Departament de Física
Universitat de les Illes Balears

Programa Oficial de Postgrau de Ciències Experimentals i Tecnologies (Física).
Doctor per la Universitat de les Illes Balears

Numerical study of intense cyclogenesis events in the Mediterranean basin

Tesis doctoral

Lluís Fita Borrell

Directors:
Dr. Climent Ramis Noguera
Dr. Romualdo Romero March

A la Laura,
als de casa

La ciència és com l'art,
però amb lògica i matemàtiques

Agraïments

Tota la tsasca d'investigació s'ha dut a terme dins del *Grup de Meteorologia* del *departament de física* de la *Universitat de les Illes Balears*. Sense l'ajuda, la paciència i la seva infrestructura, la meva tasca hauria estat impossible. Molt agraït a la confiança que em féu el Dr. Climent Ramis, quan m'oferí la beca FPI i incorporar-me al grup al juny del 2003, sabedor que ha realitzat un doble esforç. Car, altres compromisos que adquirí a posteriori no m'ha permés tenir més temps amb ell per a poder aprendre'n molt més del que he après. Al Dr. Romualdo Romero, el qual sense ell, la seva gran capcacitat de traball i paciència, res no hauria estat possible. Climent i Romu, gràcies per permetre desenvolupar-me en la meva indisciplina i independència.

Al Dr. Víctor Homar per les profundes reflexions i meditacions al voltant de la meva recerca durant llargues i enriquidores converses. Al Dr. Joan Cuxart per l'ajuda en dubtes sobre la capa límit. A totes les persones que formen i havien format part del grup de meteorologia. Tot el temps passat amb vosaltres no ha estat temps perdut, car, tot i que em treieu temps per a fer la meva recerca, els vostres dubtes, comentaris, reptes i problemes han estat un estímul que m'ha dut a adquirir molts altres coneixements. No dubteu que he après molt més jo de vosaltres. A en Toni, Marional, Alberto i Ángel, per tot allò que us he fet compartir, patir i créixer plegats.

A en Krisitian Horvath del *Državni Hidrometeorološki Zavod* per la tasca i enriquiment comú del qual en segueix una bona amistat. Al Dr. Eduardo García de la *Univerdiad de León* per la tasca comuna realitzada. Al Dr. Kerry A. Emanuel del *Massachusetts Institute of Technology* per permetre'm treballar amb ell. A les llargues i iniciàtiques converses amb el Dr. Chuck Doswell III de *The University of Oklahoma*. A en Joan Campins del l'*Agencia Estatal de Meteorología* per l'ajuda donadada. A en Toni Borràs per agunatarme els desvariejos al cubicle. A la comunitat i mentalitat open-source.

A totes aquelles altres persones que m'he trobat pel camí i que sense el seu suport hagués estat impossible tirar endavant una tesi lluny de casa i lluny de tot, vosaltres heu estat el meu sosteniment. La llista és llarga, però especial agraïment (en ordre alfabètic): Arancha, Benet, Cesc, Joan Miquel, Marga, Maria, Maria del Mar, Marta, Noelia, Pau, Sara, Tanja, Toni. A totes les altres persones que han fet de casa meva l'*Hostal Lluís*, que ha estat una de les experiències més intenses i engrescadores de la meva vida. A totes les persones de la travessa i a les seves amistats que m'han permés re-conèixer, redescobrir i gaudir de l'illa de Mallorca, les seves persones i la seva cultura.

A uns companys de camí de Barcelona com l'Isaac en Quim, Makarres i FpD. A tothom que em va ajudar a començar-lo iseguir-lo, Héctor, Carles Albert, la gent de Salt i la de l'A. E. Pare Claret.

Contents

Chapter 1

Introduction

The relation between humanity and atmospheric phenomena is still at the beginning of the 21st century, a matter of necessity, hope and fear. The atmosphere provides the suitable environment for life, but at the same time, destruction and death. It is a complex system with several different aspects interacting at the same time, such as: the sun, seas, mountains, coastal-lines, terrestrial rotation, humanity, and much more. It provides a double challenge. One is related to its inherent complexity and the ways to understand it. And the other is about the mechanisms that the humanity can develop to mitigate the negative impacts of hazardous weather (e.g. large hail, heavy precipitation, strong winds, tornadoes, hurricanes, etc). The better the atmosphere is understood, the lower can be the impacts that are suffered from its nature.

Results obtained from the study of some of the negative atmospheric phenomenas will be presented. This document is devoted to the study of strong cyclogenesis (formation of a cyclone) in the scope of the Mediterranean basin. It is focused in the analysis of some episodes where a strong cyclone developed or a strong social impact occurred as a result of the formation of a cyclone. Cyclones can generate a large list of consequences in some cases related with severe weather (weather phenomena with a high potential destructive effect on the environment or the societies) such as: heavy precipitation, strong winds, strong snow falls, tornadoes, large hail. As a result of it, floods or flash floods and high sea-waves can be derived. They can be considered one of the most suffered atmospheric phenomena all around the world. Giving a little more of knowledge about cyclones and their formation, might help to prevent their strong impacts in our societies.

Different aspects, that play a role during the formation of a cyclone, have been analysed. The study of the roles of different features of the environment that contribute, enhance or provoke the formation of a cyclone is done throughout tools and techniques applied on the results obtained from atmospheric numerical simulations. Although, numerical models presented some limitations of accuracy and confidence due to approxi-

mations and simplifications that they contain, they provided a good tool for carry out a complete description of dynamics and thermodynamics of the atmosphere, which is very helpful in the study of the gas layer that surrounds the Earth.

The study of the cyclogenesis has been focused on the characteristics of one specific region. The localisation of the knowledge into a specific region of the planet should not be a penalty for the results. It should be considered as a way to consolidate, confirm and verify the assumptions, theories and concepts developed for other regions. The validation of theories and concepts in different regions might contribute to enhance their accuracy and avoid restrictions such as case dependencies or regional particularities. At the same time, it helps in the recognition of the specific aspects of each region. In this way, studied phenomena become better understood in the region, and their potential negative impact can be mitigated.

The selected laboratory has been the Mediterranean basin due to the interest of the author and the scientific team (Grup de Meteorologia de la Universitat de les Illes Balears[1]) with which the activity has been carried out. The Mediterranean Sea is a blue bridge that connects a wide range of cultures, societies and states. It is a densely populated region and presents a large wide of characteristics and peculiarities that can be found all around the world. This makes the Mediterranean basin a perfect region to develop the studies of the extra tropical cyclogenesis (out of tropical regions and without tropical characteristics), since a large variety of cyclogenesis types can be developed.

Numerical analyses of extreme cyclogenic events have been carried out using the MM5 model. MM5 (version 3.2 to 3.7) primitive equations non-hydrostatic model has been developed by the Pennsylvania State University and the National Center for Atmospheric Research (NCAR)[2] (Grell et al., 1995). Results of numerical simulations have been analysed with numerical tools and methodologies. Selected methodologies help in to the analyses of dynamics, influences and evolution of a wide range of features involved in the episodes. Two methodologies have mainly been used ; Piecewise Potential Vorticity inversion technique in the non linear version developed by Davis and Emanuel (1991) and/or the Factor Separation technique (Stein and Albert, 1993).

Piecewise PV Inversion technique has been used to modify the initial conditions of the simulations. In this way, a sensitive study to changes in the initial conditions of the simulations could be done (Huo et al., 1999; Romero, 2001). This methodology allowed to determine which pieces of a PV anomaly field are relevant for the case, and their role in the evolution of the episode could be derived.

[1] http://www.uib.es/depart/dfs/meteorologia/

[2] http://www.mmm.ucar.edu/mm5/mm5-home.html

Factor Separation technique allows the study of the role of isolated factors of the environment as well as interactions between two or more factors (Homar et al., 2002a). The results should clarify what dynamic role has been developed by the specific feature or interaction during the evolution of the case.

The techniques have been used to analyse some episodes occurred in the Mediterranean basin. The variety of the analysed cases is wide and should help to provide a main scope of the cyclogenesis in the Mediterranean basin. Baroclinic and barotropic mechanisms (Hoskins et al., 1985) are usually present in the Mediterranean cyclogenesis. At the same time, mountain range lee cyclogenesis (Buzzi and Tibaldi, 1978) and thermal low (Alonso et al., 1994) formation also have an important role. These and other aspects have been analysed in: the November 9-12th 2001 West Mediterranean case (Fita et al., 2007b), an intercomparison between 11 deep cyclogenetic cases occurred all over the basin (Fita et al., 2006), a strong hail event in the Ebro basin over the Iberian Peninsula (García-Ortega et al., 2007) and in the extreme Bura episode in Croatia during the November of 2004 (Horvath et al., 2006).

The cyclogenesis study is concluded by the analyses of a particular kind of Mediterranean systems. These systems have the appearance of a tropical storm and occurred only above maritime regions. They exhibited a well-defined rounded cloud structure in cyclonic rotation and some of them also showed a clear cloud-free zone in the centre. Although they have strong similarities with the tropical cases and are related to heavy rains and strong winds, they did not reach the hurricane intensity. The dynamics of the environment where they are developed have been analysed with a conceptual model of hurricane (Fita et al., 2007a). Factor separation technique has been used to analyse the dynamics and sensitivity of this kind of tropical-like storms (Fita et al., 2008b,c) that is similar to the air-sea mechanism (Emanuel, 1986) developed by the hurricanes, but altered by an upper level trough (Emanuel, 2005). Finally, a satellite-based methodology for the improvement of numerical simulations of these episodes (Fita et al., 2008a) has also been developed.

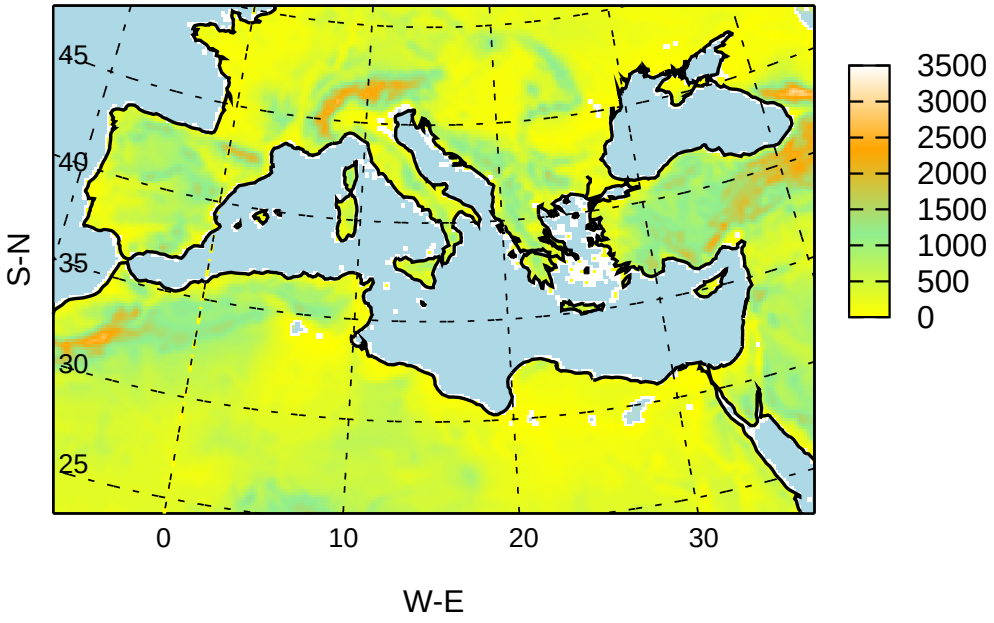

Figure 1.1.1: Mediterranean basin with the orography (colour shaded)

1.1 Mediterranean characteristics

The Mediterranean basin is defined as the land region that is surrounding the Mediterranean Sea (See figure 1.1.1). It reaches approximately the region comprised between 5 degrees West to 35 degrees East and 30 to 45 degrees North. Mediterranean sea is almost a closed sea that has a small connection (narrowest part is about 27 km) to the Atlantic ocean in its west extreme. It is a small sea with two major river tributaries: Nile river in its south-east extreme and the Rhône in its North-West extreme. It is mainly rounded by mountainous systems some of them with peaks above the 3000 m. Southern part of the basin is mainly dominated by extreme hot and dry desert areas. It has an irregular coastal line and relatively wide islands. Due to its morphological characteristics, Mediterranean basin has specificities unique in the world and it has been widely studied. *Plinius Conference on Mediterranean Storms* is a specific European Geosciences Union Topical Conference devoted to the Atmospheric behaviour in the Mediterranean area[3].

[3]web page of the 10th edition: `http://meetings.copernicus.org/plinius10`

Western part of the Mediterranean basin is surrounded by important mountain ranges (see top figure 1.1.2). Alps, Pyrenees and Atlas ranges have mountains that are overpasses 3000 m. Moreover, Iberian peninsula (south-eastern mountains are higher than 3000 m), Corsica, Sardinia and Sicily islands are also mountainous land surfaces. Another aspect of the ranges is their orientation. Western Mediterranean most relevant mountain ranges are latitudinal oriented and they do not have an important blocking effect to the westward general circulation of the air. Eastern part of the basin (see bottom figure 1.1.2) is less mountainously encircled. Highest mountains are on the north and southern and eastern part is almost flat. At the same time, no large islands are located in this part of the sea.

In spite of the non-blocking effect of the mountain ranges on the general circulation in the Mediterranean basin, they have an important role on specific atmospheric flow conditions that become relatively usual in the Mediterranean area. One of this atmospheric patterns, in which orography plays an important role, is in the lee cyclogenesis. In this case, cyclone formation occurs when a strong flow is blocked by a mountain range. Inward zone becomes a high pressure zone, meanwhile in the down wind or leeward zone pressure falls. It is frequent that Alps or Atlas (Buzzi and Tibaldi, 1978; Buzzi and Speranza, 1983; Horvath et al., 2006) ranges recipe southward winds and consequently Alps and Atlas lee zones are cyclogenetic zones. In fact, Alps lee region is one of the most cyclogenetic zones in the world (Reiter, 1975; Alpert et al., 1990; Maheras et al., 2001; Trigo et al., 1999, 2002; Campins et al., 2006).

Another characteristic effect derived from the mountainous Mediterranean coasts are the flash-floods episodes. Due to the proximity of the mountains to the coastal lines, Mediterranean maritime areas are very abrupt. Shallow, short and highly step torrents are distributed allover the Mediterranean basin. Due to its characteristics, relatively strong precipitation can provoke fast and important growing in the rushing streams (one example is found in the Montserrat episode, in North Eastern part of Iberian peninsula on June of 2000, Martín et al. (2007); Amengual et al. (2007)).

Aside of the intensification of the rainfall effects on the runoff, mountain ranges play an important role in the localisation of the precipitation. Low level air-flows over sea surfaces acquires usually high quantities of moisture (see a scheme on figure 1.1.3). When one of these flow patterns reaches the coast and hit a mountain range air-flow is upward promoted. A result of it, due to its high moisture content, strong cloud or even convection can be developed and heavy rainfall can occur (Romero et al., 1997; Doswell et al., 1997; Ramis et al., 1998). Both mountain derived effects on rainfall (fast floods and localisation of precipitation) produce high impact weather in the Mediterranean zone. Large list of cases with large number of fatalities, casualties and economic costs can be found allover the Mediterranean zone that follow a similar pattern of heavy and very localised precipitation.

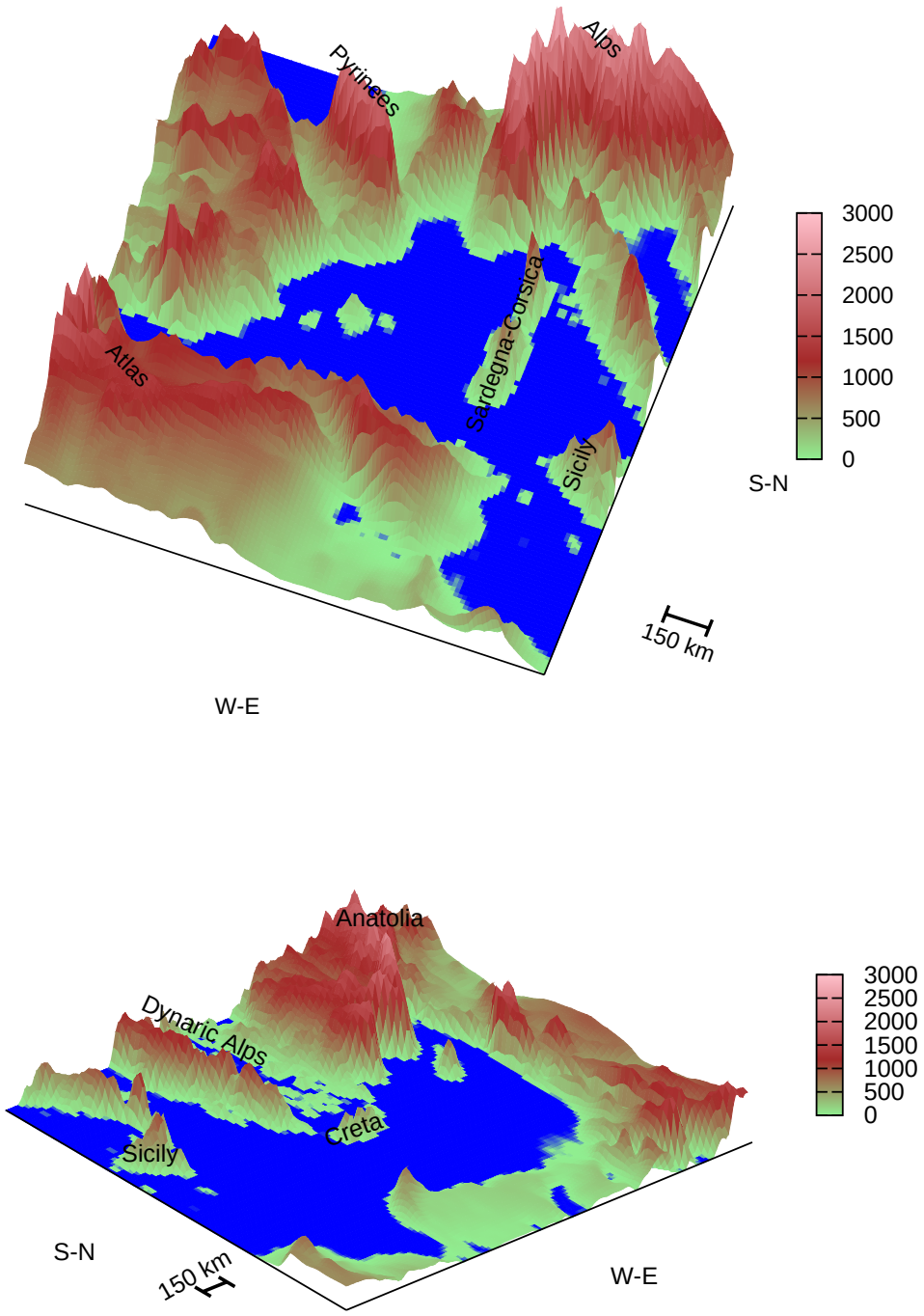

Figure 1.1.2: 3-dimensional representation of the orography of the Mediterranean basin. Western (top), Eastern (bottom)

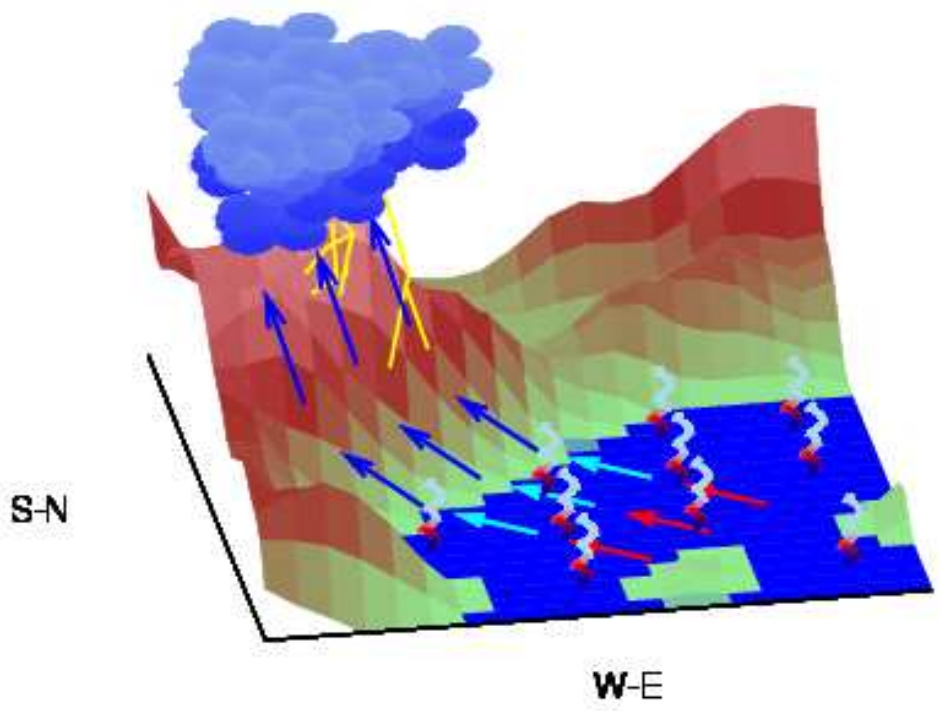

Figure 1.1.3: Schematic representation of the orographic effect on the Eastern coast of the Iberian peninsula. Warm air (red arrows) advects above sea surface gains moisture (spirals as evaporation from sea). Wet and warm air (blue arrows) reaches coastal line. Due to orographic effect, air ascends and cools and moisture might be condensed. Formation of clouds would provoke heavy rainfalls if the situation persists for a long period of time.

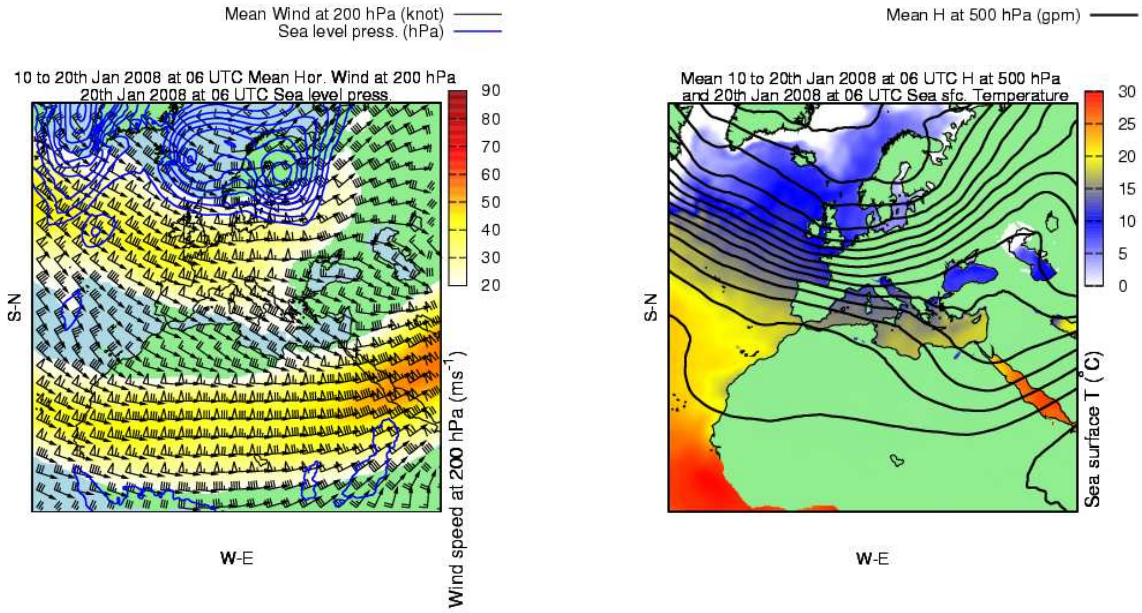

Figure 1.1.4: Atmospheric situation over Central mid-latitudes. Left panel: Mean horizontal wind at 200 hPa (vectors in barbs notation; triangle: 50 knot, pennant: 10 knot, half pennant: 5 knot), sea level pressure at 20 Jan. 2008 at 06 UTC (top), from 950 hPa to 1010 hPa (every 4 hPa, blue line) and mean horizontal wind speed at 200 hPa (ms^{-1}, colour shaded). Right panel: Sea surface temperature ($^{\circ}C$, colour shaded) at 20th Jan 2008 at 06 UTC (top) and mean geopotential height at 500 hPa (black line, every 50 gpm). Mean values from 10 to 20th January 2008 at 06 UTC

In order to mitigate these effects a large number of studies (Homar et al., 1999; Romero, 2001) and projects have been carried out devoted to this topic. Some of the most recent inter-governmental projects have been: MEDiterranean EXperiment on "Cyclones that produce high impact weather in the Mediterranean" (MEDEX[4], WMO recognised project), or EU – Interreg IIIB projects HYDROPTIMET[5] and AMPHORE[6].

Mediterranean basin is affected by two major features of the global circulation. During the summers (see figure 1.1.5), subtropical jet shifted polarward and flows above the

[4] http://medex.inm.uib.es/
[5] http://hydroptimet.medocc.org/
[6] http://amphore.medocc.org/

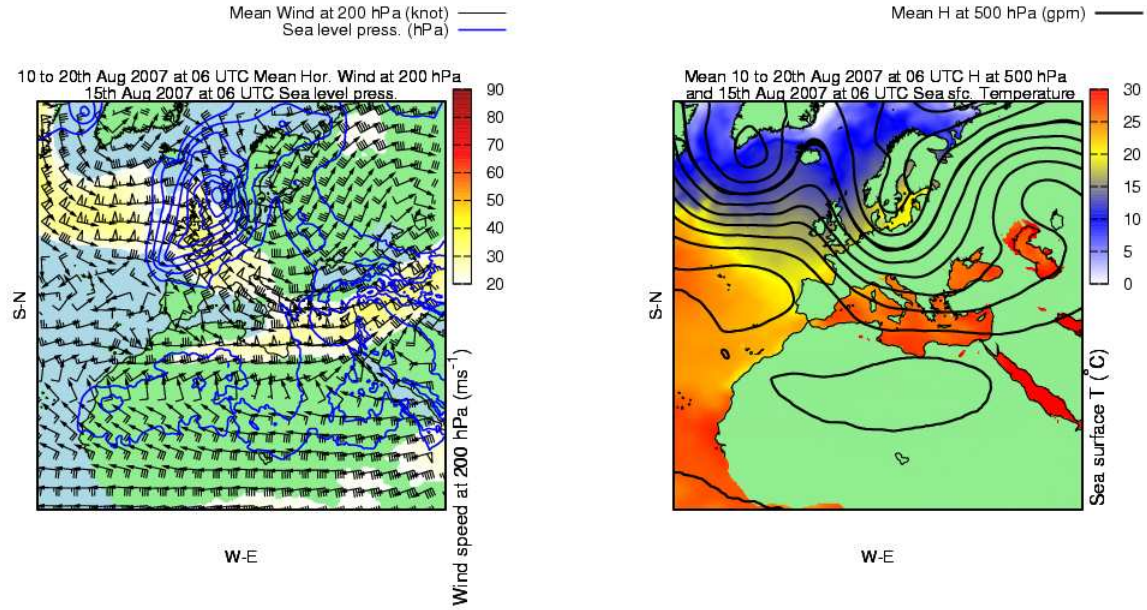

Figure 1.1.5: As in figure 1.1.4, but on 15th Aug. 2007 at 06 UTC and mean values from 10 to 20th August 2007 at 06 UTC

southern part of the basin. At the winter, intrusions of polar air usually reach the region (see figure 1.1.4). The effect of these two major patterns in the basin is reflected as a strong seasonality of the atmosphere in the Mediterranean area. Spring and Autumn are the seasons during which both flow patterns can occasionally be relatively close provoking a strong instabilisation of the air in the area. Moreover, high temperature of the Mediterranean Sea in Autumn, due to high isolation during summer, provides a third major element of instability in the area. By this way, for example Western Mediterranean basin has the largest amounts of precipitation and cyclone activity during Autumn (Campins et al., 2006; Reiser and Kutiel, 2007b). The persistence of the Azores anticyclone generates a North Atlantic blocking of the general flow that has a strong impact on the Western part of the Mediterranean basin. Eastern region is affected by the moist advections from the equatorial tropics of Africa (Krichak et al., 2004).

Geographical and general dynamic circulation patterns define the Mediterranean basin as a warm sea surrounded by mountains. Dry and hot advections of air from the southern deserted regions can interact with cold wet/dry air masses. At the same time, mountain ranges enhance the formation of cyclones as a consequence of the mountain-lee cyclogen-

esis. Strong isolation on the terrestrial areas allow the formation of shallow thermal lows (Alonso et al., 1994). All the aforementioned conditions make the Mediterranean basin as one of the most cyclogenetic regions in the world (Reiter, 1975). At the same time, atmospheric systems present a complex evolution and dynamics due to the high number of features interacting in the basin.

Strong and continuous cyclone formation in the Mediterranean area presents different particularities and dependencies. Alps-lee cyclogenetic zone is the largest one and presents its maximum activity in winter season (Trigo et al., 1999, 2002; Campins et al., 2000, 2006). Western Mediterranean area presents a duality of cyclogenesis. One kind are deep cyclones or Atlas-lee formed. Another kind of shallow but numerous cyclones are summer thermal formation of lows over the Iberian and Sahara land regions (Alonso et al., 1994). Eastern part of the cyclogenetic activity is mainly driven by the sea thermal origin, Turkish mountains or incoming Atlas cyclones (Maheras et al., 2001).

Coastal lines of the Mediterranean sea are mountainous and densely populated. For this reason, coastal lines are very sensitive to any kind of atmospheric phenomena. Fatalities and strong economical and social impacts can occur quite often allover the basin (see compilation in the MedEx database[7]) some times in the presence of weak systems. The potentiality of destruction from atmospheric phenomena in the region claims to an accurate study of the severe weather conditions. With the adequate response of the involved actors, the negative impact of the atmospheric phenomena in the Mediterranean basin can be properly mitigated. See statistical social and economical impact of weather phenomena in the EM-DAT: The OFDA/CRED International Disaster Database[8] and Dartmouth Flood Observatory[9]. Principal natural disasters that occurred in the Mediterranean basin are mainly derived from atmospheric phenomena (see figure 1.1.6).

Complexity and variety of characteristics of the Mediterranean basin become the adequate combination of features, in which a large variety of phenomena can be developed. It has been studied and shown how extreme weather (tornadoes, heavy rainfalls, large hail or extreme winds) highly frequent in the North American great plains also occurred in the European and Mediterranean zones (Tous and Romero, 2006). There is even an European Conference on Severe Storms (ECSS[10]) dedicated to this topic.

Waterspouts and tornadoes have been reported allover the Mediterranean area (Gayà et al., 2001; Homar et al., 2003a). Moreover, storm activity has been characterised also by mesocale convective systems (MCSs) activity with strong and fatal consequences (Romero

[7] http://medex.inm.uib.es/

[8] http://www.emdat.be/

[9] http://www.dartmouth.edu/~floods/archiveatlas/index.htm

[10] http://essl.org/ECSS/

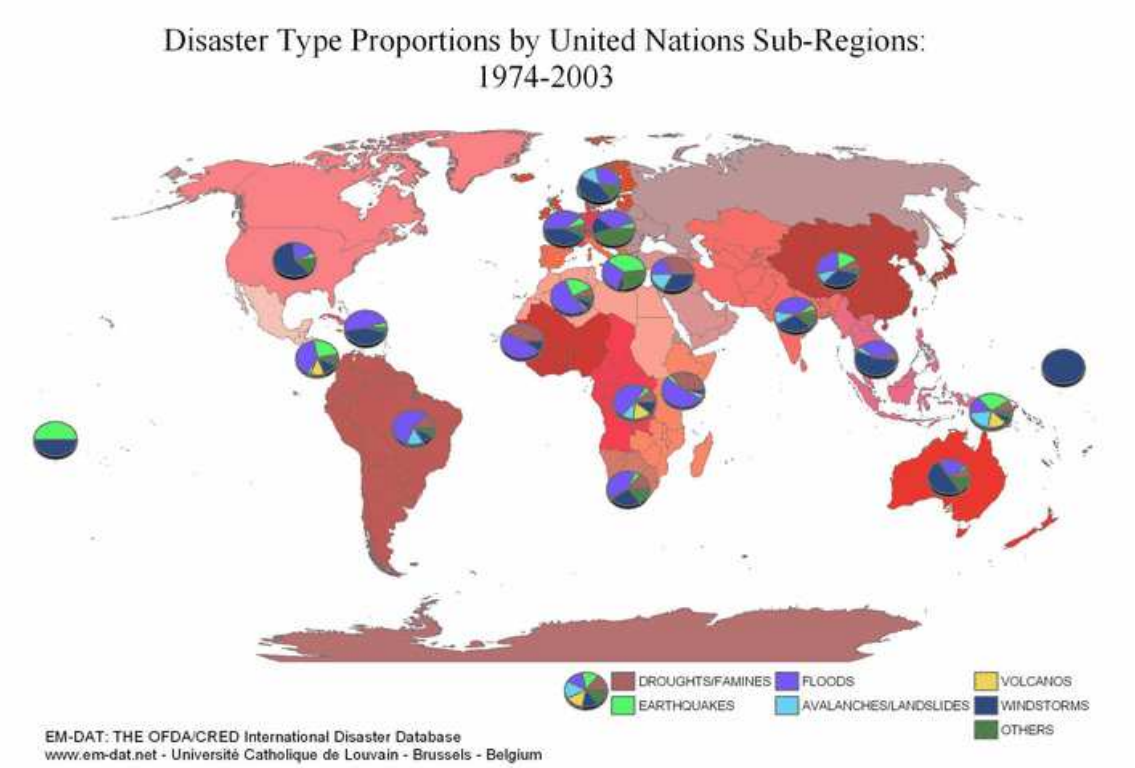

Figure 1.1.6: Disasters type allover the world. Source *EM-DAT: The OFDA/CRED International Disaster Database* `www.emdat.be` *Université Catholique de Louvain Brussels (Belgium)*

et al., 2001, 2000). Moreover extreme hail events (Tudurí et al., 2003; García-Ortega et al., 2007) or even strong snowfalls (Tayanç et al., 1998; Cucurull et al., 2004; Houssos et al., 2007). It has also also found that Mediterranean basin presents a tropical-like storm activity (Rasmussen and Zick, 1987; Businger and Reed, 1989; Homar et al., 2003b; Fita et al., 2007a). Another atmospheric phenomena strongly linked to the sea is found in a atmospheric-induced tsunamis or meteotsunamis like '*rissaga*' in Balearic islands (Ramis and Jansà, 1983), *marubbio* in Sicily or *milghuba* in Malta (Monserrat et al., 2006). In these cases oceanic barotropic waves induced by pressure fluctuations of the atmosphere are enhanced when they reach the coast throughout specific resonance conditions.

A large number and variety of atmospheric phenomena within the Mediterranean basin has been described. Moreover Mediterranean basin presents a complex climatological pattern with large and wide fluctuations of atmospheric characteristics in zones, seasons and year to year. Rainy patterns are not constant and present a wide fluctuation in climatological amounts allover the basin (Reiser and Kutiel, 2007b), and large differences from Western zone to Eastern one (Reiser and Kutiel, 2007a). Different synoptic patterns are related to strong precipitations specifically for each region, according to their relative position with respect to the Mediterranean Sea. In general Eastern Mediterranean Sea heavy precipitation events are related to westerly flows, meanwhile for example in the western region of the Iberian peninsula to easterly flows (Romero et al., 1998, 1999). Event climatological fluctuations of rainy extreme events is also found allover the Mediterranean region (Alpert et al., 2002).

Climate change scenarios project a warmer and dryer Mediterranean climate (IPCC, 2007). Increase of temperatures are projected to be higher than global values, with hotter and longer summer periods. At the same time, rainy days are likely to decrease with an increase of summer drought episodes. Even some studies project the possibility of a tropical cyclones in the late 21st century (Gaertner et al., 2007).

Chapter 2

Methodology

Numerical methodologies are very powerful in the study of the atmosphere. Real observations are sparse and they are taken with low temporal frequencies. This lack of observations does not give an entire view of the real state of the environment. A useful way to correct this lack of knowledge of the atmosphere can be approximately solved with the use of atmospheric numerical models. Numerical models give an approximation to the real evolution of the atmosphere. They are computational simplifications of a big portion of the atmospheric knowledge. However, in comparison to the observations, they give a complete and continuous spatial and temporal description of the environment and of its evolution.

Numerical methodologies applied in the results of numerical models can bring a kind of information that is very difficult to be obtained from the observations. Numerical tools can give a detailed information of a large variety of dynamic or structural details that the observations can not provide. However, one should maintain a contact with the information obtained from the observations. Numerical results should be verified, tested and contrasted with the best approach of the reality obtained from the observations. At the same time, it must bear in mind that numerical results are obtained from the approximated perspective given by a numerical model and the lack of knowledge of some atmospheric processes.

2.1 Atmospheric numerical model

Atmospheric numerical models try to solve the equations that describe the dynamical and thermo-dynamical behaviour of the atmosphere (a brief list of available atmospheric numerical models is provided in table 2.1.a). Numerical models are a useful tool, since atmospheric equations are non linear and they do not have an analytical solution. Thus, the numerical solution of the equations is the unique (for the moment) way to solve them. Atmospheric numerical models solve the equations in different ways. At the same time,

Table 2.1.a: Alphabetically ordered brief list of numerical models giving the name of the model or the centre that has develop it accompanied with a web-source of information

Name	**web access**
Aladin	http://www.cnrm.meteo.fr/aladin/
Arpege	http://www.meteofrance.com/FR/index.jsp
BOLAM-QBOLAM	http://www.isac.cnr.it/dinamica/bolam/index.html
COSMO	http://cosmo-model.cscs.ch/
ECMWF	http://www.ecmwf.int/
GEM	http://collaboration.cmc.ec.gc.ca/science/rpn/gef_html_public
GEM-LAM	http://www.msc-smc.ec.gc.ca/
GFS (new AVN)	http://www.emc.ncep.noaa.gov/modelinfo/
GME	http://www.dwd.de/en/en.htm
HadCM	http://www.metoffice.gov.uk/research/hadleycentre/models/modeltypes.html
Hirlam	http://hirlam.org/
IGCM	http://www.met.rdg.ac.uk/~mike/dyn_models/igcm/
Lokal	http://www.dwd.de/en/en.htm
MASS	http://www.meteosimtruewind.com/
Meso-NH	http://mesonh.aero.obs-mip.fr/mesonh/
MM5	http://www.mmm.ucar.edu/mm5/mm5v3/
RAMS	http://bridge.atmet.org/users/software.php
UKWMO	http://www.metoffice.gov.uk/
WRF	http://www.wrf-model.org/index.php

some models give multiple available configurations. As result of it, the computation is not unique and it is case, model and configuration dependant.

The development of the atmospheric numerical model is strongly related to the history of the computation and the capacity of management of digital information. The degree of complexity and confidence in the models has been increasing in parallel with the growing of the computational capacities and research (g.e.: MM4 was a hydrostatic model of the MMM community until the MM5[1] non-hydrostatic version of the model was released on July 31st 1999). A numerical model is based in different pieces or modules. Each one of these modules has a specific function with its degree of simplification, approximation or complexity.

[1] http://www.mmm.ucar.edu/mm5/mm5-home.html

- **Atmospheric equations:** The atmosphere is a mixture of different gases. However, due to the spatial and temporal scales in which it is studied it is treated as a fluid. Fluids such as oceans, atmosphere or magma are described by the *Navier-Stokes* equations (Bluestein, 1992). The NS-equations (also known as *primitive equations*) give the dynamics of a given state of a continuous system. These equations are nonlinear, and multi-coupled equations of six variables ($\vec{V}, T, q$ and p). Numerical models solve these equations in different degrees, throughout the simplification of some terms of the equations. Initial versions of the models (g.e.: MM4, Hirlam, ...) were hydrostatic, in which equation for third coordinate is substituted by the hydrostatic approximation (pressure, height and density have the relation: $\delta p = -g\rho\delta z$). Actual models try to deal with the complete complexity of the equations including the non-hydrostatic terms. The computation of the equations is solved in different ways such as: finite differences, finite volumes and spectral.

- **Resolution:** Numerical models are used to compute spatially and temporally the variables that describe the atmosphere. In order to carry out this computations space and time need to be discretized (the variable will be computed at specific spatial and temporal values; some assumptions are made within the unresolved temporal and spatial scales). The degree of discretization will give the resolution of the simulation. In finite volumes or finite differences models the space is usually discretized in horizontal regular net of grid points. This regular horizontal nets of points are not homogeneously distributed vertically. The density of horizontal grids are usually higher in the lower than in the upper levels of the atmosphere. In spectral models, the resolution is given by the lowest wave of the spectra of typically a Gaussian spectral distribution. In order to avoid grid troubles in the poles, some models use a triangular net of points (GME).

- **Global and limited area models:** Two big groups of numerical models can be established. The are the global and the limited area models. Global models are used to simulate the dynamics of the atmosphere allover the planet. Limited area models are used to simulate a fraction of the atmosphere. Usually, global models present less complexity than the limited area ones. Limited area models allow a major precision and detail in the simulations. Climate global models such as HadCM3 use a horizontal resolution of 2.5 terrestrial degrees. Meanwhile mesoscale limited area models such as Meso-NH can be used in simulations with a horizontal resolution of 500 m or even less.

- **Terrain characteristics:** Terrestrial information needs to be provided in order to have a realistic simulation. Thus, geographical coordinates are provided, as such as the morphology of the earth surface. Topography and orography information are also inserted in the model. At the same time is included the information of land-

use such us: forest/urban characteristics, kind of vegetation, ice, desert, land/water mask. Assuming at the same time, particular characteristics to each category such as albedo, moisture, emissivity, roughness length, thermal inertia.

- **Initial and boundary conditions:** In order to simulate the 'real' atmosphere the initial state introduced in the models should be as accurate as possible. Initial conditions are used as the first state from which numerical model will start. They are mainly derived from combination of observations and numerical adjustments through atmospheric models. Atmospheric models are used as a way to obtain the entire state of an atmosphere described by the equations in agreement with the observations. The generation of an entire state of the atmosphere with concordance on observations is mainly used in the global models. Global models will compute a forecast of the entire planetary atmosphere initiated with the numerical adjustment of the observations. Numerical adjustment of the observations is carried out with different tools or methodologies such as 3DVAR (Lorenc et al., 2000; Barker et al., 2003), Kalman Filter (Evensen, 2003), or 4DVAR (Rabier et al., 1998). Limited area models also use initial conditions, however, due to their spatial limitations, they need information about the state of the atmosphere at the limits of their domain of integration. With the boundary conditions a limited area model acquires the state of the surrounding atmosphere. These surrounding conditions are mainly derived from other global simulations. By this way, specific local simulations are maintained in concordance with the entire state of the atmosphere. Thus, structures outer of the area that were not present in the initialisation of the simulation are properly introduced in later stages. There are different centres that generate the global simulations used as initial and Boundary conditions. They are carried out every day in a large variety of temporal (usually every 12 or 6h) and horizontal resolutions (from 2.5 to 0.25 degrees). Most of them are generated by state agencies like: NCEP, ECMWF, Deutscher Wetterdienst, Meteo France or UK Met Office. They can be atmospheric analyses or global forecasts. ECMWF (Uppala et al., 2005) and NCEP have been developed a new set of re-analyses in which have been used the best numerical adjustments with all the available sources of observations and measurements.

- **Observations:** Some models allow the insertion of observations in the simulations. With the observations is ensured a better representation of the real state of the atmosphere and the capture of smaller features that are not represented in the global analyses of a low resolution. The global standard network of observations of the WMO [2] are one of the major sources of observations. A source of observations are the 3h or 1 hourly surface observations taken from the land surface or ships and the rawinsonde at every 12 hours. Network of observations are sparse and they are

[2] `http://www.wmo.in`

insufficient to give a detailed description of the state of the atmosphere. Last years techniques have been developed that allow to introduce other kind of observations like satellite or radar data. At the same time complex methodologies of adjustment between observations and model simulations have been developed. Two of these are observation nudging (Stauffer and Seaman, 1990) and 4DVAR variational method (Rabier et al., 2000).

- **Physical processes:** Within dynamics of the atmosphere there is a wide variety of processes that are developed at different scales and strates. Some of these processes such as: evaporation, condensation, rain, convection, take place on different scales of time and space (synoptic, mesoscale and microscale). All them are related with each other and they present different characteristics and behaviours. At the same time, different aspects of the atmosphere occurs in specific regions (g.e.: drop formation, eadies in the boundary layer). Some of these processes have a high complexity or even are not well known. Due to the difficulty and limited computational resources in order to simulate these aspects with the primitive equations, some of them are not simulated directly and are simulated with a scheme. A scheme is a simplified representation of the process with which is attempted to reproduce the phenomena. These schemes are applied on specific zones of the simulation, when according to appropriate conditions of the prognostic variables, the phenomena can be developed. As a result of the application or activation of the scheme, general dynamics of the atmosphere (computed via the *Navier-Stokes* equations) would be altered by the interaction of the general dynamics of the atmosphere with the particular outputs of the schemes at a given grid point (e.g.: increasing of the temperature as a result of a drop formation simulated by the cloud-microphysics scheme). There is a large variety of schemes and they present different degrees of complexity. Even though schemes are secondary aspects of the fluid dynamics, the processes simulated with them can have a strong impact in the simulations. Changes in the selection of one scheme can induce significant differences between simulations of the same episode (Wisse and de Arellano, 2004; Fita et al., 2008a).

- **Nesting:** Limited area models are used to study in detail some atmospherics events. In order to increase the detail, different regions of one area are usually defined. In these subareas or domains, different temporal and spatial resolutions are used. By this way, a major detail is obtained from a region with a minimal increase of the computational cost. Different domains established an order of levels or hierarchy where a 'mother' domain is defined. Smaller domains use the outputs of the bigger domains as their initial and boundary conditions of the atmosphere. *Two-way nesting* is established when the results of smaller domain are allowed to influence simulation in the bigger domain.

- **Coupling:** In some studies have been started to couple atmospheric models to other

numerical models such as ocean in the global clime models such as: HadCAM, runoff (Amengual et al., 2007) or contaminant dispersion (Grell et al., 2000).

In spite of the impossibility to solve all the factors and processes involved in the atmosphere, the results of the models are reasonably good (Buzzi and Tibaldi, 1978; Alpert et al., 1995; Leslie et al., 1998; Lagouvardos et al., 1999; Pytharoulis et al., 2000; Wisse and de Arellano, 2004) and their results are improving in time (WMO, 2002). Dynamics of the phenomena obtained from numerical simulations seem to be quite similar to the phenomena that occurred in the atmosphere. Numerical results of the models are quite well corresponded with the observations and measurements. There are basically two elements that avoid a complete success of the numerical models: lack of knowledge and technical computational limitations. Moreover, it must bear in main the strong non-linear behaviour of the atmosphere (with a fractal dimensionless bigger than 6 Lorenz (1991); Zeng et al. (1992)) makes impossible a perfect numerical simulation of the system (Lorenz, 1963). In some cases, major aspects of the atmosphere are actually significantly well simulated. However, small scale events such as; localisation and value of strong precipitation, tornadoes or fog are sometimes not well captured. Unfortunately most of severe weather episodes are related to small scale aspects of some events. This fact must aim to improve numerical atmospheric models allowing a correct forecast of these phenomenas. During recent years, a statistical use of atmospheric models has been made. It is assumed that forecast statistics of an ensemble of different simulations (using multi model, multi physical, perturbed or other ways of generation of the members) of the same phenomena will provide a better result that an unique simulation (Toth and Kalnay, 1993; Molteni et al., 1996; Toth and Kalnay, 1997; WMO, 2006).

2.1.1 MM5

Equations

MM5 model (last version 3.7, Grell et al., 1995) is a mesoscale nonhydrostatic primitive equation limited area model. Numerical solution of the equations is done by the finite differences method and it allows two-way nested coupling between different domains. MM5 solves the *Primitive equations* in a vertical terrain following coordinates (x,y,σ). Vertical coordinate σ is defined following the orography of the domain (see equation 2.1.1).

$$\sigma = \frac{p - p_{top}}{p_{surf} - p_{top}} \tag{2.1.1}$$

where p, pressure; p_{top}, highest pressure value; p_{surf}, surface pressure. σ takes the interval between 0 (top) and 1 (surface). The dry version of the equations are discussed.

- **pressure**

$$\frac{\partial p'}{\partial t} - \rho_0 g w + \gamma p \nabla \cdot \vec{V} = -\vec{V} \cdot \nabla p' + \frac{\gamma p}{T}\left(\frac{\dot{Q}}{C_p} + \frac{T_0}{\theta_0} D_\theta\right) \tag{2.1.2}$$

where p', nonhydrostatic perturbation of the hydrostatic pressure (p_0, $p = p_0 + p'$)). Hydrostatic pressure presents a lineal relation with the density (ρ), gravity (g) and with differential of height (δz), [according to $\delta p = -\rho_0 g \delta z$]; ρ_0, hydrostatic density; g, gravity; w, vertical velocity; $\gamma = C_p/C_v$; $C_{p(v)}$, thermal capacity of the air preserving pressure(volume); $\vec{V} = (u, v, \dot{\sigma})$, speed vector; $\nabla = (\partial_x, \partial_y, \partial_\sigma)$, differential operator; $\dot{Q}$, heat changes with the environment; T_0, temperature of the buoyancy term ($\rho_0 = p_0/R_d T_0$); θ_0, potential temperature of reference; D_θ, viscosity and turbulent dissipation term of heat. This equation establishes a relation of the temporal variations of pressure (Ist term in the left) with: updrafts/downdrafts of the fluid ($\rho_0 g w$), convergence/divergence ($\gamma p \nabla \cdot \vec{V}$), pressure advections ($-\vec{V} \cdot \nabla p'$) and thermal variations (last term of equation)

- **Momentum** $u = \vec{V} \cdot \hat{e}_x$ (x component of the speed)

$$\begin{aligned} \frac{\partial u}{\partial t} + \frac{m}{\rho}\left(\frac{\partial p'}{\partial x} - \frac{\sigma}{p^*}\frac{\partial p^*}{\partial x}\frac{\partial p'}{\partial \sigma}\right) &= -\vec{V} \cdot \nabla u + v\left(f + u\frac{\partial m}{\partial y} - v\frac{\partial m}{\partial x}\right) \\ &- ew\cos\alpha - \frac{uw}{r_{earth}} + D_u \end{aligned} \tag{2.1.3}$$

where m: map scale factor; $p^* = p_{surf} - p_{top}$, pressure differences (σ coordinates); f, Coriolis term; $u\frac{\partial m}{\partial y}, v\frac{\partial m}{\partial x}, r_{earth}$, terrestrial curvature terms; $e = 2\Omega\cos\lambda$, Coriolis component (λ, latitude); $\alpha = \phi - \phi_c$, ϕ longitude, ϕ_c, central longitude; D_u, dissipative term due to friction and turbulence following $\hat{e}_x$ direction. From the equation is obtained that the variations of the momentum in the $\hat{e}_x$ direction are made by variations on the pressure field (IInd term), advection of the momentum ($\vec{V} \cdot \nabla u$, nonlinear term), variations respect to the curvature (terms with ∂m and r_{earth}) and as a reflect of rotation of the Earth (terms of Coriolis, fu and $ew\cos\alpha$)

- **Momentum** $v = \vec{V} \cdot \hat{e}_y$ (y component of the velocity)

$$\begin{aligned} \frac{\partial v}{\partial t} + \frac{m}{\rho}\left(\frac{\partial p'}{\partial y} - \frac{\sigma}{p^*}\frac{\partial p^*}{\partial y}\frac{\partial p'}{\partial \sigma}\right) &= -\vec{V} \cdot \nabla v - u\left(f + u\frac{\partial m}{\partial y} - v\frac{\partial m}{\partial x}\right) \\ &+ ew\sin\alpha - \frac{vw}{r_{earth}} + D_v \end{aligned} \tag{2.1.4}$$

- **Momentum** $w = \vec{V} \cdot \hat{e}_\sigma$ (z(σ) component of the velocity)

$$\begin{aligned} \frac{\partial w}{\partial t} - \frac{\rho_0}{\rho}\frac{g}{p^*}\frac{\partial p'}{\partial \sigma} + \frac{g}{\gamma}\frac{p'}{p} &= -\vec{V} \cdot \nabla w + g\frac{p_0}{p}\frac{T'}{T_0} - \frac{gR_d}{C_p}\frac{p'}{p} + e(u\cos\alpha - v\sin\alpha) \\ &+ \frac{u^2 + v^2}{r_{earth}} + D_w \end{aligned} \tag{2.1.5}$$

where R_d, universal constant for dry air.

- **Thermodynamics**

$$\frac{\partial T}{\partial t} = -\vec{V} \cdot \nabla T + \frac{1}{\rho C_p}\left(\frac{\partial p'}{\partial t} + \vec{V} \cdot \nabla p' - \rho_0 g w\right) + \frac{\dot{Q}}{C_p} + \frac{T_0}{\theta_0} D_\theta \tag{2.1.6}$$

Thermal variations are derived from thermal advections ($\vec{V} \cdot \nabla T$), dynamics of the fluid (IInd term), heat fluxes ($\dot{Q}/C_p$) and frictional and turbulence dissipative effects (last term)

- Expansion of the advective terms

$$\begin{aligned} \vec{V} \cdot \nabla \chi &\equiv mu\frac{\partial \chi}{\partial x} + mv\frac{\partial \chi}{\partial y} + \dot{\sigma}\frac{\partial \chi}{\partial \sigma} \\ \dot{\sigma} &= -\frac{\rho_0 g}{p^*} w - \frac{m\sigma}{p^*}\frac{\partial p^*}{\partial x} u - \frac{m\sigma}{p^*}\frac{\partial p^*}{\partial y} v \end{aligned} \tag{2.1.7}$$

Advective terms 2.1.7 add a coupled and nonlinear term in the equations. It is expanded and solved at the second order.

- Divergence term expansion is shown in equation 2.1.8

$$\begin{aligned} \nabla \cdot \vec{V} &= m^2 \frac{\partial}{\partial x}\left(\frac{u}{m}\right) - \frac{m\sigma}{p^*}\frac{\partial p^*}{\partial x}\frac{\partial u}{\partial \sigma} + m^2 \frac{\partial}{\partial y}\left(\frac{v}{m}\right) - \frac{m\sigma}{p^*}\frac{\partial p^*}{\partial y}\frac{\partial v}{\partial \sigma} \\ &- \frac{\rho_0}{p^*} g \frac{\partial w}{\partial \sigma} \end{aligned} \tag{2.1.8}$$

- Difussion terms
In order to control growing of nonlinear instabilities and remove small scale computational noise, an experimental diffusion scheme is used (Grell et al., 1995; Xu et al., 2001; Zängl, 2002) in all the tendencies of the prognostic variables ($\nabla_t \chi$). In MM5 horizontal second order diffusion is applied in the boundaries of the coarse domain and fourth-order diffusion at the inner points. Another second-order vertical diffusion term is also applied on the physical sub-grid transport following mixing-length theory. The second order form of the horizontal diffusion term is

$$F_{H2\alpha} = p^* K_H \vec{\nabla}^2_\sigma \chi \tag{2.1.9}$$

where χ, any prognostic variable at level σ, $p^* = p_{sfc} - p_{top}$, pressure different between surface and top level; K_H, diffusion coefficient. The fourth-order form is

$$F_{H4\alpha} = p^* K'_H \vec{\nabla}^4_\sigma \chi \tag{2.1.10}$$

Fourth-order diffusion term is applied on any prognostic variable (χ) at all sigma levels that there is not any intersection with the lower-most half-sigma surface at any grid point. $\vec{\nabla}^2, \vec{\nabla}^4$ are applied on sigma constant surfaces. It is established the relation between diffusion coefficients of different order,

$$K_H^{'} = \Delta s^2 K_H \tag{2.1.11}$$

Second order diffusion coefficient K_H (see equation 2.1.12) is obtained according to a background value K_{HO} accompanied with a term proportional to the deformation of the flow.

$$K_H = K_{HO} + 0.5k^2(\Delta s)^2 \left[\left(\frac{\partial u}{\partial x} - \frac{\partial v}{\partial y} \right)^2 + \left(\frac{\partial v}{\partial x} + \frac{\partial u}{\partial y} \right)^2 \right]^{1/2} \tag{2.1.12}$$

where $K_{HO} = 3.0 \times 10^{-3}(\Delta x)^2/\Delta t$ and to ensure computational stability a upper limit has been imposed $K_H \leq (\Delta x)^2/(64\Delta T)$ in MM5v3.7 version; Δx, horizontal grid distance; k, von Kármán constant, Δt, temporal increment. Has been shown how the background term is dominant at all levels and locations in contrast to the deformation term (Xu et al., 2001).

Land Use data type

MM5 numerical model simulates with three different classifications of terrain: old 13 (PSU/NCAR), USGS (see table 2.1.b for the 24 categories of vegetation data from U.S. Geological Survey - USGS[3] specifications used in MM5 model) and SiB (North-American 17-category data used by Simple Biosphere model, from USGS). At the same time, MM5 model works with different classifications of soil data. Both tables are provided at different resolutions from 1 terrestrial degree (about 111.0 km) to 30 sec. (about 0.925 km)

Cumulus Schemes

These schemes determine the subgrid processes that occur within a cumulus cloud, like vertical fluxes, transportation between cloud species and convective rainfall. Convection is activated for a given trigger and need a closure in order to determine the strength. MM5 has 7 different cumulus schemes with different uses, purposes and approximations (see stable 2.1.c. This scheme can not be activated for grid lengths smaller than 5 km. In this case, cumulus processes are simulated directly by the primitive equations.

[3] `http://www.usgs.gov/`

Table 2.1.b: Characteristics of the 24 USGGS vegetation categories used in MM5. albedo (%, third column), moisture available (%, 4th col.), surface emissivity (% at 9 μm, 5th col.), roughness length (cm, 6th col.) and thermal inertia ($cal\ cm^{-2}k^{-1}s^{-1/2}$, 7th col.) For the Summer (15th April - 15th October, first sub-col) and winter (15 October - 15 April, second sub-col). Source MM5 model notes

Number	**Vegetation Description**	**Albedo** (%)		**Moisture Avail.** (%)		**Sfc. Emissivity** (% at 9 μm)		**Roughness Length** (cm)		**Thermal Inertia** ($cal\ cm^{-2}k^{-1}s^{-1/2}$)	
		Sum	Win	Sum	Win	Sum	Win	Sum	Win	Sum	Win
1	Urban and Built-Up Land	15	15	10	10	88	88	80	80	0.03	0.03
2	Dryland Cropland and Pasture	17	23	30	60	98.5	92	15	5	0.04	0.04
3	Irrigated Cropland and Pasture	18	23	50	50	98.5	92	15	5	0.04	0.04
4	Mixed Dryland/Irrigated Cropland and Pasture	18	23	25	50	98.5	92	15	5	0.04	0.04
5	Cropland/Grassland Mosaic	18	23	25	40	99	92	14	5	0.04	0.04
6	Cropland/Woodland Mosaic	16	20	35	60	98.5	93	20	20	0.04	0.04
7	Grassland	19	23	15	30	98.5	92	12	10	0.03	0.04
8	Shrubland	22	25	10	20	88	88	10	10	0.03	0.04
9	Mixed Shrubland/Grassland	20	24	15	25	90	90	11	10	0.03	0.04
10	Savanna	20	20	15	15	92	92	15	15	0.03	0.03
11	Deciduous Broadleaf Forest	16	17	30	60	93	93	50	50	0.04	0.05
12	Deciduous Needleleaf Forest	14	15	30	60	94	93	50	50	0.04	0.05
13	Evergreen Broadleaf Forest	12	12	50	50	95	95	50	50	0.05	0.05
14	Evergreen Needleleaf Forest	12	12	30	60	95	95	50	50	0.04	0.05
15	Mixed Forest	13	14	30	60	94	94	50	50	0.04	0.06
16	Water Bodies	8	8	100	100	98	98	.01	.01	0.06	0.06
17	Herbaceous Wetland	14	14	60	75	95	95	20	20	0.06	0.06
18	Wooded wetland	14	14	35	70	95	95	40	40	0.05	0.06
19	Barren or Sparsely Vegetated	25	25	2	5	85	85	10	10	0.02	0.02
20	Herbaceous Tundra	15	60	50	90	92	92	10	10	0.05	0.05
21	Wooden Tundra	15	50	50	90	93	93	30	30	0.05	0.05
22	Mixed Tundra	15	55	50	90	92	92	15	15	0.05	0.05
23	Bare Ground Tundra	25	70	2	95	85	95	10	5	0.02	0.05
24	Snow or Ice	55	70	95	95	95	95	5	5	0.05	0.05

Table 2.1.c: Main characteristics of the MM5v3 cumulus schemes

Scheme name	**Main characteristics**	**Recomm. resol. (km)**
Anthes-Kuo	driven by moisture convergence (M_t) parametrised heating and moistening profiles moistening depends on RH critical threshold $M_t \geq 3. \times 10^{-6} kgm^{-2}s^{-1}$ cloud-depth $\Delta\sigma \geq 0.3$	> 30
Grell	simple scheme driven by compensation of mass flux clouds as stability agents steady-state updraft and downdraft circulations mixing with environment at top and bottom	10-30
Arakawa-Schubert	Three parts: static, dynamic, feedback Multi-cloud scheme with updrafts and downdrafts cloud population	> 30
Fritsch-Chappel	driven by temporal releasing of instability (CAPE) representation of up/downdrafts Mass-flux type compensation scheme	20-30
Kain-Fritsch	sofisticated scheme up/downdraft given by cloud-mixing temporal releasing of CAPE mass-flux considerations	
Betts-Miller	relaxation following a post-convective sounding no explicit downdrafts	> 30
Kain-Fritsch 2	Improvement of Kain-Fritsch Add Shallow convection	

The Kain-Fritsch scheme (Kain and Fritsch, 1990, 1993) and its improved version (Kain, 2004) is one of the most used cumulus parameterisation in the *Grup de Meteorologia del departament de física de les Illes Balears* (UIB-Meteo. group). It is structured (following brief description of Kain (2004)) in three parts: the convective triggering func-

tion, the mass flux formulation and the closure assumptions.

- *The trigger function:* A parcel of air is obtained from a vertical mixing following adjacent layers from surface until 60 hPa. Lifted condensation level for this parcel (T_{LCL}) is compared to the environmental one (T_{ENV}) (usually $T_{LCL} \leq T_{ENV}$). According to the observational suggestion that environment makes easier convection, a relation between thermal perturbation (δT_{vv}) of the parcel and the grid resolving vertical motion is established (with a vertical threshold value). A potential convective parcel of air will be given by this parcel of air, that its mixed temperature and the grid-resolved derived anomaly becomes higher (positive buoyancy) than the environmental temperature ($T_{LCL} + \delta T_{vv} > T_{ENV}$). Vertical velocity of the upper part of the LCL is computed at each layer following a Lagrangian methodology that includes environmental effects. Deep convection will be activated when the Lagrangian computed vertical velocity keeps positive until a cloud height of about 3-4 km. In case of fail values, this methodology is repeated following an iterative process in which iterative parcels are recomputed according to the elevation of its lowest layer until a threshold of 300 hPa.

- *Mass flux computation:* A steady-state entraining-detraining plume model for the equivalent potential temperature (θ_e) and water vapour q_v will determine the convective updrafts in the scheme. Plume model establishes that high(low) parcel buoyancy and moist(dry) environment promotes entrainment(detainment). Convective downdrafts are lived on a fraction of evaporation of the total condensate generated within the updraft. This fraction of evaporation is given by precipitation efficiency and established the mass relative magnitudes between up/downdrafts according to other downdrafts parameters such as: starting/ending levels, relative humidity profile and characteristics and amounts of entrained air. Downdraft is finished when it reaches the surface or it becomes warmer than its environment. Finally the net convective mass flux (defined as the compensation between environment and transports within up/downdrafts) at any level of the column is established to be zero.

- *Closure:* Closure assumptions are reached when 90% of CAPE of the column is removed according to balance of environmental mass fluxes and up/downdrafts. CAPE is computed within the convective parcel and is vanished by a combination of lowering θ_e in the convective parcel and warming the environment aloft. The convective time scale (within the limits of 1/2 and 1 hour) is determined according to the advective time scale in the cloud layer. Scheme has a feedback effect on the tendency of temperature, water vapour and cloud water mixing ratios.

Planetary Boundary Layer schemes

Planetary boundary layer (commonly referred as PBL) describes the first levels of the atmosphere in contact with the surface (Stull, 1988). It presents a variable range of

dimensions and usually the air in this layer presents turbulent characteristics. Under turbulent dynamics, from which the flow presents unpredictable fluctuations in the three directions of the flow, has powerful mixing properties. PBL is a clear example of the utility of the schemes in the numerical weather models, since it has not been completely resolved. In contrast to the general fluid mechanic equations, a complete set of equations that could explain the turbulence have not been already proposed. Some assumptions and approximations are done in order to provide a properly way to complete the set of equations that try to describe the turbulence. These approximations and assumptions can vary significantly and are derived from the observations. Therefore, PBL schemes can present significant differences. MM5 model has 7 PBL schemes (see table 2.1.d).

In the UIB-Meteo. group, Eta (Janjić, 1990, 1994) and MRF (Troen and Mahrt, 1986; Hong and Pan, 1996) schemes are the most used PBL schemes. A short description of each scheme is given:

- **MRF:** Regime conditions of the PBL are given by $|z_h/L|$, z_h, height of the mixed layer (determined by the bulk Richardson number, equation 2.1.14, $\mathcal{B}_r$); L, Monin-Obukhov length (see equation 2.1.15), in terms of the momentum diffusivity $\mathcal{K}_m$ (equation 2.1.13).

$$\mathcal{K}_m = u_* k z \Phi_m^{-1} \left(1 - \frac{z}{h}\right)^P \tag{2.1.13}$$

$$h = \mathcal{R}_i \frac{T_0 |\vec{v}(h)|^2}{g(\theta_v(h) - \theta_0)}, \quad \begin{cases} \mathcal{R}_i = \dfrac{\dfrac{g}{\overline{\theta}_v}\dfrac{\partial \overline{\theta}_v}{\partial z}}{\left[\left(\dfrac{\partial \overline{U}}{\partial z}\right)^2 + \left(\dfrac{\partial \overline{V}}{\partial z}\right)^2\right]} \\ \mathcal{B}_r = \dfrac{g \Delta \overline{\theta}_v \Delta z}{\overline{\theta}_v [(\Delta \overline{U})^2 + (\Delta \overline{V})^2} \end{cases} \tag{2.1.14}$$

$$L = \frac{-\overline{\theta_V} u_*^3}{k g (\overline{w' \theta_V'})_s} \tag{2.1.15}$$

where u_*, surface friction velocity, k von Kármán constant, Φ_m, nondimensional shear, z, height above ground and h boundary layer height; $\overline{\theta}_v$, averaged value of virtual temperature; $\overline{U}, \overline{V}$, averaged values of wind speed, $(\overline{w'\theta_V'})_s$, vertical turbulent flux of temperature fluctuations at the surface

  - Stability: $\Phi_m = 1 + \dfrac{4.7z}{L}$

Table 2.1.d: Brief description of MM5v3 PBL schemes

Name	**Characteristics**	**Vertical resolution**
Bulk	two regimes: stable, unstable bulk coefficients	coarse ($\delta z > 250\ m$)
High-Resolution Blackdadar	four stability regimes nonlocal mixing implicit vertical diffusion scheme driven by Monin-Obukhov similarity	high
Burk-Thompson	prediction of TKE local vertical mixing not call SLAB Louis scheme for surface exchange coefficients	coarse/high
Eta	prediction of TKE local vertical mixing driven by Monin-Obukhov similarity allow use of Noah-LSM surface scheme 2.5 order scheme	high
MRF	countergradient transport theorem nonlocal mixing driven by bulk Richardson number allow use of Noah-LSM surface scheme implicit vertical diffusion scheme	high
Gayno-Seaman	prediction of TKE conservation of liquid-water potential temperature allow coupling between cloud-topped PBL better for saturated situations	high
Pleim-Chang	based on Blackadar scheme can only be used with Pleim-Xiu LSM surface scheme asymmetric convective model	high

– Instability: $\Phi_m = (1 + \frac{7z}{L})^{-1/3}$

1. $\mathcal{B}_r \geq 0.2$ Nighttime stable conditions
2. $0.0 < \mathcal{B}_r < 0.2$ Damped mechanical turbulent conditions
3. $\mathcal{B}_r = 0.2$ Forced convection conditions
4. $\mathcal{B}_r < 0.0$ Free convection conditions

Surface temperature is computed according to a *scaled virtual temperature excess* as follows:

$$\theta_T = C\frac{(\overline{w'\theta'_v})_0}{w_s h} \tag{2.1.16}$$

Eady diffusivities of moist (q), momentum (m; u and v) and temperature (t) are computed following the Prandtl number ($\mathcal{P}r$, equation 2.1.17) imposing that heat and momentum fluxes match at the top of the surface layer

$$\mathcal{P}r = \frac{\mathcal{K}_t}{\mathcal{K}_m} = \left[\frac{\Phi_t}{\Phi_m}\left(\frac{z}{L}\right) + k\frac{z}{h}C\right]^{-1} \tag{2.1.17}$$

where Φ_m, Φ_t, momentum (m) and humidity/temperature (t) adimensional gradients with a nonlinear term in the formulation of the fluxes. k approach (Louis, 1979) is applied for the diffusion in the free atmosphere, keeping the diffusion in the free atmosphere:

– $\mathcal{R}ig > 0$, stably stratified free atmosphere; $f_{m,t}(\mathcal{R}ig) = e^{-8.5\mathcal{R}ig} + \frac{0.15}{\mathcal{R}ig + 3.0}$, and $\mathcal{P}r = 1.5 + 3.08\mathcal{R}ig$

– $\mathcal{R}ig \leq 0$, neutral and unstably stratified free atmosphere; same as in previous regime but replacing in $\Phi_m, \Phi_t(z/L) \rightarrow \Phi_m, \Phi t(\mathcal{R}ig)$.

where $\mathcal{R}ig = (g/T)(\partial\theta_v/\partial z)(|\partial U/\partial z|)^{-2}$, local gradient Richardson number. MRF becomes very sensible to the surface fluxes (heat and evaporation) and water content of the surface.

- **Eta:** The 2.5 dimensional local mixing model governed by turbulent kinetic energy (TKE) is described by the system of equations as follows as in (Mellor and Yamada,

1982):

$$\begin{cases} \dfrac{d}{dt}\dfrac{q^2}{2} - \dfrac{\partial}{\partial z}\left[\ell_q S_q \left(\dfrac{\partial}{\partial z}\dfrac{q^2}{2}\right)\right] = \mathcal{P}_s - \mathcal{P}_b - \epsilon \\ \mathcal{P}_s = -\overline{wu}\left(\dfrac{\partial U}{\partial z}\right) - \overline{wv}\left(\dfrac{\partial V}{\partial z}\right) \\ \mathcal{P}_b = \beta g \overline{w\theta_v},\ \epsilon = \dfrac{q^3}{B_1 \ell} \\ -\overline{wu} = \mathcal{K}_M \dfrac{\partial U}{\partial z},\ -\overline{wv} = \mathcal{K}_M \dfrac{\partial V}{\partial z} \\ -\overline{w\theta_v} = \mathcal{K}_H \dfrac{\partial \Theta_v}{\partial z},\ -\overline{ws} = \mathcal{K}_H \dfrac{\partial S}{\partial z} \\ \mathcal{K}_M = \ell_q S_M,\ \mathcal{K}_H = \ell_q S_H \\ S_M(6A_1A_2G_M) + S_H(1 - 3A_2B_2G_H - 12A_1A_2G_H) = A_2 \\ S_M(1 + 6A_1^2 G_M - 9A_1A_2G_H) - S_H(12A_1^2 G_H + 9A_1A_2G_H) = A_1(1 - 3C_1) \\ G_M = \dfrac{\ell^2}{q^2}\left[\left(\dfrac{\partial U}{\partial z}\right)^2 + \left(\dfrac{\partial V}{\partial z}\right)^2\right],\ G_H = -\dfrac{\ell^2}{q^2}\beta g \dfrac{\partial \Theta_v}{\partial z} \end{cases} \tag{2.1.18}$$

where $S_q, \beta, A_1, A_2, B_1, B_2, C_1$, empirical constants; $q^2/2$, ℓ, master length. Capital letters is for motions resolved by the dynamical part of the model, and lower case are for the turbulent fluctuations. v, denotes virtual potential temperature; S passive quantity. $\mathcal{K}_M, \mathcal{K}_H$, vertical turbulent exchange coefficients for momentum (M) and heat (H). $\mathcal{P}_S, \mathcal{P}_b$, production of the TKE by shear (S) and buoyancy (b); ϵ, dissipation; in order to avoid zero determinant the following thresholds are imposed: $G_H \leq 0.0024$ and $G_M \leq 0.36 - 16 G_H$. Master length scale ℓ is computed as follows:

$$\begin{cases} \ell = \dfrac{\ell_0 k z}{\ell_0 + k z} \\ \ell_0 = \alpha \dfrac{\displaystyle\int_{P_{sfc}}^{P_{top}} dq\ |z| q}{\displaystyle\int_{P_{sfc}}^{P_{top}} dq\ q} \\ \lim\limits_{z \to 0} \ell = kz \\ \lim\limits_{z \to \infty} \ell = k \\ \ell \leq \ell_{max} = 0.53 q \left(\beta g \dfrac{\partial \Theta}{\partial z}\right)^{-1/2} + H \end{cases} \tag{2.1.19}$$

where α, empirical constant; $P_{top/sfc}$, top and surface pressures; k, von Kármán constant. An improvement of the model has been applied (Janjić, 1994), in which a marine viscous sublayer has been defined and an upper level limit has been imposed in to the master length scale ℓ_{max}; H, constant. Boundary layer height is fixed

according to the drop of TKE for a specific threshold:

$$\begin{cases} 0.5min(0.6, TKE_{max}) & TKE_{max} > 1.2 \\ kL & TKE_{max} < 0.4 \end{cases} \tag{2.1.20}$$

Owing to the vertical differences of mixing between Eta and MRF schemes, significant differences between characteristics of the simulated PBL are obtained. It has been shown how the nonlocal or local vertical mixing properties can affect processes such as strong convective rain over land (Hong and Pan, 1996; Wisse and de Arellano, 2004) or even tropical-like systems such as medicanes (Fita et al., 2008a).

One of the most relevant difference between simulated PBL is the strength of the mixing developed within the layer. MRF scheme (similar characteristics presents Blackadar scheme, Fita et al. (2008a)), show stronger rates of mixing than Eta scheme. At the same time, diurnal cycle of the boundary layer (PBL characteristics during day and night in one day) is much more marked in the nonlocal mixing scheme than in Eta scheme. Wisse and de Arellano (2004) found that Eta capping inversion at the top of the boundary layer is stronger than in the MRF scheme.

Table 2.1.e: Brief description of MM5v3 moist microphysics schemes

Name	**Characteristics**
Dry	no vapour or clouds
Stable Precipitation	grid saturation immediately as rain nonconvective precipitation no rain evaporation no cloud prediction
Warm Rain (Hsie)	cloud and rain are separated 3D fields no ice phase
Simple Ice (Dudhia)	adaptation with ice of Hsie scheme different arrays for ice, rain and snow no supercooled water snow melt at melting layer
Mixed-Phase (Reisner 1)	cloud ice and snow arrays same processes as Simple Ice supercooled water gradual melting of the snow
Goddard microphysics	prediction of graupel suitable for cloud-resolving models
Reisner 2 (graupel)	concentrations for graupel and ice suitable for cloud-resolving models strong improvements along MM5 versions
Schultz	ice and graupel simple and efficient

Explicit Moisture schemes

These schemes provide the information about the processes that occur between the water species that form the cloud. It also provides part of the resultant tendencies in the trends of the prognostic fields, as well as radiation information due to cloud formation. In MM5 model there are 8 schemes (see table 2.1.e).

Most used moisture scheme in the UIB-Meteo. group is the Reisner 2 (graupel) scheme (Reisner et al., 1998). Reisner2 model is specially designed to avoid the lack of accuracy in the determination of the supercooled liquid water (hereafter, SLW) in the winter storms over North America. It was started as a bulk rain model with mixing ratios of cloud water (q_c), rain (q_r), snow (q_s). Low predictions of SLW suggest the addition of a mixing ratio of cloud ice (q_i) and graupel (q_g) with the addition of a prediction of the

number concentration of cloud ice (N_i) with a prescribed prediction of the N_s and N_g as function of their precipitation rates $N_{o,s}$, $N_{o,g}$. Last improvement of the moist microphysics included explicit predictions of the N_s and N_g species with remarkable improvement in the simulations.

A brief description of the dynamics between species follows similar structure as in (Ikawa and Saito, 1991):

- **Prognostic mixing ratios**

$$\left\{\begin{array}{rcl}
\dfrac{\partial q^* q_v}{\partial t} &=& -\mathcal{ADV}(p^* q_v) + \mathcal{DIV}(p^* q_v) + \mathcal{D}(q_v) + p^* \sum_{\ell}^{\Gamma(q_v)} \varsigma_\ell \mathcal{P}_\ell \\
\dfrac{\partial q^* q_c}{\partial t} &=& -\mathcal{ADV}(p^* q_c) + \mathcal{DIV}(p^* q_c) + \mathcal{D}(q_c) + p^* \sum_{\ell}^{\Gamma(q_c)} \varsigma_\ell \mathcal{P}_\ell \\
\dfrac{\partial q^* q_r}{\partial t} &=& -\mathcal{ADV}(p^* q_r) + \mathcal{DIV}(p^* q_r) + p^* \sum_{\ell}^{\Gamma(q_r)} \varsigma_\ell \mathcal{P}_\ell - \mathcal{P}_{rprc} \\
\dfrac{\partial q^* q_i}{\partial t} &=& -\mathcal{ADV}(p^* q_i) + \mathcal{DIV}(p^* q_i) + \mathcal{D}(q_i) + p^* \sum_{\ell}^{\Gamma(q_i)} \varsigma_\ell \mathcal{P}_\ell \\
\frac{\partial q^* q_s}{\partial t} &=& -\mathcal{ADV}(p^* q_s) + \mathcal{DIV}(p^* q_s) + p^* \sum_{\ell}^{\Gamma(q_s)} \varsigma_\ell \mathcal{P}_\ell - \mathcal{P}_{sprc} \\
\dfrac{\partial q^* q_g}{\partial t} &=& -\mathcal{ADV}(p^* q_g) + \mathcal{DIV}(p^* q_g) + p^* \sum_{\ell}^{\Gamma(q_g)} \varsigma_\ell \mathcal{P}_\ell - \mathcal{P}_{gprc}
\end{array}\right. \tag{2.1.21}$$

- **Prognostic number concentrations**

$$\left\{\begin{array}{rcl}
\dfrac{\partial p^* N_i}{\partial t} &=& -\mathcal{ADV}(p^* N_i) + \mathcal{DIV}(p^* N_i) + \mathcal{D}(N_i) + p^* \left\{ \sum_{\ell}^{\Xi(N_i)} N_\ell + \dfrac{\rho}{m_{io}} \sum_{\ell}^{\Phi(N_i)} \mathcal{P}_\ell \right. \\
& & \left. - \dfrac{N_i}{q_i} \sum_{\ell}^{\Psi(N_i)} \mathcal{P}_\ell \right\} \\
\dfrac{\partial p^* N_s}{\partial t} &=& -\mathcal{ADV}(p^* N_s) + \mathcal{DIV}(p^* N_s) + p^* \left\{ \sum_{\ell}^{\Xi(N_s)} N_\ell + \dfrac{\rho}{m_{so}} \sum_{\ell}^{\Phi(N_s)} \mathcal{P}_\ell \right. \\
& & \left. - \dfrac{N_s}{q_s} \sum_{\ell}^{\Psi(N_s)} \mathcal{P}_\ell \right\} - N_{sprc} \\
\dfrac{\partial p^* N_g}{\partial t} &=& -\mathcal{ADV}(p^* N_g) + \mathcal{DIV}(p^* N_g) + p^* \left\{ \sum_{\ell}^{\Xi(N_g)} N_\ell + \dfrac{\rho}{m_{go}} \sum_{\ell}^{\Phi(N_g)} \mathcal{P}_\ell \right. \\
& & \left. - \frac{N_g}{q_g} \sum_{\ell}^{\Psi(N_g)} \mathcal{P}_\ell \right\} - N_{gprc}
\end{array}\right. \tag{2.1.22}$$

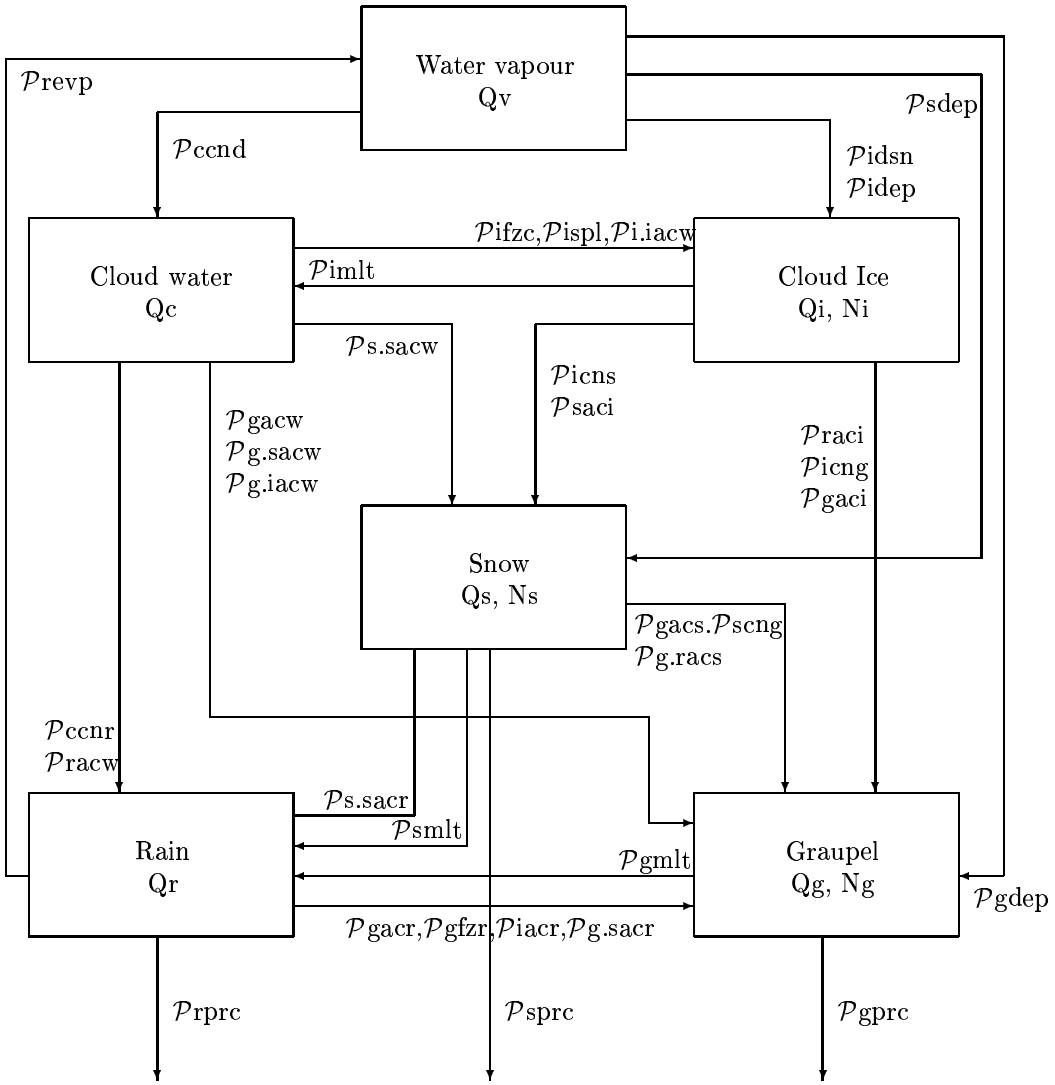

Figure 2.1.1: Schematic representation of the processes between species contained in the Reisner2(graupel) explicit moisture scheme of the MM5 model according to Ikawa and Saito (1991) formulation. Abbreviations for the species χ are: χdep, depositional growth; χmlt, melting; χprc, precipitation; χag, aggregation; χcn$\aleph$, conversion of χ to $\aleph$; χfz$\aleph$, freezing of $\aleph$ to χ; χac$\aleph$, collection of $\aleph$ by χ; $\chi.\aleph$acγ, generation of χ as result of collection of γ by $\aleph$; idsn, initiation of q_i; ispl, ice multiplication processes

where, $p^* = p_{sfc} - p_{top}$, pressure differences between surface and top; $\mathcal{D}$, diffusion on subgrid-scale turbulence; $\mathcal{ADV}, \mathcal{DIV}$ 3-dimensional advection and divergence terms (equation 2.1.23, m, map scale factor, $\sigma = (p - p_{top})/p^*$, terrain-following vertical coordinate). $\mathcal{P}_\ell$, source/sink mass terms; $\mathcal{N}_\ell$, source/sink number terms than can be: depositional growth, melting, precipitation, aggregation, conversion, freezing, collection, generation as result of a collection and ice initiation and multiplication processes. As example: $\mathcal{P}_{rprc}$, precipitation of cloud water. Γ, Ξ, Φ, Ψ, processes related to source/sink of each species.

$$\begin{cases} \mathcal{ADV}(p^*\chi) = m^2 \left(\dfrac{\partial p^* u\chi/m}{\partial x} + \dfrac{\partial p^* v\chi/m}{\partial y} \right) + \dfrac{\partial p^* \chi\dot{\sigma}}{\partial \sigma} \\ \mathcal{DIV} = m^2 \left(\dfrac{\partial p^* u/m}{\partial x} + \dfrac{\partial p^* v/m}{\partial y} \right) + \dfrac{\partial p^* \dot{\sigma}}{\partial \sigma} \end{cases} \tag{2.1.23}$$

- **Size distribution**

$$\begin{aligned} N_\chi = \frac{N_{o,\chi}}{\lambda_\chi},\ \rho Q\chi &= \int_0^\infty dD\chi\ \rho_\chi \frac{\pi}{6} D\chi^3 N_{o,\chi} exp\left(-\lambda\chi D\chi\right) \\ &= \frac{\pi \rho_\chi N_{o,\chi}}{\lambda\chi^4} \begin{cases} N_{o,\chi} = N_\chi \left(\dfrac{\pi \rho_\chi N_\chi}{\rho q_\chi} \right)^{1/3} \\ \lambda_\chi = \left(\dfrac{\pi \rho_\chi N_\chi}{\rho q_\chi} \right)^{1/3} \end{cases} \end{aligned} \tag{2.1.24}$$

where, ρ_χ, density of an hydrometer ($\chi = (v, c, r, i, s, g)$); ρ, density of dry air. The changes in the number of concentration (N_χ) or mixing ratio ($\mathcal{P}_\chi$) of meteor χ due to precipitation is given by:

$$\begin{cases} N_{\chi prc} = -\dfrac{\partial \overline{U}_{n\chi} \rho g N_\chi}{\partial \sigma}, & \overline{U}_{n\chi} = \dfrac{a_\chi \Gamma(1 + b_\chi)}{\lambda_\chi^{b\chi}} \\ \mathcal{P}_{\chi prc} = -\dfrac{\partial \overline{U}_\chi \rho g q_\chi}{\partial \sigma}, & \overline{U}_\chi = \dfrac{a_\chi \Gamma(4 + b_\chi)}{6\lambda_\chi^{b\chi}} \end{cases} \tag{2.1.25}$$

where $\overline{U}_{n\chi}$, number-weighted terminal velocity; $\overline{U}_\chi$, mass-weighted terminal velocity; $g = 9.81\ ms^{-2}$, gravitational acceleration; a_χ, b_χ, constants. Precipitation terms are computed at each split time steps $\Delta t'$, ensuring numerical stability $\overline{U}_\chi \Delta t'/\Delta x < 1$, with the size of $\Delta t'$ based on the maximum value of $U_\chi \Delta t/\Delta z$ in the column where Δt, model time step.
Finally, each process of formation of species has its own expression. These processes are listed below for each species:

- ice: *nucleation, freezing of cloud droplets, multiplication process, depositional growth of cloud, riming growth of cloud*

- snow: *conversion from cloud ice, aggregation among, depositional growth and melting, collection of cloud ice*
- graupel: *conversion from cloud ice, generation by collisions between rain water and cloud ice, snow conversion, collisions between rain water and snow, generation via freezing of rain water, depositional growth and melting, production by collection of cloud water*
- rain: *conversion from cloud water, collection of cloud water, sublimation/evaporation*
- cloud water: *conversion from water vapour, melting of cloud ice*

In order to prevent zero values of some species, the total sum of source/sink terms are adjusted by the sum total of the rates. Negative values are considered as null values. Finally some constrains are imposed in some species:

$$\begin{cases} \textit{cloud ice} & \dfrac{0.5\times\rho q_i}{0.8 m_{s,o}} < N_i < \dfrac{100\rho q_i}{m_{i,o}} \\ \textit{snow} & \left(\dfrac{N_{o,s}}{1000}\right)^{3/4}\left(\dfrac{\rho q_s}{\rho_s \pi}\right)^{1/4} < N_s < (1000 N_{o,s})^{3/4}\left(\dfrac{\rho q_s}{\rho_s \pi}\right)^{1/4} \\ \textit{graupel} & 10^{-7}\times\left(\dfrac{\rho q_g}{m_{g,o}}\right) < N_g < 100\times\left(\frac{\rho q_g}{m_{g,o}}\right) \end{cases} \quad (2.1.26)$$

Radiation schemes

These schemes provide the radiative effects in atmosphere (cloud interaction, clear sky and/or absorvation) radiative effects at surface (longwave absorbation/emission, albedo, surface fluxes) and thermal column tendencies due to vertical radiative flux divergence. MM5 has 4 radiation schemes and also it can be switched off. Main characteristics of these schemes are summarised in table 2.1.f.

Most used radiation scheme in the UIB-Meteo. group is the Cloud scheme (Dudhia, 1989).

This scheme computes the radiative effects in the vertical resolution of the model in vertical layers 50 hPa thick. The net absorption at each level results in radiative heating. It computes down/upward fluxes of longwave radiation (usually of terrestrial origin) and the downward flux of shortwave radiation (of solar origin), taking into account the solar angle. Resultant net flux at the ground is used for the land surface scheme. Each radiative flux is compute separately with the following characteristics:

- **Longwave scheme:** Temperature-dependent emissivity in clear-air follow an accurate fitting for the water vapour absorption bands in a clear-air conditions from

Table 2.1.f: Brief description of MM5v3 radiation schemes

Name	**Characteristics**	
None	no effects in the atmosphere surface still active	Surface radiation active in these two options
Simple cooling	cooling as function of temperature no cloud interaction no diurnal cycle climatological mean cooling profile surface still active	surface short/longwave flux for ground temperature uses total content of water vapour of the column uses RH to determine low/mid/high cloud fractions coarse grids or no microphysics
Cloud	atmospheric effects according to model cloud provides long/shortwave fluxes	
CCM2	multiple spectral short/longwave bands cloud treated on resolved ones or RH fraction suitable for coarse grid scales suitable for long time integrations provides surface radiative fluxes	
RRTM longwave	uses correlated-k model for the effects of absorption spectrum considering water vapour, CO_2 and O_3 can be combined with cloud-radiation shortwave scheme accurate and efficient	

polar to tropical ($\epsilon(u)$).

$$\begin{cases} \epsilon(u) = \sum_{i=0}^{i=4}(a_i + \overline{T}b_i)x^i & u \geq 10gm^{-2}, \quad x = ln(u) \\ \epsilon(u) = \sum_{i=0}^{i=4}(c_i + \overline{T}d_i)y^i & u < 10gm^{-2}, \quad y = u^{1/2} \end{cases} \tag{2.1.27}$$

where u, water vapour path; $\overline{T}$, u-weighted $T - 250\ K$; a_i, b_i, c_i, d_i constants. At the tropics e-type absorption is included in the computation. It is missed cloud ceiling conditions from which an error of up to $20Wm^{-2}$ is made. Therefore Up/Downward fluxes at any layer are computed as:

$$F_{u/d} = \int_0^1 d\epsilon_{u/d} B(T) \tag{2.1.28}$$

where $B = \sigma T^4$, frequency-integrated Planck function; σ Stefan's constant. Clouds are assumed as horizontally uniform grey bodies (without wavelength preferences). Downward longwave flux on the top is assumed to be only from CO_2 stratospheric emission. Cloud liquid water (c), ice (i) and water vapour paths are derived from model data with absorption lengths of 60 m for 0.1 gm^{-3} cloud water to 3000 m for 0.1 gm^{-3} of rain water. CO_2 effects are on the infrared spectrum. Thus the band is divided (with a thermal dependency) in carbon/noncarbon spectrum. Each species has its own assumptions and characteristics. They are all together computed in order to obtain the total net emissivity (ϵ_{tot}).

$$\epsilon_{tot} = 1 - T_v T_c T_p \begin{cases} T_v = 1 - \epsilon_v & vapour \\ T_c = exp(-\alpha_c u_c) & cloud\ water \\ T_p = exp(-\alpha_p u_p) & rain\ \&\ snow \end{cases} \tag{2.1.29}$$

With the flux profiles, heating rate is defined as:

$$\mathcal{R}_T = \frac{\partial T}{\partial t} = \frac{1}{\rho C_p}\frac{\partial}{\partial z}(F_d - F_u) = -\frac{g}{C_p}\frac{\partial}{\partial p}(F_d - F_u) \tag{2.1.30}$$

- **Shortwave scheme:** Reflected or backscattered components of the solar radiation are treated as secondary effects. Clear-air scattering and absorption (mainly from water vapour) and cloud scattering are included. At the same time is taking into account the solar zenithal angle, giving the downward flux as:

$$S_d(z) = \mu S_0 - \int_z^{top} dS_{cs} + dS_{ca} + dS_s + dS_a \tag{2.1.31}$$

where μ, solar zenithal cosine; S_0, solar constant. Albedo and absorption of all cloud, precipitation and water vapour are treated as one type of cloud with theoretical

values (as function of $ln(w/\mu)$, w vertically integrated liquid water path) taking into account solar zenith angle. Heating rate is given by:

$$\mathcal{R}_T = \mathcal{R}_T^{longwave} + \frac{1}{\rho C_p}\frac{\partial}{\partial z}S_{abs} \tag{2.1.32}$$

where S_{abs}, absorption term of $S_d(z)$ (equation 2.1.31)

Surface schemes

These schemes simulate effects of land and water in the atmosphere. Ground temperature is computed from radiative net fluxes and boundary layer characteristics. It provide surface sensible and latent heat flux, sub-soil temperature and moisture profiles and can provide tendencies of snow-cover or surface moisture availability. MM5 model has 4 surface schemes (see table 2.1.g).

Most used soil scheme in the UIB-Meteo. group is the Five-Layer soil model (Dudhia, 1996). Two important assumptions are removed from the force-restore scheme: constant tunning for 24 h cycle periods and immediately uniforming distribution of the heating through the slab. The Five-layer soil model works at higher vertical resolution (5 layers, see table 2.1.g), that will allow a faster response of the surface and more addequated propagation depth in the ground of the changes (with a nominal downward propagation at 3cm/hour). Substrate temperature at 31 cm is kept constant. Transfer of heat ($\mathcal{F}$ in Wm^{-2}) follows one-dimensional diffusion equation as the heat flux:

$$\mathcal{F} = -K\rho_s c_s \frac{\partial T_s}{\partial z} \tag{2.1.33}$$

where K is the soil thermal diffusivity ($m^2 s^{-1}$); ρ_s, soil density; c_s, specific heat capacity ($Jkg^{-1}K^{-1}$). Heating is proportional to flux convergence:

$$\frac{\partial T_s}{\partial t} = -\frac{1}{\rho_s c_s}\frac{\partial \mathcal{F}}{\partial z} \tag{2.1.34}$$

After the computation of the diffusion at a given depth $\mathcal{F}(z)$ (equation 2.1.33), heating can be computed assuming that $\mathcal{F}(z=0)$ at the surface is known as the net sensible, latent and radiative flux. In MM5 soil's thermal diffusivity (K), is taken from the thermal inertia χ ($Jm^{-2}K^{-1}s^{-1/2}$) following the relation $\chi = \rho_s c_s K^{1/2}$. By this way, temperature only depends in χ for a given $\rho_s c_s$ and K. MM5 takes a fixed an intermediate K took between sand and clay soils of $K' = 5 \times 10^{-7} m^2 s^{-1}$. This value fixes a numerical stability criterion for the thermal variation of

$$1 > 2\frac{K\Delta t_{soil}}{\Delta z^2} \tag{2.1.35}$$

Table 2.1.g: Brief description of the MM5v3 soil schemes

Name	**Characteristics**
Force-restore (Blackadar)	prediction of ground temperature 2-layer model fixed thermal substrate as diurnal average surface temperature
Five-layer Soil Temperature	soil temperature prediction in 5 layers layers thickness: 1, 2, 4, 8, 16 cm better response to high frequency changes than force-restore substrate fixed by diffusion
Noah LSM	four layers at: 10, 30,60 and 100 cm soil predictions of: temperature, water/ice, canopy water and snow cover demands of additional inputs of: soil texture, $< T_{sfc} >_{anual}$ seasonal vegetation and initial soil temperature and moisture can use albedo datasets use of percentage land-use and soil data prediction of surface and under-ground run-off and snow depth
Pleim-Xiu LSM	two layer model:; 1cm, 1m prediction of soil temperature and moisture prediction of canopy and evapotranspiration allow data assimilation for the initialisation of soil moisture use of percentage land-use and soil data optional plant-growth and leaf-out algorithms

Table 2.1.h: A brief description of a short list of MM5v3 additional schemes

Name	**Characteristics**
LEVSLP	solar slope
OROSHAW	Topography shadowing
IPOLAR	polar physics sea-ice fraction sea-ice snow/ice fluxes ice nuclei conc from Meyers
Shallow convection	prediction of shallow convection non-precipiting clouds strong entrainment, small radius uniform clouds without downdrafts
IFSNOW	snow cover effects

A very simple initialisation of the temperature profile is carried out for this scheme. It is assumed a linear dependant in depth vertical profile (considered as the steady solution of the diffusivity equation). However, is well known, that initial soil temperature is dependent on previous days temperature, but considerations of these order make mandatory the use of a much more complex soil scheme (as Noah LSM).

Other schemes

A large variety of phenomena has also taken into account in the MM5 model. They attain to a large different processes with different order of importance (see table 2.1.h)

FDDA

A Four-Dimensional data assimilation (FDDA) is a way to introduce observational information into numerical simulation. FDDA technique can also be seen as a way to continuously link and dynamical couple successive observations using a numerical model. This technique is actually applied in the global models in two different ways: *dynamic initialisation*, a complete set of observations are introduced into a atmospheric model in order to obtain a complete 3-dimensional dynamically integrated representation of the initial state of the atmosphere; *nudging*, during the period of simulation of a model, diagnostic fields are driven 'towards' the observations according to a dynamical forcing.

FDDA technique has been applied in its *nudging* procedure. It is know also as *Newtonian relaxation*. The gradual forcing of the numerical simulation is assumed to be soft

enough that the fields remain in appropriated balance conditions. Assimilated observations can be of any type: statistical grid derived from different origins, or even, they can be individual measurements (weighted assimilated as simple Cressman-type functions (distance-weighted) or more sophisticated methodologies).

The modification of numerical simulations using observations from different sources has been shown as a successful way to improve the results (Stauffer and Seaman, 1990; Leslie et al., 1998; Zou and Xiao, 1999; Fan and Tilley, 2002; Ducrocq et al., 2002; Davolio and Buzzi, 2004; Orlandi et al., 2004; Lagouvardos and Kotroni, 2005). MM5 model (Grell et al., 1995) uses a four-dimensional data assimilation (FDDA) tool based on a Newtonian-relaxation or nudging (Stauffer and Seaman, 1990) applied on the prognostic equations. Artificial tendency terms are added in the prognostic equations derived from the difference between the simulated and observed value at the given grid point. This artificial tendency term is added in the prognostic equations according to a given spatial and temporal window of influence of the observations or gridded analyses.

- **Analysis nudging:** Nudging term will be proportional to the 'difference' between simulated and analysed fields at every grid point. Prediction of variable $\chi(\vec{x},t)$ is given as:

$$\begin{aligned}\frac{\partial p^*\chi}{\partial t} &= \mathcal{F}(\chi,\vec{x},t)+\mathcal{G}_\chi\cdot W_\chi(\vec{x},t)\cdot\epsilon_\chi(\vec{x})\cdot p^*(\overline{\chi}_0-\chi)\\ &+ \mathcal{G}_{p^*}\cdot W_{p^*}(\vec{x},t)\cdot\epsilon_{p^*}(\vec{x})\cdot\chi(\overline{p}^*_0-p^*)\end{aligned}\qquad(2.1.36)$$

  where, $\mathcal{F}$, physical forcing terms of the model (advection, Coriolis, etc.); χ, model dependent variables; $\vec{x}$, independent spatial variables; t time. $p^* = p_{sfc} - p_{top}$, pressure difference between surface and top. Terms of the equation with $\mathcal{G}_\chi$ and $\mathcal{G}_{p^*}$ are respectively the nudging terms for χ and p^*. Nudging of surface pressure (included in p^*) must be accompanied by an 'appropriated' change of the vertical structure of the column above. Since there is not an unique possible adequate vertical structure it is not frequent to nudge surface pressure and is fixed a $\mathcal{G}_{p^*}\equiv 0$. Four-dimensional weight function W, determines the spatial and temporal variation of $\mathcal{G}_\chi$. ϵ is the analysis quality factor (from 0 to 1); $\overline{\chi}_0$, estimation of the observation by χ analysed to the grid. $\mathcal{G}_\chi$ must satisfy the stability criterion $\mathcal{G}_\chi \leq 1/\Delta t$. $\mathcal{G}_\chi$ must be small enough to ensure: model ability to adequately solve mass-momentum imbalances imposed by the observations and the generation of model atmospheric features not included in the analysis. Avoiding very small values that will derive to any influence of the observations and a growing of the amplitude of errors of the simulations. Typical values are $10^{-4}\ s^{-1} \leq \mathcal{G}_\chi \leq 10^{-3}\ s^{-1}$. For a simple situation in which is assumed that $W(\vec{x},t)\equiv 1$, $\partial p^*/\partial t = 0$ and observational analysis is

perfect and time invariant, is obtained that:

$$\frac{\partial \chi}{\partial t} = \mathcal{G}_\chi(\overline{\chi}_0 - \chi) \tag{2.1.37}$$

with solution:

$$\chi = \overline{\chi}_0 + (\chi_i - \overline{\chi}_0)e^{-\mathcal{G}\chi t} \tag{2.1.38}$$

where χ_i, initial value of χ at starting nudging time. According to this exponential tendency towards the nudging observation, one obtain a threshold of influence of the nudging observation associated to a e-folding time $\tau_\mathcal{G}$, according to $\tau_\mathcal{G} = 1/\mathcal{G}_\chi$. This implies that high frequency observations will not be retained (for a giving $\mathcal{G}_\chi = 10^{-3}\ s^{-1}$, $\tau_\mathcal{G} \approx 0.93\ h$)

- **Observational nudging:** In this implementation, nudging equation 2.1.36 will be carried out for that observations that are included within a radius of influence (R) and temporal window (δt) at every grid point at each model time step. Tendency for $\chi(\vec{x}, t)$ with $\mathcal{G}_{p^*} \equiv 0$ is:

$$\frac{\partial p^* \chi}{\partial t} = \mathcal{F}(\chi, \vec{x}, t) + \mathcal{G}_\chi \cdot p^* \frac{\left[\sum_{i=1}^{N} W_i^2(\vec{x}, t) \cdot \gamma_i \cdot (\chi_0 - \overline{\chi})_i\right]}{\sum_{i=1}^{N} W_i(\vec{x}, t)} \tag{2.1.39}$$

where $\mathcal{F}, \mathcal{G}_\chi$, have same meaning as before; i, ith observation; within a radius R and δt time at a given grid point; χ_0, observed value of χ; $\overline{\chi}$, model's prognostic variable interpolated to the observation; γ, observational quality factor (0 to 1, instrument errors and representativity). Assuming a perfect observation control quality $\gamma \equiv 1$, therefore the four-dimensional weighting function for the ith observation:

$$W(\vec{x}, t) \equiv w_{xy} w_\sigma w_t \begin{cases} w_{xy} = \begin{cases} \dfrac{R^2 - D^2}{R^2 + D^2} & 0 \le D \le R \\ 0 & D > R \end{cases} \\ w_\sigma = \begin{cases} 1 - \dfrac{|\sigma_{obs} - \sigma|}{\mathcal{R}_\sigma} & |\sigma_{obs} - \sigma| \le \mathcal{R}_\sigma \\ 0 & |\sigma_{obs} - \sigma| > \mathcal{R}_\sigma \end{cases} \\ w_t = \begin{cases} 1 & |t - t_0| < \tau/2 \\ \dfrac{(\tau - |t - t_0|)}{\tau/2} & \tau/2 \le |t - t_0| \le \tau \\ 0 |t - t_0| > \tau \end{cases} \end{cases} \tag{2.1.40}$$

where, w_{xy}, horizontal weight; w_σ, vertical weight; w_t, temporal weight; R, radius of influence; D, distance from the grid point to the ith observation; $\mathcal{R}_\sigma$, vertical radius of influence (usually small, 0.01 or even less); σ_{obs}, vertical position of ith observation; σ, vertical coordinate of the grid point; t, model-relative time; t_0, model-relative time of the ith observation; $\tau = \delta t/2$, half period of the time window δt.

2.1.2 Axisymmetric cloud resolving model

A modified version of the axisymmetric, nonhydrostatic, cloud-resolving model of Rotunno and Emanuel (1987) is used. The model has been modified to ensure global energy conservation, including dissipative heating. Any development in such a model must occur owing to Wind-Induced Surface Heat Exchange (WISHE), since baroclinic instability is absent in axisymmetric geometry. It assume the air-sea description and characteristics of a tropical storm (Emanuel, 1986).

The model is run with a radial grid size of 3.75 km and vertical level separation of 300 m. The model is initiated with a weak vortex (described by an overall radial size and a radius of maximum azimuthal wind, see equation 2.1.43) and a vertical sounding. A vertical sounding is used to determine the initial condition of the atmosphere. It is applied to all the radial grid points of the model. Consequently, an initial horizontally homogeneous environment is established. From gradient balance, the pressure distribution is established. Some other assumptions and simplifications are (with the constant values given in table 2.1.i):

- Hydrostatic and gradient wind balance

$$\frac{dp}{dz} = -\rho g \qquad \frac{V_{gr}}{R} + fV_{gr} = -g\frac{\partial z}{\partial n} \tag{2.1.41}$$

- Neutrality to Slantwise moist convection

$$M \equiv v + fx \quad \frac{du}{dt} = f(M - M_g) \quad \frac{dw}{dt} = B = \gamma_m(s' - s'^*) \qquad M = s^* \ (SlantwiseNeutrality) \tag{2.1.42}$$

- Initial vortex

$$v(r,z,0) = \frac{z_{sponge} - z}{z_{sponge}} \left\langle \left\{ v_m^2 \left(\frac{r}{r_m}\right)^2 \left[\left(\frac{2r_m}{r + r_m}\right)^3 - \left(\frac{2r_m}{r_0 + r_m}\right)^3 \right] + \frac{f^2 r^2}{4} \right\}^{1/2} - \frac{fr}{2} \right\rangle \tag{2.1.43}$$

Table 2.1.i: Values of some constants in the axisymmetric cloud resolving model

Coriolis Parameter ($10^{-5}s^{-1}$)	9.0	Surf. Drag Coefficient (10^{-3})	1.1
Ratio of Exch. Coeffs. (C_T/C_D)	1.0	Wind-Dep. Surf. Flux ($10^{-5}\ sm^{-1}$)	4.0
Horizontal Mixing Length (m)	200.0	Radiative Time Scale (h)	12.0
Cap. on rad. cooling (C/day)	2.0	Precipitation Fall Speed (ms^{-1})	7.0
Lowest perm. T in sounding (K)	133.0	SST Anomaly Amplitude (K)	0.0
SST Anomaly Decay L (km)	100.0	Large Time Step (s)	10.0
Nbr. small time steps/Delt	5	Asselin Filter constant	0.1
Sponge layer damping coeff.	0.01	Radius of Outer Wall (km)	1500.0
Altitude of Upper Boundary (km)	25.0	Number of sponge layer levels	5
End Time (days)	10.0	Threshold water content (gKg^{-1})	0.2

- "Sponge" layer limit convection in height near tropopause
- Eye in solid body rotation
- Constant sea surface temperature
- Compressible, axisymmetric flow
- Explicit cumulus convection imposing conservation of potential equivalent temperature
- Two dimension turbulence model, on azimuthal average following (Smagorinsky, 1963) and (Lilly, 1962)
- Newtonian cooling

$$R \equiv -\frac{\theta - \overline{\theta}}{\tau_R} \tag{2.1.44}$$

- Rigid lid at upper boundary condition
- $w = 0\ cms^{-1}$ on surface
- Open lateral boundary conditions

2.2 Piecewise PV Inversion

General state of the atmosphere is given by natural variables or state-variables: Temperature (T), Wind speed (u, v, w), Humidity (given by mixing ratio q, or relative humidity RH) and pressure (p). There are another set of variables that are combinations of the state-variables that contribute to a better analysis, understanding or forecasting of the atmosphere. One of these variables is the *Potential Temperature* (θ, equation 2.2.1).

$$\theta = T\left(\frac{p_0}{p}\right)^{\frac{R}{C_p}} \tag{2.2.1}$$

where T, temperature at a giving height; p_0, reference pressure; p, pressure at a giving height; R, ideal gas constant for dry air ($287\ Jkg^{-1}K^{-1}$); C_p, specific heat at constant pressure for dry air ($1005.7 \pm 2.5 Jkg^{-1}K^{-1}$).

Potential temperature is an adiabatically conservative variable. This implies that an air parcel which does not exchange heat with the environment (adiabatic process) preserves the potential temperature. The most useful way with which an air parcel exchanges heat with the environment is done throughout the transitions between water phases. By this way, when an air parcel moves without changes in its water phases, the movement is done following a potential isothermal surface. Potential temperature is the temperature that might have an air parcel that adiabatically moves from a reference pressure value (usually 1000 hPa) to another one. The definition of this temperature allows to study the thermal vertical structure of the atmosphere without the effects on vertical pressure changes. In some way it represents the temperature that might have an air parcel at a given height in an ideal dry atmosphere. Thus, one can obtain an idea of the state of the atmosphere. From this point of view, potential temperature is very useful as a way to determine the stability of a forced vertical movement of an air parcel (Bluestein, 1992). The stability of vertical movements of air parcels determine the chance of development of large variety of atmospheric phenomenas such as clouds.

There are a large variety of combined variables (CAPE, divergence, thickness, etc.). Each one helps in the study of a specific aspect of the atmosphere. One of these variables is the *Vorticity*.

- **Vorticity:** It is obtained when the curl operator ($\vec{\nabla}\times$) is applied on the conservation of motion equation (in terms of the Reynolds decomposition $\chi = \overline{\chi} + \chi''$) according to Bluestein (1992):

$$\frac{\partial}{\partial t}\left[\varepsilon_{pqi}\frac{\partial}{\partial x_q}\rho_0\overline{u}_i\right] = - \frac{\partial}{\partial x_j}\left[\overline{u}_j\varepsilon_{pqi}\frac{\partial\overline{u}_i\rho_0}{\partial x_q}\right] - \frac{\partial}{\partial x_j}\left[\rho_0\overline{u}_i\varepsilon_{pqi}\frac{\partial\overline{u}_j}{\partial x_q}\right]$$

$$
\begin{aligned}
&- \varepsilon_{pqi}\frac{\partial}{\partial x_q}\frac{\partial}{\partial x_j}\rho_0\overline{u_j'' u_i''} - \varepsilon_{pqi}\frac{\partial}{\partial x_q}\frac{\partial p'}{\partial x_i} \\
&- \varepsilon_{pqi}\frac{\partial}{\partial x_q}\left[\frac{\partial p_0}{\partial x}\delta_{i1} + \frac{\partial p_0}{\partial y}\delta_{i2}\right] + \varepsilon_{pqi}\frac{\partial}{\partial x_q}\frac{\alpha'}{\alpha_0^2}g\delta_{i3} \\
&- 2\varepsilon_{pqi}\varepsilon_{ijk}\Omega_j\frac{\partial \rho_0\overline{u}_k}{\partial x_q}
\end{aligned}
\tag{2.2.2}
$$

where ρ, density; u, velocity components; α, specific volume; p, pressure; g, gravity; Ω, Coriolis term; i, j, p, q, coordinates; ε, permutation symbol; δ, Kronecker delta in Einstein summation. It is known that the curl of a gradient is always null ($\nabla\chi = 0$), thus $\varepsilon_{pqi}(\partial/\partial x_q)(\partial p'/\partial x_i) = 0$. One can define a density-weighted mesoscale vorticity ω_p (equivalent to $\omega_p = \nabla \times \rho_0\vec{V'}$), and the equation is rewritten as:

$$
\begin{aligned}
\frac{\partial \omega_p}{\partial t} = &- \frac{\partial}{\partial x_j}(\overline{u}_j\omega_p) - \varepsilon_{pqi}\frac{\partial}{\partial x_j}\left(\rho_0\overline{u}_i\frac{\partial \overline{u}_j}{\partial x_q}\right) - \varepsilon_{pqi}\frac{\partial}{\partial x_q}\frac{\partial}{\partial x_j}(\rho_0\overline{u_j'' u_i''}) \\
&- \varepsilon_{pqi}\frac{\partial}{\partial x_q}\left[\frac{\partial p_0}{\partial x}\delta_{i1} + \frac{\partial p_0}{\partial y}\delta_{i2}\right] + \delta_{i3}g\varepsilon_{pqi}\frac{\partial}{\partial x_q}\frac{\alpha'}{\alpha_0^2} \\
&- 2\varepsilon_{pqi}\varepsilon_{ijk}\Omega_j\frac{\partial \rho_0\overline{u}_k}{\partial x_q}
\end{aligned}
\tag{2.2.3}
$$

each individual term of the equation is related to:

- $\dfrac{\partial \omega_p}{\partial t}$: local tendency of vorticity
- $\dfrac{\partial}{\partial x_j}(\overline{u}_j\omega_p)$: gradient of the flux
- $\varepsilon_{pqi}\dfrac{\partial}{\partial x_j}\left(\rho_0\overline{u}_i\dfrac{\partial \overline{u}_j}{\partial x_q}\right)$: *tilting term*, vorticity transferation between 3-dimensional spatial components as a result of velocity shear
- $\varepsilon_{pqi}\dfrac{\partial}{\partial x_q}\dfrac{\partial}{\partial x_j}(\rho_0\overline{u_j'' u_i''})$: source/sink subgrid term
- $\varepsilon_{pqi}\dfrac{\partial}{\partial x_q}\left[\dfrac{\partial p_0}{\partial x}\delta_{i1} + \dfrac{\partial p_0}{\partial y}\delta_{i2}\right]$: larger-scale source/sink term due to curvature of the synoptic-scale horizontal pressure gradients
- $\delta_{i3}g\varepsilon_{pqi}\dfrac{\partial}{\partial x_q}\dfrac{\alpha'}{\alpha_0^2}$: *selenoidal term*, source/sink due to gradients in density. In shallow flows ($\alpha'/\alpha_0^2 \sim \rho_0\theta'/\theta_0$) differential heating produces changes in the vorticity field
- $2\varepsilon_{pqi}\varepsilon_{ijk}\Omega_j\dfrac{\partial \rho_0\overline{u}_k}{\partial x_q}$: *solid-body rotation*, source/sink term due to rotation of earth

In atmospheric sciences, vertical component of the vorticity is a large source of information. Then is defined the Vorticity (ζ, equation 2.2.4) that gives the capacity of a fluid to locally rotate (Holton, 1979). It comes as a result of apply the curl operator ($\vec{\nabla}\times$) to the conservation of motion equation. That means, the capacity of a given flow to present rotation of radial distribution of its kinematic properties. It could be clockwise rotation ($\zeta < 0$), other to the other sense ($\zeta > 0$).

$$\zeta = \hat{k} \cdot \nabla \times \vec{V} = \frac{\partial v}{\partial x} - \frac{\partial u}{\partial y} \tag{2.2.4}$$

A vectorial expression for the vertical component of the vorticity ζ (Holton, 1979):

$$\begin{aligned} \frac{D\zeta}{Dt} = & - (\zeta + f)\left(\frac{\partial u}{\partial x} + \frac{\partial v}{\partial y}\right) - \frac{s\omega\cos\phi}{a}v + \left(\frac{\partial w}{\partial y}\frac{\partial u}{\partial z} - \frac{\partial w}{\partial x}\frac{\partial v}{\partial z}\right) \\ & + \left(\frac{\partial p}{\partial x}\frac{\partial \alpha}{\partial y} - \frac{\partial p}{\partial y}\frac{\partial \alpha}{\partial x}\right) \end{aligned} \tag{2.2.5}$$

The 'natural' coordinates form (equation 2.2.6) express the *vorticity* in an useful intuitive form from which the sources and sinks of vorticity can be clearly obtained. Then it is obtained that the *Vorticity* might change to the shear in the perpendicular direction to the velocity field (first term), and to the curvature of the flow (second term, see figure 2.2.1).

$$\zeta = V\frac{\partial \theta_b}{\partial s} - \frac{\partial V}{\partial n} \tag{2.2.6}$$

Absolute vorticity (η) is obtained, when the Coriolis term is included in the vorticity ($\eta = \zeta + f$) equation.

- **Potential Vorticity:** It is a generalisation of the *vorticity*. One dry formulation was given by (Ertel, 1942, equation 2.2.7). The potential term of the equation takes in to account the capacity of the particle of air developing vorticity. It is a conservative variable under adiabatic and frictionless conditions. An expression of the *potential vorticity* (hereafter, PV):

$$\begin{aligned} q &= \frac{1}{\rho}\vec{\eta} \cdot \vec{\nabla}\theta \\ q &\simeq \frac{g\kappa\pi}{p}\left[\left(f + m^2\Delta\psi\right)\frac{\partial^2\phi}{\partial\pi^2} - m^2\left(\frac{\partial^2\psi}{\partial x\partial\pi}\frac{\partial^2\phi}{\partial x\partial\pi} + \frac{\partial^2\psi}{\partial y\partial\pi}\frac{\partial^2\phi}{\partial y\partial\pi}\right)\right] \end{aligned} \tag{2.2.7}$$

where ρ, density; $\vec{\eta}$, absolute vorticity; θ, potential temperature; ψ, stream function lines; $\phi = gz$, geopotential height; p, pressure; g, gravity; $\kappa = R_d/C_p$; $\pi =$

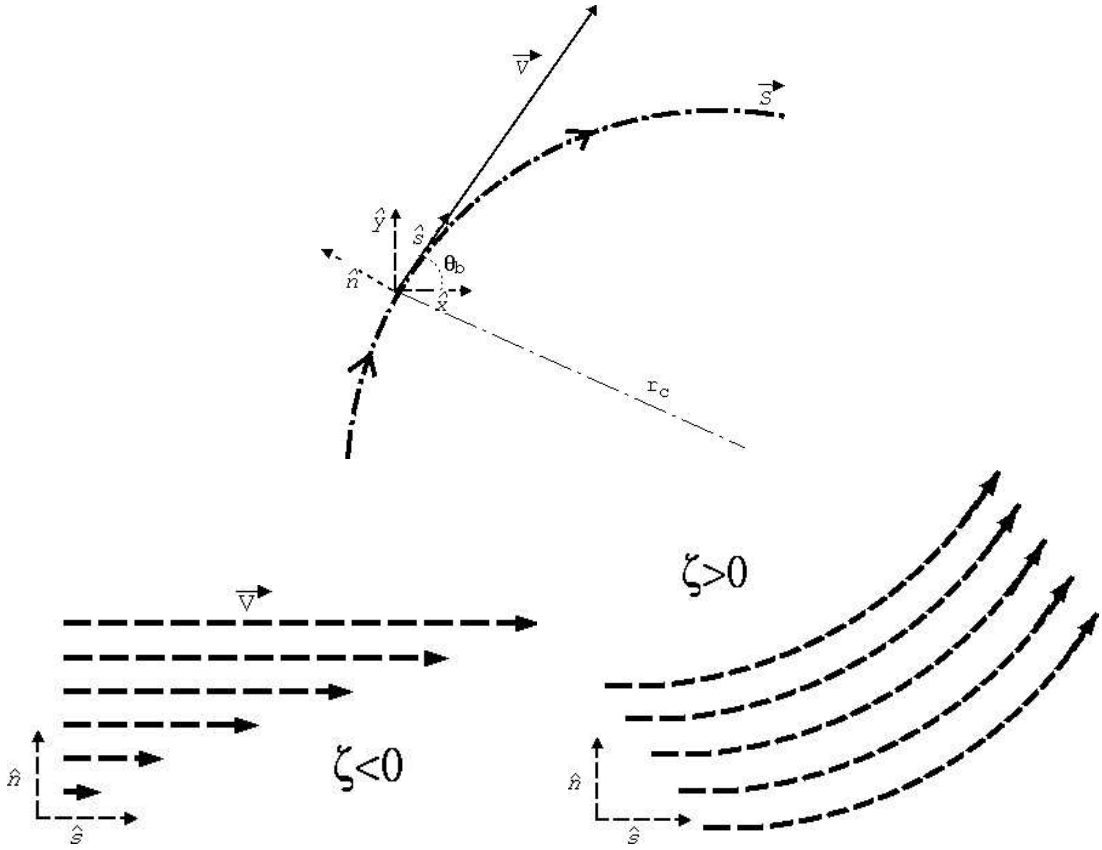

Figure 2.2.1: Top panel: Decomposition of the wind vector to its natural coordinates $(\hat{n}, \hat{s})$. Bottom left panel: A perpendicular wind shear to the direction of movement generates negative vorticity $(\frac{\partial V}{\partial n} > 0)$. Bottom right panel: A curvature $(\frac{\partial \theta_b}{\partial s} \neq 0)$ of a permanent flow $(\frac{\partial V}{\partial n} = 0)$ is depicted as positive vorticity

$C_p(p/p_0)^\kappa$, Exner function (as vertical coordinate). PV field has been shown (Hoskins et al., 1985) as a powerful diagnostic variable with which dynamically unstable regions of the flow (such us high rotational regions and strong gradients of wind) can be identified. PV presents significant values in zones of the flow that can be precursors of significant changes. Therefore, a specific case can present a strong sensitivity in the distribution of the PV field. As a result of PV properties, a large variety of atmospheric phenomena can be explained with the PV. *PV-thinking* is the way in which a set of processes is explained using the PV.

PV-thinking

As a result of the frictionless and adiabatic preservative characteristics of the PV, a large variety of atmospheric processes can be more clearly explained. PV point of view of some processes might help to better understand some phenomena. At the same time, some powerful tools (such as piecewise PV inversion and analysis of PV tendencies) can be derived from the variable.

Potential vorticity combines flow properties and thermal characteristics of the atmosphere. Some of the discussion of atmospheric phenomena using PV thinking are based in the *Stokes'* theorem (combination of the vorticity $\vec{\nabla} \times \vec{U}$ and the circulation $\vec{U} \cdot d\vec{l}$ equation 2.2.8) and the stability of the atmosphere (depicted by the Brunt-Väisälä frequency or buoyancy frequency N, equation 2.2.9). Explanations that will follow will be based on the conservation of the PV under adiabatically and frictionless conditions.

$$\oint \vec{U} \cdot d\vec{l} = \int_A \int dA(\vec{\nabla} \times \vec{U}) \cdot \hat{n} \tag{2.2.8}$$

$$N^2 = \frac{g}{\overline{\theta_v}} \frac{d\overline{\theta_v}}{dz} \tag{2.2.9}$$

where $\oint$, integration following a closed line; $\int_A \int dA$ surface integration; $\vec{U}$, vector field; g, gravity, $\overline{\theta_v}$, averaged virtual temperature between two layers; $d\overline{\theta_v}/dz$, vertical variation of potential potential temperature between two layers.

- **PV, adiabatic process and change of thickness:** Under adiabatic ($\theta = ct$) and frictionless ($\nu = 0$) assumptions potential vorticity is preserved ($q = ct$, equation 2.2.10; Holton (1979)). Applying Stokes' theorem, if an air parcel changes its thickness, this will change vorticity (ζ, see figure left 2.2.2).

$$q = (\zeta + f) \frac{\partial \theta}{\partial p}\bigg|_{(\theta = ct, \nu = 0)} = ct \tag{2.2.10}$$

- **PV and orography:** Taking the expression of vorticity 2.2.11 under preservative conditions ($q = ct$), on changes in the height (δz) will produce changes of vorticity (ζ). As a given example, in right figure 2.2.3 are shown the changes that suffers a parallel and constant ($\zeta = 0$) West flow when it interacts with a S-N mountainous range.

$$q = \frac{\zeta + f}{\delta z} = ct \tag{2.2.11}$$

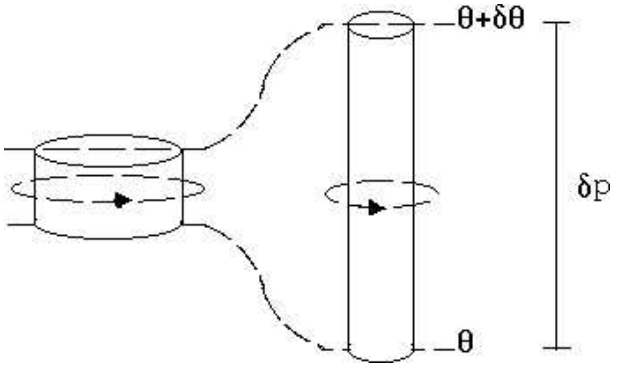

Figure 2.2.2: Expression 2.2.10 gives a relation between thickness or vertical dimension (δp) of a vortex and its absolute vorticity ($\zeta + f$). On frictionless and adiabatic conditions, changes of the thickness of the vortex will derive on changes in its vorticity (assuming not meridional movement $f = ct$), since potential vorticity (q) should not change

- η **& divergence:** Following the conservation of the vorticity, a dynamical property of the vorticity (see figure 2.2.4) could be obtained from the equation of the evolution of the absolute vorticity η (equation 2.2.12). First term of the equation is the divergence; second term relates the generation of vertical velocity due changes on the orientation of the flow; the last term is the selenoidal term from which, η is generated due to changes in pressure/density

$$\begin{aligned} \delta_t \eta = \frac{d}{dt}(\zeta + f) &= -(\zeta + f)\left(\frac{\partial u}{\partial x} + \frac{\partial v}{\partial y}\right) - \left(\frac{\partial w}{\partial x}\frac{\partial v}{\partial z} - \frac{\partial w}{\partial y}\frac{\partial u}{\partial z}\right) \\ &+ \frac{1}{p^2}\left(\frac{\partial \rho}{\partial x}\frac{\partial p}{\partial y} - \frac{\partial \rho}{\partial y}\frac{\partial p}{\partial x}\right) \end{aligned} \tag{2.2.12}$$

- **PV and cloud formation:** Another way to express the potential vorticity q is given by equation 2.2.13. A source of q is obtained from the study of the third term of the equation. During the formation of the clouds, due the condensation of huge amounts of water vapour a lot of heat is released. Latent Heat release from the condensation is developed in low-middle levels of the troposphere. As a result of it, this levels are warmed. Just below the zone of maximum heating, the level increases its stability. Due to the third term of the equation 2.2.13 positive potential vorticity is induced. The presence of positive potential vorticity at middle-low levels has been shown as a mechanism that enhance the cyclogenetic processes (Hoskins et al., 1985; Romero, 2001; Homar et al., 2002a). Middle-low levels positive PV emphasises, reinforces and catalyses coupling situations between upper and low levels disturbances, low level vorticity or instability (Davis and Emanuel, 1991).

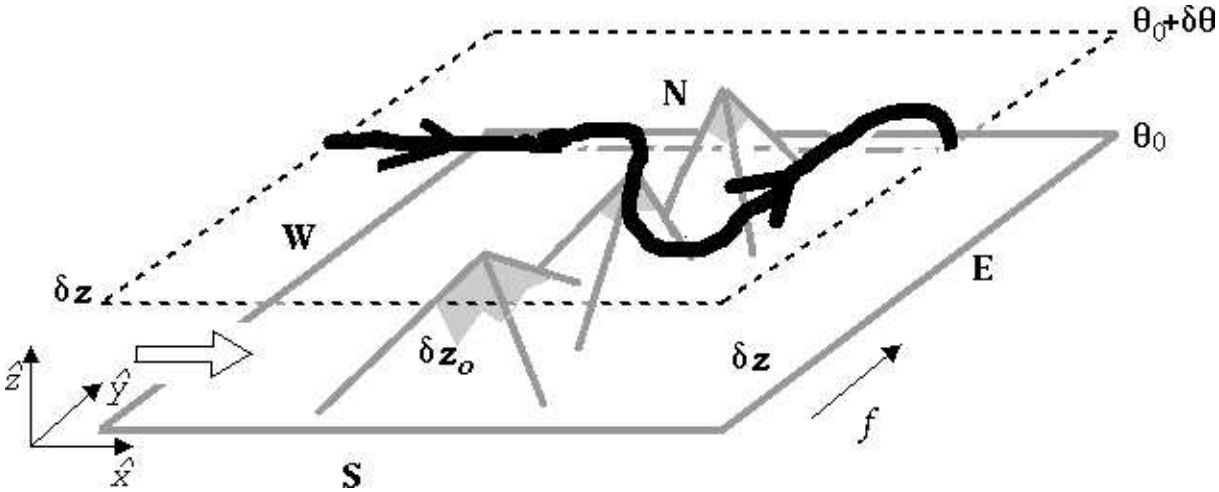

Figure 2.2.3: A constant West flow ($\zeta = 0$) reaches a S-N mountain range. In an adiabatic processes potential isothermal surfaces follow orography of the surface. Meanwhile, upper-level isothermal surfaces keep almost constant. As a result of it, flow decreases significantly its thickness ($\delta z_0 < \delta_z$). Due to the conservation of the Potential Vorticity q, relative vorticity ζ should change. In northern hemisphere where Coriolis term (f) increases towards the North pole, relative vorticity might decrease. Once the air-parcel overpasses the mountain range it is in a region with less Coriolis term with no height variation. In order to preserve the potential vorticity, flow should increase its rotation and it turns back to the north. When the air parcel reaches the original latitude that it was before the mountain range it has a northward component. This northward component should be compensated with negative vorticity (anticyclonic rotation). This process will be periodically reproduced until the flow reaches the initial arrotiational movement

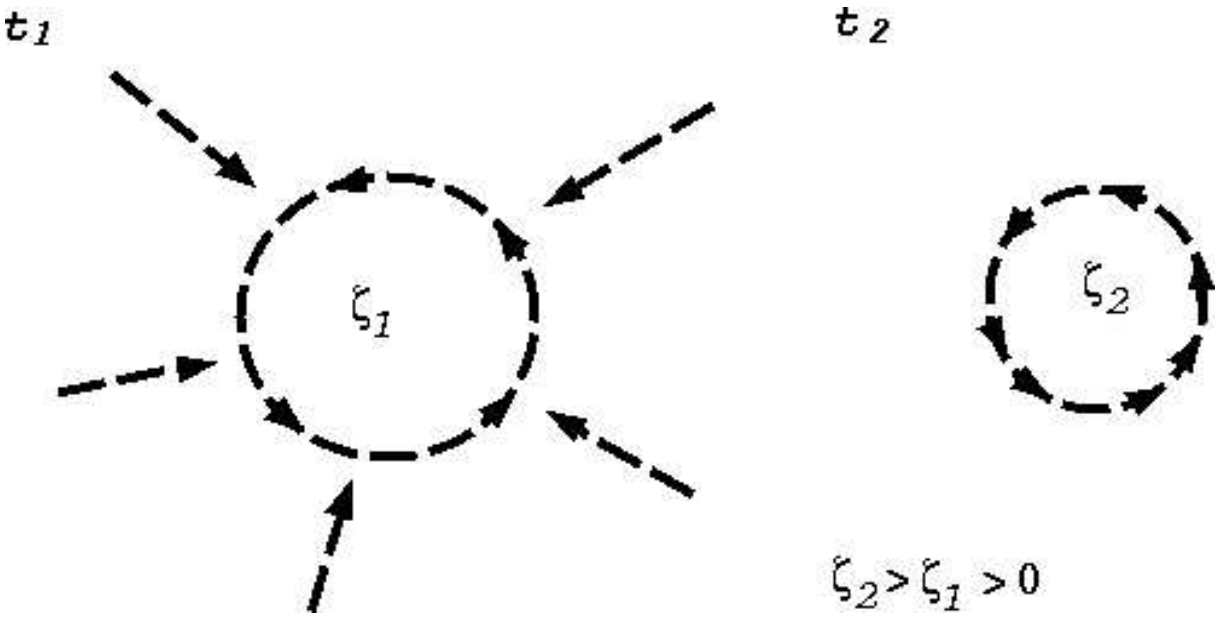

Figure 2.2.4: In a region of positive vorticity there is a convergence of the flow. Some time later air parcels should change the area that enclosed their streamlines. In order to keep constant the circulation, mean vorticity will increase. This process from which the vorticity is enhanced by convergences of the flow is common in cyclogenic processes. The search of convergence zones has been related to unstable zones and useful for the weather forecasters

$$q = \frac{1}{\rho}\Big[\frac{\partial\theta}{\partial x}\Big(\frac{\partial w}{\partial y} - \frac{\partial v}{\partial z}\Big) + \frac{\partial\theta}{\partial y}\Big(\frac{\partial u}{\partial z} - \frac{\partial w}{\partial x}\Big) + \frac{\partial\theta}{\partial z}\Big(\frac{\partial v}{\partial x} - \frac{\partial u}{\partial y} + f\Big)\Big] \qquad (2.2.13)$$

2.2.1 Invertibility principle

The invertibility principle of the Potential Vorticity establishes that for a given distribution of PV, assuming a balance equation between the wind and the temperature field and for a given boundary, top and bottom conditions; one can obtain its state-variables (without humidity) at all the space (Hoskins et al., 1985). According to this procedure the PV-related balanced state of the atmosphere will be obtained. The balance condition commonly used is a flow in wind and thermal balance with the expression:

$$\Delta\phi = \vec{\nabla}\cdot f\vec{\nabla}\psi + 2m^2\left[\frac{\partial^2\psi}{\partial x^2}\frac{\partial^2\psi}{\partial y^2} - \left(\frac{\partial^2\psi}{\partial x\partial y}\right)^2\right] \qquad (2.2.14)$$

where ϕ, geopotential height; ψ, streamfucntions; m, map factor; f, Coriolis factor.

The PV Inversion used in the UIB-Meteo. group follows the scheme proposed by Davis and Emanuel (1991). Nonlinear *Charney balance equation* (Charney, 1955, equation 2.2.14) has been taken as the appropriate form to give the balance condition. *Dirichlet* boundary conditions are imposed and *Neumann* top and bottom conditions (equation 2.2.15; f, Coriolis term) following Hakim et al. (1996).

$$\frac{\partial\phi}{\partial\pi} = f\frac{\partial\psi}{\partial\pi} = -\theta \qquad (2.2.15)$$

The solution of the PV Inversion does not have an unique solution. Obtained inverted fields will obey the chosen balance condition. Thus, the election of an appropriate balance equation will dominate the results of the inversion. It can be proved that nondivergent winds (winds with a smaller irrotational part than the nondivergent) are reasonably close to the balance flows (Davis and Emanuel, 1991). Therefore, it can be assumed that the inverted fields are a good approximation of the flow. If the chosen invertible relation is linear, the solution will be also linear. Therefore, a combination of PV distributions can be also inverted obtaining a combination of solutions. By this way, initial PV field can be disgregated in various pieces allowing a particular study of each piece. In the same way, any linear combination of operation of the PV distribution can be inverted. By this way, choosing a linear methodology to do the inversion different PV regions or individual pieces related to different features of the event can be indepently analysed. Allowing the study of different features of the environment to which they are related. These individual components of the PV field will be identified with relevant anomalies from a reference state of

the atmosphere, and then inverted to produce the initial perturbations in the simulations.

The *piecewise PV Inversion technique* in the meteorologic group of the UIB has mainly been used to perform sensitivity studies to changes in the initial conditions of the simulations of the cases of study. PV features in the PV field are obtained as PV anomalies at the initial conditions. These PV anomalies (hereafter, PVp) are derived according to a 7 to 10-day temporal averaged PV field for all the period of the case (and centred at the maximal strength of the event). It is assumed that the background flow is partially captured by the averaged composite of fields. Computing the PVp at the beginning of the simulation, might allow to capture the specific features that were present in the initial conditions and contributed to generate the episode. The inverted fields obtained for each anomaly are used to linearly modify the initial conditions of the simulations and perform, by this way, a sensitivity test to the changes introduced. Since inverted fields are driven by a balance condition, one can be sure that the modifications will not introduce any inconsistency between the state variables (if huge modifications have not been introduced). Since a linear inversion has been used, linear modifications carried out with the PV anomalies (or their resultant inverted fields) have also a solution. Inverted fields ($I\_\Xi = \{I\_H, I\_T, I\_U, I\_V\}$) obtained from an anomaly p_i are used to modify linearly (usually change of strength or shifts of the anomalies, see equation 2.2.16) the initial fields ($\Xi_{initial}$).

$$\Xi' = \Xi_{inicial} \pm \begin{cases} \%I\_\Xi p_i \\ I\_\Xi p_i(x+\chi, y+\gamma, z+\kappa) \end{cases} \tag{2.2.16}$$

PV Inversion is numerically solved throughout an iterative resolution of two-dimensional elliptical equations (commonly Green functions). This technique is known as a successive overrelaxation method (SOR)[4] (Barrett et al., 1994) and will be applied at each vertical level.

According to the methodology previously described it is necessary to illustrate some conditions that might comply the domain. Selected PV anomaly can not be close to the boundaries of the domain. PV Inversion presents a sensitivity to low latitudes due to low Coriolis values. At the same time, PV Inversion has problems to invert high resolution gradients or extreme values in the PV field. Selected domain should be big enough to capture all the PV anomalies that interact during the episode. At the same time, one should not introduce huge modifications and should be sure that the resultant environment is similar enough to the original initial conditions. Some not initially present incoming PV features during the event can derive erroneous conclusions. In order to prevent this in small domains, one could apply the modification of the boundary conditions at each time step that they are assimilated into the domain. This continuously application of the technique used to modify the fields, should be only applied to weak modifications in order to

[4] `http://mathworld.wolfram.com/SuccessiveOverrelaxationMethod.html`

prevent strong discontinuities between simulated and boundary fields.

Theoretically, a positive(negative) surface thermal anomaly can be related to a formal positive(negative) PV anomaly located below the bottom boundary (Bretherton, 1966; Thorpe, 1986; Horvath et al., 2006). Thus, the surface thermal anomaly studied in this work (a bottom boundary in the PV inversion method) is going to be treated as an underground PVp. By this way, the inverted balanced fields will be equivalent to the inverted fields that one can obtain from a PV anomaly under the ground that would produce the same surface thermal anomaly.

2.2.2 PV-based prognostic equations

One can also apply the PV Inversion technique to the prognostic equation of the PV. The closed system of PV-based prognostic equations (Davis and Emanuel, 1991) is used to solve the geopotential height tendency equation. Geopotential height (ϕ) and stream function (ψ) are first obtained from a given PV distribution (q) via the non-linear **PV inversion technique** (explained also in Davis and Emanuel (1991)). The geopotential height, stream function and PV tendencies (ϕ^t, ψ^t, q^t, respectively) can be calculated after applying the tendency operator to the **Charney nonlinear balance equation** (equation 2.2.17), **Ertel's PV definition** (eq. 2.2.18) and the **Ertel's PV conservation equation**, under the frictionless and diabatic form (eq. 2.2.19).

$$\begin{aligned}\nabla^2\phi^t &= \vec{\nabla}\cdot f\vec{\nabla}\psi^t + 2m^2\left[\frac{\partial^2\psi^t}{\partial x^2}\frac{\partial^2\psi}{\partial y^2} + \frac{\partial^2\psi}{\partial x^2}\frac{\partial^2\psi^t}{\partial y^2}\right.\\ &- \left. 2\,\frac{\partial^2\psi}{\partial x\partial y}\frac{\partial^2\psi^t}{\partial x\partial y}\right] \end{aligned} \tag{2.2.17}$$

$$\begin{aligned}q^t &= \frac{g\kappa\pi}{p}\left[\left(f + m^2\nabla^2\psi\right)\frac{\partial^2\phi^t}{\partial\pi^2} + m^2\frac{\partial^2\phi}{\partial\pi^2}\nabla^2\psi^t\right.\\ &- m^2\left(\frac{\partial^2\psi^t}{\partial x\partial\pi}\frac{\partial^2\phi}{\partial x\partial\pi} + \frac{\partial^2\psi}{\partial x\partial\pi}\frac{\partial^2\phi^t}{\partial x\partial\pi}\right.\\ &+ \left.\left.\frac{\partial^2\psi^t}{\partial y\partial\pi}\frac{\partial^2\phi}{\partial y\partial\pi} + \frac{\partial^2\psi}{\partial y\partial\pi}\frac{\partial^2\phi^t}{\partial y\partial\pi}\right)\right] \end{aligned} \tag{2.2.18}$$

$$\begin{aligned}q^t &= -m(\vec{v}_\psi + \vec{v}_\chi)\cdot\vec{\nabla}q - \omega^*\frac{\partial q}{\partial\pi}\\ &+ \overbrace{\frac{g\kappa\pi}{p}\left[\eta\cdot\vec{\nabla}\left(\frac{d\theta}{dt}\right) + \vec{\nabla}\theta\cdot\vec{\nabla}\times\vec{F}\right]}^{DIABI} \end{aligned} \tag{2.2.19}$$

where $\mathcal{DIABI}$ indicates the diabatic term of the equation. The formulation of the horizontal wind is partitioned in non-divergent and irrotational parts according to equations 2.2.20:

$$\begin{cases} \vec{v}_\psi = m\hat{k} \times \vec{\nabla}\psi \\ \vec{v}_\chi = m\vec{\nabla}\chi \end{cases} \tag{2.2.20}$$

In the above equations m is the map factor, $\kappa = \frac{R_d}{C_p}$, and $\pi = C_p \left(\frac{p}{p_0}\right)^\kappa$ is the Exer function used as vertical coordinates in the formulation. From the **omega equation** (eq. 2.2.21) the vertical velocity ($\omega^* = \frac{d\pi}{dt} = \frac{\kappa\pi}{p}\omega$) can be solved:

$$\begin{aligned} f\eta\tfrac{\partial}{\partial\pi} & \left[\pi^{1-\frac{1}{\kappa}}\frac{\partial}{\partial\pi}\left(\pi^{\frac{1}{\kappa}-1}\omega^*\right)\right] + m^2\nabla^2\left(\frac{\partial^2\phi}{\partial\pi^2}\omega^*\right) \\ - \quad & m^2 f\frac{\partial}{\partial\pi}\left(\frac{\partial\omega^*}{\partial x}\frac{\partial\psi}{\partial x\partial\pi} + \frac{\partial\omega^*}{\partial y}\frac{\partial\psi}{\partial y\partial\pi}\right) \\ + \quad & \left(f\frac{\partial\eta}{\partial\pi}\frac{\frac{1}{\kappa}-1}{\pi} - f\frac{\partial^2\eta}{\partial\pi^2}\right)\omega^* \\ = \quad & m^3\nabla^2[(\vec{v}_\psi + \vec{v}_\chi)\cdot\vec{\nabla}\theta] \\ + \quad & mf\frac{\partial}{\partial\pi}[(\vec{v}_\psi + \vec{v}_\chi)\cdot\vec{\nabla}\eta] - m^2\vec{\nabla}f\cdot\vec{\nabla}\left(\frac{\partial\psi^t}{\partial\pi}\right) \\ - \quad & 2m^4\frac{\partial}{\partial\pi}\left[\frac{\partial^2\psi^t}{\partial x^2}\frac{\partial^2\psi}{\partial y^2} + \frac{\partial^2\psi}{\partial x^2}\frac{\partial^2\psi^t}{\partial y^2}\right. \\ - \quad & \left. 2\frac{\partial^2\psi}{\partial 10\partial y}\frac{\partial^2\psi^t}{\partial x\partial y}\right] \\ + \quad & \overbrace{\nabla^2\left(\frac{d\theta}{dt}\right)}^{\mathcal{DIABII}} \end{aligned} \tag{2.2.21}$$

where $\mathcal{DIABII}$ indicates the diabatic term of the equation. Finally with the **continuity equation** the system is closed (eq. 2.2.22):

$$m^2\nabla^2\chi + \pi^{1-\frac{1}{\kappa}}\frac{\partial}{\partial\pi}(\pi^{\frac{1}{\kappa}-1}\omega^*) = 0 \tag{2.2.22}$$

Lateral homogeneous ($\phi^t = \psi^t = q^t = \omega^* = \chi = 0$) and *Neumman top and bottom* (eq., 2.2.23) boundary conditions are used for the tendencies:

$$\frac{\partial\phi^t}{\partial\pi} = f\frac{\partial\psi^t}{\partial\pi} = -\theta^t$$

$$= -m(\vec{v}_\psi + \vec{v}_\chi) \cdot \vec{\nabla}\theta - \omega^* \frac{\partial \theta}{\partial \pi} \tag{2.2.23}$$

Zero vertical velocity on the top of the domain and topographic vertical velocity on the surface are imposed.

The role of different PV anomalies can be studied by solving the previous system of equations for the geopotential height tendency (an indicator of cyclogenetic/cyclolitic processes) Romero (2008).

2.3 Factor Separation

Factor separation technique (Stein and Albert, 1993) allows to determine individual and mutual sensitivities of a forecasted field to a set of factors. It is a way to study the role of each factor or synergy during the evolution of the selected forecasted field of a numerical simulation. The collection of factors must be made of independent factors. That means that can not be any direct relation between them (g.e.: a specific mountain and its range could not be two different factors).

It is taken a forecasted field f. If for a factor ξ that affected the variable f is made a continuous modification $\xi = c\xi \; with \; 0 \leq c \leq 1$, the forecasted variable will suffer also a continuous modification $f = f(\xi) = f[\xi(c)]$. This characteristics will be also reproduced by a set of various parameters c_i. It is considered as first approximation that the function can be decomposed in two main parts, a dependant term $\hat{f}(c)$ (where $\hat{f}\,|_{c=0} = 0\,,\;\; c = c_1, ..., c_n$ as function of a continues modification) and another one that it is non-dependant of all factors called $\hat{f}(0) \equiv f_0$ (see equation 2.3.1).

$$f(c) = \hat{f}_0 + \hat{f}(c) \tag{2.3.1}$$

The free term is redefined as $f(0) \equiv f_0$, and $f(c_i) \equiv f_i$. For an unique factor the decomposition of the forecasted field is shown in equation 2.3.2.

$$\begin{aligned} \hat{f}_0 &= f(0) \\ \hat{f}(1) &= f(1) - f(0) \end{aligned} \tag{2.3.2}$$

For a given set of n parameters the decomposition can be done (see equation 2.3.3). It is shown that for a given set of n factors, is needed 2^n simulations to compute the decomposition. Following this procedure, the individual and synergies of the factors are obtained.

$$\begin{aligned} f_0 &= f(0,0,...,0) = \hat{f}_0 \\ f_i &= \hat{f}_i + \hat{f}_0 \\ f_{ij} &= \hat{f}_{ij} + \hat{f}_i + \hat{f}_j + \hat{f}_0 \\ f_{123...n} &= \hat{f}_{123...n} + ... + \sum_{i,j,k=1,2,3}^{n-2,n-1,n} \hat{f}_{ijk} + \sum_{i,j=1,2}^{n-1,n} \hat{f}_{ij} + \sum_{i=1}^{n} \hat{f}_i + \hat{f}_0 \end{aligned} \tag{2.3.3}$$

As an example is shown the effects ($\hat{f}_i \equiv e_i$) for a set of three factors 1,2 and 3 (equation 2.3.4). *Effect* is understood as the role that has had the factor during the forecasting

of the field. Synergetic effects are only the effect of the mutual interaction without the counting part of the individual effect. Is unusual provide synergies of three or four factors, due to the difficulty to give an appropriated physical meaning of a triple or four factor synergy.

$$\begin{aligned} e_0 &\equiv \hat{f}_0 = f_0 \\ e_i &\equiv \hat{f}_i = f_i - f_0 \\ e_{ij} &\equiv \hat{f}_{ij} = f_{ij} - (f_i + f_j) + f_0 \\ e_{123} &\equiv \hat{f}_{123} = f_{123} - (f_{12} + f_{13} + f_{23}) + (f_1 + f_2 + f_3) - f_0 \end{aligned} \tag{2.3.4}$$

2.3.1 Differential application

FS results present a great dependency on the number of factors. All those effects due to factors that have not been selected remain as hidden or unknown synergies in the factor separation results or the basic simulation s_0. That ambiguity in the results can be treated in two different ways: applying the fractional approach of the FS technique (Krichak and Alpert, 2002), and/or studying the response of the pure effects to a change in the number of factors that are used in the FS (Alpert et al., 1995).

- **Fractional approach:** it tries to deal with the hidden factors summarised in the interaction of a specific factor with the environment (hidden factors). Considering interactions with the environment, FS equations are rewritten as:

$$\begin{aligned} f_0 &= \hat{f}_0 \\ f_{a0} &= \hat{f}_0 + \hat{f}_a + \hat{f}_{a0} \\ f_{b0} &= \hat{f}_0 + \hat{f}_b + \hat{f}_{b0} \\ f_{ab0} &= \hat{f}_0 + \hat{f}_b + \hat{f}_b + \hat{f}_{a0} + \hat{f}_{b0} + \hat{f}_{ab0} \end{aligned} \tag{2.3.5}$$

  where $\hat{f}_{\chi 0}$, contribution of interaction of the factor χ with the background or hidden factors; $\hat{f}_\chi$, pure contributions of factor χ. The solution of the system keeps as:

$$\begin{aligned} \hat{f}_0 &= f_0 \\ \hat{f}_a &= f_{a0} - f_0 - \hat{f}_{a0} \\ \hat{f}_b &= f_{b0} - f_0 - \hat{f}_{b0} \\ \hat{f}_{ab} &= f_{ab0} - (f_{a0} + f_{b0}) + f_0 - \hat{f}_{ab0} \end{aligned} \tag{2.3.6}$$

  where usually $\hat{f}_{a0}, \hat{f}_{b0}, \hat{f}_{ab0}$ are neglected. In order to study hidden synergies an intercomparison of the considered effects (factors a, b) to gradual strengths of modification of each factor ($\hat{f}_{-k\chi},\ k = [0, 1]$) can be done. If the importance of the factor

or synergy is not linear with the strength of modification ($\hat{f}_\chi(k)$ *not* $\propto k\hat{f}_\chi$) implies that this factor must have a strong nonlinear interaction with a non-considered factor ($\hat{f}_{\chi 0}$). Fractional approximation of the FS technique multiplies the number of simulations by a minimum value of 3 (that means three-degree strengths of modification of the factor). This growths considerably the computational cost of the studies and limits its application.

- **Collection of factors:** The modification of the group and number of selected factors does not need additional simulations. In this method a pure effect (an effect related only to one factor, f_a) is selected. The effectivity of this factor is recalculated for each possible group of factors of the study (a, b, c) as follows:

$$\begin{array}{lcll} \hat{f}_a & = & f_a - f_0^a & \\ \hat{f}_a & = & f_a - f_0^{a,b} & \rightarrow \hat{f}_a \notin f_{ab} \\ \hat{f}_a & = & f_a - f_0^{a,c} & \rightarrow \hat{f}_a \notin f_{ac} \\ \hat{f}_a & = & f_a - f_0^{a,b,c} & \rightarrow \hat{f}_a \notin f_{ab}, f_{ac}, f_{abc} \end{array} \tag{2.3.7}$$

where, f_0^a, simulation without factor a (corresponding to a FS of one factor a); $f_0^{a,\chi}$, simulation without factors χ, k (corresponding to a FS of two factors a, χ); $f_0^{a,b,c}$, simulation without factors a, b, c (corresponding to a FS of three factors a, b, c).

Due to the aforementioned increasing consequence of the hidden synergies, the same factor will have less effect in a three factor study, than in a two factor study (see F_a surface diminishing as the number of factors increase in figure 2.3.1). However, the differences between effects should be linearly proportional to the number of factors included if the selected factor is an important factor for the evolution of the studied system. A difference on the behaviour of the effect as function of the collection of factors, could be a reflection of the synergy of this effect with another factor not included in the study, however this synergy would remain hidden and unknown in the result.

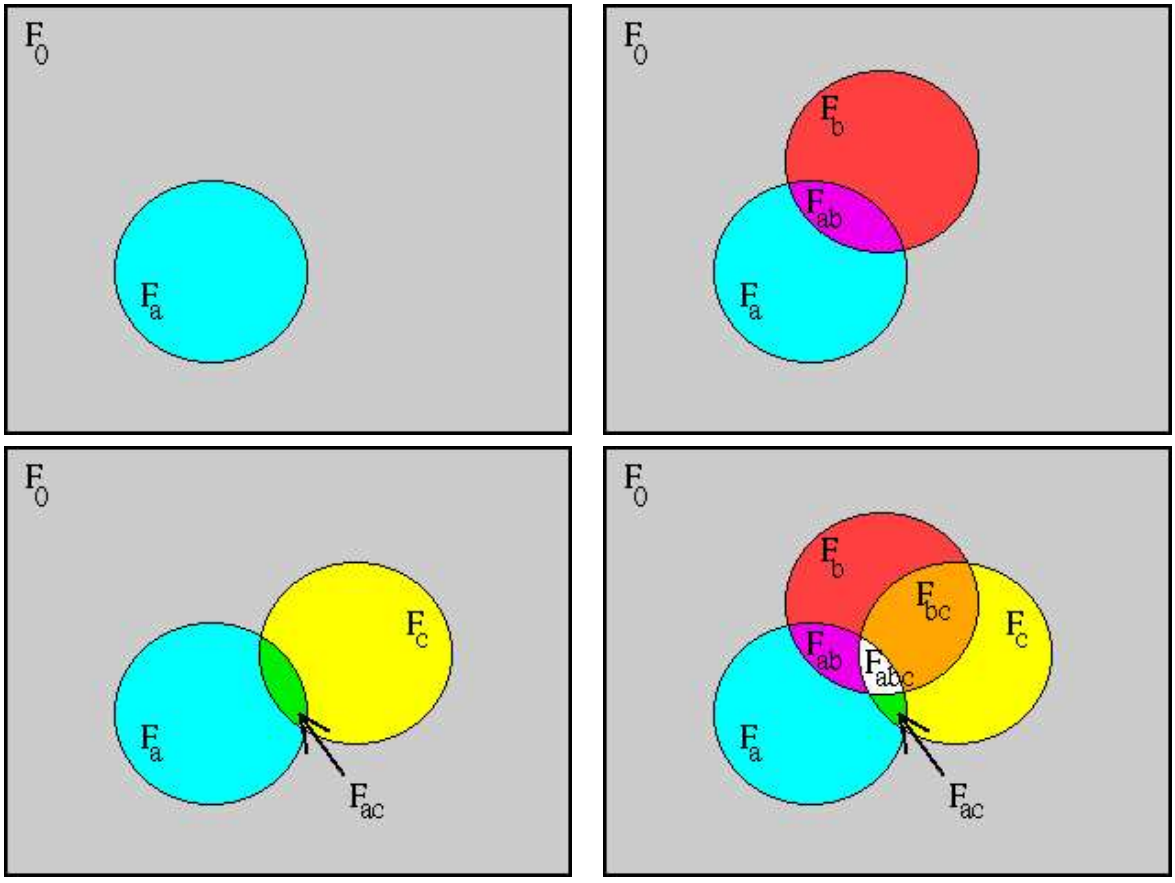

Figure 2.3.1: Representation of the factor separation for a factor F. Top left panel: FS for one factor a. Top right panel: FS for two factors a, b. Bottom left panel: FS for two factors a, c. Bottom right panel: FS for three factors a, b, c. Surface of F_a, diminishes as function of the selected factors

Chapter 3

Dynamical aspects of the cyclogenesis

Articles on which this chapter is based:

Ll. Fita, R. Romero and C. Ramis, 2006: *Intercomparison of intense cyclogenesis events over the Mediterranean basin based on baroclinic and diabatic influences*, Adv. in Geosci. (Proceedings PLINIUS 2006), **7**, 333-342

L. Fita, R. Romero and C. Ramis, 2007: *Objective quantification of perturbations produced with a piecewise PV Inversion technique*,Ann. Geophys., **25**, 2335-2349

Dynamical aspects of cyclogenesis is studied in two different manners. First study is focused on the role and influence of atmospheric features present at the beginning of a particular deep cyclogenetic case. Second study is a climatology of different cyclogenetic dynamical features of 11 cases that occurred allover the Mediterranean basin.

3.1 Baroclinicity

It is a way of development, growing and enhancing of cyclones. Basically it consists in the mutual interaction between upper and low level disturbances. One of the singularities of the mechanism is that coupling between disturbances reinforce each one and it can last a large period of time.

A favourable environment in which cyclones can be developed in the Northern hemisphere is based in the presence of a meridional low level horizontal thermal gradient and an upper level trough. Mediterranean basin often presents strong horizontal thermal gradients due to the coexistence of dry and warm air masses from the North African arid plateau and the north continental cold air masses. By this way, baroclinicity (see figures 3.1.1 and 3.1.2 for a schematic description) is one of the most common ways from which the cyclones develop in the Mediterranean basin. A deep and accurate study of the developing mechanism might help to improve forecasting of high impact hazardous weather as much as mitigate potential high destructive impact of cyclones on the densely habitated Mediterranean coastal lines and abrupt mountain ranges. Baroclinic development is a very frequent way of cyclone growing in the Mediterranean basin.

Baroclinic mechanism will interact with other phenomena that can enhance or mitigate the cyclogenic role. These other influences could be: sea surface, orography, coastal lines, surface fluxes, cloud formation. Meanwhile cloud formation is going on, large amount of water vapour is condensating in drops. As a result of it, large quantities of heat at middle levels are released due to latent heat of condensation. The warming of middle levels will influence in the development of the cyclone (see explanation in methodology section 2.2). Due tot the complexity of the Mediterranean basin all these influences (or even others) could have a role and they should be taken into account. Non linearities that are derived from these features will add complexity into the atmospheric phenomena. Thus baroclinicicty studies and other kind of meteorological studies in the Mediterranean basin become complicated due to the large amount of features, mechanism and relations that develop at the same time.

3.1.1 November 2001 case

In order to study the baroclinic mechanism in a Mediterranean case, November 2001 strong cyclone has been selected (Fita et al., 2007b). The 9th-12th November 2001 cy-

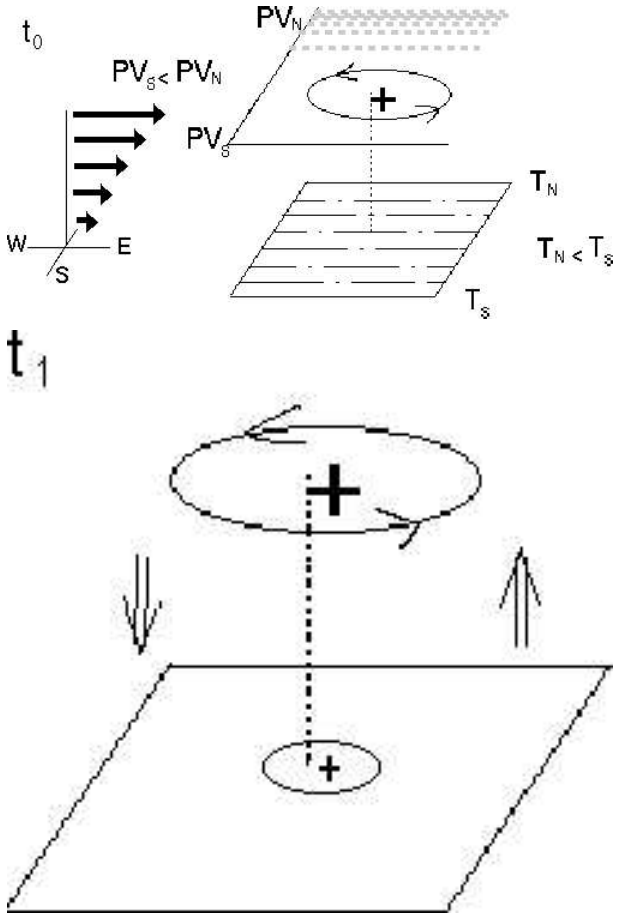

Figure 3.1.1: **Baroclinic Mechanism:** At initial time t_0, low levels present a pole-ward thermal gradient (dot-dash line), meanwhile at upper levels there is a positive PV anomaly (circle with arrows) and an westerly flow with a vertical shear (thick arrows). According to North hemisphere characteristics, temperature of the air is higher in south latitudes ($T_S > T_N$), and PV is higher in northern latitudes ($PV_S < PV_N$, reservoir in the polar zone shown as dashed thick gray lines). Upper level PV anomaly induces (t_1) cyclonic vorticity everywhere in the space that also influenced the surface (surface + circle). At the same time, in the front(back) zone of the PV anomaly upward(downward) motions of the air are developed (according to the ω equation (eq. 2.2.21), double arrows)

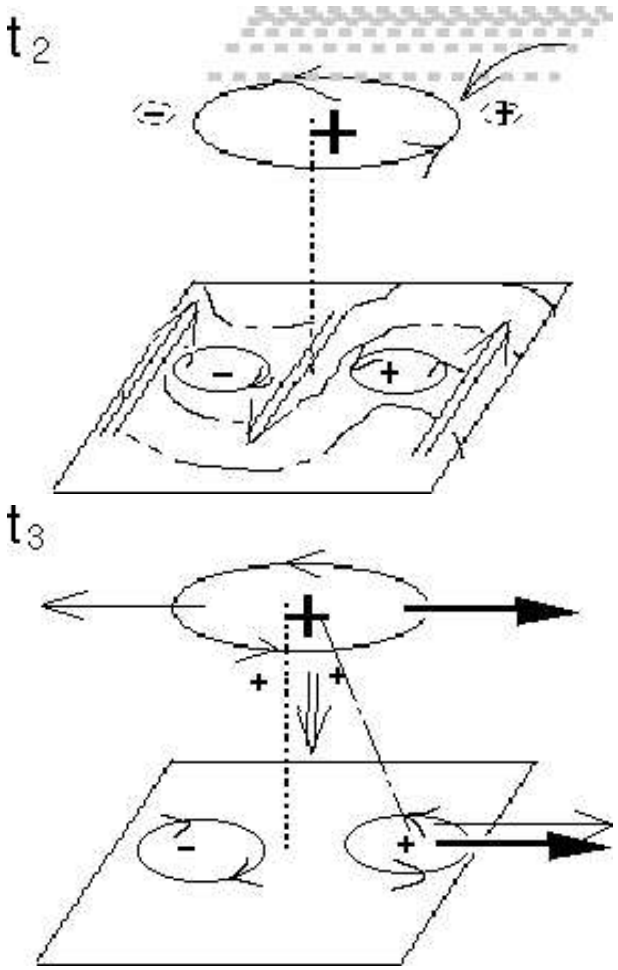

Figure 3.1.2: **Baroclinic Mechanism continuation:** As a result of the surface cyclonic induced circulation (t_2), surface thermal gradient curves its morphology and two rotational flows are generated: cyclonic (below of the frontal region of the PV anomaly) and anticyclonic (below the back region). The curvature of the horizontal thermal gradient increases thermal gradient, from which the surface rotational induced flows are enhanced. As a result of it, more warm south air is advected to the cold north region and vice-versa (double arrows). Surface pair of cyclonic/anticyclonic vortexes also influenced upper levels (small +/-, circles) and the frontal region of the PV is affected by positive PV advections from the polar reservoir. This PV advection will contribute to growth the PV upper level anomaly. Individual movements (in t_3 thin arrows) will separate upper and surface disturbances, but the background flow (thick arrows) and the influences provoke a coupling between disturbances. This coupling creates a reinforce of each anomaly. This phase-coupling between disturbances can last for large periods of time creating strong and deep cyclones.

clone has been described by the author as one of the most intense events in the Western Mediterranean basin during the last 25 years. The cyclone has been classified as a deep episode in the three-dimensional climatology done by Campins et al. (2006). It has been also widely studied (Davolio and Buzzi, 2004; Tripoli et al., 2005; Argence et al., 2006). In 24 hours a strong and deep vortex was formed. As a result, heavy precipitation and strong winds were recorded in Algiers and in the Balearic Islands. Seven hundred people died as a result of severe floods in Algiers, and 4 people died in Balearic Islands, where sustained winds of 30 ms^{-1} and precipitation above 200 mm/24 h were recorded and about two million trees felt down in the Mallorca Island.

The case is a clear and strong example of Pettersen-Smeybe class B cyclone evolution (Pettersen and Smebye, 1971), in which a cyclone is formed in a pre-existing upper level trough environment. The genesis and evolution of the case presents similar characteristics to the case occurred in December 1979 in the Western Mediterranean basin (Homar et al., 2002a). On 10th November 2001, a disturbance was formed at surface to the south of the Atlas mountains range (see figure 3.1.3, with the ECMWF analyses maps). A significant upper level disturbance was located over central Europe, extending from the Iberian peninsula to the Baltic Sea. This upper level disturbance shows a structure of two high PV positive anomalies (C0, C1, see labels in figure 3.1.3). Over the Mediterranean Sea there was a post storm situation with residual convective activity (not shown). As a result of the surface African low and the upper level disturbance, strong thermal gradients developed over the western Mediterranean basin. The low level cyclone moved northwards meanwhile the upper level disturbance translated southwards. While the low level low crossed the Atlas mountains, the upper level PV positive centres described a singular relative rotational movement, attributed to their interactions through PV advection. Mutual interaction between different positive PV vortices has been shown as an important factor that contributes to the cyclogenesis (Hakim et al., 1996). Although in this case, there was not a merge of the PV centres.

On 10th November at 18 UTC a strong interaction between upper level and low level disturbances was established. This is identified in figure 3.1.4 as the closeness between upper level disturbance (see the tropopause fold, or free cloud area), and a strong cyclonic cloud structure (cyclone, indicated by curved arrows). These configurations of proximity between strong surface thermal gradients and upper level trough disturbances become the ideal environmental conditions, under an appropriate vertical wind shear, to produce the baroclinic growth of disturbances. It has been described as one of the most important baroclinic processes from which deep cyclones can be formed (Hoskins et al., 1985; Bleck, 1990). From that time the cyclone crossed the Algerian coast and reached its mature state (Nov. 11th at 00 UTC), while strong cloud formation was present in the area. Strong winds were produced at surface (33 ms^{-1} sustained wind records were registered on Balearic Islands between 11th November 00 UTC and 06 UTC). Some time later the

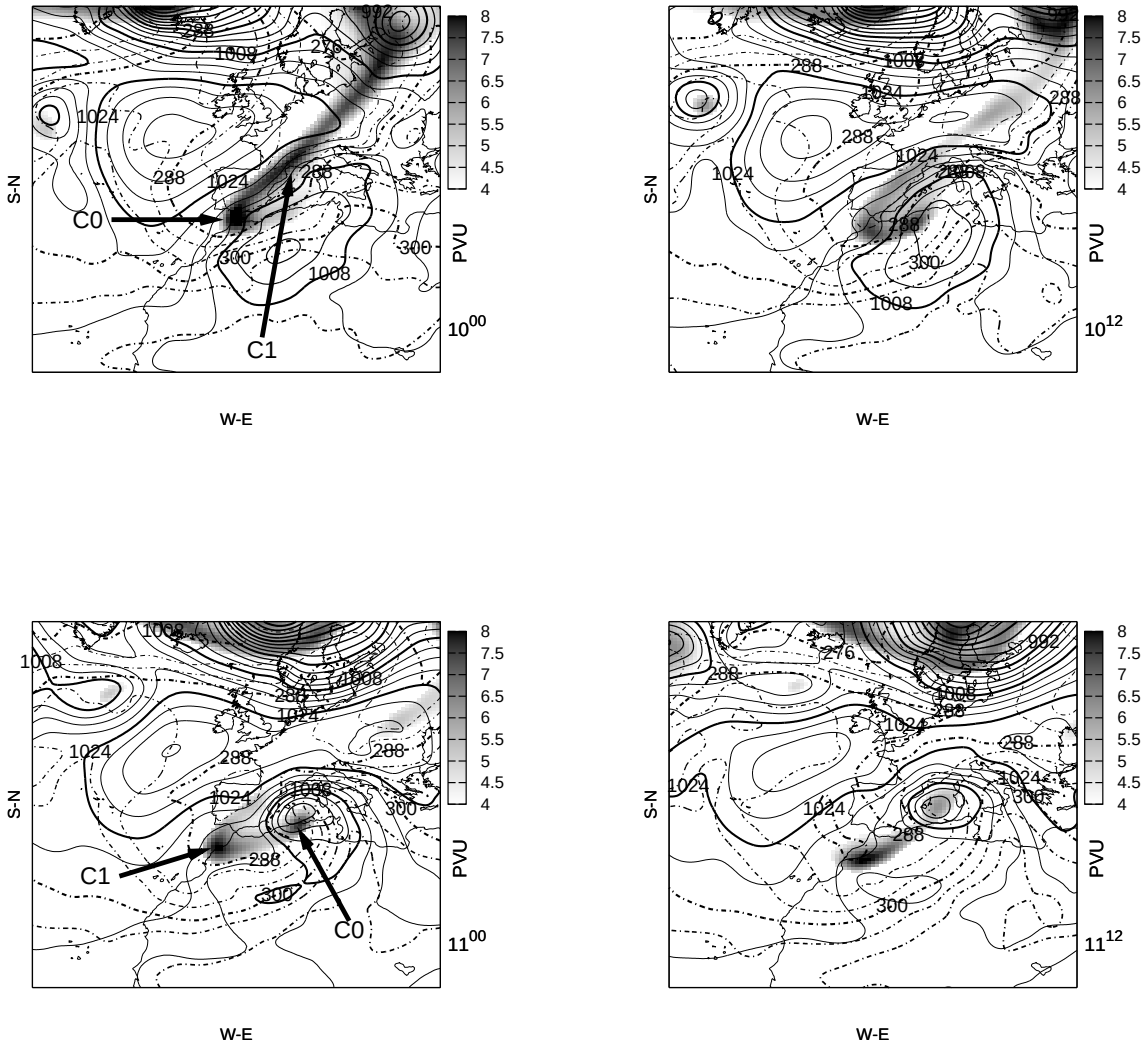

Figure 3.1.3: Sea level pressure (every 4 hPa, solid line), Potential temperature at 850 hPa (every 4 K, dashed line) and Isentropic Ertel PV at 330 K (1 PVU=$10^{-6} m^2 K s^{-1} kg^{-1}$, coloured field) from ECMWF analyses on Nov. 10th 2001 at 00 UTC (top left), Nov. 10th at 12 UTC (top right), Nov. 11th at 00 UTC (bottom left) and Nov. 11th at 12 UTC (bottom right)

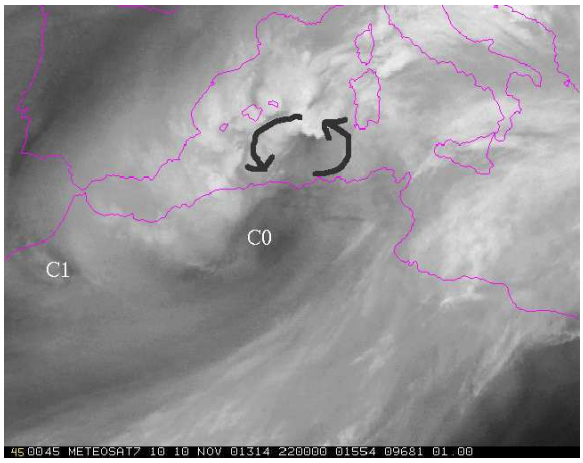

Figure 3.1.4: Normalised Water Vapour METEOSAT7 image on Nov. 10th 2001 at 22:00 UTC. EUMETSAT source

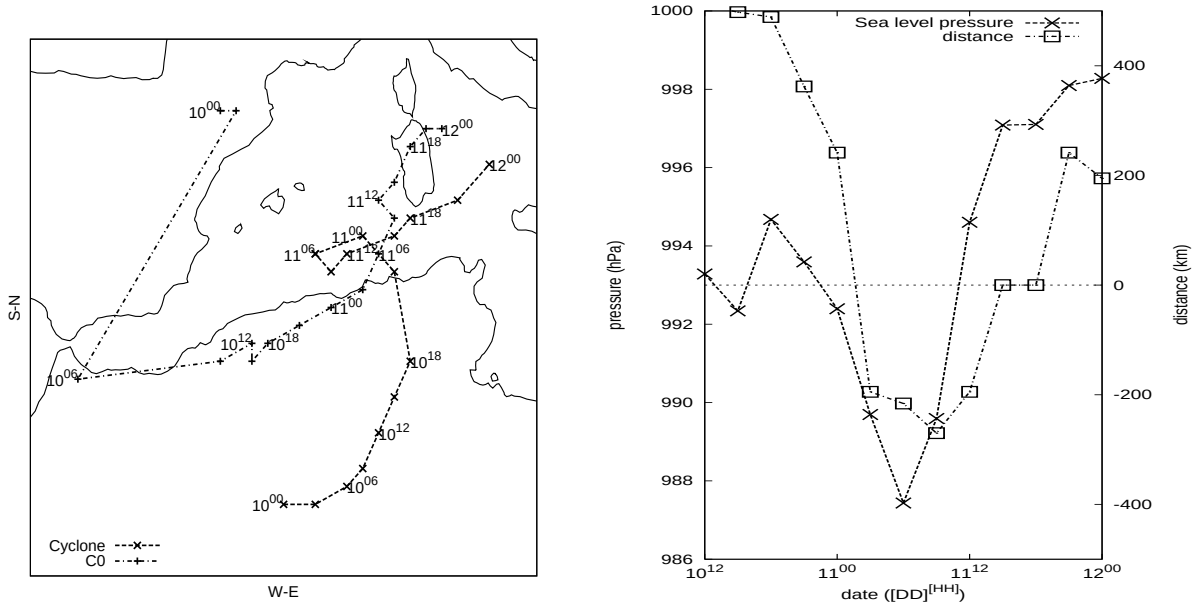

Figure 3.1.5: Control simulation results. Left panel: Evolution of the position of the cyclone (dashed line) and the C0 (slash-dot line), date of position is included ($[DD]^{[HH]}$). Right panel: Evolution of the central pressure of the cyclone (hPa, y-axis left) and its relative horizontal distance with C0 (km, y-axis right) since Nov 10th at 12 UTC. Relative horizontal distance is the distance between the positions of the centre of C0 and the cyclone. Positive(Negative) values of the relative distance occur when the cyclone is located eastward(westward) from C0

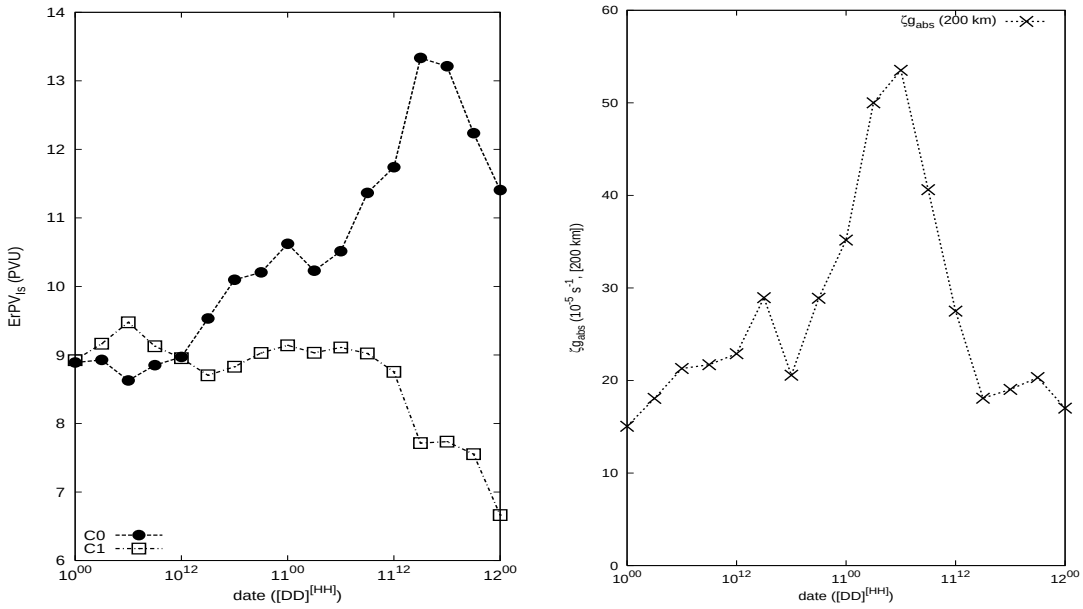

Figure 3.1.6: Left panel: Simulated central value (PVU) of the two upper level vortices C0 and C1, that are embedded within the upper level trough. Right panel: Evolution of the geostrophic vorticity calculated at 200 km (defined like in (Campins et al., 2000)) using a constant Coriolis value of $C_0 = 8.25 \times 10^{-6}\ s^{-1}$, and density $\rho = 1.225 kgm^{-3}$

upper-low levels interaction weakened because of the southward movement of the upper level disturbance and northward motion of the cyclone. At this point the cyclone weakened and described an eastward movement while it approached to the Sardinia Island.

The case will be studied using the MM5 nonhydrostatic primitive equation mesoscale model (Grell et al., 1994). A control simulation is run with one domain with a horizontal resolution of 54 km and 23 vertical levels. The simulated period comprises the interval between Nov. 10th 2001 at 00 UTC and Nov. 12th 2001 at 00 UTC. Control simulation will prescribe the main characteristics of the cyclone that will be compared to the simulated cyclones obtained from the PV-based sensitivity tests. All MM5 simulations will be run in the same configuration based on a graupel(reisner2) scheme for the explicit moisture processes, Kain-Fritsch scheme for the cumulus convection, mrf parametrisation for the planetary boundary layer and the 'rrtm' scheme (long wave) for the atmospheric radiation.

In order to track the baroclinic mechanism, the trajectories of 'C0' (the southwestern upper level PV vortex inside the upper level trough on Nov. 10th at 00 UTC, figure 3.1.3 of ECMWF analyses) and the surface cyclone are analysed. During the initial phase of the evolution, control simulation results show that meanwhile the upper level positive

vortex C0 moved southward, the cyclone moved northward. By this way the low-level disturbance and C0 got closer (Nov. 10th at 12 UTC in figure 3.1.5). While the relative horizontal distance between upper and low level disturbances decreased, the cyclone and C0 increased their intensity as a reflection of the baroclinic theory of phase coupling between upper and low level disturbances (Hoskins et al., 1985). However, the cyclone reached its mature state on a negative baroclinic-phase (C0 is located east relative to the cyclone, figure 3.1.5 on Nov. 11th at 00 UTC).

In this phase of the cyclone evolution, the cyclone reached the Mediterranean coast. Latent Heat Flux from the Sea surface and the vigorous release of latent heat due to a strong cloud formation at mid levels (see Water Vapour satellite image in figure 3.1.4) could contribute to the intensification of the cyclone. Intensification of cyclones due to the diabatic effects induced by the sea has been detected in other cases like in the North Atlantic 'bombs' (Sanders and Gyakum, 1980; Kuo et al., 1991a,b), or other Mediterranean cases (Homar et al., 2002a; Romero, 2001). Moreover, the block-phase mutual interaction of the baroclinic process is also shown by the increasing central value of the C0 (figure 3.1.6). A significantly different behaviour between the two upper level vortices is observed in the same figure. Whereas C0 became deeper, the other centre (C1) remained constant during the mutual interaction period (Nov. 10th 15 UTC to Nov. 11th 00 UTC, see figure 3.1.6). It is shown how C0 preserves its PV during the African phase of the cyclone. However, when the cyclone reached the Sea, strong diabatic processes are developed and C0 suffered an important increasing of its PV value (not shown). Meanwhile C1 conserves its PV during almost all the period of simulation.

During the African phase of the cyclone evolution (from Nov. 10th 00 UTC to Nov. 10th 18 UTC), the cyclone shows low vorticity (see figure 3.1.6). When the cyclone reached the sea it attained the mature state (Nov. 11th 00 UTC), depicted as: lowest surface central pressure value (988 hPa) and strong geostrophic vorticity (more than $30 \times 10^{-5} s^{-1}$ at the centre of the cyclone, computed using 200 km resolution geopotential data as in Campins et al. (2000)).

This episode is studied with the piecewise PV inversion technique following a new methodology of quantification of the initial modification.

3.1.2 Quantification of the initial modification

Piecewise PV Inversion technique combined with perturbed numerical simulations have been used as a tool to dynamically study different various of atmospherics systems (Hakim et al., 1996; Huo et al., 1999; Romero, 2001; Homar et al., 2002b; Argence et al., 2006). This technique can offer useful information about mechanisms and roles of wide range of features involved in the life cycle of the event. Although numerical solutions are well-

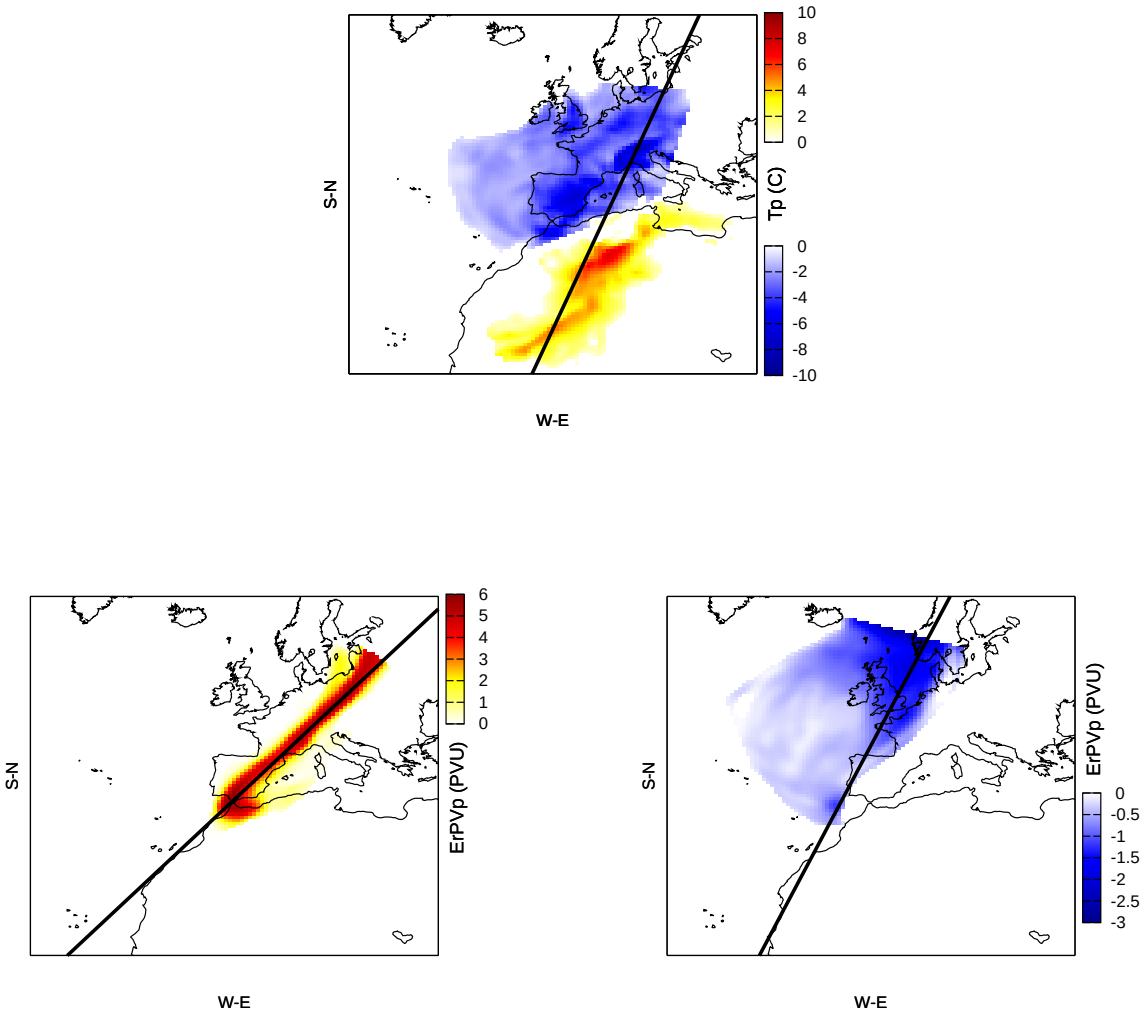

Figure 3.1.7: Surface thermal anomaly defined as ErPVpTerm (top; yellow-red, positive values; white-blue, negative values), Upper level PV perturbation (300 hPa) related to upper level trough defined as ErPVp01 (bottom left), Upper level PV perturbation (300 hPa) related to North Atlantic High defined as ErPVpHigh (bottom right), different scales are used. Solid lines show different vertical cross sections

defined throughout the set of equations, some uncertainties and subjectivities arise in its application, that can deeply influence the results. Some of these case dependent aspects are: set of balance equations used in the inversion, boundary conditions for the inversion, computation of reference state from which will be defined the PV anomalies (zonal mean, temporal mean, number of members to establish an average, etc), morphology and magnitude of the anomalies and degree of modification of the initial conditions.

In order to diminish subjectivity in the procedure, an objective way to quantify the initial modification introduced in the perturbed simulations is proposed as a method to quantify the latter aspect of the technique. The quantification of the perturbation is expressed as the mean absolute variation of the total energy between the initial and the modified fields, considering the whole horizontal domain of simulation and all vertical levels. The capability to compute the "total amount" of the introduced modification makes possible an objective control of one important aspect of the PV inversion technique, favouring meaningful intercomparisons of perturbed scenarios.

Selected anomalies might be morphologically and spatially different. The modification of the model initial conditions derived from these might be significantly different. In order to compare the roles of the PV anomalies, a 'normalisation' of the perturbation should be done. Then, one could be sure that the total amount of change introduced by means of the inverted fields remains initially constant among the simulations, independently of the size and strength of the anomaly. Thus the results can be adequately intercompared; meanwhile, the nonlinear evolution of the atmosphere will show the sensitivity of the event to changes in the initial conditions as differences between the derived simulations.

PV Inversion technique applied at each PV anomaly produces three-dimensional balanced fields (geopotential, temperature, stream function/horizontal wind). Since inverted fields are obtained for all the space, the normalisation or quantification of the perturbation requires a three-dimensional variable, and since PV inverted fields represent all atmospheric variables (except humidity), the index used for the normalisation should be a combination of these variables. The *total energy* (Bluestein, 1992) has been chosen as a plausible function. Using the energy, an energy-derived dynamical study of each anomaly can be accomplished. It can be an useful information from which a deeper understanding of the role of the collection of features can be obtained. This is possible since total energy can be split in three components: kinetic ($\delta\mathcal{ENG}_{kin}$), potential ($\delta\mathcal{ENG}_{pot}$) and internal energy ($\delta\mathcal{ENG}_{int}$). The grid point energy ($\mathcal{ENG}$) is obtained from the integration of the volumetric density of energy ($\delta\mathcal{ENG}$) across the volume of the grid point ($\delta\mathcal{V}$, see equations 3.1.1).

$$\mathcal{ENG} = \delta\mathcal{ENG}_{kin}\delta\mathcal{V} + \delta\mathcal{ENG}_{pot}\delta\mathcal{V} + \delta\mathcal{ENG}_{int}\delta\mathcal{V}$$

$$\begin{aligned} \delta\mathcal{ENG}_{kin} &= \frac{1}{2}\|\vec{v}\|^2\rho = \frac{1}{2}(u^2+v^2)\rho \\ \delta\mathcal{ENG}_{pot} &= gH\rho \\ \delta\mathcal{ENG}_{int} &= C_vT\rho \\ \delta\mathcal{V} &= \frac{ds\Delta p}{\rho g} \end{aligned} \tag{3.1.1}$$

where $\|\vec{v}\|$, wind speed; ρ, density; g, gravity; H, geopotential height; C_v, heat capacity at constant volume; T, temperature; ds, areal size of the grid point; Δp, pressure variation between bottom and top of the grid cell.

PV inverted fields used to modify the initial conditions generate a change of the total amount of energy in the atmospheric domain of the simulation. It is proposed to compute the energetic modification as the mean absolute variation of the total energy ($\mathcal{MAV}$, equation 3.1.2). Root Mean Square Variation ($\mathcal{RMSV}$) could have been proposed, but contributions of big and small energetic variation values are differently weighted in the $\mathcal{RMSV}$, since the differences are squared in the calculation.

$$\mathcal{MAV}_\chi = \frac{\sum_{i,j,k}^{Ni,Nj,Nk} |\chi_{mod}(i,j,k) - \chi_{ref}(i,j,k)|}{Ni \times Nj \times Nk} \tag{3.1.2}$$

where $\chi_{mod}(i,j,k)$ is the modified energy at each grid point; $\chi_{ref}(i,j,k)$ the unperturbed field and N_i, N_j, N_k, the number of grid points in each direction.

The proposed normalisation of the perturbations is realised by imposing the same energy variation in the initial conditions for each anomaly. Although each PV anomaly will modify with a different pattern the environment, the total amount of introduced/removed energy is forced to be the same. This condition will be condensed on a given percentage of the inverted balance fields to be used to modify the initial conditions.

However, one can not infer directly that an increase or decrease of the available energy to the environment will produce deeper or weaker systems. Any information about changes in morphology and position of the features in the fields, from which genesis and maintenance of the atmospheric systems are explained, must be also considered. Since zonal, meridional or vertical relations between features can dominate significantly the dynamics of a phenomena. That is the case of baroclinic instability as it was shown by Robinson (1989). The study of the impact and related dynamics of the energetic changes introduced by modifications of the initial conditions are out of the objectives of this study. They can be considered as a step further procedure once the certainty in the objective quantification can be verified.

The proposed quantification method of the piecewise PV inversion derived perturbations can be applied as a general methodology in dynamic meteorology. The application to various events would allow an objective intercomparison between cases independently of the morphology, characteristics and origin of the selected anomalies. This method of quantification could contribute to the PV study and analysis based on the most important features involved in the evolution of the cyclones or other atmospheric phenomena.

Energetic quantification of the modification introduced in the initial conditions will be used as a way to study the sensitivity to three different aspects of the case: upper level trough, low level thermal disturbances and environment (see equation 3.1.1). Quantification methodology fixes the total amount of modification introduced for each PV anomaly to be the same (from an energetic point of view). In the November 2001 case, the Upper level disturbances (ErPVp01 and ErPvpHigh) are clearly stronger than the surface thermal one (ErPVpTerm in figure 3.1.7). In order to avoid extremely high modification of the initial conditions or high percentages of modification with the inverted fields for one PV anomaly, the surface thermal anomaly will be used as reference. Thus a 70% of modification made with the PV inverted fields from the surface thermal anomaly is fixed as the reference. This reference of percentage of modification with the inverted fields of ErPVpTerm anomaly fixes an energy perturbation ($\mathcal{MAV}$, equation 3.1.2) of about 0.145 PJ (PJ $= 10^{15}$ J) on the initial conditions. This energy value is used to fix the total amount of variation of the inverted fields of the upper level anomalies. In order to obtain the percentage of modification in the initial fields with the inverted fields for the other two PV anomalies, a Newtonian or bisection iterative numerical method (Arfken, 1985) is used. This method is used to obtain the percentage of the inverted fields from ErPVp01 and ErPVpHigh that preserves the same amount of energy variation as the ErPVpTerm modification. Basically in the bisection method, next numerical value introduced in the iterative process is obtained as an average from the last to pair of values that are higher or lower than the desired result. The results of this numerical computation are summarised in table 3.1.a.

Different perturbation energy profiles are derived from the anomalies as it is shown in figure 3.1.8. ErPVpTerm influences much more the low levels, whereas ErPVp01 and ErPVpHigh influence strongly the upper levels. ErPVp01 is more evenly distributed in the vertical than ErPVpHigh, depicting the structural differences between troughs or cut-off lows and anticyclones acting as upper level blocking features (Hoskins et al., 1985; Thorpe, 1986).

Figure 3.1.9 gives spatial information on the impact of each anomaly over the initial conditions. It shows the three-dimensional effect on the total energy. ErPVpTerm extracts and adds energy to the environment. Since ErPVpTerm anomaly is aimed to capture the surface baroclinicity of the initial environment, it has been constructed with

Table 3.1.a: Percentage of modifications of the inverted fields of each anomaly (%) used to modify the initial conditions following the bisection method. Mean absolute variation of the total energy ($\mathcal{MAV}$ in PJ, $10^{15}J$) introduced on the initial conditions (+, increasing case; -, decreasing case)

Final values		**ErPVpTerm**		**ErPVp01**		**ErPVpHigh**	
		%	δ_{ENG}	%	δ_{ENG}	%	δ_{ENG}
+	$\mathcal{MAV}$	70	0.14504	8.8780	0.14504	7.6002	0.14505
-	$\mathcal{MAV}$	70	0.14508	8.8002	0.14509	7.6401	0.14508

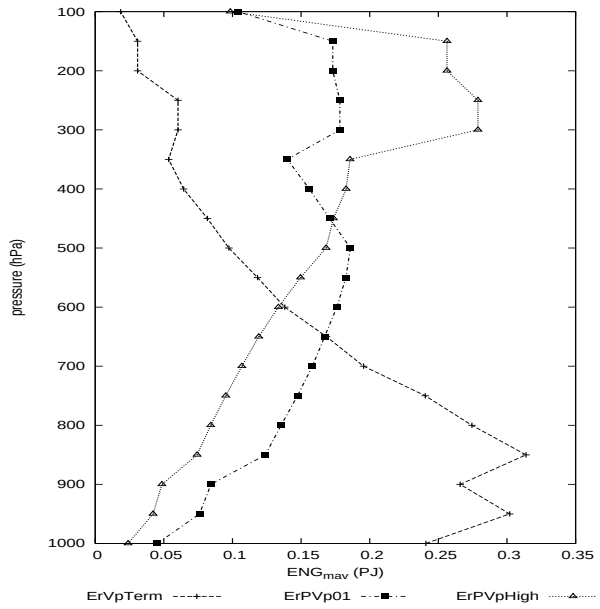

Figure 3.1.8: Vertical profile of the mean absolute energy variation ($\mathcal{MAV}$) of the initial conditions according to the positive percentage found for each anomaly. ErPVpTerm (cross), ErPVp01 (filled square), ErPVpHigh (triangles). Note that the same area is enclosed by each curve (same total energy)

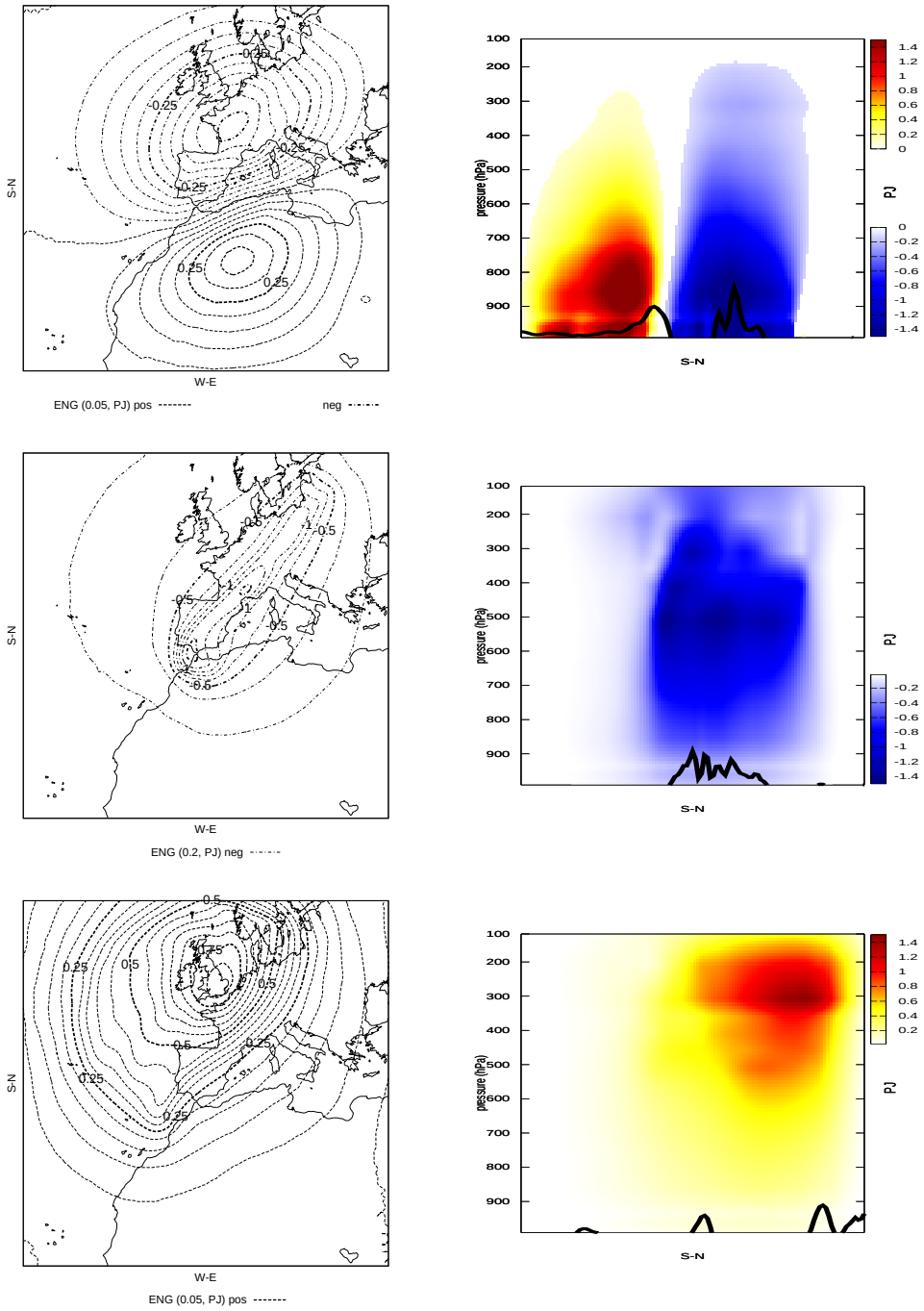

Figure 3.1.9: Energy variations (PJ, $10^{15}J$) introduced after the modification of the initial conditions (Nov. 10th 2001 at 00 UTC), according to each positive percentage of modification of the PV Inverted fields of each anomaly; ErPVpTerm (top), ErPVp01 (middle), ErPVpHigh (bottom). At 500 hPa (left) and following vertical cross sections defined at figures 3.1.7 (right)

both the positive and negative surface thermal anomaly. Perturbations carried out with positive(negative) thermal anomaly is related to a decrease(increase) of the total energy. Upper level positive(negative) potential vorticity perturbations are related to a decrease(increase) of the total energy (see figure 3.1.13). Results of ErPVpTerm anomaly (top panel in figure 3.1.13) does not show and upward decrease profile as the $\mathcal{MAV}$ value (dash and cross line in figure 3.1.8). This is because ErPVpTerm is based on both positive and negative thermal anomalies (top figure 3.1.7). As a result the inverted fields increase/decrease the energy of the environment. Figure 3.1.13 gives the averaged total variations of this energy (thus allowing compensation between terms), meanwhile in $\mathcal{MAV}$ computation this is not allowed since absolute values are used.

The perturbation energy partition among kinetic, potential and internal for each anomaly is shown in figures from 3.1.10 to 3.1.12 and 3.1.13. ErPVpTerm is related to a variation of the internal and potential energies. The effect is almost constant at all vertical levels. ErPVp01 and ErPVpHigh energy contributions are broadly similar. These anomalies have an important effect on the potential and internal energy, with the maximum energy variation found at upper levels. Significant perturbations of the kinetic energy are also found at upper levels, where the anomalies are defined. ErPVp01 has the highest impact on the potential energy, while ErPVpHigh on the internal energy.

However, one can not infer directly that an increase or decrease of the available energy to the environment will produce deeper or weaker systems. As it has been shown, increasing the upper level positive PV anomaly induces a significant decrease of potential and internal energy in spite that a strong upper level positive PV anomaly is usually related to strong cyclogenesis (Pettersen and Smebye, 1971; Hoskins et al., 1985). Energy impacts are shown as horizontally averaged values. Any information about changes in morphology and position of the features in the fields, from which genesis and maintenance of the atmospheric systems are explained, is not provided. Energetic implications for the baroclinic instability (Robinson, 1989) is out of the objectives of this study.

The sensitivity to changes in the initial conditions will be derived from the differences between the collection of simulated cyclones. The impacts on the simulated trajectories, central pressure value and central vorticity of the cyclones will be examined. Besides, a short description of the upper level vortex (C0) properties and evolutions will be given. The computation of the vorticity characteristics of the cyclones follow the criteria of Campins et al. (2000), where a 200 km grid length mesh is used.

Generally, in terms of central pressure values of simulated cyclones, is shown a symmetric response between positive and negative modifications of the initial fields (see figure 3.1.16). That is, the simulated two cyclones as a result of modification of the initial conditions adding or removing a percentage of the inverted fields of one perturbation, show

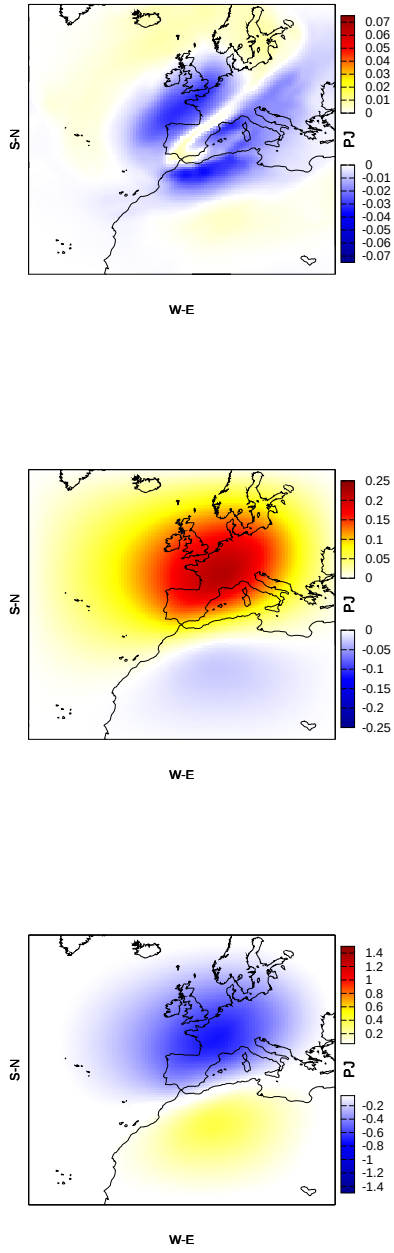

Figure 3.1.10: Energy variations (PJ, $10^{15}J$) introduced after the modification of the initial conditions (Nov. 10th 2001 at 00 UTC), according to the positive percentage of modification of the PV Inverted fields for anomaly ErPVpTerm. At 500 hPa for the kinetic term (top), internal (middle) and potential (bottom)

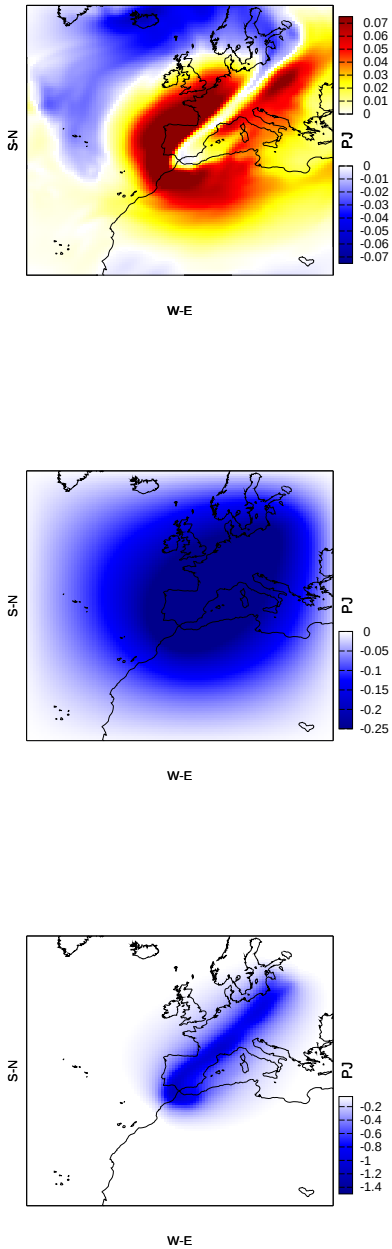

Figure 3.1.11: As in figure 3.1.10, but for the ErPVp01 anomaly

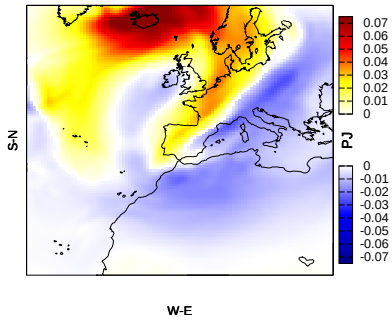

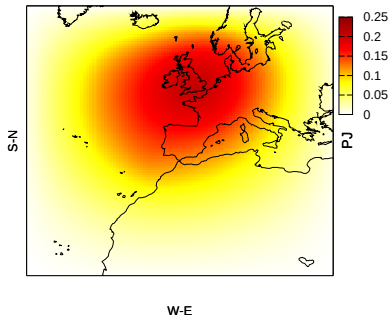

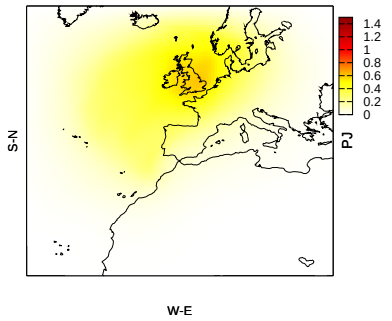

Figure 3.1.12: As in figure 3.1.10, but for the ErPVpHigh anomaly

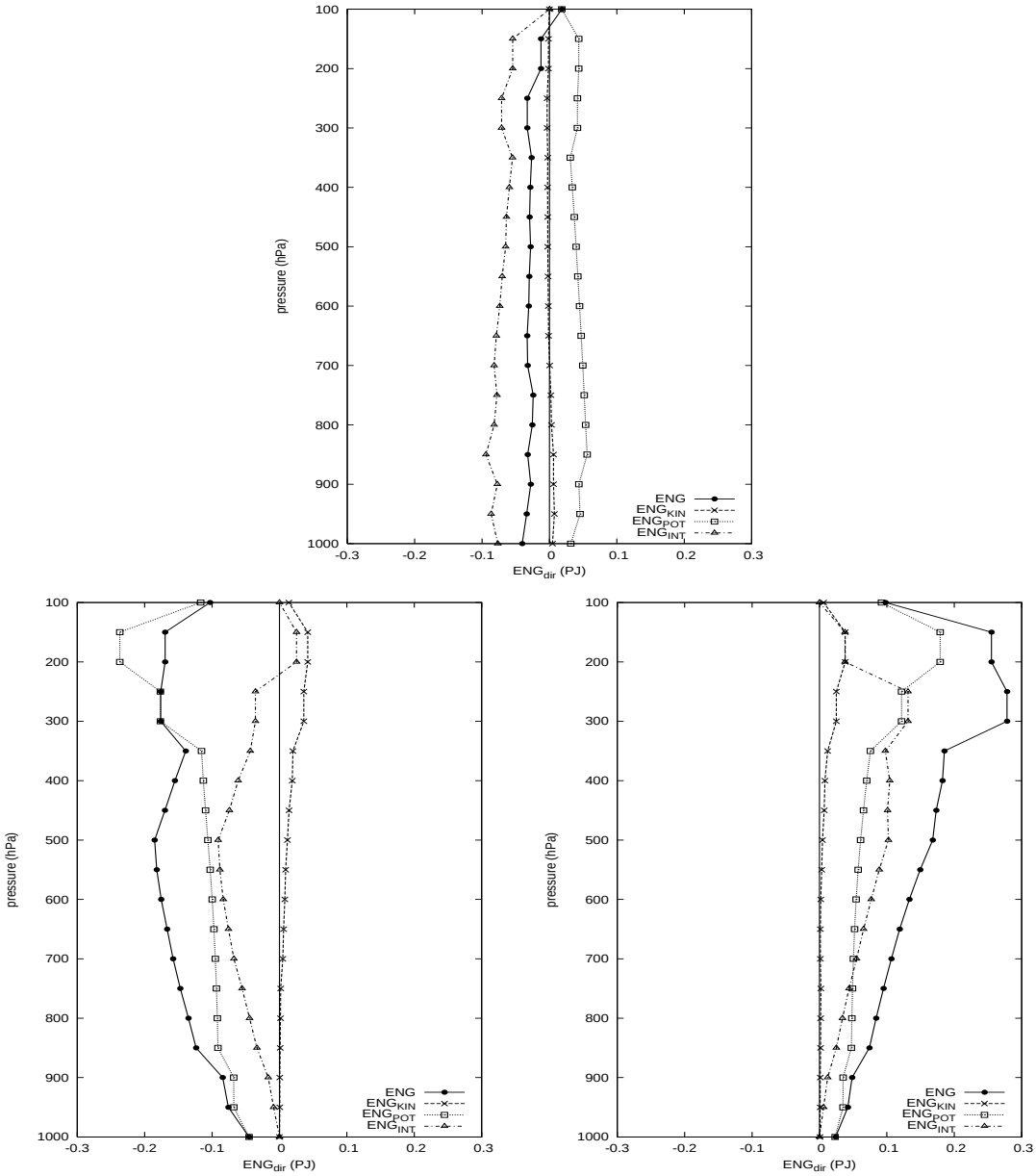

Figure 3.1.13: Vertical profiles of the horizontally averaged total variations of energy (in PJ, $10^{15}J$) according to the positive percentage of modification for each anomaly. Total energy variation (solid line, filled circles), Potential energy ($\mathcal{ENG}_{pot}$, dotted line with squares), Kinetic energy ($\mathcal{ENG}_{in}$, dashed line with crosses), Internal energy ($\mathcal{ENG}_{int}$, dot-dash line with triangles). ErPVpTerm (top), ErPVp01 (bottom left), ErPVpHigh (bottom right)

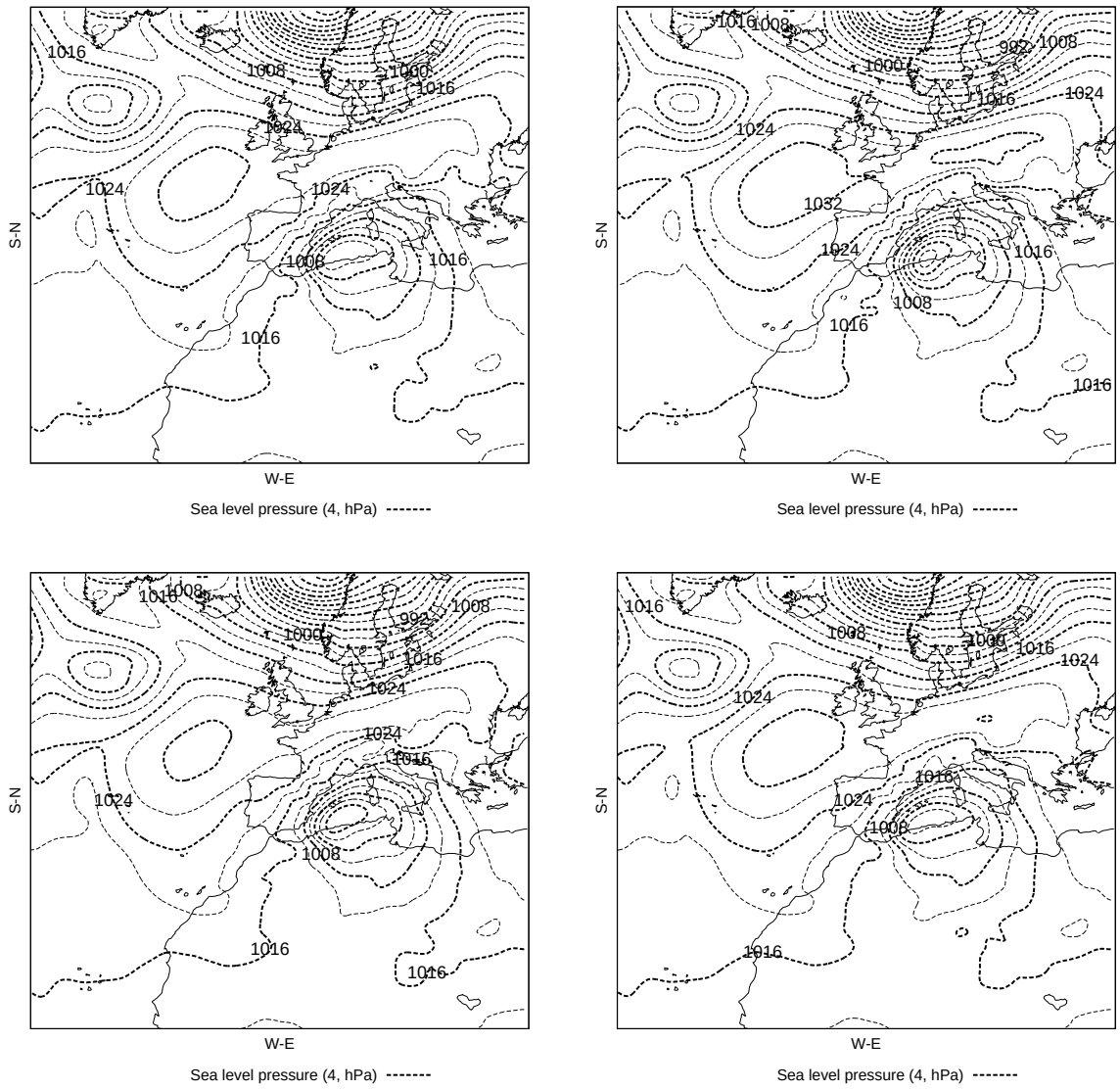

Figure 3.1.14: Sea level pressure at the mature state of the cyclone (Nov. 11th 00 UTC). Lines every 4 hPa. For the control simulation (top left), +ErPVpTerm (top right), +ErPVp01 (bottom left) and +ErPVpHigh (bottom right)

the same variations, with opposite sign, from the control one. These differences are not very strong owing to the small degree of modification introduced.

3.1.3 Sensitivity to upper level trough

The cyclone simulated through the ±ErPVp01 perturbations reveals significant impacts of the upper-level trough. The effects are most notable during the mature state of the cyclone on Nov. 11th at 00 UTC. The simulated cyclones and the C0 centres describe similar trajectories as the control ones (see lines with squares in figure 3.1.15). However, the evolution of the central surface pressure values and the C0 magnitudes have been changed (see lines with squares in figures 3.1.16, 3.1.17). Low differences are observed between the final PV values of C0 between the +ErPVp01 and -ErPVp01 cases (figure 3.1.17), probably due to diabatic influences.

Initially the perturbation of ErPVp01 is localised at upper levels, where the trough is altered (central pressure of the cyclones for ±ErPVp01 cases are initially only $\pm 1 hPa$ different than the control one). During initial phase the cyclones preserve similar vorticities (see figure 3.1.18), but they change significantly their dimensions (not shown). Stronger or weaker upper level PV vortex do not produce any strong effect on the trajectory of the disturbances (similar trajectories as the control one are obtained, see figure 3.1.17). However, a weaker upper level disturbance (-ErPVp01 case) decreases the upper-low level interaction and this is depicted as a shallower mature cyclone. With a stronger upper level trough (+ErPVp01 perturbation) cyclone moves faster than the control one (figure 3.1.15). Significant geostrophic vorticity differences are obtained at the mature stage of the cyclone (Nov. 11th at 00 UTC, figure 3.1.18), as a reflection of the changes in the vorticity advections due to a stronger(weaker) upper level trough. In the last phase of the evolution of the cyclone, C0 value is similar to the control one, but central pressure values of the cyclone are clearly different (about $\pm 2 hPa$), possibly related to changes in the relative phase between C0 and the cyclone at this ending phase. Like for the ErPVpTerm anomaly simulations, small differences between positive/negative cases in the maximum growth rate of the cyclone is also observed for this anomaly.

3.1.4 Sensitivity to low level thermal disturbances

The modification of the low level environmental baroclinicity (± ErPVpTerm) reveals significant variations with respect to the control simulation during the initial and last phases of the cyclone evolution. These differences are the largest ones among all the set of perturbations at the initial phase of the simulations. According to the results, the differences in the initial position of the cyclone are about 480 km (see figure 3.1.15), and for the initial central pressure value of the cyclone approx. $\pm 4 hPa$ (see figure 3.1.16).

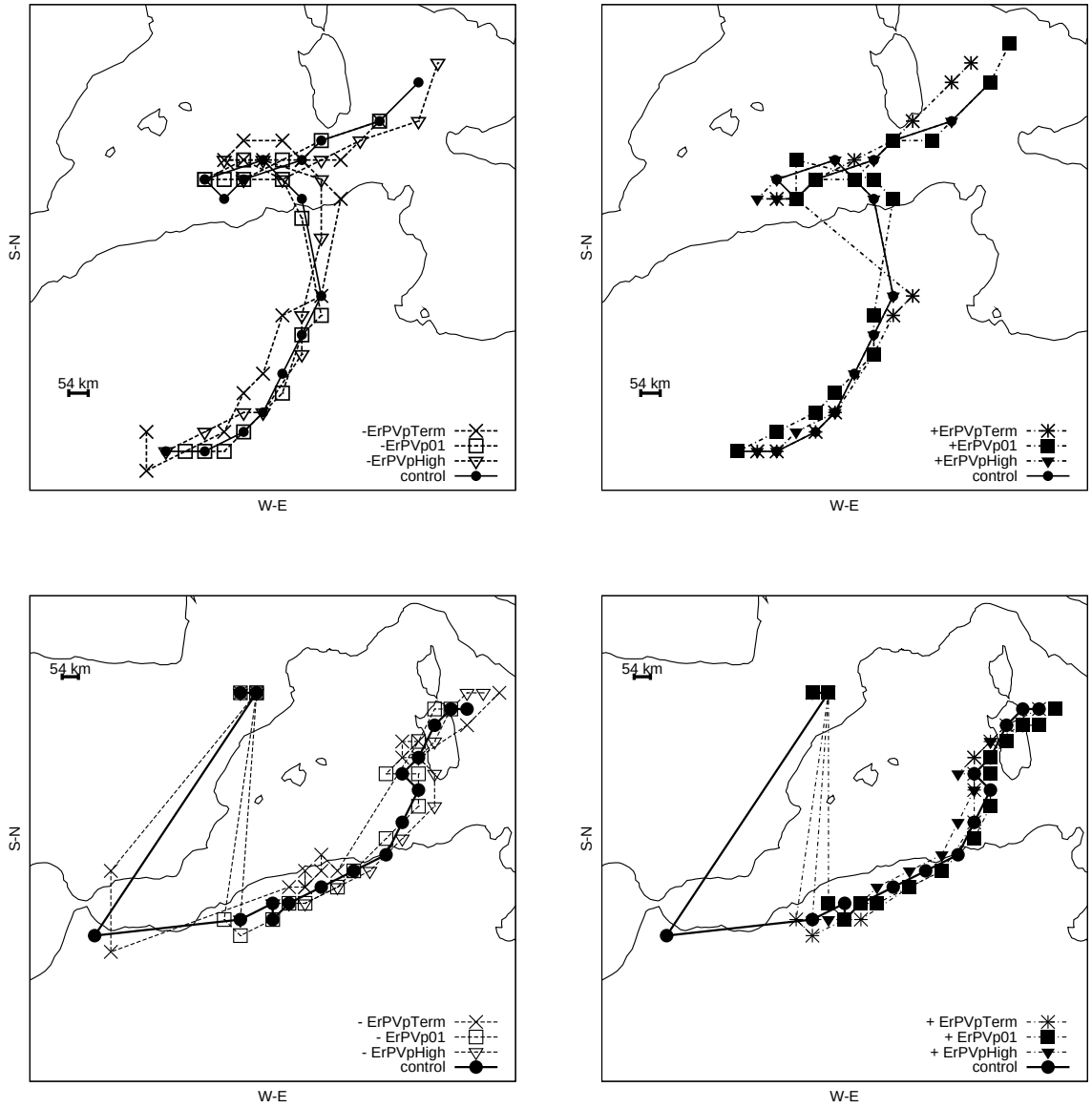

Figure 3.1.15: Top panels: Trajectories of the cyclone obtained from the initially perturbed simulations. Bottom panels: Trajectory of C0 for the different simulations. For the negative modifications (left), for the positive modifications (right). According to values on table 3.1.a. -ErPVpTerm (simple cross), +ErPVpTerm (full cross), -ErPVp01 (empty square), +ErPVp01 (filled square), -ErPVpHigh (empty triangle), +ErPVpHigh (filled triangle)

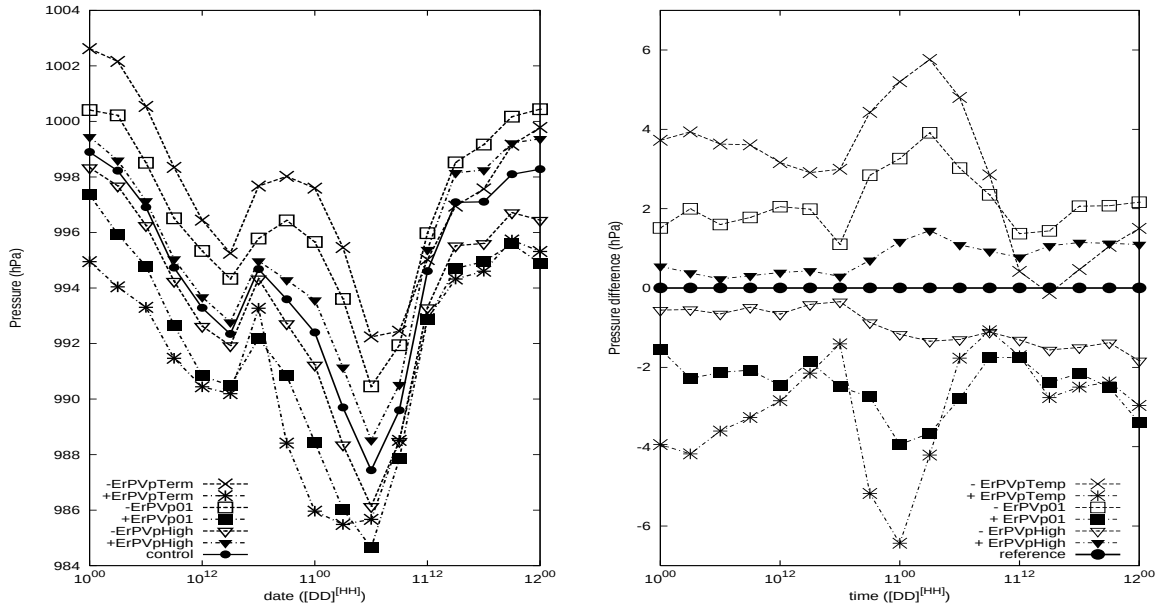

Figure 3.1.16: Labels as in figure 3.1.15, but Left panel: evolution of the central pressure of the cyclone. Right panel: evolution of the central pressure of the cyclone rescaled to control simulation results

At the same time, the simulated cyclones show strong variations in their vorticity (about $\pm 5\ s^{-1}$ at 200 km gridmesh point, in figure 3.1.18). As a result of the change in the initial position of the cyclone, the interaction between the upper and low level disturbances has also changed (the relative phase between the disturbances is significantly changed in comparison to the other simulations, figure 3.1.17).

In the -ErPVpTerm(+ErPVpTerm) case (perturbation of the initial conditions by subtracting(increasing) the fields related to the horizontal thermal anomaly) the initial trajectory of the cyclone is clearly different from the control one (see the two dashed lines with crosses in figure 3.1.15). The mature cyclones at Nov 11th 00 UTC show the largest variations with the control one: on the lowest central pressure value ($\pm 6\ hPa$, figure 3.1.16), relative distance with C0 (between 100-200 km in figure 3.1.17) and central value of the upper level trough C0 about 1 PVU less than in the control one, (figure 3.1.17). ErPVpTerm perturbations have a deep impact when the cyclone crosses the Atlas mountains, modifying the relation between the cyclone and the upper level trough. It is shown in the phase-relative-distance (figure 3.1.17). As result of it, the perturbed cyclone from -ErPVpTerm changes to a negative relative phase (C0 is located in an eastern position relative to the cyclone) 9 hours later than the +ErPVpTerm cyclone.

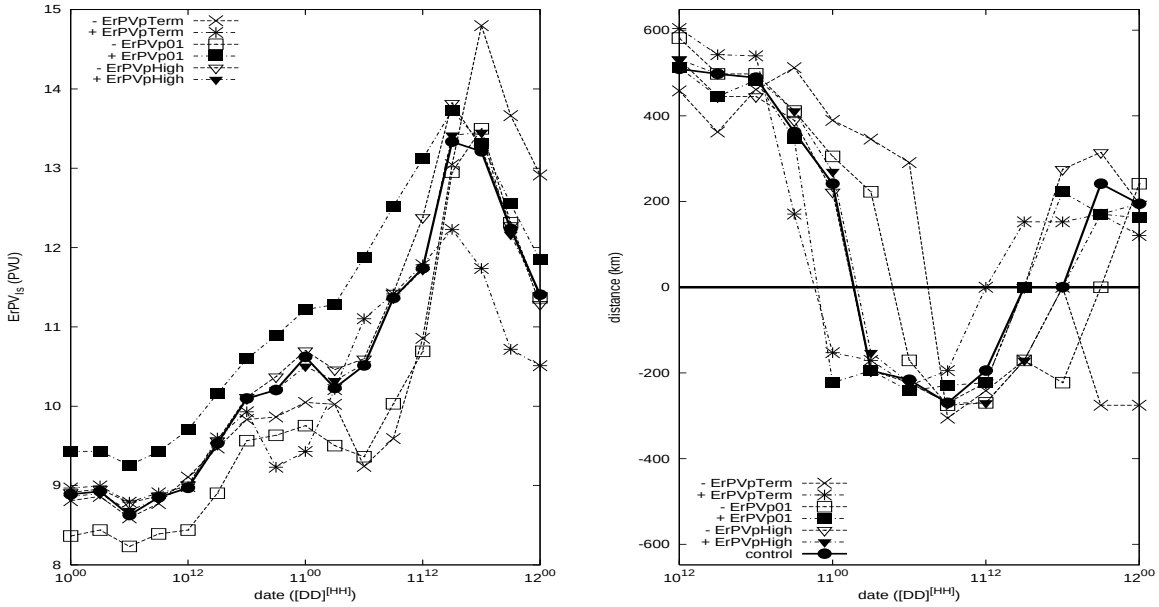

Figure 3.1.17: Labels as in figure 3.1.15, but Left panel: evolution of the C0 central value (PVU). Right panel: Evolution of the relative distance (km) between C0 and cyclone, positive(negative) sign denotes eastward(westward) relative position of the cyclone (starting date on Nov. 10th at 12 UTC)

Initially the C0 simulated from the ± ErPVpTerm perturbations are similar respect to the control one. However, at the mature state of the cyclone, C0 values are about 1 PVU lower (see figure 3.1.17). The strong differences may be related to the change of phase of the mutual interaction with the surface cyclone attributed to the baroclinic deepening processes. This aspect is also reflected in the +ErPVpTerm cyclone simulation. The cyclone exhibits a stronger vorticity than the control one (see figure 3.1.18) associated to a deeper cyclone and stronger North Atlantic high, which results in much stronger surface pressure gradients (see figure 3.1.14). During the dissipative phase of the cyclone (from 11th Nov. at 12 UTC to 12th Nov. at 00 UTC), the differences with the control cyclone become strong. The final position is clearly shifted about 54 km from control one on both cases (figure 3.1.15), the central pressure value is changed about $\pm 2hPa$ (figure 3.1.16), and final values of C0 are stronger (about $\pm 1.5PVU$, figure 3.1.17). At the end of the simulated period lower vorticity of the -ErPVpTerm cyclone is obtained because of the smaller dimensions of the cyclone in comparison to the +ErPVpTerm one (not shown). The strongest deepening of the cyclone occurred between Nov. 10th at 18 UTC and Nov. 11th at 06 UTC (see figure 3.1.16). In contrast with the strong sensitivity to the ErPVpTerm anomaly, the growth rate of the cyclone does not vary significantly (about -8 hPa/12 hours in positive case and -6 hPa/12 hours in the negative).

3.1.5 Sensitivity to to the Atlantic high pressure zone

The cyclones obtained in the simulations with the ErPVpHigh anomaly present the lowest sensitivities. The differences with respect to the control simulation are rather low until the last phase of the cyclone. The largest variations are obtained in -ErPVpHigh case. A weaker North Atlantic anticyclone (as a result of the -ErPvpHigh initial perturbation) can help to a faster movement of the Mediterranean disturbance, owing to a weaker blocking of the anticyclone. That is, a weaker North Atlantic high pressure zone might allow a faster movement of the cyclone and changes in the advections from higher latitudes. Final values of the C0 centre and relative distances between low and upper level disturbances do not differ from the control one (see figure 3.1.17), but final phase trajectories are significantly shifted from the control one (see lines with triangles in figure 3.1.15).

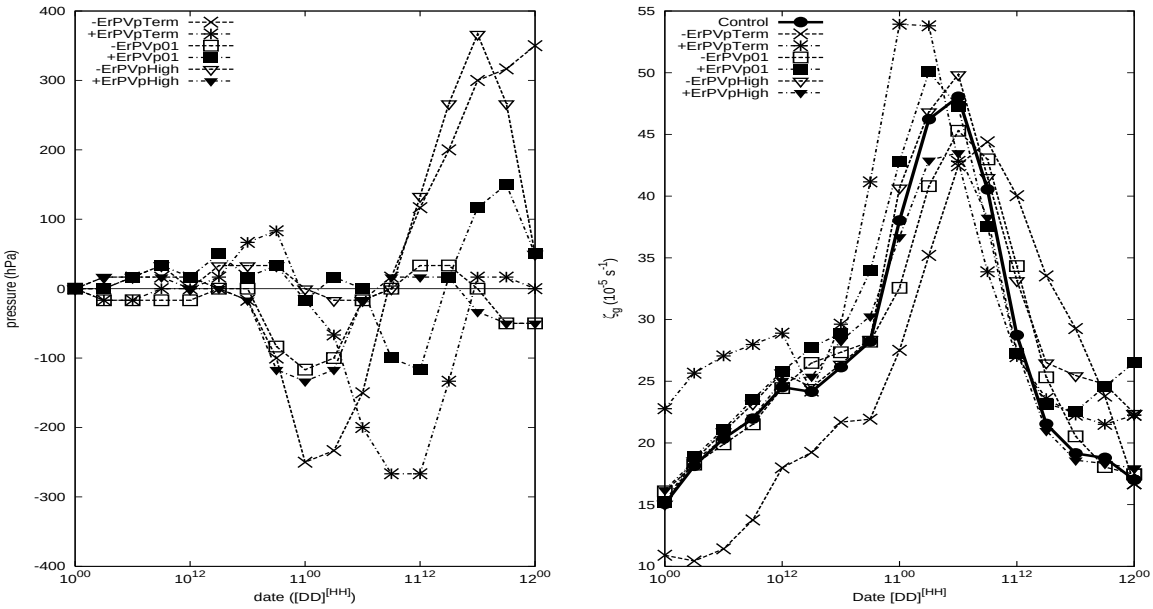

Figure 3.1.18: Labels as in figure 3.1.15, but Left panel: evolution of the depth of the cyclone rescaled to control simulation results (defined as the first minimal vorticity value above the centre of the cyclone, left). Right panel: evolution of the vorticity of the cyclone at distance of 200 km (defined like in (Campins et al., 2000)). Each figure has been temporally filtered through a mobile-average filter of 3 time-points

3.2 Intercomparison throughout Mediterranean basin

Mediterranean basin presents unique geographical and morphological characteristics that might derive to a cyclgonesis in the all basin with particularities and specific processes. The existence of a characteristic Mediterranean cyclogenesis could be shown with a climatology of roles and influences of some features involved in the cyclogenesis in the area.

In order to evaluate the cyclogenesis allover the basin a climatology of 'dynamical' aspects is made (Fita et al., 2006). It is investigated the possible similarities and differences among the selected cases of the relative weight of cyclogenesis. The study is done through the analysis of the role of cyclogenetic factors on the cyclone evolutions as function of cyclone type and geographical area.

The climatology is obtained from the study of eleven Mediterranean cyclones. As dynamical aspects, some evolving features of the atmosphere that are involved and related to the cyclone's evolution are considered: The upper level PV anomaly associated to the undulating tropopause (PVp above 700 hPa, with a relative humidity (RH) less than 70 %), the low level PV anomaly (PVp under 700 hPa, drier than 70 % together with surface thermal anomalies (Bretherton, 1966)) and the diabatically induced PVp (PVp below 500 hPa, with humidity higher than 70 %). The inclusion in the study of diabatically induced PVp aims to isolate the effects associated with latent heat release in the cyclone cloudy structure. The thermal anomaly induced by massive water vapour condensation at mid-upper tropospheric levels enhances the static stability above and this is reflected as a distinct PV positive anomaly (Hoskins et al., 1985; Davis and Emanuel, 1991)

The eleven selected cyclones have been chosen from the MEDEX[1] data base. This data base has been constructed from contributions of different National Weather Services, research institutes and universities of the entire Mediterranean basin. The cyclones have been classified in terms of their social impact. These 11 cases (see table 3.2.a) have been chosen from the most severe MEDEX group, usually involving deep cyclogenesis. These cases have been selected trying to encompass all the Mediterranean basin. Cyclones have been classified according to a geographical area of evolution and to a typology of formation. Geographical classification is chosen from three main areas of the Mediterranean basin: Western (from Eastern coast of Iberian peninsula until Sardegna-Corsica Islands), Central (from Sardegna-Corsica Islands until Peloponnese) Eastern (from Peloponnese until Middle-East). Has been determined three typologies of formation of the cyclone: Alpine lee (cyclogenesis at the lee of the Alps mountains), African (cyclone originated in the north African region) and Marine (cyclogenesis above the sea).

The dynamical study is based on solving the geopotential height tendency due to

[1] `http://medex.inm.uib.es`

Table 3.2.a: Table of the 11 selected cases. 1st col. indicates the name of the case ([DD]/[MM]/[YY]), 2on col. indicates the date of cyclone's mature state ([DD]/[MM]/[YY]) and P_{min} indicates minimum central pressure value (hPa) and corresponding time according to ECMWF analysis. 3rd col. indicates the Mediterranean region where the cyclone evolved. 4th col. indicates cyclogenesis area

Case	**maximum depth** (P_{min})	**Med. region**	**cyclone type**
6-9/10/96	7/10 06 (1003.6)	Central	Alpine lee
16-18/03/98	16/03 00 (984.1)	Eastern	African
6-9/11/99	7/11 06 (997.5)	Central	Alpine lee
13-16/10/00	15/10 06 (1001.9)	Western	African
9-13/11/01	11/11 00 (993.0)	Western	African
23-24/11/01	25/11 12 (989.3)	Eastern	Alpine lee
3-4/12/01	2/12 12 (997.7)	Eastern	Maritime
14-15/12/01	14/12 00 (1005.5)	Western	Maritime
6-8/05/02	7/05 00 (993.0)	Western	African
13-14/07/02	14/07 00 (1002.8)	Central	African
8-10/10/02	12/10 06 (997.8)	Western-Central	Maritime

the different factors using the prognostic system of equations proposed by Davis and Emanuel (1991) see section 2.2.2. Via this PV-based set of prognostic equations, the impact of each PV anomaly could be studied by switching on and off those anomalies in the atmospheric state and combining the results for the height tendency using the Factor Separation technique (Stein and Albert, 1993). Both, the individual effects as well as their mutual interactions could be properly isolated with such methodology. The methodology is solved on ECMWF global analyses fields (every 6 hours) that comprise all the period of evolution of each cyclone.

This methodology contributes widen the perspective of the dynamical aspects of the cyclones. A large variety of Mediterranean cyclonic climatologies have been done (Campins et al., 2000; Picornell et al., 2001; Campins et al., 2006). All of these climatologies have been focused in morphological aspects of the cyclones such as central pressure value, vorticity and trajectories. The methodology based on the geopotential height tendency gives information about the dynamical processes involved in the cyclone evolution. Dynamical aspects are shown as their direct or interaction effect on the evolution of the cyclone. These effects or synergies are objectively quantified trying also to give some information about the couplings between features that are involved in the cyclogenesis. By this way a new main view of the dynamics of the cyclogenesis in the Mediterranean basin can be obtained. Detailed information of the principal features of the cyclogenesis

is given once one have selected and detected the most important ones. That allows to made intercomparisons of the roles of the same features involved in different cases. At the same time can be found the existence of specific characteristics of the cyclone evolution in the Mediterranean basin.

3.2.1 Description of cases

Each case represents a different cyclone evolution over the Mediterranean basin. Their major characteristics are briefly described (see MEDEX database for more details at `http://medex.inm.uib.es`) as well as depicted trajectories in figures 3.2.1 to 3.2.11:

1. *6-9/10/96*: An upper level cut-off evolved into the Mediterranean basin, from which the cyclone was created off the coastal line of Algiers. The eastward progression of the cut-off produced an evolution of the cyclone over the sea toward the east.

2. *16-18/03/98*: A north African thermal low was developed to the south of the Atlas mountains. Through the interaction with an upper level trough, the cyclone moved over the Sahara desert and entered into the Mediterranean Sea across the Egyptian coast when it reached the mature state.

3. *6-9/11/99*: This cyclone can be considered as an Alpine-lee cyclogenesis (Buzzi and Tibaldi, 1978). The mature cyclone moved Southeastward over the Mediterranean Sea.

4. *13-16/10/00*: A thermal low over African plateau interacted with an upper level trough. The cyclone moved toward the Mediterranean Sea over Algiers following a northward trajectory. When the cyclone reached the sea, the low reached the mature state.

5. *9-13/11/01*: This case is very similar to the previous one (*13-16/10/00*). In this case the cyclone is deeper and stronger.

6. *23-24/11/01*: The cyclone presented two phases. An Alpine-lee cyclone moved from the Golf of Genoa following the Adriatic Sea forced by an upper level trough. Meanwhile the upper level trough became a cut-off, the cyclone moved then northeastward and reached the Black Sea where it attained its mature state.

7. *3-4/12/01*: A low latitude upper level disturbance induced a cyclone over the Cyprus island region. The cyclone stayed on the region during all its life cycle.

8. *14-15/12/01*: An upper level cut-off moved southwestward from the Central Europe region. As a result, a cyclone was developed on the lee of the Alps mountains.

9. *6-8/05/02*: Another case similar to *16-18/03/98* where the interaction between an African thermal low and an upper level trough induced a cyclone which reached the mature state when it entered in the Mediterranean basin in front of the coast of Algeria.

10. *13-14/07/02*: A thermal North African cyclone interacted with an upper level trough. In this case the cyclone moved into the Mediterranean basin across the coastal region of Tunis, and moved northward to Balkan countries.

11. *8-10/10/02*: An Atlantic cyclone moved southeastward owing to the southeastward movement of an upper level trough. The cyclone crossed the north of Spain and moved eastward along the Mediterranean Sea reaching Greece.

In this case the following effects are isolated and labelled as (See section 2.3 for the meaning of the effects):

- E_0: Effect of the Background flow
- E_1: Effect of the Upper level PVp (P <700 hPa, RH<70 %)
- E_2: Effect of the Low level PVp (P >700 hPa, RH<70 %)
- E_3: Effect of the Diabatic PVp (P >500 hPa,RH>70 %)
- E_{ij}: Effect of the synergy E_i & E_j
- E_{123}: Effect of the synergy of the three anomalies

The study is focused on the effects of each factor on the most relevant total geopotential height tendency signal (at 925 hPa) that governs the cyclone evolution from its genesis to its decay. The most relevant geopotential height tendency zone responsible for the cyclone evolution is detected at each time-step. Geopotential height tendency and sea level pressure fields are visually intercompared in order to detect the most related geopotential height tendency to the cyclone evolution. Most related geopotential height tendency zone has been selected in two ways: as the closest enclosed tendency zone or the enclosed tendency zone where the cyclone moves the next step. This geopotential zones are defined as an enclosed tendency threshold and/or geometrical line defined sections of the tendency. A spatial-average of the effects of each factor/interaction on the selected height tendency is depicted for each time-step. By this way effects should reflect the evolution of the characteristics of the cyclone and/or its movement. Negative values indicate deepening and/or movement of the cyclone, whereas positive values would act to fill or slow the disturbance.

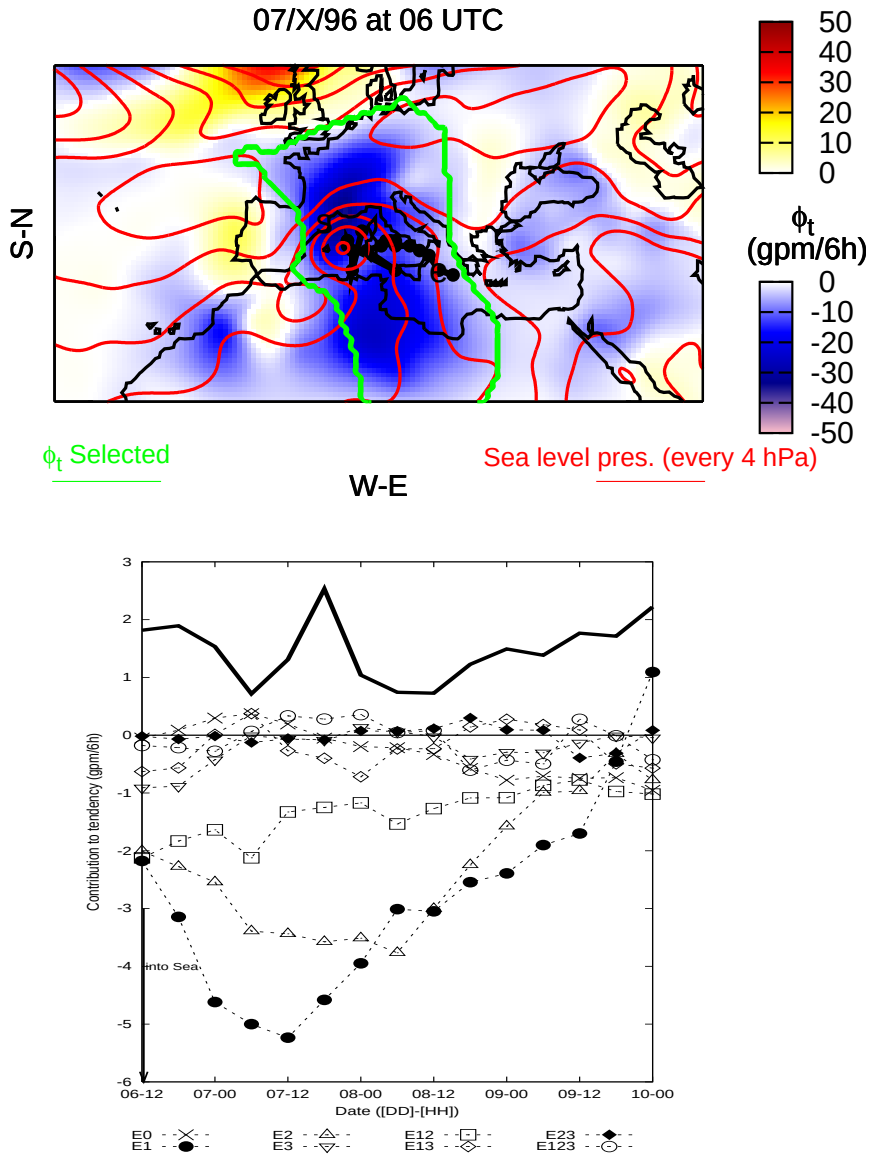

Figure 3.2.1: 'Alpine lee' & Central Mediterranean case 6-9/10/96. On left panel: Cyclone trajectory (solid thick line with circles), ϕ^t at 925 hPa (white to red positive, white to blue negative, every 10 gpm/6h), Sea level pressure (dot line, every 4 hPa) and geopotential height tendency signal used to compute the effects (thick dash-dot line) at mature cyclone time. Labels indicate starting (s) and ending (e) central cyclone position. Right panel: Evolution of the space-average tendency by each factor/interaction filtered with a three-step moving filter (dashed lines, and corresponding symbols as defined in bottom figure). Black arrows show when the cyclone reached/left the Sea. The cyclone central pressure evolution is shown as the solid thick upper line (no scale).

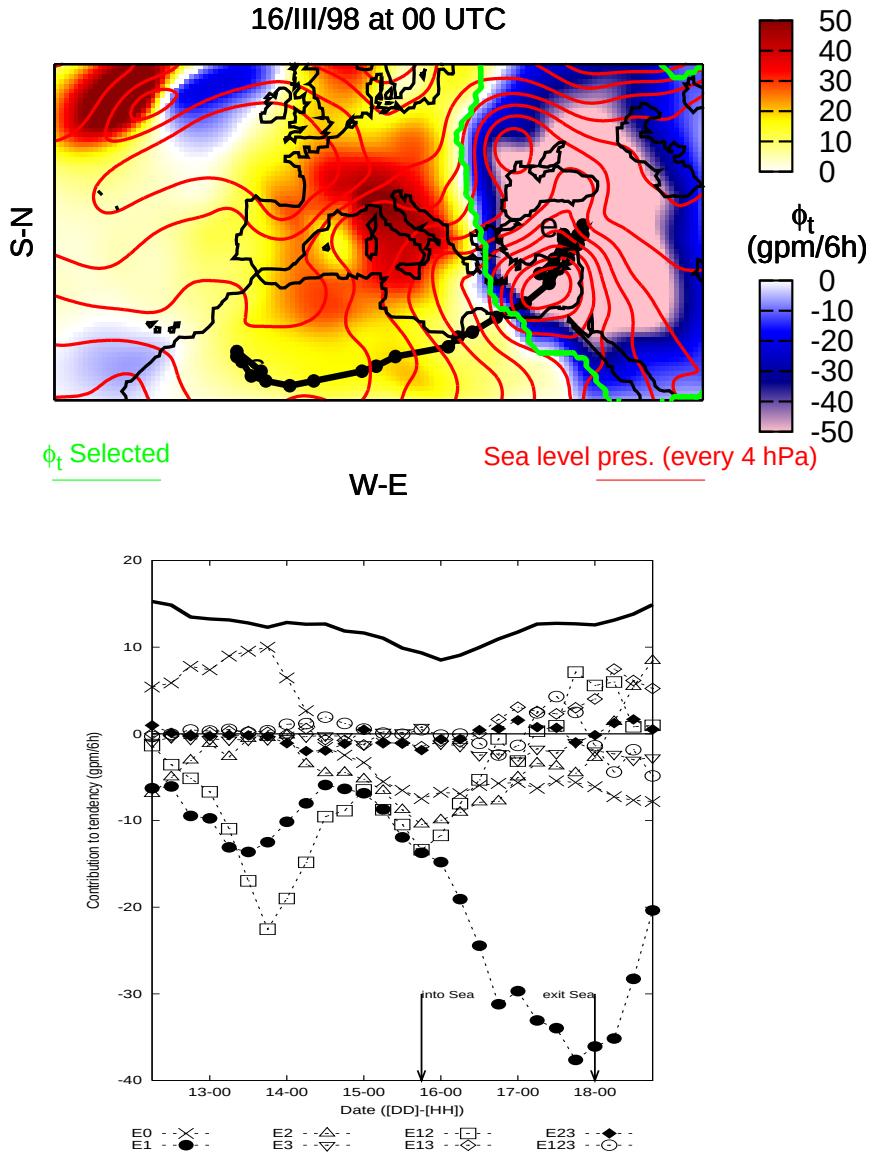

Figure 3.2.2: As in figure 3.2.1 for 'African' & Eastern Med. case 16-18/03/98

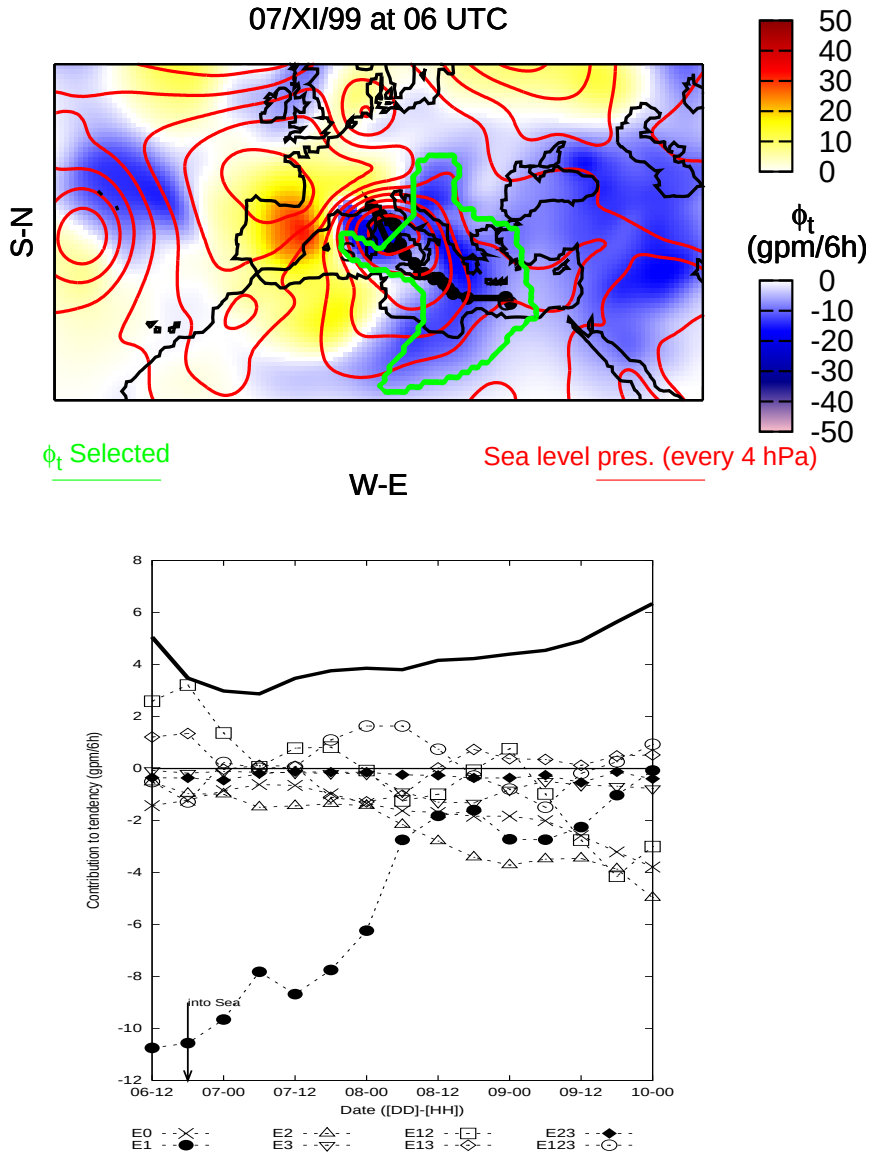

Figure 3.2.3: As in figure 3.2.1 for 'Alpine lee' & Central Med. case 6-9/11/99

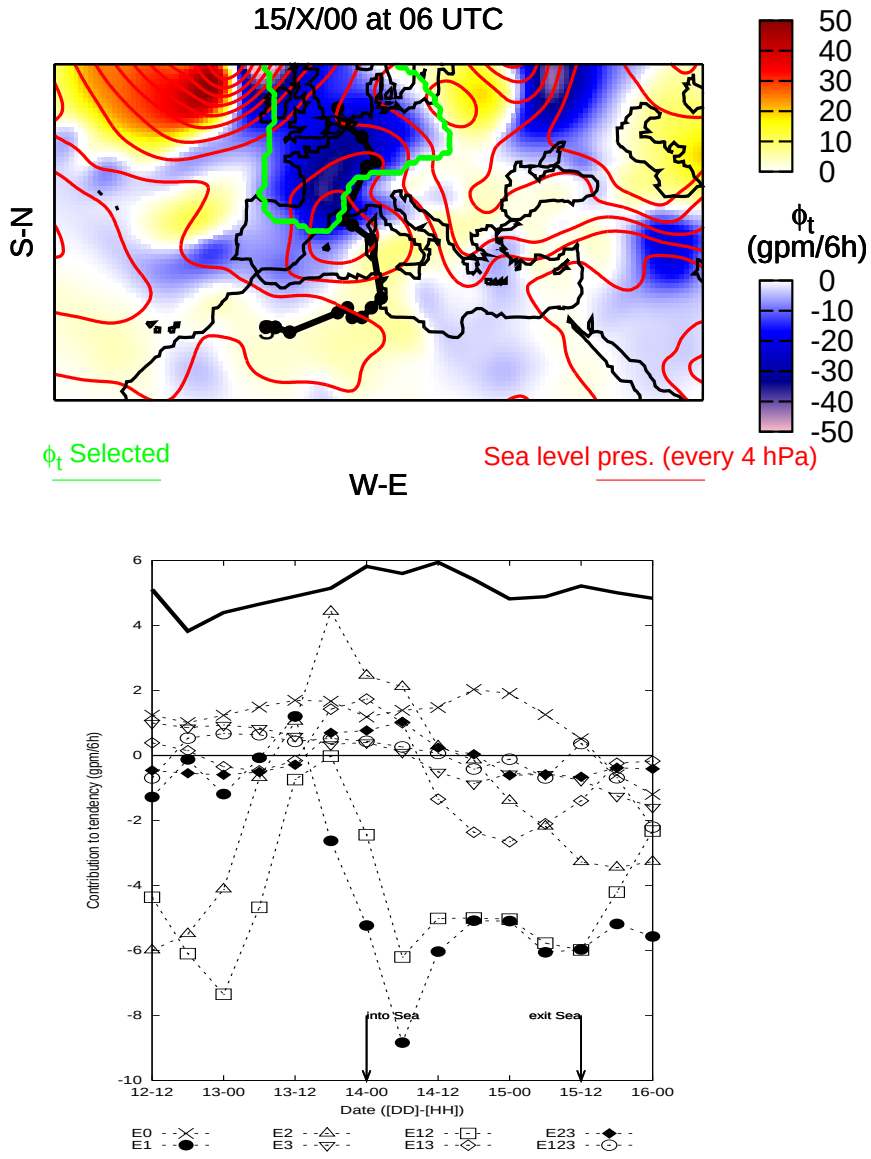

Figure 3.2.4: As in figure 3.2.1 for 'African' & Western Med. case 13-16/10/00

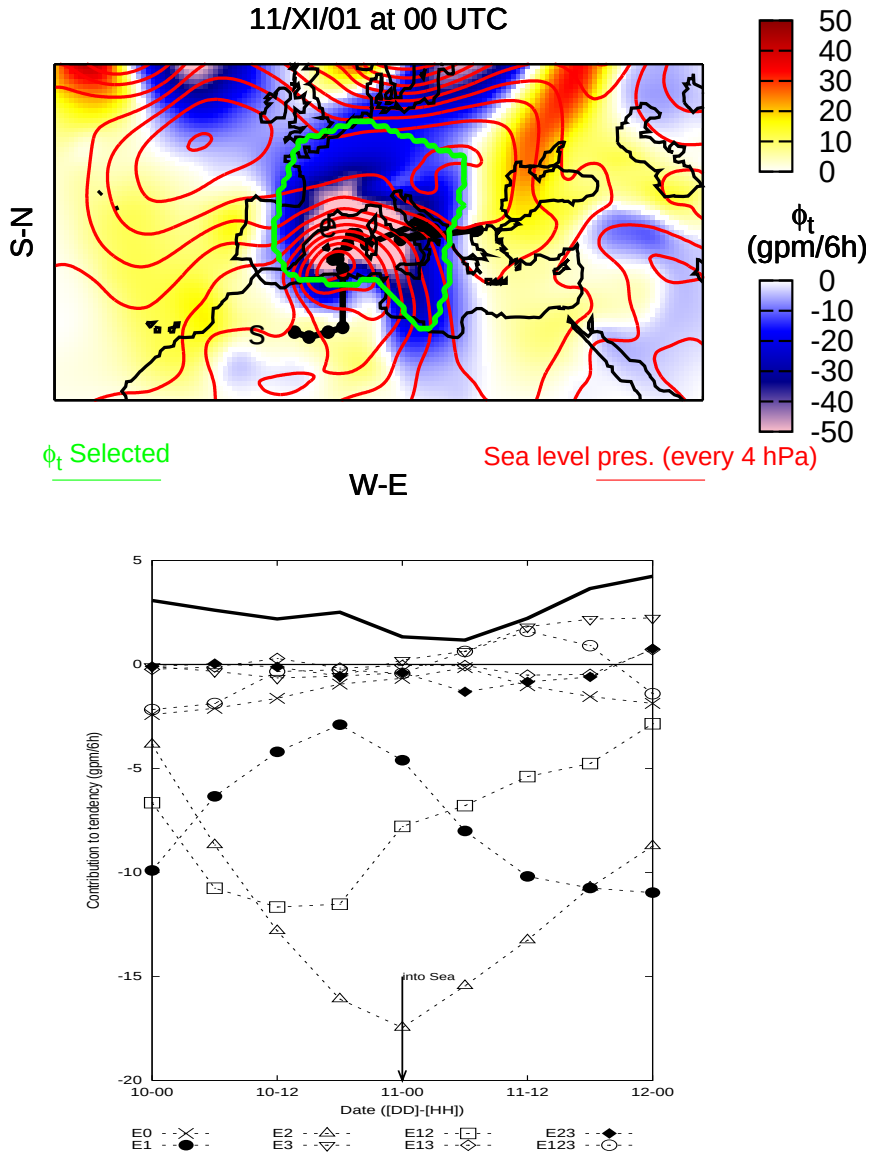

Figure 3.2.5: As in figure 3.2.1 for 'African' & Western Med. case 9-13/11/01

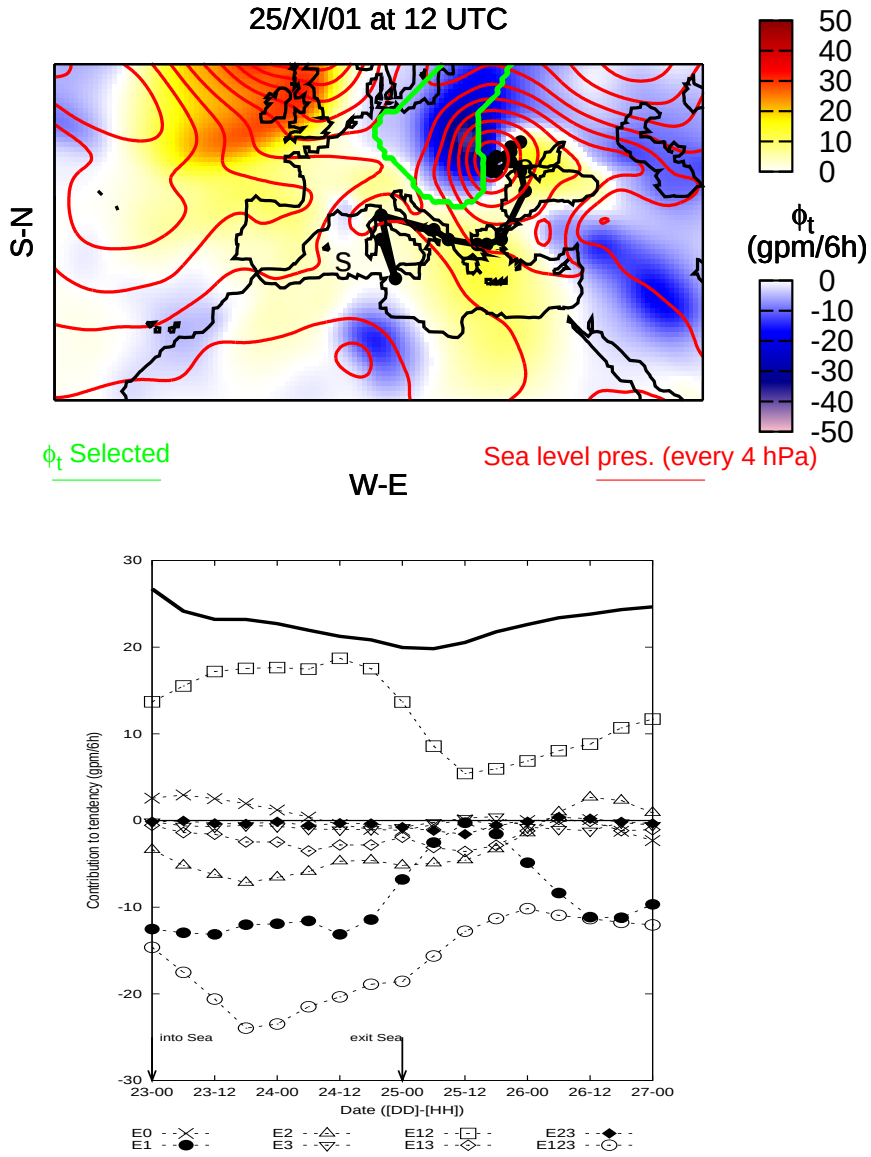

Figure 3.2.6: As in figure 3.2.1 for 'Alpine lee' & Eastern Med. case 23-24/11/01

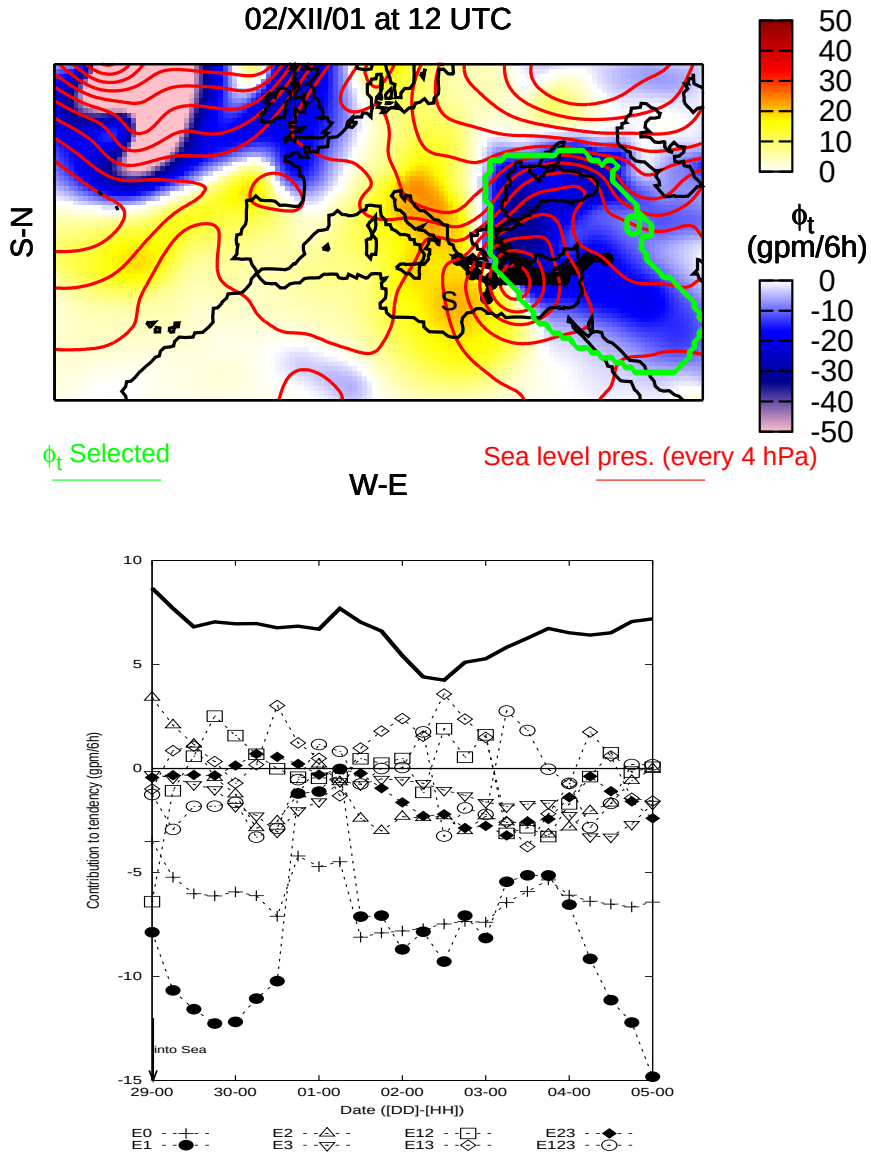

Figure 3.2.7: As in figure 3.2.1 for 'Maritime' & Eastern Med. case 3-4/12/01

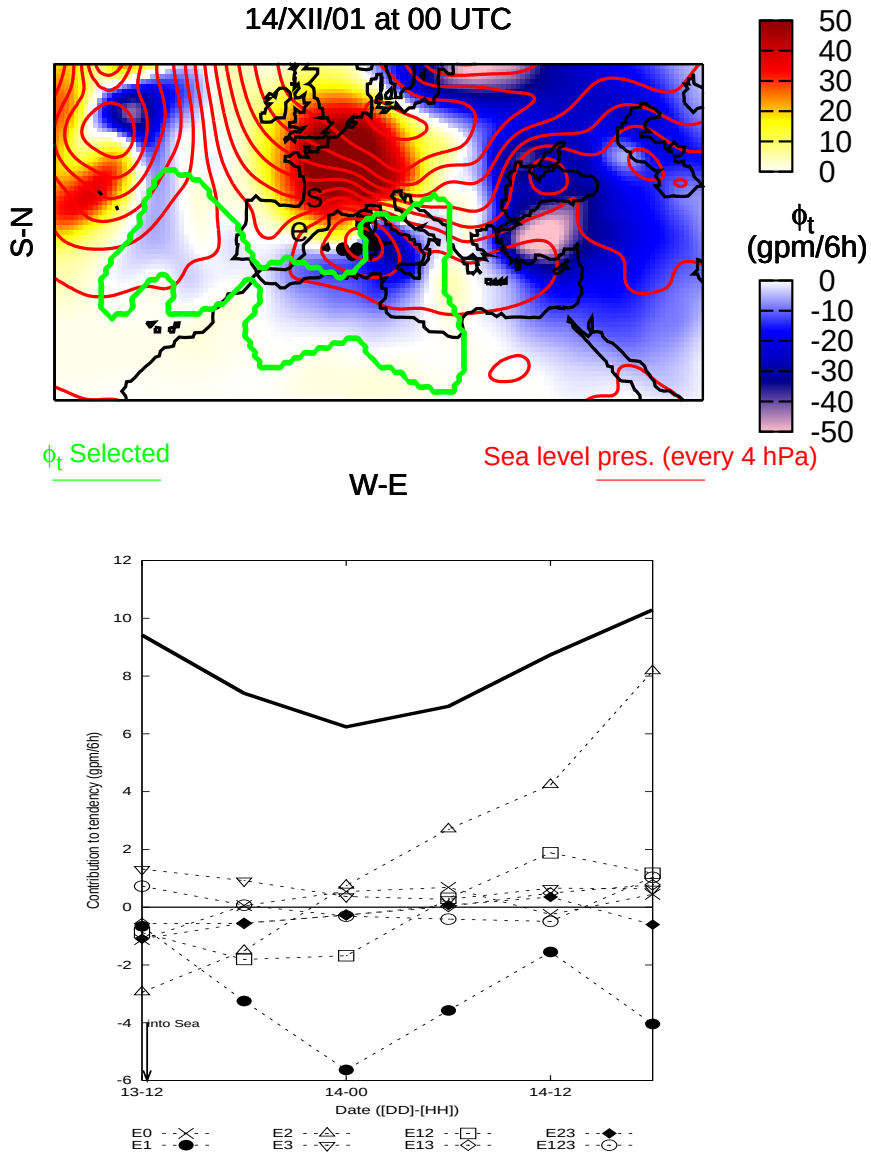

Figure 3.2.8: As in figure 3.2.1 for 'Maritime' & Western Med. case 14-15/12/01

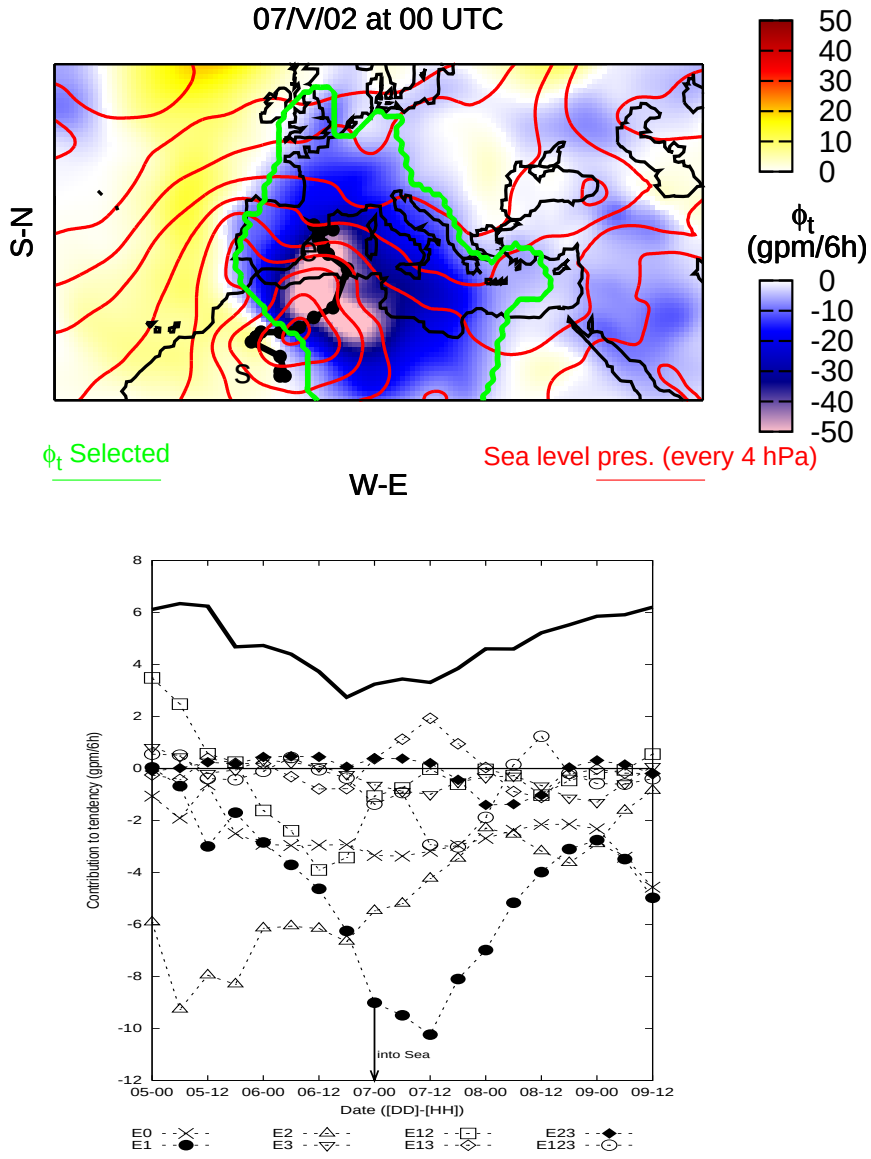

Figure 3.2.9: As in figure 3.2.1 for 'African' & Western Med. case 6-8/05/02

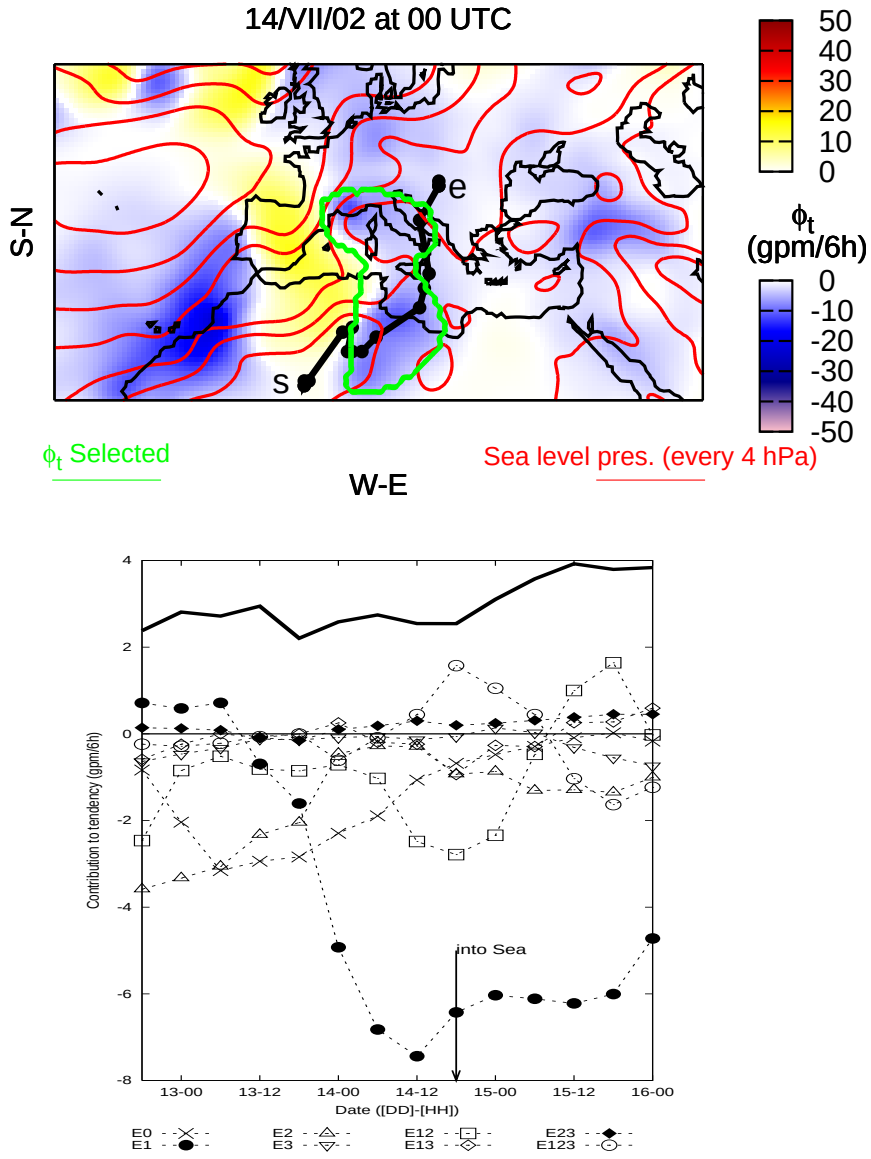

Figure 3.2.10: As in figure 3.2.1 for 'African' & Central Med. case 13-14/07/02

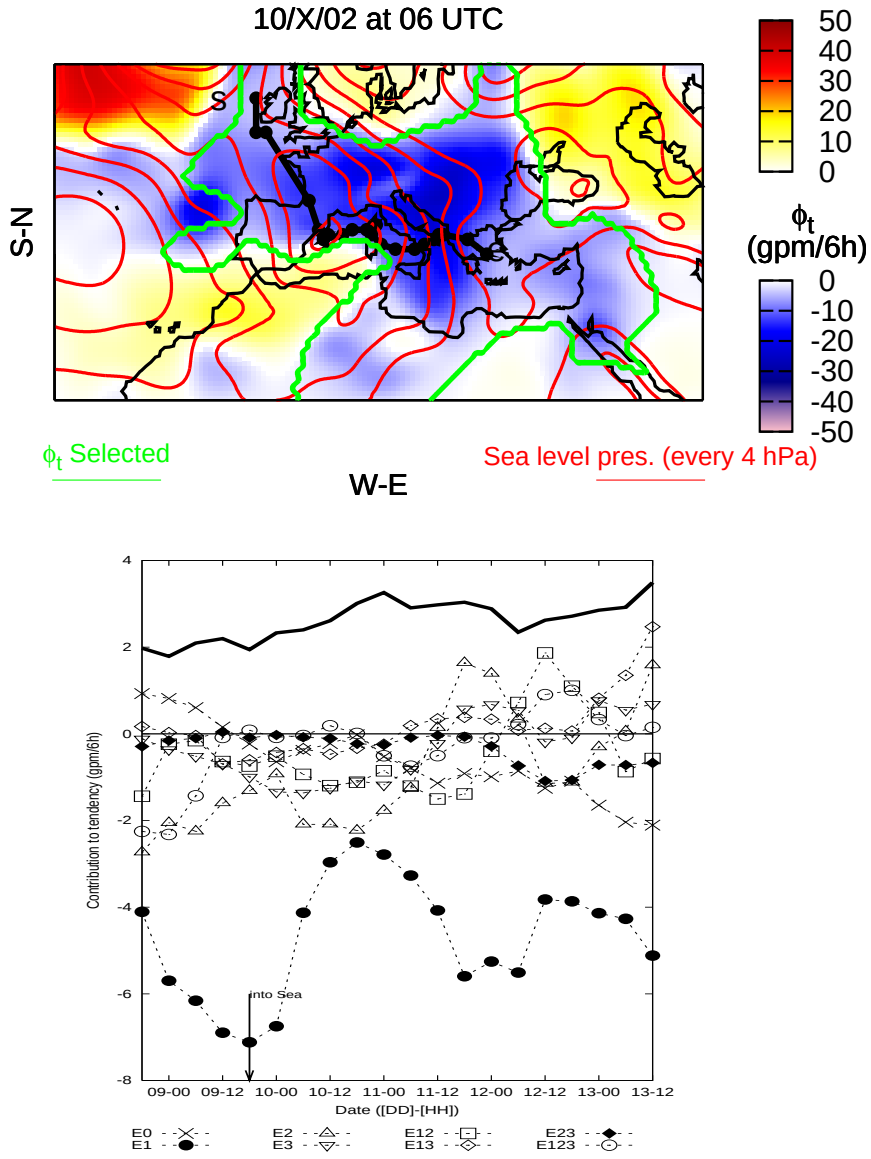

Figure 3.2.11: As in figure 3.2.1 for 'Maritime' & W-Central Med. case 8-10/10/02

3.2.2 Results

From figure 3.2.1 to 3.2.11 the results for each cyclone are shown. The results are generally case dependent with respect to the importance of the selected effects and the role of each one. However some conclusions can be emphasised: Generally the upper level PVp (effect E_1) is the most relevant (showing the important role of the baroclinicity over the Mediterranean basin, like in 13-14/7/02 and 14-15/12/01 cases). It is noticeable that in almost all of the selected cases a significant upper level trough or cut-off was present during the cyclone evolution (not shown).

Low level PVp (E_2) & synergy E_{12} mainly play secondary roles (like in cases shown in figures 3.2.4, 3.2.5 and 3.2.11). This result depicts the importance of the role of the dry low level PV. Positive surface layer PV can be related to a surface layer thermal anomaly (Bretherton, 1966). Many times a surface thermal anomaly is evolves into the baroclinic development of disturbances. Low level PV might be also related to a surface thermal anomaly and at the same time to the thermal anomaly associated to the cyclone (in some Mediterranean cases related to the North African warm and dry plateau).

The background flow (E_0) is mainly responsible for the displacement of the disturbance (e.g. in figure 3.2.10 of case 13-14/07/02; where this weak cyclone moved northward due to general circulation reflected by this factor). In this case, cyclone does not follow an usual eastward movement due to influence of an upper level trough elongated meridionally (see figure 3.2.12).

The effects related with the diabatically induced PVp (E_3, E_{13} and E_{23}) present the lowest contribution, even for the cyclones presenting high deepening process when reaching the sea (leading to mature state) like in figures 3.2.2 and 3.2.5. Note that the above effects are related with the role of diabatically-generated PV, not with the diabatic forcing itself as it is included in the right hand sides of equations 2.2.19 and 2.2.21. Thus PV at low levels might reflect a part of the diabatical aspects of the latent heat release due to strong cloud formation. Moreover ECMWF analyses (with a grid mesh of about 0.3 degrees) could be not fine enough to capture this effect as positive PV at low level with high moist values. Explicit consideration of the diabatic terms of the equations as new factors should be developed in order to confirm these hypothesis.

Factors are often cyclogenetic and cyclolitic probably owing to different phases of evolution of the cyclone or to the complex topographical configuration of the basin and other evolving interactions involved in baroclinic developments. One of these influences is the upper-level-low level interaction (Hoskins et al., 1985). For example E_2 and E_{12} change sign in 8-10/10/02 case owing to the change of vertical tilt of the upper and low level disturbances (see figure 3.2.13). Another kind of influence is the cyclone position

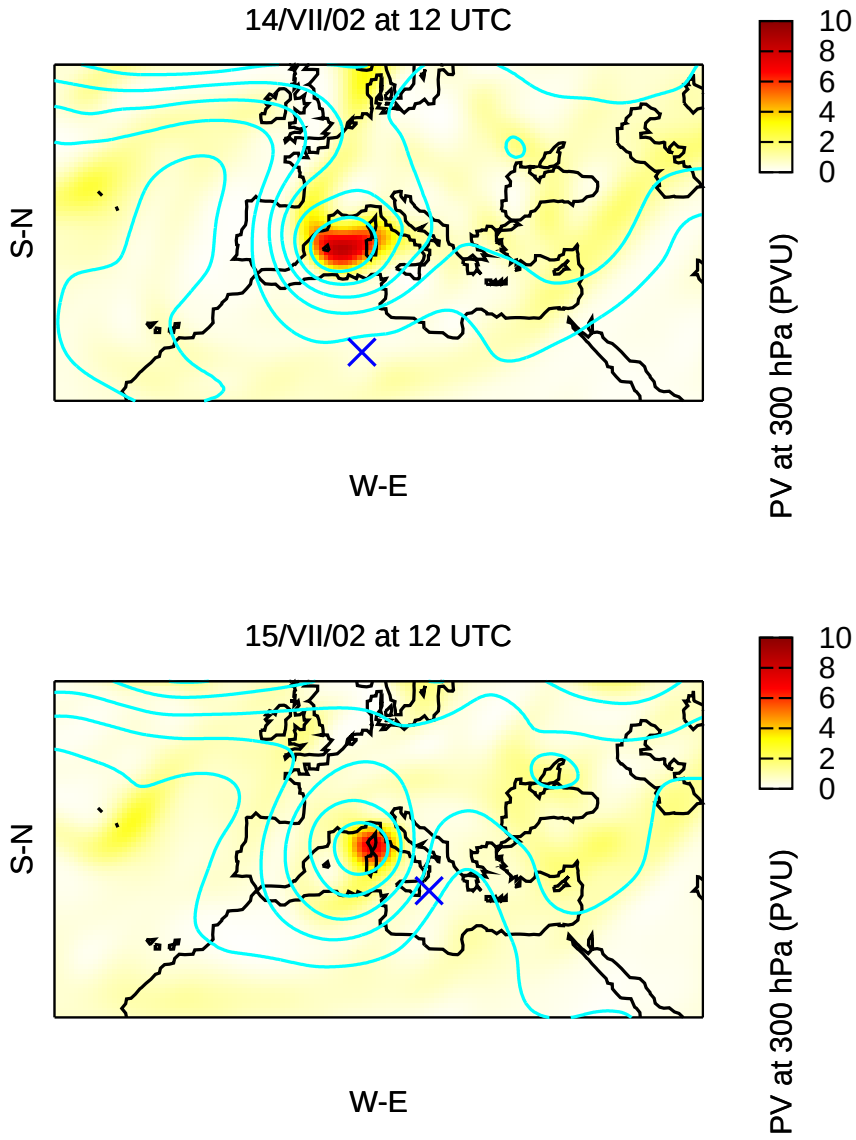

Figure 3.2.12: Potential Vorticity at 300 hPa (dashed), geopotential height (every 50 gpm, solid light blue line) and position of the centre of cyclone (blue cross) for the 13-14/07/02 case on 14th at 12 UTC (left) and on 15th at 12 UTC (right)

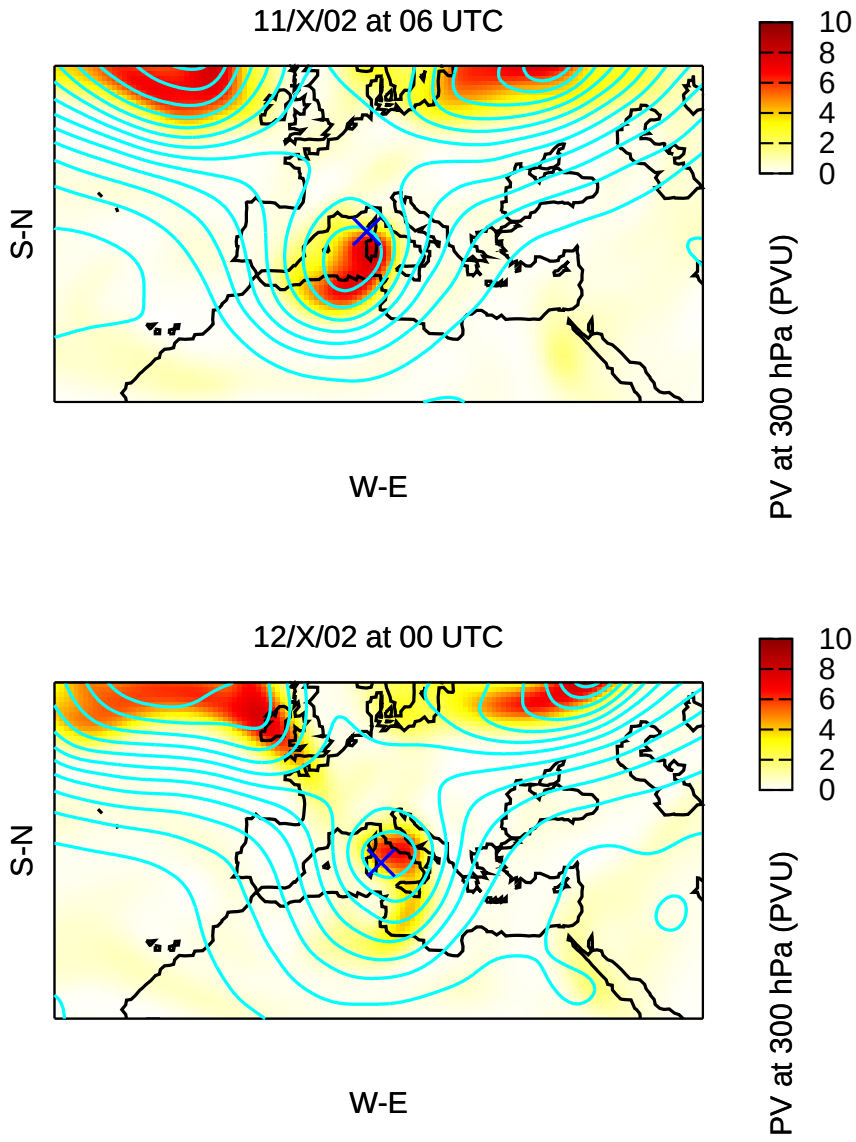

Figure 3.2.13: As in figure 3.2.12, but for the 8-10/10/02 case on 11th at 06 UTC (left) and on 12th at 00 UTC (right)

relative to the orography and background flow. For example, E_0 became cyclogenetic until the cyclone moved over the Tunis planes on case 16-18/03/98. At this time-step (about 14th 12 UTC), background flow loses its cyclolitic role in the cyclone evolution. It is notorious to see that background flow is in leeward geographical disposition with Atlas range. However, cyclone is a little bit further of the lee cyclogenetic ideal position (see figure 3.2.14).

Cyclogenesis events in the Mediterranean have often been classified attending to affected geographical zone, social impact, NWP performance and/or deepening rate (e.g. MEDEX database, see `http://medex.inm.uib.es`). In this work the emphasis is made on the role of evolving and interacting dynamical aspects of the synoptic-scale circulation as represented by PV anomalies, and it is hoped that the approach can be extended and refined to perform a dynamical climatology of deep cyclogenesis events in the Mediterranean basin. The results presented do not close the question, but seem to indicate that some dynamical differences in Mediterranean cyclogenesis can be related to the nature and track location of the disturbance.

3.2.3 Geographical sensitivity

Western & Central Mediterranean cyclones seem to be mainly dominated by PV anomalies E_1, E_2 and their synergy E_{12} (as is shown by 3.2.5). In contrast eastern Mediterranean cyclones show a non unique principal factor dependence. They are dominated by a variety of effects of distinct nature like E_{12}, E_1, E_{123} or E_0 as it is shown in figures 3.2.2 and 3.2.6. This apparent regional characteristic of the Mediterranean cyclones could be attributed to the different kinds of cyclone owing to the origin of formation that present different influences with large variety of characteristics. Western and central cases are mainly North African plateau and Alps lee cyclones. However, the Eastern cyclones present different genesis zones and trajectories. Eastern geographical area presents the most extent maritime area without any large orographical or island influence. Moreover, South-Eastern part of the Mediterranean basin is basically constituted by desertic plains and Crete and Cyprus islands are the major islands.

3.2.4 Dynamical sensitivity

'African' cyclones (like in figures 3.2.2 and 3.2.10) are mainly dominated by Upper level disturbances (factor E_1) or the synergy E_{12}. 'Maritime' cyclones (shown in figures 3.2.7 or 3.2.11) seem to be dominated mainly by E_1 and in lower degree by the background flow (E_0 effect). This should reflect the inexistence of orographic features that might influence in the synoptic driven trajectory of the cyclone. The selected 'Alpine Lee' cyclones (like in figures 3.2.1 and 3.2.3) seem to present three phases: an initial dominated by the role of the upper level tropopause disturbance (factor E_1), a second one dominated by E_2 prob-

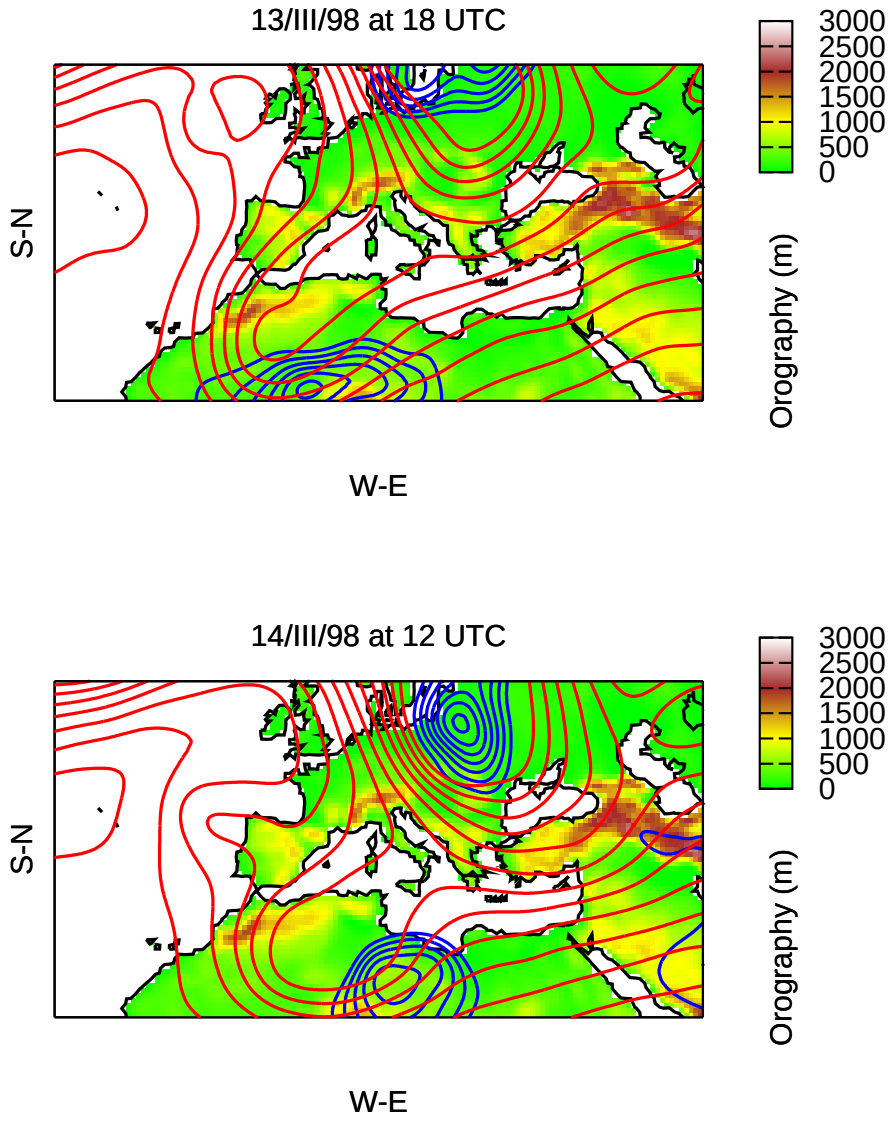

Figure 3.2.14: Orography (dashed) geopotential height at 500 hPa (every 50 gpm, solid red line) and sea level pressure (every 2 hPa lower than 1010 hPa, solid blue line) for the 16-18/03/98 case on 13th at 18 UTC (left) and on 14th at 12 UTC (right)

ably related to the induced PV banners of a lee cyclogenesis, and later maritime phase dominated by E_2 probably due to the role of the moist processes. Finally it is sometimes obtained a compensation between large cyclogenetic and cyclolitic effects (e.g. E_{123} and E_1 cyclogenetic effects are compensated by E_{12} and E_0 on 23-24/11/01 case during the initial steps of the evolution of the cyclone).

A larger and deeper study should be done with more cases in order to obtain more general results and better representation of the population of cyclones over the Mediterranean Sea. However, the presented approach, carried out with 11 cases, attempts to correct the lack of number of cases with the election of an appropriated set of cases that incorporate cyclones of different geographical areas and different dynamical evolution. At the same time wider number of factors should be used to ensure a correct capture of the most important features involved in the Mediterranean cyclogenesis.

Chapter 4

Thermal and topographic lee influences

Articles on which this chapter is based:

E. García-Ortega, L. Fita, R. Romero, L. López, C. Ramis and J.L. Sánchez, 2007: *Numerical simulation and sensitivity study of a severe hail-storm in northeast Spain*, Atmos. Res., **83**, 225-241

K. Horvath, Ll. Fita, R. Romero and Branka Ivancan-Picek, 2006: *A numerical study on the first phase of a deep Mediterranean cyclone: Cyclogenesis in the lee of the Atlas Mountains*, Meteorologische Z. 1, **15**, 133-146

4.1 Thermal influences

In specific regions, where a strong isolation is reproduced, lows can be generated. As a result of strong and continuous radiation, land surface can be strongly heated. Air above the surface is also heated and reach high temperatures. Increase of the buoyancy produce an upward motion of the air, decreasing the surface pressure. This cyclogenetic mechanism is known as the thermal-low (Alonso et al., 1994), due to the thermal origin of the cyclone. This could be the case of the initial surface disturbance of two studied cases: November 9-12th 2001 case and November 11-14 2004 case. In both cases, a weak surface disturbance was present above the hot and dry North African plateau south of the Atlas mountains.

The increasing of buoyancy due to solar radiation might have an effect as precursor of strong convection. At the end of a diurnal period with strong isolation, air above the surface may be very unstable and in the afternoon deep convection, heavy rain or even extreme weather can be developed. This peculiarities are very common for example in the Iberian peninsula during summer (Font, 1983). As an other consequence of the increase of buoyancy, in strong isolated regions weak and shallow lows are frequently generated (Campins et al., 2006). Convective phenomena usually have local characteristics and their effects usually affect small areas. In some locations this solar triggered convection might have local influences. One of this zones is the central part of the Ebro river basin (see figure 4.1.1).

The Ebro river basin run allover the Northwestern part of the Iberian peninsula and it is orientated NWSE. The Ebro is valley is bordered by the mountainous range of the Pyrenees to the north, the Iberian mountainous System to the southwest, and the Mediterranean Sea to the east (see figure 4.1.1). Due to its topographical characteristics, the Ebro basin is a corridor for the entrance of two types of air masses: one cold downward the basin of Atlantic origin, and another one of warm and moistened air flowing upward the Ebro basin incoming from the Mediterranean Sea.

Usually these two air of masses merge in an area of the basin known as the Central Ebro valley. The convergence of these two types of air masses is reproduced in an area in which high temperatures are registered during the summer months. By this way triggering effects of the solar radiation at the end of the day can be enhanced due to the convergence of these two air masses. This peculiar configuration makes hailstorms a frequent phenomena during these months. In fact, the Ebro Valley is one of the areas in Europe with the highest number of cases of severe convective phenomena. There are 20 thunderstorms per year in the southern part of the Valley (Font, 1983). These storms are usually of the warm-based cloud type (Sánchez et al., 1999) and most of them can be classified as multicellular, whereas supercells only represent 3% of all cases (Sánchez and Fraile, 1992).

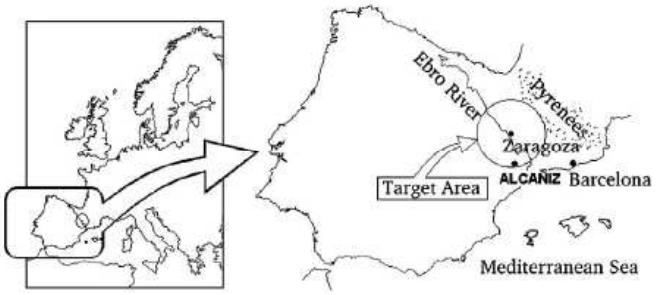

Figure 4.1.1: Target area

Font (1983), basing his studies on the analysis of maps on a synoptic scale, attributes the development of thunderstorms to the release of latent instability by strong surface heating. This author claims that the topography plays a fundamental role in this development when there is cold air at medium and high tropospheric levels. However, more recent studies including numerical simulations of a mesoscale system, such as the one carried out by Ramis et al. (1999), demonstrate the importance of a thermal mesolow in a hail event in Catalonia. A similar mesoscale structure was the triggering factor in the catastrophic flash flood over the Spanish Pyrenees in the summer of 1996 (Romero et al., 2001). Tudurí et al. (2003) also conclude that the presence of a mesolow of thermal origin is a fundamental factor in the development of a chain of hailstorms in the Ebro Valley in the summer of 2001.

4.1.1 Extreme hail event on August 16th 2003

The impacts and sensitivities of these kind of phenomenas are examined in the August 16th 2003 severe hail event occurred in the town of Alcañiz in the Ebro Valley in Spain (García-Ortega et al., 2007). This storm brought with it intense rain and hail precipitation that caused severe floods, damaged cars and street furniture. On August 16th 2003, between 1525 and 1820 UTC, a severe storm broke over the town of Alcañiz (41.02° N, 0.08° W), province of Teruel (in the Ebro Valley, figure 4.1.1). Rain gauges registered a maximum accumulated precipitation of 115 mm in slightly over 3 h. Within this time span, an intense hail fall affected the town and its surroundings for over half an hour, and hailstones of up to 12 cm were registered. Satellite images (not shown) provided information of the storms which originated over the Central part of the Ebro Valley and the existence of a mesoscale convective system generated over the Alborán Sea (southern part of the Spanish Mediterranean coast) that moved northwards. A C-band radar with a high time resolution was used to follow up the horizontal and vertical structure of the storm.

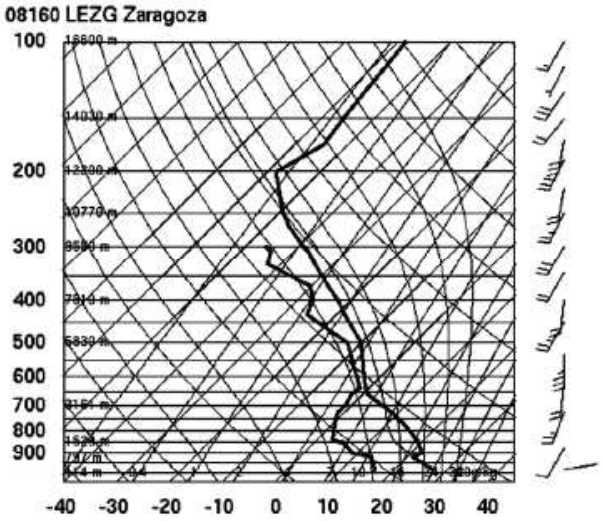

Figure 4.1.2: Skew-T plot of the Zaragoza sounding on 16th August 2003 at 12^{00} UTC

Observations

Infrared images from Meteosat show that by 10^{30} UTC a convective cloud mass started developing in the Central Ebro Valley, moving from NW to SE. Between 15^{30} and 18^{30} UTC the satellite images confirm that the cloud top temperature of the air mass over Alcañiz was between -60 and -65 $^{\circ}C$. The cloud band associated with this air mass was subsequently pushed northwards by mid and high tropospheric winds, causing small disperse storms in the Pyrenees in the late evening. The 12^{00} UTC sounding in Zaragoza (figure 4.1.2) registered winds from the south at mid and high tropospheric levels. There is also a layer of instability in the lower first meters, and an area of conditional instability around 925 hPa, just before a layer of stability at 900 hPa. The Convective Available Potential Energy (CAPE) reveals favourable conditions for convective developments, going from 161.4 Jkg^{-1} at 00^{00} UTC to 672.5 Jkg^{-1} at 12^{00} UTC. In this same time interval, the Lifted Index went from -0.82 to -1.46.

A C-band radar with a high time resolution was installed close to Zaragoza, about 100 km from Alcañiz. This radar provided information on the horizontal and vertical structure of the storm with a spatial resolution of 1 km. The radar images show that the storm originated at approximately 15^{25} UTC. The radar echoes were almost stationary, indicating that the storm moved very little during its active life. At 15^{40} UTC, the maximum reflectivity factor of the storm reached 48 dBZ at an altitude of 11,000 MSL, with an echo top of 18 km. These values remained nearly unchanged for about an hour. At approximately 16^{50} UTC, the intensity of the storm decreased, but from 17^{10} UTC the storm gained renewed intensity, with a maximum reflectivity factor, Zmax, between 42

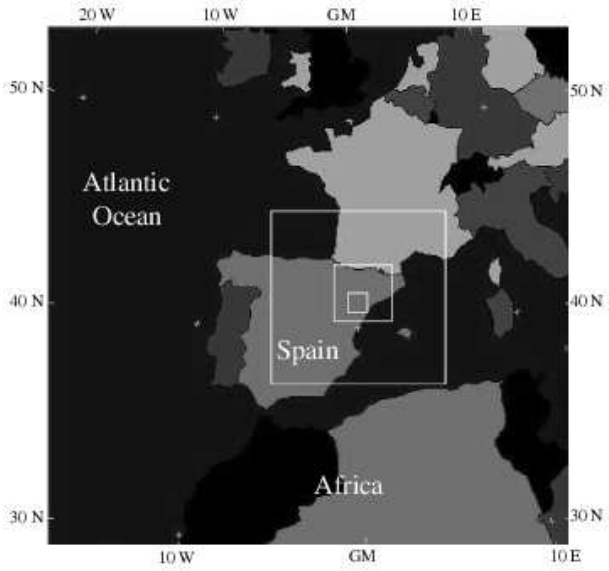

Figure 4.1.3: The four domains used for numerical simulations

and 47 dBZ until 17^{40} UTC, when the storm started dwindling until it was completely dispersed by 18^{30} UTC. Rain gauges in Alcañiz registered a maximum accumulated precipitation of 115 mm in just over 3 h. In this time there was an intense hail fall in Alcañiz that lasted over half an hour, with hailstones between 5 and 12 cm.

4.1.2 Sensitivity to orography and solar radiation

A number of numerical simulations were carried out in four domains that include synoptic, and mesoscales. The first aim of this study was to test whether or not the model could represent the conditions in which the severe storm in Alcañiz occurred, at both synoptic and mesoscale. Furthermore, it aims at studying whether or not the simulation at a higher resolution is capable of reproducing the event well enough. The information provided by the radar has been essential in order to locate the storm in time and space, and thus establish a comparison with the output of the model. Finally, the importance of topography and solar radiation has been studied in relation with the origin of this particular severe storm, considering not only their individual relevance, but also the contribution of the combination of both factors in locating the storm in time and space.

Four 151 × 151 grid domains, using Lambert's conformal projection, were set up to obtain the highest resolution over the area of interest (figure 4.1.3). The coarse domain has a resolution of 18 km, covering western Mediterranean areas, eastern mid-latitude Atlantic areas and the north of Africa (domain 1). The three other nested domains (do-

mains 2, 3 and 4) are centred in the study area with a resolution of 6, 2 and 0.67 km, respectively. Vertically, 23 terrain-following-levels have been considered. The model output intervals used are 6, 3, 1 and 0.5 h, respectively. The four domains interact with each other through a two-way nesting strategy. Initial and boundary conditions for the coarse domain a reconstructed from the analysis of the ECMWF. The source data of the 25-category classified global coverage USGS (see table 2.1.b). As for the period of time covered by the experiments, a 36-h long simulation was performed, from August 16th at 00^{00} UTC to August 17th at 12^{00} UTC, to ensure a stable behaviour of the model during the time of the storm.

MM5v3 simulations were performed with the Kain-Fritsch convective parameterisation scheme was used for domain 1. In domains 2, 3 and 4, no convective scheme has been introduced and convective processes are fully explicit simulated with the primitive model equations. The moisture scheme used was the Reisner graupel scheme, the parameterisation scheme used to represent the planetary boundary layer processes is the MRF scheme (see section 2.1.1 for a better explanation).

Model validation and diagnosis

The numerical study requires a control run that reproduces closely the observed meteorological aspects of the event. The model simulation must reproduce the observations for a run to be considered useful, keeping in mind the difficulty involved in achieving accuracy in the results when simulating an event on a convective scale with four domains, with the smallest one having a grid domain of only 0.67 km.

The simulation results show that the model reproduced reasonably well the evolution on a synoptic scale of the domains observed in the ECMWF analysis at all tropospheric levels. The simulation in domain 1 (left panel in figure 4.1.4) shows that at 300 hPa and at 12^{00} UTC there is a trough over the Iberian Peninsula with a low over Galicia moving eastward until 18^{00} UTC. As a result, an upper-level flow from SSW is found over the study zone. A similar topography is observed at 500 hPa, with a cold air mass affecting the region of Aragón and the Mediterranean coast, with temperatures below -12 °C to the east of the geopotential trough moving eastward (right panel in figure 4.1.4). This cold air mass has to be taken into account, as it will cause increasing instability before the trough arrives.

On the other hand, left panel in figure 4.1.5 shows a strong temperature gradient over the Iberian Peninsula at 850 hPa moving NWSE, with temperatures from 10 °C in the north Atlantic coast of Galicia to 19 °C in the Mediterranean coast, with a maximum of 22 °C to the south of Alcañiz. Right panel in figure 4.1.5 corresponds to domain 2 and shows a thermal mesolow at 12^{00} UTC over the Central Ebro Valley. This low becomes

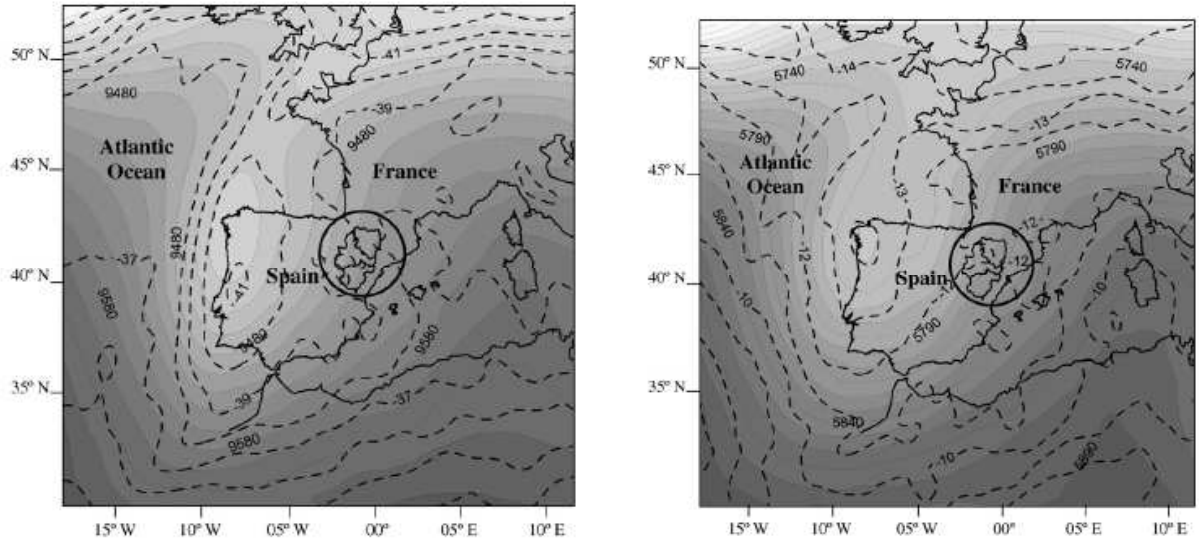

Figure 4.1.4: Left panel: Geopotential height (gpm, shaded areas) and temperature (°C, dashed line) at 300 hPa at 12^{00} UTC on 16th August 2003, as simulated by the model (domain 1). Right panel: Geopotential height (gpm, shaded areas) and temperature (°C, dashed line) at 500 hPa at 12^{00} UTC on 16th August 2003, as simulated by the model (domain 1). The circle comprises the area of study

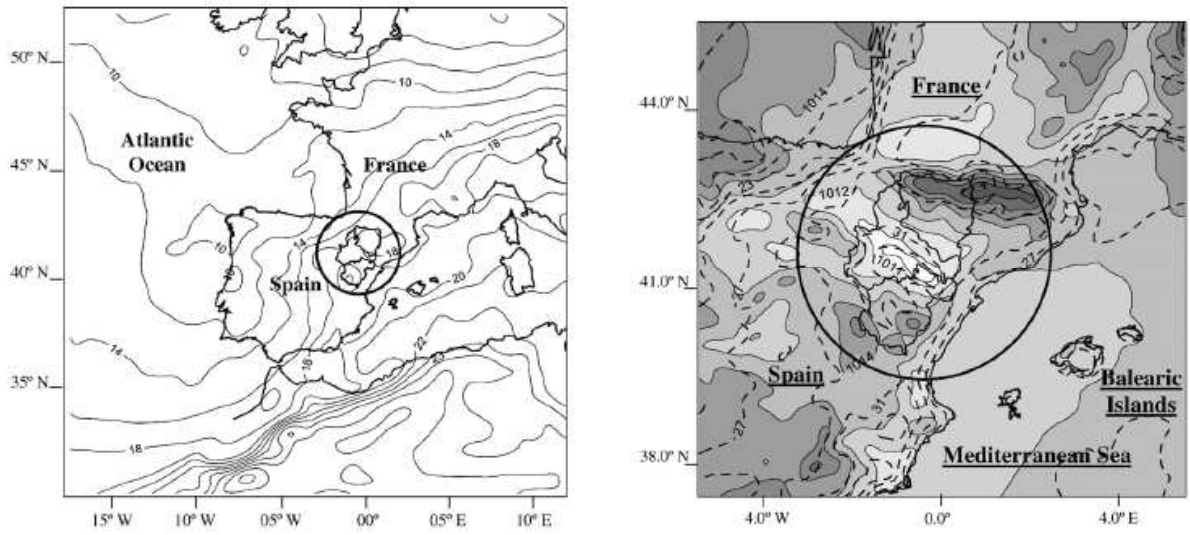

Figure 4.1.5: Left panel: Temperature (°C) at 850 hPa at 12^{00} UTC on 16th August 2003, as simulated by the model (domain 1). Right panel: Sea level pressure (hPa, shaded) and surface temperature (°C, dashed line) at 12^{00} UTC on 16th August 2003, as simulated by the model (domain 2). The circle comprises the area of study

more marked in the study zone. The figure highlights that the area of Alcañiz registers temperatures of over 31 °C. Between 12^{00} and 15^{00} UTC there is a strong increase in the relative surface humidity in the study zone (not shown), soaring from 40% to over 75%. Left panel in figure 4.1.6 corresponds to domain 3 and shows the surface wind field from the Mediterranean Sea entering the Ebro Valley, and reaching Alcañiz by 12^{00} UTC. This wind field associated with the thermal mesolow supplies warm air from the Mediterranean Sea, which had in those days temperatures higher than average in that time of the year, with a high content of water vapour. The surface inflow, the convergence area shown in figure 4.1.6 (left panel) around Alcañiz, and the thermal mesolow, overlapping on a favourable synoptic environment, with a deep trough and a cold front arriving from NW, are enough to trigger convection.

Figure 4.1.6 also shows the total precipitation field. This field comprises, on the one hand, the northern part of the domain until the Pyrenees, and on the other hand, the Ebro Valley near Alcañiz. The shaded areas over Alcañiz indicate the highest intensity in precipitation. As far as precipitation in the Pyrenees is concerned, there were some isolated storms, but the radar range and the mountainous profile of this area have hindered the gathering of additional information about this fact. If we compare the results of the simulation with the actual study zone, according to the radar data (right panel figure

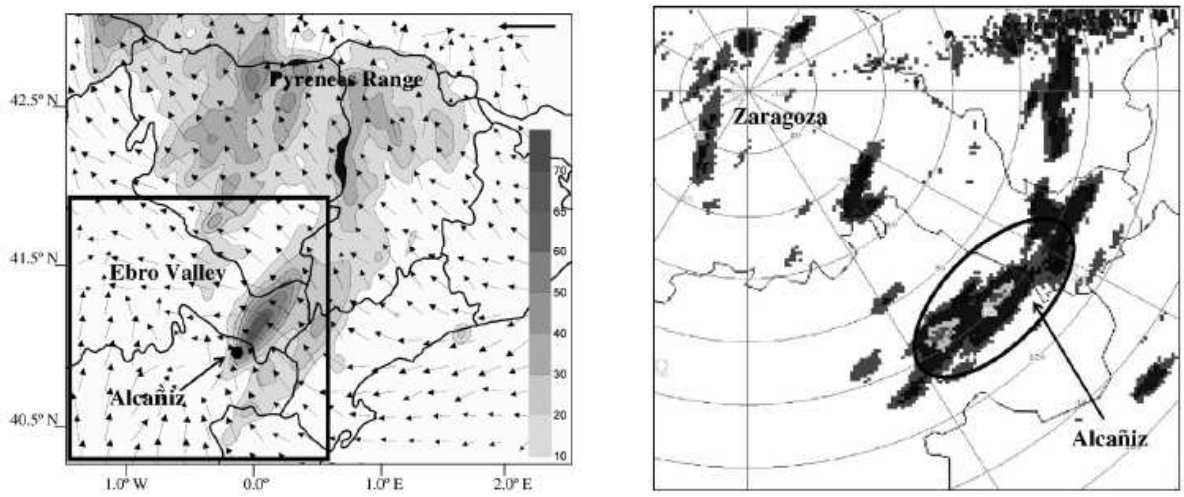

Figure 4.1.6: Left panel: Simulated surface wind field at 12^{00} UTC. Arrow on upper right-hand corner corresponds to 12 $ms{-}^{1}$. Simulated precipitation field (control simulation) recorded from 00^{00} UTC to 19^{00} UTC on 16th August 2003. Precipitation is in mm (domain 3). The box in the lower left is shown enlarged in right panel. Left panel: Accumulated precipitation areas provided by the C-band radar in Zaragoza recorded from 00^{00} UTC to 19^{00} UTC on 16th August 2003. The highlighted area indicates the zone affected by the severe storm

4.1.6) it may be stated that the simulation reproduces quite closely the area affected by the severe storm. The point that establishes the maximum precipitation estimated by the radar moves only 15 km to the SW of the maximum precipitation point, according to the model. However, the maximum precipitation recorded by the rain gauges in Alcañiz was 115 mm, whereas the model gives a maximum precipitation value of 85 mm.

In addition, the model simulates reasonably well the environment and the convective activity causing the severe hail event in the area of Alcañiz. The model locates very precisely the area with the most intense precipitation, although it underestimates the amount registered. Taking into account that the present study is focused on one single severe storm, and considering the difficulty of reproducing these events on a convective scale, the results found are so satisfactory that a more in-depth analysis of the causes of the event will be done, using this simulation as a control simulation for a sensitivity study.

Radar vs. simulation

The radar was simulated on domain 4 between 15^{30} and 18^{30} UTC to analyse whether or not the model was capable of reproducing the spatial and temporal evolution of the storm. Radar data are supplied every 3.5 min approximately, while the model output interval in domain 4 is 30 min. Because of this, a statistical comparison was carried out. The average values of the radar reflectivity factor were calculated at intervals of 30 min, and the data were compared to the simulation of the radar reflectivity factor averaged every 30 min.

In reference to spatial evolution, it is interesting to observe (figures 4.1.7 to 4.1.11) that there is quite a high degree of similarity. Between 15^{30} and 17^{00} UTC the radar shows how the storm moves slowly towards the NE. The same behaviour is observed in the simulation.

The radar images show that around 17^{00} UTC the storm starts dissipating in its central and northeastern parts, whereas the southwest regains activity, although to a smaller extent. Similarly, the simulation shows a decrease in the intensity of the storm, followed by a renewed activity in the SW of domain 4. The intensity of this new nucleus increases between 17^{00} and 17^{30} (figure 4.1.10).

The most intense hail event occurred between 16^{00} and 16^{30} UTC. The maximum value of the maximum radar reflectivity factor, $Zmax = 54dBZ$, was registered at 16^{13} UTC (not shown). The simulation shows that the intensity of the storm reaches its maximum values between 16^{00} and 16^{30} UTC, coinciding with the data from the radar.

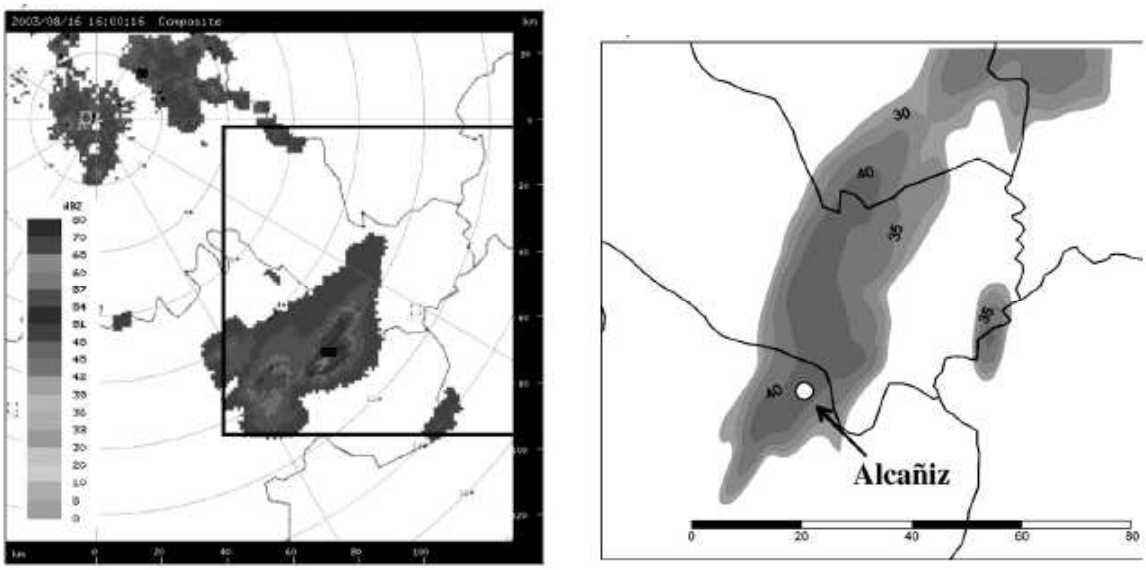

Figure 4.1.7: Composite reflectivity factor (dBZ, according to the scale) provided by the radar at 16^{00} UTC. b) Zoom to the box in figure 4.1.7a showing the simulated reflectivity factor averaged between 15^{30} and 16^{00} UTC (domain 4)

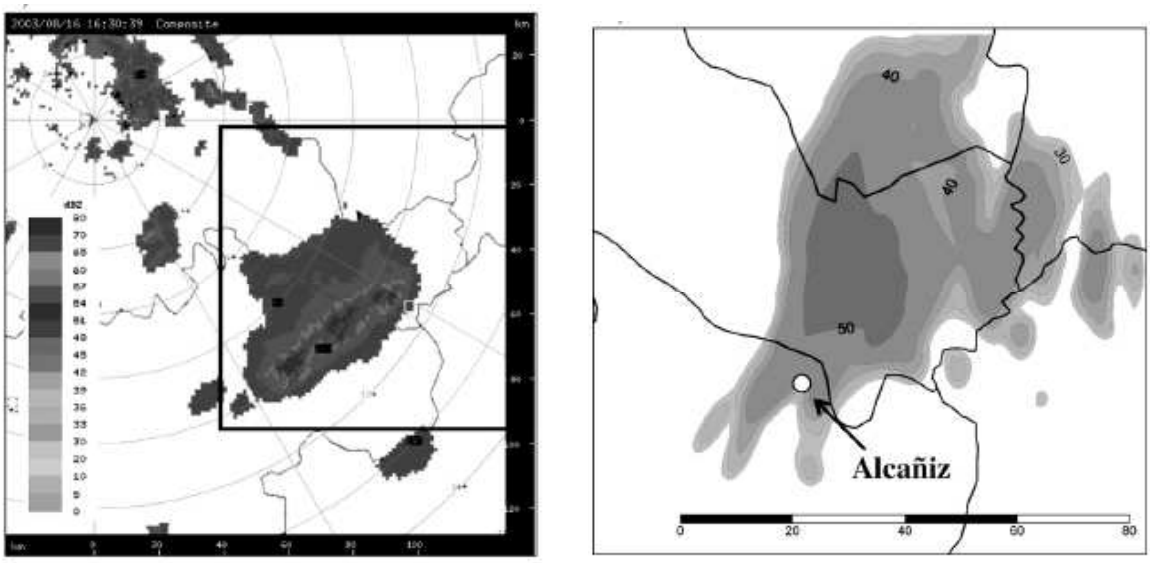

Figure 4.1.8: The same as in figure 4.1.7, but at time radar 16^{30} UTC and zoomed averaged reflectivity between 16^{00} and 16^{30} UTC

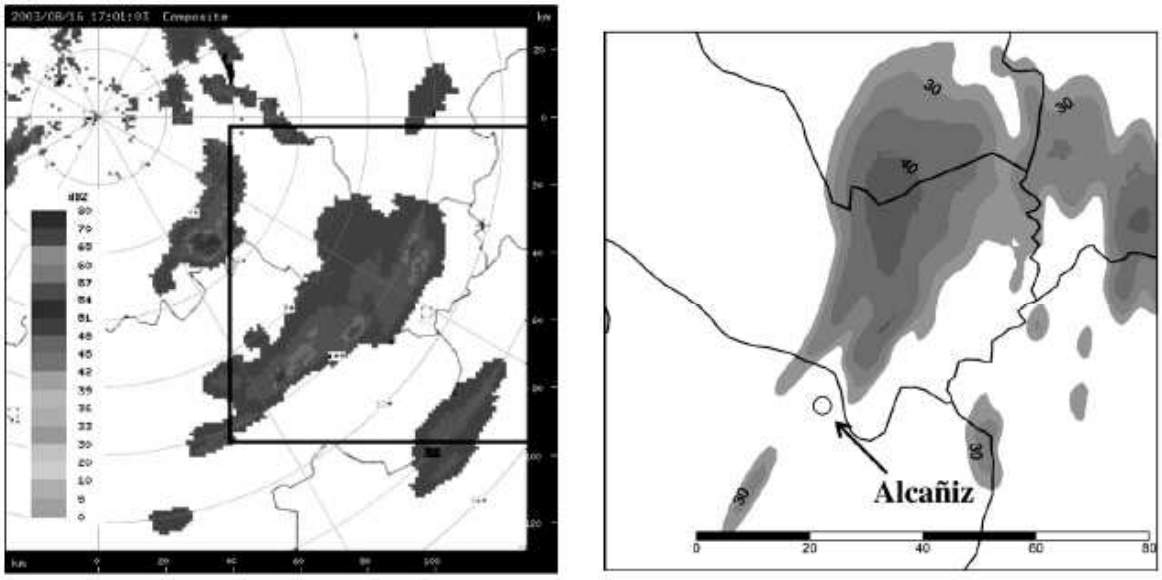

Figure 4.1.9: The same as in figure 4.1.7, but at time radar 17^{00} UTC and zoomed averaged reflectivity between 16^{30} and 17^{00} UTC

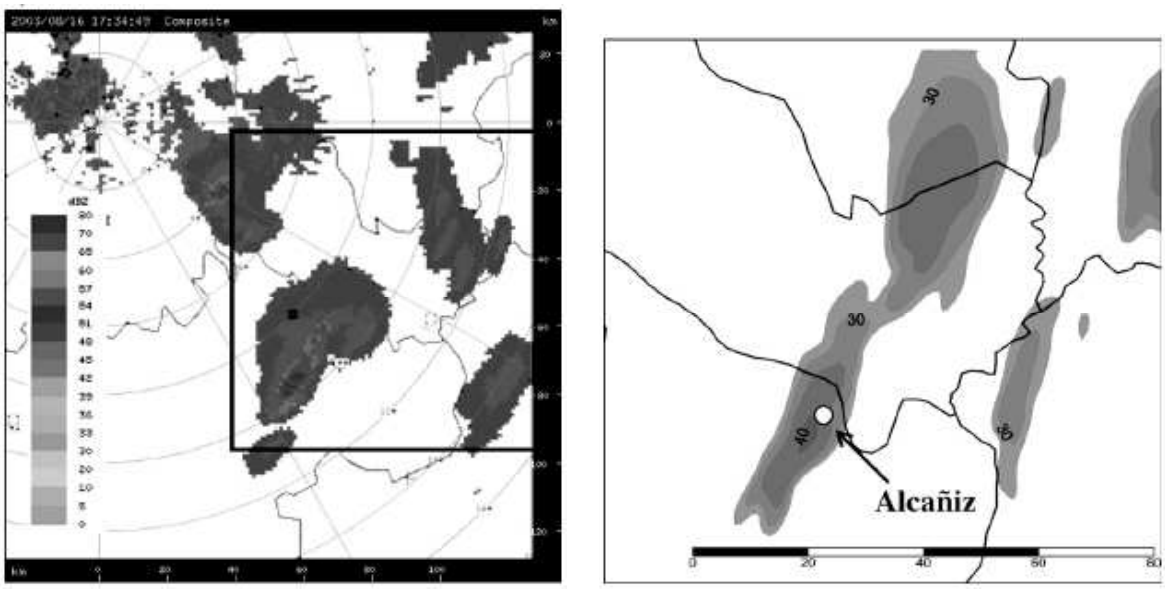

Figure 4.1.10: The same as in figure 4.1.7, but at time radar 17^{30} UTC and zoomed averaged reflectivity between 17^{00} and 17^{30} UTC

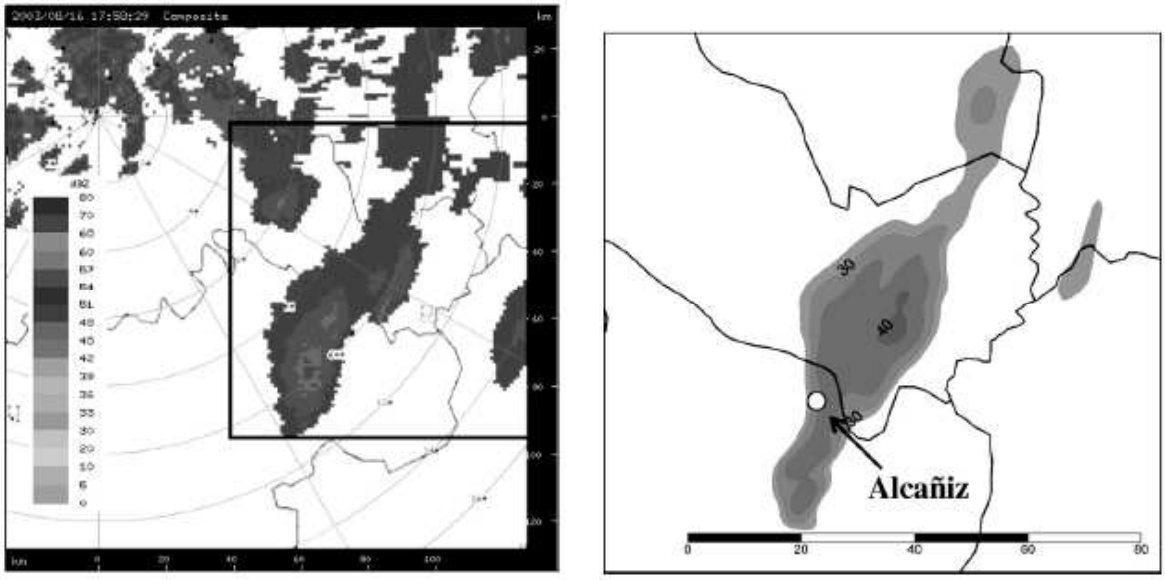

Figure 4.1.11: The same as in figure 4.1.7, but at time radar 18^{00} UTC and zoomed averaged reflectivity between 17^{30} and 18^{00} UTC

Sensitivity experiments

Once the most relevant synoptic and mesoscale-scale components in the development of the episode have been diagnosed, and once the satisfactory performance of the model in the simulation of the storm has been confirmed, it would be interesting to determine which factor has the strongest impact on the formation of the storm.

As mentioned above, the occurrence of a thermal mesolow is a feature common to various cases of severe convective phenomena studied in the Ebro Valley, and it was also present in the storm in Alcañiz. The peculiar topography of Alcañiz, to the south of a valley that forms a corridor to the Mediterranean Sea between the Pyrenees and the Iberian Mountains, fosters the inflow of warm and humid air from the sea and the lifting of low-level parcels. In other words, the topography induces changes in the low-tropospheric wind field. The high temperatures of the summer (solar radiation) influence the development of the thermal mesolow and play a fundamental role in the convective episode. These two factors, solar radiation (factor 1) and topography (factor 2), have been studied with respect to the effects they may have on the formation of the mesolow, as well as on the spatial distribution and the intensity of the precipitation.

The factor separation technique by (Stein and Albert, 1993) has been used in order to determine the quantitative of these effects (See section 2.3).

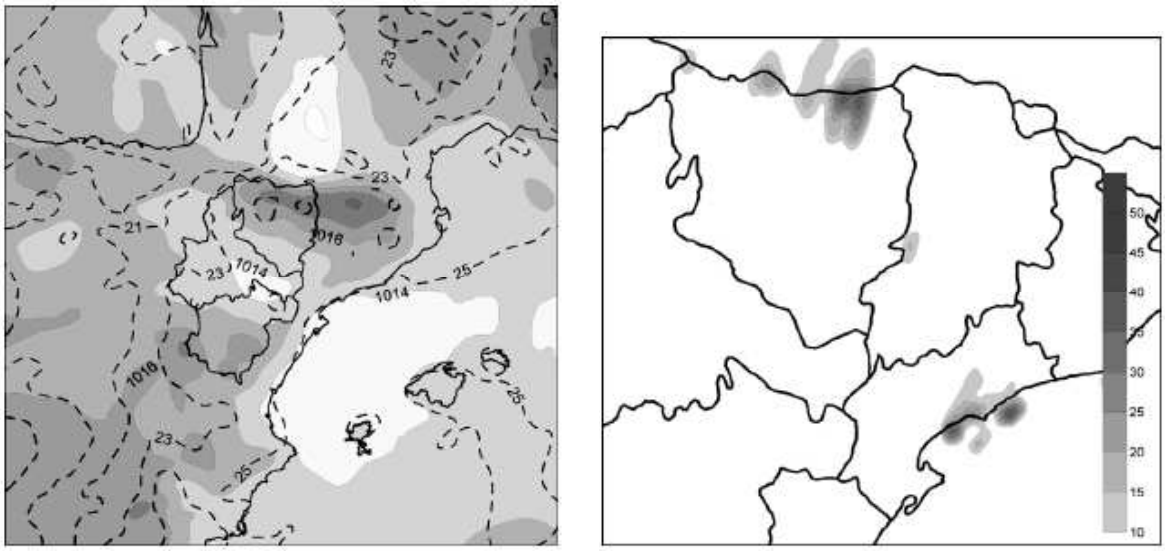

Figure 4.1.12: Left panel: Sea level pressure (hPa, shaded) and surface temperature (°C) at 12^{00} UTC on 16th August 2003, as simulated by the no-radiation experiment S2 (domain 2). Right panel: Simulated precipitation field induced by terrain (e_2) from 00^{00} UTC to 19^{00} UTC on 16th August 2003. Precipitation is in mm (domain 3)

The experiment with neither solar radiation nor topography S0 (not shown) shows no precipitation at all in Northeastern Spain, with only a maximum of 10 mm in a very small area over the Mediterranean Sea.

If solar radiation is left out (experiment S2, left panel in figure 4.1.12), the mesolow is less intense than in SC. The temperature in the area of Alcañiz at 12^{00} UTC is only 24 °C (compared to 33 °C in the control simulation). As far as topography is concerned, it clearly influences the form of the mesolow along the Ebro Valley. As a result, the total precipitation field induced by topography (e_2, right panel in figure 4.1.12) is substantially different from the one obtained in the control simulation, with less precipitation in the Pyrenees. In addition, no precipitation occurs in the area of Alcañiz and it is limited to only a small area of the Mediterranean coast, where the temperature is higher. This precipitation starts at a later time than in the control simulation, at 18^{00} UTC, coinciding with the arrival of a high cold front.

In the simulation with flat terrain (experiment S1, left panel in figure 4.1.13) the mesolow spreads in all directions, since its geometry is not conditioned by the valley. The temperature in Alcañiz is somewhat lower than in the control simulation, reaching T =

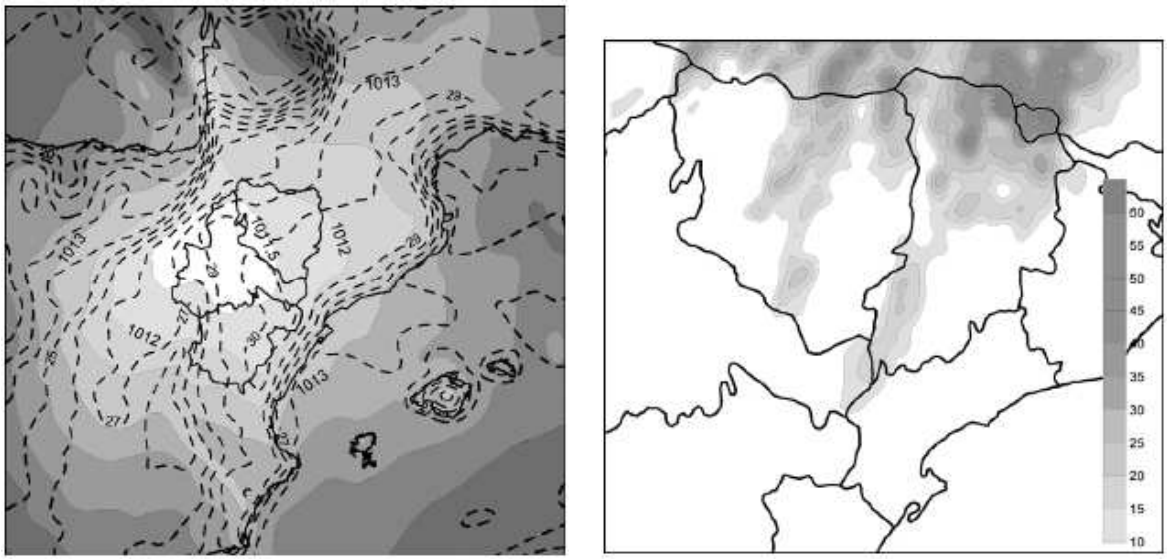

Figure 4.1.13: Left panel: Sea level pressure (hPa, shaded) and surface temperature (°C) at 12^{00} UTC on 16th August 2003, as simulated by the flat terrain experiment S1 (domain 2). Right panel: Simulated precipitation field induced by solar radiation (e_1) from 00^{00} UTC to 19^{00} UTC on 16th August 2003. Precipitation is in mm (domain 3)

30°C, and the low-level inflow from the Mediterranean Sea is not present. Consequently, the total precipitation field induced by solar radiation (e_1, right panel in figure 4.1.13) comprises a larger area than in e_2, drawing a map similar to the control simulation in the Pyrenees, but with lower precipitation rates, and affecting Alcañiz only to a small extent with 10-15 mm.

These results show that neither of the two factors in isolation can explain the precipitation caused by the severe storm in Alcañiz. Therefore, synergic effects of the two factors have been studied. The interaction of topography and solar radiation is essential to determine the places where rain actually fell and those where it did not fall.

In figure 4.1.14 we see that positive values correspond to a positive contribution to the total precipitation field. It is precisely in the area where the model locates the storm in Alcañiz that the combined effects of topography and solar radiation are more important (darker shaded areas). In contrast, the interaction of these two factors causes the opposite effect in other areas of Northeastern Spain, as shown in figure 4.1.14 shaded in light grey.

This case study leads to the conclusion that the mesoscale synoptic situation seems to have a rain potential by itself, but the thermal low of the valley causes an inflow of

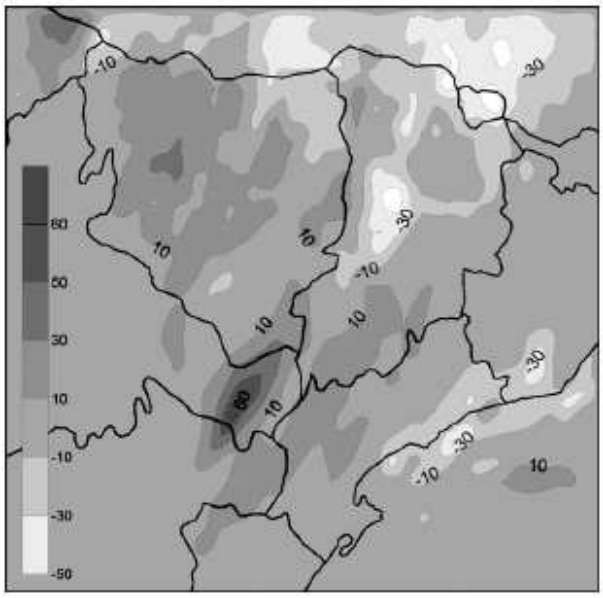

Figure 4.1.14: Simulated precipitation field induced by the interaction between topography and solar radiation (e_{12}) from 00^{00} to 19^{00} UTC on 16th August 2003. Precipitation is in mm (domain 3)

moist air from the Mediterranean Sea and updrafts in the area, occasionally generating convective clouds. The topography, together with solar radiation, contributes to highly localised and intense precipitation in the study zone.

4.1.3 Sensitivity to thermal anomaly using PV inversion

PV anomalies theory (Thorpe, 1986) indicates that above a positive PV anomaly there is a thermal positive anomaly above and a cold one below. This characteristics of the thermal anomaly will be used to study the sensitivity to the surface thermal anomaly present in the initial conditions of the simulation. Namely, it was shown (Hoskins et al., 1985) that a surface thermal anomaly can be regarded as an equivalent to a concentrated PV anomaly contained in a thin surface layer. The term surrogate PV has been introduced and widely used in referring to the surface potential temperature anomaly (Reed et al., 1992; Huo et al., 1998), since the potential temperature anomaly is mathematically treated like a PV anomaly under the ground surface (Bretherton, 1966).

In order to study the sensitivity to this 'formal' PV anomaly, piecewise PV inversion technique will be used. In this case surface thermal anomaly is identified as the signature instead of a PV anomaly. Piecewise PV inversion technique (Davis and Emanuel, 1991)

usually apply zero bottom conditions. If a given thermal anomaly is chosen as the bottom conditions and no PV anomaly is selected, PV inversion technique will provide the inverted fields related to the bottom condition. This could also be understood as the inversion of the surrogate PV related to the thermal anomaly. Inverted fields of a surface thermal anomaly of November 11-14th 2004 case are shown in figure 4.1.15. It is show how a positive surface thermal anomaly is related to a cyclonic rotation of the flow (bottom right panel in figure 4.1.15) and a pressure fall (top right panel in figure 4.1.15).

Thermal anomaly in November 11-14th 2004 case

The cyclone of the November 2004 episode (Horvath et al., 2006) was initiated over the hot and dry environment of the Atlas lee. Due to the characteristics of the zone, it could be said, that it was initially formed as a thermal low (see figure 4.2.2).

Sensitivity studies to thermal low anomalies with the piecewise PV inversion technique are carried out in the study of the November 11-14th 2004 episode described in the following section. It has also been applied in the baroclinic study of the November 9-12th 2001 cyclone episode (see chapter 3).

It is carried out a simulation where initial surface thermal anomaly has been weakened (figure 4.1.15). Resultant initial cyclone is about 5 hPa lower and 4 K colder at 925 hPa, and shifted to the north than the initial cyclone (see figure 4.1.16). Although the initial cyclone has been changed, the evolution of this cyclone does not vary significantly from the original one. This results can be a signature of the strong role of the surface thermal anomaly in the formation of the cyclone, but with a low impact in the trajectory of the cyclone.

It was shown in the control run that the cyclone was attached to the small barotropic area in the beginning of the cyclogenesis. However, this area also corresponded to the strongest low-level PV values, associated with the strong primary PV banner near the SW edge of the mountain. In order to separate the influence of the thermal anomaly and low-level PV, a simulation with orography, but without thermal anomaly was performed.

The difference between initial low-level temperatures of the sensitivity simulation and the control run is shown on figure 4.1.16a. The broad Atlas-scale thermal anomaly perturbation reached 4 K in the temperature field at 925 hPa, with associated mean sea level pressure increase of 5 hPa. Accordingly, the long baroclinic zone in the Atlas lee was significantly weakened. On a smaller scale, the shape of the isolines near the SW Atlas edge indicated weakening of the "secondary" thermal anomaly in the lee of the High Atlas, the place where the cyclone was initiated.

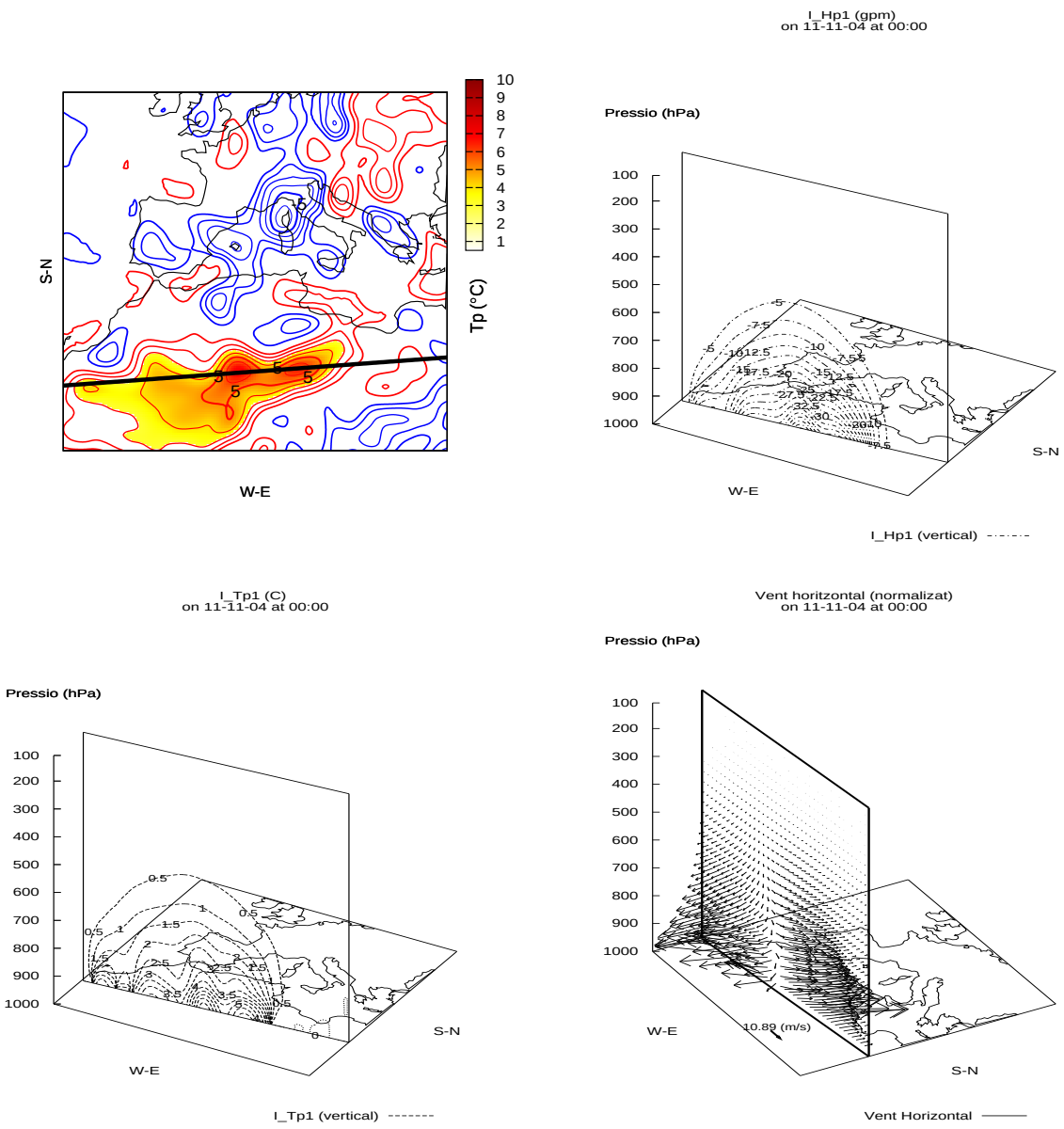

Figure 4.1.15: Top left panel: Thermal anomaly (solid line every 1°C; blue: negative anomaly, red: positive anomaly) and selected surface thermal anomaly (shaded area), dashed line indicates vertical cross sections. Top right panel: Cross section of the geopotential anomaly (every 2.5 gpm) due to the surface thermal anomaly. Bottom left panel: Vertical cross section of the thermal anomaly (every 0.5 °C). Bottom right panel: Vertical cross section of the wind anomaly (rescaled, see bottom vector). It is shown how a positive surface thermal anomaly induces a pressure and a cyclonic rotation of the above air.

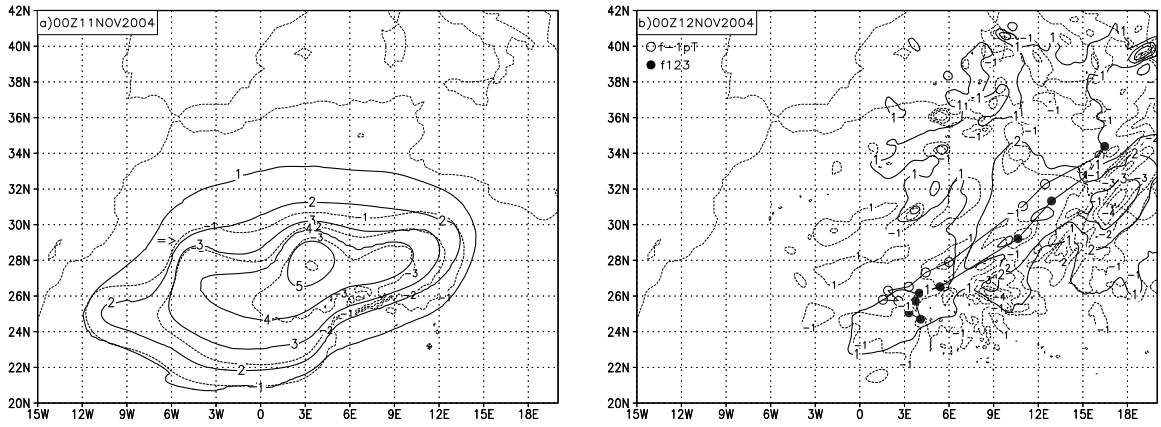

Figure 4.1.16: Definition of the thermal anomaly subtracted from the initial conditions at 11 Nov 2004 00 UTC (a). Fields denote a difference between the modified initial fields for the thermal anomaly sensitivity experiment and the original initial fields of the control run. The initially positive mean sea level pressure modifications (hPa) is plotted in continuous line and the initially negative temperature modification at 925 hPa in dashed. The arrow denotes the lee of the High Atlas mountains and removal of the "secondary" thermal anomaly. The structure of the thermal anomaly perturbation after 24 hours of simulation at 12 Nov 2004 00 UTC (b), defined as a difference described above. The cyclone trajectories in the experiment with thermal anomaly removed (f-1pT) and in the control run (f123) were superimposed on the figure, starting from 12 Nov 00 UTC, plotted every 6 hours

At 12 Nov 00 UTC, the approximate time of cyclogenesis in the lee of the Atlas, the initially removed thermal anomaly was strongly stretched out and already partly advected over the Mediterranean Sea with little effect in the Atlas lee (figure 4.1.16b). This suggests that the atmospheric conditions in the lee of the High Atlas at cyclone initiation time were only slightly changed by the removal of the thermal anomaly perturbation. It can be verified from the figure that the relative differences in the area of interest reached up to 1 K and 1 hPa. The dipole structure of the thermal anomaly perturbation in the lee of the High Atlas denoted weakening of the baroclinic zone and frontally induced low-level PV before the cyclone commencement. Further inspection of the low-level atmospheric conditions at 12 Nov 00 UTC (figure 4.1.17ab) showed that the surface baroclinic zone was somewhat weaker compared to the control run, in accordance with figure 4.1.16b, while the barotropic zone near the cyclone initiation point was more uniform. In this barotropic zone, a slightly weaker cyclone centre was located more inside the secondary thermal anomaly, closer to the mountain and orographic PV banner then in the control run. However, already at 12 Nov 12 UTC, there was no notable difference in the cyclone centre intensity or surface baroclinicity in the area of interest (figure 4.1.17c-d). Nevertheless, the cyclone centre was positioned closer to the mountain and continued to take that path in its further development (figure 4.1.16b).

The simulation showed that a thermal anomaly in the lee of the Atlas built up rather quickly, practically during the 24-hour interval preceding the cyclogenesis. Thus, little reliance could be made on the separation of low-level PV and thermal anomaly influences on the intensity of cyclone initiation in our simulation experiments. However, it seems that the location of the cyclone initiation showed sensitivity to thermal anomaly positioning in the mountain lee (see topographic configuration of the domain in figure 4.1.18).

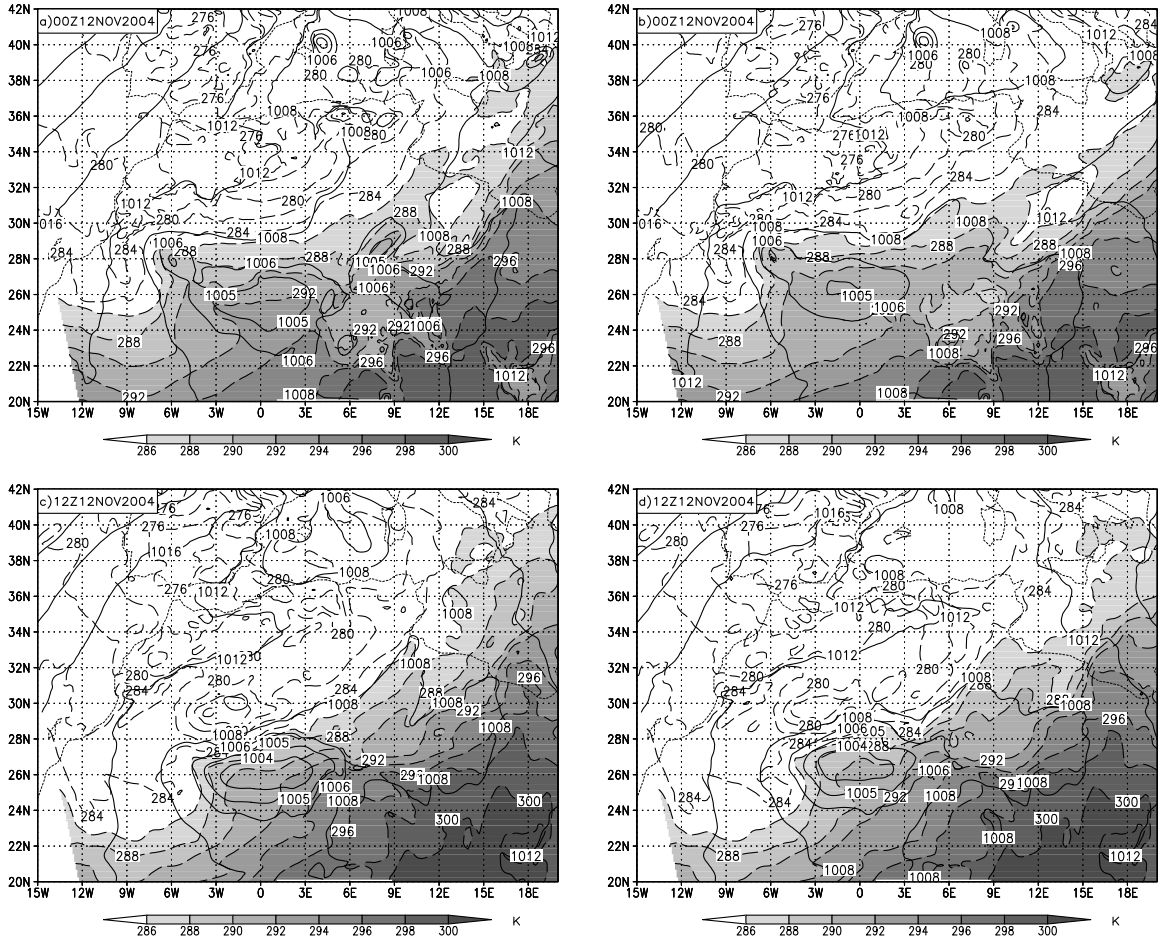

Figure 4.1.17: Model forecasts (shown on a zoomed domain) of the control run (a) and the thermal anomaly sensitivity run (b) at 12 Nov 2004 00 UTC and the control run (c) and the thermal anomaly sensitivity run (d) at 12 Nov 2004 12 UTC. Mean sea level pressure (hPa) is shown in continuous line (above 1008 hPa every 4 hPa, under 1006 hPa every 1 hPa). Temperature is plotted in dashed line (every 2 hPa) with shaded values over 286 K

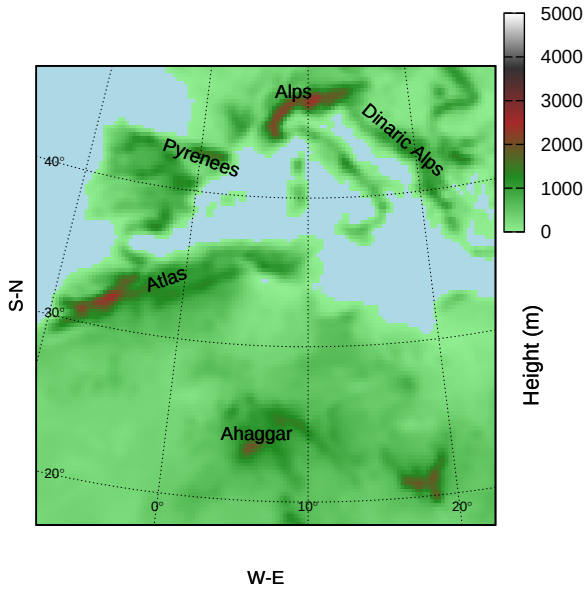

Figure 4.1.18: Topography of the domain of interest

4.2 Topographic lee influences

In the November 11th-14th 2004 case, an Atlas lee cyclogenesis (see figure 4.2.1). In contrast to the Alps-lee cases, Atlas cases present the singularity that their development is above extreme hot and dry area.

4.2.1 Extreme Bura case on November 11-14th 2004

During this case, a large upper-level trough was present above the Iberian peninsula on Nov. 11th (figure 4.2.2). This upper level trough was clearly depicted by the water vapour satellite image (EUMETSAT source) as a dry water vapour content (black zone in figures 4.2.7 and 4.2.8). At the same time, old signs of instability were present in the Adriatic Sea zone (between November 7th and 8th where recorded about 180 mm of precipitation in Albania).

Synoptic pattern is dominated by a high pressure zone that determined the flow in the North African region. At low levels a permanent northwestern flow affected the Atlas

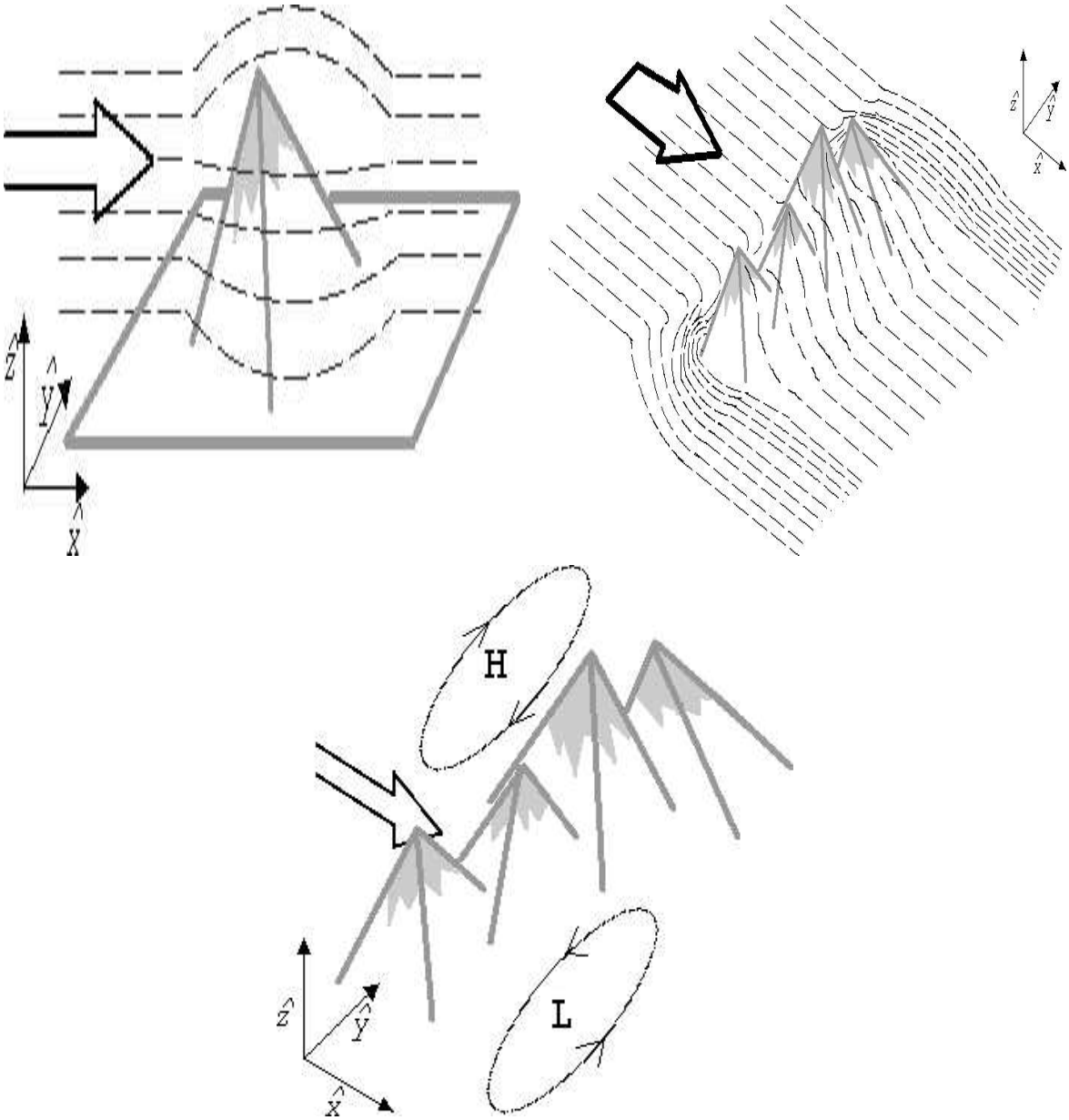

Figure 4.2.1: **Lee cyclogenesis:** Mountains block the flow of a persistent synoptic wind (top left and right panels). In the windward side if the flow could not overpass the mountains, air becomes compressed and the pressure increased and a High pressure disturbance is created. In the leeward the diminishing of the air decreases the pressure and a low pressure disturbance is generated. By this way, a dipole system is established (bottom panel)

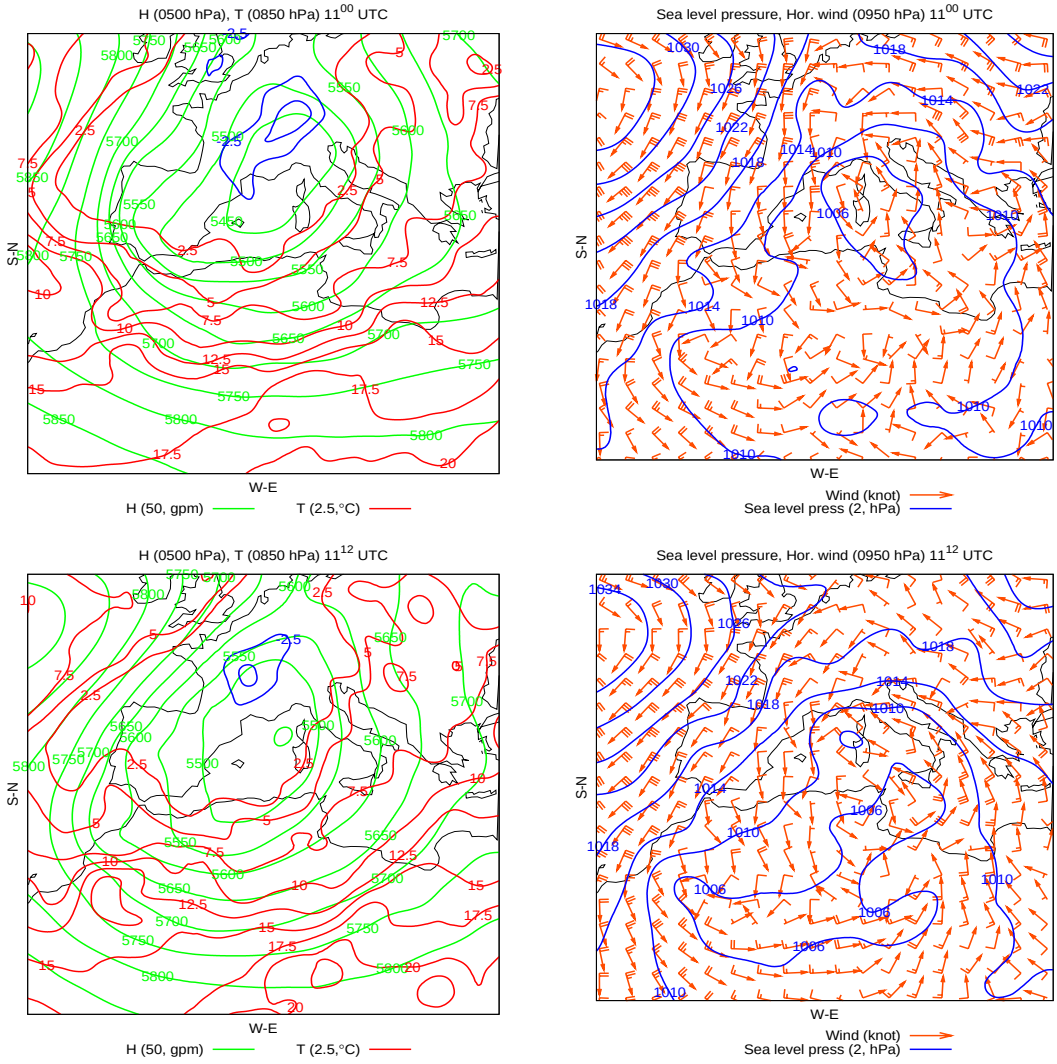

Figure 4.2.2: NCEP analyses evolution of the case. Left panel: Geopotential height (H) at 500 hPa (every 40 gpm, green line) and Temperature at 850 hPa (every 2.5 °C; red line, positive values; blue line, negative values). Right panel: Sea surface pressure (every 4 hPa, blue line) and horizontal wind at 950 hPa (orange barbs notes; large: 10 kt, short: 5 kt). On Nov. 11 at 00^{00} UTC (top), and at 12^{00} UTC (bottom)

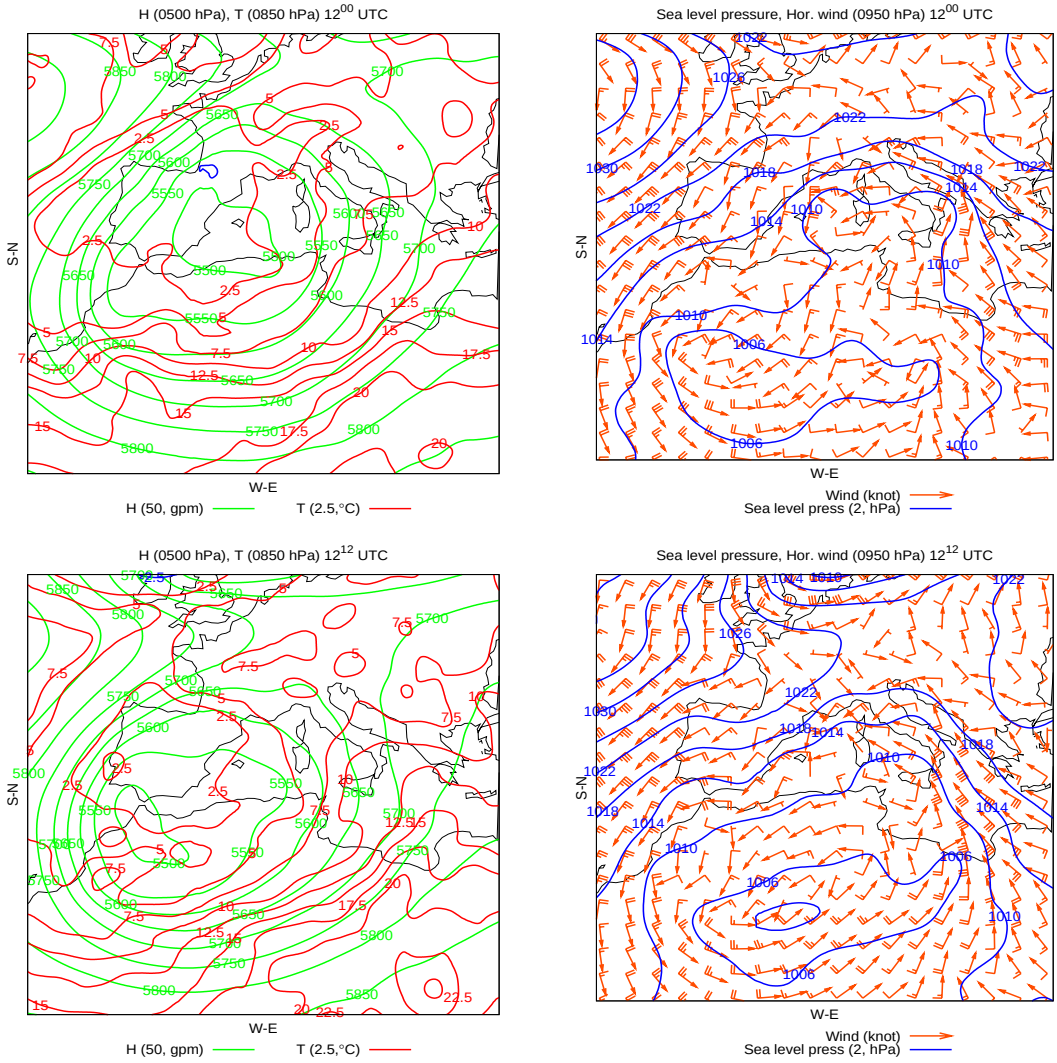

Figure 4.2.3: As in figure 4.2.2, but on Nov. 12th at 00^{00} UTC (top) and 12^{00} UTC (bottom)

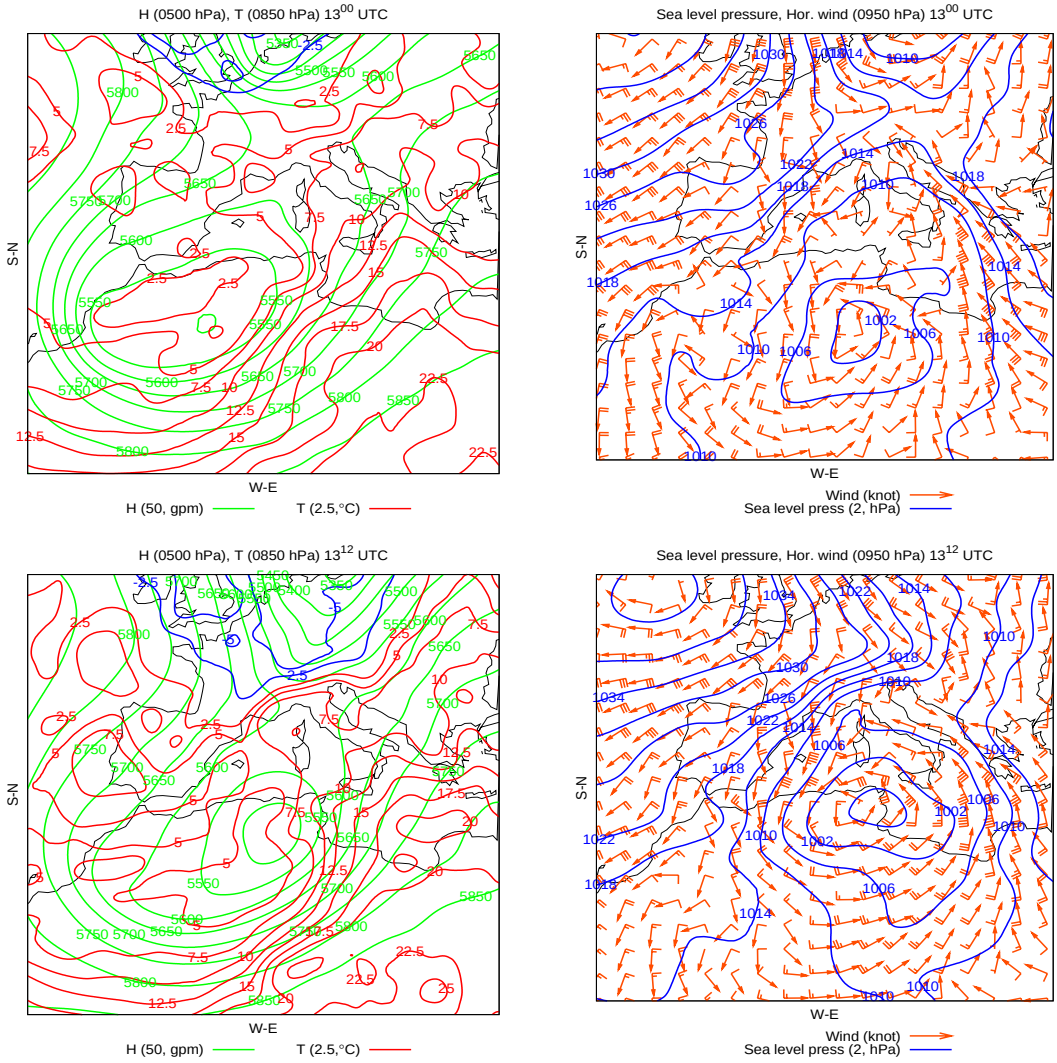

Figure 4.2.4: As in figure 4.2.2, but on Nov. 13th at 00^{00} UTC (top) and 12^{00} UTC (bottom)

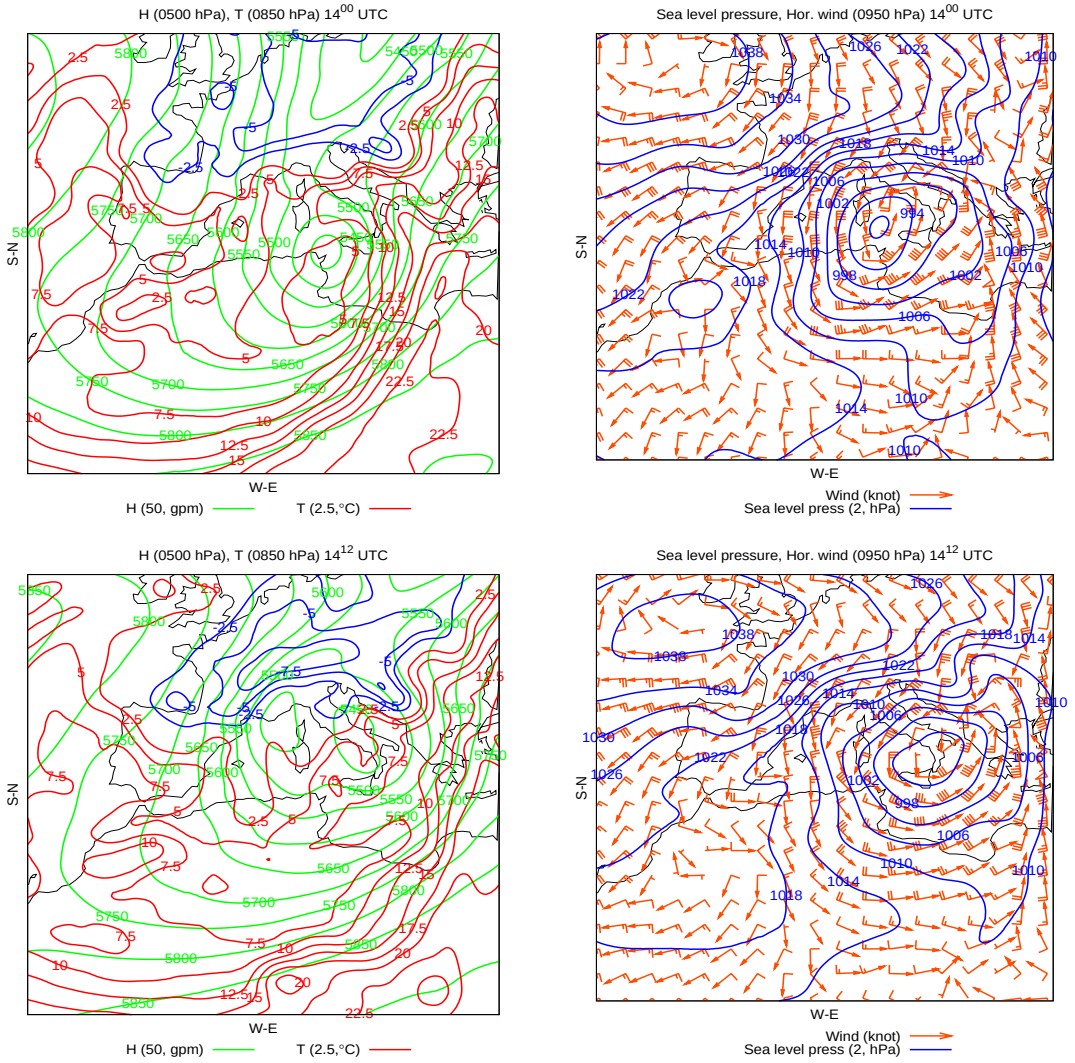

Figure 4.2.5: As in figure 4.2.2, but on Nov. 14th at 00^{00} UTC (top) and 12^{00} UTC (bottom)

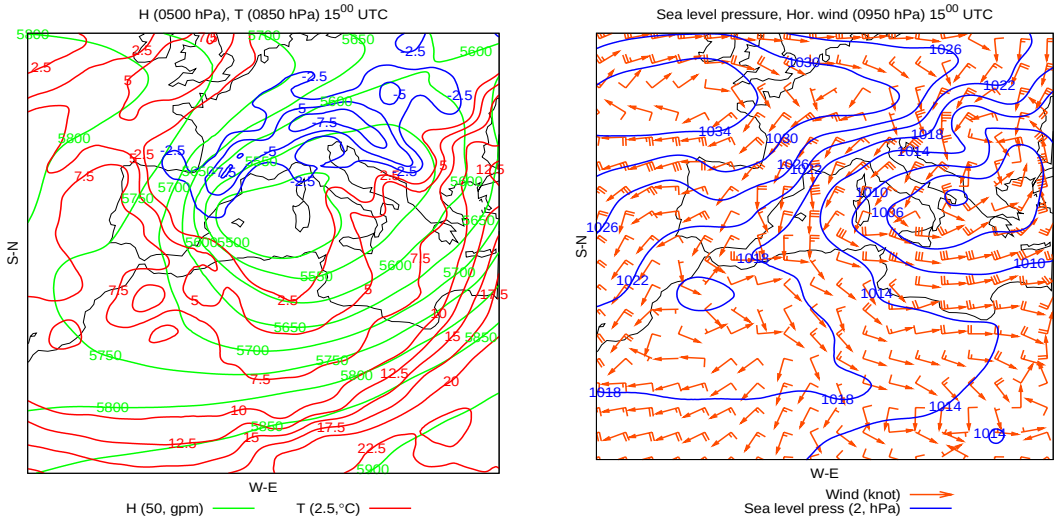

Figure 4.2.6: As in figure 4.2.2, but on Nov. 15th at 00^{00} UTC

range and in the southern part of the Atlas range there was an important longitudinal thermic gradient (figure 4.2.2 on Nov. 11 at 00^{00} UTC). Initially the flow kept blocked by the Atlas, but after a low detraiment the flow could overpass the range and the initial disturbance started to growth (Nov. 11th at 12^{00}). At the same time, intense radiative fluxes are simulated in the African plateau (about 400 Wm^{-2}, not shown). Upper level trough moved southward and the surface disturbance moved eastward following longitudinal thermal gradient at the south lee of the Atlas range (figure 4.2.3, Nov. 12th 12^{00}). From this moment, eastward movement of the cyclone and the upper level trough became very similar (might be a signature of the acouplement between upper and low level disturbances). The coupling between disturbances and the surface thermal gradient established the needed circumstances that allow the development of the baroclinic mechanism (Hoskins et al., 1985).

Cyclone kept growing during the Atlas lee and the coupled phase between upper level and low level disturbances. When the cyclone reached the coastal line of Tunisia (Nov. 13th 12^{00}, figures 4.2.4 and 4.2.8) it experimented a strong and fast deepening, from which it reached its mature state. At the same moment, it can also be seen above the Mediterranean Sea a secondary thermal gradient with a SW-NE direction. Meanwhile the cyclone started to decay it was moving towards the NE (14-15 Nov., figures 4.2.5 4.2.6). At this step of the cyclone evolution, strong convective activity is depicted by the satellite images at the South of Italy (figure 4.2.8, Nov. 14th 12^{00}). In concordance with a high pressure zone in the Atlantic Sea, a strong pressure gradient was established allover the Alps and Dynaric Alps. According to this distribution of pressures, strong winds can be developed

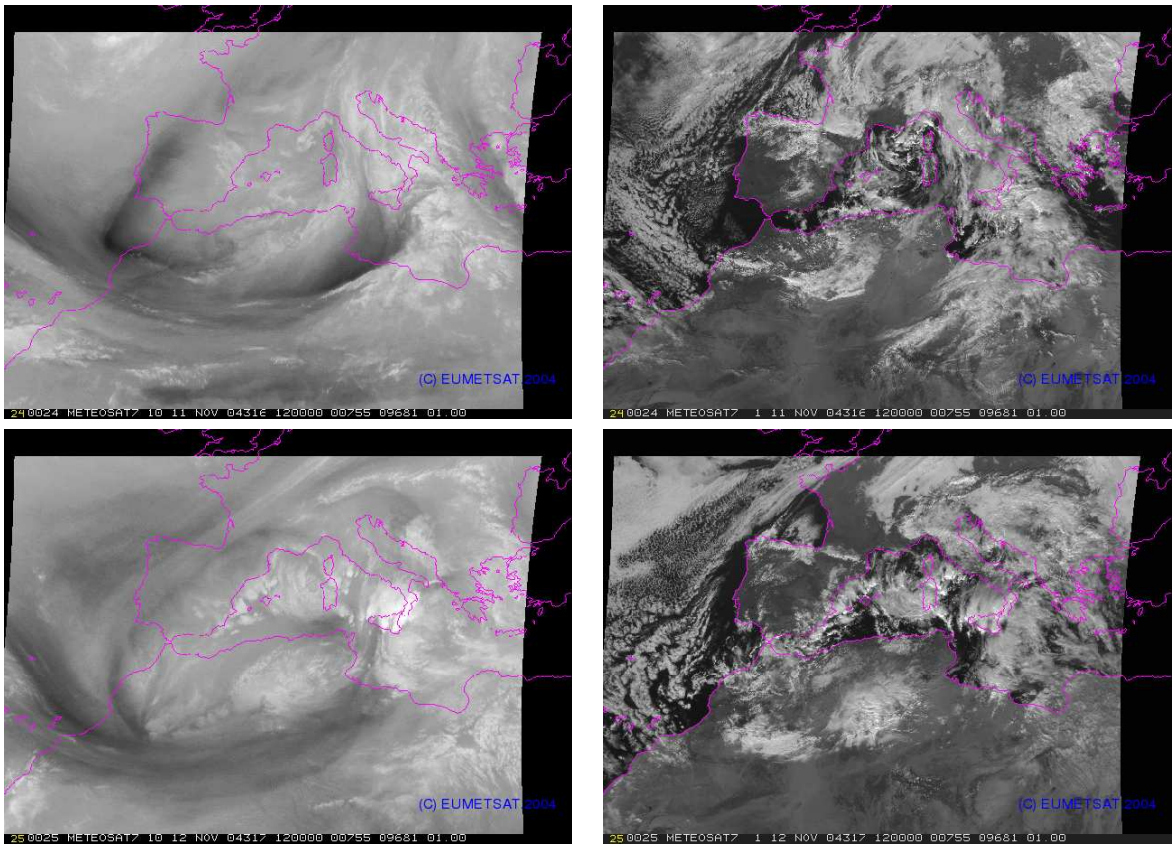

Figure 4.2.7: METEOSAT7 images for the vapour water channel (left) and the visible channel (right). On Nov. 11th at 12^{00} (top) and Nov. 12th at 12^{00} (bottom). Upper level trough is identified as the dark free cloud area due to the upper level downdrafts of dry air from higher levels. Cloudy zone seen in the visible channel image at the south of the Atlas mountains corresponds with the cyclone. Images with the collaboration of Ángel Luque)

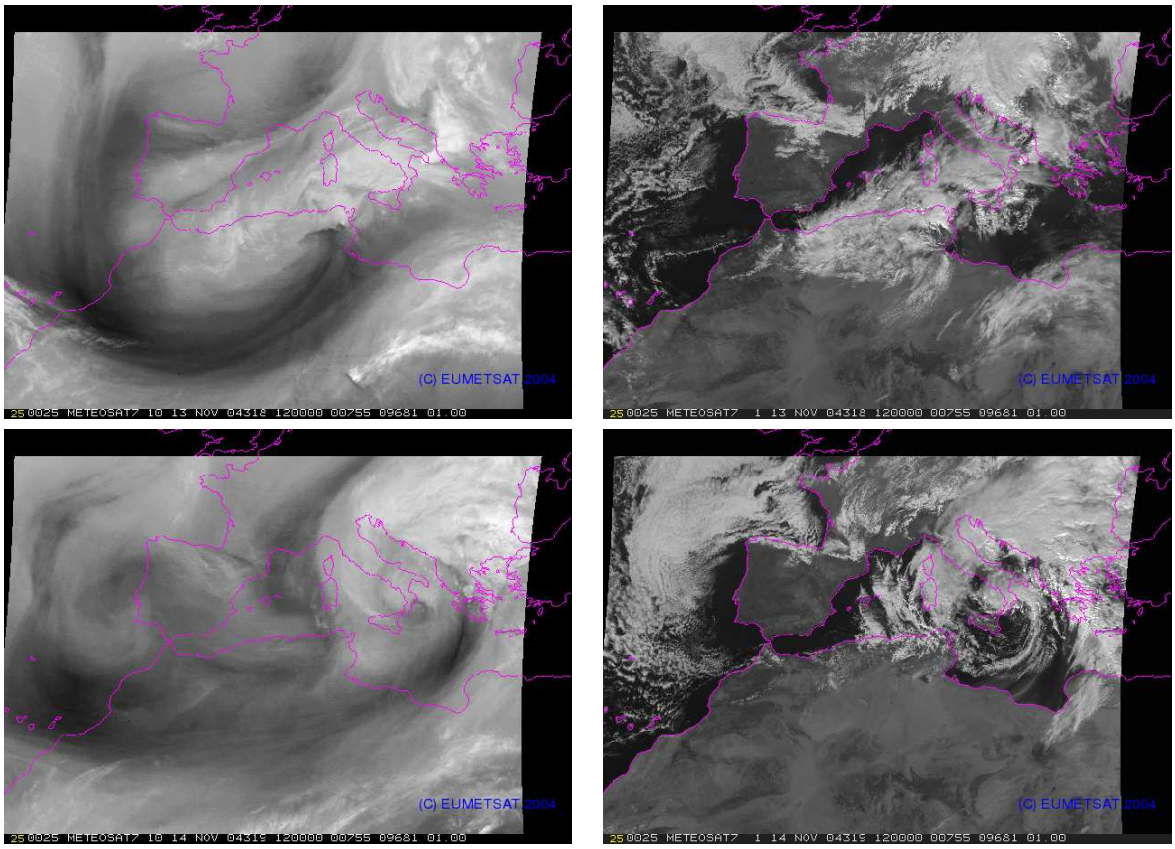

Figure 4.2.8: As in figure 4.2.7, but on Nov. 13th at 12^{00} (top) and Nov. 14th at 12^{00} (bottom). The movements of the cyclone observed in the visible channel image (right panels) corresponded with the movements of the upper level trough (dark zones in the water vapour channel images, left panels)

in the Rhône river basin and in the North base of the Adriatic Sea known as Bura winds. During this period of time, heavy precipitation were recorded in the south of Italy (about 200 mm/24h) and extreme Bura winds in the Croatia region (sustained winds about 35 ms^{-1} and gust winds about 60 ms^{-1}). 60 ms^{-1} gust winds have been established as the strongest gust wind record in Croatia.

Mediterranean phase of the cyclone is out of interest in the study of Atlas lee cyclogenesis. However, such kind of strong and quick deepening of the cyclones, have also been observed in other Mediterranean cases (Romero, 2001; Homar et al., 2002a) and in the North Atlantic bombs Sanders and Gyakum (1980); Sanders (1986) or similar cases Gyakum (1983a,b); Uccelini et al. (1985); Whitaker et al. (1988); Kuo et al. (1991a); Huo et al. (1995). The deepening process is associated to the strong amount of water evaporation from the sea and the strong formation of clouds. Large amounts of water vapour and heating at middle levels contribute significantly to deep the cyclone in a short time (Hoskins et al., 1985; Davis and Emanuel, 1991).

Validation of control simulation

The synoptic evolution of the lee cyclone in the control simulation (figure 4.2.9) shows that mean sea level pressure fields, system movement and deepening were moderately well simulated, experiencing some time delay in the process evolution. The upper-evel potential vorticity core at 300 hPa level reached 14 PVU at the time it was advected over the Atlas region (figure 4.2.9c). This cut-off upper tropospheric low induced a closed upper-air circulation as indicated by geopotential height distribution. Towards the end of the analysed period (figure 4.2.9d), which is approximately the time when the cyclone left the lee and entered the Mediterranean (14 Nov 00 UTC), the upper-level potential vorticity anomaly weakened, probably at the expense of interaction with the low-level vortex. The axis of the lee cyclone had a slightly negative tilt that tended to get more neutral with time. All of the aforementioned facts agree with the (Pettersen and Smebye, 1971) cyclone type B, and are in close resemblance with the lee cyclogenesis synoptic features.

In a mesoscale analysis of the model run, we investigated the lower tropospheric conditions. As mentioned in evolution of the system, strong northerly winds together with high surface sensible heat flux created an Atlas-sized thermal anomaly already on 10 Nov, far prior to the cyclogenesis. However, soon upon its creation, cold air crossed the lower NE part of the Atlas range and reduced the thermal anomaly to the lee of the High Atlas Mountains (figure 4.2.10a). A strong shear line is visible on 12 Nov 0 UTC as primary orographic PV banner of a considerable horizontal distance starting over the SW Atlas edge and overcoming 2.5 PVU in intensity (figure 4.2.10b). At the same time, two frontal low-level PV sources are visible: the first one corresponding to the front that

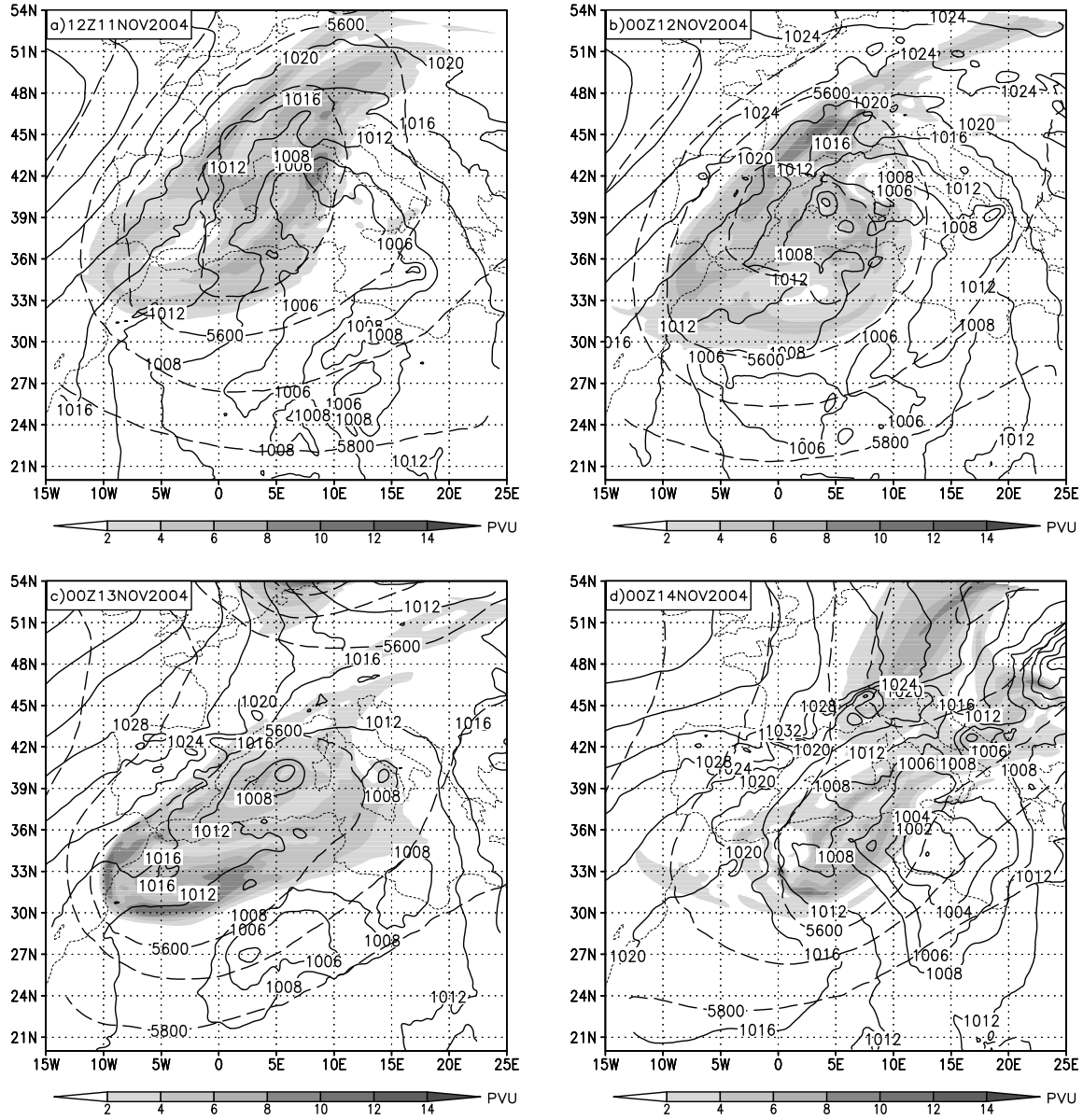

Figure 4.2.9: Model forecast of synoptic scale evolution at 11 Nov 2004 12 UTC (a), 12 Nov 2004 00 UTC (b), 13 Nov 2004 00 UTC (c) and 14 Nov 2004 00 UTC (d). Mean sea level pressure contours are plotted in continuous line with 4 hPa above 1008 hPa and 2 hPa below 1008 hPa values. Upper-level potential vorticity values at 300 hPa are shaded (white under 2 PVU black over 14 PVU), while geopotential at 500 hPa is plotted in dashed (every 100 gpm)

crossed the central and the northern part of Atlas and the second one more away to the east. They belonged to the same initial baroclinic zone and were separated due to the temporary orographic blocking of the first and quick outbreak from the Mediterranean of the second. In this period and subsequent hours, the very cyclone centre was located in a small quasi-barotropic zone and an area of enhanced low-level PV. During the 12t h of November, the cyclone moved northward towards the Mediterranean area. Low-level PV banners weakened, as a mere consequence of the reduced daytime stability. At 13 Nov 00 UTC (figure 4.2.10c), the orographic primary PV banner merged with the frontal one, forming a continuous source of low-level PV far away from the mountain. At the time, the cyclone centre started to be attached to the frontal baroclinic zone and stayed that way until the end of the analysed period. Orographically induced PV banner seemed to feed the low-level cyclone, resembling some of the documented cases of Alpine lee cyclogenesis (Aebishcer and Schär, 1998). On 14 Nov 00 UTC (figure 4.2.10d), which is the last time-sequence of our analysis, roughly corresponding to the time the cyclone left the lee and entered the maritime area, the cyclone centre reached 1000 hPa depth and was characterised with a well defined frontal structure.

Despite of the fact that differences between model simulations and ECMWF analysis (not shown) reveal that the model simulation of the investigated process was of limited quality, it is believed that its features were captured reasonably well enough to make the case appropriate for the sensitivity study and deduction of factor contributions in this lee cyclogenesis event.

4.2.2 Sensitivity tests

Control run of the case exhibits a good correspondence with the satellite-based observations (see figure 4.2.8). However, the maritime phase of the simulated cyclone does not match very well with the NCEP analyses and the observations. That could be a reflection of the lack of accuracy of the MM5 mesoscale model for simulations that least for a long period.

In previous sections upper-level potential vorticity (PV), orography and surface sensible heat flux (SSHF) were identified as main factors affecting this cyclogenesis event. A series of simulations will be addressed out in order to qualitatively analyse the contributions of these factors and their mutual synergies to the mean sea level value and cyclone centre position. This study will done with the aim of the factor separation technique (Stein and Albert, 1993). As mentioned previously, for that purpose 8 simulations had to be done. Thus, to address the orographic contributions to the process, the Atlas Mountains were removed from the terrain field. Secondly, surface sensible heat flux was withheld in a series of simulations, allowing for a determination of the influence of the associated surface forcing. Finally, an upper-level potential vorticity anomaly was removed from the

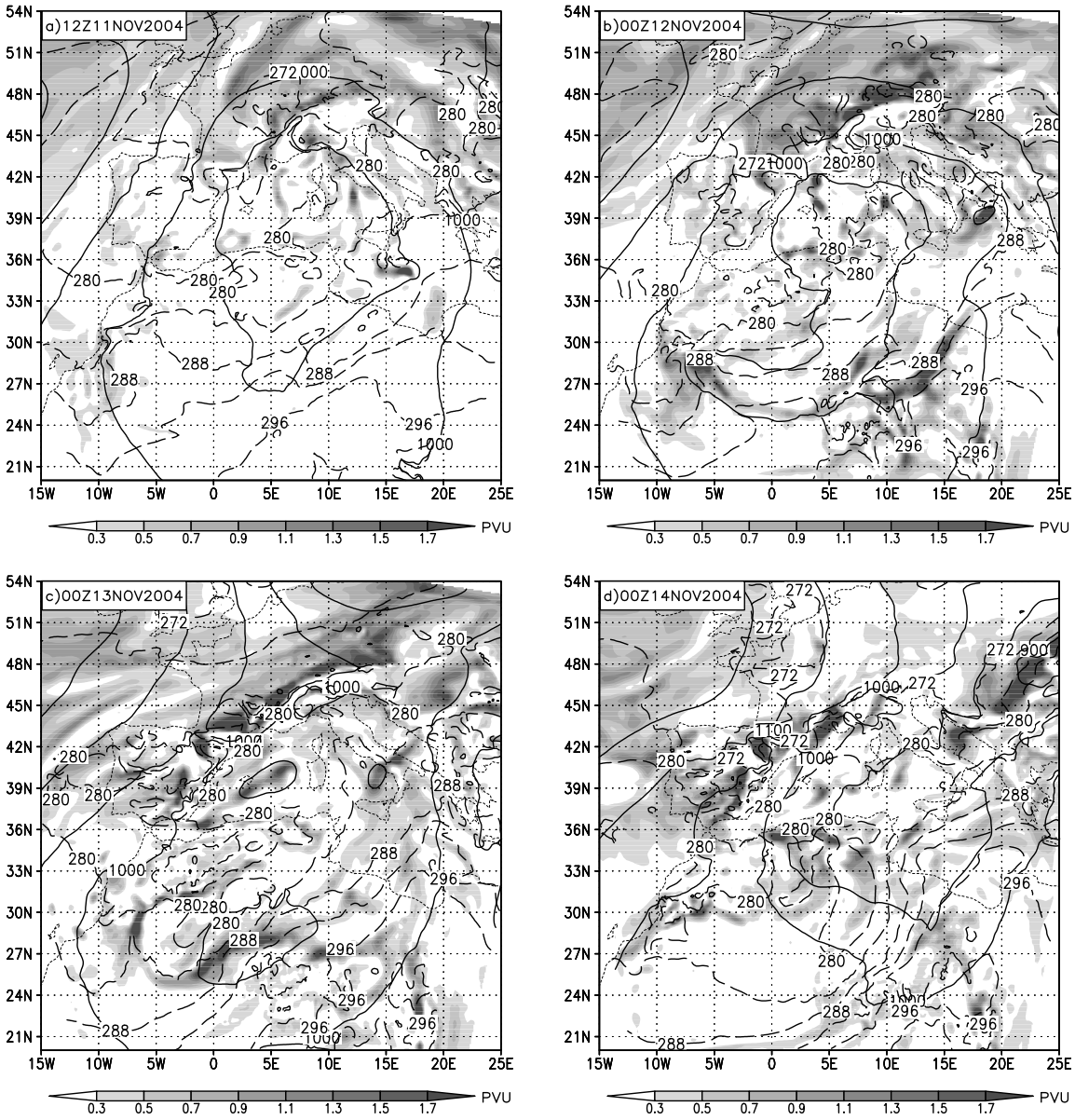

Figure 4.2.10: Model forecast of low-level conditions at 925 hPa at 11 Nov 2004 12 UTC (a), 12 Nov 2004 00 UTC (b), 13 Nov 2004 00 UTC (c) and 14 Nov 2004 00 UTC (d). Low-level potential vorticity is shaded (white under 0.3 PVU and black over 1.7 PVU). Geopotential is continuous line (every 50 gpm), while temperature is in dashed (every 4 K)

initial conditions to address the role of upper-level dynamical processes in the cyclogenesis.

The *Surface Latent Heat Flux* (here and after, LHF) and the *Sensible Surface Heat Flux* (here and after, SSHF) are related to the exchanges between earth surface and atmosphere. Due to the extremely dry conditions of the North African plateau, LHF will be not considered in the study. Preliminary results with this factor do not show a clear role of the flux.

Throughout the sensible surface heat flux (SSHF) the heat exchange between earth surface and the atmosphere is carried out (see figure 4.2.11). Surface is heated by the solar radiation (shortwave). Incoming radiation is used in different processes such as: diffusion to the ground, absorption into water surfaces (Sea, lakes or rivers), radiation in longwave form and/or atmospheric heating. This atmospheric surface originated induced heating is the first factor that heats/cools the first layers of the atmosphere Stull (1988). It could be considered as the source of energy that will produce the turbulence in the Boundary layer. Due to the extremely hot conditions of the north African plateau, it is assume that SSHF might have an important role in the development of the cyclone (Kuo et al., 1991b).

The removal of the upper-level potential vorticity anomaly from initial conditions was performed by applying the piecewise PV inversion scheme (Davis and Emanuel, 1991) described in section 2.2. The inversion was performed at the simulation starting time (11 Nov 00 UTC) using the NCEP/NCAR the 10-day averaged fields were centred at 12 Nov 00 UTC. However, in simulations with a total upper-level PV anomaly removed, the cyclone was excessively changed, both in intensity and in path. Thus, in order to keep the similarity with the real case, a PV perturbation used for our sensitivity study addressed only half of the total PV anomaly (figure 4.2.12). This later resulted in an upper-level PV anomaly that e.g. on 12 Nov 06 UTC reached 8 PVU at 300 hPa level, compared to the almost 14 PVU associated with the original upper-level PV anomaly. This should be kept in mind when considering the quantitative contributions of the upper-level potential vorticity and its interactions.

The influence of the Atlas mountainous range is realised removing all the topography of the mountain range from the simulation (height is fixed to 1 m allover the domain of the range, see figure 4.2.13). SSHF is studied throughout modifications in the boundary layer scheme used in the simulations. PBL used scheme is a high resolution modified version (Zhang and Anthes, 1982; Zhang and Fritsch, 1986) of Blackadar scheme (Blackadar, 1979). The SSHF is switched off in the scheme computations. By this way, PBL will be generated without the heating of the surface. Radiative heating from the sun will be heating the soil without any exchange with the atmosphere. Upper level PV anomaly will be studied via the piecewise PV Inversion.

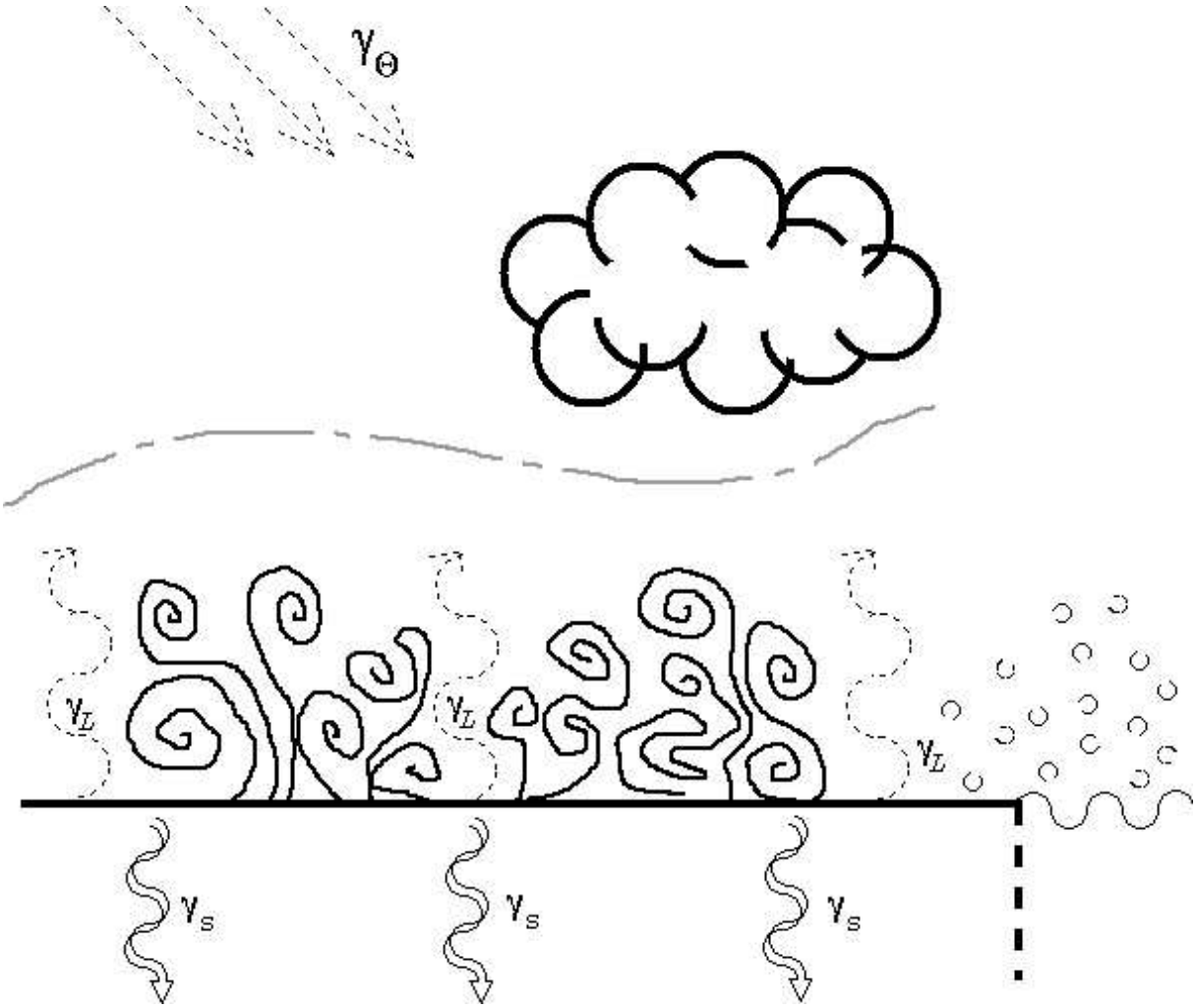

Figure 4.2.11: **Radiative balance:** Solar radiation (parallel and downdraft arrows, shortwave radiation γ_Θ) heats the surface. A fraction of the heat is emitted as longwave radiation (curved arrows, γ_L), which is partially absorbed by the water vapour of the clear-air, liquid water content of the clouds, CO_2. Another fraction (SSHF) heats the lowest layers of the troposphere from which the turbulence (spirals) is generated within the boundary layer (gray slash-dot line). Another fraction of the solar radiation is diffused in to the ground (γ_s, double curved arrows). Finally, another fraction evaporates the humidity of the soil surface, or the water of rivers, lakes or seas (opened circles)

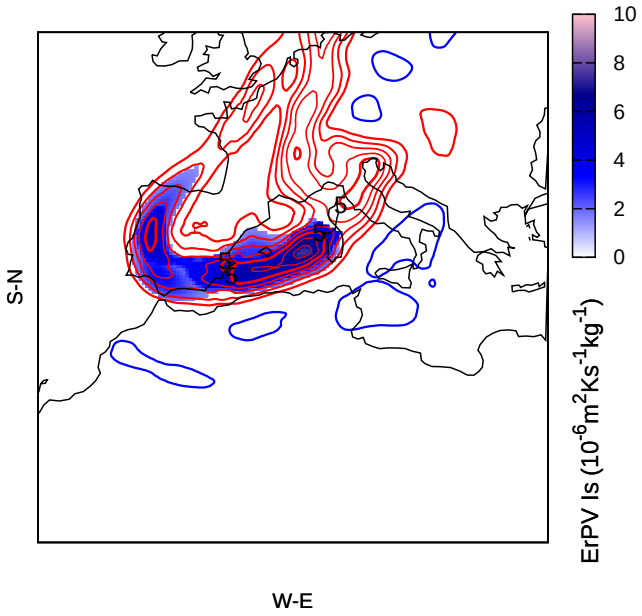

Figure 4.2.12: *Ertel Potential Vorticity* anomaly on Nov. 14th at 00^{00} UTC (solid line every 1 $PVU = 10^{-6}m^2Ks^{-1}kg^{-1}$). PV anomaly selected feature f_3 (shaded region, PV units)

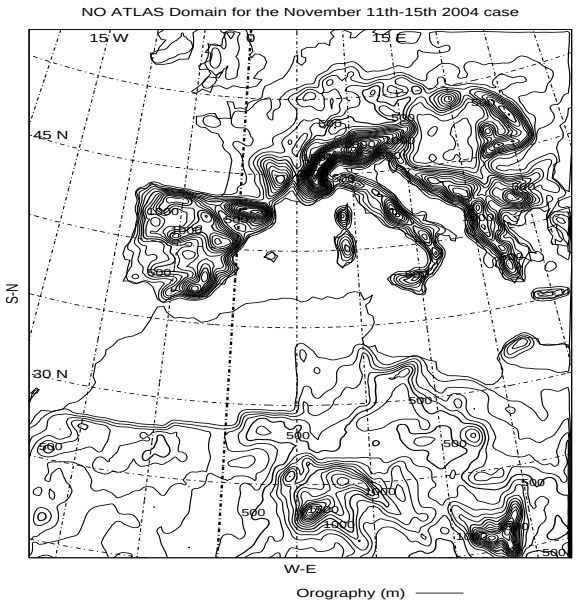

Figure 4.2.13: Orography after the removing of the mountain ranges of the Atlas f_1

Resultant selected sensitives are labelled as follows:

- e_0: Other effects
- e_1: Atlas range effect
- e_2: SSHF effect
- e_3: Upper level PV anomaly fraction effect at the initial conditions
- e_{12}: Synergy between Atlas and SSHF
- e_{13}: Synergy between Atlas and Upper level PV anomaly
- e_{23}: Synergy between SSHF and Upper level PV anomaly
- e_{123}: Triple synergy

A time evolution of the factor contributions to the mean sea level pressure value illustrates the dominance of different processes at different stages of the cyclone development (figure 4.2.14). The analysis focused on the period starting from 12 Nov 00 UTC (24 hours after the simulation initiation) that is the approximate time of cyclogenesis commencement in the simulation. The apparent cyclogenetic influence of upper-level PV in

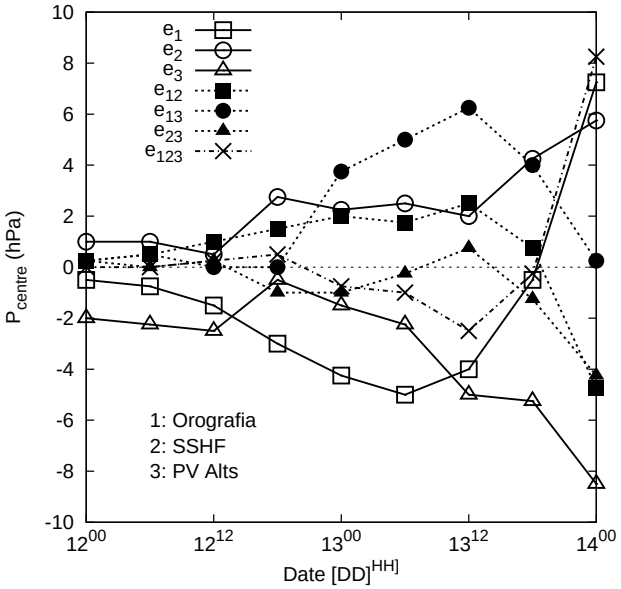

Figure 4.2.14: Temporal evolution of the effects of each factor on the control simulated central pressure of the cyclone (hPa)

the start of the analysed period (12 Nov 00 UTC, e_3 effect, line with empty triangles in figure 4.2.14) probably merely reflects the change in initial conditions. Namely, a removal of upper-level PV perturbation caused a warming of the low-level cold air impinging on the Atlas, thus reducing the intensity of the thermal anomaly and the associated pressure low. That is the reason why, before the cyclogenesis commenced, a mean sea level pressure was somewhat higher in the background simulation (with all factors excluded, f_0 simulation) than in the simulation with the upper-level PV perturbation included (f_3).

The first pronounced cyclogenetic influence was an orographic one (effect, e_1, line with empty squares in figure 4.2.14), starting around 12 Nov 00 UTC, cumulatively exerting 5 hPa deepening on the cyclone. This influence was associated with a frontal retardation and creation of the thermal and low-level PV anomalies in the lee of the High Atlas that were not present in simulations without orography. At that time and in subsequent hours, the cyclone centre was mostly attached to the quasi-barotropic lee area, marking the first phase of the lee cyclogenesis. At 13 Nov 06 UTC, an orographic influence first diminished (e_1), and then became strongly cyclolytic (destruction of a cyclone). This type of duality of orographic influence was already noticed in a study of the Alpine cyclogenesis by Alpert et al. (1995) and was probably due to cyclone movement out of the favourable lee area.

Similar results were achieved in Tsidulko and Alpert (2001), although the cyclogenetic influence of orography in their analysis does not seem to be so intensive as in this study.

The upper-level potential vorticity perturbation (effect e_3, line with empty triangles in figure 4.2.14) started to contribute to cyclogenesis at the time its strongest core got advected over the Atlas lee at 12 Nov 18 UTC. Its influence was in the subsequent period associated with reduced stability of the troposphere and a creation of a slightly stronger thermal anomaly at the surface (inclusion of the upper-level PV perturbation cooled the air impinging on the Atlas). Furthermore, stronger positive vorticity advection at upper levels induced greater low-level vertical velocities (e.g. in accordance with the omega equation, 2.2.21) and stronger low-level convergence, resulting in a more intense low-level vortex development. Stronger winds at lower levels resulted in the more intense cyclonic circulation and the stronger shear line in the lee. In other words, a cyclonic circulation of the upper-level potential vorticity anomaly propagated vertically (downward) to the middle and lower atmosphere, in accordance with conclusions derived from similar experiments for the Alpine lee cyclogenesis (Tsidulko and Alpert, 2001) and in idealised numerical experiments on the Sharav cyclone (Egger et al., 1995) However, as later analysis is going to show, the difference between the speeds of advection in simulations that define the upper-level PV perturbation influence (referred as e_3) indicates that part of its strong cyclogenetic influence in the end of the analysed period could be partially related to moist processes over the Mediterranean Sea.

The most pronounced contribution of sensible surface heat flux (effect e_2, line with empty circles in figure 4.2.14) seems to be the afternoon cyclolysis. It is evident that surface heat flux enables heat exchange between the atmospheric planetary boundary layer (PBL) and the surface. Thus, in the simulation without surface sensible heat flux, absorbed energy during the daytime (when SSHF is directed upwards) caused higher ground temperatures, but lower surface air temperatures near the ground and a less intensive planetary boundary layer. In this environment, a weaker PBL and less vertical mixing contributed to a stronger baroclinic zone and more intensive cyclone deepening. A similar cyclolytic influence in the early stage of the cyclone development has been noticed in work done by Kuo et al. (1991a), although their case took place over the sea. Furthermore, a horizontal air temperature gradient in the surface baroclinic zone was stronger then the horizontal ground temperature gradient at the same location. Thus, when enabled, the heat exchange tended to increase the horizontal temperature gradient in the ground, and decrease it in the low-level atmosphere, weakening the baroclinic zone and cyclone deepening. Finally, it is proposed that exclusion of SSHF affected the radiation balance at different levels in the atmosphere. In absence of SSHF, during the daytime, ground temperature was higher than in the presence of SSHF. This situation enhanced the longwave earth radiation, which became the main heat exchange factor between the ground and the atmosphere, since latent heat flux over the arid Atlas lee was rather small.

In contrast to SSHF that transferred the heat more locally to the surface boundary layer (and indirectly to the whole PBL through turbulent mixing), longwave terrestrial radiation was absorbed the most where the humidity was the highest. Throughout this process, cloudy areas in the free troposphere gained more, while the surface layer gained less heat energy compared to the control run. Thus, the PBL was less intensive contributing to a stronger surface baroclinicity and cyclogenesis as described above. On the other hand, the moist free troposphere was less stable due to increased heating. The heating of the moist free troposphere is known for its strong contributing to a cyclone deepening. For example, in Alpert et al. (1995), latent heat release was identified as one of the main contributors to cyclone deepening. Although the underlying mechanism was clearly not the same, the final effect in terms of a heat supply to the free troposphere seems to be qualitatively similar.

The afternoon cyclogenetic effect of SSHF noticed in the study seems to oppose the findings of Alpert and Ziv (1989), who investigated the generation mechanism of the Sharav cyclones with modified two-level linear baroclinic model suggested by Phillips (1954). Thus, their study mostly considered global to regional scale analysis that can be captured by quasi-geostrophic balanced dynamics. This result seems to indicate the scale dependence of the SSHF influence, and the importance of mesoscale frontal dynamics and boundary layer processes representation in the model, in order to fully determine the role of surface sensible heat fluxes in lee cyclogenesis events.

It is interesting to note the contribution of the synergy between orography and upper-level potential vorticity (e_{13}, line with filled circles in figure 4.2.14) on the mean sea level pressure values. The influence was clearly cyclolytic during the 18-hour period, starting from 12 Nov 18 UTC. It will be shown later in the analysis of cyclone paths, that it seems to be connected to the cyclone destruction at the orographic obstacle on the way to the Tunisia area. After that, on 13 Nov 12 UTC and subsequent hours, the synergy contributed to the cyclone recovery. At that time lower and upper-level vortices were tilted to the favourable western direction with height. Rough estimates of geopotential at 300 hPa and mean sea level fields on 13 Nov 12 UTC gave a horizontal dimension of the upper-level trough wave of L=60, and a separation of the centres of around 0.15L. If these numbers were applied to the idealised conceptual models of low-level-upper-level vortex interaction or linear instability theory (Bretherton, 1966; Hoskins et al., 1985), the waves would tend to hold themselves against the zonal flow (i.e. against differential advection), growing and reinforcing each other. This qualitative consideration seems to be roughly applicable at the end of the analysed period, when low-level and upper-level centres tended to be almost locked in phase.

It has been observed that an inclusion of SSHF in the simulations strengthens the upper-level PV. This is in qualitative agreement with the cyclogenetic synergy of SSHF

and upper-level PV (e_{23}, lines with full triangles in figure 4.2.14) seemed to show in the afternoons. Other synergies (e_{12}, e_{12}, e_{123}) did not seem to exert a significant impact on the cyclone centre deepening/filling, except in the very end of the analysed period. The corresponding results at that time should be interpreted with care, because of the cyclone centre spread at the end of the simulations. Namely, in some simulations the cyclone centres entered the Mediterranean, while in others still stayed on the continent. In this way, possible moisture processes could have influenced the results. However, the role of moist processes is out of the scope of this study and will not be analysed here.

Cyclone centre paths in factor separation simulations are shown in figure 4.2.15. A cyclone centre path for the simulation with the total upper-level PV anomaly removed from the initial conditions (F_PV) is added to the picture. Considering the latter first, we can see that without upper-level PV anomaly in the initial conditions the cyclone initiation point and movement were excessively changed. The shallow cyclone was indeed formed in the lee of the Ahaggar Mountain (refer to figure 4.1.18), dominated by a weak advection of the upper-level PV from the boundary conditions over that area. Thus, the analysis suggests that strong upper-level PV advection is crucial for the cyclogenesis in the lee of the Atlas to occur.

The influence of orography on cyclone paths was clearly resolved the four closest cyclone paths to the Atlas range corresponded to the four simulations with orography included (F1, F12, F13, F123 trajectories in figure 4.2.15). Therefore, in the first place orography tended to move the location of cyclone initiation to the favourable lee area where orographically induced low-level PV and thermal anomalies were the strongest. In addition, it continued to keep the cyclone path deeper inside the lee area. In contrast, inclusion of the upper-level PV perturbation (factor 3) moved the position of the cyclone formation away from the mountain. It seems that the stability of the lower atmosphere on the windward side of the Atlas played an important role in localising the formation place. Namely, in simulations with the upper-level PV perturbation included, the lower atmosphere was less stable underneath. A closer look reveals that in those simulations (F3, F23), cold air parcels on the windward side were able to cross the mountain more efficiently and moved the thermal anomaly more to the south-east. Adversely, in simulations without the upper-level PV perturbation, the low-level stability was stronger and the air was forced to go around the obstacle, creating a thermal anomaly deeper inside the mountain lee. Diffluence of the cyclone paths in simulations with a variable intensity of the upper-level PV anomaly indicates that upper level dynamical factors have a potential to account for the variability of the cyclone paths towards the Mediterranean Sea. Inspection of the cyclone path in the simulation with orography and upper-level PV perturbation (F13) included showed that the cyclone ran into the orographic obstacle on the way to the Mediterranean Sea. The associated land-rise (hill) the cyclone crossed was almost 500 meters, and was not experienced in other simulations of interest (f0, f1 and

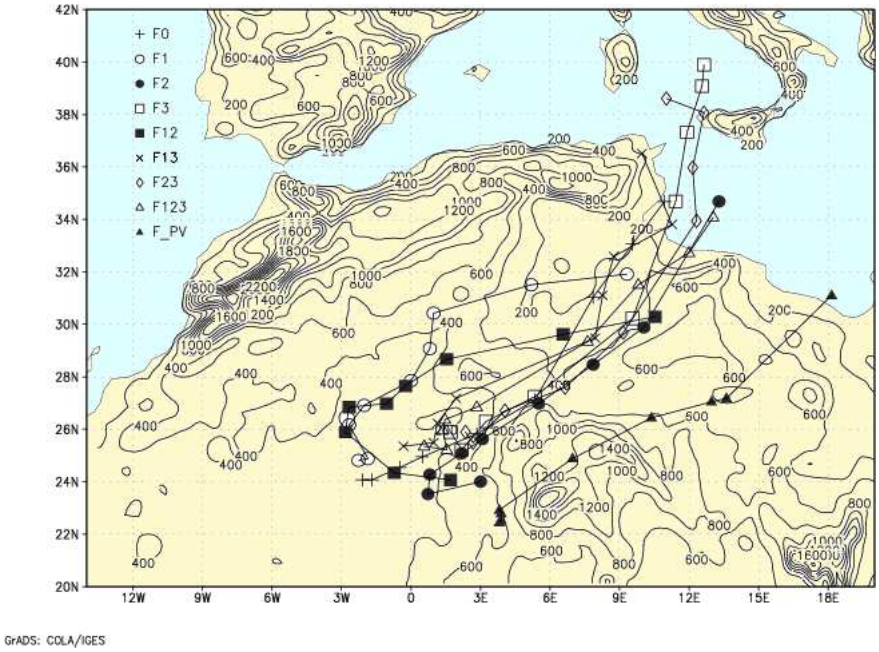

Figure 4.2.15: Simulated trajectories of the different simulated cyclones. On F0 (equivalent to f_0 in equation 2.3.4), F1 (f_1): simulation only with the topography, F2 (f_2): only SSHF, F3 (f_3): only PVp, F12 (f_{12}): without PVp, F13 (f_{13}): without SSHF, F23 (f_{23}): without top orography, F123 (f_{123}, control simulation): with the three factors, F_ PV: simulation without the entire upper-level PV anomaly PVp. Symbols denote position of the cyclone every 6 hours

f3, refer to equation 2.3.4) to such an extent. Thus, this unique cyclone path, and the destruction over the hill could have been the reasons for the strong cyclolytic influence the analysed synergy tended to produce. This idea qualitatively resembles the studies on tropical cyclones passing over the island terrain (g.e. Bender et al., 1987) that reported a strong cyclone filling as the cyclone passes the land disturbance. However, this cyclolytic influence lasted for 18 hours and it is not clear whether this type of orographically induced cyclone filling can be held responsible for the cyclolysis in the whole period.

There were significant differences noted in the times the cyclone reached the Mediterranean Sea. The two slowest cyclones were attached to orographically (f1, f12), while the two fastest ones to upper-level potential vorticity dominated simulations (f3, f23). As expected, sensible heat flux did not have a significant impact on the cyclone track variability. The aforementioned strong dependency indicates that the orographic influence was to keep the cyclone in the mountain lee, while upper-level potential vorticity induced a faster advection of the low-level pressure system to the Mediterranean Sea.

Chapter 5

Medicanes: Tropical-like Mediterranean storms

Articles on which this chapter is based:

L. Fita, R. Romero, a. Luque, K. Emanuel and C. Ramis, 2007: *Analysis of the environments of seven Mediterranean tropical-like storms using an axisymmetric, nonhydrostatic, cloud resolving model*, Nat. Hazard. Earth Sys., **7**, 41-56

L. Fita, R. Romero and C. Ramis, 2008: *Sensitivity study of Mediterranean tropical-like storms. part I: Sensitivity of air-sea mechanism in three storms*,Ann. Geophys., **submitted**

L. Fita, R. Romero and C. Ramis, 2008: *Sensitivity study of tropical-like storms. part II: Verification, dynamics and structure of January 1995 medicane*,Ann. Geophys., **submitted**

Different studies have revealed the existence of tropical-like storms evolving in the Mediterranean basin (in the following, the 'medicane' [Medi-*terranean*+*Hurri*-cane] term is adopted to refer to these systems). A rounded cloud structure surrounding a cloud free area in the centre associated with strong winds, heavy precipitation and high vorticity is a common aspects of medicanes. These are rare cases, however since, about 40 cases during the last 25 years allover the Mediterranean basin have been detected from satellite images and bibliography done by the *Grup de Meteorologia* of *Deparatament de física* of the *Universitat de les Illes Balears* (a web page[1] has been prepared with animations of satellite pictures of the detected cases). Some of the cases have been previously analysed and studied from different perspectives and using different techniques (Rasmussen and Zick, 1987; Businger and Reed, 1989; Lagouvardos et al., 1999; Pytharoulis et al., 2000; Reed et al., 2001; Homar et al., 2003b). Conclusions obtained from these studies reflected the singularity of the characteristics of the phenomena in the Mediterranean basin. Despite its low occurrence, this type of strong cyclogenesis over open sea areas has an important interest due to its potential destructiveness and the high populated Mediterranean coastal line.

Since the initial description of a tropical storm occurred South of the Sicilian Island done by Ernst and Matson (1983), different studies have been devoted to medicanes. Rasmussen and Zick (1987) provided a satellite-based description of a medicane occurred at the end of September 1983. Moreover, through the analysis of soundings they verified the warm core structure of the system and made the hypothesis about the important role of the sea surface temperature (SST) and the strong convective activity associated to these phenomena. Businger and Reed (1989) classification of the small and strong vortex generation associated to a cold air mass gave a first main frame of these kind of phenomena. The term 'polar low' was applied to those extratropical small and deep cyclones originated in sea areas related to a cold upper level air mass or synoptic disturbance. Medicanes were classified as a subclass of "polar low" developed in the Mediterranean basin. They associated this phenomena to an upper level low with a strong convective activity induced by a warm sea from which strong heat and moist surface fluxes were generated. Basically, on a pre-existing high convective and cyclonic environment, convection is enhanced by the existence of an upper level cold low. Self organisation of the convection around a small vortex contributes to the formation of a deep and small cyclone enhancing convection mechanism. Instead of the baroclinic aspects of the Mediterranean basin, the initial studies of medicanes related the evolution of these systems to convective processes, more typical from tropical environments. By this way, the evolution and maintenance of these systems was supposed to be a combination of different mechanisms such as baroclinicity, conditional instability of second kind (CISK), air-sea interaction and barotropy.

The application of atmospheric limited area numerical models gave the opportunity

[1] `http://www.uib.es/depart/dfs/meteorologia/METEOROLOGIA/MEDICANES/`

to confirm such theories. These models are able to simulate medicane systems with a pretty good correspondence with the observations, helping to describe the evolution of the storms over the data-avoided oceanic areas. As examples, ETA and RAMS models were used by Lagouvardos et al. (1999), UK Met. Office Unified Model for the same case by Pytharoulis et al. (2000), and MM5 simulations were done for two cases: January 1982 (Reed et al., 2001) and September 1996 (Homar et al., 2003b). Warm core evidences of the systems are obtained from these simulations as well as characteristic radial wind profiles. Exploiting the flexibility of the numerical models, sensitivity studies can be carried out in order to verify observational hypotheses and to obtain a better understanding of the phenomena. Sensitivity tests of the storms (Lagouvardos et al., 1999; Reed et al., 2001; Homar et al., 2003b) confirm the important role of the different mechanisms theoretically emphasised for the medicane formation and evolution. A large set of parameters have been tested: diabatic processes such as latent heat release from convection and latent heat flux from the sea (hereafter, LHF) are key mechanisms in the medicane; sensible surface heat flux (hereafter, SSHF) and SST played also an important role in the medicane evolution; Homar et al. (2003b) showed an evolution of the September 1996 medicane initially dominated by upper level induced mechanisms and a second phase dominated by LHF and diabatic processes. Reed et al. (2001) revealed a high sensitivity of the simulation of the January 1982 case to the initial conditions (as an initial surface vortex). These same studies have revealed that these Mediterranean systems can have the strength of a tropical storm (more than 33 ms^{-1}).

Previous described observational sparse model-based studies revealed that principal reinforce mechanisms of medicanes are related to sea surface temperature and the presence of an upper level anomaly (Rasmussen and Zick, 1987). The use of present nonhydrostatic models operated at higher resolution than older ones should be able to confirm and reveal new fine and deep structures of these systems. Such studies like (Lagouvardos et al., 1999; Pytharoulis et al., 2000; Reed et al., 2001; Homar et al., 2003b) also presented a strong small vortex related to heavy precipitation and a warm core. These studies also confirm main mechanisms of reinforce and maintenance such as: strong diabatic processes related to vigorous and deep convection, latent heat release from cloud formation at middle altitudes, vigorous latent heat fluxes from the sea and the initial driven role of the baroclinicity due to a prior upper level cold low. Sensitivity test shown that without latent heating due to the strong convection developed by deep cumulus, these systems can not be developed (Homar et al., 2003b). A lower influence is attributed to surface fluxes and upper level trough, latent heat flux from the sea surface and in lower degree, sensible surface heat flux. Another important role is attributed to the SST value as it is shown by Homar et al. (2003b). Although, uncertinities due to the lack of observations related to maritime characteristics of the systems decrease the success of the simulations of the models (Reed et al., 2001).

Air-sea interaction mechanism (Emanuel, 1986) has also been proposed as responsible for the medicane evolution. However, Mediterranean environment is very different than the tropical one (Reiter, 1975). Maritime Tropical environments exhibit homogeneous atmospheric characteristics over most of the low latitudes region. They are characterised by warm temperatures and high humidities (e.g. mean annual values of temperature and humidity at 1000 hPa for the West Indies are respectively 24.3 $^{\circ}C$ and 79%; Jordan (1958)). Tropical environments show also a low seasonal trend (annual spread of the temperature at all levels is lower than 10 $^{\circ}C$ Jordan (1958)).

Main characteristics of the Mediterranean basin like elevated surrounding orography, small sea and warm and dry air advections from the North African plateau might influence the Mediterranean tropical-like systems. Thus, Mediterranean cases evolve within a more complex environment than the homogeneous tropical one and in order to capture the entire influences due to the complexity of the environment (see figure 1.1.2), their study should be done with full physics primitive equations numerical models like MM5 if an adequate simulation will be obtained (Fita et al., 2007a).

The existence of an upper level cold low above warm and moistened low level air is assumed as the triggering environment from which medicanes are formed (Emanuel, 2005). By this way, medicanes can be developed above sea within a surface temperature (see SST distribution during the January 1995 case in figure 5.0.1) colder than the 26 °C, threshold below which a hurricane can not be formed (Emanuel, 1986).

5.1 Description of studied cases

Seven cases have been studied with different techniques, purposes and methodologies. Each one affected different areas and occurred at different periods of time (see all their trajectories in figure 5.1.1). A general description of the cases has been obtained from the satellite images. The trajectory of the storms is derived through human-base eye localisation. All cases exhibited similar characteristics from the satellite perspective. A highly stormy environment was present during the initial phase of the systems (in some cases, convection with cloud top temperatures as cold as 200 K was observed, not shown). Cloud systems started to gain cyclonic rotational movement meanwhile cloud formation was enhancing. Rotational movement of the clouds increased rapidly and a well shaped circular cloud system was formed. In the centre of the cloud structure, a free cloud area (an eye-like structure) was visible. The hurricane-like aspect of the storm was visible at different periods of the storm evolution, and lasted for different amounts of times (see table 5.1.a, for more details). Then, the storm diminished in intensity and finally disappeared (generally 1 day later), mainly when the storm reached the coast.

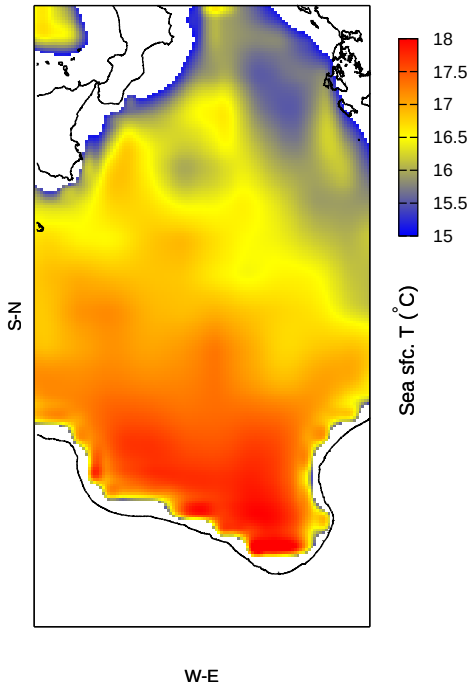

Figure 5.0.1: Sea surface temperature in the zone of evolution of the medicane. It is unchanged during all the period of simulation

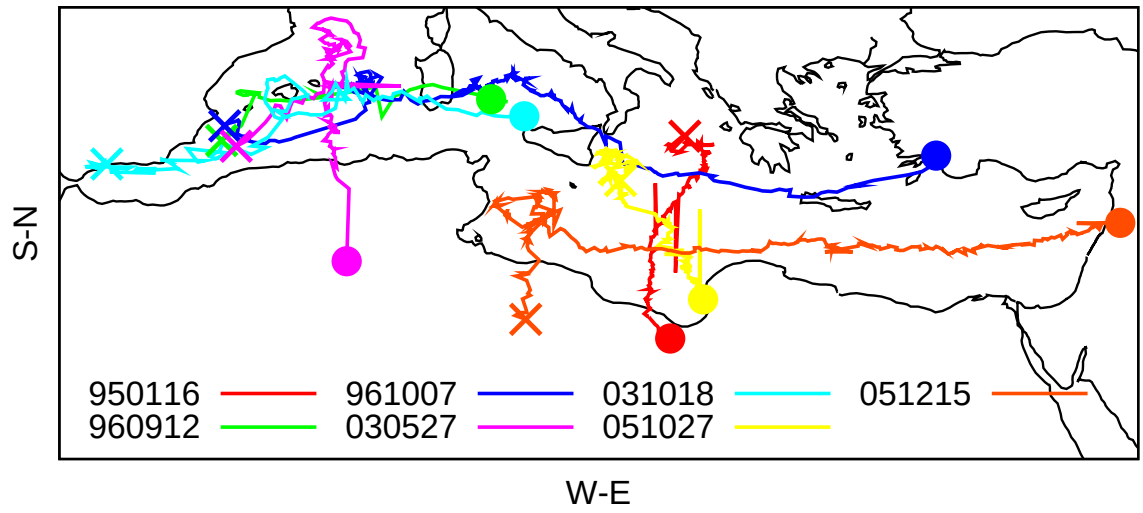

Figure 5.1.1: Storm trajectories derived from satellite imagery. See legend for case-description. Cross beginning of the storm. Full circle end of the storm

All cases presented similar synoptic characteristics (see figures from 5.1.2 to 5.1.9). An upper level trough was present during all the evolution of the cases. At low levels convergence of cold and warm air masses was present in the zone where the medicanes evolved at the initial phase of the cyclones. However, no particularly high relative humidities or deep column positive vorticity values, presumed in the tropical systems, were detected. Synoptic atmospheric environments obtained from ECMWF analyses did not show any particular difference from previous climatological Mediterranean studies of cyclonegensis and cyclone evolution (Reiter, 1975; Campins et al., 2000). 24 hours before the eye formation the environment (see table 5.3.b) was not supportive of strong thunderstorms according to calculated instability indices (Tudurí and Ramis, 1997). The presence in the area of a strong surface horizontal thermal gradient (bottom panels in figures 5.1.3 to 5.1.9) is an indication of the baroclinicity typical of the Mediterranean basin. As has been said, the presence of an upper level trough is assumed to be a necessary aspect to make possible the development of this kind of tropical-like storms (Emanuel, 2005): thermodynamic vertical disequilibrium in which the medicane is rooted is established between relatively high Sea Surface Temperature (SST) and the cold air associated with the upper level cold low. Thus a medicane might reflect the combination of two different storm genesis mechanisms: strong convection due to the vertical thermodynamic disequilibrium characteristics of tropical systems, and the baroclinic mechanism typical of the Mediterranean latitudes (Fita et al., 2007a). Meanwhile the coldest SST from which a hurricane can be formed is 26°C (Emanuel, 1986), SST in January 1995 case in figure

Table 5.1.a: Selected environments related to a tropical-like Mediterranean storm. First col. indicates label storm. 2^{nd} col.: Storm initial date (on [DD]/[MM] $[HH]^{[MI]}$ format), 3^{rd} col.: Storm ending date, 4^{th} col.: Eye beginning, 5^{th} col.: Eye ending

case	**Storm Beg.**	**Storm End**	**Eye Beg.**	**Eye End**
950116	$14/01\ 12^{00}$	$18/01\ 20^{00}$	$15/01\ 07^{00}$	$18/01\ 06^{30}$
960912	$11/09\ 21^{00}$	$13/09\ 02^{30}$	$12/09\ 07^{30}$	$12/09\ 12^{00}$
961007	$06/10\ 03^{30}$	$11/10\ 03^{00}$	$07/10\ 05^{30}$ $08/10\ 06^{00}$	$07/10\ 06^{30}$ $10/10\ 12^{00}$
030527	$25/03\ 12^{00}$	$28/05\ 04^{30}$	$27/05\ 08^{30}$	$27/05\ 15^{30}$
031018	$17/10\ 00^{00}$	$19/10\ 04^{00}$	$18/10\ 12^{30}$	$18/10\ 13^{30}$
051027	$26/10\ 20^{30}$	$29/10\ 14^{30}$	$28/10\ 10^{00}$	$28/10\ 12^{00}$
051215	$13/12\ 05^{00}$	$16/12\ 12^{15}$	$14/12\ 08^{00}$ $15/12\ 06^{00}$	$14/12\ 15^{15}$ $15/12\ 14^{15}$

5.0.1, for example was only 15.7°C, high enough to activate the air-sea thermodynamic disequilibrium due to the presence of very cold air advected southward by the baroclinic disturbance (see table 5.3.b). Environments related to tropical-like storms are detected in all seasons; however, a great preponderance occurs during Autumn. Studied storms of these environments reached different durations (larger than two days). Some storms travelled large distances (across almost all Mediterranean basin, see figure 5.1.1). All of them showed a high cyclonic rotation and less than 500 km in radius.

January 1995
This case occurred during January 1995 in the south of the Ionic Sea (see figure 5.1.2). In this case the medicane is formed within the area of influence of deep convection that reached the South of Italy and the Albanian coast. In the January 1995 case the eye-wall cloud structure was visible for about 1 day while the system moved southward about 500 km (see table 5.1.a).

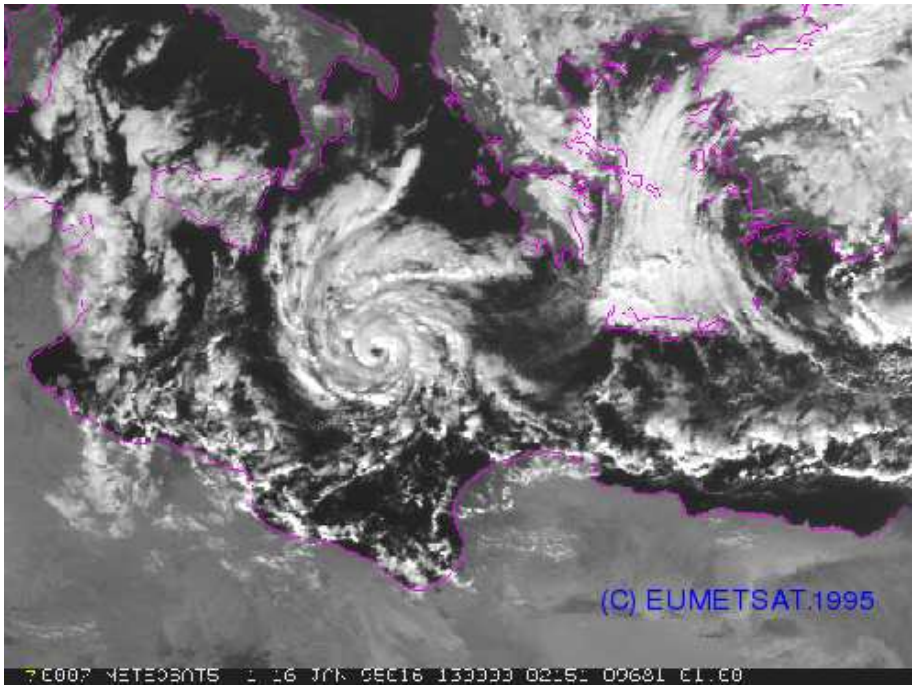

Figure 5.1.2: Main characteristics of the January 1995 medicane case. Normalised satellite visible image channel at maximum intensity moment corresponding to '950116' case on January 16th 1995 at 13^{00} UTC (source METEOSAT-5, top).

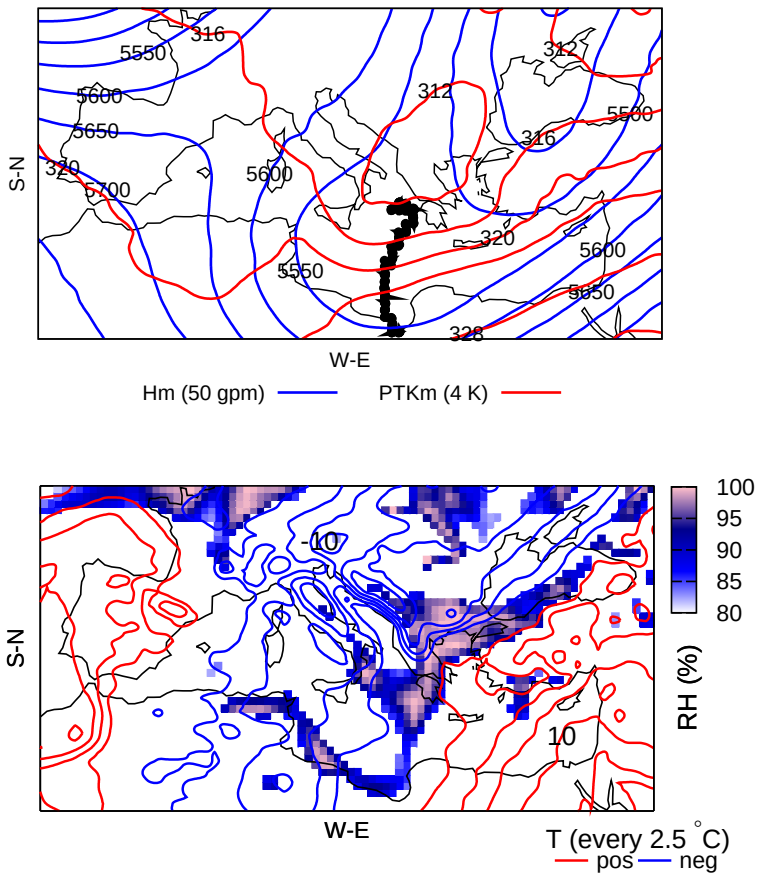

Figure 5.1.3: Main characteristics of the January 1995 medicane case. Top panel: Time averaged ECMWF analysis (during all the storm period see table 5.1.a) geopotential height (500 hPa, blue solid line, every 50 gpm) and time averaged potential temperature (300 hPa, red solid line, every 4 K). Thick solid lines with points showed storm trajectory obtained from satellite images. Bottom panel: Relative humidity at 925 hPa (above 80 %, shaded) and temperature at 850 (red line: positive values, blue line: negative values, every 2.5 $^{\circ}C$) at the beginning of the storm on Jan. 14th at 12^{00} UTC.

September 1996

This case affected the Balearic Islands (see middle panel in figure 5.1.4). Deep convection occurred in the Balearic Sea, between Valencia coast and Balearic Islands, meanwhile a weak cyclonic system was offshore the coasts of Argel. A weak vorticity centre evolved from the south following the Iberian coastal line. When this system reached the convective zone the medicane started to develop. September 1996 case, vanished in one day after it overpassed Sardegna Island.

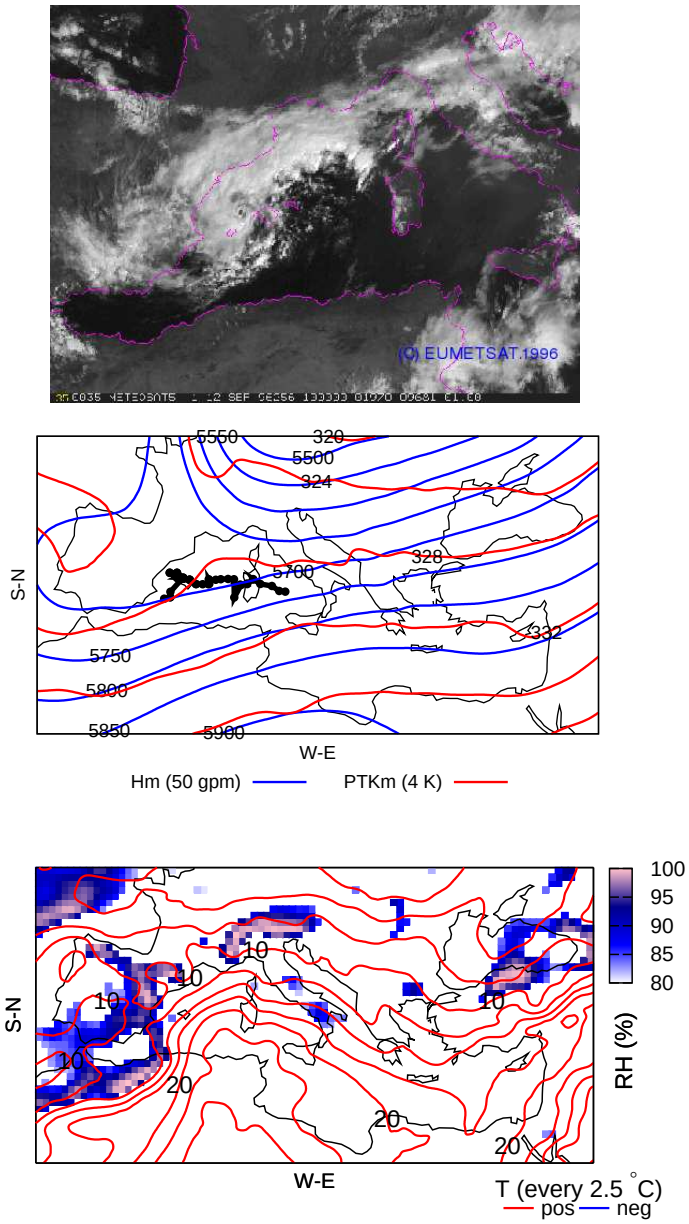

Figure 5.1.4: As in figures 5.1.2 and 5.1.3, but for the September 1996 medicane case. Satellite maximum on September 12th 1996 at 10^{00} UTC (METEOSAT-5, top). Beginning of the storm is on Sept. 12th at 00^{00} UTC.

October 1996

This case started as a storm system Southwest of the Balearic islands. It gained vorticity as it moved westward. Before it reached Sardegna island it shown a clear eye in the centre of spiral clouds. When it was overpassing Sardegna it lost it hurricane-like morphology, that it recovered again when it reached again the Sea between the island and Italy (see table 5.1.a with the two eye-detected period). The system moved south-eastward, overpassed close to the Strait of Messina and died as storm residual system South of the Peloponnese peninsula.

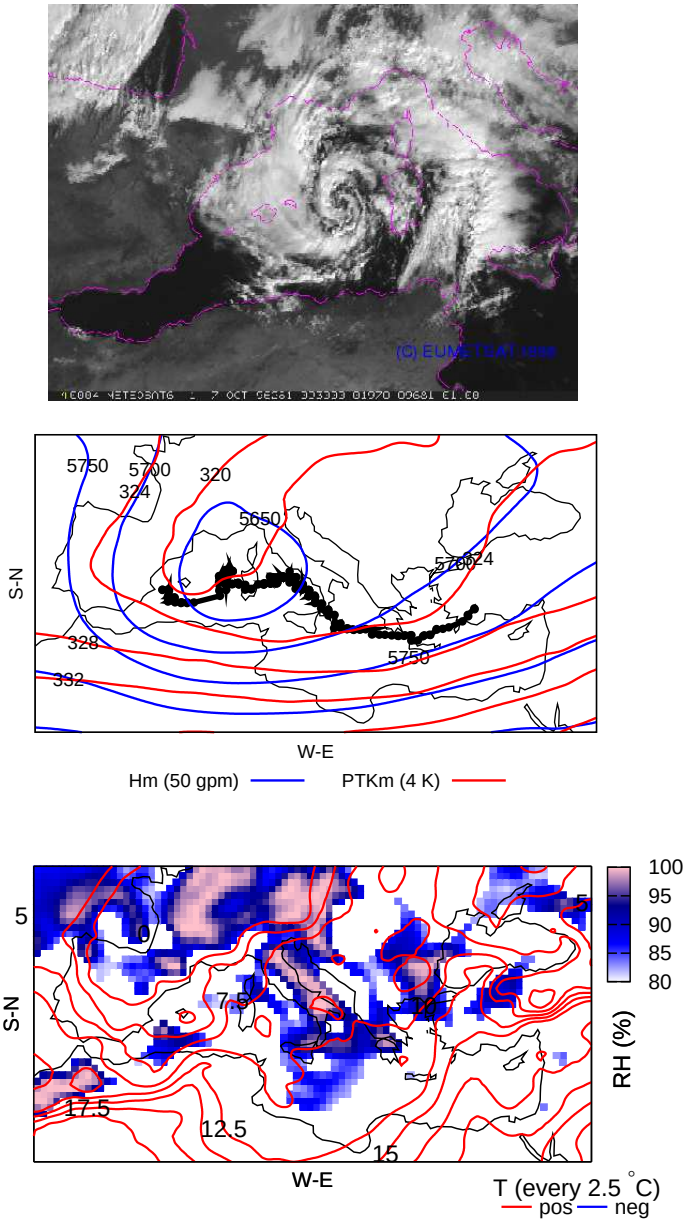

Figure 5.1.5: As in figures 5.1.2 and 5.1.3, but for the October 1996 medicane case. Satellite maximum on October 7th 1996 at 09^{30} UTC (METEOSAT-6, top). Beginning of the storm is on Oct. 6th at 06^{00} UTC.

May 2003

This episode occurred during May of 2003 in the Western Mediterranean basin. A cyclonic system was initially present between North of Balearics and Sardegna Islands. The vortex system evolved from a coma shape cloud structure to a medicane, while moving. Southwards and overpassing Balearic Islands. Strong vorticity of the cloud systems was observed but a cloud free area was not clearly identified.

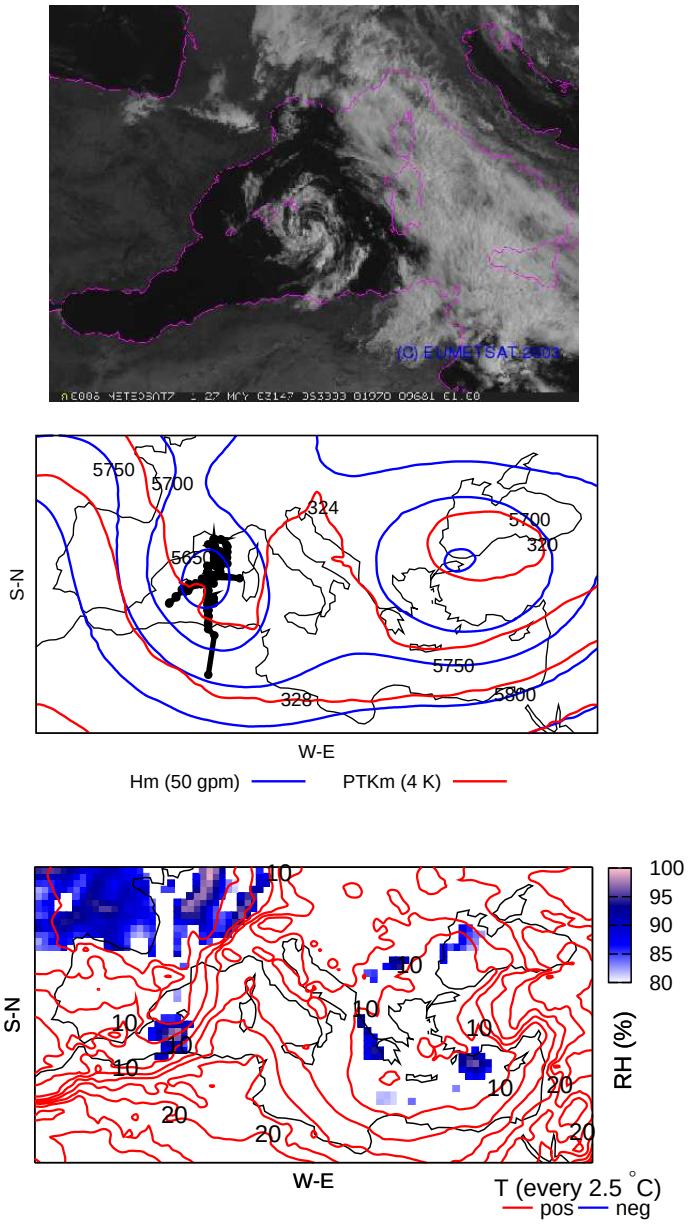

Figure 5.1.6: As in figures 5.1.2 and 5.1.3, but for the May 2003 medicane case. Satellite maximum on May 27th 2003 at 08^{30} UTC (METEOSAT-7, top). Beginning of the storm is on on May 25th at 12^{00} UTC

October 2003

This case developed in the Western Mediterranean basin. A weak vortex initiated to the south of the Iberian peninsula, evolved along the eastern coast of Spain until it reached an area with thunderstorm activity located between Iberian peninsula and Balearic Islands. Later, convective cloud cluster acquired a cyclonic rotation and formed the medicane. It moved westward until it disappeared when it overpassed the Sardegna island.

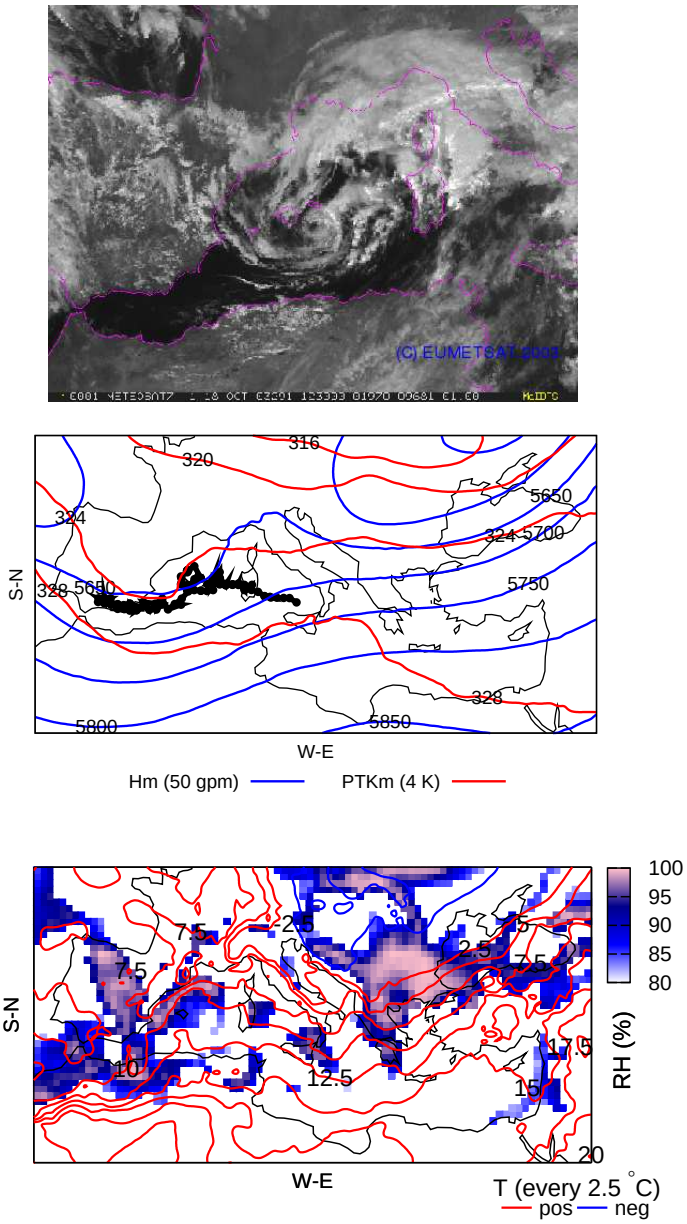

Figure 5.1.7: As in figures 5.1.2 and 5.1.3, but for the October 2003 medicane case. Satellite maximum on October 18th 2003 at 12^{30} UTC (METEOSAT-7, top). Beginning of the storm is on Oct. 17th at 00^{00} UTC.

November 2005

This case started as a strong storm system in the eastern coast of Tunis. It moved north-eastward until the South of the Strait of Messina. It stopped at this point and gained vorticity. Once it started cyclonicity to rotate it moved southward and disappeared in front of the North African coast at the Gulf of Sidra.

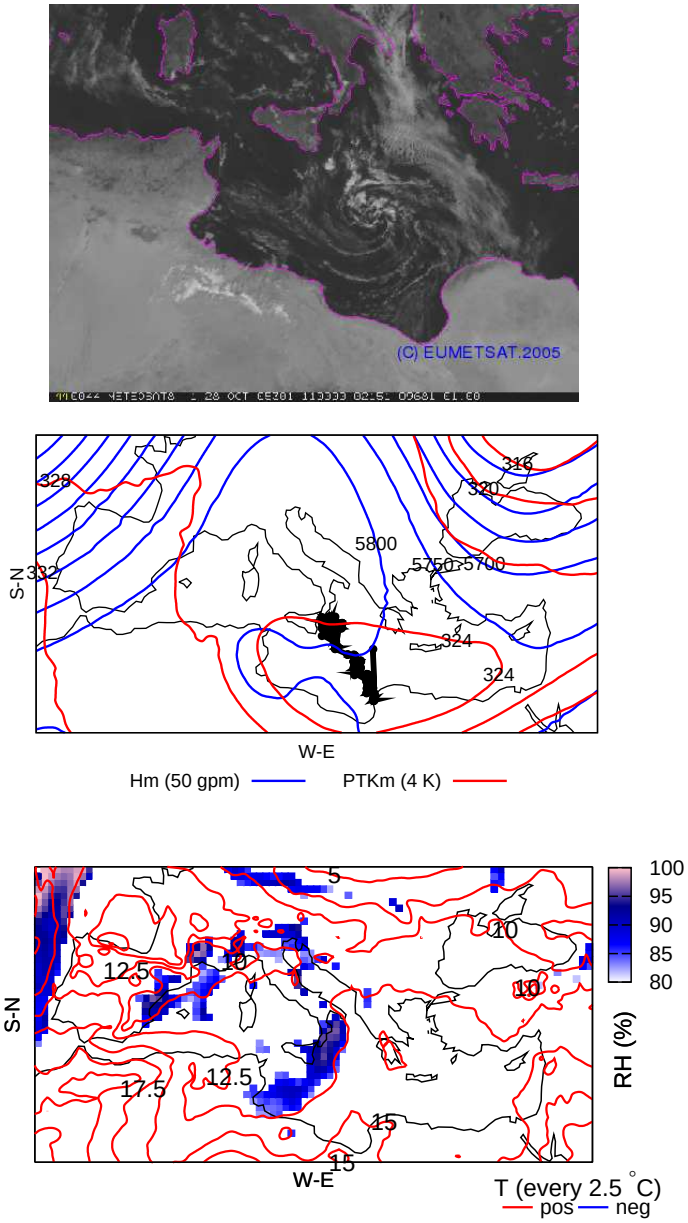

Figure 5.1.8: As in figures 5.1.2 and 5.1.3, but for the October 2005 medicane case. Satellite maximum on October 28th 2005 at 11^{00} UTC (METEOSAT-8, top). Beginning of the storm is on Oct. 26th at 18^{00} UTC.

December 2005

A weak vortex from the inland of North Africa reached a strong storm system located in the eastern coast of Tunis. Storm system acquired cyclonic rotation and moved eastward. Close to the Golf of Sidra round cloud structure with a cloud free centre as an eye was observed. It acquired again the eye-like centre structure when it was moving South of the Crete island (see two eye-formed periods in table 5.1.a). It vanished as storm system when it reached the eastern extreme of the Mediterranean basin.

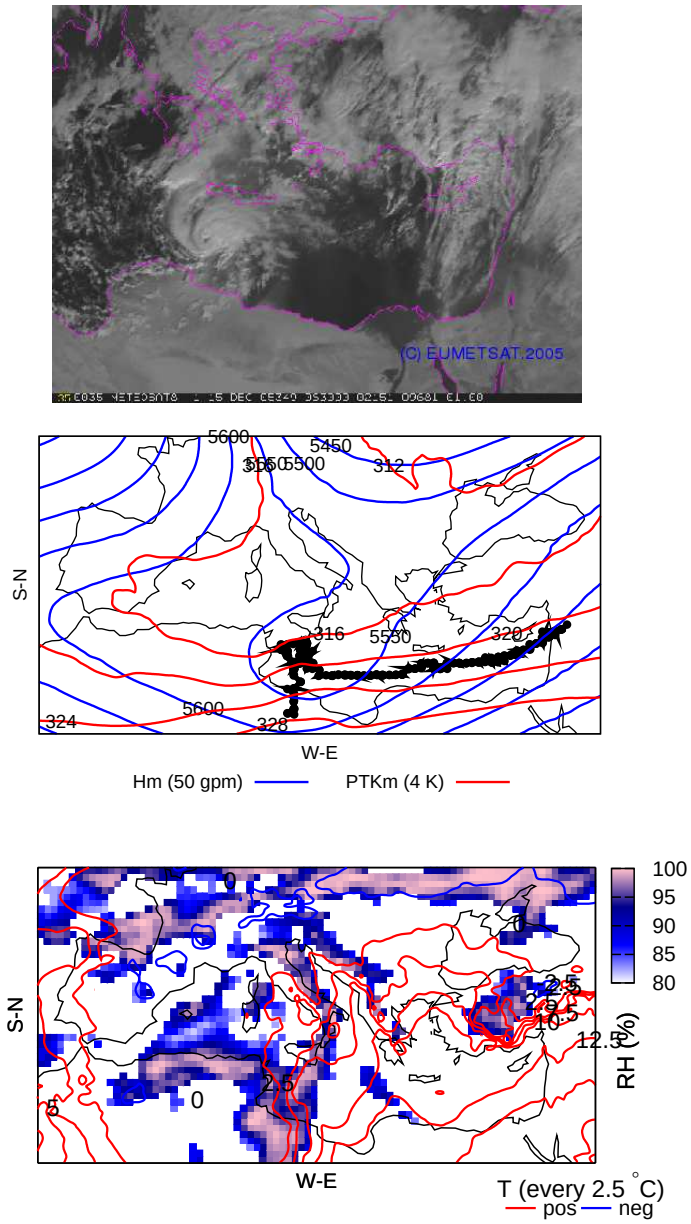

Figure 5.1.9: As in figures 5.1.2 and 5.1.3, but for the December 2005 medicane case. Satellite maximum on 15/12/05 at 08^{30} UTC (METEOSAT-8, top). Beginning of the storm is on Dec. 13th at 06^{00} UTC.

5.2 Air-sea mechanism

Air-sea mechanism (Emanuel, 1986) starts from the assumption that tropical cyclones are developed and maintained by the self-induced strong fluxes of moist and enthalpy originated above sea surfaces. Previous description of formation of tropical cyclones assume that convection was maintained by the moist convergence in the boundary layer of a quasi-balanced vortex (Charney and Eliassen, 1964; Ooyama, 1964). Air-sea mechanism does not assume an environmental CAPE value as the triggering mechanism as in previous descriptions, but it needs a genesis driven by a finite amplitude disturbance as a weak vortex. A feedback is established between radial temperature gradients and radial gradients of sea-air heat transfer associated with gradients of surface wind speed. Transfer of the moist and heat acquired from the Sea surface is driven by cumulus convection. By this way, environment keeps locally neutral to slantwise moist convection. This assumption provides a thermal and kinematic structure of the tropical storm in which combination of buoyant/centrifugal potential of boundary layer air is null. From which is derived a neutral buoyancy of the air in the boundary layer when it lifts along surfaces of constant angular momentum (Emanuel, 1983). It has assumed a well-mixed boundary layer that is inviscid and thermodynamic reversible and the gradient wind approximation can be applied.

Air-sea mechanism describes a tropical mature storm as an axisymmetric structure, with upward constant angular momentum air-parcels trajectories in the free atmosphere and a boundary layer with three distinct regions (eye, wall and outer zone; see schematic representation in figure 5.2.1). Outer zone is characterised by an inward increasing of the azimuthal wind speed with constant surface relative humidity and strong turbulent exchange at the top of the boundary layer. Eye wall zone is depicted as satured air with maximum azimuthal wind speed and strong updrafts (becoming the most responsabile flows for the moist transport instead of the turbulent transport $\overline{(\omega'\theta_E)}_h = 0$ as it is shown in figure 5.2.1). Eye zone is characterised by unsaturated air and subsidence.

The development and maintains of a tropical storm following air-sea mechanism can be described by the trajectory that follows an air particle within a tropical storm. It is assumed that the gain of energy is only obtained from the sea surface. Throughout a constant thermal inward movement to the centre of the storm air particle acquires energy (A-B section of figure 5.2.1). Strong amount of heat and moist is acquired at constant temperature. When the air particle reaches the wall zone it is adiabatically upward decompress transported following constant angular momentum surfaces (B-O section of figure 5.2.1). By radiative Newtonian cooling, air particle loses its heat at the outer part of the storm (O-O' section of figure 5.2.1). Air-mass circulation it would be enclosed by adiabatic compression by turbulent mixing with surrounding air (O'-A section of figure 5.2.1). This description of the energy budget within a tropical storm allows an ideal

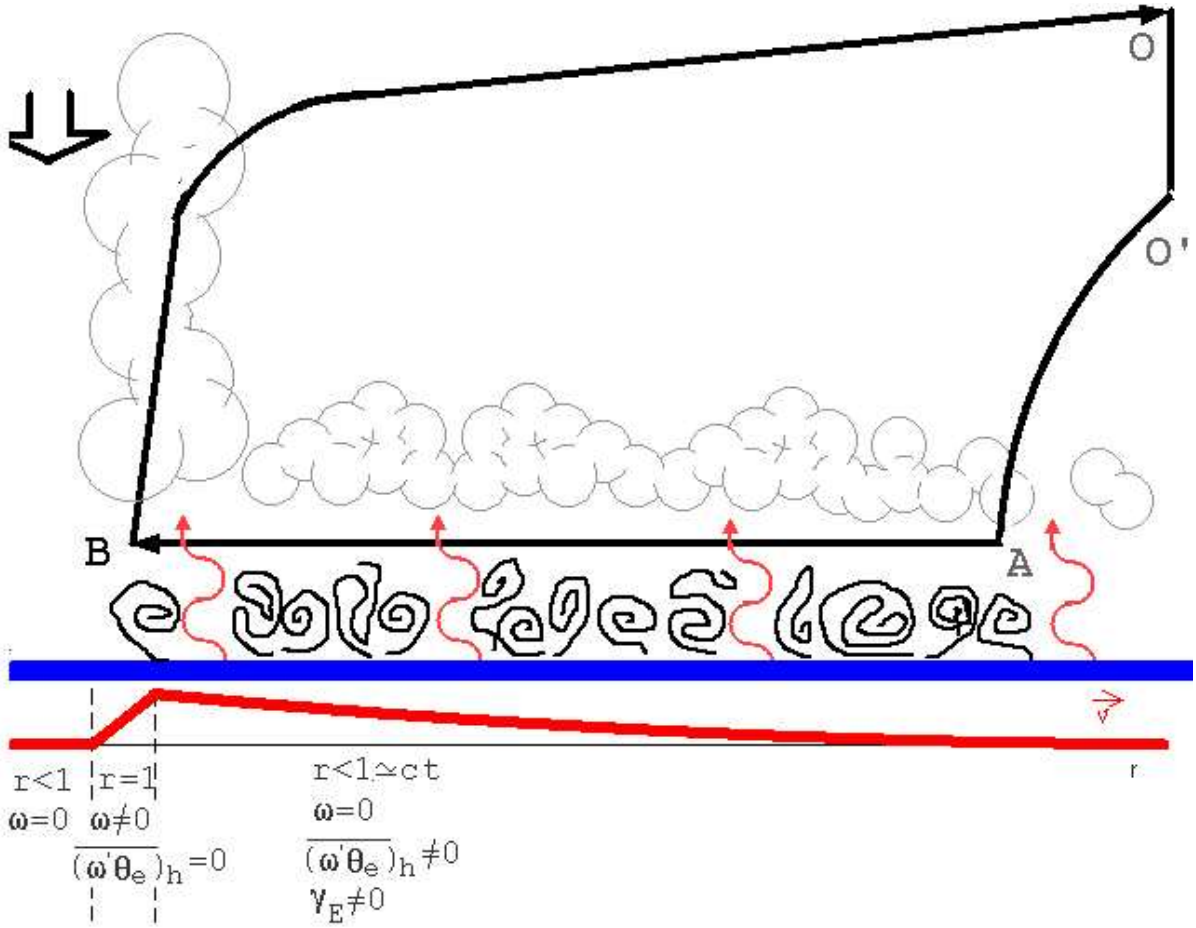

Figure 5.2.1: Radial structure of a tropical steady storm. $\vec{v}$, azimuthal wind (thick red line below); PBL regions (dashed lines, from left to right: eye, wall, outer zone); r, relative humidity; ω, vertical velocity; $\overline{(\omega'\theta_E)}_h$, turbulent vertical transport of moist entropy; γ_E, Ekman pumping

treatment of the storm as a Carnot heat engine (Emanuel, 1986, 1995).

Air-sea mechanism provides a relation between the dimension of the tropical storm, the radius with the maximum azimuthal wind speeds, the pressure fall at the centre of the storm and the thermal relation between the sea surface temperature and the upper level temperature at the outer region of the storm in which the radiative cooling occurred. At the same time provides a 26°C minimum sea surface temperature threshold below which a tropical storm would not be formed.

Main characteristics of the tropical storm according to air-sea mechanism are:

- Radial distribution of moist entropy θ_e

$$\ln \theta_e = \ln \theta_{es} - \frac{C_D}{C_\theta} \frac{1}{C_p(T_B - T0)} \left(V^2 + \frac{1}{2} f r V \right)$$

  where θ_{es}, surface moist entropy; T_B, absolute temperature at the top of the boundary layer; T_0, outflow temperature; f, Fourier.

- Radius length of the storm r_0

$$r_0^{2+2\beta} \approx r_{max}^{2\beta} 2\epsilon \frac{C_\theta}{C_D} \frac{T_B}{T_S} \frac{L q_a^*}{f^2} (1 - RH_{as})(1 + \beta) \tag{5.2.1}$$

  where r_{max}, radius of maximum wind; T_s, surface temperature.

- Wind $|\vec{V}\|$ radial distribution

$$V(r) \begin{cases} V \approx r^{\chi/2} & r < r_{max} \\ V \approx r^{-\beta} & r > r_{max} \end{cases} \tag{5.2.2}$$

$$\chi \equiv \frac{2\left[1 - \epsilon\left(1 + \frac{L q_a^*}{R T_s}\right)\right]}{2\frac{C_D}{C_\theta} - 1} \tag{5.2.3}$$

$$\beta \equiv 1 - \epsilon \left(1 + \frac{L q_a^* RH_{as}}{R T_s}\right) \tag{5.2.4}$$

$$\epsilon \equiv \frac{T_B - T_0}{T_B} \tag{5.2.5}$$

  where C_D/C_θ, Ratio exchange coefficients; q_a^*, saturated mixing ratio of the ambient; RH_{as}, relative humidity of the ambient at the surface;

- Eye-pressure

$$\ln \pi_{cs} \simeq \frac{-\left(\frac{T_B - \overline{T}_{out}}{T_B}\right) \frac{L q_a^*}{C_p T_S} (RH_c - RH_a)_s + \frac{1}{4} \frac{f^2 r_0^2}{C_p T_B}}{1 - \left(\frac{T_B - \overline{T}_{out}}{T_B}\right) \left(1 + \frac{L q_a^* RH_{CS}}{R T_S}\right)} \tag{5.2.6}$$

where $\overline{T}_{out}$, weighted averaged outflow temperature; RH_c, relative humidity at the centre, RH_{cs}, surface relative humidity.

- V max

$$V_{max}^2 = \frac{C_\theta}{C_D}\epsilon L q_a^*(1-RH_{as})\frac{1-\frac{1}{4}\frac{f^2r_0^2}{\beta RT_B}}{1-\frac{1}{2}\frac{C_\theta}{C_D}\epsilon\frac{Lq_a^*(1-RH_{as})}{\beta RT_S}} \tag{5.2.7}$$

- pressure distribution

$$\ln\pi = \frac{-\frac{1}{2}\epsilon\frac{C_\theta}{C_D}\frac{Lq_a^*}{C_pT_B}(1-RH_{as})+\frac{1}{4}\frac{f^2r_0^2}{C_pT_B}}{\beta-\frac{1}{2}\frac{C_\theta}{C_D}\epsilon\frac{Lq_a^*}{RT_s}(1-RH_{as})} \tag{5.2.8}$$

5.3 Sensitivities of Medicane environments with cloud model

Medicanes have a structure similar to that of tropical systems. Thus a numerical model for tropical systems (Rotunno and Emanuel, 1987) is used to study a collection of 7 Mediterranean atmospheric environments related to tropical-like cases (see description in figures 5.1.2 to 5.1.9). Cloud model simulations will be used as a tool to study the Mediterranean environments in which seven medicanes were formed and to examine the limitations arising from the model assumptions. It is not attempted to simulate the real cyclones, but rather to assess the potentialities of the environments to support this kind of extreme windstorms. The model is an axisymmetric cloud resolving model employed to simulate under idealised, homogeneous conditions, tropical systems such as hurricanes and tropical storms. The results of the numerical simulations allow one to determine similarities and differences between the storms in the Tropical and Mediterranean environments. The air-sea interaction theory of tropical cyclones shows that the steady-state of these storms can be idealised by a Carnot engine, with good agreement between the theoretical maximum wind speed (or potential intensity) and observed values in the Tropics. However, the Mediterranean basin (Reiter, 1975) presents characteristics significantly different from those of tropical regions (Jordan, 1958; Emanuel, 2003) and different results might be obtained in the real Mediterranean environment.

The effect in the simulated medicane of the sea surface temperature, dimension and strength of the initial perturbation from which the medicane will grow, and the stability of the air (Emanuel, 2003, 1986) will be analysed with the cloud model (see section 2.1.2).

Moreover, a recent study (Romero and Emanuel, 2006), applied an empirical index of tropical cyclone genesis to the medicane cases. The results showed systematically high values of the index for all the events and therefore its value as a forecasting parameter. The index is based, among other environmental factors, on the potential intensity (or maximum attainable wind speed) of tropical cyclones derived from the air-sea interaction theory (Emanuel, 2003). The theoretical potential intensity (Bister and Emanuel, 1998) can be compared with the -simulated and observed- intensity of the selected medicane events.

The seven environments for this study have been selected from satellite imagery and previously published papers on tropical-like storms. That is, these events have been selected because they exhibited in the satellite visible channel a rounded and clear-eye cloud structure (see figures 5.1.2 to 5.1.9). As it has been mentioned, more than seven cases (Lagouvardos et al., 1999) have been detected. However, only the cases for which satellite images were accessible at the time of the study could be analysed. Once a storm was selected (see table 5.1.a), the storm was tracked using visible, infrared and water vapour

satellite channels. The storm trajectory was chosen from the centre of the storm, or from the position of the eye (when it was visible). The formation, maintenance and dissipation of tropical-like storms are all of interest to this study. For this reason, the chosen trajectory comprises the entire lifetime of the storm and not only when a clear eye and rounded cloud structure are clearly observed.

Soundings derived from ECMWF analyses have been used to initialise the cloud model. These soundings do not show special environmental aspects (see table 5.3.b). Sea surface temperature (SST) was not warmer than climatological values (Reiter, 1975). Generally, the synthetic soundings exhibit significant instability (values of index CAPE higher than 700 Jkg^{-1}) and high amount of precipitable water in the air column (higher than 22 mm). However, these values are not rare in comparison with characteristic Mediterranean storm situations (Tudurí and Ramis, 1997). Thus, the atmosphere did not show any specific characteristic from which any particular precursor signature of medicane formation could be obtained.

Two types of observation have been also used to complete the general description of medicanes. Synoptic observations and observations derived from satellite measurements have been used. Synoptic observations have been taken from BUFR files from ECMWF (pilot and surface observations). Records within a 1000 km radius from the cloud-eye position have been selected from this database. Due to the maritime characteristics of the medicanes, the information obtained has been very sparse. However, maximum and minimum values showed characteristics of tropical systems (see table 5.3.a). Wind speeds measurements confirmed the tropical storm strength of the medicanes. The lack of synoptic observations over the sea has been alleviated by the use of SSMI or QSCAT satellite-sensors information (SSMI source). Wind derived from satellite images above the sea is obtained. These sensors on board polar-orbiting satellites can measure wind speed remotely from the analysis of the sea roughness in the microwave radiative spectrum area. These data and more information about the sensors and techniques are freely available via the web page `www.ssmi.com` from the Remote Sensing System enterprise. Remote wind speed measures have 25 km spatial resolution over open sea and covers a range of wind speeds from 0 to 33 ms^{-1} for ssmi (50 ms^{-1} on QuikSCAT). See satellite-derived wind for 051215 event on figure 5.3.1.

The control simulation for all the cases covers a 10-day period and the outer radius of the model is set at 1000 km. The initial vortex had an overall radial dimension of 100 km width, and a maximum wind speed of 5 ms^{-1} at 25 km radial distance from the centre. This vortex specification is assumed to be close to the initially weak vortexes observed in the satellite images. Initial atmospheric conditions are taken from ECMWF analyses. A synthetic atmospheric sounding is interpolated from ECMWF analysis 24 hours before the eye formation at the central storm position (see figure 5.3.2). General atmospheric

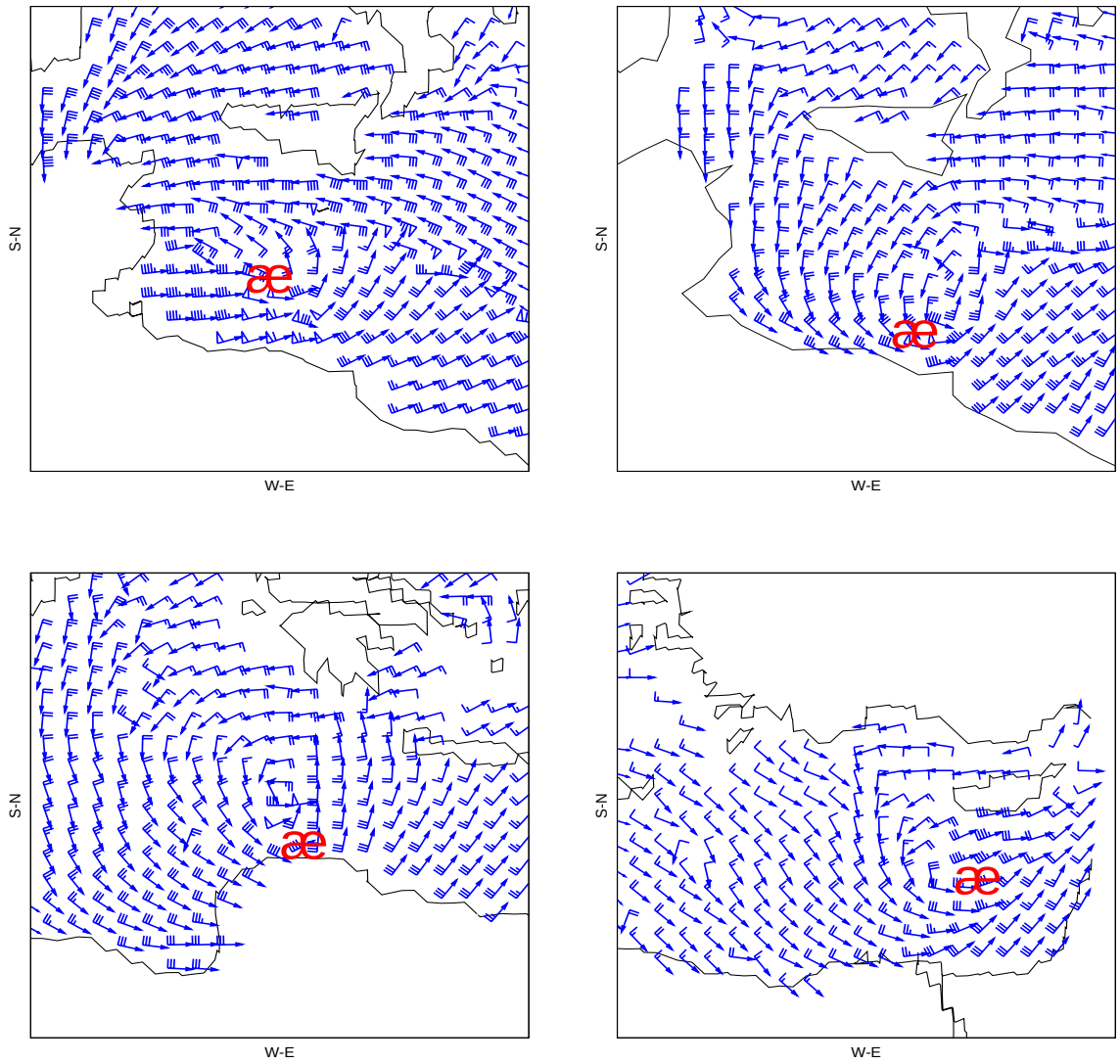

Figure 5.3.1: QuikSCAT satellite wind derived field (every 2 grid points) on 13/12/05 at 17^{30} UTC (top left), 15/12/05 at 14^{18} UTC (top right), 15/12/05 at 17^{06} UTC (bottom left) and 16/12/05 at 03^{54} UTC. Red big æshows centre position of the 051215 medicane on corresponding time observed from Meteosat satellite images. Missed wind derived values correspond with heavy precipitation zones or areas out of the satellite range. æ symbol is proposed as medicane indication (keeping § for hurricane)

Table 5.3.a: Storm observed characteristics (BUFR files-pilot, synop sources- from ECMWF). The selected values corresponded to the maximum values of observations closer than 1000 km to the storm trajectory (when exhibited eye-rounded cloud structure) and date and position of the observation ($[DD]^{[HH]}$; latitude, longitude). Col 1: Case label, col 2: minimal pressure (hPa), col 3: maximum surface wind speed (ms^{-1}) and col 4: maximum surface temperature (K). Maximum wind (53.0 ms^{-1}) of 961007 storm is perhaps not correct

case	Pmin (hPa)	max sfc. wind (ms^{-1})	max temp. (K)
950116	1009.0 (16^{06}; 35.60,18.40)	26.0 (16^{12}; 35.30,18.70)	13.3 (16^{06}; 35.60,18.40)
960912	998.4 (12^{12}; 39.55,2.73)	24.0 (12^{09}; 40.80,2.20)	24.9 (12^{15}; 38.28,-0.55)
961007	1004.8 (07^{06};39,87,4.23)	19.0 (07^{12};37.30,5.6)	17.4 (07^{12}; 37.30,5.6)
	997.0 (09^{00}; 40.30,12.40)	53.0 (09^{06}; 38.20,15.55)	24.1 (09^{09}; 39.10,9.52)
030527	1012.5 (27^{09}; 39.87,4.23)	13.0 (27^{18};37.2,3.50)	21.7 (27^{12}; 39.55,2.73)
031018	1024.0 (18^{12}; 39.87,4.23)	13.0 (18^{12};37.10,4.3)	22.1 (10^{18}; 37.10,4.30)
051027	1021.2 (28^{18}; 35.0,16.0)	5.0 (28^{18};35.0,16.0)	23.1 (28^{18}; 35.0,16.0)
051215	991.0 (14^{06};35.5,12.6)	25.0 (14^{12}; 33.5,13.3)	19.7 (14^{13}; 35.5,12.6)
	993.5 (15^{12}; 33.6,24.9)	18.0 (15^{12}; 33.6,24.9)	17.6 (15^{12}; 34.1,25.7)

conditions are presented in table 5.3.b. Sea surface temperature is also obtained from the ECMWF analyses. ECMWF SST is based on daily NCEP SST analyses generated from ship, buoy and satellite observations (see more information on ECMWF web page `http://www.ecmwf.int`)

General results from the cloud resolving model emphize the potentiality of the environments to support medicanes, but the simulation features are in low agreement with observations. Generally, the model simulations overestimate storms characteristics (see figures 5.3.3 and 5.3.4, as example for all the cases). Simulated storms become much stronger than the observed ones, having deeper cores, stronger winds and wider eye structures. Moreover, simulated storms form and evolve more slowly than the observed ones and do not show any signs of dissipation over the ten-day period.

A numerical evaluation is carried out comparing the winds derived from satellite measurements (SSMI or QUICKSCAT) to the simulated ones. The radial distribution of the winds is divided in radial sections about 12.5 km. For each section an average wind speed is calculated. Numerical simulations overestimate storm strength. In order to obtain a more adequate intercomparison, wind values are not taken when the simulated storm is steady state. Simulated wind values are taken at different time-steps according

Table 5.3.b: Sounding main characteristics for each case [DD]/[MM] $[HH]^{[MI]}$, at ([latitude], [longitude] position), and **SST**: Sea surface temperate (K), **C**: Cape (J/kg), **Sh**: Showalter index (C), **PW**: Precipitable water (mm), **C15**: Convective Instability between 1000 and 500 hPa layers (deg.), **SRH**: Storm relative helicity (m^2s^{-2}), **T15**: Thickness between 1000 and 500 hPa layers (m).§, soundings not corresponding to time storm position, because at this time storm was over land. † null Cape is undetermined because of humidity numerical overestimation at some verticals levels of the sounding

case	**S. date (lat., long.)**	**SST**	**C**	**Sh**	**PW**	**C15**	**SRH**	**T15**
950116	14/01 12^{00} (37.9, 18.9)	15.7	27.8	4.28	15.8	1.8	-16.3	5348
960912	12/09 $00^{00,\S}$ (38.3, 1.2)	24.3	1840	0.38	41.0	-13.5	79.3	5647
961007	06/10 06^{00} (38.4, 1.2)	22.0	1284	0.92	20.6	-10.8	-141.3	5439
	07/10 12^{00} (40.4, 6.3)	20.9	932	0.57	24.9	-9.4	-46.2	5503
030527	26/05 06^{00} (42.4, 4.3)	17.1	$0.0^{\dagger}$	2.36	25.4	2.3	1077	5493
031018	17/10 $12^{00,\S}$ (37.2, -0.7)	22.3	946.9	-1.56	33.9	-8.4	-63.6	5544
051027	27/10 12^{00} (30.8, 12.6)	25.6	1043	-2.08	30.5	-12.6	8.9	5621
051215	13/12 12^{00} (33.8, 12.6)	20.1	376.5	-0.71	22.0	-5.5	43.2	5439
	14/12 06^{00} (35.6, 13.8)	18.2	0.1	3.27	18.4	-0.4	43.7	5462

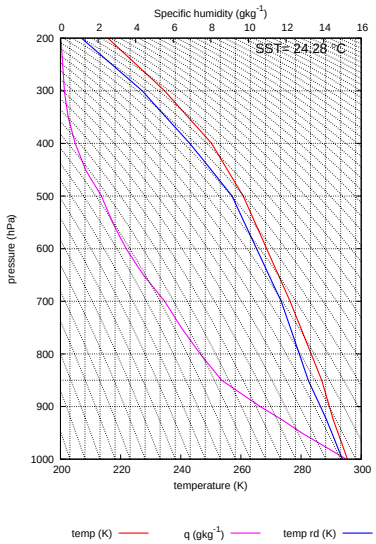

Figure 5.3.2: Synthetic sounding from ECMWF analysis used to simulate the environment labelled '960912'. bottom x-axis temperature (K), y-axis pressure (hPa), top x-axis water content (gkg^{-1}). Dry temperature (red line), dew point temperature (blue line), water content (pink line). SST (Sea Surface Temperature, $°C$)

to the time when maximum wind speeds are reached and are maintained above different thresholds. It has been taken the simulated values at the 4^{th} day of simulation (reached maximum winds about 20 ms^{-1}), the 5^{th} day (reached maximum winds about 25 ms^{-1}) and the 6^{th} day (reached maximum winds about 30 ms^{-1}). Winds derived from satellite measurements are taken when the eye of the storm is observed. A radial distribution of the derived winds is assumed and the distribution is positioned at the centre of the eye. The combined results do not show a good agreement between satellite measurements and model results (see figure 5.3.5). Intensity and decay of the wind profile are underestimated by the model. This disagreement may come from the low satellite grid resolution, sparse satellite data, irregular temporal resolution due to the polar orbit tracks, the failure of the model to simulate the systems adequately and/or subjectivity of the arbitrary choice of the time at which the intercomparison is made.

In order to understand modelled medicane behaviour, sensitivity tests are performed. A value of 26 $°C$ is often indicated as the coldest SST at which a hurricane can develop in tropical regions (Emanuel, 1986). As has been shown in the Mediterranean cases (see table 5.3.b), the SST does not show a critical value (e.g.: on 950115 case, the SST obtained from ECMWF was 15 $°C$; see SST distribution in 5.0.1). Obviously, at the 'high' latitudes of the Mediterranean region under preceding cold intrusions at mid-upper levels,

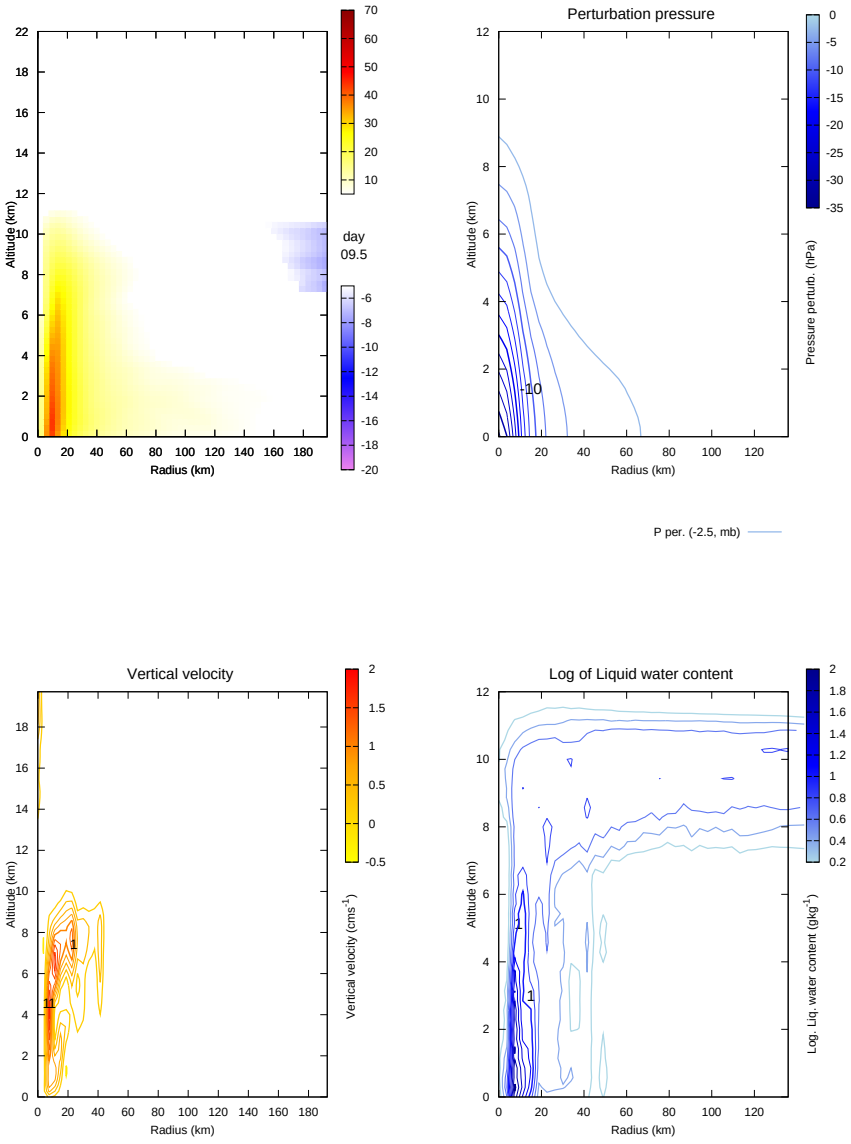

Figure 5.3.3: Simulation results of '960912' storm. x-axis radial distance (km) from storm centre at the left, y-axis height (km). Top left panel: Azimuthal velocity (every 5 ms^{-1}, shaded). Top right panel: Pressure anomaly (every, -2.5 hPa). Bottom left panel: Vertical velocity (every 0.2 cms^{-1}). Bottom right panel: Logarithmic liquid water content (every 0.2 gkg^{-1})

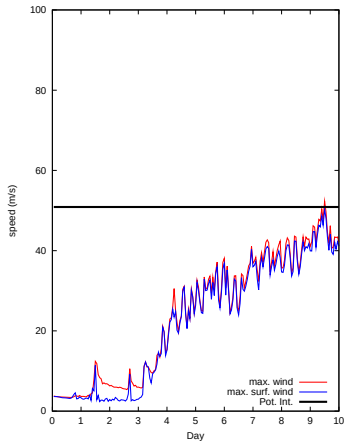

Figure 5.3.4: Evolution of the theoretical potential intensity of the storm (thick black line). maximum wind speed (blue line), and maximum surface wind speed (red line) evolution of the 960912 storm obtained from the model. Day of simulation (x-axis), speed (ms^{-1}, y-axis). Simulation obtained from the 'control' configuration of the initial vortex;$r_{max} = 25\ km,\ v_{max} = 5\ ms^{-1},\ r_0 = 100\ km$ using sounding plotted on figure 5.3.2

the thermodynamic disequilibrium between sea and air can be established with significantly cooler SST values, compared to tropical cases.

To study the sensitivity to the SST, a pair of simulations in which SST has been increased and decreased 5 $°C$ is carried out. It is assumed that the cloud model is able to produce adequate surface fluxes (in concordance to the new SST) after a 'spin-up' time. The study of the sensitivity to the degree of convective instability and moisture content is done by increasing and decreasing 30 % of the humidity value at each point of the sounding used to initialise the axisymmetric model. Previous simulations of tropical cyclones (Rotunno and Emanuel, 1987) do not show an important dependence on the nature of the initial vortex. However, the Mediterranean cases have smaller dimensions (diameter less than 500 km), for which the size of the initial vortex might play an important role. For this reason, a sensitivity test is also carried out by changing the dimension of the initial vortex. In one simulation the initial vortex has been reduced ($r_{max} = 15\ km,\ v_{max} = 5\ ms^{-1},\ r_0 = 50\ km$). In the other simulation, the vortex has been enlarged ($r_{max} = 25km,\ v_{max} = 5\ ms^{-1},\ r_0 = 500\ km$). Another simulation test has been run by changing the surface temperature distribution of the initial vortex. From potential vorticity theory, it is known that positive thermal anomalies are associated with a cyclonic movement of the air around its area (Hoskins et al., 1985; Thorpe, 1986). Thus, in order

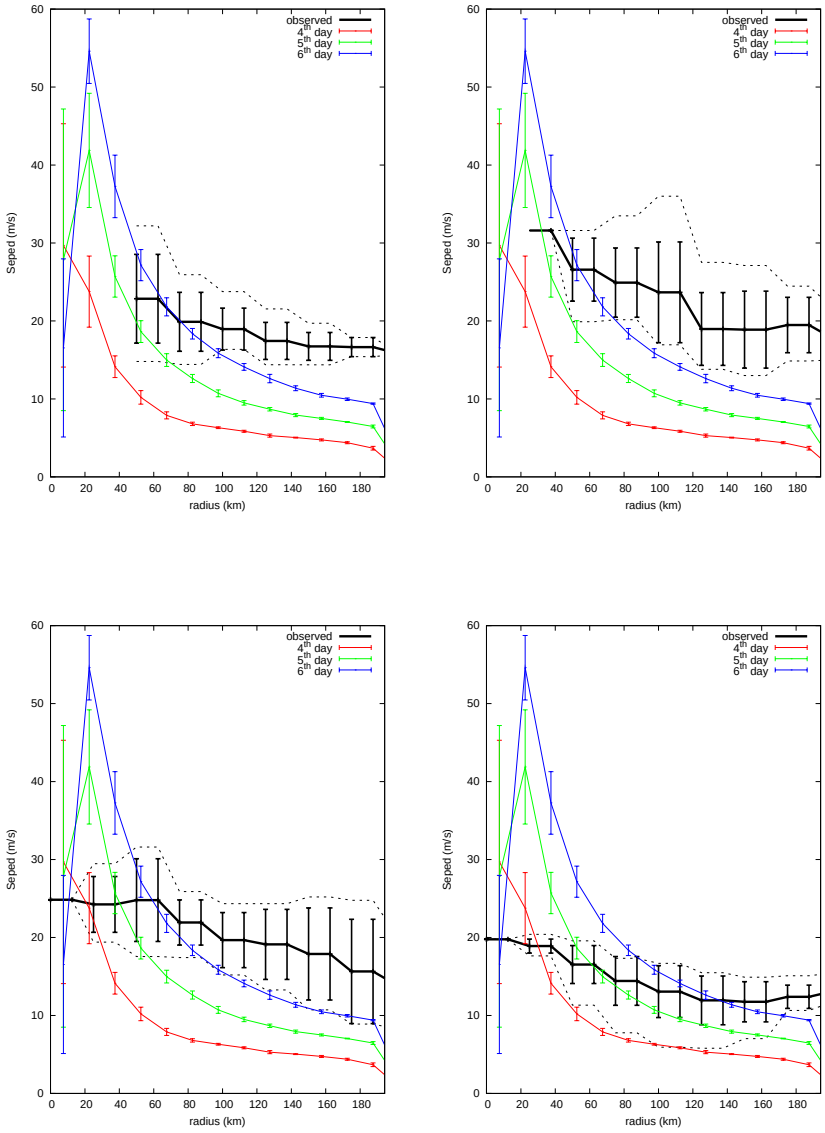

Figure 5.3.5: Comparison between radial cloud model simulated wind profile (colour lines) at different time steps (4th day, red; 5th day, green; 6th day, blue) and wind speed satellite derived measurements for 961007 case at different time steps. Each wind speed value is a radial average every 12.5 km from the centre of medicane (on 0 at x-axis, km). Mean speed values (y-axis, ms^{-1}). Solid colour error lines values correspond to simulated results at the time of initial formation of the system. Solid black error lines are satellite derived measurements. Dashed black lines above(below) corresponded with the maximum(minimal) wind speed value at the corresponding radii. Satellite measurements on 8/10/96 at 21^{00} UTC (top left), 8/10/96 at 18^{06} UTC (top right), 9/10/96 at 06^{24} UTC (bottom left) and 10/10/96 at 12^{00} UTC. In both cases, error bars are calculated as standard deviation from the values used to compute the average

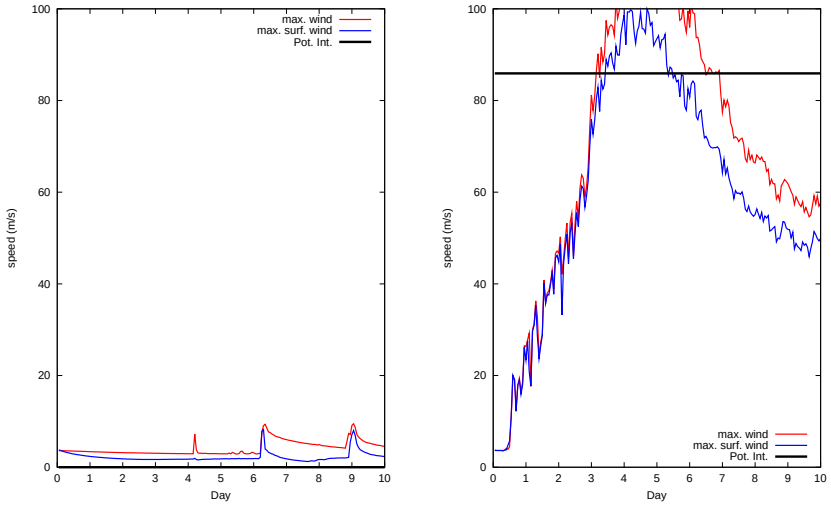

Figure 5.3.6: As in figure 5.3.4, but cooling 5 $°C$ SST (left) and increasing 5 $°C$ Sea surface Temperature (right).

to obtain a warmer initial vortex, the initial maximum azimuthal velocity is increased without changing the vortex dimensions ($r_{max} = 25\ km,\ v_{max} = 15\ ms^{-1},\ r_0 = 100\ km$). Sensitivity tests results will be shown with plots of the evolution of the maximum wind speed at all levels, maximum surface wind speed and potential intensity. Potential intensity is the theoretical maximum wind speed that can attain the steady-state storm according to the air-sea interaction theory (Bister and Emanuel, 1998).

For the sake of brevity, only the sensitivity results of the 960912 environment will be shown. The sensitivities obtained for the 960912 case are quite representative of the sensitivities obtained from the other cases. Sensitivity test simulations results (see figure 5.3.6) show a high impact of changes in the sea surface temperature. In some cases, the system is not formed when the SST has been cooled 5 $°C$ (e.g.: 960912 case). When the SST has been increased 5 $°C$ a much more intense and larger system is obtained, reaching hurricane strength (wind speeds faster than 33 ms^{-1}). On 960912 when SST has been increase 5 $°C$, potential intensity derived from the cloud model simulation is extremely high (maximum wind speeds over 100 ms^{-1}). This value would explain a high potentiality of the environment resulting from a combination of the prescribed vertical sounding and the SST. This result should not been taken as a high simulation of the specific storm, but as a mere potential test of the environment.

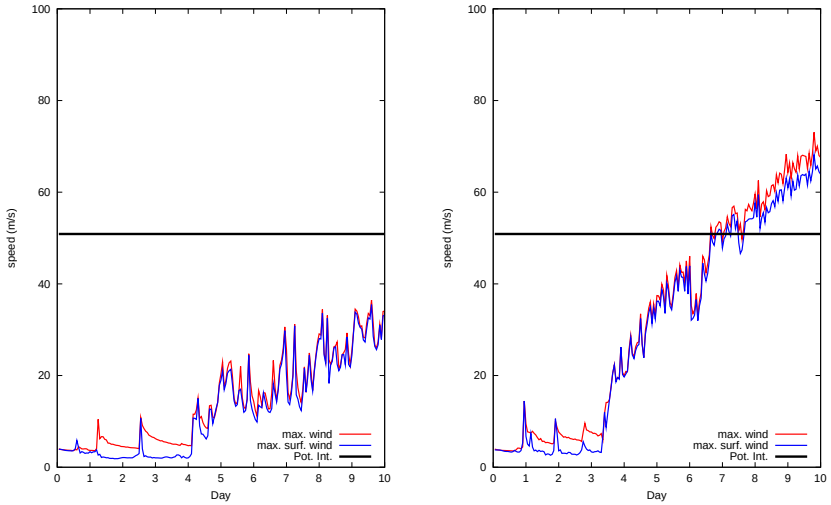

Figure 5.3.7: As in figure 5.3.4, but using a smaller initial vortex ($r_{max} = 15\ km$, $v_{max} = 5\ ms^{-1}$, $r_0 = 50\ km$, left) and with a wider initial one ($r_{max} = 25km$, $v_{max} = 5\ ms^{-1}$, $r_0 = 500\ km$, right)

5.3.1 Sensitivity on dimension of initial vortex

Changes in the dimension of the initial vortex size had a minor effect on the storm simulations (see figure 5.3.7). However, a weaker storm is obtained when the initial vortex is smaller. Besides, the storm takes more time to develop (it is assumed that development is reached when the model simulates maximum wind speeds higher than 20 ms^{-1}). With a larger initial vortex, the storm is formed a bit faster and is quite a bit stronger. On changes on the initial weak vortex, significant changes on the self organisation of the system are introduced (Rotunno and Emanuel, 1987). A weaker initial vortex is less able to organise properly convection than a stronger one.

5.3.2 Sensitivity on initial humidty

The initial relative humidity has a strong effect on the simulations (see results on figure 5.3.8). In a dryer environment, the results are not much different from the control simulation. However, a much more intense system is simulated when the humidity is increased. Moreover, the system is formed much faster than in the control simulation (2 days instead of 4 days). It is shown that high initial moisture in the atmosphere is not a necessary ingredient to generate a medicane in the environment. However, high humidity

emphasises and increases the medicane genesis.

5.3.3 Sensitivity on initial vortex strength

Finally, sensitivity tests on the core temperature of the initial vortex show a clear influence on the speed of formation of the storm (see figure 5.3.9). The simulated storm is formed much faster than in the control case. At the same time, a significantly stronger system is simulated. The environments have not been changed. However, changes on the characteristics of the initial vortex produce changes on the formation and organisation processes of the system.

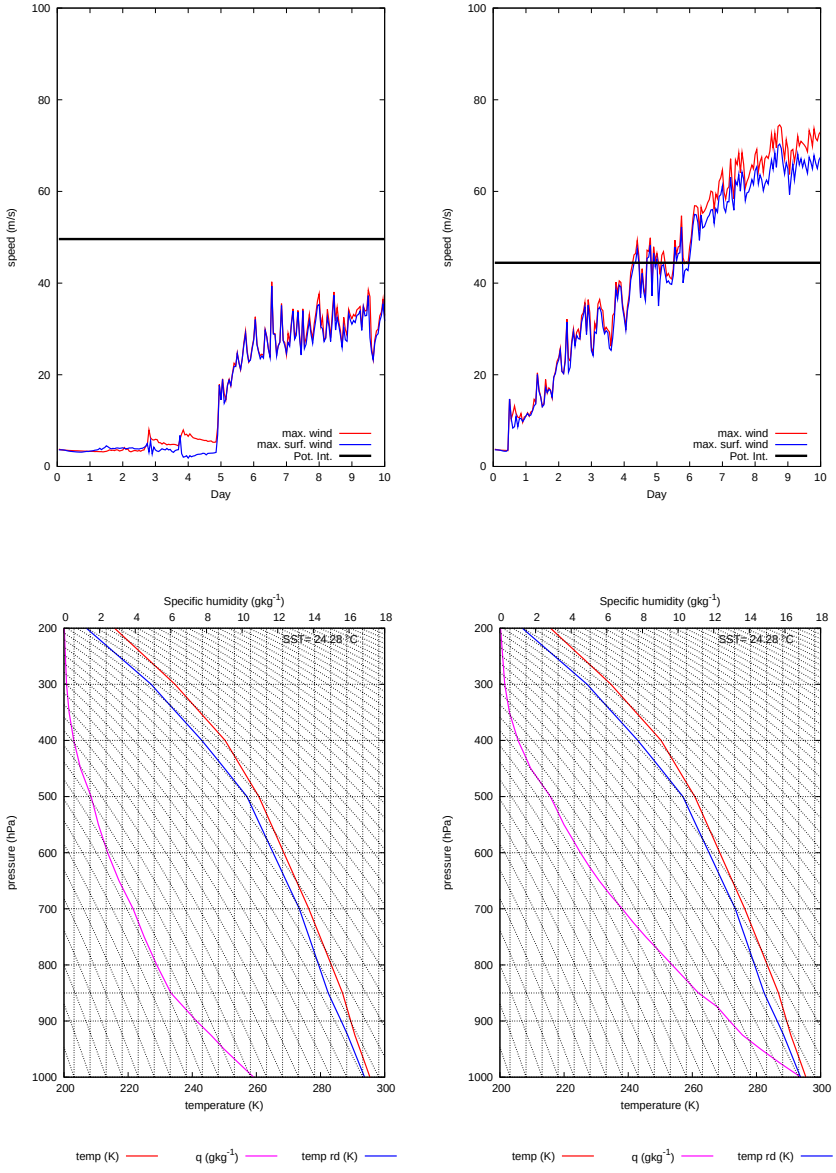

Figure 5.3.8: As in figure 5.3.4, but drying 30% (bottom left) initial vertical relative humidity profile (top left) and increasing 30% (bottom right) initial vertical relative humidity profile (top right)

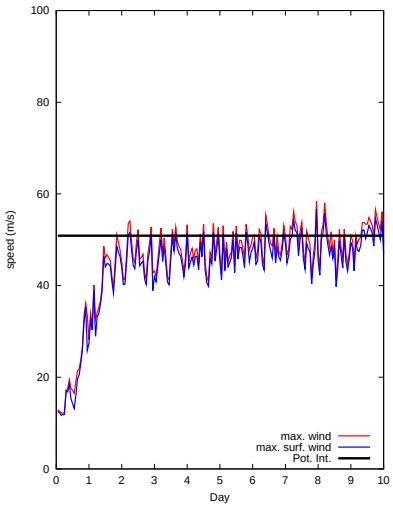

Figure 5.3.9: As in figure 5.3.4, but increasing maximum speed of initial vortex (warmer vortex, $v_{max} = 15\ ms^{-1}$)

5.4 Air-sea mechanism sensitivity study in 3 Medicanes

In order to asses the air-sea interaction in the medicane evolution, a sensitivity test of four factors: sea surface temperature (SST), latent heat flux from the sea (LHF) Upper level PV anomaly and sea surface temperature (SST) is carried out with the MM5 v3.7 numerical model (Grell et al., 1995). This sensitivity test is developed through the factor separation technique (Stein and Albert, 1993). Three different cases are studied (see figures 5.1.2, 5.1.3, 5.1.4 and 5.1.6 respectively for the January 1995, September 1996 and May 2003 cases), attempting to generate a more general scope of the sensitivities. The three selected cases attained different regions, intensities and periods of the year. Due to the large number of simulations needed to deal with the four selected factors (16) short and clear cases are selected: January 1995 south Ionic Sea case (studied previously by Lagouvardos et al., 1999; Pytharoulis et al., 2000), September 1996 Western Mediterranean case (Homar et al., 2003b) and May 2003 Western Mediterranean case.

Storm direct measurements obtained from BUFR data archived in the ECMWF, show a 'tropical storm' strength of the selected medicanes wind speeds less than 33 ms^{-1}). Like the satellite information, BUFR observations reflect the weakness of the 030527 medicane case in comparison with the strong activity of the 950116 and 960912 cases (see table 5.3.a).

5.4.1 Sensitivity methodology and control simulations

Air-sea interaction (Emanuel, 1986) has been assumed as an important mechanism in the medicane evolution. In order to study the role of the mechanism a complete sensitivity study of the medicane events to four aspects involved in it is carried out.

Surface fluxes SSHF and LHF are well correlated with the surface wind and the temperature of the sea surface (Emanuel, 1986; Schulz et al., 1996). Changes on the fluxes or/and in the SST will modify strongly the energy source of the storm. On the other hand, previous studies suggest that the thermodynamic disequilibrium necessary for the development and maintenance of Mediterranean tropical-like storm is activated by an upper level cold low (Emanuel, 2005; Fita et al., 2007a). In order to verify this hypothesis an additional sensitivity analysis to the upper level disturbance will be carried out. With the selection of these four factors, one attempts to capture the most important aspects that influence the energy budget of the air-sea interaction mechanism.

MM5 v3.7 mesoscale model will be used for the numerical determination of the sensitivities. The sensitivity study will be realised by modifying or switching off some aspects

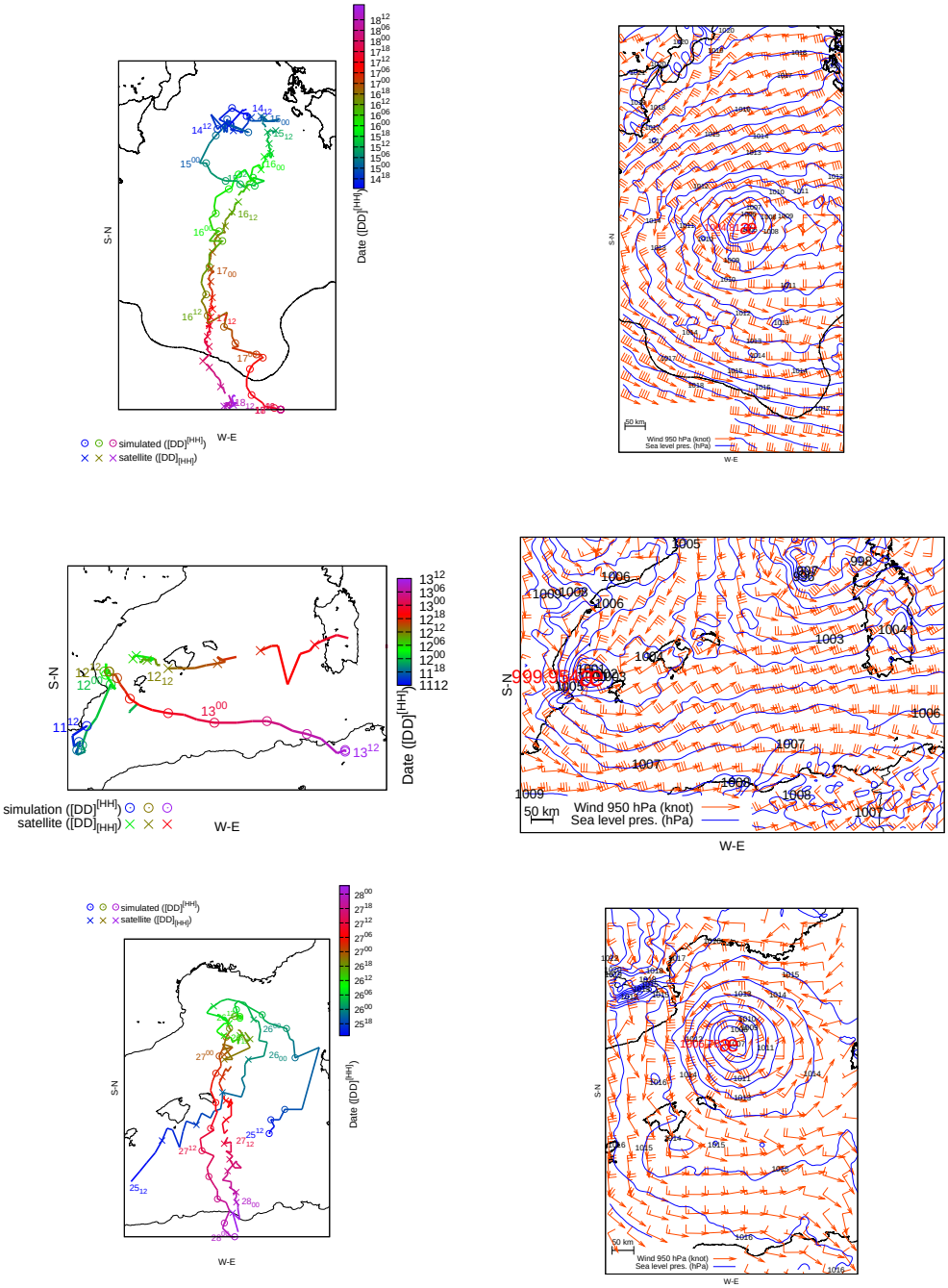

Figure 5.4.1: Left panels: MM5 simulated medicane trajectories (line with empty circles) and satellite derived medicane trajectory (line with crosses) coloured according to date. Case 950116 (top), 960912 (middle) and 030527 (bottom). Right panels: Sea level pressure (blue line, every 1 hPa), and horizontal wind at 950 hPa (barbs notation: triangle: 50 knot; pennant: 10 knot; half pennant: 5 knot) on Jan. 16th 1995 at 00 UTC (top), September 12th at 15 UTC (middle, medicane is the the small vortex in front of the Eastern Iberian Peninsula coast) and May 27th 2003 at 00 UTC (bottom). æ symbol is proposed as medicane indication (keeping § for hurricane)

of the numerical model or the environmental conditions of the simulations. ECMWF analyses and BUFR observation files (WMO, 2007) have been used for the initial and boundary conditions of the simulations. Two-way nested domains of varying dimensions and 15 and 5 km horizontal resolutions with 23 vertical levels are applied on the regions of the three studied medicanes. The cloud microphysical scheme of graupel(Reisner2) (Reisner et al., 1998) has been selected. Kain-Fritsch (Kain and Fritsch, 1993; Kain, 2004) cumulus scheme has been only activated in the first domain. Thus convection will be explicitly simulated by the primitive equations of the MM5 model in the second domain. It is assumed that 5 km horizontal resolution is high enough as to enable this procedure. A simple Blackadar scheme (Blackadar, 1979; Zhang and Anthes, 1982) is used to model the planetary boundary layer (PBL) processes. Cloud Radiation scheme is used (Dudhia, 1989). See MM5 reference for information and characteristics of each selected scheme (Grell et al., 1995). From each cyclone the simulated fields every 3 hours for the 15 km resolution domain (domain 1), and every hour for the 5 km resolution domain (domain 2) will be obtained. January 1995 case from Jan. 14th at 06 UTC to Jan. 18th at 00 UTC will be simulated; September 1996 case from Sep. 11th at 12 UTC to Sept. 13th at 12 UTC and May 2003 case from May 25th at 12 UTC to May 28th at 00 UTC. However, results during the most important phase of the storms and for the periods during which set of simulations present a vortex structure with similarities to the studied cases will only be shown.

Control simulations (i.e. those simulations with the full physics and environmental characteristics) of each case (outputs in figure 5.4.1) reveal the genesis of a small strong vortex assumed to represent a tropical-like storm. However, simulated trajectories show a temporal and spatial shift with respect to the observed ones on the satellite images. Genesis zones are significantly away from the observed areas (except for the January 1995 case) and the simulated vortexes start earlier. Nevertheless, all control simulations are able to simulate a tropical-like storm (denoted by the warm core of strong and small vortex, see figures 5.4.1, 5.4.2 and 5.4.3). There is a strong difference between the trajectory of the September 1996 medicane simulated in this study and in Homar et al. (2003b). In that study NCEP analyses as boundary conditions and MM5 v3.3 version model were used. These simulations will be assumed good enough for the purposes of the subsequent sensitivity study.

Azimuthal and time averaged vertical-cross sections of the simulated mature storms reflect the characteristic structure of a tropical cyclone (figures 5.4.2 and 5.4.3). This averaged state of the storm shows a wall structure in the relative humidity and wind speed fields (at about 20 km from the centre for the 950116 case). Besides, a free cloud eye is reflected according to the simulated vertical motion since subsidence is present in the core of the storm. For September 1996 and May 2003 cases, MM5 does not simulate a structure as clear as in January 1995 case (see figure 5.4.3).

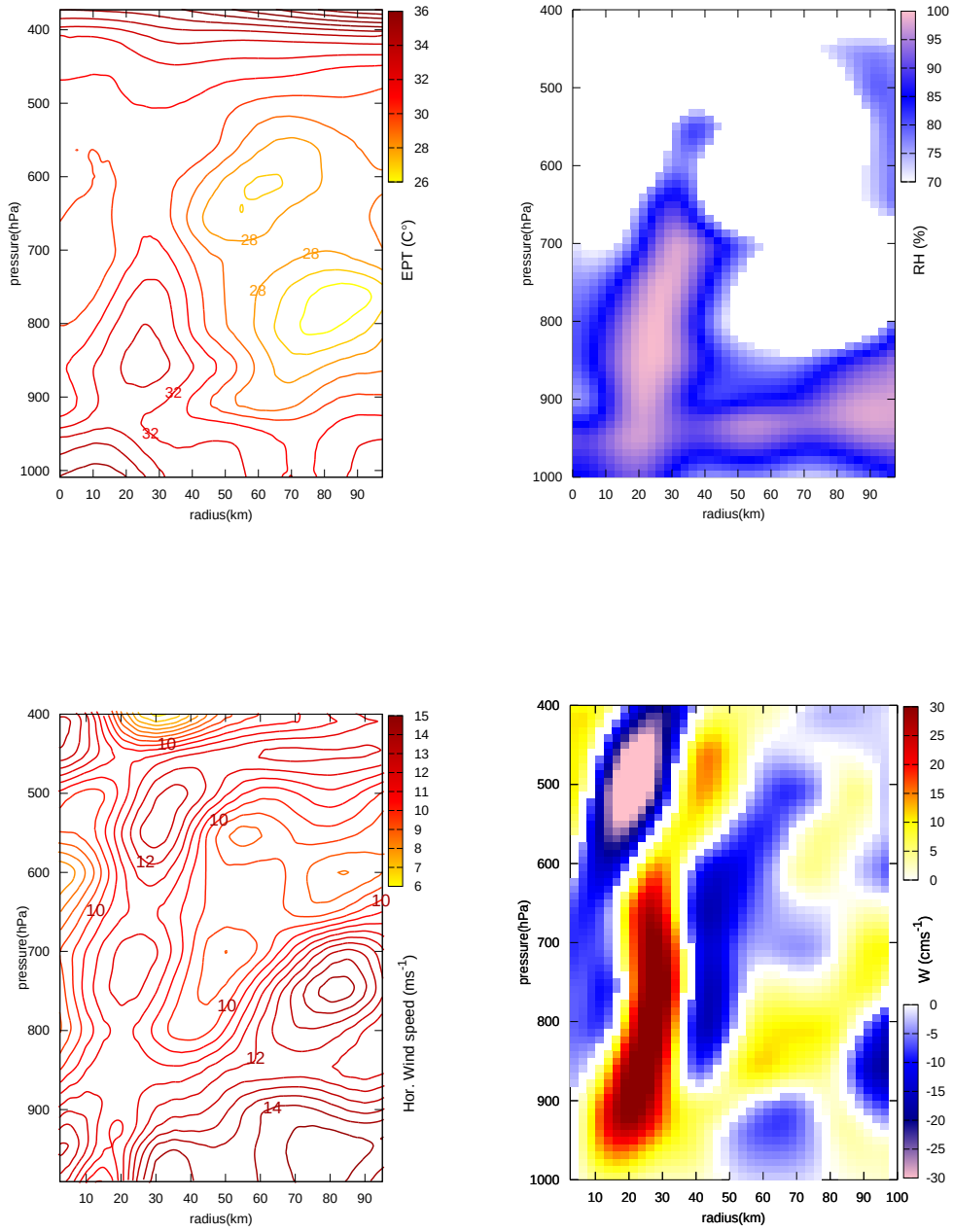

Figure 5.4.2: Vertical cross-section from the centre of the storm, showing the time-azimuthal averaged fields of MM5 simulated 950116 medicane during the period of maximum intensity (from 15th Jan. 95 at 16 UTC to 16th Jan. 95 at 05 UTC). x-axis (radial distance from the centre of the storm, km), y-axis (pressure, hPa). Top left panel: Equivalent Potential Temperature (every 1. $°C$). Top right panel: Relative Humidity from 70 % (shaded). Bottom left panel: Horizontal velocity (lines every 0.5 ms^{-1}). Bottom right panel: Vertical velocity (cms^{-1}, shaded)

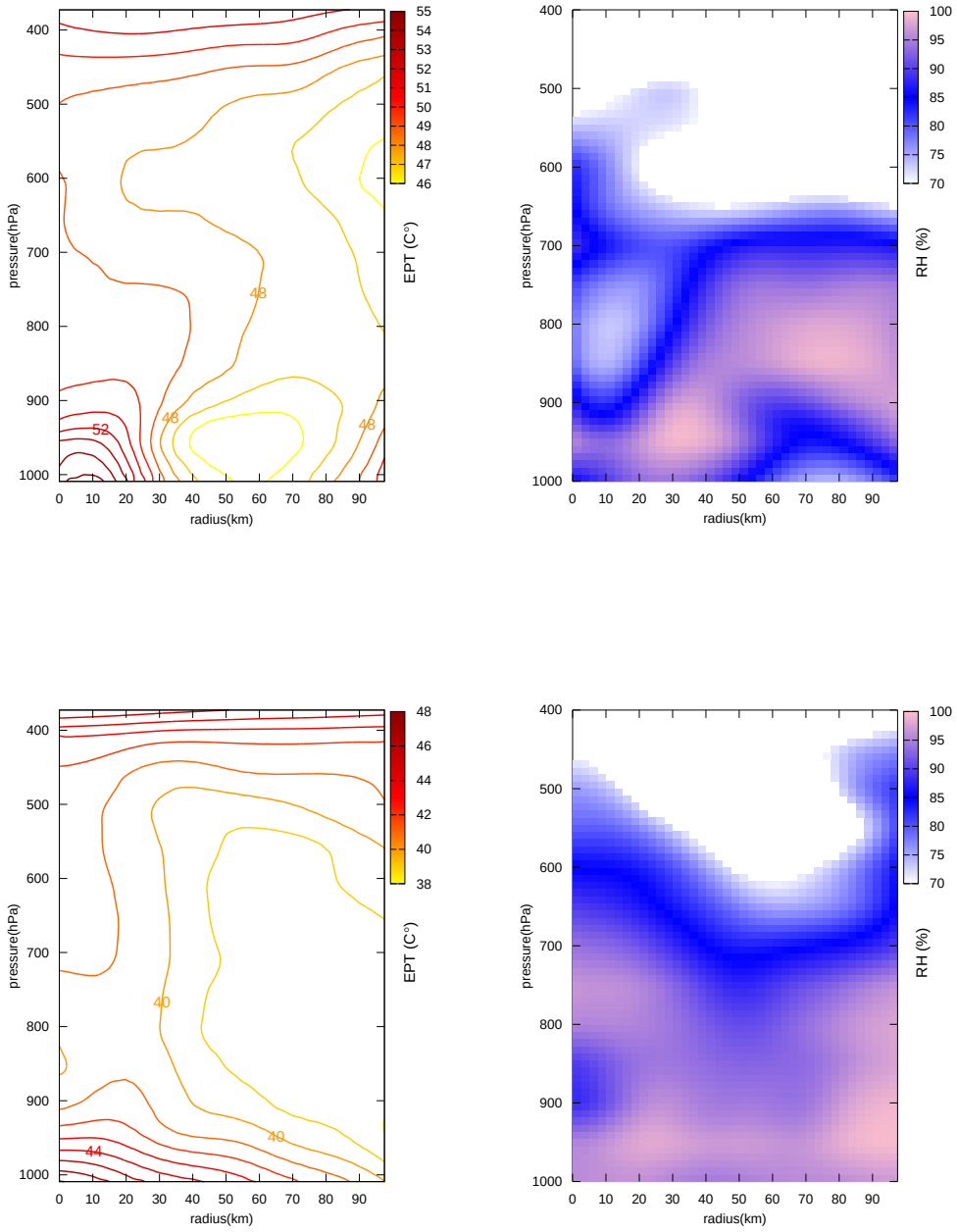

Figure 5.4.3: As in figure 5.4.2, but for 960912 medicane (top) during the period of maximum intensity (from 12th Sept. 96 at 07 UTC to 12th Sept. 96 at 17 UTC) and 030527 medicane (bottom, from 26th May 03 at 11 UTC to 26th May 03 at 20 UTC). Left panels: Equivalent Potential Temperature (every 1. $^{\circ}C$). Right panels: Relative Humidity from 70 % (shaded)

For the sensitivities studies on the latent and sensible surface fluxes will be switched off in the numerical computation of the PBL for all the grid points (LHF is only switched off in grid points located above the sea). The effects of Sea surface temperature will be studied by means of simulations where SST has been decreased $5°C$ from its original value obtained from the ECMWF analyses. Upper level disturbance effects will be studied through the PV Inversion technique. Usually, PV Inversion technique is used to modify the initial conditions of the numerical simulations in order to find sensitivities to these changes (Huo et al., 1999; Romero, 2001). Due to the small dimensions of the selected biggest domain, however, upper level disturbances are not fully captured at the first time step of the simulations. Therefore, the PV Inversion technique is used to modify the upper level characteristics at all the boundary condition times over the ECMWF analyses. Potential Vorticity anomaly field is computed at each ECMWF analyses time (00, 06, 12 and 18 UTC) during the period of MM5 simulations. The inversion of the positive PV anomaly enclosed between 500 hPa and 100 hPa 150 km (10 grid point) away from the border of the first domain is done. Then a subtraction of the 10% of the inverted fields obtained from these selected PV anomalies will be applied to generate the modified boundary conditions at each time step. Thus, the net effect is referred to a slightly weaken the intensity of the upper-level troughs or cut-off lows initially located of later incoming into the simulated domain.

The factor separation (FS) technique (Stein and Albert, 1993) is used to study the effects of the selected factors (1) LHF, (2) SSHF, (3) Upper level PV and (4) SST on a forecast field f. According to this technique, 16 different simulations are necessary to isolated the full collection of individual and synergistic effects due to these four factors (see table 5.4.a). The effect on a forecasted field of individual factors and their synergies is explained in section 2.3

It is very difficult to find a plausible physical meaning of quadruple and even triple synergies due to the complexity of the dynamics of the problem. Therefore, results will be discussed up to the triple synergies only. However, e_{1234} results will be also given, but not interpreted.

Medicanes are the result of both baroclinic development (precursor environment) and the air-sea interaction (genesis and maintenance mechanism). This study focuses on the later dynamical process. Thus, FS on the simulated medicane it self (identified in the simulations as a minimum sea level pressure zone of high vorticity, with circular morphology and small dimensions) will be focused. Numerically simulated fields will be examined around the centre of small vortex. These medicane centred fields will be used in equation 2.3.4 to compute the effect of the 4 factors through the FS technique. Thus, a Lagrangian application of the FS technique will be done in contrast to a previous study which applied

Table 5.4.a: Description of the factors that are included (1) in each effect. LHF factor means a boundary layer without latent heat flux from the sea. SSHF factor means a boundary layer without sensible surface heat flux. ULPV factor means a decrease of 10% of the upper level PV. SST factor means a Sea surfer temperature 5°C colder

effect	**LHF**	**SSHF**	**ULPV**	**SST**
e_0	0	0	0	0
e_1	1	0	0	0
e_2	0	1	0	0
e_3	0	0	1	0
e_4	0	0	0	1
e_{12}	1	1	0	0
e_{13}	1	0	1	0
e_{14}	1	0	0	1
e_{23}	0	1	1	0
e_{24}	0	1	0	1
e_{34}	0	0	1	1
e_{123}	1	1	1	0
e_{124}	1	1	0	1
e_{134}	1	0	1	1
e_{234}	0	1	1	1
e_{1234}	1	1	1	1

FS following the trajectory given by the 'control' simulation of the medicane Homar et al. (2003b). FS defines the effects on a forecast field due to a linear decomposition of the roles of each factor. A Lagrangian use of the FS can be done if it is considered the system it self as a result of the linear combinations of the different systems simulated by each set of factors.

The effects computed according to each methodology differ significantly (see an example in figures 5.4.4 to 5.4.6). However, from a general point of view, effects in both methodologies seem to preserve in some how the sign of their role and even their dual phase dynamics.

The study is focused in three scalar forecasted fields: sea level pressure value at the centre of the storm (Sea lev. pres.), relative vorticity (RVOR) at the centre of the storm at 950 hPa and maximum azimuthally averaged horizontal wind at 950 hPa ($HWind_{max}$, within a radii of 200 km from the centre of the storm). A relation exists between the pressure value at the centre of the storm and the maximum horizontal wind speed (Emanuel, 1986). A cyclogenetic or enhancing role of the air-sea interaction effects will be related to a decrease of the central pressure value of the system and increase of the horizontal wind speed and relative vorticity at the centre.

5.4.2 Sensitivity results

Results of the sensitivity tests will be in three different ways: storm trajectories obtained by each simulation, temporal evolution of the individual and synergistic effects on the three variables. Positive(negative) values for these effects indicate that the corresponding factor increases(decreases) the analysed storm attribute.

Simulated storm trajectories shown similar characteristics in all medicanes (see figure 5.4.7). Trajectories of medicanes are significantly modified with respect to the control one when the upper level trough is altered (simulations without factor 3). Changes in the upper level structure of the trough play two main roles: altered the vertical disequilibrium between upper air and lower-level air and radiative cooling at outer and upper-level parts of the energetic cycle of the air-sea interaction. On the January 1995 case the trajectory of the medicane in the simulation where the upper level disturbance has been modified (f_{124}) is very different to the rest (see top panel left in figure 5.4.7), but without strong differences with respect to the central pressure values (see figure 5.4.8).

Simulated trajectories of the medicanes do not show a clear relation with respect to the trajectories of the upper level maximum vorticity centres (see figure 5.4.9). However, a momentaneous strong influence in the trajectory of the medicane can be observed when upper level vorticity centres are significantly close in space and time to the position of

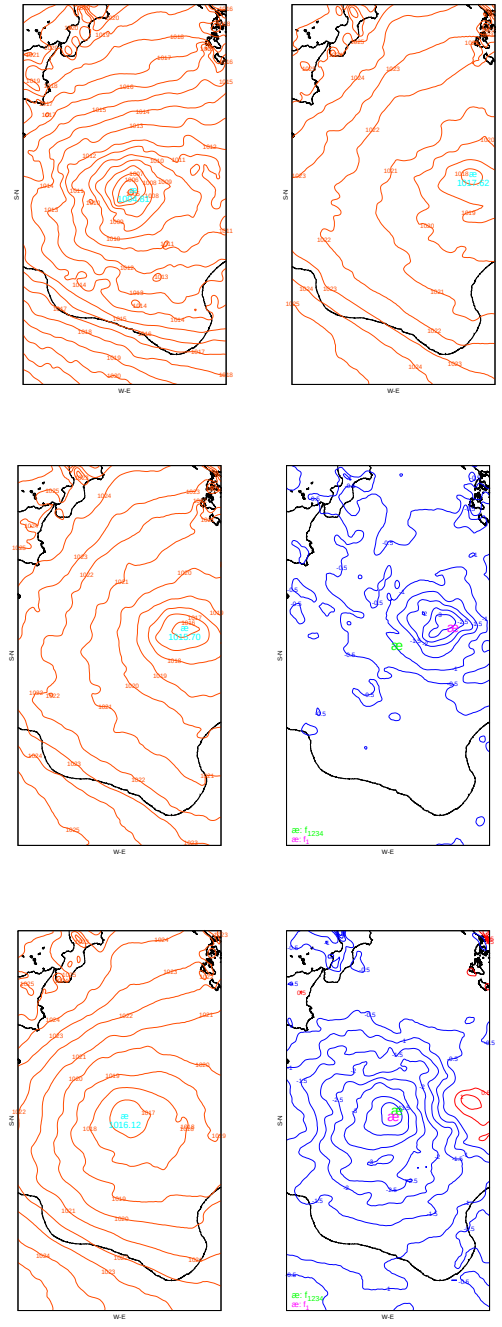

$$f_i^{cont} = f_i(x_{cont}, y_{cont})$$
$$f_i^{lagr} = f_i(x_i, y_i)$$

$f_0^{cont} = 1019.72$ hPa
$f_1^{cont} = 1020.40$ hPa
$f_2^{cont} = 1016.18$ hPa
$f_3^{cont} = 1019.25$ hPa
$f_4^{cont} = 1020.57$ hPa
$f_{1234}^{cont} = 1005.81$ hPa

$e_1^{cont} = -0.85$ hPa
$e_1^{lagr} = -1.92$ hPa

$e_3^{cont} = -4.39$ hPa
$e_3^{lagr} = -1.5$ hPa

Figure 5.4.4: Simulated sea level pressure (every 1 hPa, orange lines) on January 16th at 00 UTC; position and sea level pressure at the centre of the medicane (æ in hPa, light blue). Control simulation (f_{1234}, top left), background (f_0, top right), LHF (f_1, middle 1st), ULd (f_3, bottom 1st). 2-dimensional effect on sea level pressure (every 0.5 hPa; blue lines negative; red positive) and medicane position according to the control simulation (æ green) simulation only with the factor i (æ pink) on January 16th at 00 UTC for the LHF (e_1, middle 2nd), ULd (e_3, bottom 2nd). Effects values following control simulation (Eulerian form; $e_i^{cont} = f_i^{cont} - f_0^{cont}$), according to the position of each medicane (Lagrangian form, $e_i^{lagr} = f_i^{lagr} - f_0^{lagr}$)

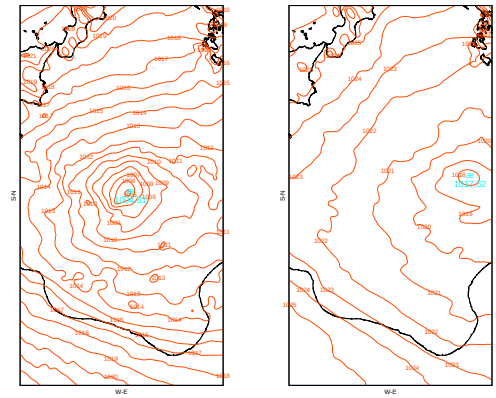

$$f_i^{cont} = f_i(x_{cont}, y_{cont})$$
$$f_i^{lagr} = f_i(x_i, y_i)$$

$$f_0^{lagr} = 1015.70 \text{ hPa}$$
$$f_1^{lagr} = 1016.69 \text{ hPa}$$
$$f_2^{lagr} = 1016.12 \text{ hPa}$$
$$f_3^{lagr} = 1016.75 \text{ hPa}$$
$$f_4^{lagr} = 1017.62 \text{ hPa}$$
$$f_{1234}^{lagr} = 1004.81 \text{ hPa}$$

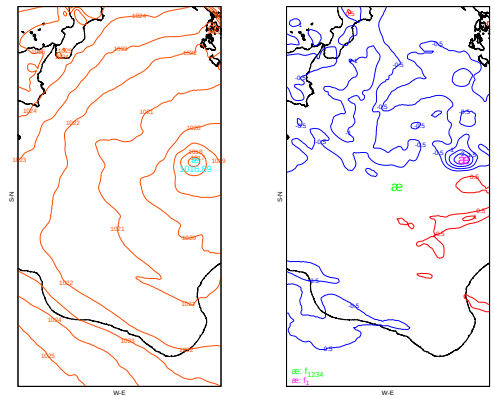

$$e_2^{cont} = -0.17 \text{ hPa}$$
$$e_2^{lagr} = -0.93 \text{ hPa}$$

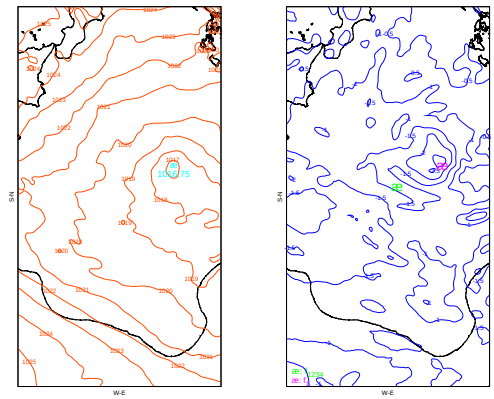

$$e_4^{cont} = -1.32 \text{ hPa}$$
$$e_4^{lagr} = -0.87 \text{ hPa}$$

Figure 5.4.5: As in figure 5.4.4, but for SSHF (f_2, middle 1st), SST (f_4, bottom 1st). SSHF (e_2, middle 2nd), SST (e_4, bottom 2nd)

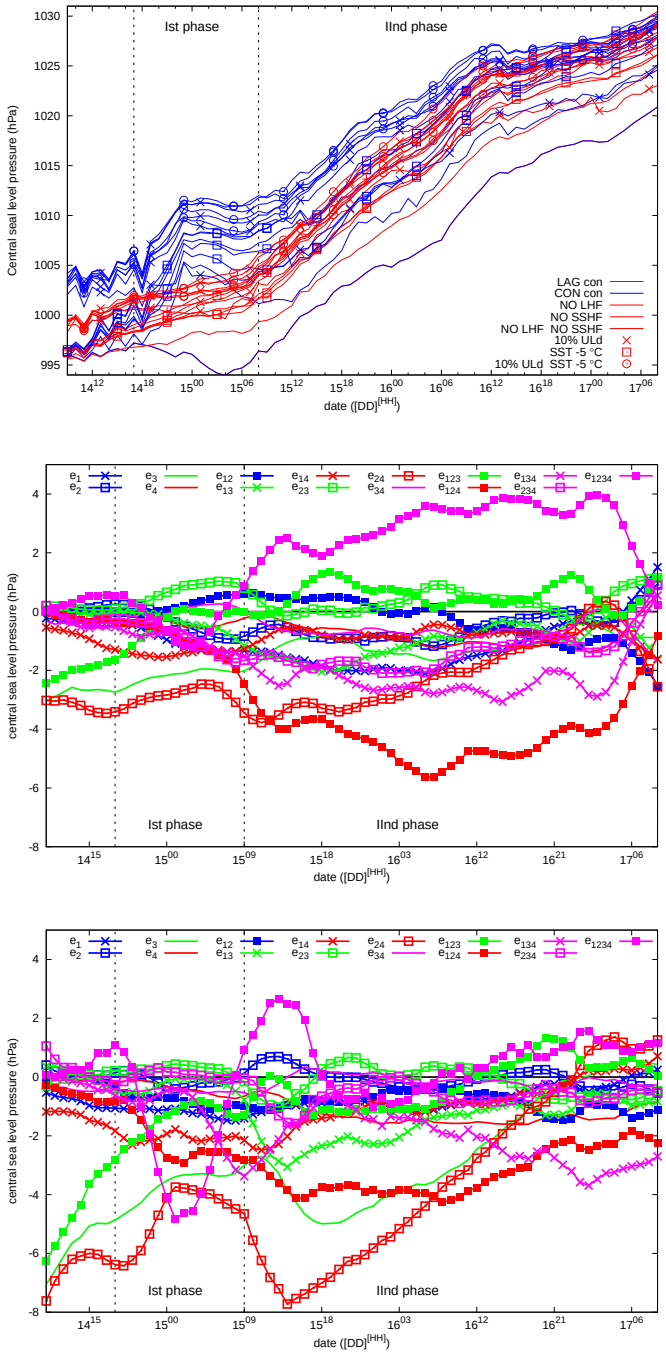

Figure 5.4.6: Top panel: Temporal evolution of the pressure at the centre of the simulated medicane (red lines) and following trajectory of the medicane of the control simulation (blue lines); solid lines without surface fluxes (f_{1234}, f_{234}, f_{134}, f_{34}), lines with crosses with -10% ULd (f_{124}, f_{24}, f_{14}, f_4), with a SST 5° colder (f_{123}, f_{23}, f_{13}, f_3), with -10% ULd and SST -5° (f_{12}, f_2, f_1, f_0). Effects on central sea level pressure on control simulation (middle), central pressure of each simulated medicanes (Lagrangian, bottom)

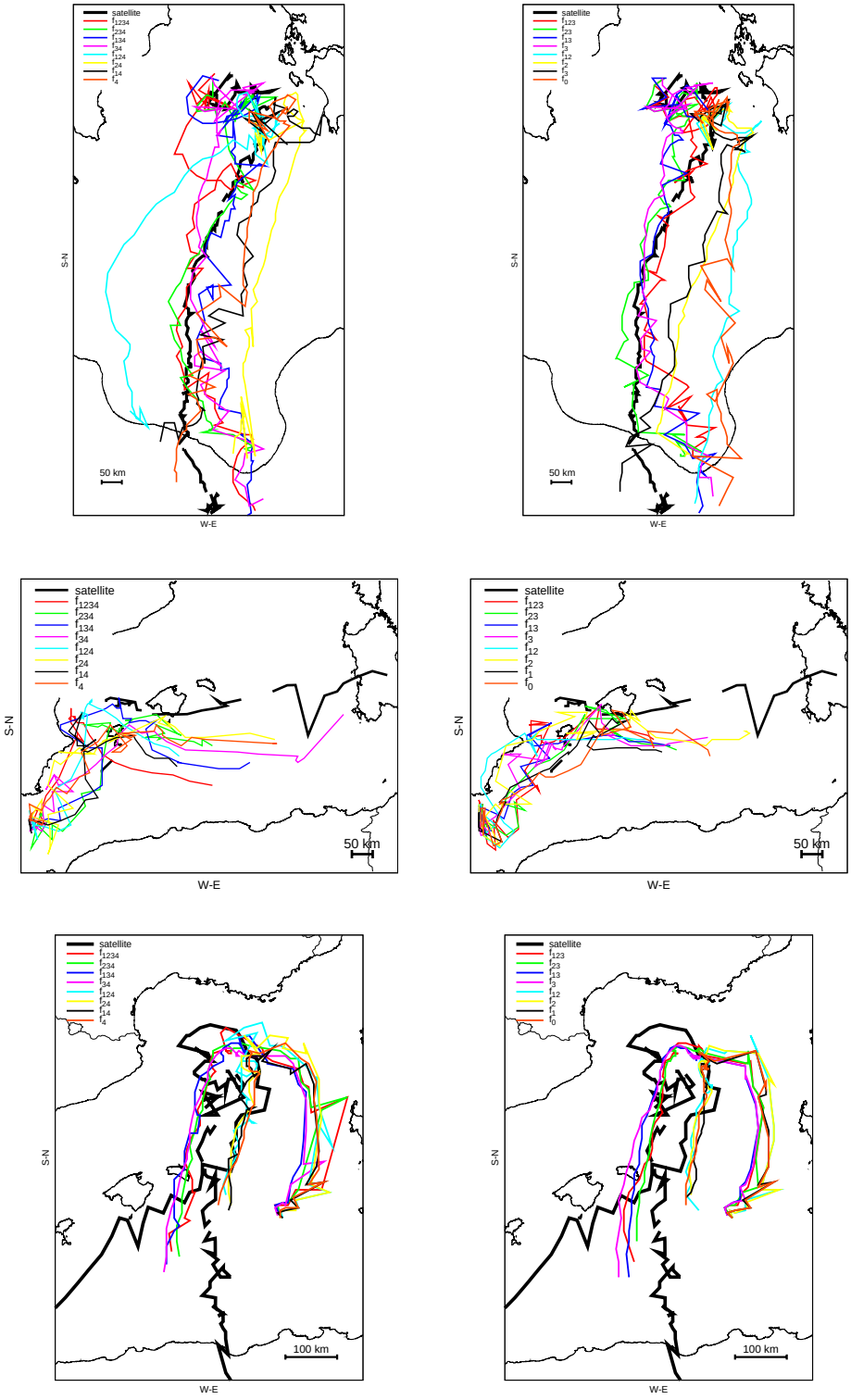

Figure 5.4.7: Simulated trajectories for each simulation. See legend for notation of the lines. January 1995 case (top), September 1996 (middle) and May 2003 case (bottom). Strong differenced blue-light line in 1995 case (top left) is the simulated trajectory of f_{124} experiment

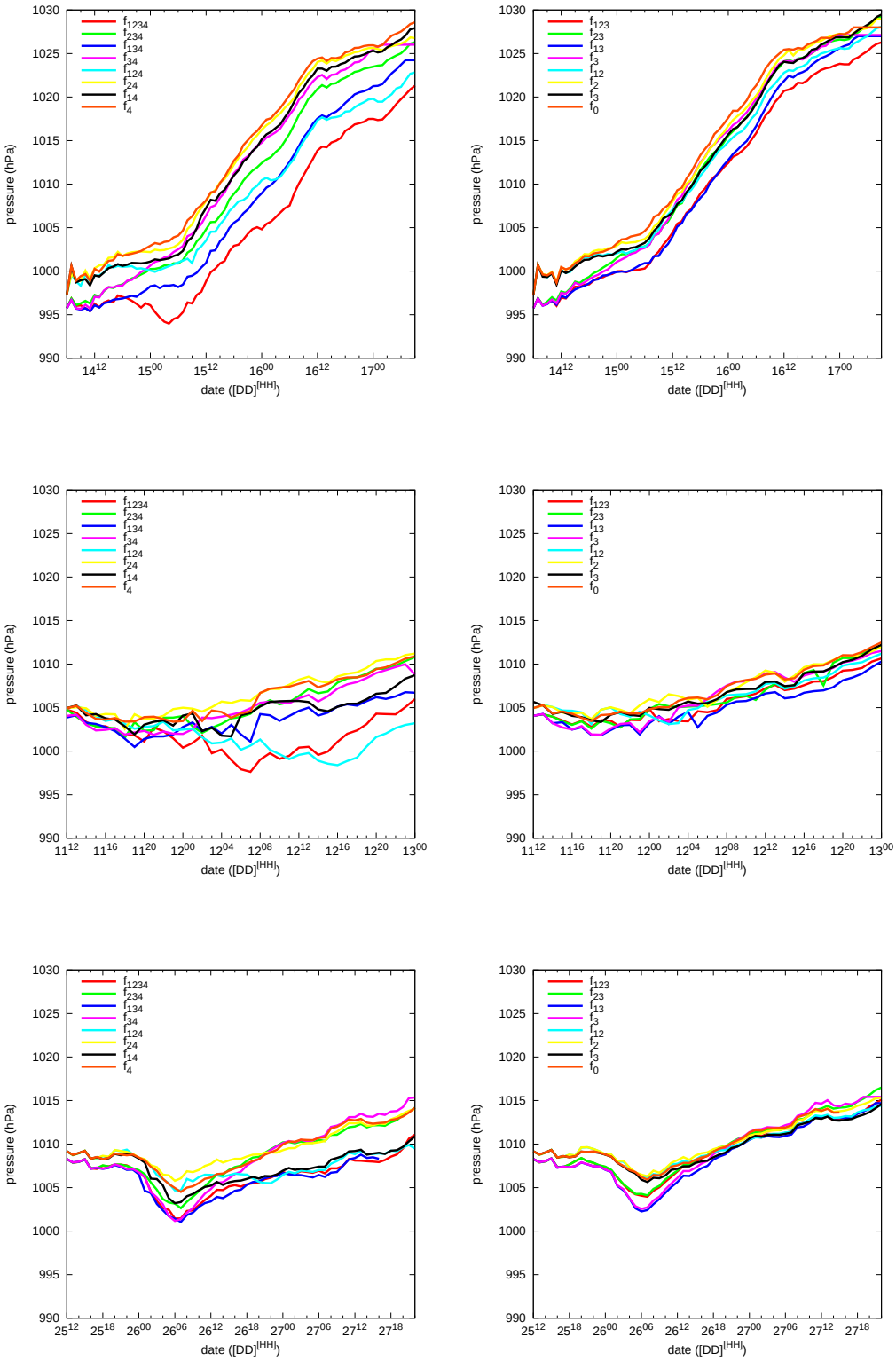

Figure 5.4.8: As in figure 5.4.7 but for the simulated sea level pressure at the centre of the medicane

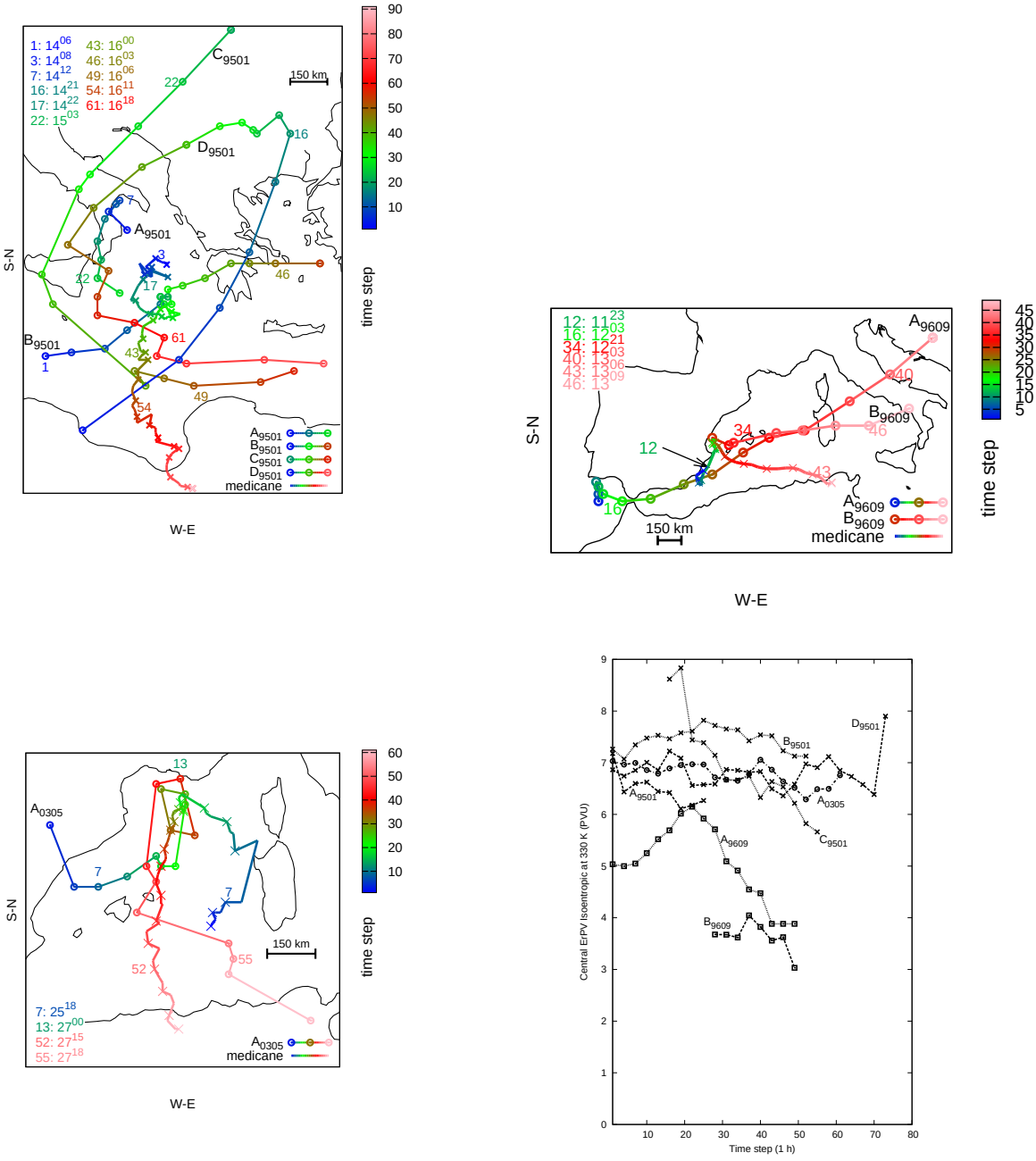

Figure 5.4.9: Trajectories of different Ertel PV maximum centres (coloured lines with circles, at 330 K isentropic surface, labelled as Ξ_{case}) related with the medicane evolution (coloured line with crosses) each circle/cross denotes 3h time-step. Colour lines changes with time step according to colour bar. January 1995 case (top left), September 1996 case (top right) and May 2003 case (bottom left). Date of position of each disturbance is indicated at different time-steps (see dates of time-steps at each graph in $[DD]^{[HH]}$ format). Ertel PV values evolution of each centre (bottom right, $PVU = 10^{-6} m^2 K s^{-1} kg^{-1}$)

the medicane. Some momentaneous similarities might be a reflect of a short-lasted coupling between upper and low-level disturbances (Hoskins et al., 1985; Bleck, 1990) not maintained due to a slower movement of the medicane with respect to the movement of upper-level disturbance assumed to be as a consequence of friction surface phenomena. On January 1995 case (top left panel in figure 5.4.9), initial movement of the medicane follows (shifted about 200 km below) similar trajectory as the A_{9501} maximum. Movement loop on the medicane trajectory occurs with a temporal and spatial coincidence with upper level maximum B_{9501}. South-southeast-ward movement of the medicane seems to be influenced also by the similar tendency of the upper-level maximum centres and the flow pattern attributed to an elongated N-S upper level disturbance.

In the September 1996 case, at the same moment that upper level maximum overpasses the zone where the medicane is located, storm system starts an eastward movement similar to the upper level maximum centres (top right panel in figure 5.4.9). Initial phases of the movement of the May 2003 medicane are dominated by the flow derived by the upper level disturbance (see bottom left panel in figure 5.4.9). Medicane and upper level maximum centre trajectories are temporal and spatial coincidence for a period of time in which upper level maximum centre draws a loop and medicane keeps almost fixed. Once upper level maximum moves southward, medicane also starts to move southwardly.

The temporal evolution of the Ertel PV maximum centres on an isentropic surface (330 K) show that there is a small non-conservative evolution of the Ertel PV. The change of PV values on isentropic surfaces is related to diabatic processes such as deep convection (Hoskins et al., 1985). This is illustrated in the azimuthal averaged radiative tendency and PV values (figure 5.4.10), showing a relation between positive radiative warming and PV positive values at low levels.

Simulated trajectories show also a strong dependency on SST. Almost all these simulated trajectories are clearly different from the other when SST is cooled (simulations containing factor 4 $f_{\chi 4}$).

As has been said (see chapter 2) FS results present a great dependency on the number of factors. That ambiguity in the results can be treated in two different ways: applying the fractional approach of the FS technique (Krichak and Alpert, 2002), and/or studying the response of the pure effects to a change in the number of factors that are used in the FS (Alpert et al., 1995).

Another aspect that could be controlled is the degree of modification introduced when one factor is studied. Intercomparison between results could be improve if in some manner one could equalise the degree of modification of each factor to a same common value. By this way, the resulting effects can be unambiguously associated to a true sensitivity,

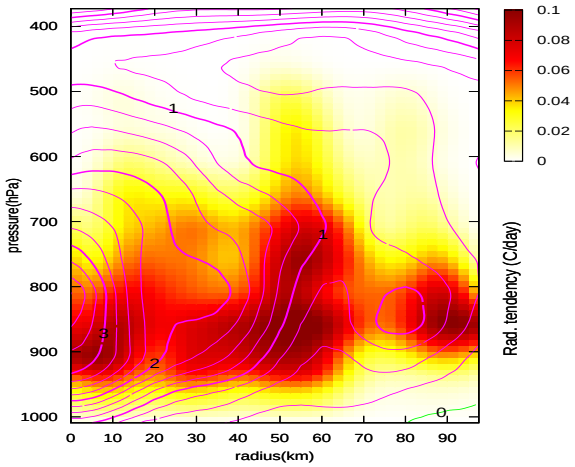

Figure 5.4.10: As in figure 5.4.2, but for the radiative tendency ($°C/day$, shaded) and PV values (PVU, lines)

avoiding the dependency into the strength and morphology of the introduced change (a similar procedure can be found in (Fita et al., 2007b)). In this sensitivity study this has not been considered, due to the difficulty to establish a correct manner to find a same common value. LHF and SSHF are completely removed from the simulations, SST is cooled 5°C and Upper level PV is only modified a 10% of its strength. Each factor have a different impact in the simulations: LHF, SSHF change the dynamics of the atmosphere. Upper level changes affect energy of the whole atmosphere, meanwhile SST modifies the energy content of the Sea.

Due to the limitation in the computational resources, the study on the response of the effects is only done through the modification of the group of selected factors.

5.4.3 Collection dependence

The dependence on the collection of factors of the three fields shows significant differences (see figure 5.4.11). The central sea level pressure of the storm presents more proportionality to the number of factors than the other two fields. The more complex response of the azimuthally-averaged wind speed and relative vorticity may be due to the fact that these fields have been derived from the model prognostic state variables. It is shown how

the non proportionality to the number of factors of some effects is reproduced in the three variables (like in e_{13} in January 1995 and September 1996 cases and e_{12} for May 2005). At the same time, no clear correspondence among effects of Sea lev. press and $HWind_{max}$ are obtained (theoretically development of air-sea mechanism establishes a relation between both variables).

The role of the effects varies among the three cases. All the storms show the strongest sensitivity to the LHF (collection $\{1\}$) and the SST (collection $\{4\}$). Almost all the effects are cyclogenetic, except SSHF in the May case (collection $\{2\}$, top left panel in figure 5.4.14). January 1995 case shows a more linear response than May 2003 case, and this linearity is very poor in the 960912 case. This result could be a reflection of the different characteristics of the storms. January 1995 would be a more similar to a prototype tropical-like storm, May 2003 case more baroclinic-like and September 1996 somewhat within. The four selected factors are shown to be more appropriate to study the January 1995, and September 1996 cases rather than May 2003 case. Such inadequate selection of factors is well observed on the collection sensitivity for the SSHF effect when looking the value of the sea level pressure at the centre of the storm for the 030527 case (top right on figure 5.4.14).

These poor results obtained in the May 2003 case for this effect (large differences and not correlated sensitivities) could also be explained by the interaction with other factors not considered in the study, such as: mixing of the thermal surface gradient due to boundary layer turbulence, diurnal cycle effects (day/night activation/suppression of the turbulence with a maximum at the end of the day, explain a phase of the effect about 18 h is in $\{2\}$ computation of e_2). On a study of an Atlas lee cyclogenetic phase of a cyclone, an afternoon increasing role of SSHF factor was also obtained (Horvath et al., 2006). Besides, the low spread obtained for the Upper level effect (e_3, bottom left panel of figure 5.4.14) might reflect the relevance of this factor in the case.

Similar high group-dependence is obtained for the Upper level PV effect (e_3) of the 960912 case. The non linearity with respect to the number of taken factors is observed and the effect-dependence does not exhibit similar trends or relation between groups (bottom left panel in figure 5.4.13). This wide behaviour could be attributed to the proximity of the Iberian peninsula and the Balearic Islands during the evolution of the case. Orography interactions of a hurricane has been related to its weakening (Bender et al., 1987). Bear in mind that latent heat release of convection (LHR) is a key parameter for the the storm (Homar et al., 2003b) and it has not been considered. The role of this not considered or hidden factor is reflected in the strong non proportionality for the Upper level PV effect to the number of factors. At the same time, almost all the groups with this factor on the other pure effects group-dependence curves have the largest differences with respect to the other ones (see in figure 5.4.13, curves $\{1,3\},\{2,3\},\{3\},\{3,4\}$). This result reflect

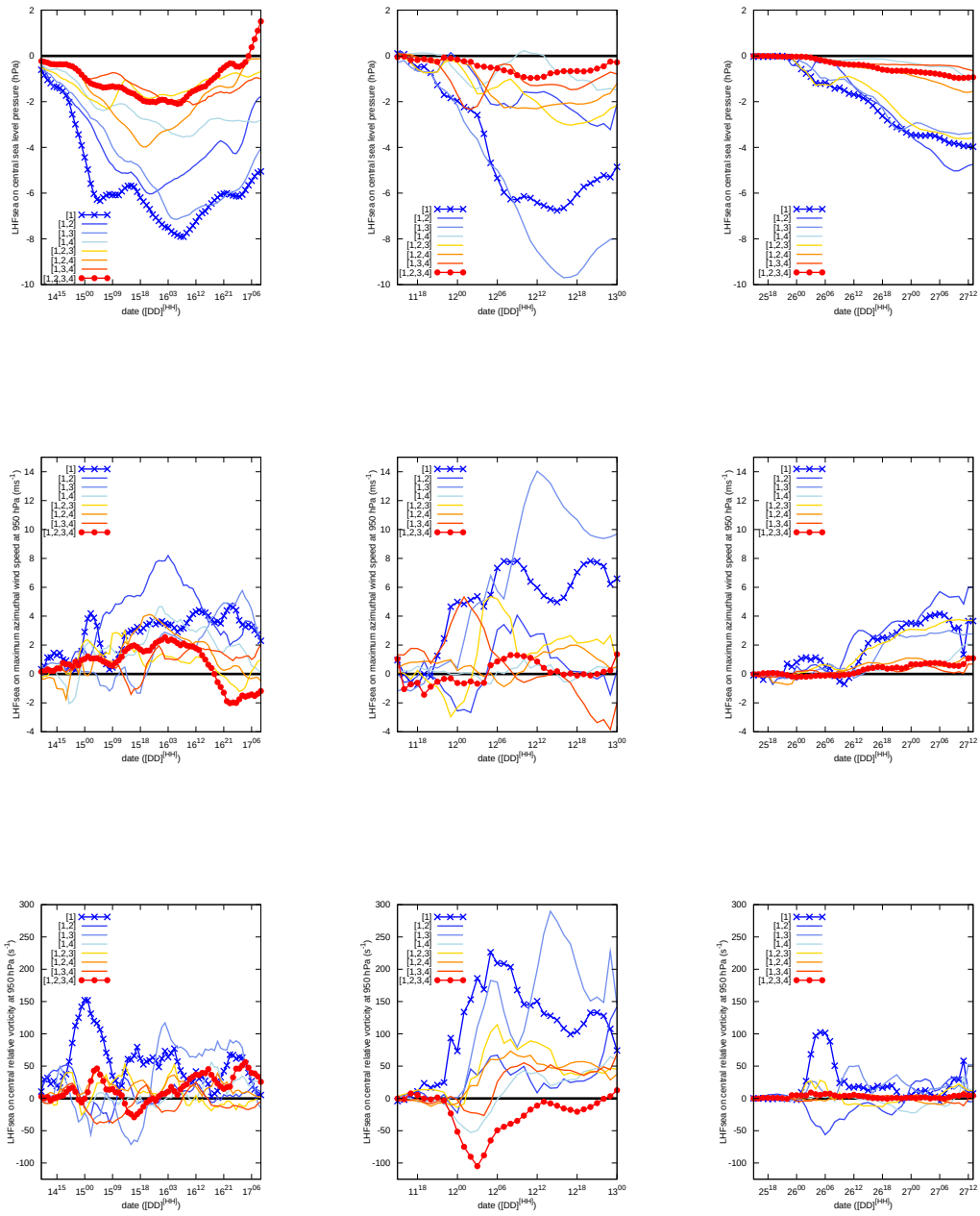

Figure 5.4.11: Collection-dependence of the LHF effect on the sea level pressure at the centre of the storm (top), the maximum azimuthal averaged horizontal wind speed at 950 hPa (middle), and the central relative vorticity at 950 hPa (bottom), for the 950116 case (left), 960912 case (middle) and the 030527 case (right). Results have been filtered with a mobile average filter of five time steps. $\{1\}$ FS effectivity of LHF (e_1) for factor 1; $\{i, j\}$ FS e_1 for two factors i, j; $\{i, j, k\}$ FS e_1 for three factors i, j, k and $\{1, 2, 3, 4\}$ FS e_1 for four factors. Factor 1: LHF, 2: SSHF, 3: Upper level PV, 4: SST. See legend for correspondences with lines

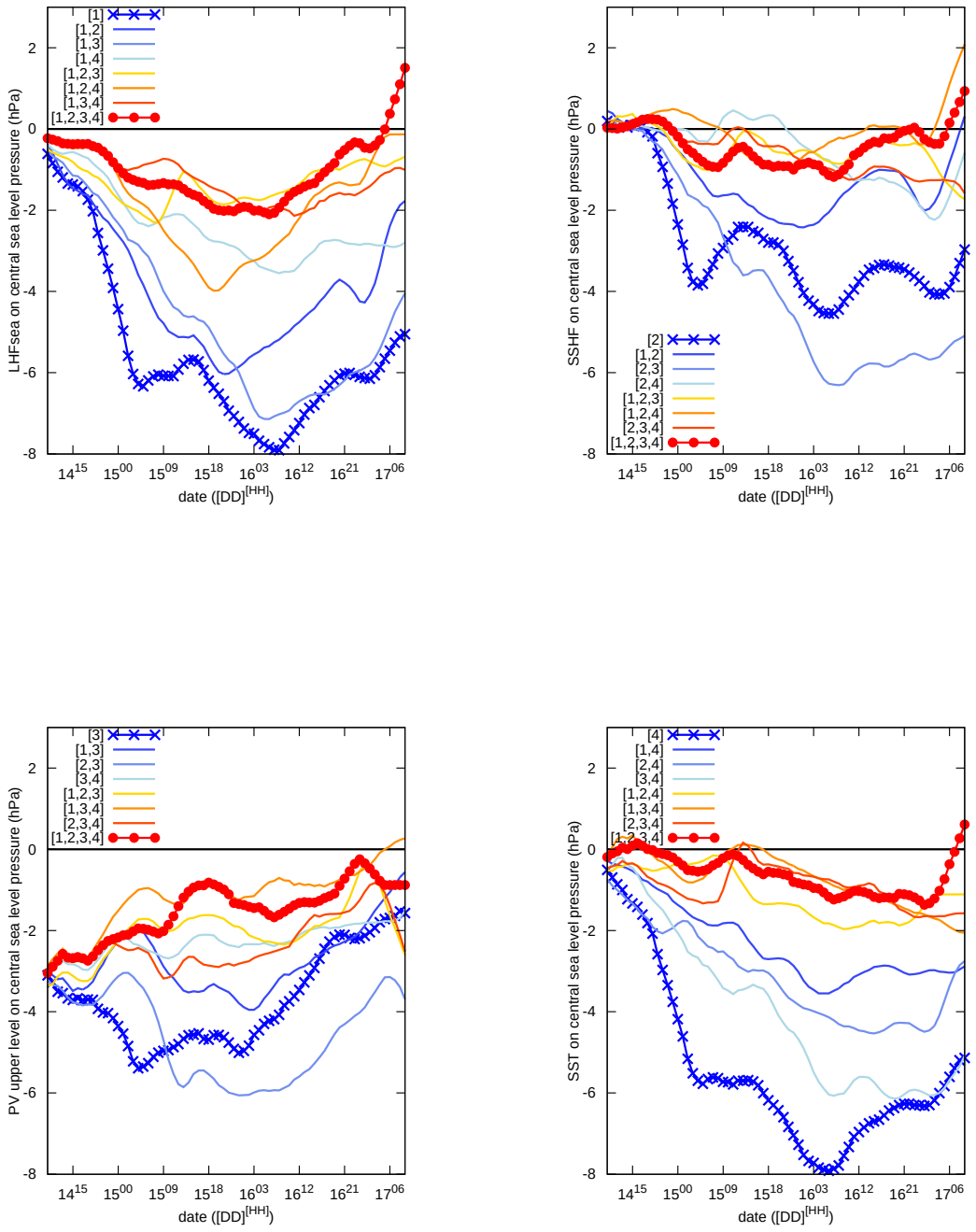

Figure 5.4.12: Collection-dependence of the 950116 case of the effects on the sea level pressure at the centre of the storm (hPa). LHF (top left), SSHF (top right), Upper level PV (bottom left), SST (bottom right). Results have been filtered with a mobile average filter of five time steps. Legend of the lines follows same structure like in figure 5.4.11

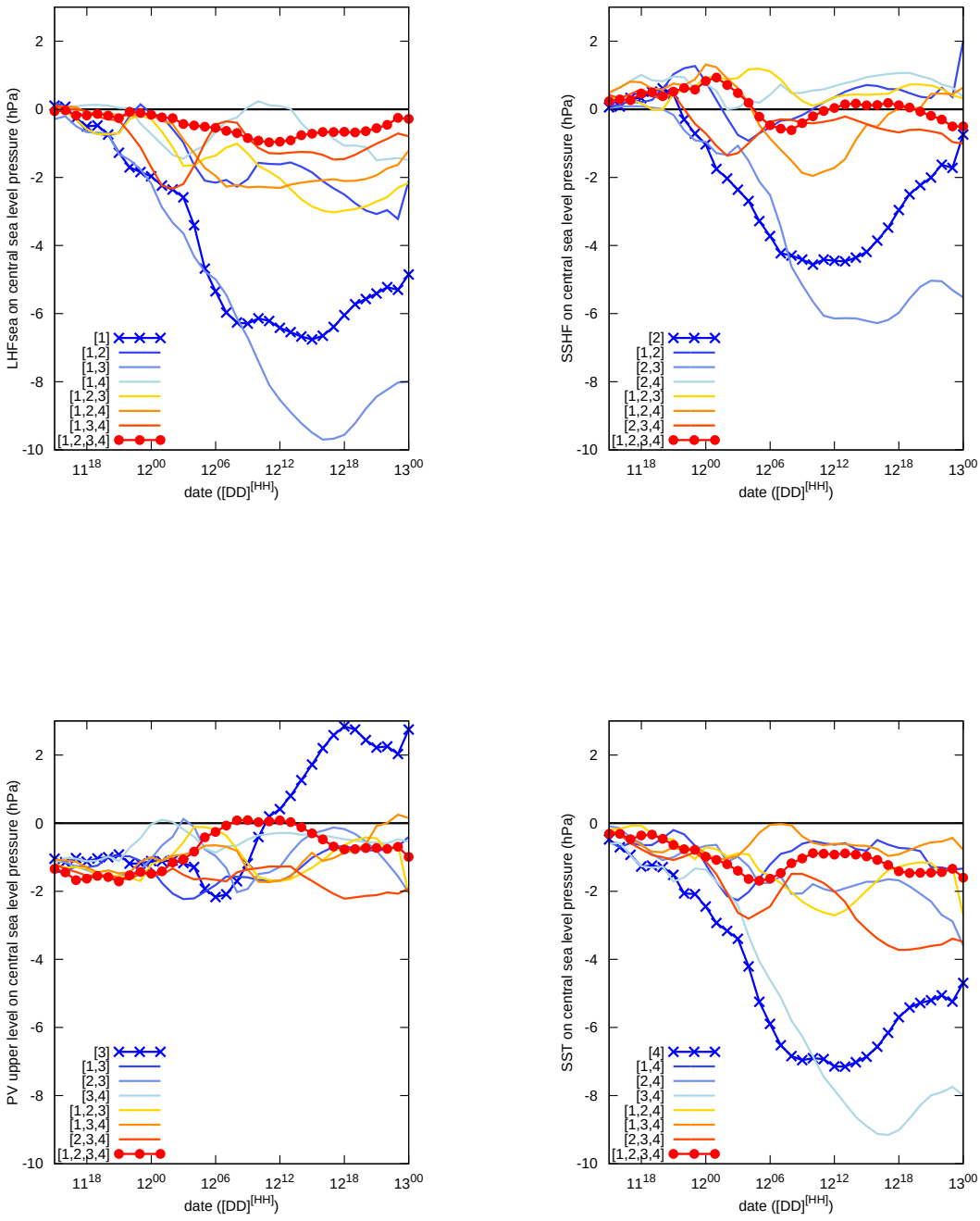

Figure 5.4.13: As in figure 5.4.12 but for the 960912 case (different scale)

the importance of the LHR on the enhancing role on upper level disturbances or on their influences in low-level disturbances (Hoskins et al., 1985; Davis and Emanuel, 1991).

In the sea level pressure value at the centre of the storm of the 950116 case, different 'goodness' are obtained (see figure 5.4.12). The four effects show anomalous dependence when they are obtained from a pair FS with the Upper level PV ($\{1,3\}$ curve in e_1(LHF effect), $\{2,3\}$ curve in e_2(SSHF effect), $\{3,4\}$ for e_4(SST effect), results that reflect some PV processes related to other factors not included in the study such as: PV diabatic generation due to the latent heat release on the strong and deep cloud formation into a medicane and/or Upper-low level PV interaction as a consequence of the baroclinic processes, and/or non PV related interactions between boundary layer and free layer, friction effects (related to efficiency of heat and moist transport from sea to cloud free layer driven by boundary layer). Secondary high sensitivity of the effectivity of the factors is obtained in the synergies with the SST factor ($\{1,4\}$ curve in e_1(LHF),$\{2,4\}$ curve in e_2(SSHF) $\{3,4\}$, $\{1,3,4\}$ curves in e_3(UPV), $\{1,4\}$ curve for e_4(SST)). Effects of SSHF factor show the lightest results during the mature phase of the medicane (between Jan. 15^{16} and 16^{05} UTC, figure 5.4.12). Giving a signature of the complex diabatic processes developed in the boundary layer of the storm like possible sea spray effect, and/or PBL processes related to strong turbulence, convection and winds poor influenced by the SSHF.

5.4.4 Temporal dependence

Effects on the pressure field of the cyclones are very diverse and depended strongly on the time step (see figures 5.4.15 to 5.4.17). From a general perspective, one can detect that 950116 and 030527 cases are different than 960912 case. These notorious differences might be related to the different nature of the cases: 950116 case shows a clear tropical-like structure (a clear and long-lasting central eye is observed see figure 5.1.2); 030527 case shows strong low-level vorticity, but an eye is not observed (see figure 5.1.6); 960912 case exhibits a clear eye (see figure 5.1.4), but for a short period of time (less than 5 hours, see table 5.1.a). These differences between the cloud structures of the storms could confirm the different nature of the systems. Meanwhile 950116 case would be mainly a system in which convection has strongly been self-organised around a vortex, 030527 case could reflect a major dominance of the baroclinic processes, and 960912 case could be the result of a combination of both processes. These aspects should be confirmed by the results.

Temporal evolution of the effects is divided in two phases in order to obtain a better understanding of the systems and as a way of summarise the results. This two-phase evolution is observed (see figure 5.4.15) as a change of the most relevant effects of the medicane evolution. First phase reached the formation of the system, meanwhile second phase reached mature state and dissipation. First phase is taken some time later of the

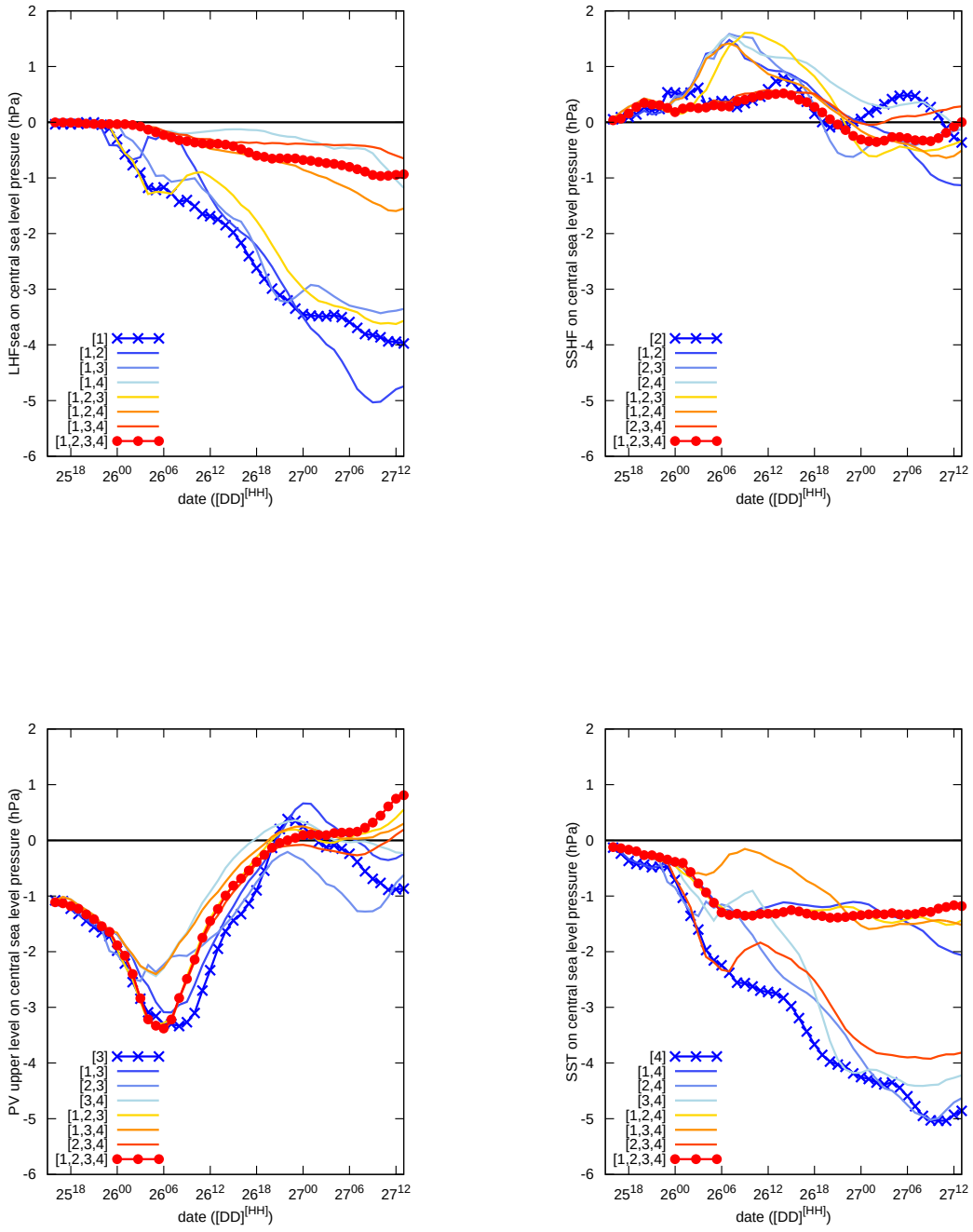

Figure 5.4.14: As in 5.4.12 but for the 030527 case (different scale)

Table 5.4.b: Phases of evolution of each medicane based on effect trends. Dates are in $[DD]^{[HH]}$ format

Medicane	Ist phase	IInd phase
950116	$14^{18} - 15^{17}$	$15^{18} - 17^{09}$
960912	$11^{22} - 12^{04}$	$12^{05} - 13^{00}$
030527	$26^{00} - 26^{11}$	$26^{12} - 27^{22}$

beginning of the simulations in order to avoid spin-up model processes and to make sure that the specific formation of the system is captured. Periods of the phases for each case are shown in the table 5.4.b. The total integrated effect per hour of each factor has been computed during each phase as a temporal integration of the effect at each time step divided for the length of the phase (negative and positive values is allowed, see results in tables 5.4.c, 5.4.d and 5.4.e). By this way is obtained a general idea of the mean role per hour of the effect during each phase.

There is a change of importance between the two phases. Meanwhile the fifth most important effects in the 3 variables (central sea level pressure, maximum azimuthally averaged horizontal wind speed at 950 hPa and relative vorticity at the centre of the storm) in the first phase are: $e_3, e_{24}, e_{14}, e_{134}$, on second phase they are: e_{14}, e_{123}, e_{124}, e_{134}. It is shown the dominance of the baroclinic evolution of the first phase (shown by strong role of e_3) as such as the triggering effect of the surface moist and heat fluxes derived from sea (factor number 4). Coinciding results of the polar low dynamics derived from a three-dimensional nonlinear geostrophic momentum model (Montgomery and Farrell, 1992). However, in second phase the evolution of the system is dominated by the heat of evaporation from the sea influenced by boundary layer and upper level disturbance (LHF as number 1 appeared in all the most important factors). Second phase reveal a more complex dynamics (triple synergies are important), as a possible reflection of the role of the air-sea mechanism. Some particularities for each case and variable can be given.

Effects on central pressure

During the formation phase, effects show a main clear enhancing role for the January 1995 case (2 cyclolitic of the 15 effects), meanwhile for May 2003 is not that clear (9 and 10). Results reveal that in selected cases the initial phase of the central sea level pressure effect is mainly driven by Upper level disturbance (effect e_3), the synergy between LHF and SST (effect e_{14}), synergy between SSHF and SST (e_{24}) and in lower degree by different synergies between the surface fluxes and SST. This dual dependence reflects the interaction between

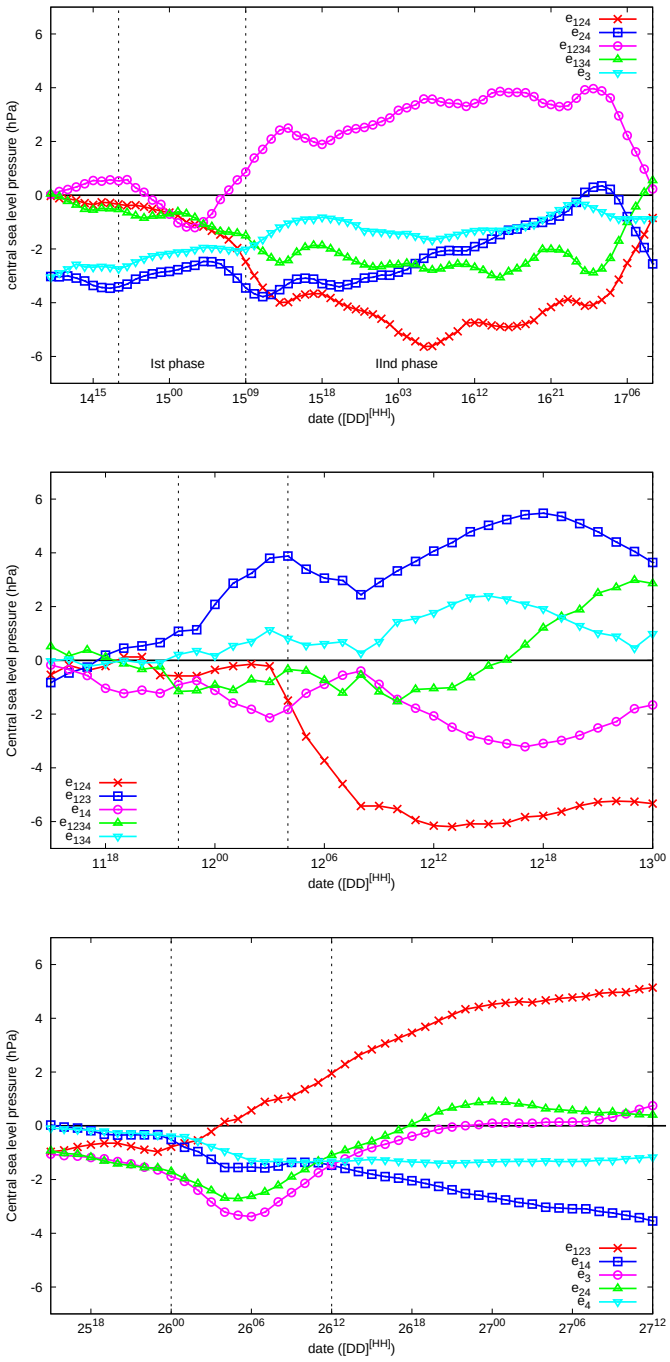

Figure 5.4.15: Temporal evolution of the fifth most important effects on the sea level pressure at the centre of the storm. January 1995 medicane (top), September 1996 medicane (middle) and May 2003 medicane (bottom). Results have been filtered with a mobile average filter of 5 time-steps (5 h). Vertical slashed lines mark each phase (labelled in top panel).

the baroclinic and diabatic sea surface induced processes assumed to be necessary for the formation of a medicane. Upper level disturbance as a way to enhance vorticity at the surface trough the baroclinic development and increasing vertical thermodynamic disequilibrium with the warm and moistened air above sea surface from which air-sea mechanism can be established in the Mediterranean area (Emanuel, 2005). The existence of a low level weak vortex has been shown as a necessary element from which a tropical-storm developed (Rotunno and Emanuel, 1987). This dynamical genesis aspect is shown by September 1996 case in which approaching movement of the upper level disturbance towards the zone of formation of the system (in which deep convection was developing, see figure 5.4.9) can be associated to a surface weak vortex around which convection is organised and the medicane is generated. Importance of the SST is a signature of its high influence on the heat and moist vertical transport in the boundary (as it is described in bulk parametrisation of the LHF and SSHF fluxes (Emanuel, 1986)) that acts as the initial source of heat and moisture for the convection. In all the cases, secondaries effects are synergies between SST, the LHF and SSHF fluxes. Some particular behaviours could be obtained from each case. The most clear is found in 030527 case a strong peak of the effectivity of the upper level disturbance (e_3 as line-circles in figure 5.4.15 on 26th at 06 UTC), could reflect a typical baroclinic Mediterranean role of the storm rather than a tropical like.

Secondary phases do not present a clear similarity between cases. Moreover, cyclogenetic and cyclolitic effects are present during this phase. Nevertheless, during this phase medicanes reached their mature state, but with the results of the three cases, one can not derive a general description of a medicane dynamics. Cyclones do not reflect the same effects with cyclogenetic/cyclolitic changes of some effects among episodes, and their stronger effects are different. January 1995 case reflect a multi-dependence during this phase. Double and triple synergies between the four different factors are the most important effects. This aspect could be a signature of the importance of the air-sea interaction for the development of the 950116 case. Different result is obtained for the September 1996 case. Instead synergies are still important effects, they exhibited a mixture of cyclolitic and cyclogenetic roles. This can be an indication of a short period of importance of the air-sea mechanism for the case. Bear in mind that in September 1996 case a cloud central free cloud area (eye) was only observed for few hours. May 2003 case does not show a similar dominance of the synergies like in the other two cases. A clear enhancing role is obtained from the SST and LHF. SST effect on the LHF (e_{14}, and the individual effect e_4 see table 5.4.c) is probably relevant because storm formation is mainly due to the moist fluxes from the sea, rather than as a consequence of a vertical disequilibrium as a combination of upper level disturbances and surface warm and moistened air. Important increasing in time cyclolitic role of the e_{123} effect is obtained for the three cases. Cyclolitic role of the e_{123} becomes stronger as more baroclinic-like is the storm (see significant differences between cyclolitic roles of the effect in table 5.4.c

Table 5.4.c: Averaged effects (hPa/hour) of each factor during the different phases of the cases at the central pressure value of the medicane. See table 5.4.b for the period of each phase

	950116		**960912**		**030527**	
	Ist phase	IInd phase	Ist phase	IInd phase	Ist phase	IInd phase
1st	e_{24} (-3.07)	e_{124} (-4.28)	e_{123} (2.84)	e_{124} (-5.47)	e_{3} (-2.87)	e_{123} (4.23)
2nd	e_{3} (-2.36)	e_{1234} (2.97)	e_{12} (-1.80)	e_{123} (4.41)	e_{24} (-2.35)	e_{14} (-2.65)
3rd	e_{14} (-1.51)	e_{134} (-2.35)	e_{14} (-1.66)	e_{14} (-2.16)	e_{14} (-1.39)	e_{4} (-1.37)
4th	e_{1} (-1.04)	e_{24} (-2.10)	e_{24} (-1.64)	e_{13} (-1.44)	e_{4} (-1.11)	e_{1} (-0.70)
5th	e_{124} (-0.98)	e_{234} (-1.43)	e_{3} (-1.62)	e_{134} (1.41)	e_{1234} (-0.94)	e_{134} (-0.53)
6th	e_{134} (-0.97)	e_{1} (-1.27)	e_{4} (-1.24)	e_{4} (-1.32)	e_{23} (0.76)	e_{124} (-0.47)
7th	e_{234} (-0.91)	e_{3} (-1.15)	e_{1234} (-1.18)	e_{24} (-1.08)	e_{234} (-0.64)	e_{24} (0.29)
8th	e_{23} (0.70)	e_{13} (-1.08)	e_{2} (0.83)	e_{1} (-0.71)	e_{134} (0.52)	e_{12} (0.29)
9th	e_{123} (-0.46)	e_{4} (-0.85)	e_{234} (-0.78)	e_{23} (-0.57)	e_{123} (0.43)	e_{13} (-0.24)
10th	e_{2} (-0.35)	e_{14} (-0.79)	e_{134} (0.62)	e_{34} (-0.54)	e_{2} (0.35)	e_{3} (-0.17)
11th	e_{13} (-0.35)	e_{34} (-0.63)	e_{124} (-0.42)	e_{12} (-0.42)	e_{1} (-0.22)	e_{234} (-0.17)
12th	e_{4} (-0.33)	e_{2} (-0.55)	e_{23} (0.30)	e_{3} (-0.38)	e_{124} (0.16)	e_{1234} (0.14)
13th	e_{1234} (-0.30)	e_{123} (0.54)	e_{1} (-0.25)	e_{1234} (0.18)	e_{12} (0.06)	e_{23} (0.07)
14th	e_{12} (0.20)	e_{23} (0.33)	e_{34} (0.20)	e_{234} (0.14)	e_{13} (-0.02)	e_{2} (-0.03)
15th	e_{34} (-0.06)	e_{12} (-0.31)	e_{13} (-0.18)	e_{2} (-0.13)	e_{34} (-0.02)	e_{34} (-0.01)

among January 1995, September 1996 and assumed more baroclinic May 2003 case). In other baroclinic studies a cyclolitc role was attributed to the surface fluxes (Kuo et al., 1991a; Horvath et al., 2006) due to a weakening of the surface baroclinic conditions that is proposed to be reinforced in the e_{123} synergy that includes the upper-level disturbance. At the same time, synergy is also proposed to be related to the strength of the capping inversion at the top of the PBL. Surface fluxes define PBL characteristics, meanwhile upper-level disturbances promotes mid-level instability. Their mutual interaction might be related to weaker differences between PBL and free atmosphere layers. Changes on the characteristics of the capping inversion introduced changes in the important energy budget (trough the $\overline{(w'\theta_e)}_h$, see figure 5.2.1) at the top (h) of the boundary layer at outer regions of the medicane (Emanuel, 1986).

Effects on maximum averaged horizontal wind speed

Effects on the maximum azimuthally averaged horizontal wind speed present a large variety of roles (figure 5.4.16). Looking to the fifth more important ones, a quite different sensitivities is obtained for both phases of each medicane (see table 5.4.d). Same factors like, e_{123}, e_{134} have different effectivity sign in 950116 and 960912 cases. This merge of roles and effects of the factors, could be a reflection of the mixture of mechanisms from which the system is developed, since no clear baroclinic or tropical-like structure is formed. In lower degree the initial dominance of the upper level disturbance (e_3) and SST and surface fluxes synergies (e_{24}, e_{14}) as in previous effect is also shown.

During the second phase of the storm evolution, the main effects on the maximal horizontal wind speed at 950 hPa become better identified, since their roles become stronger and much more well defined as a reflection of the well-formed structure. This is summarised in less number of principal effects for the three cases than in the formation phase (see table 5.4.d). Storms are still reinforced by surface factors, meanwhile upper level disturbance lost importance. In January 1995 case three of the five most important effects are the same than in the effects on the central sea level pressure (e_{124}, e_{134}, e_{24}). Moreover the effects present the same behaviour. Cyclogenetic effects e_{124}, e_{24}, e_{134} increase the wind speed of the system. This well correspondence between effects, could reflect a well formation of the case as a tropical-like storm driven by the air-sea mechanism.

Effects on relative vorticity

Effects on the Relative Vorticity at 950 hPa at the centre of the storm (see figure 5.4.17) clearly show the previous defined two phases of the evolution of these kind of systems. There is a clear signal of the formation of the 960912 and 030527 medicanes in the vorticity effects (see middle and bottom plots in figure 5.4.17), which are null until the storms

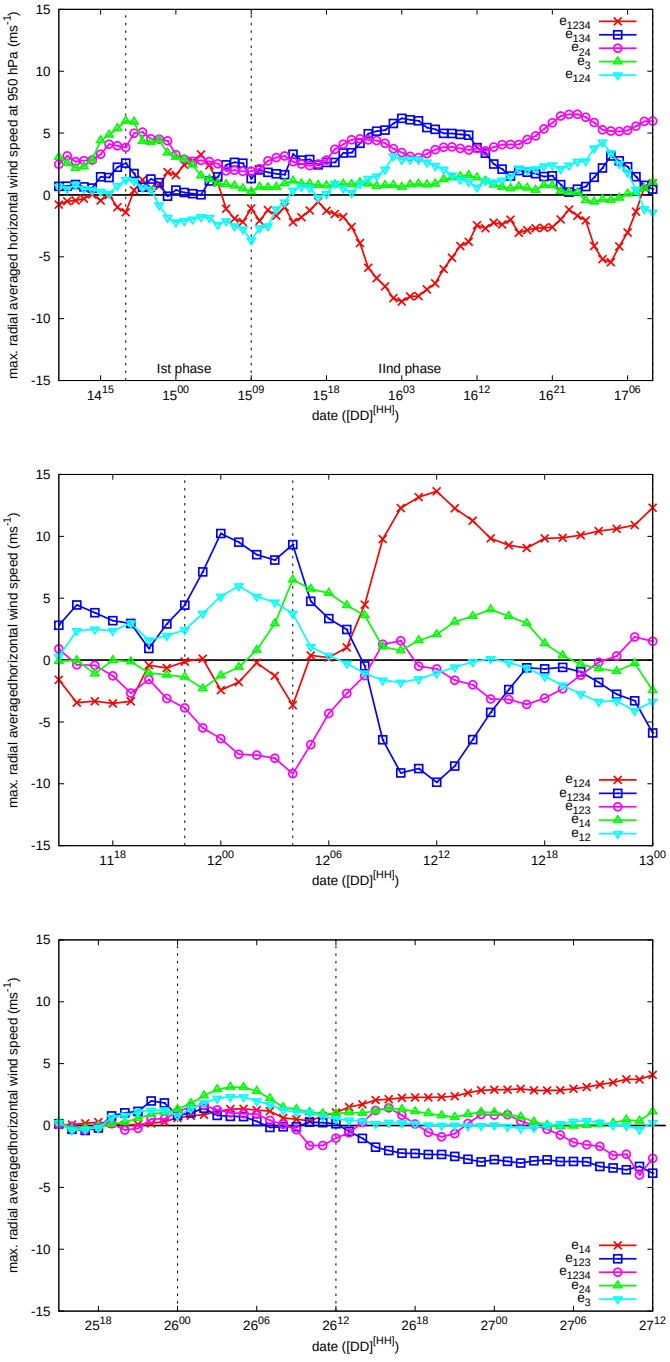

Figure 5.4.16: As in 5.4.15, but for the maximum azimuthally averaged horizontal wind speed at 950 hPa.

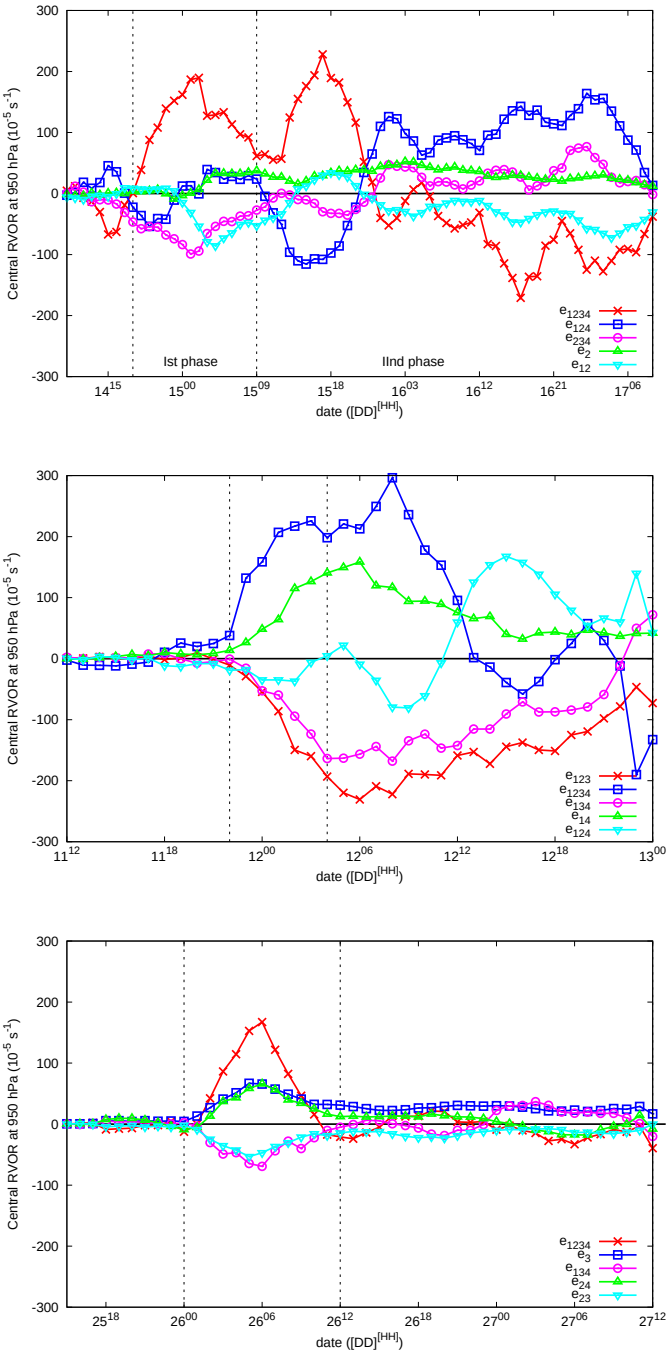

Figure 5.4.17: Like in 5.4.15 but for the Relative Vorticity ($10^{-5}s^{-1}$) at 950 hPa at the centre of the storm.

Table 5.4.d: Averaged effects (ms^{-1}/hour) of each factor during the different phases of the cases at the maximal azimuthal averaged horizontal wind speed at 950 hPa of the medicane. See table 5.4.b for the period of each phase

	950116		**960912**		**030527**	
	Ist phase	IInd phase	Ist phase	IInd phase	Ist phase	IInd phase
1st	e_{24} (3.57)	e_{24} (4.23)	e_{1234} (9.58)	e_{124} (8.67)	e_{24} (2.22)	e_{14} (2.74)
2nd	e_{3} (3.04)	e_{1234} (-3.54)	e_{123} (-7.79)	e_{34} (2.73)	e_{3} (1.69)	e_{123} (-2.57)
3rd	e_{14} (1.73)	e_{134} (3.06)	e_{12} (5.43)	e_{14} (2.52)	e_{14} (0.98)	e_{134} (0.99)
4th	e_{124} (-1.35)	e_{14} (1.83)	e_{4} (2.22)	e_{1234} (-2.48)	e_{2} (-0.59)	e_{24} (0.72)
5th	e_{134} (1.29)	e_{124} (1.33)	e_{134} (-2.03)	e_{123} (-2.15)	e_{123} (0.54)	e_{1} (0.54)
6th	e_{234} (1.04)	e_{13} (1.19)	e_{13} (1.29)	e_{134} (-1.86)	e_{1234} (0.49)	e_{1234} (-0.48)
7th	e_{23} (-1.01)	e_{34} (1.06)	e_{2} (-1.22)	e_{234} (-1.73)	e_{124} (-0.48)	e_{124} (-0.42)
8th	e_{1} (0.93)	e_{2} (-0.97)	e_{124} (-1.14)	e_{12} (-1.08)	e_{23} (0.31)	e_{13} (0.29)
9th	e_{1234} (0.82)	e_{234} (0.79)	e_{1} (-0.62)	e_{1} (0.45)	e_{12} (0.28)	e_{12} (-0.23)
10th	e_{13} (-0.47)	e_{1} (0.74)	e_{3} (0.49)	e_{13} (0.40)	e_{234} (-0.23)	e_{23} (0.16)
11th	e_{123} (0.34)	e_{3} (0.67)	e_{34} (-0.38)	e_{2} (0.35)	e_{13} (0.17)	e_{4} (0.11)
12th	e_{2} (-0.32)	e_{4} (-0.66)	e_{14} (-0.35)	e_{3} (-0.31)	e_{1} (-0.14)	e_{3} (0.10)
13th	e_{4} (0.25)	e_{123} (-0.30)	e_{23} (-0.34)	e_{23} (0.28)	e_{4} (0.09)	e_{2} (0.11)
14th	e_{34} (-0.07)	e_{12} (0.24)	e_{234} (-0.21)	e_{24} (0.20)	e_{34} (0.06)	e_{234} (0.09)
15th	e_{12} (-0.06)	e_{23} (-0.10)	e_{24} (0.17)	e_{4} (-0.01)	e_{134} (0.04)	e_{34} (-0.01)

Table 5.4.e: Averaged effects (10^{-5} s^{-1}/hour) of each factor during the different phases of the cases on the Relative Vorticity at the centre of the medicane at 950 hPa. See table 5.4.b for the period of each phase

	950116		**960912**		**030527**	
	Ist phase	IInd phase	Ist phase	IInd phase	Ist phase	IInd phase
1st	e_{1234} (125.47)	e_{124} (59.74)	e_{1234} (195.71)	e_{123} (-167.27)	e_{1234} (72.67)	e_3 (27.25)
2nd	e_{234} (-65.51)	e_2 (32.49)	e_{234} (-102.27)	e_{134} (-110.14)	e_3 (43.79)	e_4 (22.71)
3rd	e_{12} (-32.62)	e_{23} (-29.15)	e_{123} (-97.85)	e_{1234} (84.33)	e_{234} (38.18)	e_{124} (22.45)
4th	e_{134} (-19.29)	e_{24} (-27.90)	e_{23} (84.71)	e_{13} (83.29)	e_{134} (-36.87)	e_{123} (-16.36)
5th	e_1 (18.61)	e_{12} (-25.26)	e_{14} (78.75)	e_{14} (80.82)	e_{24} (34.02)	e_{23} (-14.48)
6th	e_2 (14.29)	e_{14} (-24.98)	e_{34} (76.78)	e_{12} (65.53)	e_{23} (-30.63)	e_{34} (-12.49)
7th	e_{34} (13.30)	e_1 (17.36)	e_{13} (73.88)	e_{24} (61.31)	e_{14} (20.17)	e_{134} (8.52)
8th	e_{123} (11.58)	e_{234} (16.69)	e_{24} (73.36)	e_{124} (55.91)	e_4 (18.28)	e_{1234} (-6.80)
9th	e_3 (-9.54)	e_{1234} (-13.21)	e_2 (-69.83)	e_1 (-25.64)	e_{123} (-17.42)	e_{234} (5.51)
10th	e_4 (-9.05)	e_4 (11.53)	e_1 (-69.58)	e_{234} (-25.34)	e_{124} (12.01)	e_{24} (3.37)
11th	e_{24} (8.71)	e_{34} (-5.90)	e_{134} (-69.31)	e_{34} (19.39)	e_2 (-9.43)	e_{13} (-2.95)
12th	e_{13} (4.88)	e_3 (-2.26)	e_3 (-60.90)	e_{23} (15.24)	e_{13} (-6.88)	e_1 (1.75)
13th	e_{23} (-4.85)	e_{134} (-2.01)	e_4 (-60.14)	e_3 (-12.78)	e_1 (5.96)	e_{14} (0.32)
14th	e_{14} (1.01)	e_{13} (1.02)	e_{12} (56.66)	e_2 (-10.82)	e_{12} (-4.02)	e_{12} (-0.10)
15th	e_{124} (-0.24)	e_{123} (-0.23)	e_{124} (-29.91)	e_4 (-5.61)	e_{34} (-0.95)	e_2 (-0.04)

are starting to form (11^{21} and 25^{23} UTC, respectively). mature and dissipative phase is depicted as a change in the roles of the factors in the 950116 and 030527 cases at 15^{23} and 26^{10} UTC respectively. Similar change of the roles is observed in the 960912 case at 12^{12} UTC. The principal roles in the January 950116 shown a mixture of factors and cyclolitic/cyclogenetic effects (see top panel in figure 5.4.17). On the other hand, 960912 and 030527 main effects follow two different characteristics. One group of the factors maintain their effect after the genesis of the meso-cyclone (as it is shown by the fifth most important effects of 960912 in the table 5.4.e). Other group of factors only are effective during the initial period of formation of the system (shown by fifth most important effects of 030527 case). The difference between effects of the cases, can be another evidence of the strong dynamical differences between two tropical-like episodes of 950116 and 960912 and a not well defined tropical-like 030527 case.

5.5 Sensitivity study on January 1995 medicane

January 1995 case has been described as the clearest case of tropical-like structure among the three studied cases in the previous section. In addition, from a collection of about 40 cases, the January 1995 event shows the most clear hurricane-like structure on satellite imagery[2].

MM5 model has been shown as a quite adequate tool to simulate tropical storms, like hurricane Andrew (Liu et al., 1997) and Mediterranean tropical-like systems (Reed et al., 2001; Homar et al., 2003b). Since MM5 numerical simulations provide a quite good simulation of the episode (see previous section), a detailed study of the air-sea mechanism in this case can be done.

Analysis of January 1995 case is done following azimuthal averages of 16 radius (100 km long) taken equidistributed at all directions from the centre of the storm. Azimuthal averaged values assume axisymmetry of the storm. Moreover, provides an unique way to represent the results with spatial and temporal independence. However, due to average computations, obtained fields are smoothed and some details are missed. Moreover, azimuthal averaged values are used as a way to ensure that the values of the fields are describing the global characteristic of the system. Analysis is carried out in two ways: a study of the correspondence of the characteristics of MM5 simulated case with the air-sea idealised characteristics, and factor separation results for four selected factors: sea surface temperature (SST), latent heat flux from sea (LHF), sensible surface heat flux (SSHF) and Upper level cold low on a different set of variables.

5.5.1 Methodology of 2-d effects

In order to study the role of the air-sea mechanism, the effect of four factors as well as their synergies are analysed. Simulation without any factor is carried out with sea surface temperature (SST, factor 4) cooled 5°C, sensible surface heat flux (SSHF, factor 2) and latent heat flux from the sea (LHF, factor 1) are switched off in the PBL scheme. Finally, upper level disturbances (ULd, factor 3), selected as all the potential vorticity (PV) field between 500 and 100 hPa, is decreased a 10% of its value at each time when the boundary conditions on the coarse domain (global analyses from ECMWF) are actualised (every 6 hours). Instead FS provide a way to analyse the effect of the tetra- synergy it is not analysed due to the high complexity and large variety of non-linear roles that are included in this synergy (see table 5.4.a for a description of each simulation). It is assumed that selected four factors provide a complete scope of the energetic cycle of the air-sea mechanism. However, one should bear in mind that the latent heat release of the

[2] http://www.uib.es/depart/dfs/meteorologia/METEOROLOGIA/MEDICANES/

strong, deep and vigorous cloud formation essential for the development of these storms, as it was shown in another similar case by Homar et al. (2003b).

Study of the non-linearity of the effects on some point characteristics of the storm (central sea level pressure, vorticity and maximum azimuthal averaged wind speed) has been done in the previous section. Here the 2-dimensional effects of the factors following 16-radius azimuthal averaged fields (with a radius of 100 km from the centre of the storm) will be presented. Previous studies (Homar et al., 2003b; Horvath et al., 2006) used FS in the study of a single characteristic of the system (central pressure), others one (Stein and Albert, 1993; Romero et al., 1997; Homar et al., 1999; García-Ortega et al., 2007) showed the effects on 2-dimensional patterns. In this case, FS technique is applied in a Lagrangian way (following the centre of the simulated system) that provided results will be focused on the structure of the system by itself. Thus, FS is not focused on the results on a single control simulation, otherwise on the simulated feature that wants to be studied. Showing the results on azimuthal averaged vertical sections of the storm is the proposed way from which a generic scope of the role of the effect should be obtained in both sense: the structure and induced dynamics. The azimuthal averaged effects should provide a detailed view of the roles according to their relative position within the studied feature. This increases the complexity of the study, since an interpretation of the effect should be provide taking into account its positional dependence. At the same time that a tropical-like storm has strong dynamically differentiated eye, wall and outer regions.

5.5.2 Validation of control simulation

Validation

Simulated trajectory and vertical structure of the cyclone present quite semblances with the satellite-based tropical-like observed structure and storm trajectory (see figure 5.5.1). At the same time, radial perspective of the simulated storm present clear tropical characteristics (see figure 5.5.2). Unfortunately sparse observations are in this maritime area and a verification following few ship measurements can only be done.

In order to analyse the goodness of the MM5 simulation of the case, BUFR files from ECMWF were used. According to specifications of the observational stations they can provide observations every 3, 6 or 12 hours. In this case 7 ship measurements available during mature phase of the storm (when a clear eye was observed) are considered.

Simulated trajectory of the storm is quite similar to the satellite-based derived one. However, simulated trajectory presents a temporal shift. Numerical storm evolves much faster and last less time that the observed (see figures 5.5.1 and 5.5.3). Instead poor temporal coincidence between observed and simulated trajectories of the storm, a com-

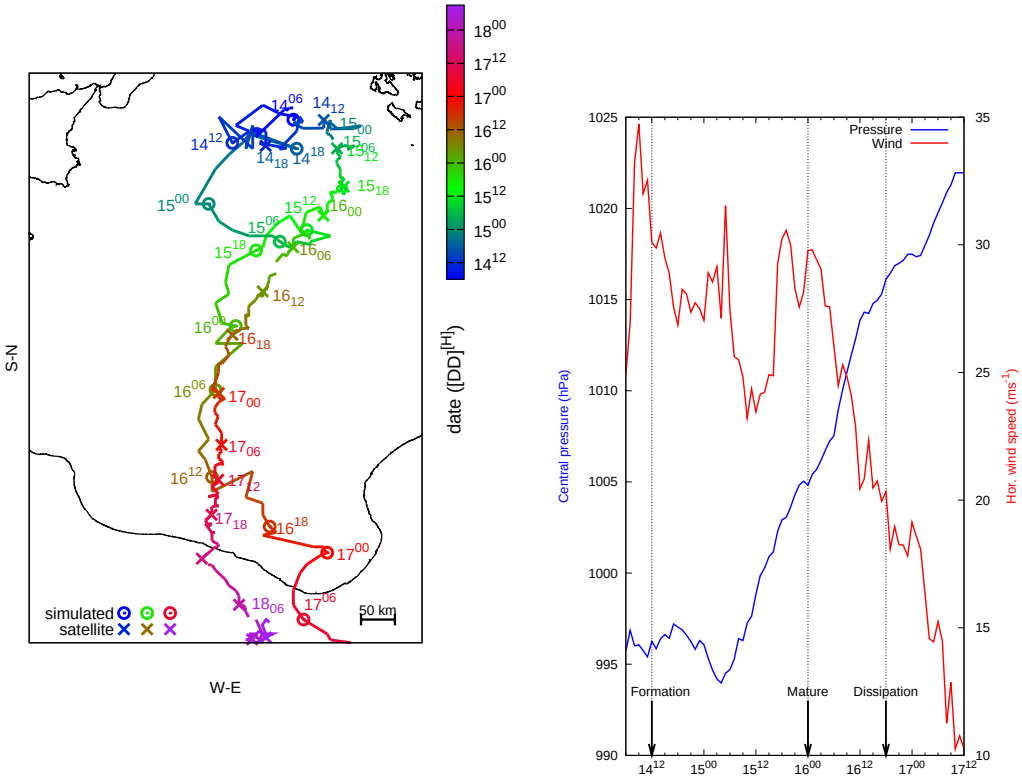

Figure 5.5.1: Control simulation results (f_{1234}). Left panel: MM5 simulated (line with circles and dates in $[DD]^{[HH]}$ format) and satellite derived (line with crosses and dates in $[DD]_{[HH]}$ format) medicane trajectories for the 950116 case with the corresponding date ($[DD]^{[HH]}$, format). Line colour according to box. Right panel: Temporal evolution of the simulated sea level pressure at the centre of the storm (blue line, hPa) and maximum horizontal wind speed at 950 hPa within a radius of 200 km from the centre (red line, ms^{-1}) date in $[DD]^{[HH]}$ format

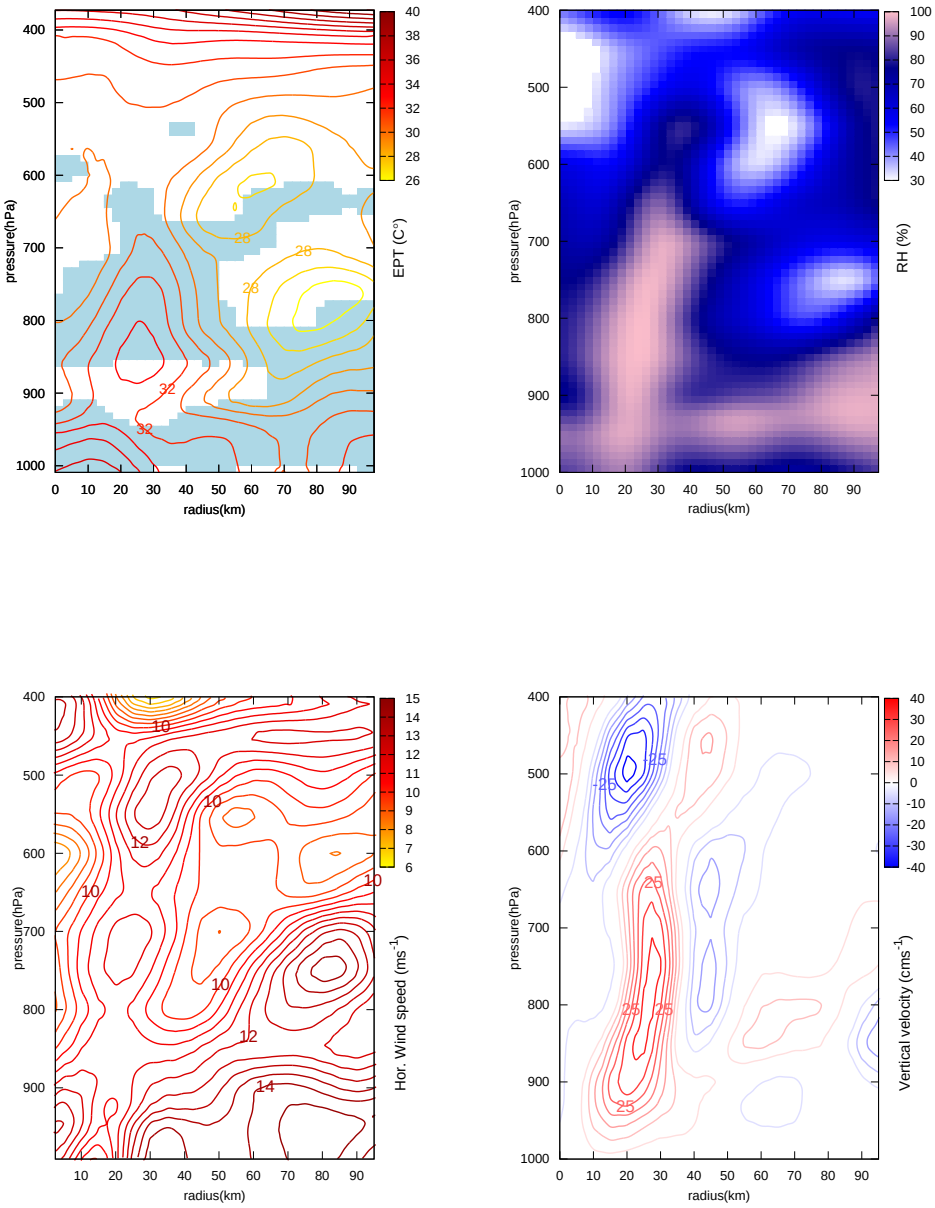

Figure 5.5.2: Averaged time-azimuthal fields (from the centre of the storm) of MM5 control simulated 950116 medicane during the period of maximum intensity (from 15th Jan. 95 at 16 UTC to 16th Jan. 95 at 05 UTC, defined as maximum horizontal wind speed and radial surface pressure gradient). x-axis (radial distance from the centre of the storm, km), y-axis (pressure, hPa). Negative vertical gradients of EPT are blue shaded ($\partial_z EPT < 0$, convective instability). Top left panel: Equivalent Potential Temperature (coloured line, every 1. $°C$). Top right panel: Relative Humidity from 30 %. Bottom left panel: Horizontal velocity (lines every 0.5 ms^{-1}). Bottom right panel: Vertical velocity (lines every 5 cms^{-1}), upward (red line), downward (blue line)

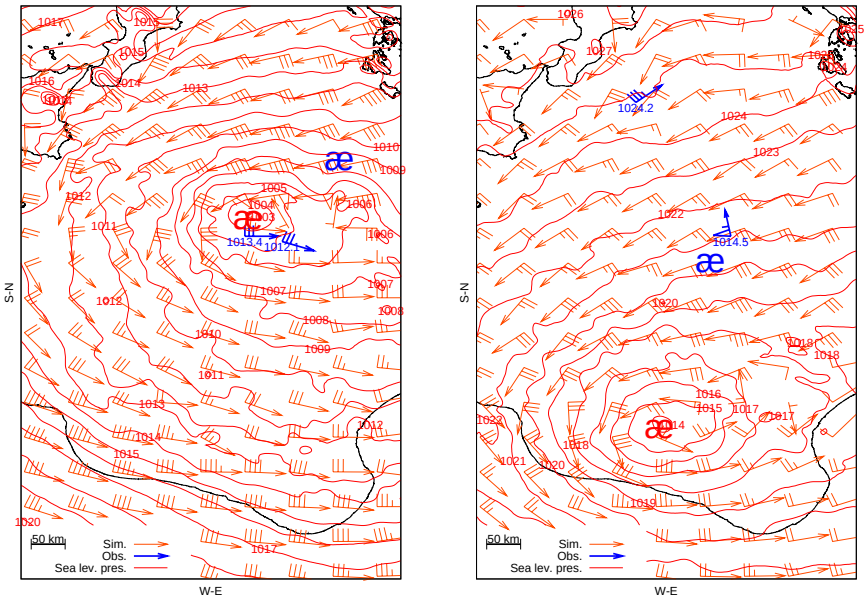

Figure 5.5.3: MM5 Control simulation results results for the January 1995 case (in reds; wind speed at 950 hPa, Sea surface pressure field every 1 hPa and centre of the medicane cross) and the observations (in blue: wind, surface pressure and satellite-based position of the medicane). On January 15th at 18 UTC (left), and January 16th at 12 UTC (right). Symbol æ denotes medicane keeping § for hurricane

parison among the structures of simulated and observed storms is attempted to be done. Trajectory and warm-core simulated structures are taken as realistic enough to assume well correspondence with observed one and for the porpoises of the study. Since at least, a tropical-like cyclone is obtained in the MM5 simulations and the role of different features related to the air-sea mechanism want to be studied.

Obtained fields during the maximum intensity of the simulated storm (between January 15th at 16 UTC and 16th 05 UTC, defined as a horizontal wind maximum at 950 hPa close to the centre of the storm in figure 5.5.1, and stronger radial pressure gradients) are compared to the observations meanwhile an eye-like structure in the centre of the storm can be observed on satellite imagery (from January 15th at 07 UTC to 18th at 06 UTC). Observed characteristics of the storm are taking as a composite of all the measurements located at the corresponding distance of the centre of the storm at the moment of the measurement. Resultant storm is considered to have preservative structure avoiding temporal changes or evolutions of its characteristics. Should beard in mind that this validation have strong approximations: an artificial construction of the characteristics of the observed storm and comparison will be made between smoothed simulated fields (they are spatial and time averaged) and punctual observations. However, according to the available observations, and knowing the temporal shift of the simulations, this methodology is the proposed most accurate way from which the validation of the simulated mature state of the medicane can be done with sparse and temporally shifted ship measurements.

MM5 simulation presents a deeper low pressure disturbance with winds increasing radius ward (see figure 5.5.4). A warm core can be derived (the centre of the storm is warmer that the outer values, bottom left). Moreover a possible wall can be derived from the maximum humidity value and lowest boundary layer height at a distance of 10 km from the centre of the storm (bottom right). Observational composite presented somewhat similar to a tropical-like storm (cross values). Inner low core is warmer with a maximum wind speed and humidity and low cloud base. However, observational and simulated values are quite different. The most notorious difference is that meanwhile MM5 gives a deeper low than the observational compose one (top left), observations give a stronger wind profile (top right).

Vortex characteristics

In order to analyse main characteristics of the mature state of the medicane, some vortex mean fields are computed. Following to the trajectory of the storm, grid boxes of 400x400 km are taken of different fields centred at the storm maximum intensity (between January 15 at 16 UTC and 16th at 05 UTC). Equivalent potential temperature at 850 hPa (EPT), relative vorticity at 950 hPa (RVOR), geopotential height at 500 hPa (H), sea level pressure and mixing ratio at 2 m (Q) give an idea of a rounded clear structure (see

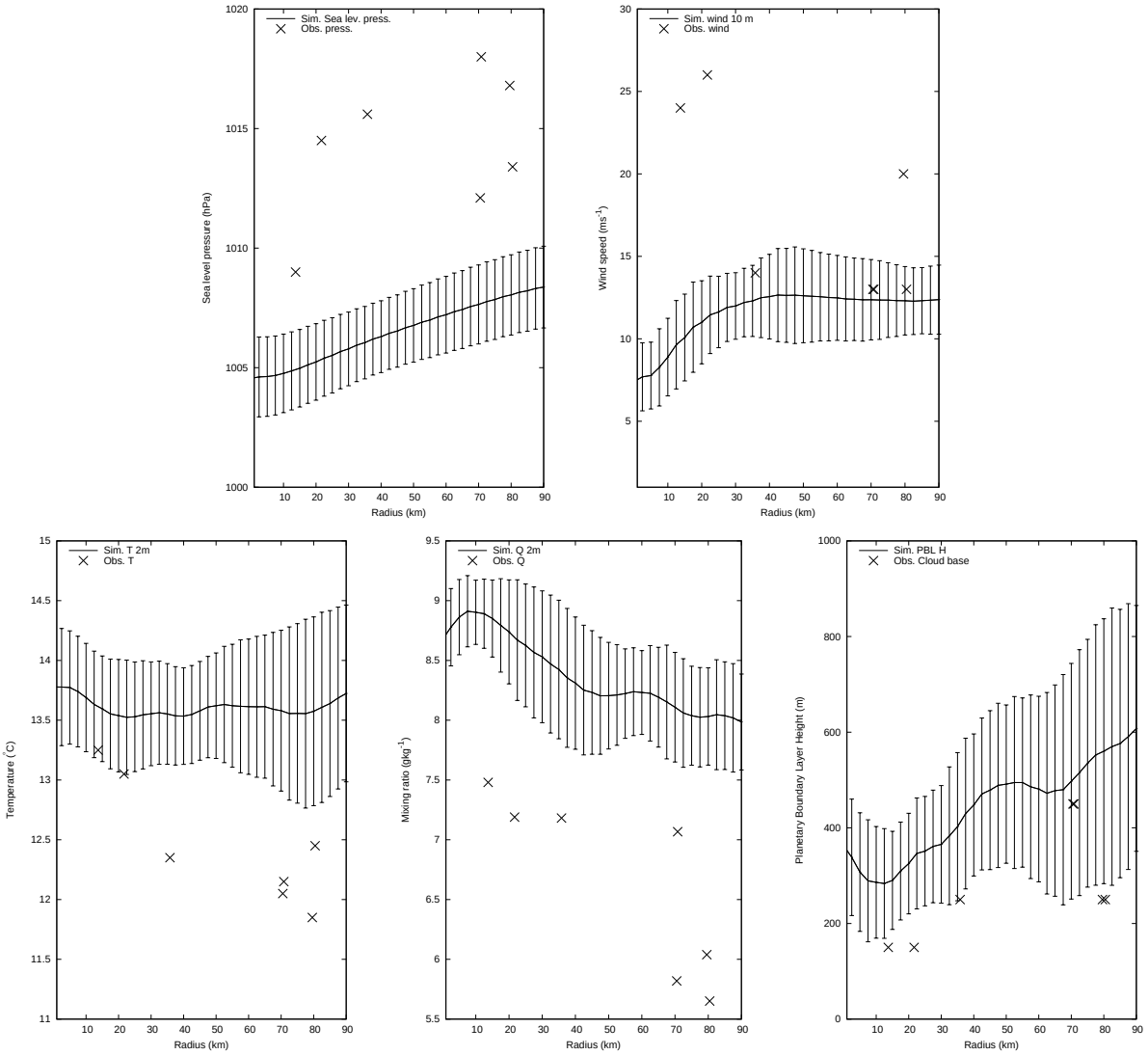

Figure 5.5.4: Radial distribution from the centre of the storm of the MM5 control results for the January 1995 case azimuthal and time averaged values during the maximum intensity of the storm (between January 15th at 16 UTC and 16th 05 UTC) and observations during the existence of an eye (from January 15th at 07 UTC to 18th 06 UTC). Each value has been referred to its individual position of the storm. Sea level pressure (hPa, top left), Wind speed at 10 m (ms^{-1}, top right), Temperature at 2 m (°C, bottom left), Mixing ratio at 2 m (gkg^{-1}, bottom middle) and simulated planetary boundary layer height (m) and observed base of the clouds (m, bottom right). Bars show standard deviation of azimuthal averaging

figure 5.5.5). However, Radiative tendency at 850 hPa RADTEND), temperature at 2 m (T2), planetary boundary layer height (PBLHGT), horizontal and vertical wind at 500 hPa and isoentropic Ertel potential vorticity (ErPV Is) (see figures 5.5.6 and 5.5.7) do not give any kind of clear organised structure.

It is shown how the storm is structured as a warm core low with high vorticity and quasi-saturated centre (see figure 5.5.5). Significant down drafts are obtained during the mature phase of the storm at its centre (see top right panel in figure 5.5.6). At the same time, horizontal wind field do not show an enclosed homogeneous vortex circulation (see figure 5.5.7). It is also obtained that the storm presented a maximum wind profile in the back part of the storm (northern region).

The non-vortex characteristics of the storm are more evident at low levels than at upper levels (see figure 5.5.7). A clear lower winds zone is extended eastward and it is reflected at all levels. This could be a signature of the environmental influences of the upper level anomalies that presented a clear meridional distribution (see ErPV Is field in bottom right panel in figure 5.5.6). It should be also mentioned the shifted relative distribution of the upper and low level disturbances. Geopotential height minimum (top right panel in figure 5.5.5), is shifted eastward from the centre of the storm. The persistence of the shift between upper and low level disturbances is also shown by the horizontal wind profile in which there is a coincidence of a minimal wind intensity (see middle and bottom figures in figure 5.5.7). The no clear existence of an axisymmetric vortex structure of the storm can be considered as a reflect of the weakness of the tropical characteristics of the storm as air masses with different thermal characteristics that confluence at the central part of the medicane (see top left panel in figure 5.5.6). This point is also mentioned by Montgomery and Farrell (1992) in the polar lows as a possible reflect of the warm air swirl by cold air. Finally frictional effects are shown in the wind profile, since wind strength at 950 hPa is stronger than at 2 m (see figure 5.5.7).

5.5.3 PBL Air-sea structure correspondence

As has been said, MM5 numerical simulations present a cyclone with tropical-like characteristics. Assuming well enough coincidence of the behaviour of the simulated storm, MM5 simulations will be used to study the importance of the air-sea mechanism in these type of Mediterranean tropical-like storms.

General characteristics of the planetary boundary layer (hereafter, PBL) of the storm do not present a clear structure as it is described by theory. Temporal evolution of simulated regime (defined throughout the Bulk Richardson number and Monin-Obukhov length) shows a pattern in which a signature of a wall and three related PBL zones can

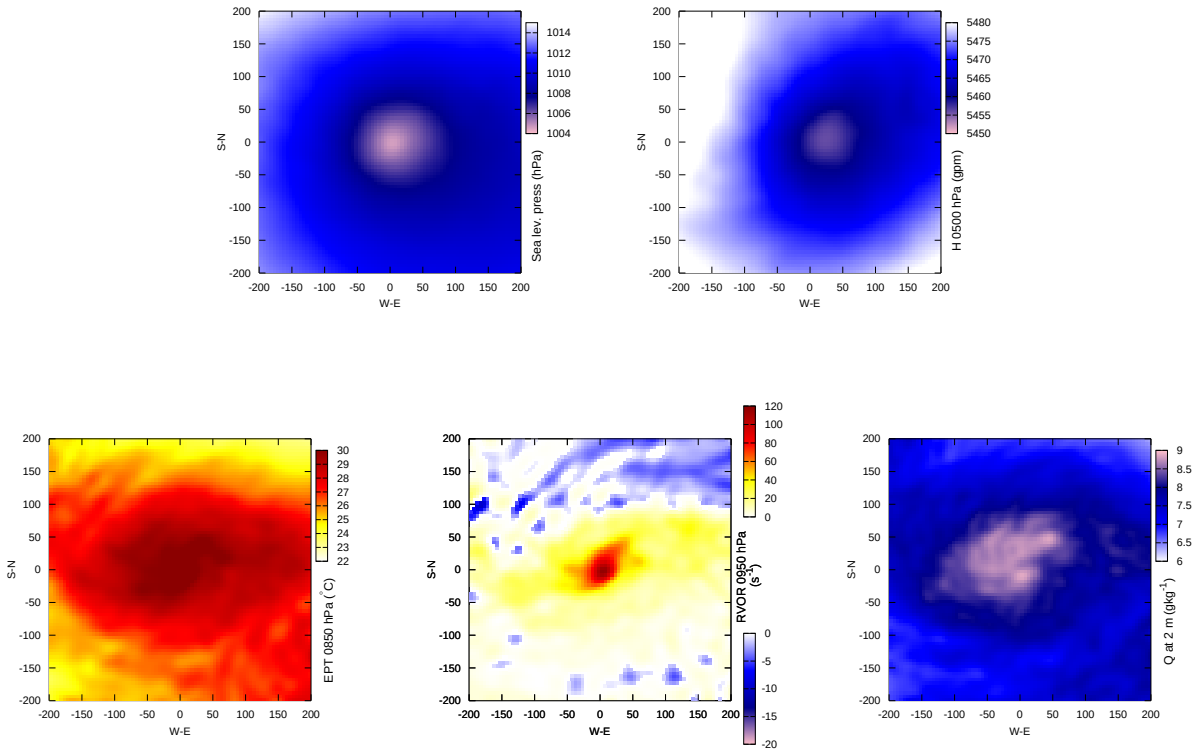

Figure 5.5.5: Time averaged fields in a grid box of 400x400 km centred at the centre of the storm following its trajectory during its maximum intensity (From January 15th at 16 UTC to 16th at 05 UTC). For the Sea level pressure (hPa, top left) and Geopotential Height at 500 hPa (gpm, top right). Equivalent Potential Temperature at 850 hPa (°C, bottom left), Relative vorticity at 950 hPa (s^{-1}, bottom middle) and Mixing ratio at 2 m (bottom right, gkg^{-1})

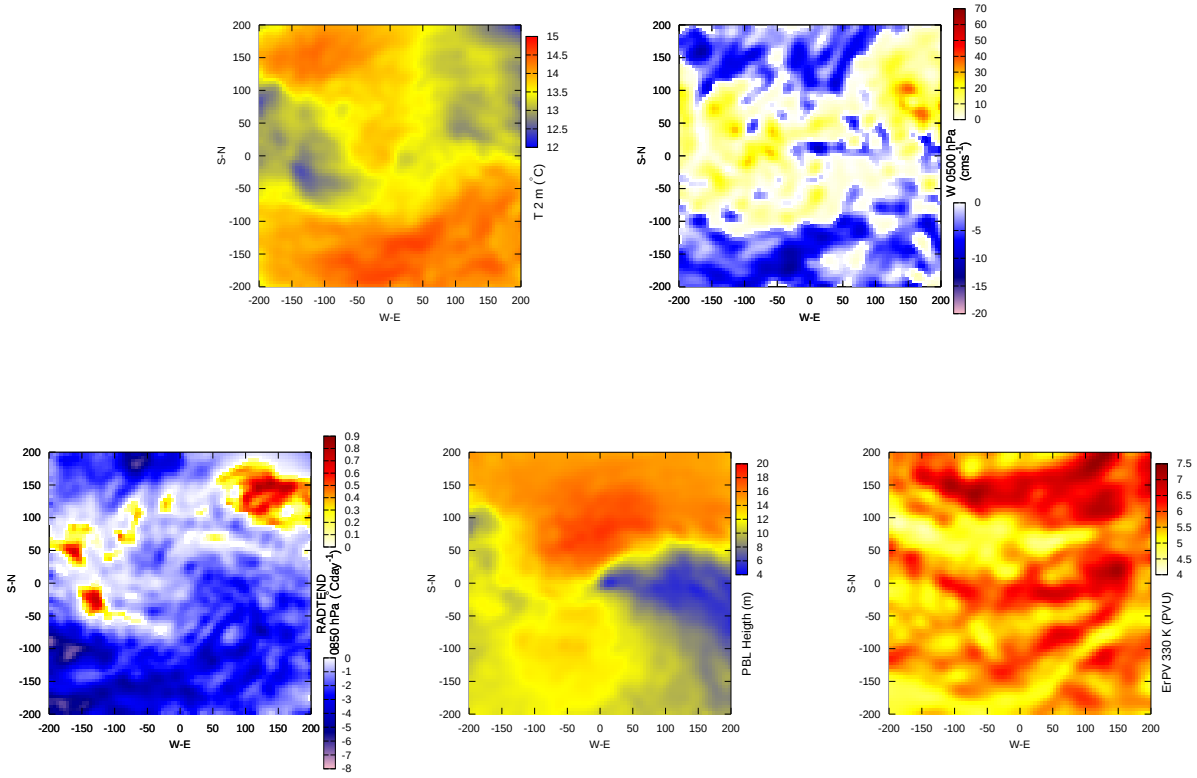

Figure 5.5.6: As in 5.5.5, but for the Temperature at 2 m ($^{\circ}C$, top left), vertical velocity at 500 hPa (cms^{-1}, top right), radiative tendency at 850 hPa ($^{\circ}Cday^{-1}$, bottom left), planetary boundary layer height (m, bottom middle) and Ertel potential vorticity on an isentropic surface at 330 K ($PVU = 10^{-6}m^2Ks^{-1}kg^{-1}$, bottom right)

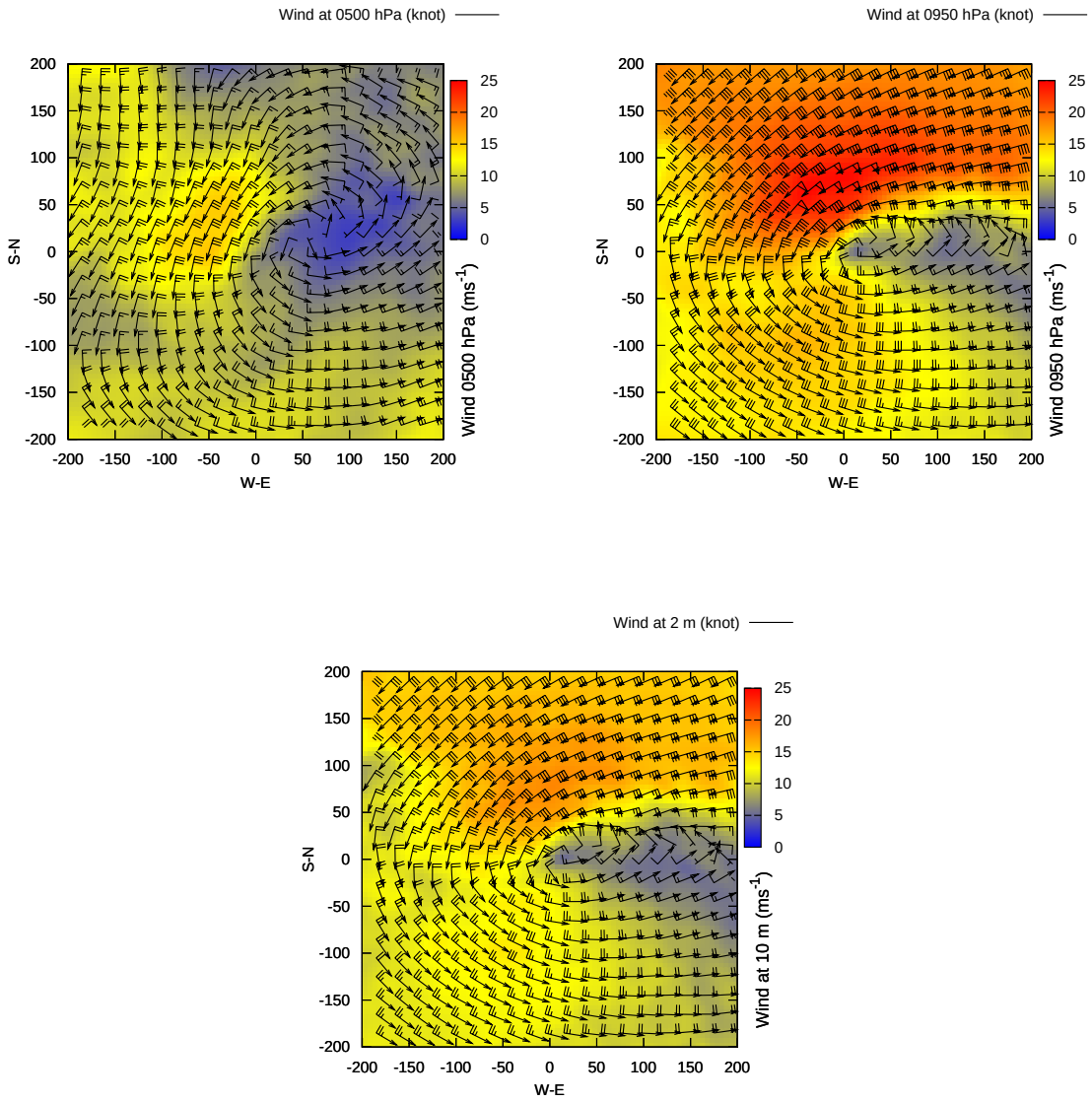

Figure 5.5.7: As in 5.5.5, but for horizontal wind speed at 500 hPa (ms^{-1}, top left), at 950 hPa (ms^{-1}, top right) and at 10 m (ms^{-1}, bottom), superimposed in barb notation (triangle 50 knot, full pennant 10 knot and half pennant 5 knot)

be observed. At specific times three boundary regimes are simulated and presented a well agreement with an eye-wall-convection regions (see figure 5.5.8). Changes in PBL regime have correspondence with the lowest and most saturated region of the radius section that can be identified with the wall zone. Due to subsidence in the eye, this zone should present a stable boundary layer, meanwhile MM5 boundary layer scheme gives a free convective regime. Blackadar PBL is a simple scheme that considers only two regimes (Grell et al., 1995): free-convection and nocturnal regime given by a comparison between the critical and the bulk Richardson Richardson numbers (Stull, 1988). The simplicity of the scheme might not be accurate enough to provide an adequate view of the PBL.

However, temporal evolution of boundary layer characteristics reflect the complete establishment of tropical-like characteristics of the storm (See figure 5.5.8); it is shown how the centre of the storm is warming due to warm core characteristics (see increasing centre temperature in thermal evolution in the top right panel). At the same time, inner regions presented the lowest turbulent characteristics (lowest values of the friction velocity, u_*, bottom right panel) and the enhancing of the eye as a wider section with the lowest boundary layer heights (top left panel). However, as has been seen in temporal evolution of the central pressure (see right panel in figure 5.5.1), surface pressure increases with time (bottom panel in figure 5.5.8).

5.5.4 Effects on the vertical radial structure

Effects obtained for the January 1995 case have a relatively good relation to the dynamics of the air-sea interaction (see previous section). For a more detailed study effects on 16 azimuthal averaged vertical cross sections of the system from the centre of the storm are shown. These radial vertical cross sections are taken at three time steps. One on January 14th at 12 UTC (six hour after the starting time of the simulations avoiding model spin up effects), on January 16th at 00 UTC (at mature state of the system) and during dissipation phase on January 16th at 18 UTC.

The effects of the factors could be focused in two principal aspects of the storm; thermodynamic aspects such as temperature, humidity and cloudiness and dynamical aspects such us geopotential height and wind field. Even so, air-sea mechanism establishes a thermodynamic base for the formation and evolution of a tropical storm that makes possible the treatment of a hurricane as a Carnot engine (Emanuel, 1986, 1995). Thus a well understanding of the evolution and structure of the EPT can give a wide idea of the thermodynamic aspects of the system, even though other characteristics are not well described by the variable. Some important aspects obtained from other variables will be also mentioned when it is necessary, since some factors could have a strong impact on specific other aspects of the system.

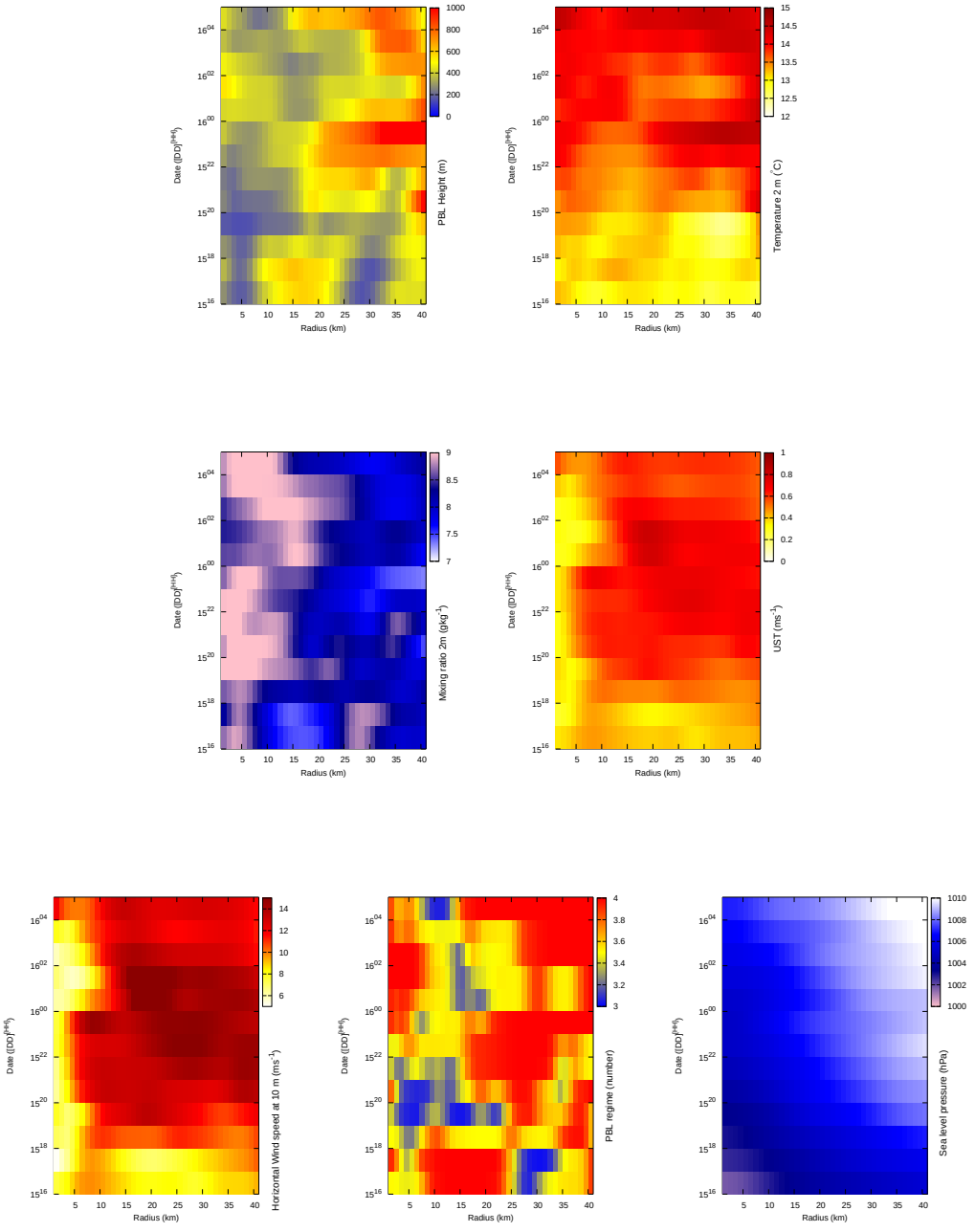

Figure 5.5.8: Temporal evolution (from January 15th at 16^{00} to January 16th 05^{00} UTC) of azimuthal averaged values PBL Height (top left), Temperature at 2 m (top right), mixing ratio (gkg^{-1}, middle left), u_* (ms^{-1}, middle right), wind speed at 10 m (ms^{-1}, bottom left), PBL regime (3: Forced convection, 4: Free convection; bottom middle) and Sea level pressure (hPa, bottom right)

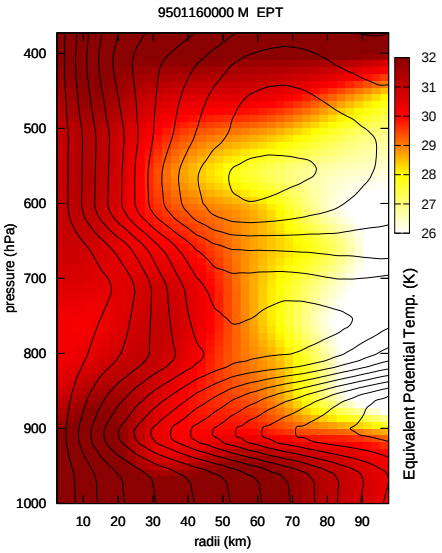

Figure 5.5.9: Storm centred azimuthal averaged vertical cross section of constant angular momentum surfaces M ($m^2 s^{-1}$, solid lines) and equivalent potential temperature (K, shaded) on 16th January 1995 at 00 UTC. x axes radius distance from centre, y axes pressure)

If the air-sea mechanism is active during the medicane evolution, in somehow vertical cross sections of the fields exhibit some peculiarities of the tropical-like structure of the storm. Radial azimuthal averaged vertical cross section of the simulated mature state of the storm (see figure 5.5.9), have some similarities with the radial structure of a hurricane (Rotunno and Emanuel, 1987) (see figure 5.2.1). Constant angular momentum surfaces draw two distinct zones: at low level, surfaces are radially equi-distributed; at mid-levels, surfaces show up-outward distribution. A warm core structure is also shown with a signature of an eye-wall.

Effects are given at a specific moment of the simulation, which provide a time-dependant description of the result. However, they provide a not smoothed view of the storm that is given by averaged fields in storm's mature phase discussed in the validation subsection. Moreover, azimuthal averaged fields assume axis-symmetric structure of the storm, and an unique and equal radius for all the periods of the storm, that might help to

obtain an objective scope of the phases of the cyclone. Due to hurricane-like characteristics of the storm, effects might have two distinguished values: at the centre and outer regions.

Effects during formation

At the beginning of the storm (January 14th at 12 UTC) a weak vortex about 800 hPa height, and a radii about 40 km is observed (see top left in figure 5.5.10). It is shown the positive role of the surface fluxes in the storm as it was found by Kuo et al. (1991b). LHF warms and moistens the surface layers (e_1, top right), meanwhile SSHF (e_2 bottom left) warms and dries surface layers and deepens the storm cooling, moistening and increasing wind speed at its centre (not shown). Enhancing effect in the core of the vortex, might be a reflect of the positive role of the SSHF in maritime low disturbances described by Mak (1997). Upper level disturbances (ULd hereafter, effect e_3, bottom middle), provokes a decrease of the EPT all over the storm, except at the top of the centre of the vortex, where the column of air at this zone is moistened and vorticity is raised until 700 hPa as a result of the factor (not shown). Meanwhile induced down drafts of upper air dried. At this moment, control simulation (in the f_{1234}) disturbance is beneath an upper level cold pool zone (not shown).

The synergy between the SSHF and the Upper level disturbances e_{23} (bottom right in figure 5.5.10) has a differenced role in the centre of the vortex and the outer regions, with a vertical dependence according to the height of the vortex. It plays a role heating and drying the centre of the storm, meanwhile the environment is cooled and moistened. At the same time it reduces the wind speed at the centre of the storm (not shown). In terms of the baroclinic development of the vortex, it plays a cyclolitic role, but it has a positive effect towards the characteristics of an hurricane-like eye and it destabilises the environment of the vortex. SST enhances the turbulent mixing and transports in the surface (see bulk parametrisation of LHF and SSHF fluxes, Emanuel (1986)) and the synergy (e_{24}, left panel in figure 5.5.11) has a stronger equivalent effect than in the e_2 pure effect.

Similar role is obtained by the triple synergy e_{124} (middle) between surface fluxes (LHF and SSHF) and SST from which a tropical driven effect on the evolution of the storm can be derived. Mid level humidity is enhanced and cloud formation is promoted at outer regions of the vortex (Cloud liquid water at middle levels is enhanced (not shown)). At the same time it reduces wind speed and vorticity at the centre of the storm increasing wind speed at outer regions (not shown). Finally, e_{234} reproduces the same pattern of the SSHF by it self (right). It is remarkable that the mutual interaction of two factors e_{23} without taking into account influences of SST has the opposite sign. This result shows the

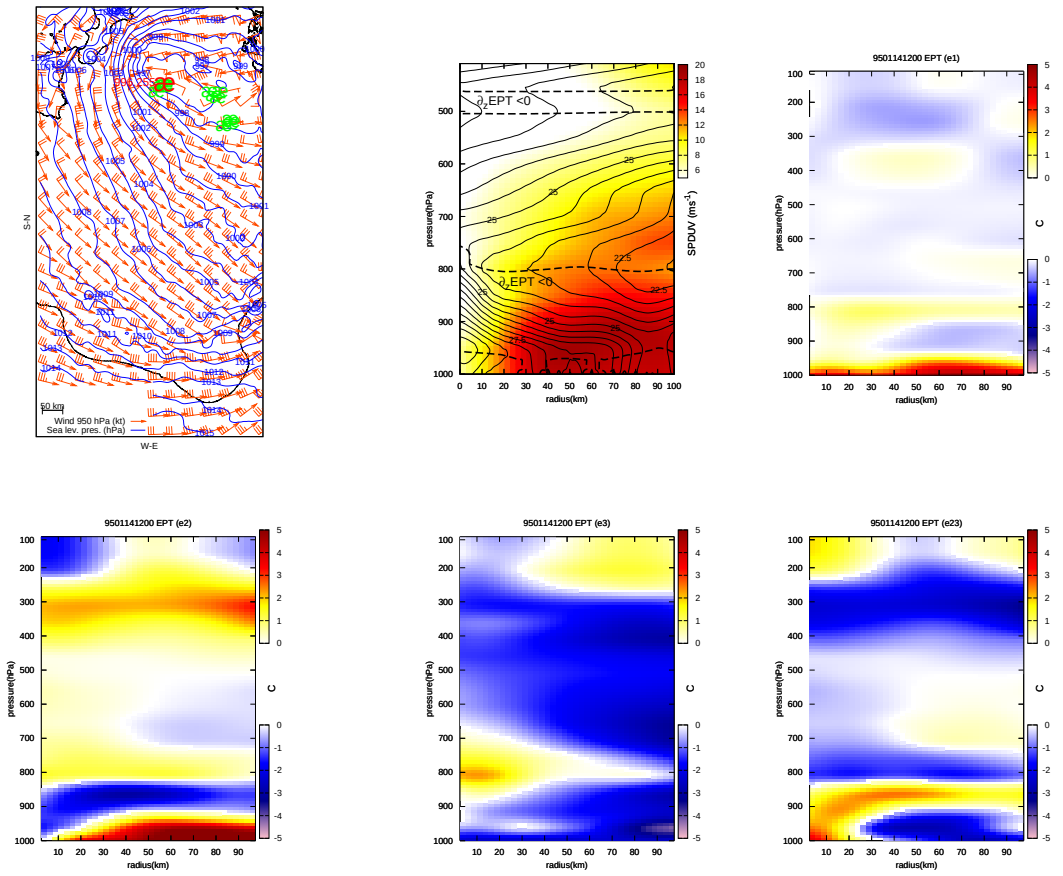

Figure 5.5.10: Values on January 14th at 12 UTC. Top left panel: Control simulation sea level pressure (f_{1234}, simulation; every 1 hPa, blue lines), horizontal wind at 950 hPa (orange vectors in barb notation; triangle: 50 kt, pennant 10 kt, half pennant 5 kt) and central position and pressure of the storm (red æ, red label in hPa), rest of simulated medicanes positions (green æ). Top middle panel: Control simulation vertical cross sections of azimuthal averaged horizontal wind speed (shaded in ms^{-1}) and equivalent potential temperature (EPT, solid lines in $°C$, convective instability zone $\partial_z EPT < 0$ is shown as thick dashed line). Rest of panels: Azimuthal averaged effects on EPT (dashed in $°C$; blues: negative effect, reds: positive effect). e_1 (LHF, top right), e_2 (SSHF, bottom left), e_3 (ULd, bottom middle), e_{23} (SSHF and ULd synergy, bottom right)

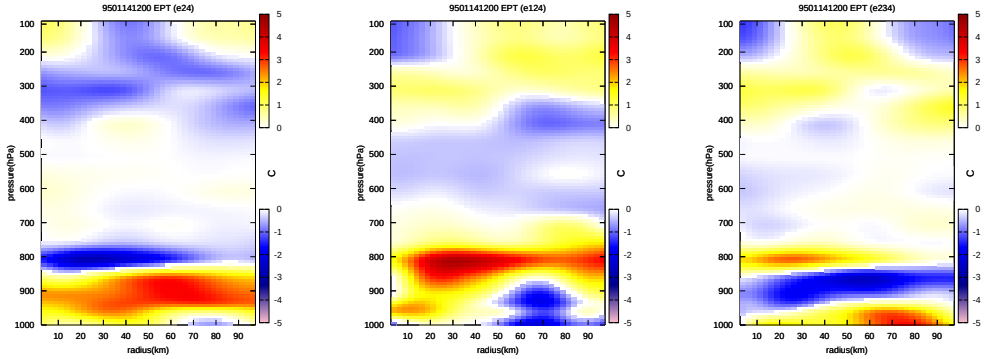

Figure 5.5.11: As in figure 5.5.10 but for e_{24} (SSHF and SST synergy, left), e_{124} (LHF, SSHF and SST synergy, middle) and e_{234} (SSHF, ULd and SST synergy, right)

complexity of non linear processes that are involved in the mutual interactions between factors.

Effects at mature phase

Mature state of the medicane (January 16th on 00 UTC, see left and middle plots in figure 5.5.12) is described as a cyclone with a height of 600 hPa and a radii about 100 km. Radii of the eye seems to be about 10 km with the base of the wall at 30 km (zone with the maximum wind speeds). In control simulation, at this moment, upper level disturbance and medicane are completely coupled, since upper level central minimum height (about 5470 gpm at 500 hPa) is located above the centre of the medicane (not shown). In comparison to the formation phase of the system, it is shown a more unstable structure of the storm according to the greater convective instable zone ($\partial_z EPT < 0$ in figure 5.5.12 top middle panel).

Surface fluxes preserve the same role that they have in the initial phase. However, LHF (e_1 effect at top right plot in figure 5.5.12) has increased significantly its influence to higher levels and it has a strong pressure fall role at low levels (not shown). e_3 drys the middle levels of the system and decreases (weaker than in the initial phase) pressure allover the vertical structure of the system (middle left plot in figure 5.5.12). SST warmed low levels and has it strongest deepening role in the selected moments (not shown).

Effects of the synergies between surface fluxes (middle middle plot in figure 5.5.12)

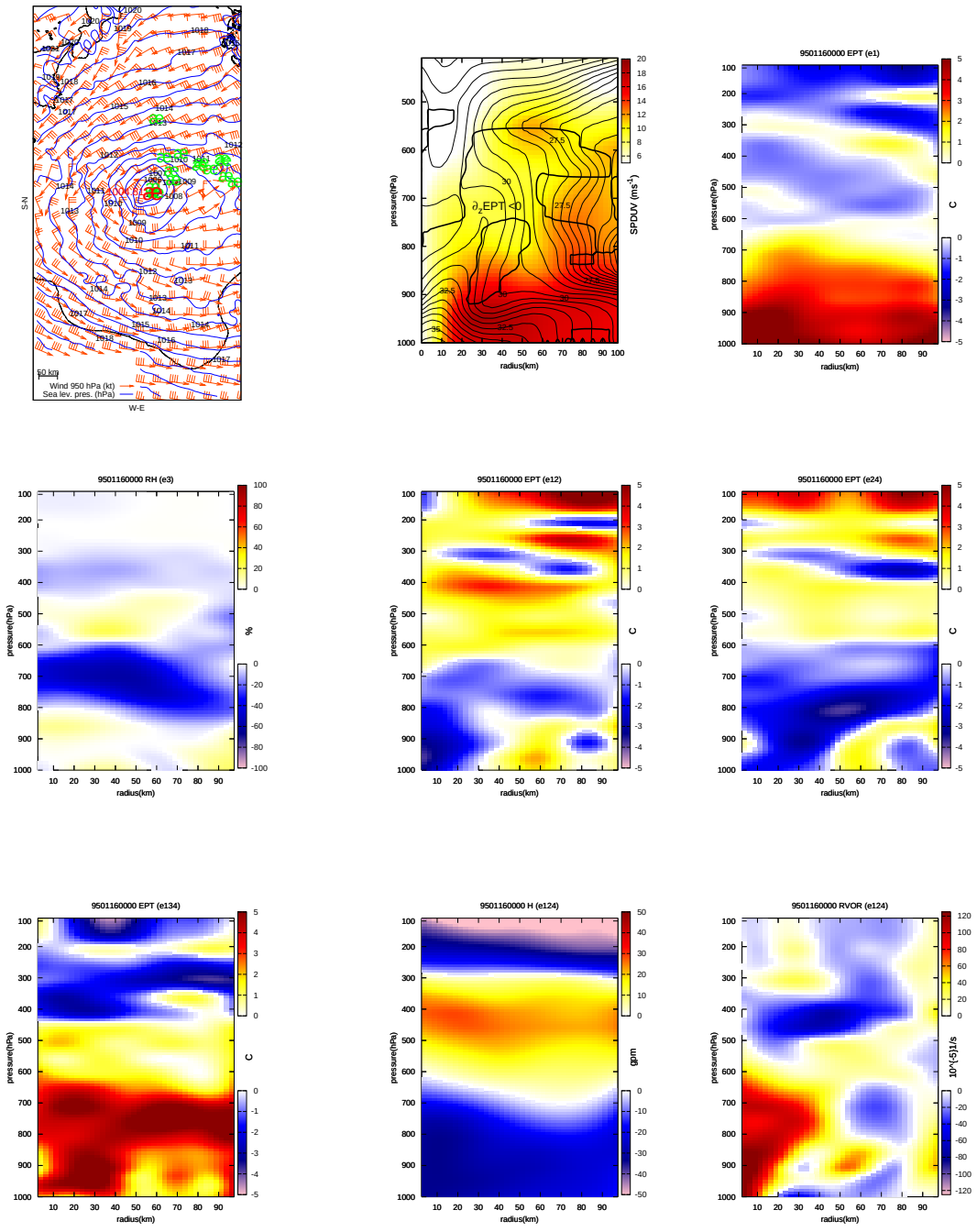

Figure 5.5.12: As in figure 5.5.10 and 5.5.11, but on January 16th at 00 UTC. Effects of e_1 on Equivalent potential temperature (EPT in $°C$, top right), e_3 on relative humidity (%, middle left), e_{12} on EPT ($°C$, middle middle), e_{24} on EPT ($°C$, middle right), e_{134} on EPT ($°C$, bottom left), e_{124} on geopotential Height (gpm, bottom middle) and of e_{124} on relative vorticity (s^{-1}, bottom right)

are most important in the core of the storm contributing to enhance its properties such as vertical low humidity profile, low wind speed velocities and low cloudiness (not shown). Synergy between LHF and ULd (e_{13}) has a dual role. It makes difficult the humidity flux following air trajectories of the air sea mechanism (middle level constant angular momentum surfaces structure as in figure 5.5.9), but deepened the system and enhanced the air-sea mechanism characteristics of the storm. Not only it helps to low the pressure, cloudiness and wind speed at the centre of the storm but it contributes to increase cloudiness, vorticity and humidity at outer region of the eye (not shown). SSHF and ULd mutual influences have a enhancing effect on the storm, since their mutual interaction reinforces their positive individual role. This synergy (e_{23}) moistened middle levels and dried the air at the top and weakened wind speed of the centre of the storm (not shown). e_{24} cooled and dried a wide zone within the storm that presents some similarities to the mid-level constant angular momentum surfaces (see middle right in figure 5.5.12). Must be noticed the antagonistic role of this effect in comparison to its role in the formation phase. It could be a reflect of the change in the dynamics of the system. During initial phase SSHF (factor 2), enhances storm reinforcing vertical transport of heat and moist to boundary layer and upper levels. However, at mature phase, SSHF enhance turbulence provoking a diminishing effect on the inward motion to the centre of the storm (maximum values of u_* are found at this phase, see figure 5.5.8).

e_{123} plays a dissipative effect (as it is shown in previous section), since it cooled and moistened the core of the system (not shown) at the same time that it decreased humidity and cloud formation in outer regions (not shown). Mutual interaction between LHF, ULd and SST plays an important enhancing role moistening and warming the air-sea mechanism trajectory pattern (e_{134}, bottom left) and promoting pressure fall and wind speed enforce at the base of the wall (not shown). Synergy between surface fluxes and SST (e_{124}) contributes strongly in the mechanical deepening (pressure fall and wind speed increasing) of the system (bottom middle, negative effect), but present other thermodynamic vanishing effects such us a cooling, moistening and enhancing cloud formation in the core (not shown). At the same time, at outer regions low level air is cooled and middle level is warmed meanwhile wind speed is increased as a result of it a strong increase of relative vorticity all over the centre of the storm is induced (see bottom right plot).

Effects during dissipation

During the dissipative phase of the storm (January 16th at 18 UTC see figure 5.5.13), control simulation (top left and middle plots in figure 5.5.13) shows a warm core structure with a radii about 50 km and a height of the vortex up to 750 hPa. At this moment the storm is not located below upper level disturbance (not shown). Simulated atmospheric conditions differ significantly among 16 simulations (see for example different lo-

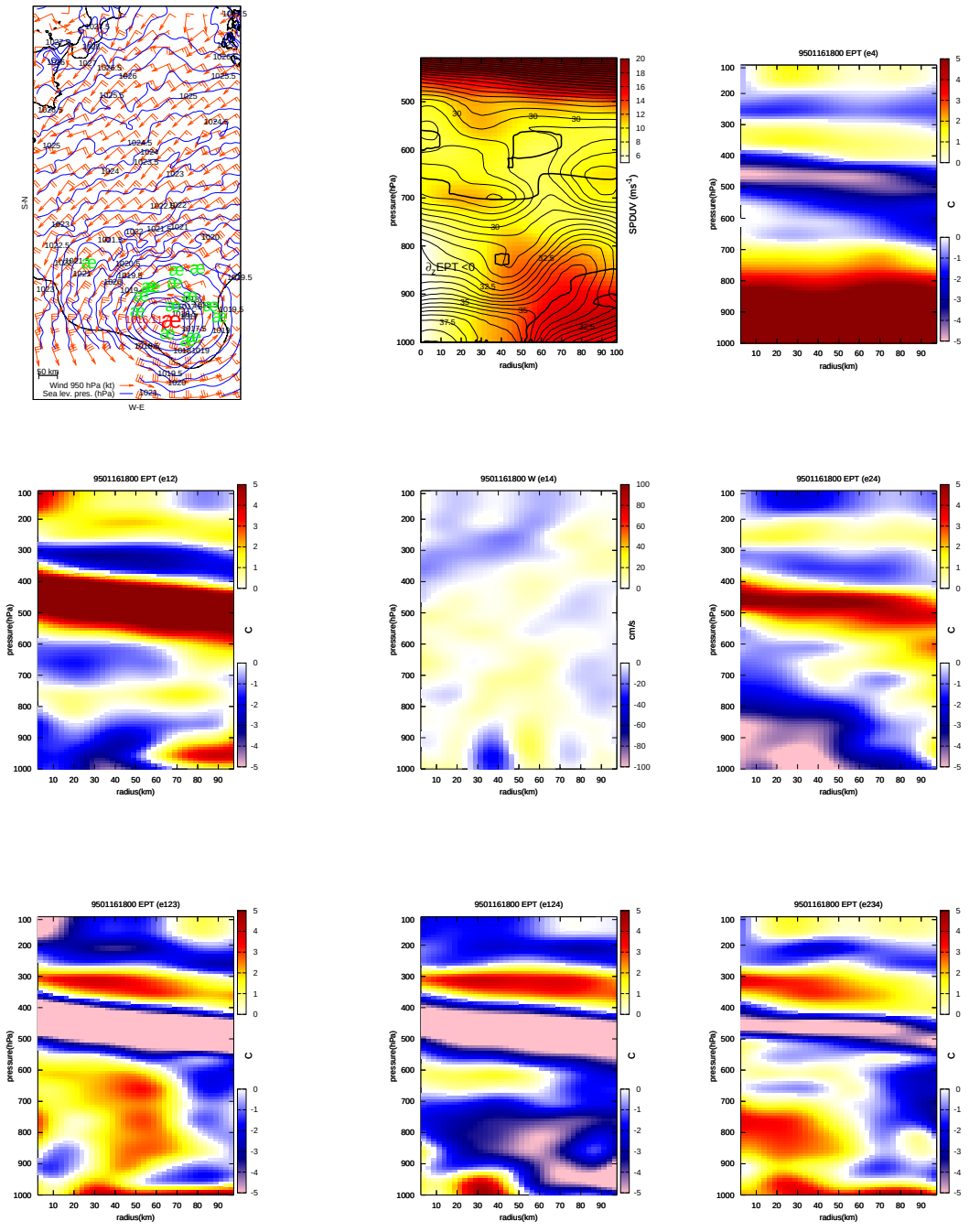

Figure 5.5.13: As in figure 5.5.10 and 5.5.11, but on January 16th at 18 UTC. e_4 on equivalent potential temperature (EPT, $°C$, top right), e_{12} on EPT ($°C$, middle left), e_{14} on Vertical velocity (cms^{-1}, middle middle), e_{24} on EPT ($°C$, middle right), e_{123} on EPT ($°C$, bottom left), e_{124} on EPT ($°C$, bottom middle) and e_{234} on EPT ($°C$, bottom right)

cations among simulated medicanes in top middle panel). Simulated tropopause heights at this time vary strongly. This is reflected in effects as strongly cooled(warmed) and decreased(increased) horizontal wind speed about 450 hPa (like in bottom left plot in figure 5.5.13). In simulations like f_{24}, f_0, simulated vortex is almost disappeared at this time (not shown). Tropopause is higher in those simulations that shown a vortex than in those that it is practically disappeared. Maximum tropopause height differences between simulations are about 150 hPa. However, in the simulations where the system is still simulated a weak structure is shown, and two differentiated patterns are separated at 40 km from the centre of the system (see top middle plot in figure 5.5.13). Keeping in main this description, effects will be only taking into account in middle and low levels.

Surface fluxes LHF and SSHF do not change their role in previous moments and they keep warming and moistening the low levels (not shown). Due to ULd the system is dried between 800-700 hPa (not shown). Due to SST low levels are warmed and moistened (top right panel in figure 5.5.13) meanwhile pressure is increased. According to the enlargement of the radius of the core, synergy between surface fluxes (e_{12}) increases and extends the same role at the mature state that it has at the centre of the storm (middle left plot in figure 5.5.13). LHF and ULd synergy (e_{13}) drys low levels and increase the horizontal wind at the centre of the storm (not shown). Synergy between SSHF and ULd e_{23} dries and diminishes horizontal wind speed at middle levels and the cyclonic rotation of the system (not shown). Effect e_{14} drys and cools low levels as such as diminishes up drafts at the base of the wall zone (middle middle plot in figure 5.5.13). As a result of the mutual interaction between SSHF and SST (e_{24}), low levels are strongly dried and cooled (middle right plot), and cloudiness in the wall zone is decreased. e_{34} dries low levels and characteristics of the wall such as wind speed, cloudiness and up drafts are diminished (not shown). Is notorious the vanishing role of the SST and its coupled interaction with surface fluxes at this phase. Must be said that this vanishing effect of the SST occurs in a region with the warmest SST (see figure 5.0.1), in contrast to previous studies (Emanuel, 1986; Rotunno and Emanuel, 1987; Homar et al., 2003b; Fita et al., 2007a) for which SST has an enhancing role. This is attributed to the vanishing phase of the storm. At this phase, low levels are almost saturated (see Q at 2m evolution in figure 5.5.8). Saturation of boundary layer has been described as a way from which dissipation of a hurricane might be done (Rotunno and Emanuel, 1987). Once boundary layer is saturated, heat and moisture transports capacity of the layer finishes and the storm loses its energy source. Thus, coupled interaction between a warmer SST and surface fluxes contributes to enhance moist into an almost saturated boundary layer favouring the dissipation of the storm.

Triple synergy e_{123} (bottom left plot in figure 5.5.13) plays an enhancing role deepening the system and enhancing the characteristics of the wall through an intensification of the wind speed, humidity and cloudiness in the zone in contradiction with the role in

previous section. It could be related to a diminishing of the saturation in the boundary layer allowing and enhance of its height (no clear ULd is shown at this position of all the storms). e_{124} cooled middle levels (bottom middle plot) but enforce the base of the wall increasing its humidity and up drafts from which more cloudiness is created (bottom middle). e_{134} moistened and cooled generally all the system (not shown) and decreased significantly the horizontal wind speed of the inner zone of the system (not shown). e_{234} moistens inner zone and cools low levels of the system. Moreover increases up drafts in the wall and also horizontal wind speed at high levels of the air-sea mechanism trajectories (bottom right plot in figure 5.5.13).

Comparison of results between point and 2-d effects

Previous to a comparison among azimuthal averaged effects and point effects some considerations should to be done. In the azimuthal averaged fields, 2-dimensional information is obtained, meanwhile the effects where obtained for an unique grid point at the centre of the storm. Due to 2-dimensional characteristics of the efectivities, simultaneous dissipating and enhancing role can be obtained, meanwhile point effects only give an unique behaviour at an individual grid point.

2-dimensional effects do not provide a clear baroclinic development at the beginning of the storm. Effects related to ULd do not have the strongest role in the baroclinic development role as it is reflected by point ones. Extratropical lows present a cold centre (Thorpe, 1986), but for example 2-dimensional e_3 and e_{23} warm the central part of the storm (see figure 5.5.10) promoting tropical-like warm core characteristics. e_{123} cyclolitc role is shown using both methodologies.

Cyclogenetic effects of the point effects on January 14th at 12 UTC such as e_{24}, e_{134} presented also an enhancing role as azimuthal averaged effects. In mature phase (January 16th at 00 UTC), point effects e_{124}, e_{24}, e_{134}, e_3 are revealed as cyclogenetic effects deepening centre of the storm, raising wind speed and relative vorticity at the centre of the storm. From vertical azimuthal averaged cross sections of the storm, effects show different enhancing/vanishing role: e_{124} shows an enhancing role in some aspects such as increasing vorticity at the centre or falling the pressure, but it cools and moistens the centre of the storm. e_{24} reduces the humidity on the theoretical trajectories (following constant angular momentum surfaces) of the particle of air. e_3 shows a vanishing effect due to the drying effect at middle levels, deepening at the same time the storm. Meanwhile e_{134} exhibited an enhancing role warming and moistening low-middle levels and decreasing the pressure of the system.

During the dissipating phase vanishing role of the synergies with the SST are obtained

with both methodologies. Punctual effects also change their role in later stages of the evolution.

Chapter 6

Assimilation of observational data in simulations

Articles on which this chapter is based:

L. Fita, R. Romero, A. Luque and C. Ramis, 2008: *Effects on numerical simulations of tropical-like Mediterranean storms of assimilating precipitation zones derived from satellite and lightning data*, Ann. Geophys., **submitted**

6.1 Effects of assimilating data in medicane simulations

Simulations of medicanes are an important challenge for the numerical models. These systems are usually small, short lasting in time and evolve above maritime areas. At the same time, maritime areas have sparse observations. Moreover, medicane formation and evolution is related to convective processes. There is a large variety of processes that trigger a convective process such as: mountain range, water source, upper level disturbance, shear, solar isolation. The lack of information of the real situation of the atmosphere could derive to a lost of a correct representation of the real conditions that will reproduce an incorrect simulation of the medicanes. Reed et al. (2001) show the sensitivity and beneficial effects on the numerical simulation when sea surface temperatures are corrected with observations. However, limited area mesoscale numerical models have shown a reasonable ability in simulating these storms (Lagouvardos et al., 1999; Pytharoulis et al., 2000; Reed et al., 2001; Homar et al., 2003b), in spite of the limited observational data given their maritime origin.

The modification of numerical simulations using observations from different sources has been shown as a successful way to improve the results (Stauffer and Seaman, 1990; Leslie et al., 1998; Zou and Xiao, 1999; Fan and Tilley, 2002; Ducrocq et al., 2002; Davolio and Buzzi, 2004; Orlandi et al., 2004; Lagouvardos and Kotroni, 2005). MM5 model (Grell et al., 1995) uses a four-dimensional data assimilation (FDDA) tool based on a Newtonian-relaxation or nudging (Stauffer and Seaman, 1990) applied on the prognostic equations.

A possible method for the improvement of medicane simulations is proposed using satellite derived information. Satellite-derived precipitation type (stratiform or convective) is used to modify humidity vertical profiles through FDDA in MM5 simulations. Lightning activity is used to mark convective points. The technique is applied in the simulation of the September 1996 case (studied by Homar et al. (2003b), see figure 5.1.4) and October 2003 (studied in Fita et al. (2007a), see figure 5.1.7).

6.1.1 Methodology

MM5 version 3.7 mesoscale model has been used to simulate these two cases. Two domains in two way interaction with a horizontal resolution of 15 and 5 km with 23 vertical levels have been defined. The domains have different dimensions and are centred at different points for each case. Initial and boundary conditions are derived from the European Center for Medium-range Weather Forecasts (ECMWF) global analyses (at 00, 06, 12, and 18 UTC). Analyses have been improved with Binary Universal Form for data Representation (BUFR) observations archived at ECMWF (in FM-94 BUFR format, see WMO

(2007)). Main MM5 physical configuration is graupel(reisner2) (Reisner et al., 1998) for moist microphysical scheme, Kain-Fritsch (Kain and Fritsch, 1993; Kain, 2004) cumulus scheme activated only in the coarse domain (5 km resolution is assumed to be high enough to resolve cumulus), and cloud scheme for radiation (Grell et al., 1995).

Three different planetary boundary layer (hereafter, PBL) schemes are used in this study in order to test the sensitivity of medicane simulations to the election of the PBL scheme. These PBL schemes are referred to as Blackadar, ETA and MRF (Grell et al., 1995). Blackadar scheme (Blackadar, 1979) computes PBL characteristics following bulk Richardson number. It does not use a Turbulent Kinetic Energy (TKE) equation and turbulent mixing is computed following an implicit vertical diffusion scheme. Eta scheme (Janjić, 1990, 1994) is 2.5 dimensional and it uses TKE with a local mixing dynamics. MRF scheme (Troen and Mahrt, 1986; Hong and Pan, 1996) which is an improvement of the Blackadar PBL scheme for higher horizontal resolutions.

Hong and Pan (1996) found that heavy rainfall events are better forecasted with MRF approximations than with a local PBL scheme (used in ETA model), due to a better representation of a well formed unstable PBL. Wisse and de Arellano (2004) show that MRF scheme produces a weaker PBL inversion with stronger vertical fluxes than ETA scheme. By this way heavier precipitation was obtained as a result of stronger transport of moist and heat to the free atmosphere. ETA scheme produces a lower vertical transport and helps to maintain a stronger inversion, as a result of it, higher values of CAPE are forecasted. Consequently ETA presents more extreme precipitation rates. These differences between vertical transports parametrised with different schemes were found more significant over maritime areas than over land (Wisse and de Arellano, 2004). Hurricane-like characteristics of the medicanes suggest that they should present a notable sensitivity to the strength of low-level transport of heat and moisture.

Satellite data from European Organisation for the Exploitation of Meteorological Satellites (EUMETSAT) and lightning datasets provided by Instituto Nacional de Meteorología (INM, Spanish Met. Office) show a deep convection (observed as cold cloud top pixels) and lightning activity during the formation phase of both storms (Luque et al., 2007). During their mature state, number of cold cloud top pixels decreased, as well as lightning activity (mostly located at these stages in warm cloud top pixels; see figures 6.1.1 and 6.1.2).

Infrared (11 μm) satellite images are used to depict stratiform or convective precipitation type. Lightning discharges are used to assist in the delineation of convective areas, assuming that all lightning activity is developed within convective cells. Once the precipitation type is obtained for each pixel, MM5 humidity vertical profile is modified according to two different vertical structures including a layer of saturated air (stratiform

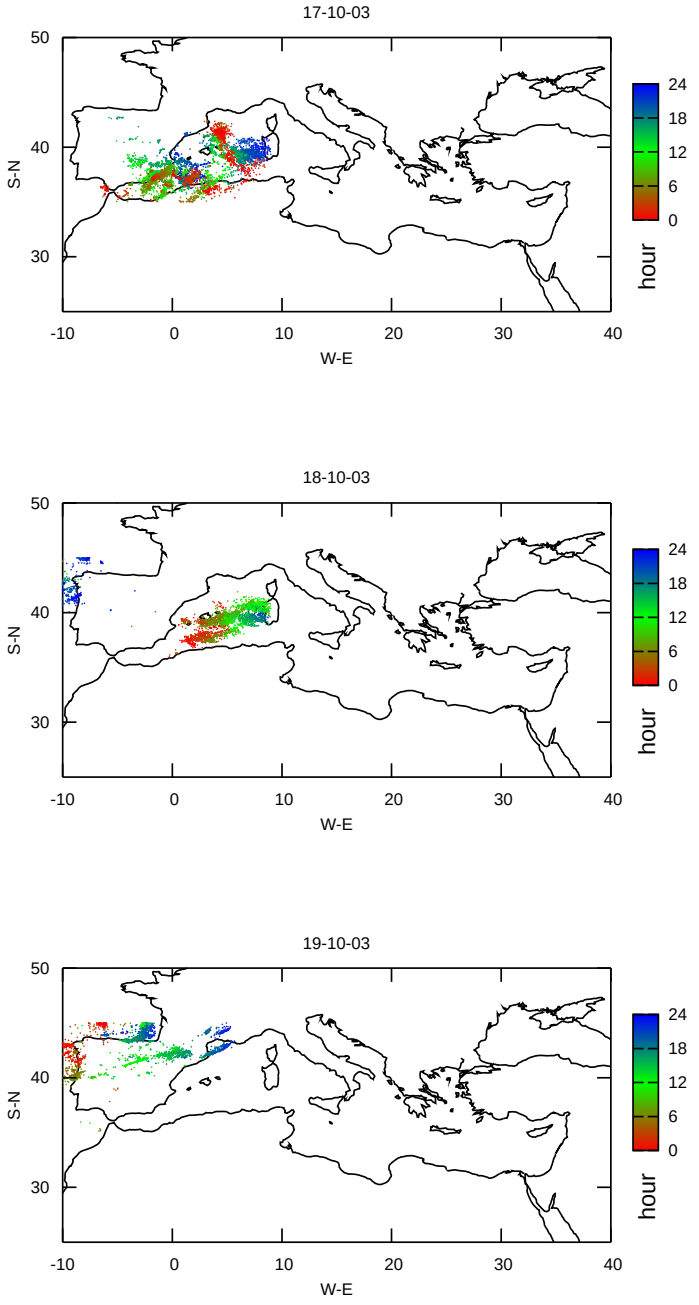

Figure 6.1.1: Lightning activity for the October 2003 case. During October 17th 2003 (top), Oct. 18th (middle) and 19th (bottom). Discharges are indicated as a point coloured according to the hour of hit (see color box). Source INM lightning detection net

or convective structure).

The Histogram Matching Technique (HMT) is used to derive rain characteristics (intensity of precipitation for a given cloud top infrared temperature value) from the satellite images (Turk et al., 2000; Kidd et al., 2003). HMT rainfall estimation curve is obtained by combining a set of simultaneous Meteosat infrared images with passive-microwave rainfall images (SSMI and AMSR sensors). In order to identify convective areas a cross-correlation methodology is applied for the tracking of cold cloud top pixels (cloud top Infrared-channel temperature lower than 239 K). Cloud pixels are tracked applying a cross-correlation method in 19 by 19 grid zones before the cloud pixel temperature change with time is calculated. Rainy points that are cooling in time are marked as convective according to the work of (Roberts and Rutledge, 2003), while the other rainy pixels are marked as stratiform. Lightning discharges (see evolution during October 2003 case in figure 6.1.1) are used to mark as convective pixels a 3x3 pixels zone centred at the discharge point even if these are outside the satellite convective area (see stratiform/convective distribution at two moments of the October 2003 episode in figure 6.1.2). Bear in mind that in the FDDA only the precipitation type will be used irrespectively of the amounts.

Following Davolio and Buzzi (2004) the humidity adjustment in the model is done following certain vertical structures associated with stratiform or convective precipitation types (see figure 6.1.3, and equation 6.1.3). By this way, it is ensured a relaxation (by factor $\mathcal{R}(\sigma)$) of the model grid point mixing ratio value ($\mathcal{Q}_m(i,j,k)$) to mid or low-level saturating mixing ratio ($\mathcal{Q}_s(i,j,k)$) consistent with the forcing, respectively, of stratiform or convective precipitation. The new humidity profiles are introduced in the simulations via analysis and observational nudging as implemented in the FDDA package of the MM5 model.

However, MM5 humidity field is expressed in terms of mixing ratio. Humidity profiles want to be saturated in some vertical levels according to a specific kind of precipitation. For that reason a computation of the saturated mixing ratio value at each grid point should be done with the model pressure and temperature values at that point (see equation 6.1.2).

$$e_s = 6.22 exp\left(\frac{17.67T}{T+243.5}\right) \tag{6.1.1}$$

$$\mathcal{Q}_s = 0.662\frac{e_s}{p-e_s} \tag{6.1.2}$$

e_s, saturated vapour pressure is given in Bolton's form (equation 6.1.1). T model temperature; p, model pressure, $\mathcal{Q}_s$ satured mixing ratio .

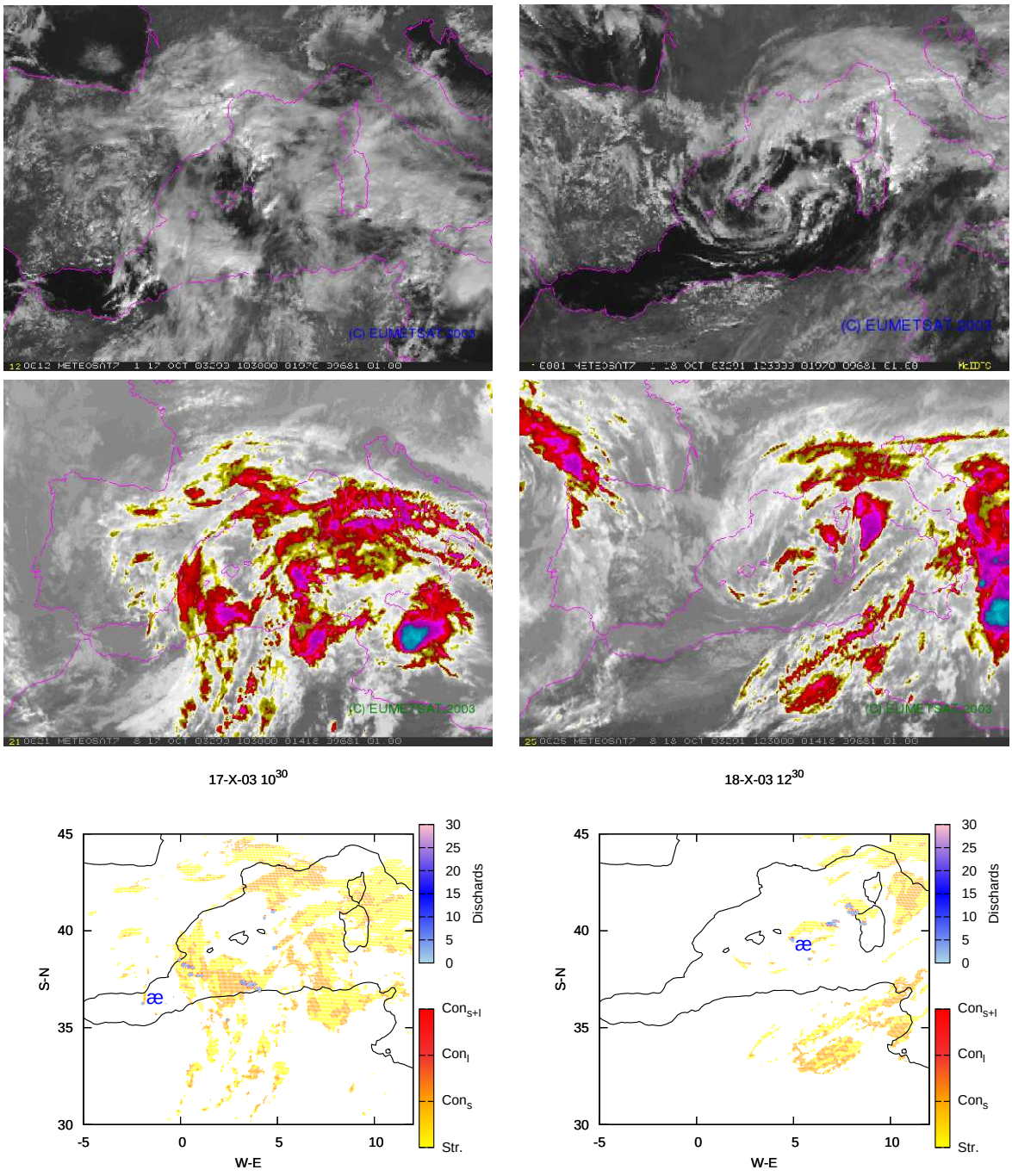

Figure 6.1.2: Visible channel (top) and coloured infrared (11 μm, bottom) images from METEOSAT-7 (Source EUMETSAT). Bottom panels: Stratiform (yellow colours), convective (orange-red colours; Con_s, satellite convective; Con_l, lightning convective; Con_{s+l}, satellite and lightning convective;) and number of discharges (blue dots). Blue æ indicates medicane position Left panels: on October 17th 2003 at 10^{30} UTC (left). Right panels: on October 18th at 12^{30} (maximum intensity)

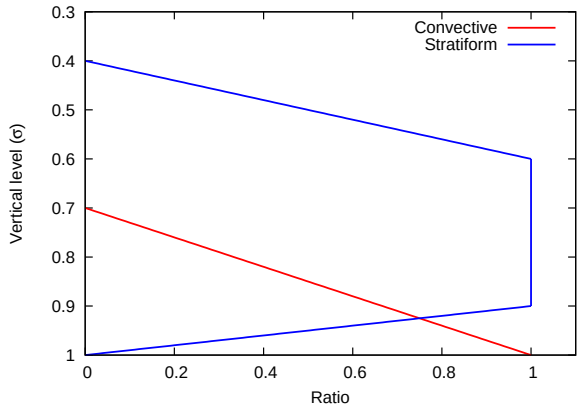

Figure 6.1.3: Vertical profile of factor $\mathcal{R}(\sigma)$ (used in equation 6.1.3) for the correction of the humidity profile in the convective precipitation (red) and stratiform (blue) precipitation areas.

$$\mathcal{Q}'(i,j,k) = \mathcal{Q}_m(i,j,k) + \mathcal{R}(\sigma)\left[\mathcal{Q}_s(i,j,k) - \mathcal{Q}_m(i,j,k)\right] \tag{6.1.3}$$

Nudging is only applied in the high resolution inner domain with a weight of 10×10^{-4} and a time window of 6 minutes from the time of the observation (full influence ± 3 minutes, linear decay ± 6 min further). Weight computation of nudging term is done every 2 model time-steps with a vertical influence of the observation between levels of 0.001 (Cressman-type).

Eight experiments are performed for each medicane case (see table 6.1.a). A control simulation (without humidity modification $\emptyset$ values). Two modifications of the MM5 simulations are done without FDDA technique, in which initial and boundary conditions for the humidity fields (i. e. analyses from ECMWF) are directly modified with the satellite derived information. First experiment applies the modifications only to the initial condition (REGRIDmod experiment). In the second experiment the procedure is carried out at each analysis time (00, 06, 12 and 18 UTC, REGRIDmod TOT experiment).

MM5 FDDA technique can be applied as analyses nudging. In this case, analyses grid point values drive tendencies of the model. Analysis nudging is done with the non-modified version of the analyses (FDDA AN exp.), and with analyses in which humidity vertical profile has been modified with satellite-based information (FDDA rhAN exp.).

Table 6.1.a: Complete set of experiments for the September 1996 case (left) and October 2003 case (right). $\Delta\vec{r}$ indicates horizontal resolution (km) of the satellite-derived information used. Δt indicates the frequency (hours) of assimilation into the simulations of the satellite-derived information. $\emptyset$ indicates no data assimilation. $\forall$, indicates maximum available resolution. t_0, indicates simulation start time

simulation	**960912**		**031018**	
	$\Delta\vec{r}$ (km)	Δt (h)	$\Delta\vec{r}$ (km)	Δt (h)
control	$\emptyset$	$\emptyset$	$\emptyset$	$\emptyset$
REGRIDmod	$\forall$	t_0	$\forall$	t_0
REGRIDmod TOT	$\forall$	6	$\forall$	6
FDDA AN	$\forall$	6	$\forall$	6
FDDA rhAN	$\forall$	6	$\forall$	6
OBS TOT	15	$\forall$	22.5	$\forall$
OBS 1h	3	1	15	1
OBS 3h	3	3	7	3

Satellite information is obtained every 30 minutes (i.e. operational frequency of METEOSAT-5 and METEOSAT-7 geostationary satellites) with a horizontal resolution about 5 km in the study zone. Modifications of vertical humidity profiles are done in the lowest 12 sigma-levels. Computational memory limitations do not allow to use together the maximum temporal and spatial resolution of the satellite information. Thus an observational nudging with full temporal resolution and reduced horizontal resolution (OBS TOT exp.) has been performed. Two additional experiments have been performed with the highest horizontal resolution that computational resources allow under a satellite information update frequency of 1h and 3h (OBS 1h and OBS 3h experiments). Table 6.1.a shows the specific configuration of each experiment. Figure 6.1.4 shows the resultant data included at the first time step of the October 2003 simulations according to each resolution.

The above experiments will be compared with respect to the control one with regard to the characteristics of the simulated medicanes and in terms of several meteograms. These meteograms are located at the genesis and evolution areas of each medicane and are drawn for different variables such as precipitable water, sensible surface heat flux, surface latent heat flux and convective available potential energy (CAPE).

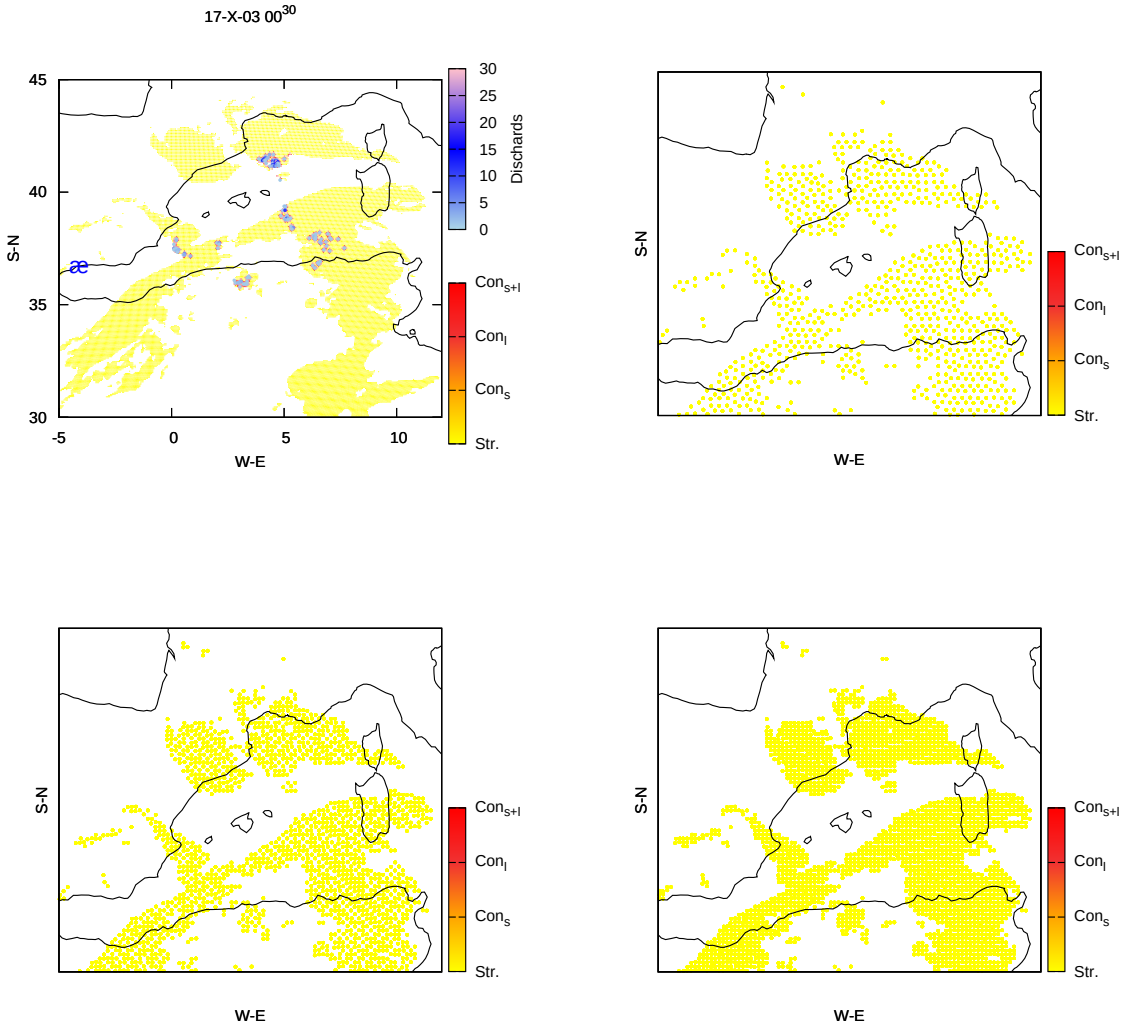

Figure 6.1.4: Rainy type of information that will be nudged (Domain 1 grid) on October 17th 2003 at 00^{00}. Original satellite-based information (top left, satellite grid), OBS TOT experiment (top right), OBS 1h 15k exp. (bottom left) and OBS 3h 7k exp. (bottom right). æ indicates position of medicane. Satellite information is from October 17th 2003 at 00^{30}, since no satellite image was available at starting simulation time

6.1.2 Results

Control simulations of the two cases with the three different PBL schemes show formation of the system but a poor agreement between simulated and observed trajectories (see figure 6.1.5). Both medicanes are formed under the western sector of an upper level trough (see figure 5.1.4 and 5.1.7 for the September 1996 and November 2003 cases respectively) characteristic of the baroclinic growing of disturbances (Hoskins et al., 1985). However, these two medicanes do not evolve closely related with the upper level disturbances since their trajectories differ with respect to the trajectory of the maximum vorticity centre of the upper level trough (see figure 6.1.6). Evolution of both medicanes is dominated by an upper level trough, but their trajectory is somewhat independent from the movement of the upper-level disturbance (at least of its vorticity maximum). It is also observed that in general, there is not a clear correspondence between low pressure values at the centre of the collection of the different simulated medicanes and maximum horizontal wind speeds (see figure 6.1.5).

Upper level disturbance exhibits sensitivity to the used PBL scheme (see figure 6.1.7). These differences between the evolutions of the upper level trough centre obtained with the three PBL schemes grow gradually in time. Changes on the characteristics of the low level peculiarities induced by the PBL processes influence the upper/low level baroclinic interaction, affecting the growing of the low level disturbance (e.g. sensible surface heat flux effect on Horvath et al. (2006)) and the diabatic behaviour of the upper level trough. Changes on the diabatic evolution of the upper level trough are also as consequence of changes on moisture content of the column of air as a reflect of different efficiencies on vertical transport from low levels induced by each pbl scheme. Less moisture content would weak convection and diabatic heating of middle levels due to latent heat release by cloud formation.

Meteograms at different locations along the medicanes path (see figures 6.1.8 and 6.1.9) show a variety of sensitivities to the selection of the PBL scheme (similar behaviour is observed for the meteograms at other points, not shown). Increase of the surface fluxes and precipitable water is a signature of the hurricane characteristics of the medicane (Emanuel, 1986). Accumulated potential energy would be used in the intensification of the system throughout convection, reflected as a decrease of CAPE values after the incoming of the medicane in the area. The strong surface winds increase surface fluxes and thus water vapour content in the lower troposphere from which cloud formation will be reinforced. Meteograms at other model grid points corresponding to later phases of the evolution of the medicanes show a similar behaviour (not shown).

Experiments involving assimilation of satellite and lightning activity information into the simulations (see table 6.1.a) produce significant modifications on the forecasts (see

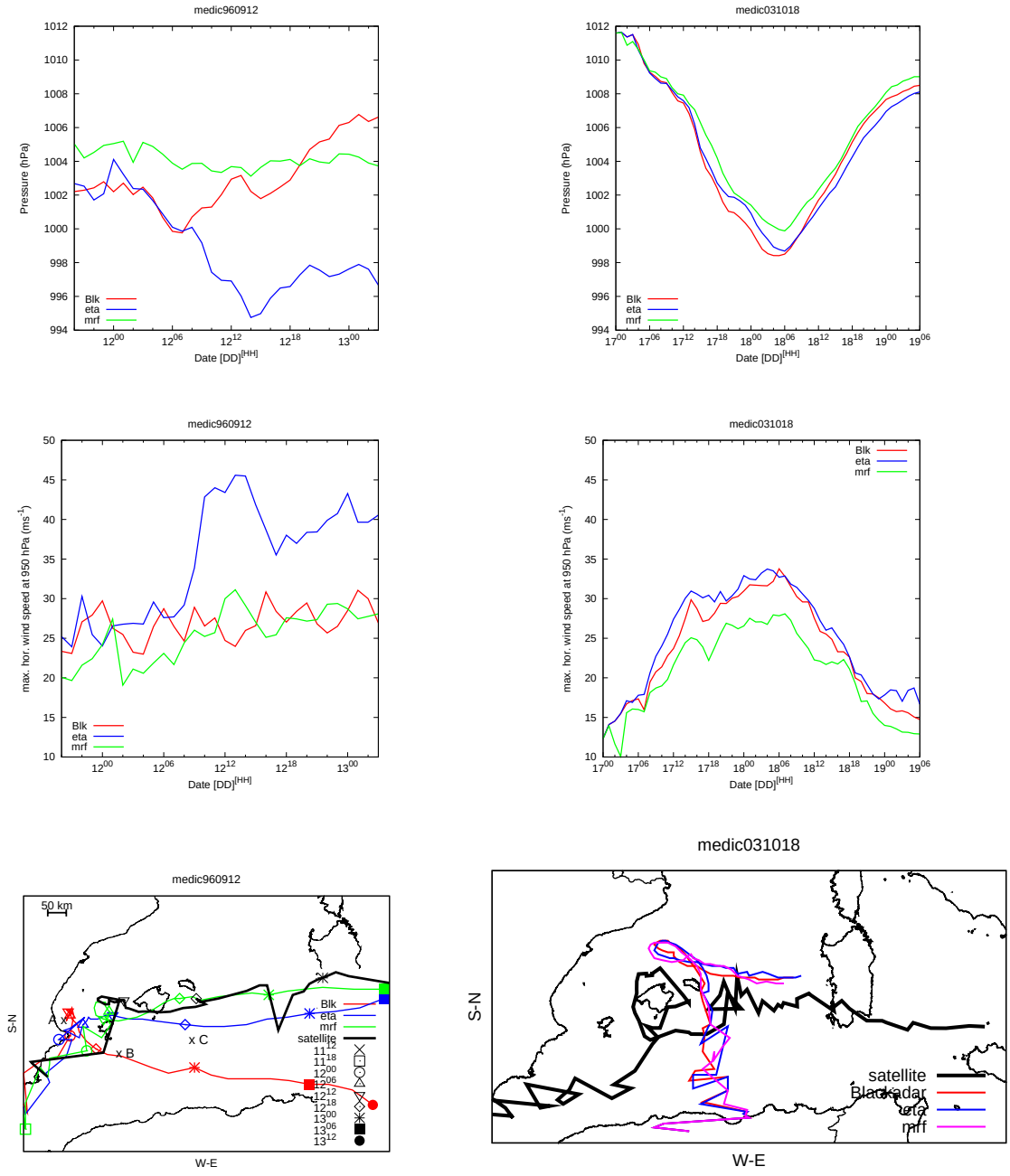

Figure 6.1.5: MM5 control simulation results with three different PBL schemes, Blackadar (red), eta (blue) and MRF (green). Evolution of the central pressure (hPa, top), maximum horizontal wind speed at 950 hPa (ms^{-1}, middle) and medicane trajectory (bottom, symbols along trajectories indicate simulation, time, see legend in graphs) compared with the satellite-based trajectory (thick black line). September 1996 case (left), October 2003 (right). A,B,C points indicate where meteograms have been obtained

figures 6.1.10 to 6.1.13). Simulated medicanes are deeper in almost all cases. According to the upper level influences previously discussed, trajectories of medicanes have changed significantly due to changes on the evolution of the upper level trough and changes in the medicane zone genesis that affected the relation between upper and low-level disturbances in the simulations (see figure 6.1.14). Regarding trajectories, these are generally worse for September 1996 case and better for October 2003 medicane, compared to the control ones.

Taylor diagrams (Taylor, 2001) of the simulated trajectories taking as reference the satellite-derived trajectory (with more than 30 values used in the statistics) are plotted (without overall bias correction) in figure 6.1.15. Taylor diagrams show higher sensitivity to the FDDA methods for the standard deviation than for the correlation. That means that the trajectories suffer a higher change in its morphology and zone of evolution than in their temporal sincrony with respect to the observed one. No smoothing of refilling techniques have been applied on the satellite-observed trajectories of the medicanes.

Experiments 'FDDA rhAN', 'OBS TOT', 'OBS 1h' and 'OBS 3h' imply a direct impact of the satellite/lightning information into the simulations. Only in these 4 experiments changes in the vertical humidity profiles are introduced at specific grid points and time steps, thus directly affecting the humidity tendency term in the model equations. In order to analyse the effect of data assimilation into the simulations, meteograms for these 4 experiments at one particular model grid point are drawn in figures 6.1.16 and 6.1.17.

Simulation results do not exhibit a significant improvement of the trajectories of the medicanes. In order to provide an objective way to compare simulated and satellite-derived trajectories and as an attempt to simplify the large amount of information, some statistical parameters are proposed (appendix A).

Simulated medicanes show slower translational speeds than the satellite observed ones (see control simulation results in figure 6.1.5). A new method to evaluate the temporal shift of two trajectories is here put in practice. The temporal shift between satellite-observed and simulated trajectories of the medicanes is objectively studied by means of the temporal dependence of bias and correlations (see $\mathcal{BIAS}^{min}_{dist}$ and PR^{max}_{bias} definitions in equations A.1.2 and A.3.15, respectively, of the appendix A). These statistical indices are iteratively recomputed using simulated trajectories that are positively or negatively displaced in time (e.g. an advanced trajectory is obtained when a simulated position at time t, $\vec{x}^t$, is changed to the position at time $t + n\Delta t$). Temporal shift between trajectories will correspond with that shift $n\Delta t$ ($\Delta t = 1$ hour) that minimises bias and maximises correlation scores. BIAS informs about the spatial proximity of the simulated and satellite-observed trajectories. Correlation is focused on the similarity between the morphologies of trajectories.

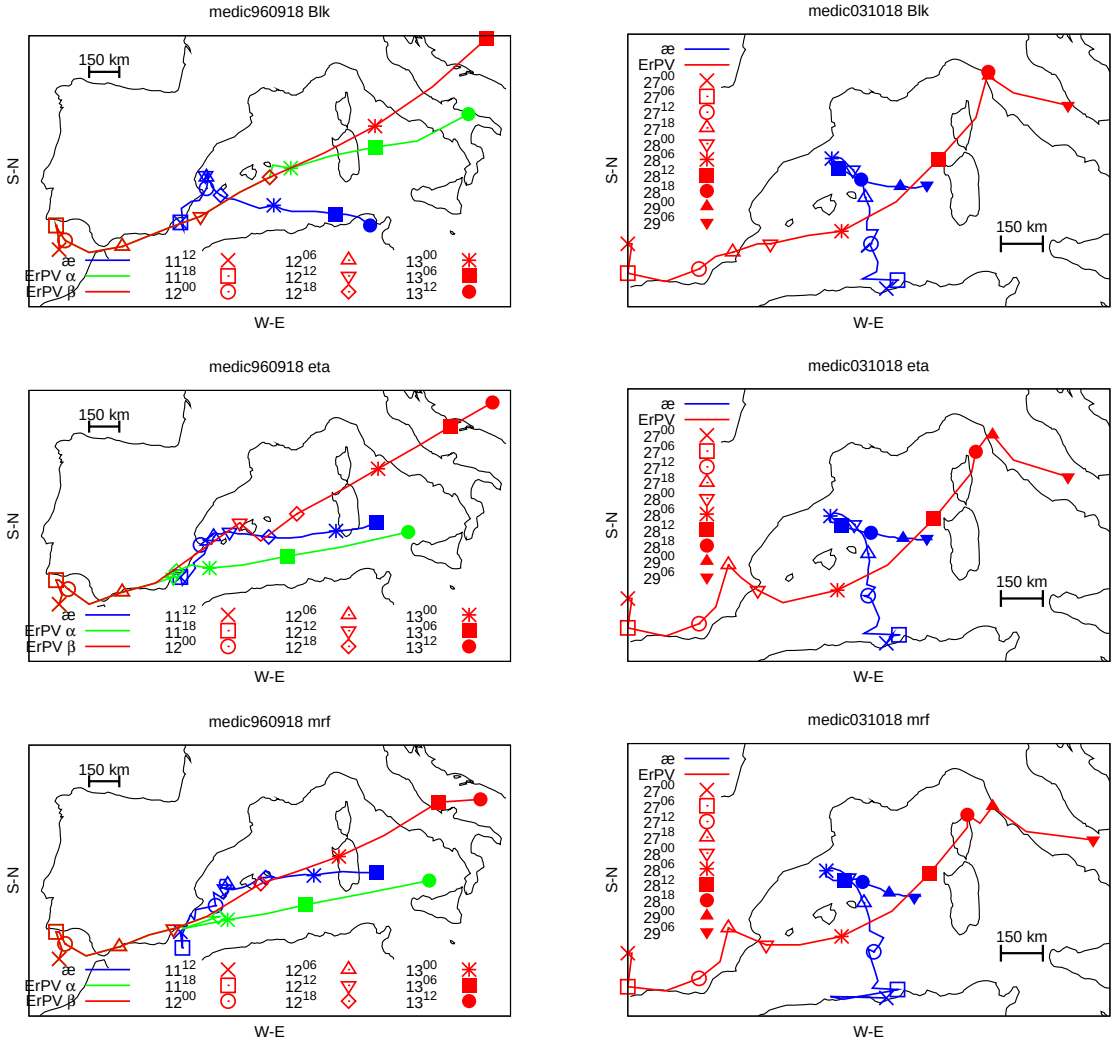

Figure 6.1.6: Evolution of Ertel PV maxima on the 330 K isentropic surface (red) related to the evolution of September 1996 (left) and October 2003 (right) medicane (blue) at different time steps (see legend). Simulations using Blackadar PBL scheme (top), ETA (middle) and MRF (bottom). In September 1996 simulation appear two maximals, α (green line), and β (red line)

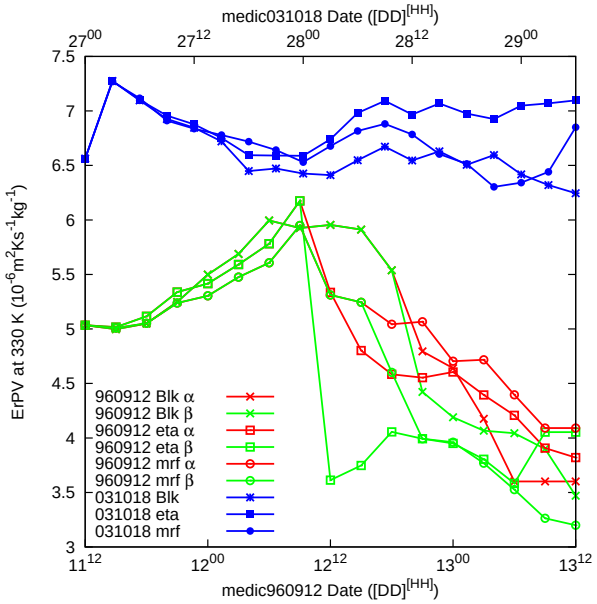

Figure 6.1.7: Temporal evolution of Ertel PV maxima on 330 K isentropic surface related to the evolution of medicanes 960912 (red) and 031018 (blue), for each PBL scheme: Blackadar (cross), ETA (square) and MRF (circle). Date/Time indicated at bottom axis for September 1996, and at top axis for October 2003 medicane. In September 1996 simulation appear two maximals, α (green line), and β (red line)

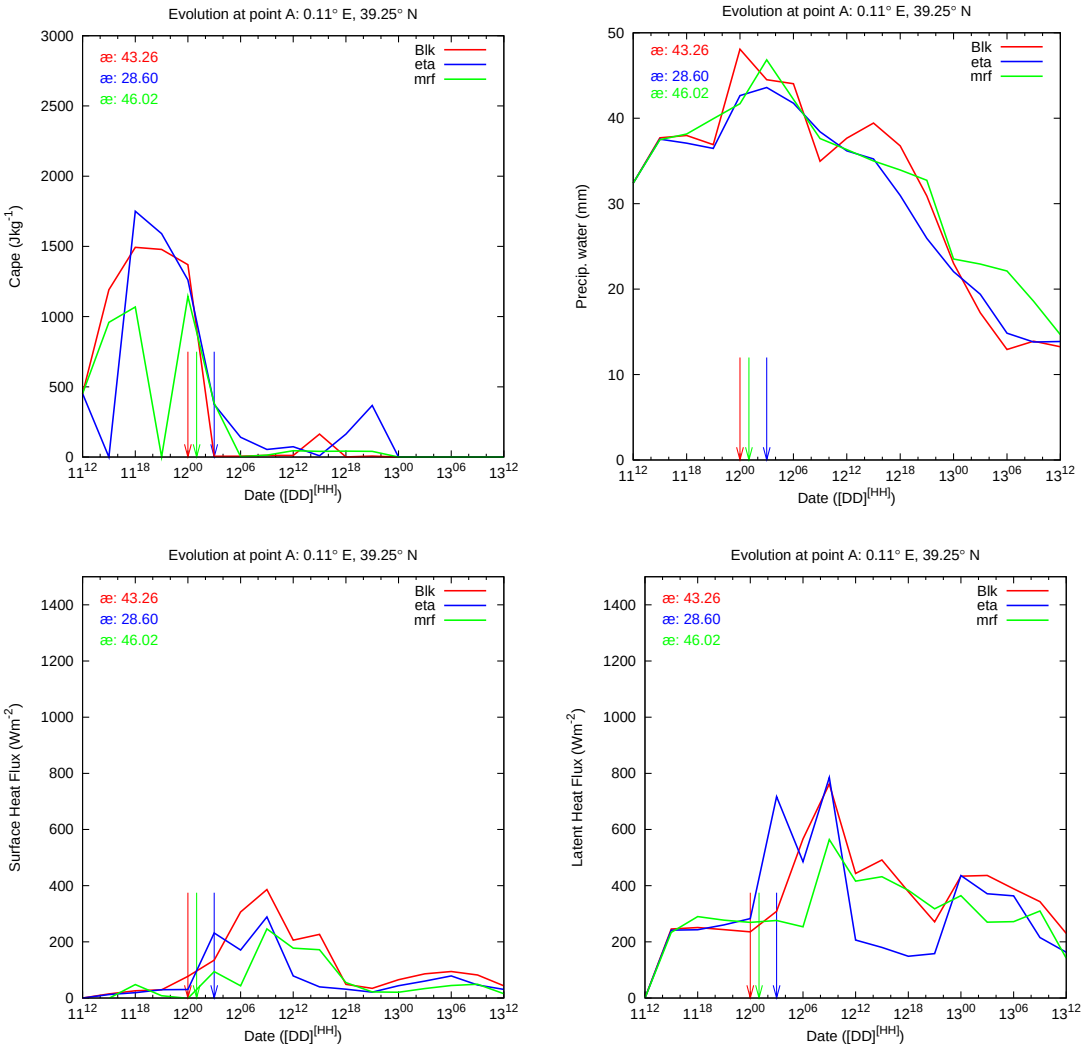

Figure 6.1.8: meteograms at point A (see left bottom panel of figure 6.1.5) for the simulation of September 1996 medicane, showing CAPE (Jkg^{-1}, top left), Precipitable water (mm, top right), surface sensible heat flux (Wm^{-2}, bottom left) and surface latent heat flux (Wm^{-2}, bottom right). Results obtained with each PBL scheme are included: Blackadar (red), ETA (blue) and MRF (green). Vertical arrows indicated the time at which the medicane simulated with each scheme passes closeliest to the point. Distances (km) of the medicane centre 'æ' to the point are indicated at the top left corner of the graphs

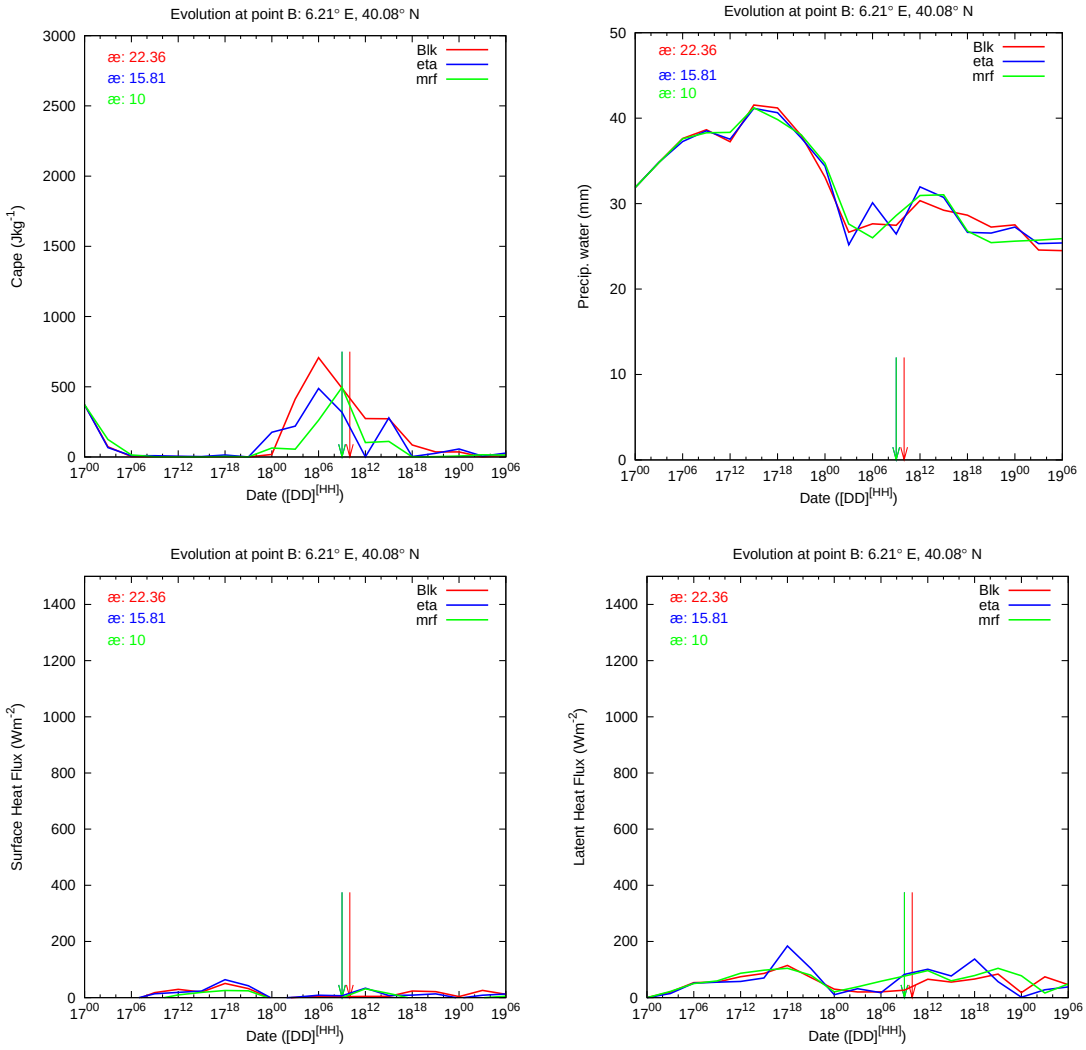

Figure 6.1.9: As in figure 6.1.8 but for the October 2003 medicane at point B (see bottom right panel of figure 6.1.5). ETA and MRF simulated medicanes arrows are superimposed since both medicanes reached the point B (right bottom panel of figure 6.1.5) at the same time, on 18th at 9 UTC

Simulated trajectories by the whole set of experiments have similar bias with respect to the satellite-based trajectory (see figure 6.1.18 as an example). It is shown how the satellite-derived information has mainly influenced the localisation in time of the medicane but it has basically left the morphology of the trajectories unchanged.

Similar dependence of $\mathcal{BIAS}_{dist}^{min}$ on temporal shift is obtained in each medicane for the group of experiments and PBL schemes (see figure 6.1.19).

Fort both cases, lowest correlation values are obtained for those simulations in which observational nudging has been applied, the best results being obtained with the 'FDDA AN' experiment. In general, larger similarity between simulated and observed trajectories are obtained in those simulations where observational nudging has not been applied (see figure 6.1.20).

For both studied medicanes, simulations with MRF scheme produce stronger systems than with Blackadar scheme. No significant differences between the nonlocal mixing schemes (Blackadar and MRF) on the evolution of the pressure at the centre, maximum wind speeds and the trajectory for each experiment are observed.

The larger differences with respect to the characteristics of simulated medicanes and meteograms among the simulations using the ETA model might be related to its local mixing characteristics. Satellite-derived information modifies vertical profiles of humidity at low levels (convective rain points) and middle levels (stratiform rain points). Blackadar and MRF PBL schemes produce a stronger vertical transport and more mixing at low levels than ETA scheme. Thus changes due to data assimilation might be weakened using the first two schemes (middle column panels in figure 6.1.17 show larger variations with respect to control ones).

September 1996

September 1996 medicane shows the strongest sensitivity on changes of the PBL scheme. In this case, last steps of the trajectory with Blackadar scheme show differences with the trajectories obtained with the other two schemes larger than 300 km. September 1996 medicane simulated with the Blackadar PBL scheme is deeper than the simulated with MRF scheme (maximum difference is about 4 hPa, see top and middle panels in figure 6.1.5) and maximum horizontal wind speeds for each simulated medicane differ also significantly (maximum differences about 10 ms^{-1}). Moreover, the deepest and strongest medicane is obtained when ETA scheme is used.

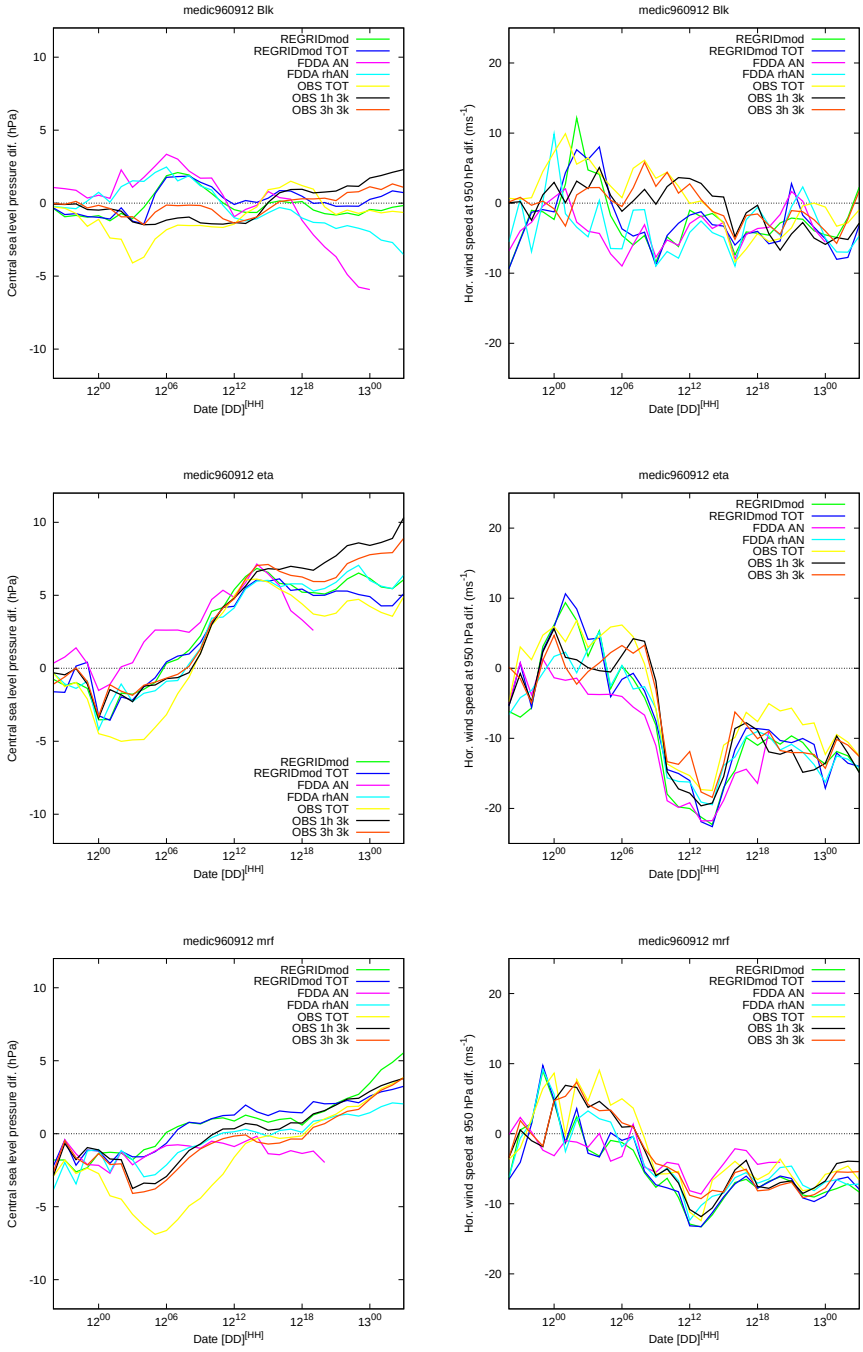

Figure 6.1.10: September 1996 medicane simulations. Left column: Central sea level pressure (hPa) referred to control value ($\mathcal{P}res_{sim} - \mathcal{P}res_{control}$). Middle column: Maximum horizontal wind speed (ms^{-1}) at 950 hPa within a radii of 200 km from the centre of the storm, referred to control value. Results are shown for the set of experiments with Blackadar PBL scheme (top), ETA (middle) and MRF (bottom). Lines colours are: Control simulation (red), REGRID mod (green), REGRID mod TOT (blue), FDDA AN (pink), FDDA rhAN (light blue), OBS TOT (yellow), OBS 1h 3k (black) and OBS 3h 3k (orange)

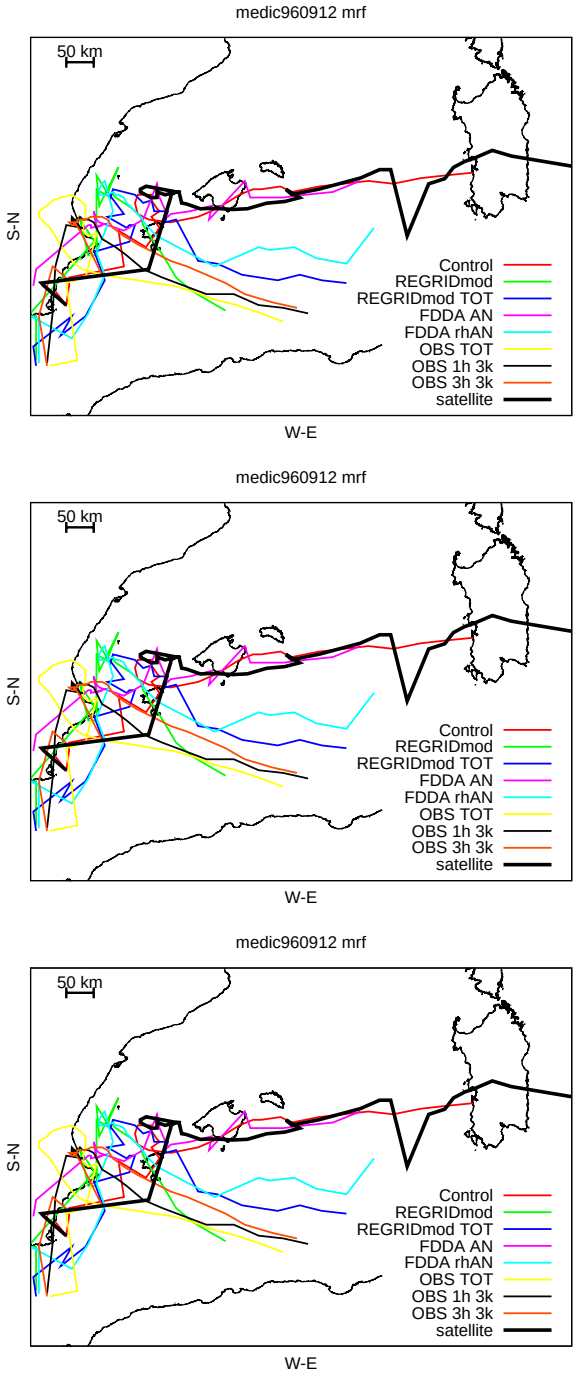

Figure 6.1.11: September 1996 medicane simulations. Trajectories of simulated medicanes. Results are shown for the set of experiments with Blackadar PBL scheme (top), ETA (middle) and MRF (bottom). Colour codification of the dots for each simulation is the same as in figure 6.1.10

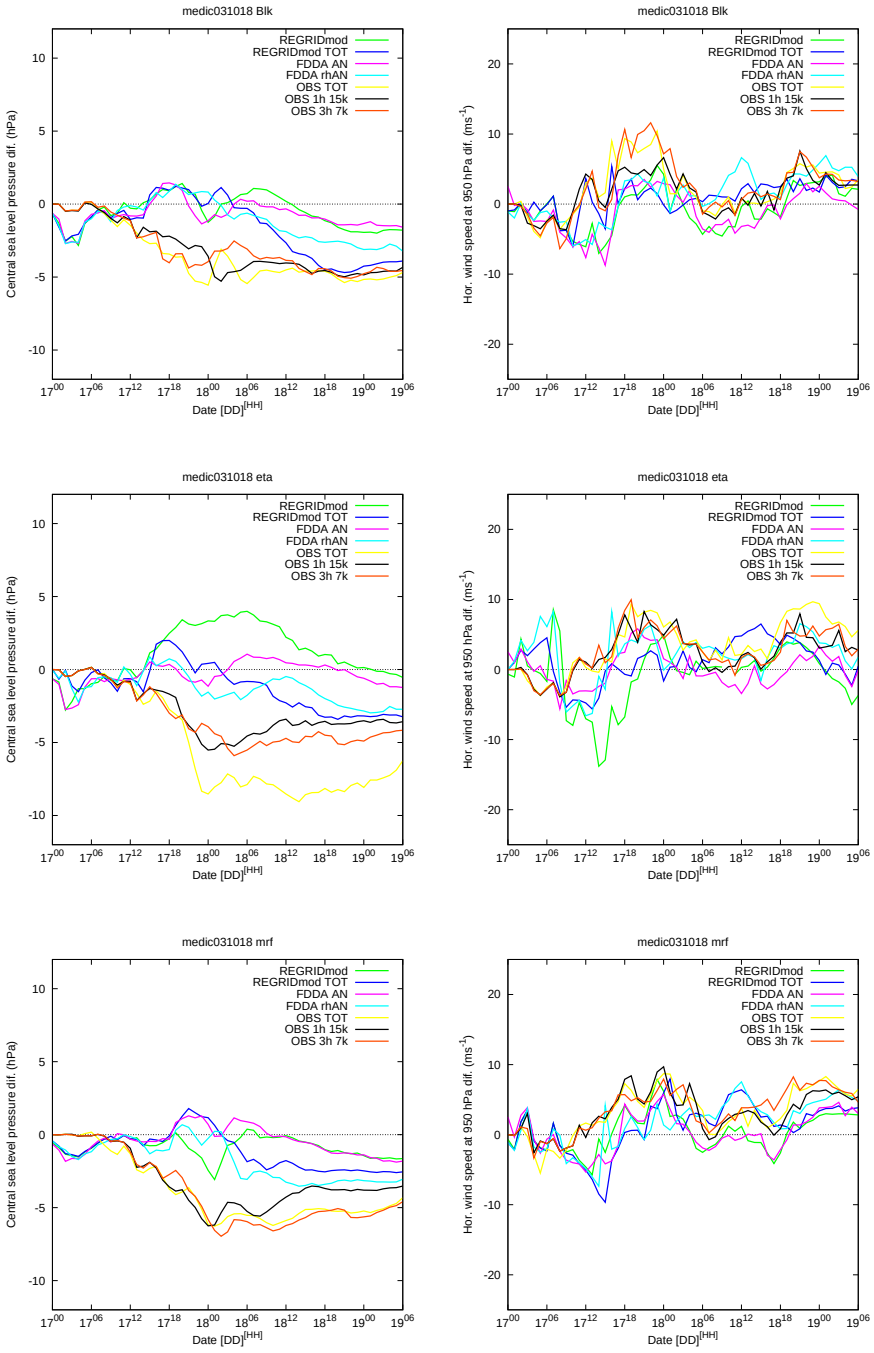

Figure 6.1.12: As in figure 6.1.10, but for the October 2003 case

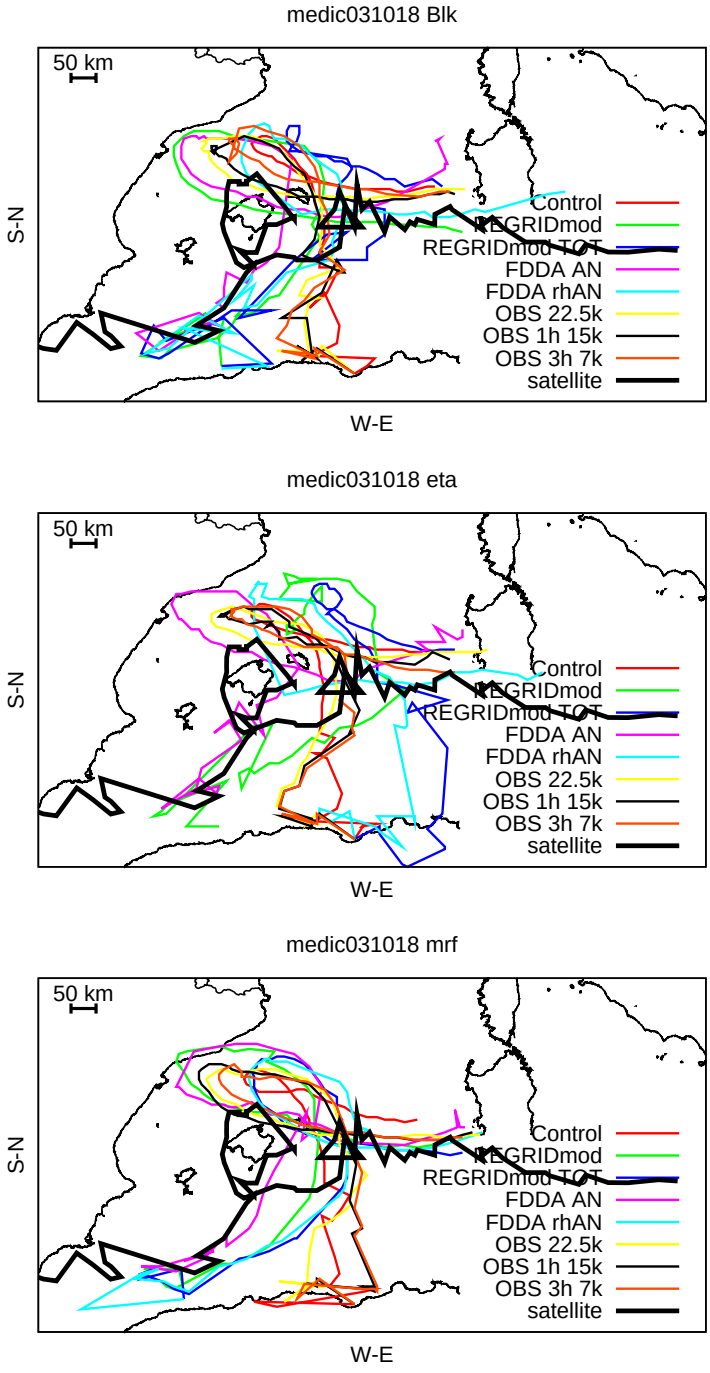

Figure 6.1.13: As in figure 6.1.11, but for the October 2003 case

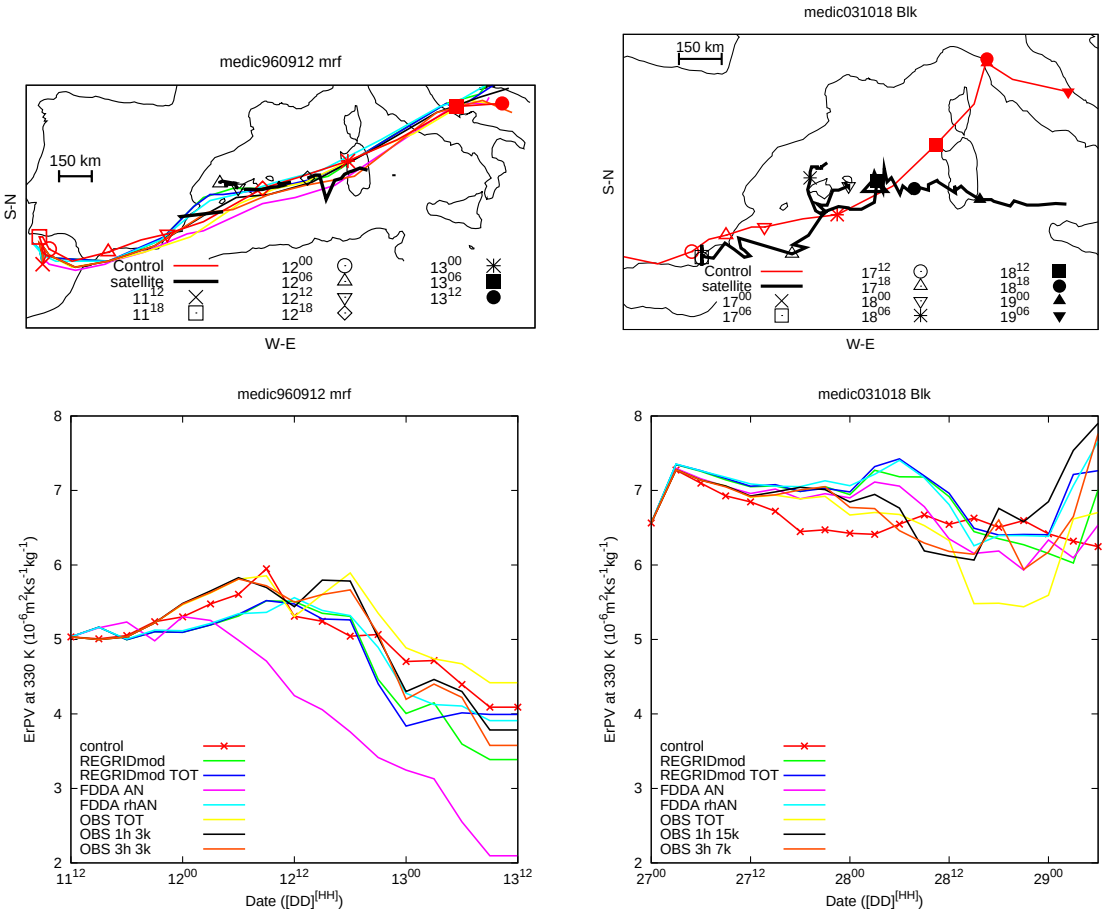

Figure 6.1.14: Top panels: Trajectories of the maximum Ertel PV closest with the medicane trajectory for each simulation. Satellite-based trajectory (thick solid line). Bottom panels: Temporal evolution of value maximum Ertel PV. For the September 1996 case with the MRF PBL scheme (left), for the October 2003 case with the Blackadar PBL scheme (right)

Evolution of September 1996 case (see left panels in figure 6.1.6) seems to exhibit a momentaneous strong relation with the upper level disturbance. The medicane is formed off the Eastern coast of the Iberian Peninsula. It grow in this region and starts to move eastwards at the same time that the centre of the trough enters over the zone (between Iberian peninsula and Balearic Islands). Associated flow to the upper level disturbance seems to drag the medicane from its genesis zone (see figure 6.1.6). The southernmost evolution of the upper level trough with Blackadar PBL scheme could explain the lower-latitude trajectory of the simulated medicane. Lower values of central pressure in ETA simulated medicane (see figure 6.1.5) could be explained by the strong overlap of the centre of the trough and the medicane (see left middle panel in figure 6.1.6) during which a mutual interaction through baroclinic development or the enhancement of the thermodynamic equilibrium between the Mediterranean Sea and the atmosphere (Emanuel, 2005) might contribute to increase the intensity of the storm.

September 1996 case shows strong sensitivity of central ErPV values of the trough to the PBL scheme. It is significant the large differences between the strength of simulated medicane with ETA PBL scheme and the other two simulations (see figure 6.1.14). During the simulation of the episode two vorticity maxima appeared (α, β, see green and red lines respectively in figures 6.1.6 and 6.1.7). Larger coupling between β upper and low level disturbances obtained with ETA pbl scheme contribute to generate a significantly deeper medicane. Maximum horizontal wind speed at 950 hPa reach hurricane intensity (over 33 ms^{-1}, see middle left panel in figure 6.1.5).

At the genesis zone of the September 1996 case (point A, figure 6.1.8), higher CAPE and Latent Heat Flux are obtained with the ETA scheme, but precipitable water is slightly lower. These results are in agreement with results of Wisse and de Arellano (2004) in which the lower magnitude of vertical transport in the ETA scheme compared with Blackadar and MRF nonlocal mixing schemes results in a less eroded capping inversion of the PBL, with higher CAPE values. Differences between PBL results are enhanced due to the maritime characteristics of the selected points where meteograms are drawn: high values of the Latent Heat Flux from sea areas and the nonlocal (Blk, MRF) vs. local (ETA) mixing properties of the schemes, result in significantly different moist vertical transport among the simulations. For a meteogram obtained at a land point (at the centre of Mallorca Island) lower differences between results are observed (not shown). Diurnal cycle at this land point is depicted with strongest signature (largest differences between day and night values) with MRF scheme. The genesis of the medicane (vertical arrows in figure 6.1.8) is accompanied by a decrease of CAPE, a transitory enhancement of precipitable water and a rise of the surface fluxes.

Simulations of September 1996 case with the satellite/lightning information show stronger medicanes than the control one during its mature phase (see figure 6.1.10), al-

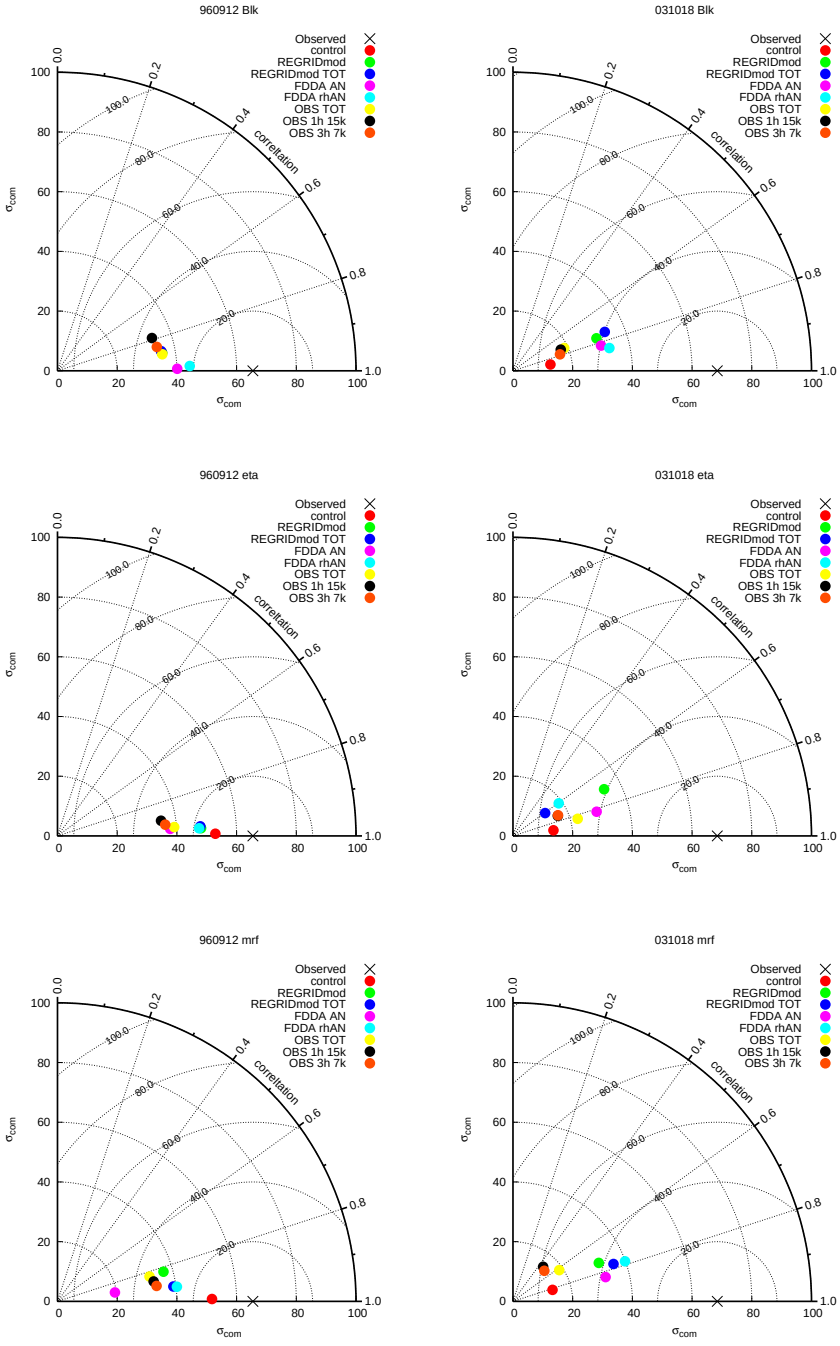

Figure 6.1.15: Taylor diagrams of simulated and satellite-observed trajectories, defined by the distances of trajectory vertices to the origin of coordinates of each domain of evolution. September 1996 (left) and October 2003 (right). With Blackadar (top), ETA (middle) and MRF (bottom) PBL schemes. σ_{com} standard deviation of the simulated trajectory (com) establishes the radius. $\mathcal{R}$, correlation between trajectories, establishes the angle respect to the abscissas. Root Mean Square Error (RMSE) is the distance between simulation dots and standard deviation of the observed trajectory (black cross). Colour codification of the dots for each simulation is the same as in figure 6.1.10

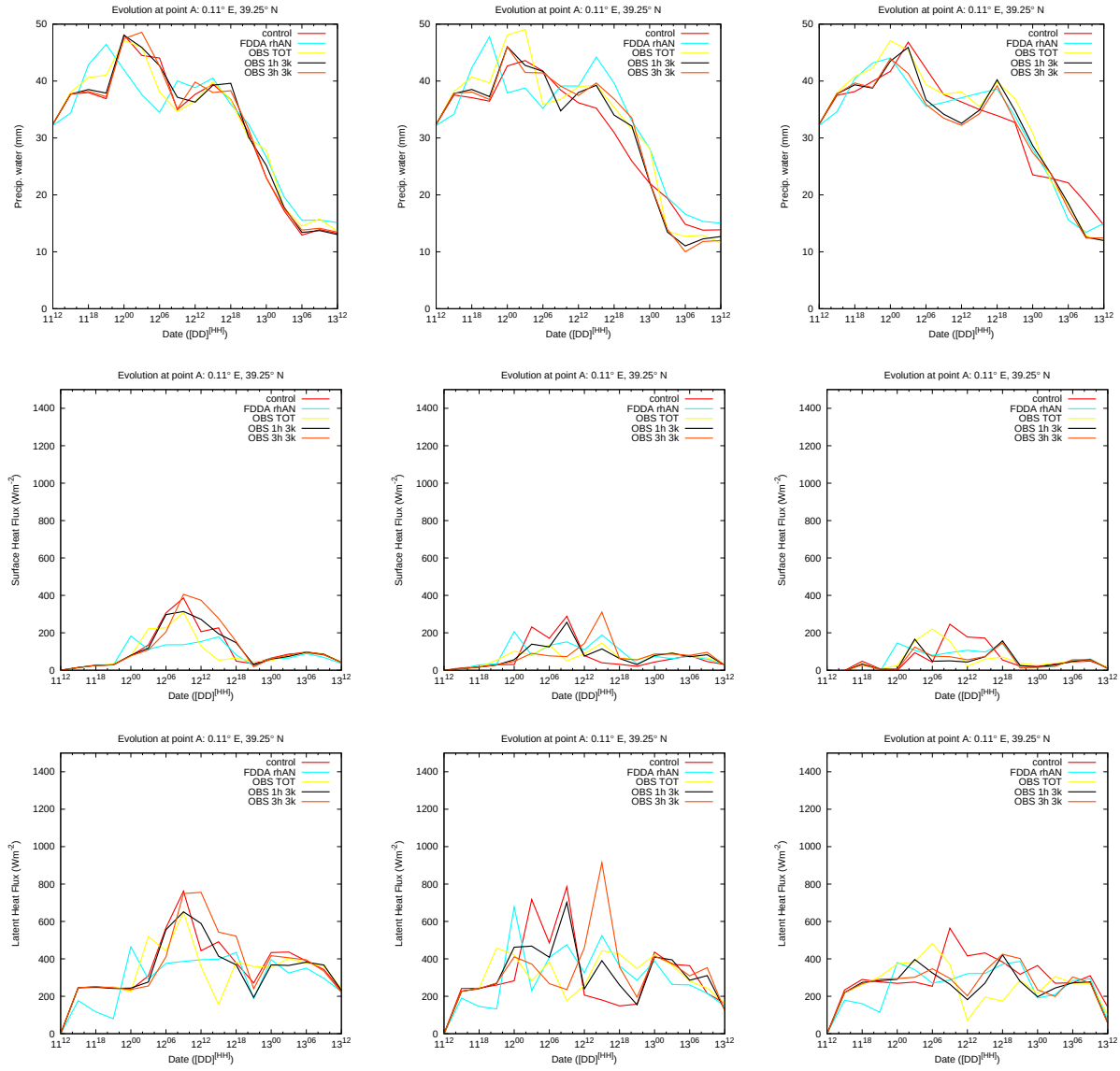

Figure 6.1.16: Evolution at point A (bottom left panel of figure 6.1.5) during September 1996 simulation of the Precipitable water (mm, top), surface sensible heat flux (Wm^{-2}, middle), latent heat flux (Wm^{-2}, bottom). For control simulation (red), OBS TOT (yellow), OBS 1h 3k (black) and OBS 3h 3k (orange), with the Blackadar (left), ETA (middle) and MRF (right) PBL schemes

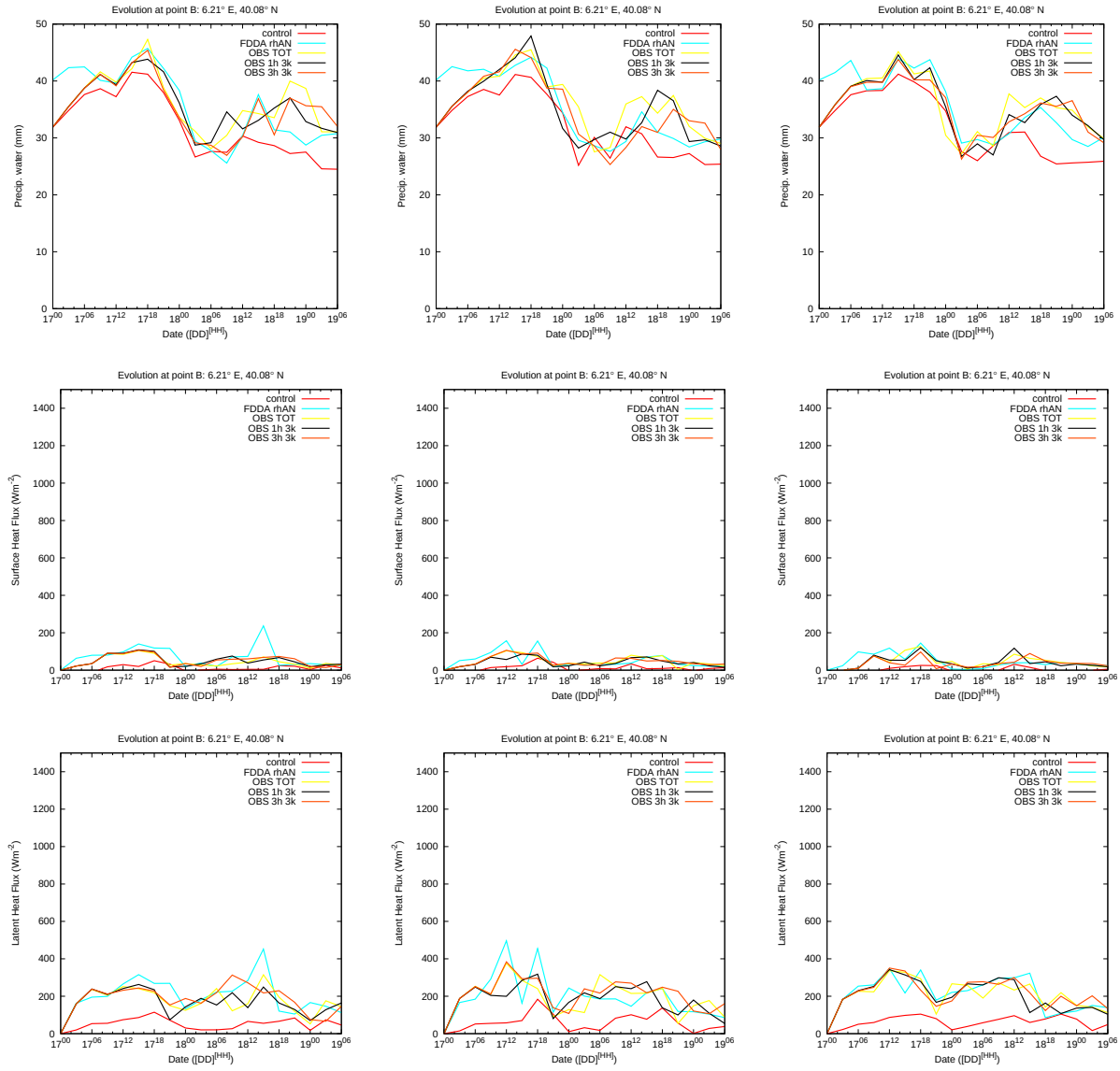

Figure 6.1.17: As in figure 6.1.16 but for the October 2003 case at point B (bottom right panel in figure 6.1.5)

though weaker medicanes are obtained at the later stages of the simulations. The largest differences on trajectory and central pressure value with respect to the control one (for all PBL schemes) are obtained with the experiment 'FDDA AN' (FDDA with unmodified ECMWF analyses). In these simulations (pink lines in figure 6.1.10), simulated medicanes are significantly weaker (they vanish before September 13th at 00 UTC) and their trajectory differ significantly from the other ones (figure 6.1.11). In these experiments, results are forced to be very similar to the ECMWF analyses, and ECMWF analyses do not fully capture the structure of the medicane owing to a poor horizontal resolution (ECMWF analyses at that time were truncated at T213, 0.5625° degrees of horizontal resolution). In FDDA AN experiment, MM5 simulated medicanes (for the three PBL schemes) present trajectories very similar to the upper level trough path (see figure 6.1.14 as an example of simulated trajectories of upper level maxima disturbance). Deepest simulated medicanes are obtained when the observational nudging is applied (experiments labelled OBS TOT, OBS 1h 3k, OBS 3h 3k; yellow, black, and orange lines in figure 6.1.10). OBS TOT experiment (coarse spatial resolution of observations that allows the highest temporal resolution of satellite information) produces the deepest medicane.

September 1996 deepest medicane is obtained by experiment 'OBS TOT' (humidity modification at every time step with the maximum computer[1] allowed spatial resolution, in this case 15 km; yellow line in figure 6.1.10). Similar tendencies of central pressure, maximum horizontal wind speed and trajectories of the simulated medicanes are obtained in the experiments using the same horizontal resolution but different temporal frequencies (experiments labelled 'OBS 1h 3k' and 'OBS 3h 3k', orange and black lines respectively in figure 6.1.10). However, experiment 'OBS 1h 3k' presents a bit stronger dissipation rate of the medicane than the lower temporal resolution experiment.

Taylor Diagrams show how the implementation of FDDA on 960912 case worsens trajectories (lower correlation and lower standard deviations). Simulated trajectories for September 1996 medicane are much closer to the satellite observed (lower Root Mean Square Error, RMSE, of the distance between simulation points and reference point in the diagrams) than October 2003. Data assimilation in September 1996 simulations modify both indexes, correlation and standard deviation, with a higher impact on the standard deviation.

No significant differences among the evolutions of precipitable water and sensible and latent heat fluxes from meteogram at the genesis zone of September 1996 are obtained with the assimilation of satellite/lightning information (see figure 6.1.16) with respect to the control one.

[1] On a PC Linux cluster with central and auxiliary nodes all with 4Gb of memory

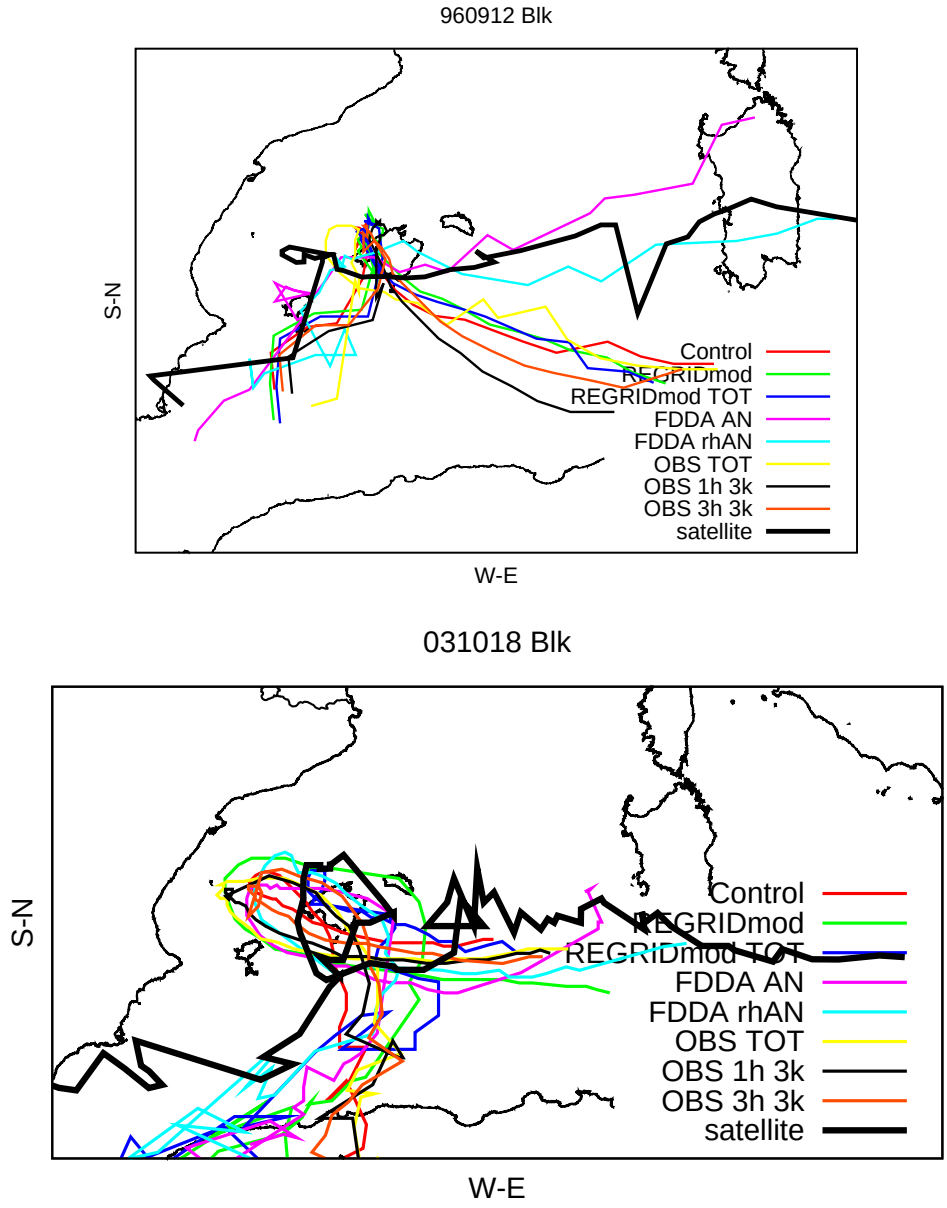

Figure 6.1.18: BIAS corrected simulated trajectories (i.e. bias is removed by traslation of the trajectories according to the spatial satellite-derived path) simulated trajectories with the Blackadar PBL scheme for each experiment. Solid black line is the satellite trajectory. For the September 1996 case (top) and October 2003 case (bottom). Colour codification of the lines is the same as in figure 6.1.10

September 1996 episode has a stronger sensitivity of $\mathcal{BIAS}_{dist}^{min}$ to the temporal shift than the October 2003 case. September 1996 episode has a symmetric response to advances/delays of the simulated trajectories. The lowest $\mathcal{BIAS}_{dist}^{min}$ values for almost all the experiments are obtained without the addition of a temporal shift in the simulated trajectories. Clearer results for the 960912 case can be attributed to the simplicity of the trajectory of the medicane in comparison to the 031018 case, in which the trajectory presents a loop. For September 1996 medicane, lowest $\mathcal{BIAS}_{dist}^{min}$ values are obtained in the experiments that do not use observation nudging (labelled REGRIDmod, REGRIDmod TOT, FDDA AN, FDDA rhAN).

No significant improvements of the BIAS corrected 'pure coordinate correlation' ($\mathcal{PR}_{bias}^{max}$) are obtained when simulated trajectories are temporally advanced or delayed (see figure 6.1.20). The introduction of a positive/negative temporal displacement in the September 1996 simulations produces a clear decrease of the correlation. None experiment or temporal shift gives better correlation results than the correlation attained by the control simulation without BIAS correction (horizontal solid black line in figure 6.1.20).

FDDA experiments with ETA PBL scheme simulate a stronger medicane, dissipation of the system occurs faster than in the control simulation using the same ETA PBL scheme (an abrupt change on 12th September 1996 at 09 UTC in middle panels of figure 6.1.10 is observed). It was shown how in the control simulation a long-lasting interaction occurs between the upper level trough β maxima and the medicane (see middle left panel in figure 6.1.6). Different trajectories of the upper level and low level centres simulated in the FDDA experiments seem to produce a reduction in the interaction between disturbances (not shown).

For September 1996, better skills (higher correlations, lower bias) are generally obtained when experiments are done with ETA PBL scheme.

October 2003

Blackadar simulation of October 2003 medicane is deeper than that one simulated with ETA scheme. However, medicane simulated with ETA scheme presents, during some periods of the evolution, the highest wind speed values.

October 2003 medicane evolution does not seem to follow so clearly the upper level disturbance as the previous case. There are not significant differences among the trajectories obtained with the different PBL schemes (see figure 6.1.5). Medicane and centre of the trough do not evolve simultaneously in this case. The closest approach between both systems does not reach 200 km (see right panels in figure 6.1.6). Therefore, October 2003 medicane might be more influenced by the general flow pattern associated with the

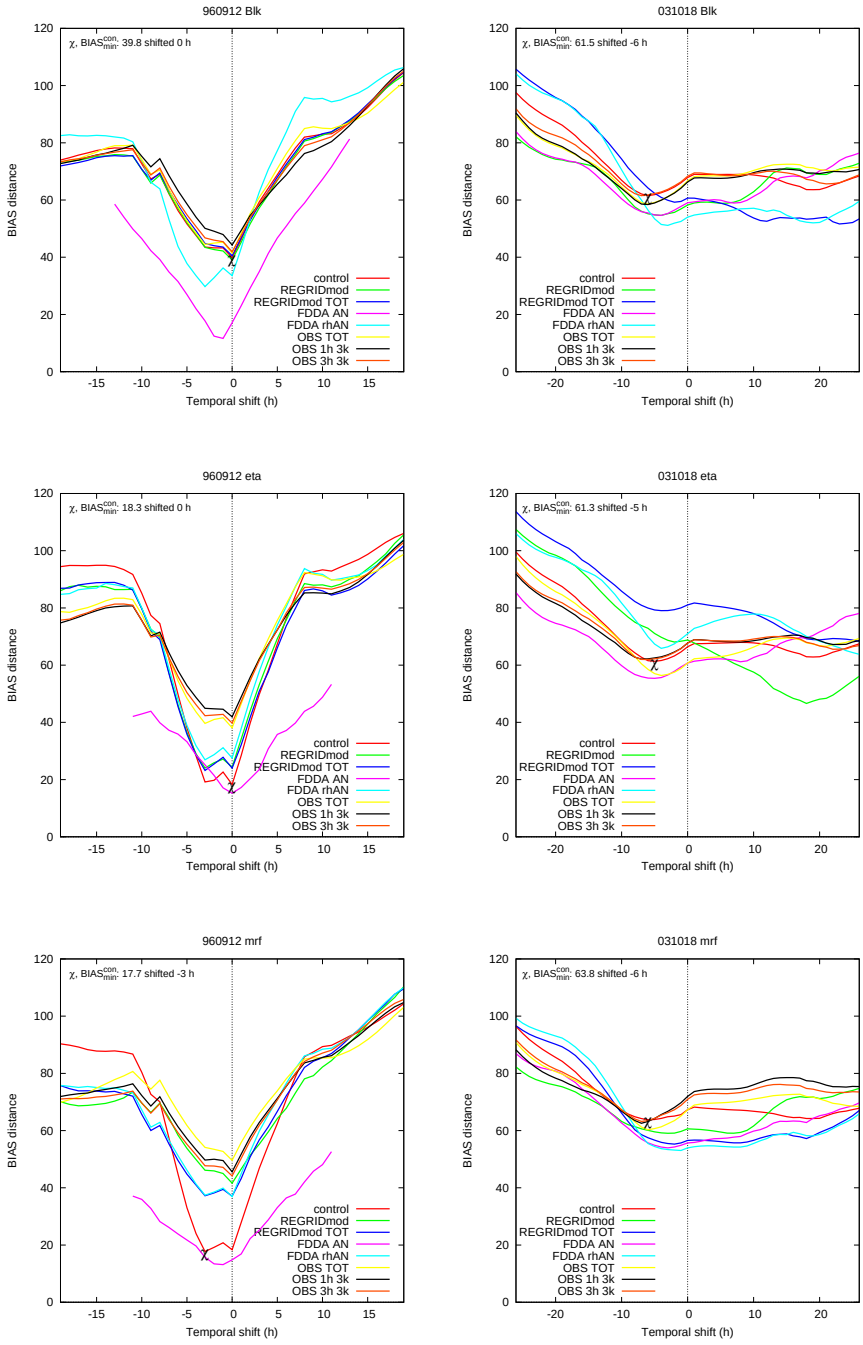

Figure 6.1.19: Dependence of the $\mathcal{BIAS}^{min}_{dist}$ of the distance between satellite-derived trajectory and simulated trajectories on temporal shift for the September 1996 (left) and October 2003 (right) cases. With the Blackadar (top), ETA (middle) and MRF (bottom) PBL schemes. Negative values mean temporal advances of the simulated trajectory and positive values mean delays. χ is the value of the minimum $\mathcal{BIAS}^{min}_{dist}$ for the control trajectory obtained for a given temporal shift. Colour reference of the lines is the same as in figure 6.1.10

upper level trough rather than by the precise movement of its centre of maximum vorticity.

October 2003 evolution of the upper level disturbances seems to be more adiabatic than September 1996 event, as a reflect of the independence between the upper-level maximum vorticity centre and medicane, for which a lower interaction between lower and upper level disturbances is established.

October 2003 case does not exhibit large differences between meteograms at formation zone (point B, figure 6.1.9) and presents lower values for all selected variables than the previous case. The intrusion of the growing medicane in the zone is also observed as a decrease of CAPE, a transitory maximum of precipitable water and an increase of surface fluxes. Larger differences in precipitable water amounts and surface fluxes intensities with respect to ETA simulation values are shown by the Blackadar and MRF meteograms in later stages of October 2003 simulations (see figure 6.1.17).

In comparison to September 1996 episode, October 2003 case reflects a lower influence of the the FDDA technique on the simulations (see figures 6.1.12 and 6.1.13).However, this case presents the strongest sensitivity of the characteristics of simulated medicane on the FDDA technique. Differences between the set of eight experiments for a given PBL scheme are larger than in previous case. There are differences between experiments for the same PBL scheme larger than 10 hPa in the central pressure value and 10 ms^{-1} for the maximum horizontal wind speeds. Upper level trough trajectories do not differ significantly, these differences becoming larger at later stages of the episode (see figure 6.1.14). This result would confirm the aforementioned low dependency of the medicane evolution on the upper level evolution, since changes in the trajectories and characteristics of the upper level maximum are weak. Deepest medicanes are related to the experiments where observational nudging is applied. In these cases, deeper pressure at the centre of the storm is also associated with stronger horizontal wind speeds.

October 2003 episode presents the strongest simulated medicanes with experiments 'OBS TOT' and 'OBS 3h 7k' (see table 6.1.a). These results, in agreement with the results obtained in the previous case, show that observational nudging for the two presented cases is more sensitive to the horizontal resolution of the data than to the temporal frequency with which the data is incorporated in the simulations.

FDDA methodology improves the trajectories of the October 2003 simulations (see figure 6.1.15) according to the decrease of the RMSE between simulated and observed trajectories, having a low impact on the correlation in contrast to its significant effect on the standard deviation.

Meteograms of precipitable water, sensible and latent heat surface fluxes at the genesis

zone of October 2003 case show higher values than in control simulation (see figure 6.1.17) when satellite/lightning data is used (similar behaviour of the variables is observed in the meteograms at other points, not shown). Bearing in mind the low sensitivity in previous case, this would mean that the humidity field is better represented in the ECMWF analyses of the September 1996 case, than in the October 2003 analyses.

October 2003 presents a clear decrease of $\mathcal{BIAS}_{dist}^{min}$ when simulated trajectories are temporally advanced with respect to the satellite one, while both increasing/decreasing effects when they are delayed. Bias results for the 2003 medicane are case dependant. A general advance about 6 hours reduces the bias ($\mathcal{BIAS}_{dist}^{min}$) between simulated and observed trajectories.

Some of the October 2003 simulations improve the pure coordinate correlation between trajectories, but temporal shift makes the results worse, even produces negative correlation values (see figure 6.1.20). Strong differences for a specific PBL with respect to the experiments are a reflect of the strong sensitivity of the October 2003 case on the FDDA technique.

For October 2003 episode the best simulation is not determined by an unique PBL scheme or experiment.

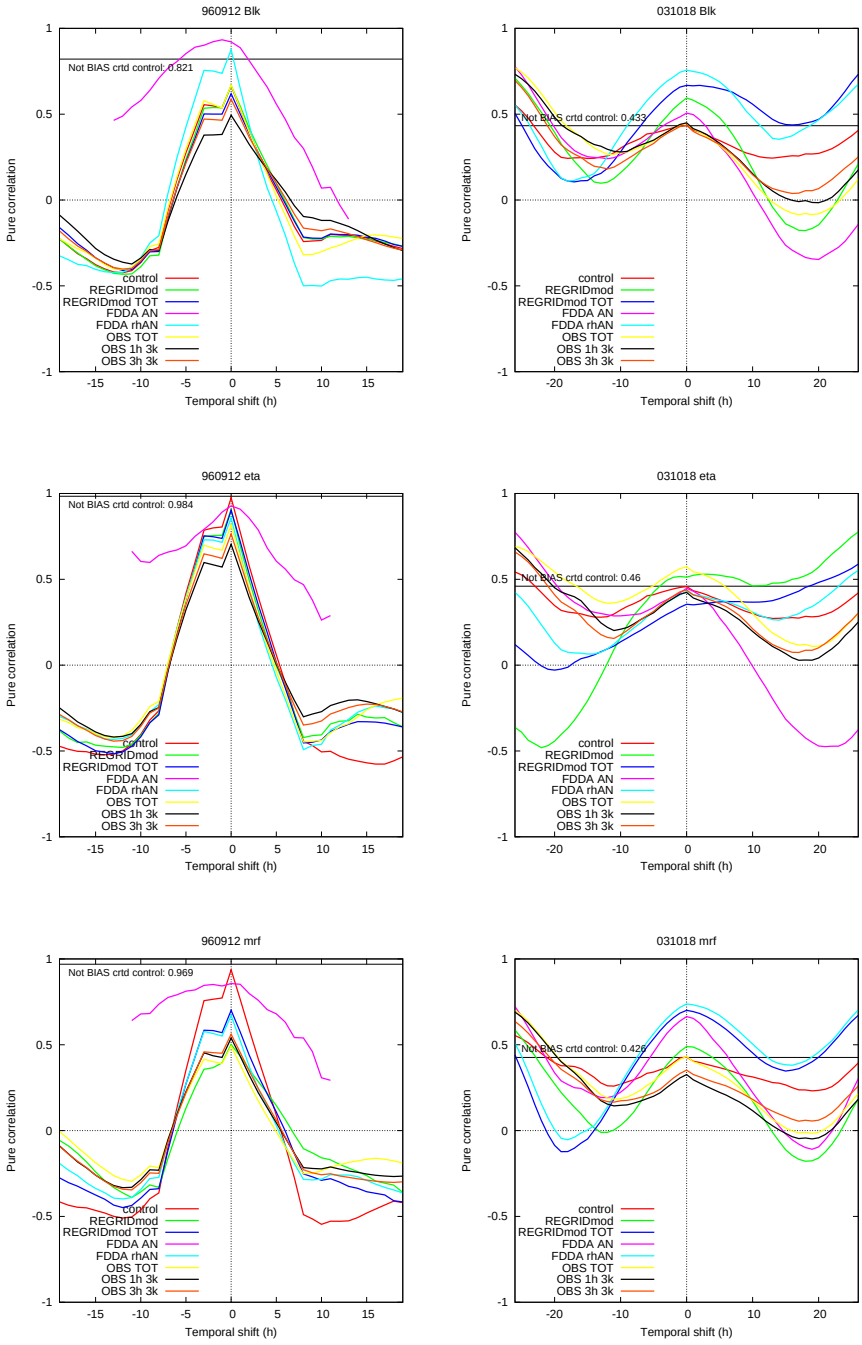

Figure 6.1.20: Dependence of the pure coordinate correlation $\mathcal{PR}^{bias}$ (bias corrected) for each experiment as function of temporal shift, for the September 1996 case (left panels) and October 2003 (right panels). With the Blackadar (top), ETA (middle) and MRF (bottom) PBL schemes. Solid black line is the correlation for the control simulation without BIAS correction. Colour codification of lines is the same as in figure 6.1.10

Chapter 7

Conclusions

A variety of Mediterranean cyclogenesis has been analysed. Although they evolved within the same environment a relative important number of different mechanisms and processes responsible for their genesis, maintenance and dissipation have been found. Three main numerical techniques: atmospheric numerical model, piecewise PV inversion and Factor Separation have been used to analyse the cyclogenesis in the Mediterranean basin. Each one provides different information from the processes allowing a robust and global view of the topic.

Conclusions obtained as result of all the developed studies are referred to two aspects: dynamical description of Mediterranean intense cyclogenesis and limitations and improvements of used numerical methodologies. It must be recognised that these conclusions have two main limitations: case dependence and numerical origin.

The non-linearity of the atmosphere limits its comprehension. Similar initial conditions might derive in different situations and phenomena. By this way, in order to obtain a wide and general perspective of the dynamics of the atmosphere a wide number of cases must be studied. Even after the study of a large number of similar episodes, due to the non linearity, a new case could be completely different. Thus, results must be seen as the particular response of the 'atmosphere' at the specific situation.

Almost all the results are based in numerical models and/or numerical techniques. Observations have only been used in some cases as a way to make, in some manner, more realistic the initial conditions of the representation of the atmosphere. Although atmospheric observations are sparse and contain errors, they constitute the most accurate and close description of the real atmosphere that we can have. Numerical methodologies constitute a well developed labour that allows: a complete description and evolution of the atmosphere based on equations and the repetition of the experiments. However without the use and validation of observations one can not be sure of the degree of nu-

merical/method artifice of its results.

Keeping in mind the previous limitations in relation to the results, the author is pretty confident in his results. A selection of different cases when it was possible has been tried in order to widen the scope of the results. In the piecewise PV inversion study of the November 2001 episode, results for a unique case are obtained. But in this study, two objectives were searched: analysis of the case and the practice of an improvement of the piecewise PV inversion numerical technique. The use of observations has been very limited, and it has been reduced to a general comparison with satellite-based trajectories or radar reflectivities. This can limit the accuracy of the results, however, there is any way to verify, contrast or validate some of the objectives of the studies, like the effects of factors or piecewise PV inversions with measurements or observations.

7.1 Strong cyclogenesis: November 2001

The 912 November 2001 Mediterranean cyclone has been studied in terms of its sensitivity to changes in the initial conditions due to three PV anomalies: the surface thermal anomaly related to the origin of the cyclone and the baroclinic initial conditions of the environment; the upper level trough related to the baroclinic growth mechanism of the cyclone; the upper level North Atlantic high pressure zone related to the environmental conditions of the upper troposphere. The anomalies show different morphologies and intensities, but since the energy-quantification of the initial modification has been applied, sensitivity results might be only attributed to the dynamical role of the anomalies. The surface thermal anomaly is revealed as the most important feature of the initial conditions for the cyclogenesis. A significant effect on the initial central pressure of the cyclone and a weak effect on its initial position are shown. Both have a strong effect on the resultant evolution of the case. The sensitivities to changes in the initial conditions due to the upper level disturbances are also important. Nevertheless, the initial impact on the structure of the cyclone is lower than for the thermal anomaly, but in later stages of the episode the impact becomes the strongest. The effects of changes in the initial conditions associated with the North Atlantic high are weak. However, in the last phase of the cyclone evolution, the initial perturbations show a notorious impact on the trajectory of the cyclone.

The sensitivity results are strongly affected by the baroclinic mechanism. It is illustrated that the diversity of simulated cyclones can be mainly explained as a function of the changes in the vertical tilt between the upper level trough and the surface disturbance. The sensitivity test to the increase(decrease) in the surface thermal anomaly shows that with similar values of the upper level disturbance, changes in the relative position and central pressure value of the surface disturbance generates deeper(weaker) and faster(slower) evolution of the simulated cyclone. This case also emphasises the mutual

interaction between anomalies, in the sense that the thermal anomaly perturbation does not affect the initial structure and intensity of the upper level disturbance, but during the simulated period, the upper level disturbance strength clearly differs between both experiments. The upper level disturbance perturbations modify both the initial central value of the cyclone and the upper level trough, but only slightly modify the relative distance between both features. These variations generate a strongly varied evolution of the cyclone. Finally, the North Atlantic high does not exhibit a significant role on the upper level disturbance, on the surface cyclone strength or on the relative position between disturbances. However, the small perturbations on the relative position between the upper and low level disturbances seem to be enough to originate significantly different final cyclones.

7.2 Intercomparison of 11 Mediterranean cyclogenesis

The results for 11 Mediterranean cyclones have been presented. Must be studied much more cases in order to obtain a much representative climatology of the Mediterranean cyclogenesis.

The effectiveness of the studied factors does not show many similarities between cases and only weak generalisations can be done, however the baroclincity of the Mediterranean basin is shown by the importance of the upper level PV anomaly. It is detectable the presence of an upper-level low in almost all the cases. Secondary role is played by dry low-level anomaly and its interaction with the upper level one. It is obtained the importance of the low-level positive PV mainly in some cases related to the baroclinic development process and/or to the thermal low genesis due to solar insolation over the North African plateau or other regions. Finally, background flow appeared to be responsible of the cyclone movement.

Moist low-level PV has been considered as a factor. The sensitivity of the 11 cases to this factor has been shown very poor. It should keep in mind that this factor only marks the moist low-level PV of the cyclone, trying by this way to deal with the diabatic aspects of the cyclogenesis. However, small sensitivity results of the factor might reflect it as an inadequate way to capture the importance of the moist-induced diabatic processes. A new approach considering directly the diabatic terms of the equations is proposed as a more correct way to capture the moist induced diabatic processes.

Factors are often cyclogenetic and cyclolitic as a probable signature of the complexity of the Mediterranean topography and the large number of factors that are reproduced in

a cyclogenesis and they have not been taking into account such as: upper level-low level interaction sensitivity on the relative position between disturbances, cyclone position relative to the orography and background flow.

Geographical differences between dynamics of cyclones can be make. Western & Central Mediterranean cyclones seem to be mainly dominated by upper and low PV anomalies and their synergy. A variety of principal factors is shown by eastern Mediterranean cyclones. This could be also related to the variety of typologies of the Eastern selected cyclones. Since Western and Central cases are generally African or Alpine lee cyclones. In contrast, Eastern cyclones have different genesis and trajectories.

Dynamical group of the cyclones show some differences. 'African' cyclones are principally driven by by Upper level disturbances or its synergy with low level PV. 'Maritime' cyclones are mainly dominated by upper level disturbances and weakly by the background flow. The selected 'Alpine Lee' cyclones shows a first phase dominated by the Upper level disturbance and a second one driven by low level disturbances. It is also shown big compensations between strong cyclolitic and cyclogenetic effects.

This methodology allow to an objective classification of the Mediterranean cyclogenesis rather that other classification based on society impacts or geographical affected areas (e.g. MEDEX database, see `http://medex.inm.uib.es`). The derived climatology is based in dynamical concepts that after an improvement of the technique can apport a general scope of the main processes related to the Mediterranean cyclogenesis. Results are not very precise, but is hoped that a significant increase of the number of cases and the appropriate selection of factors will provide significant results.

7.3 Thermal influences

This study is focused on a numerical study of a severe storm event that occurred on August 16th 2003 in Northeastern Spain. Maximum precipitation amounts of 115 mm were registered in the rain gauges of Alcañiz, the most affected town. Hailstones of up to 12 cm were registered and the town was declared a disaster zone, claiming losses of over 10 M. A C-band radar with a high temporal resolution made it possible to follow up the storm activity.

The event was characterised by a trough at mid to upper tropospheric levels. The arrival of a cold front from the NW of the Iberian Peninsula moving eastward caused high-altitude cooling. Numerical simulations were performed to examine the accuracy of the model in reproducing the severe storm of Alcañiz. The control run shows the presence of a thermal mesolow favouring the entrance of warm and humid air from the Mediter-

ranean Sea all the way up the Ebro Valley. The total precipitation field indicates that the most intense precipitation fell in the study zone, coinciding to a great extent with the radar data. The radar simulation carried out with the model proves that, even though MM5 underestimates the maximum precipitation registered, it does reproduce the spatial and temporal evolution of the storm quite closely. On a convective scale, the result of the simulation can be considered to be very satisfactory.

Besides, a numerical sensitivity study was carried out as well to analyse the factors contributing to the localisation of the intense precipitation. The roles played by topography and solar radiation were also examined, since these factors have previously been identified as relevant in severe storms in Northeastern Spain. In fact, the experiment carried out with no solar radiation shows a weakening effect on the mesolow and a reduction of the instability in the low troposphere. This hinders the activity of mechanisms triggering convection and inhibits precipitation, limiting it to small areas of the Pyrenees and the Mediterranean coast. In the experiment with flat terrain the corridor effect of the Ebro Valley on the mesolow disappears, as well as the low-level warm inflow from the Mediterranean Sea. The results conclude that the separate effects of either solar radiation or topography are not decisive by themselves in accounting for the intense precipitation caused by the severe storm of Alcañiz. However, the synergic effect of the two factors combined is fundamental for the spatial and temporal localisation of the storm, and has an inhibiting effect in other areas of Northeastern Spain.

7.4 Lee influences

This numerical sensitivity study investigated the initial phase of a deep Mediterranean cyclone that took place in the lee of the Atlas Mountains in November 2004 and caused a range of severe weather events throughout the Mediterranean region. In this numerical study, a factor separation method was applied to investigate the influences of orography, upper-level potential vorticity and surface sensible heat flux on the Atlas lee cyclone initiation and development, focused on the period until the cyclone left the lee area and entered the Mediterranean Sea.

Orography proved responsible for the first phase of the lee cyclogenesis, where a shallow cyclone was formed over a barotropic area in the lee of the High Atlas, due to frontal retardation and creation of an associated thermal anomaly. Although the orographic influence resembled the first stage of Alpine lee cyclogenesis, the orographically induced pressure drop reached 5 hPa during 24 hours and was not so rapid like in cases of Genoa cyclogenesis.

The second phase of the deepening was characterised by the cyclogenetic influence of

the upper-level potential vorticity perturbation (a part of the upper-level PV anomaly). Indeed, with a total upper-level PV anomaly removed from the initial conditions, the cyclone did not form in the lee of the Atlas, that proves that the upper-level dynamical factors are a necessary ingredient of Atlas lee cyclogenesis, in accordance with some idealised studies on Sharav lee cyclones (Egger et al., 1995). In simulations with the PV perturbation included, the low-level air was colder, resulting in the creation of a stronger thermal anomaly and associated baroclinic zone. Furthermore, the upper-level PV perturbation showed responsible for a vertical (downward) propagation of cyclonic circulation, as indicated by the increased cyclonic winds in the lower atmosphere. In other words, the influence of positive PV advection contributed to the stronger low-level convergence and more rapid cyclone initiation.

It seems that the most pronounced feature of surface sensible heat flux contribution was an afternoon cyclolysis. Namely, SSHF was accompanied with increased vertical mixing in the afternoon PBL and associated weakening of the baroclinic (and barotropic) zone, inducing less intensive cyclone deepening. Secondly, heat exchange between the ground and the surface air reduced the horizontal surface air baroclinicity, as the horizontal air temperature gradient of the baroclinic zone was bigger then the horizontal ground temperature gradient in the arid Atlas lee. And finally, it is proposed that the exclusion of surface sensible heat flux enhanced the long-wave earth radiation that tended to act as a heat supply to the moist areas (associated with the cyclone) in the free troposphere.

The synergy between orography and upper-level PV perturbation was at first cyclolytic, followed by the cyclogenetic contribution towards the end of the analysed period. The cyclolytic influence existed probably due to the fact that in the simulation with orography and upper-level PV included, the cyclone experienced filling over the terrain obstacle on the way to the Mediterranean Sea. The subsequent cyclogenetic contribution of the synergy had some potential for comparison with the low-level-upper-level vortex interaction in the second stage of Alpine lee cyclogenesis. However, at the end of the analysed period the cyclone centre positions differed significantly, not allowing a resolute conclusion.

The spread of the cyclone centres in the model simulations was shown to be a powerful tool in understanding the effect of different factors on the cyclone evolution. For instance, orography moved the cyclone initiation closer to the mountain and the favourable lee area where the thermal anomaly was the strongest and tended to keep the cyclone more stationary. On the other hand, the upper-level potential vorticity perturbation moved the cyclone formation location away from the mountain and was responsible for the faster advection of the cyclone to the Mediterranean Sea. It seems that the intensity of the upper-level PV anomaly has an influence on the subsequent cyclone movement and possibly has some potential to account for the seasonal cyclone path variability.

Another sensitivity experiment was performed to try to account for the influence of a thermal anomaly on the generation of a low-level vortex in the first stage of lee cyclogenesis. However, the simulation shown that the thermal anomaly in the lee of the Atlas built up rather quickly. It almost reached the intensity of the thermal anomaly of the control run in 24 hours since the start of the simulation, just before the cyclogenesis started. Thus, little reliance could be made on the separation of low-level PV and thermal anomaly influences on the intensity of cyclone initiation. However, it seems that the location of the slightly weaker cyclone initiation showed sensitivity to a thermal anomaly positioning in the mountain lee.

So far, the very area of the Atlas lee was subjected neither to a significant number of numerical or theoretical studies, nor to observational field campaigns like MAP. However, the arid lee area of the Atlas Mountains has some potential to attribute more precisely the influence of dynamical processes to the lee cyclogenesis due to the lack of moist processes at play. Furthermore, the vertical and horizontal scales of the High Atlas Mountains are reasonably comparable to the Alpine dimensions.

It is one of the goals of the planned MEDEX special field campaign to better monitor Mediterranean cyclones and storms, which are often not well detected by observation networks. In addition, this effort should be accompanied by an increased number of numerical and theoretical studies, specially the ones that investigate the life cycles of the high-impact deep Mediterranean cyclones.

7.5 Medicane environments

An analysis of the characteristics and behaviour of the tropical-like Mediterranean storms has been presented. The study applied a nonhydrostatic, cloud-resolving model used previously to simulate tropical cyclones in order to analyse the potentiality of seven environments in which a tropical-like Mediterranean storm occurred. Observations show that the seven analysed Mediterranean systems are of tropical storm strength. From satellite imagery, a similar morphology to the tropical cyclone systems is also obtained for the medicanes: a clear rounded cloud system, in the centre of which a free cloud zone, like an eye, is formed. Satellite imagery showed different trajectories and speeds for the movements of the medicanes.

Mediterranean systems exhibit notable differences from the tropical ones. Sea surface temperature did not play as significant role as in hurricanes. As noticed in previous work (Emanuel, 2005), high values ($> 26°C$) of sea surface temperature are not essential, in contrast to hurricanes. Thus, the vertical profile of the atmosphere, defined from the

combination of a mid-upper level cold low and a SST-controlled boundary layer, has been shown as one important aspect of medicane formation. Generally, analysed synoptic situations during medicane formation showed significant instability and high precipitable water quantities in the atmospheric column.

The cloud model simulates a 'theoretical' storm derived from an initial environment. Some assumptions and simplifications are implicit in the model. A main point is related to the energy source. It is assumed that the storm will only obtain the energy from the sea surface and related surface fluxes. The axisymmetric cloud-resolving model demonstrates that medicanes can be developed and sustained at least partially by surface enthalpy fluxes, especially if the initial environment is moist. However results showed stronger and larger potential storms in comparison to the observed ones. Simulated wind speeds were significantly stronger, and simulated cloud-eye dimensions were wider. Simulated storms are formed more slowly (mainly 3-4 days) than the 'real' ones as revealed by satellite images (mainly 1-2 days). Moreover, Mediterranean observed storms dissipated mainly in 2-3 days. Meanwhile, simulated storms were maintained for a longer period (mainly 4-5 days) and some cases did not show any weakening process. These significant differences are considered to be a sign of the complex atmospheric processes operating in the Mediterranean systems that the simplified numerical model is not able to resolve. The complex orography, the small dimensions of the basin and the continental influences from the neighbouring European and African lands are particular aspects of the Mediterranean which are not present in the largely homogeneous tropical environments. These aspects will of course modify and limit the evolution of the tropical-like systems in the Mediterranean basin. Besides, the assumptions of the cloud-resolving model do not allow one to take into account baroclinic influences which are prominent in the Mediterranean. In some cases, ECMWF analyses showed a significant horizontal thermal gradient in the region of the storm evolution, (e.g.: 950115 case). Tropical-like Mediterranean storms grow and evolve from a combination of deep convection and typical mid-latitude baroclinic processes. The axisymmetric cloud-resolving model assumes a homogeneous atmosphere. This assumed background atmosphere is also temporally invariant during the period of simulation. Spatial homogeneous and temporal invariant assumptions are inappropriate in the Mediterranean basin (Reiter, 1975). Thus, a less restrictive cloud resolving model, in which either a baroclinic environment or a time-evolving environment could be introduced, is at least necessary in order to produce realistic tropical-like storms in Mediterranean air masses. The MM5 three-dimensional numerical model was applied on two of the events to confirm that hypothesis. The results reflected a good agreement with observations and know aspects of these systems, such as warm core, the eye-wall structure and the subsidence at the centre of the storm.

The main results of the sensitivity tests of the environments, which have been computed with the tropical cloud model, showed similar results as the tropical cases. The

value of the SST is clearly important for the formation and evolution of medicanes. In the simulations, colder SST inhibited the formation of the medicanes while, warmer SST accelerated and enforced the medicane formation. The results of the simulations in which the size of the vortex was changed were significantly different from the control ones. Stronger and faster systems were formed when the initial vortex was enlarged. The importance of the vertical profile of the atmosphere for the medicane formation has been described. The sensitivity tests on the moisture content of the air column showed a deep impact on the formation and the evolution of the storm. Drier air made the formation and the evolution of the storm more difficult, while moister air enforced and accelerated the formation of the storm. Thus, the characteristics of the initial vertical profile of the atmosphere have been shown to be important influences on the evolution and formation of the medicanes. Finally, a warmer initial vortex produced a faster and stronger evolution of the simulated storms. This reflects the impact of a faster(slower) organisation of the convection induced by a stronger(weaker) rotation of the initial vortex (Rotunno and Emanuel, 1987). The good results obtained with MM5, encourages authors to use this kind of primitive equation model simulations in order to complete a more adequate model-based sensitivity test of the medicanes.

Moreover, due to the maritime characteristics of the systems, the lack of observations and records of medicanes impedes research on their development. More observations are needed for a correct understanding of medicanes.

7.6 Medicane sensitivity

High resolution simulations and the Factor Separation analysis of three tropical-like storms has give some relevant information about the role of the air-sea interaction mechanism in these systems.

Temporal and group dependences of the synergies of the cases show significant differences, as a reflection of the different behaviours of the three cases. Two phase distinctions can be made for each case. During these phases principal effects change. Instead the differences between cases, some general aspects of these kind of systems are obtained.

Beginning phases of the systems are dominated by the upper level disturbances and the interaction between surface fluxes and Sea Surface Temperature. Upper level vorticity effect at low level would contribute to the reinforce of an initial weak vortex, around which the medicane will be formed. At the same time, upper level disturbances coupled with the moistened and warm air above sea established a vertical thermodynamic disequilibrium, that is necessary for medicanes formation. In contrast, its interaction with surface fluxes

have a cyclolitc role due to a diminishing of the baroclinic conditions and the energy budget at the top of the outer region of the medicane boundary layer. Boundary layer and its high sensitivity on SST constitutes the initial source of moist and heat from which the constitution of the storm will be done.

Once the storm is well formed, air-sea interaction mechanism is revealed as a mechanism from which the system is reinforced, maintained and dissipated, as it is shown by the major importance of the multiple synergies rather than individual effects. January 1995 case has a significant different dynamics than the May 2003 case. September 1996 case shows an intermediate behaviour between the two cases, that is a reflection of a short period of tropical-like development. January 1995 case presents a dynamics mainly dominated by multiple synergies related to the SST. Meanwhile, principal effects of May 2003 case are principally related to pure effects or coupled synergies.

Group analysis dependence of the effects allows to make a relative study of that factors and they hidden synergies with that one are not taken into account in the study. From this methodology are obtained signatures of different possible strong effects not considered. Even though hidden synergies are not revealed. These various not considered factors are like: latent heat release from strong cloud formation and orography. These unresolved effects are not reflected in all the cases and effect group-dependences varies respect factors and cases. September 1996 case shows the strongest not well resolved group-dependence of the synergies for the central sea level surface pressure variable. The large number of unresolved synergies exhibited by the storm could be attributed to the short period of tropical-like behaviour and to the proximity to Eastern-Iberian coastal line, orography and islands, that are not present in the other cases and might influence its evolution.

Principal effects of each forecasted field are pretty similar for each case. It is shown that factors act in the same sense for the studied variables. Thus, cyclogenetic (cyclolitic) factors also accelerated (slow downed) and increased (weakened) the vorticity of the system. Principal deepen factors for the three cases are the upper level disturbances, SSHF and SST synergy, LHF and SST synergy, triple synergy between LHF, SSHF and SST and finally triple synergy between SSHF, Upper level disturbances and SST. Major weakening effects are triple synergy of LHF, SSHF and upper level disturbances. Differences between cases are also shown by the different computed effects. A clear temporal phased effect is shown by the effects on the relative vorticity at the centre of the storm at 950 hPa. This phased based effect is shown more clearly by 960912 and 030527 rather than by 950116 case where a mixing of effects is shown. All the obtained dynamical differences revealed January 1995 case as a system much more close to a tropical-like system than strong convective case of a small baroclinic cyclone like May 2003 case.

Air-sea mechanism was developed to describe the dynamics of a mature tropical storm. It is well known that Mediterranean characteristics are quite different from the tropical ones. MM5 simulations attempt to be a more realistic simulation of an atmospheric system. By this way, some differences respect to a theoretical model may be expected. In spite of the differences of size, strength and environment of evolution of the medicanes with respect to the hurricanes and tropics some similarities between medicanes and air-sea mechanism have been found. In the medicanes, sea surface has an important role in the heat and moist source. At the same time, a precursor role of a weak vortex has also been detected in the Mediterranean cases. Warm cores, strong inflow fluxes and strong updrafts are also obtained. However, in medicanes an upper level cold low is a key element for the formation of the systems, and in their movement. The importance of this element is shown in the SST temperatures of the medicanes (15.7, 24.3 and 17.1 °C that are significantly cooler than the threshold temperature for a tropical storm (26°C).

Results have shown a large variety of dynamics. A similar dynamical study should be done with other clear cases of tropical-like storms in order to obtain a much more concrete scope of the dynamics of the system. FS has the ability of give information about the effects of factors and synergies. A deeper knowledge of these synergies is needed in order give a better understanding and explanation of the results that provide the technique. However, some of these synergies involve complex diabatic processes that evolved in a very complex environment with a large number of uncertainties and non-linear coupled features.

7.6.1 Sensitivity of January 1995

Deep examination of the air-sea mechanism in the 950116 medicane case revealed the complexity and multiple dependences of the air-sea mechanism. Azimuthal averaged effects show different behaviour of each factor at different zones and stages of the medicane evolution. Factors can affect different regions of the structure of the storm and can reach its complete structure, be clearly focused in the central part of the storm or be important in the up-outward constant angular-momentum surfaces region. At the same time, wide differences can be found between effects that only differ in one factor with similar characteristics (like strong differences between e_{23} and e_{234} during the formation phase).

Pure effects (effects without synergies) do not change their role during the entire evolution of the system. Surface fluxes and SST basically moisten and warm the base of the storm (promoting an environment with convective instability $\partial_z EPT < 0$), meanwhile upper level disturbance cooled and dried the air beneath. No clear signature of a baroclinic development has been obtained with vertical cross sections at the formation phase of the storm. However, synergy between SSHF and ULd and triple synergy between SSHF, LHF

and SST exhibit a role from which the system acquires the tropical-like characteristics.

During mature state, almost all factors play an enhancing role. It is show how practically all the synergies and factors contributed to enhance and enforce the characteristics of the medicane. However, due to dry characteristics of the air of upper level, a vanishing role can be attributed to this factor, from which middle level air is dried. But at the same time, it contributes to maintain cold upper level air from which the medicane can close properly its energy budged.

Dissipation is characterised by a vanishing role of the synergies related to the SST, meanwhile other factors and synergies maintain in general their previous exhibited role. Moreover change of effect of the coupled SST synergies occurred in a zone where environmental conditions of growing can occur since SST presented its warmest values. This should indicate changes in the dynamics of the system that stopped the mutual reinforce interaction predicted in the tropical storms due to a saturation of the boundary layer.

In order to make an intercomparison between point and 2-dimensional effects of the study should bear in mind that the effects are calculated on different forecasted fields and in different ways. Moreover 2-dimensional effects have a spatial dependence that difficult the intercomparison, since they can present enhancing and vanishing role at the same time. No clear correspondences are obtained during the formation phase, since point effect shows a cyclogenetic development of the storm, meanwhile 2-dimensional effect upper level disturbances and synergy between sea and surface fluxes plays a deepening role with tropical characteristics. At mature state the correspondence between effects is not clear due to dual role of some effects. Meanwhile vanishing role of the synergies with SST obtained in 2-dimensional effect is partially detected by the point effect of the study.

Air-sea interaction has been studied in the particular scope of the Mediterranean tropical-like storms. In order to generalise the results for the air-sea mechanism, a similar study to the sensitivity on the same four factors could be reproduced with tropical or hurricane storms. By this way, structure and dynamics of the air-sea interaction could be better understand due to a stronger and clearer characteristics of these systems. Moreover, a deeper and more detailed study of the meaning of each factor and synergy should be done, in order to make more comprehensive the diabatic and strong nonlinear processes that reflect each synergy.

7.7 Assimilation of observational data in numerical simulations

Significant sensitivity to the choose of PBL scheme has been found for both medicanes. Nonlocal mixing PBL schemes lead to larger precipitable water quantities and more intense sensible and latent heat surface fluxes, but weaker available energy for the development of the system. Accordingly, simulations with a local-mixing scheme like ETA generated a deeper and stronger system. In September 1996 episode a notable system reaching wind hurricane intensity was obtained. No clear conclusions on which scheme is better for simulating these episodes can be obtained, since observations of the characteristics of the medicane are not available. However, deeper systems seem to be in better agreement with barograph measurements of September 1996 medicane at Palma de Mallorca (Homar et al., 2003b).

Satellite-derived images is a powerful way to obtain information at high temporal and spatial resolution over maritime areas. In this work images have been used as a method to derive precipitation type, in combination with lightning information which provides a precise way to determine convective grid points. These tools are then used to constrain MM5 vertical humidity profiles to the observed precipitation type. Medicane simulations show a high sensitivity to the representation of the humidity profile. Almost all the experiments with a modified humidity field simulated a deeper and stronger medicane. More available energy for convection and medicane growth is obtained when humidity correction is applied owing to the increase of potential instability. However, trajectories of simulated systems differ significantly from observed ones. Other satellite-based information like water-vapour channel wind speed estimations could also be retrieved and incorporated into the simulations (Leslie et al., 1998). It has not been done since the main interest of the study is to obtain the sensitivity only to changes on the humidity profile.

September 1996 medicane's trajectory is worsened when satellite information is used, meanwhile in October 2003 case it is improved. Basically, trajectories are only modified in their morphology and genesis zones. No modification of the movement speed of the medicanes is obtained with the technique. As simple modification of the initial and boundary conditions (experiments 'REGRIDmod' and 'REGRIDmot TOT') is significant enough as to generate modifications in the simulated systems. Implementation of satellite-derived information worsens both BIAS and correlation characteristics of September 1996 simulated trajectories. Best results are obtained with the 'FDDA AN' experiments (for the three PBL schemes) in which ECMWF analyses nudging is applied. Only for these experiments, simulated medicane trajectories of October 2003 event have better correlations than control simulation, although these analyses nudging experiments provide the weakest systems. No experiment is able to reduce the temporal shift between observed and

simulated medicanes. October 2003 simulated medicane reflects a delay of 6 hours with respect to the observed one from satellite.

Simulations with ETA PBL scheme seem to have a better response to the application of the observational nudging technique.

Different statistical coefficients have been presented for an objective intercomparison of simulated and observed trajectories. However, a robust object-oriented methodology appears to be necessary. This approach should be able to compare more efficiently basic aspects of the trajectories such as: morphology, genesis and evolution zone and speed of evolution.

7.8 Numerical methodologies

As a result of the objectives of some studies some modifications or new applications were done on the selected numerical techniques: MM5 numerical model, piecewise PV inversion technique and Factor separation.

7.8.1 MM5 numerical model

Presented studies show sensitivities to the SSHF. In order to make it possible, a modified version of the Blackadar PBL scheme has been made by the author. This modification cancels SSHF PBL scheme computations. This modification was made following a previous one used in the *Grup de meteorologia* of the *Universitat de les Illes Balears* in which LHF from the see was annulled.

Sensitivity studies on the SST has also been carried out. A modification on the MM5 module in which boundary conditions are acquired is made. This modification allows directly the modification of the value of the SST provided by the global analyses.

BUFR files has been used in order to improve the global analyses used as the boundary conditions of the simulations. In order to make it possible with the use of ECMWF emos libraries, a new program has been prepared. This program allows the conversion of the binary codified BUFR file to specific ascii format that MM5 module comprises.

In order to apply FDDA technique in MM5 simulations two different modifications has been made. First one consists on the modification of the boundary conditions of the simulations. In this case, the rainy type provided by satellite information was used to modify directly the vertical humidity profile of the boundary conditions. Second modification has been made in the observational nudging. MM5 humidity prognostic variable

is the mixing ratio. A modification of various subroutines of the MM5 model have been done in order to transform satured satellite-based information to the correspondent mixing ratio value into the model grid-point.

At the same time, Vis5d userfuncs have been prepared such as: azimuthal averaged vertical cross sections following a given trajectory, meteograms, soundings and grid-volume energy computations.

MM5 model is able to simulate the medicane cases as a small, strong vortex related to strong winds and precipitation. Simulation of 950116 case presents the most similar structure to a tropical-like storm. On verticals profiles of the storm, one can see patterns such as an eye-wall structure as a moist saturated area close to the centre characterised by strong up-drafts; warm core and vertical structure. However, due to the lack of observations in the maritime areas, a validation of the simulations can not be properly done. Moreover, MM5 model trajectory simulations of the cases differ significantly from the satellite-based observed ones and also exists an important delay between simulated and satellite-based observed evolutions. These significant differences between simulations and observed cases could be related to the difficult to obtain a more realistic representation of important fields like relative humidity profiles and SST over maritime areas as initial conditions in the simulations.

MM5 model is able to simulate a medicane structure in both September 1996 and October 2003 environments. Simulated tropical-like storms, however, present some differences from the observed path in satellite imagery. Simulated systems evolve more slowly, and for the October 2003 case, the storm is generated in a wrong zone. Medicanes have been shown as a meteorological feature able to increase significantly surface heat and moisture fluxes.

In order to avoid computational limitations, MM5 FDDA code should be modified to allow the nudging of higher amount of data independently of computer characteristics. Other modelling analyses such as the sensitivity to other parametrisation schemes (cumulus, explicit rain) and nudging parameters (time-window, radius of influence) should also be carried out in further steps of the study. The sensitivity of the assimilation technique to different convective/stratiform vertical humidity profiles as well as different temporal and spatial resolutions of the ingested satellite-derived data should also be established. Satellite based observational nudging could be applied in the initial steps of operational forecasts at national weather services or research centres. For the selected cases, FDDA technique has a higher sensitivity on horizontal spatial resolution of the assimilated satellite/lightning data rather than on its temporal resolution.

7.8.2 Piecewise PV inversion

Piecewise PV Inversion techniques, combined with perturbed numerical simulations, have been used as a tool to dynamically study various features of atmospherics systems. These techniques can offer useful information about mechanisms and roles of a wide range of features involved in the life cycle of the disturbances. Although numerical solutions to well-defined inversion equations are determined, some uncertainties and subjectivities arise in its application. Some of these case-dependent aspects are: computation of a reference state from which to define the PV anomalies (zonal mean, temporal mean, number of members to establish an average, etc.), morphology and magnitude of the anomalies, and degree of modification of the initial conditions. In the present study an objective procedure has been proposed as a method to quantify the latter aspect of the technique. In this way, one can diminish the ambiguity on the use of the PV Inversion technique applied to modify the initial conditions of numerical simulations.

It is proposed to use the total Mean Absolute Variation (MAV) of energy introduced, due to the modification of the initial conditions. The Root Mean Square Variation (RMSV) could have been proposed, but by squaring the values, contributions of big and small energetic variation values are differently, weighted in the RMSV calculation. The partition of the energy into mechanical, internal and kinetical energies can be useful information from which a deeper understanding of the role of the collection of features can be obtained.

Finally, the proposed quantification method of the piecewise PV inversion derived perturbations can be applied as a general methodology in dynamic meteorology. The application to various events would allow an objective intercomparison between cases, independent of the morphology, characteristics and origin of the selected anomalies. This method of quantification could contribute to the PV study and analysis based on the most important features involved in the evolution of the cyclones or other atmospheric phenomena.

7.8.3 Factor Separation

The Lagrangian application of the FS gives the opportunity to study the system as itself, since computations of values are made from grid points located within a similar dynamical environment. At the same time, it allows the study of specific spatial-correlated dynamics like air-sea interaction. However, a Lagrangian FS does not give any information related to spatial effects of the factors. For that reason, in order to complete the study, Lagrangian FS results should be accompanied with some information about the simulated trajectories.

At the same way, azimuthal averaged cross sections has been shown as a possible way

to obtain a wide and deep view of the three-dimensional processes that are involved in an atmospheric system following a Lagrangian application of the FS technique.

7.9 Final remarks by the Author

Use of new approaches, different applications and/or daring use of numerical techniques bring some success and more challenge. In presented studies, according to the knowledge of the author, different scopes of known problems have been provided such us: objective quantification of the modification throughout piecewise PV inversion technique, Lagrangian application of the factor separation, four factor separation sensitivities, satellite rain derived information on MM5 simulations and statistical tools to compare trajectories. However, new perspectives give different or modified questions that they have not been completely solved.

Author recognises that some of the directions, towards which the presented studies appointed, keep partially unsolved. Limited base of knowledge of the author is the main reason of these undetermined, not physical reason given and/or not deeply analysed aspects. This is certainly a big disillusion and something important to make notice. But in contrast, this aims the author to: keep acquiring more knowledge that should allow the explanation of unsolved aspects, follow a creative scientific way from which 'new' methodologies are proposed and provide new open questions to the scientific community.

Author also recognises the positive fact that is intrinsic of the *Grup de Meteorologia del departament de física de la Universitat de les Illes Balears*. Due to the wide, deep and solid experience of the research team in which the research has been done, author has been able to deal and propose the studies here presented. Discussions, revisions and base of knowledge has been essential to properly develop the research of the Author.

The Portland group compiler is the only licensed software used in all the presented studies. All graphics produced by the author have been drawn with the open source gnuplot tool. All documents and presentations during the period of research have been designed with LaTeX(one presentation was made in html). Computational resources, scripts and work have been based on PC-Linux platform, self-made Fortran programs and distinct shell and AWK self-made modules.

Appendix A

Statistics of trajectories

A.1 Minimum BIAS

The $\mathcal{BIAS}_{dist}$ between satellite-derived medicane trajectory $\mathcal{TRJ}_{ref}$ and trajectory of simulation used to compare $\mathcal{TRJ}_{com}$ is given by:

$$\mathcal{BIAS}_{dist} = \frac{1}{n}\sum_{t=1}^{n}\delta r(t) \tag{A.1.1}$$

where $\delta r(t) = \sqrt{\delta x(t)^2 + \delta y(t)^2}$ is the distance at time t between $\mathcal{TRJ}_{ref}$ and $\mathcal{TRJ}_{com}$. In the expression $\delta æ(t) = æ_{ref}(t) - æ_{com}(t)$, difference between $æ = [x, y]$ coordinates of the trajectories. Assuming morphological differences and different evolving zones of the trajectories, as well as different speeds of evolution of the compared medicanes, $\mathcal{BIAS}_{dist}$ would generally present a dependence on temporal shift of $\mathcal{TRJ}_{com}$. Temporal shift τ for which $\mathcal{BIAS}_{dist}$ becomes minimum (see equation A.1.2), provides an idea of this difference between translational speeds. Temporal range $\tau = [-n/2, n/2]$ is used (n number of total time-steps of length Δt) for the inspection for the adequate τ that minimise $\mathcal{BIAS}_{dist}$. Taking as inspection limits of $\pm n/2$, it is ensured a minimum number of trajectories values (n) for the statistical computation:

$$\mathcal{BIAS}^{min}_{dist} = min\left[\frac{1}{n}\sum_{t=1}^{n}\sqrt{\delta x(t,\tau)^2 + \delta y(t,\tau)^2}\right] \tag{A.1.2}$$

where $\delta æ(t,\tau) = æ_{ref}(t) - æ_{com}(t \pm \tau)$, differences between coordinates $æ = [x, y]$ of trajectory $\mathcal{TRJ}_{ref}$ at time t and trajectory $\mathcal{TRJ}_{com}$ shifted $\pm\tau = n\Delta t$, n time steps of Δt length.

A.2 Distance Correlation

Correlation (classical definition, or Pearson correlation) between satellite-derived trajectory and simulated one is given by:

$$\mathcal{R} = \frac{< \mathcal{D}_{ref}\mathcal{D}_{com} > - < \mathcal{D}_{ref} >< \mathcal{D}_{com} >}{\sigma_{\mathcal{D}_{ref}}\sigma_{\mathcal{D}_{com}}} \tag{A.2.3}$$

where $\sigma_{\mathcal{D}_\chi} = \sqrt{< \mathcal{D}_\chi^2 > - < \mathcal{D}_\chi >^2}$, standard deviation of trajectory χ, and $< \mathcal{D}_\chi >$ average position of trajectory $\chi = [ref, com]$ (equation A.2.4), and $< \mathcal{D}_\chi^2 >$, averaged quadratic distance of trajectory χ

$$< \mathcal{D}_\chi >= \frac{1}{n}\sum_{t=1}^{n} \mathcal{D}_\chi = \frac{1}{n}\sum_{t=1}^{n} \sqrt{x(t)_\chi^2 + y(t)_\chi^2} \tag{A.2.4}$$

$$< \mathcal{D}_\chi^2 >= \frac{1}{n}\sum_{t=1}^{n} \mathcal{D}_\chi^2 = \frac{1}{n}\sum_{t=1}^{n} x(t)_\chi^2 + y(t)_\chi^2 \tag{A.2.5}$$

$$< \mathcal{D}_{ref}\mathcal{D}_{com} >= \frac{1}{n}\sum_{t=1}^{n} \mathcal{D}_{ref}\mathcal{D}_{com} \tag{A.2.6}$$

A.3 Pure coordinate Correlation

It is a classical or Pearson correlation (see equation A.2.3) between observed and simulated trajectory coordinate series is computed as the correlation of two vectors ($\mathcal{R}$) made of the (x, y) coordinate series of both trajectories. With the statistics $\sigma_{\mathcal{R}_\chi} = \sqrt{< \mathcal{R}_\chi^2 > - < \mathcal{R}_\chi >^2}$, Standard deviation of trajectory χ, and $< \mathcal{R}_\chi >$ average value of trajectory $\chi = [ref, com]$ (equation A.3.8), and $< \mathcal{R}_\chi^2 >$, quadratic average value of trajectory χ

$$\mathcal{R}_\chi = \frac{1}{2n}\sum_{t=1}^{2n} R(t)_\chi \tag{A.3.7}$$

$$\mathcal{R}_\chi^2 = \frac{1}{2n}\sum_{t=1}^{2n} R(t)_\chi^2 \tag{A.3.8}$$

$$\mathcal{R}_{ref}\mathcal{R}_{com} = \frac{1}{2n}\sum_{t=1}^{2n} R(t)_{ref}R(t)_{com} \tag{A.3.9}$$

$$\tag{A.3.10}$$

where

$$R_\chi = (\mathcal{X}_{com}, \vec{\mathcal{Y}}_{com}) = (x_\chi^{t=1}, \cdots, x_\chi^{t=n}, y_\chi^{t=1}, \cdots, y_\chi^{t=n}) \tag{A.3.11}$$

A.3.1 Bias correction

The total bias $\mathcal{BIAS}_{ref}^{com}$ between compared and reference trajectories is defined as:

$$\mathcal{BIAS}_{ref}^{com} = \mathcal{BIAS}(x)_{ref}^{com} + \mathcal{BIAS}(y)_{ref}^{com} \tag{A.3.12}$$

where $\mathcal{BIAS}(æ)_{ref}^{com}$, BIAS of coordinate $æ = [x, y]$ is given by:

$$\mathcal{BIAS}(æ)_{ref}^{com} = \frac{1}{n}\sum_{t=1}^{n} æ(t)_{ref} - æ(t)_{com} \tag{A.3.13}$$

Trajectory of comparison $\mathcal{TRJ}_{com} = \left(\mathcal{X}_{com}, \vec{\mathcal{Y}}_{com}\right)$ is corrected with the $\mathcal{BIAS}(æ)_{ref}^{com}$ according to:

$$\tilde{\mathcal{TRJ}}_{com} = \left(\vec{\mathcal{X}_{com}} - \mathcal{BIAS}(\mathcal{X})_{ref}^{com}\ ,\ \vec{\mathcal{Y}_{com}} - \mathcal{BIAS}(\mathcal{Y})_{ref}^{com}\right) \tag{A.3.14}$$

A.3.2 BIAS temporal lack correction

Following $\mathcal{BIAS}_{ref}^{com}$ correction of trajectory $\tilde{\mathcal{TRJ}}_{com}$, a set of temporal shifts are performed in the trajectory ($\tilde{\mathcal{TRJ}}_{com}(\pm\tau)$) in order to obtain the τ value from which the pure coordinate correlation $\mathcal{PR}$ becomes the highest one ($\mathcal{PR}_{bias}^{max}$, see expression A.3.15). The obtained τ value provides a guidance of the temporal shift between simulated and observed trajectories:

$$\begin{aligned} \mathcal{PR}_{bias}^{max} &= max\left(\mathcal{PR}\right)[\pm\tau] = \\ max\Big([&< \mathcal{X}_{ref} > - < \tilde{\mathcal{X}}(\pm\tau)_{com} >] + \\ [&< \mathcal{Y}_{ref} > - < \tilde{\mathcal{Y}}(\pm\tau)_{com} >]\Big) \end{aligned} \tag{A.3.15}$$

Bibliography

Aebishcer, U. and Schär, C., 1998: *Low-Level Potential Vorticity and Cyclogenesis to the Lee of the Alps*, J. Atmos. Sci., **55**, 186207.

Alonso, S., Portela, A., and Ramis, C., 1994: *First considerations on the structure and development of the Iberian thermal low-pressure system*, Ann. Geophys., **12**, 457–468.

Alpert, P. and Ziv, B., 1989: *The Sharav cyclone - Observations and some theorethical considerations*, J. Geophys. Res., **94**, 18 49518 514.

Alpert, P., Neeman, B. U., and Shay-El, Y., 1990: *Climatological analysis of Mediterranean cyclones using ECMWF data*, Tellus, **42A**, 65–77.

Alpert, P., Tsidulko, M., Kirchak, S., and Stein, U., 1995: *A multi-stage evolution of an ALPEX cyclone*, Tellus, **48A**, 209–220.

Alpert, P., Ben-gai, T., Baharad, A., Benjamini, Y., Yekutieli, D., Colacino, M., Diodato, L., Ramis, C., Homar, V., Romero, R., Michaelides, S., and Manes, A., 2002: *The paradoxical increase of Mediterranean extreme daily rainfall in spite of decrease in total values*, Geophys. Res. Lett., **29**, 1–4, doi:10.1029/2001GL013554.

Amengual, A., Romero, R., Gómez, M., Martn, A., and Alonso, S., 2007: *A hydrometeorological modeling study of a flash flood event over Catalonia, Spain*, J. Hydrometeorol., **8**, 282–303.

Arfken, G., 1985: Mathematical Methods for Physicists, 3rd ed., Orlando, FL: Academic Press.

Argence, S., Lambert, D., Richard, E., Söhne, N., Chaboureau, J.-P., Crépin, F., and Arbogast, P., 2006: *High resolution numerical study of the Algiers 2001 flash flood: sensitivity to the upper-level potential vorticity anomaly*, Adv. in Geosci., **7**, 251–257.

Barker, D., Huang, W., Guo, Y.-R., and Bourgeois, A., 2003: *A three-dimensional Variational (3DVAR) Data Assimilation System for use with MM5*, NCAR Technical Note, **NCAR/TN-453+STR**, 68pp.

Barrett, R., Berry, M., Chan, T. F., Demmel, J., Donato, J., Dongarra, J., Eijkhout, V., Pozo, R., Romine, C., and Van der Vorst, H., 1994: Templates for the Solution of Linear Systems: Building Blocks for Iterative Methods, SIAM (http://www.netlib.org/linalg/html_templates/Templates.html).

Bender, M. A., Tuleya, R. E., and Kurihara, Y., 1987: *A numerical study of the effect of island terrain on tropical cyclones*, Mon. Weather Rev., **115**, 130–155.

Bister, M. and Emanuel, K. A., 1998: *Dissipative Heating and Hurricane Intensity*, Meteorol. Atmos. Phys., **50**, 2662–2682.

Blackadar, A., 1979: *High resolution models of the planetary boundary layer*, Advances in Environmental Science and Engineering 1, **1**, 5085.

Bleck, R., 1990: *Depiction of upper/lower vortex interaction associated with extratropical cyclogenesis*, Mon. Weather Rev., **118**, 573–585.

Bluestein, H. B., 1992: Synoptic-Dynamic Meteorology in Midlatitudes. Volume 1, Oxford university press, Inc.

Bretherton, F. P., 1966: *Critical layer instability in baroclinic flows*, Q. J. Roy. Meteor. Soc., **92**, 325–334.

Businger, S. and Reed, R. J., 1989: *Cyclogenesis in cold air masses*, Weather Forecast., **4**, 133–156.

Buzzi, A. and Speranza, A., 1983: *Cyclogenesis in the lee of the Alps*, Mesoscale meteorology - Theories, observations and models; Proceedings of the Advanced Study Institute, **1**, 55–142.

Buzzi, A. and Tibaldi, S., 1978: *Cyclogenesis in the lee of Alps: A case study*, Q. J. Roy. Meteor. Soc., **104**, 271–287.

Campins, J., Genovés, A., Jansà, A., Guijarro, J. A., and Ramis, C., 2000: *A catalogue and a classification of surface cyclones for the western Mediterranean*, Int. J. Climatol., **20**, 969–984.

Campins, J., Jansà, A., and Genovés, A., 2006: *Three-dimensional structure of western Mediterranean cyclones*, Int. J. Climatol., **26**, 323–343.

Charney, J. G., 1955: *The use of primitive equations of motion in numerical prediction*, Tellus, **7**, 22–26.

Charney, J. G. and Eliassen, A., 1964: *On the Growth of the Hurricane Depression*, J. Atmos. Sci., **21**, 68–75, doi:10.1175/1520-0469(1964)021⟨0068:OTGOTH⟩2.0.CO;2.

Cucurull, L., Vandenberghe, F., Barker, D., Vilaclara, E., and Rius, A., 2004: *Three-Dimensional Variational Data Assimilation of Ground-Based GPS ZTD and Meteorological Observations during the 14 December 2001 Storm Event over the Western Mediterranean Sea*, Mon. Weather Rev., **132**, 749–763, doi:10.1175/1520-0493(2004)132⟨0749:TVDAOG⟩2.0.CO;2.

Davis, C. A. and Emanuel, K. A., 1991: *Potential vorticity diagnostics of cyclogenesis*, Mon. Weather Rev., **119**, 1929–1953.

Davolio, S. and Buzzi, A., 2004: *A nudging scheme for the assimilation of precipitation data into a mesoscale model*, Weather Forecast., **19**, 855–871.

Doswell, C. A., Ramis, C., Romero, R., and Alonso, S., 1997: *A Diagnostic Study of Three Heavy Precipitation Episodes in the Western Mediterranean Region*, Weather Forecast., **13**, 102–124.

Ducrocq, V., Ricard, D., Lafore, J., and Orain, F., 2002: *Storm-Scale Numerical Rainfall Prediction for Five Precipitating Events over France: On the Importance of the Initial Humidity Field*, Weather Forecast., **17**, 1236–1256, doi:10.1175/1520-0434(2002)017⟨1236:SSNRPF⟩2.0.CO;2.

Dudhia, J., 1989: *Numerical Study of Convection Observed during the Winter Monsoon Experiment Using a Mesoscale Two-Dimensional Model*, J. Atmos. Sci., **46**, 3077–3107, doi:10.1175/1520-0469(1989)046⟨3077:NSOCOD⟩2.0.CO;2.

Dudhia, J., 1996: *A multi-layer soil temperature model for MM5*, Preprints.from the Sixth PSU/NCAR Mesoscale Model Users'Workshop 22-24, p. http://www.mmm.ucar.edu/mm5/lsm/soil.pdf.

Egger, J., Alpert, P., Tafferner, A., and Ziv, B., 1995: *Numerical experiments on the genesis of Sharav cyclones: Idealized simulations*, Tellus, **47A**, 162174.

Emanuel, K., 2003: *Tropical Cyclones*, Annu. Rev. Earth. Pl. Sc., **31**, 75–104.

Emanuel, K. A., 1983: *On Assessing Local Conditional Symmetric Instability from Atmospheric Soundings*, Mon. Weather Rev., **111**, 2016–2033, doi:10.1175/1520-0493(1983)111⟨2016:OALCSI⟩2.0.CO;2.

Emanuel, K. A., 1986: *An Air-Sea Interaction Theory for Tropical Cyclones. Part I: Steady-State Maintenance*, J. Atmos. Sci., **43**, 585–604.

Emanuel, K. A., 1995: *The Behavior of a Simple Hurricane Model Using a Convective Scheme Based on Subcloud-Layer Entropy Equilibrium*, J. Atmos. Sci., **52**, 3960–3968.

Emanuel, K. A., 2005: *Genesis and maintenance of "Mediterranean hurricanes"*, Adv. in Geoscie., **2**, 217–220.

Ernst, J. A. and Matson, M., 1983: *A Mediterranean tropical storm?*, Weather, **38**, 332–337.

Ertel, H., 1942: *Ein neuer hydrodynamischer wirbelsatz*, Meteor. Z., **59**, 271–281.

Evensen, G., 2003: *The Ensemble Kalman Filter: theoretical formulation and practical implementation*, Ocean Dynamics, **53**, 343367, doi:10.1007/s10236-003-0036-9.

Fan, X. and Tilley, J. S., 2002: *The impact of assimilating satellite-derived humidity on MM5 forecasts*, MM5 forecasts. Preprints, 15th Conference on Numerical Weather Prediction, AMS, 12-15 August, San Antonio, TX, pp. 47–50.

Fita, L., Romero, R., and Ramis, C., 2006: *Intercomparison of intense cyclogenesis events over the Mediterranean basin based on baroclinic and diabatic influences*, Adv. in Geosci. (Proccedings PLINIUS 2006), **7**, 333–342.

Fita, L., Romero, R., Luque, A., Emanuel, K., and Ramis, C., 2007a: *Analysis of the environments of seven Mediterranean tropical-like storms using an axisymmetric, non-hydrostatic, cloud resolving model*, Nat. Hazard. Earth Sys., **7**, 1–16.

Fita, L., Romero, R., and Ramis, C., 2007b: *Objective quantification of perturbations produced with a piecewise PV Inversion technique*, Ann. Geophys., **25**, 2335–2349.

Fita, L., Romero, R., Luque, A., and Ramis, C., 2008a: *Effects on numerical simulations of tropical-like Mediterranean storms of assimilating precipitation zones derived from satellite and lightning data*, Ann. Geophys., **submitted**.

Fita, L., Romero, R., and Ramis, C., 2008b: *Sensitivity study of tropical-like storms. part I: Sensitivity of air-sea mechanism in three storms*, Ann. Geophys., **submitted**.

Fita, L., Romero, R., and Ramis, C., 2008c: *Sensitivity study of tropical-like storms. part II: Air-sea mechanism in the muter phase of January 1995 medicane*, Ann. Geophys., **submitted**.

Font, L., 1983: Climatología de España y Portugal., Instituto Nacional de Meteorologa.

Gaertner, M. A., Jacob, D., Gil, V., nguez, M. D., Padorno, E., and Sánchez, E., 2007: *Tropical cyclones over the Mediterranean Sea in climate change simulations*, Geophys. Res. Lett., **34**, L14 711, doi:10.1029/2007GL029977.

García-Ortega, E., Fita, L., Romero, R., López, L., Ramis, C., and Sánchez, J., 2007: *Numerical simulation and sensitivity study of a severe hail-storm in northeast Spain*, Atmos. Res., **83**, 225–241, doi:10.1016/j.atmosres.2005.08.004.

Gayà, M., Homar, V., Romero, R., and Ramis, C., 2001: *Tornadoes and waterspouts in the Balearic Islands: Phenomena and environment characterization*, Atmos. Res., **56**, 253–267.

Grell, G., Dudhia, J., and Stauffer, D., 1994: *A description of the fifth-generation Penn State/NCAR mesoscale model (MM5)*, NCAR Technical Note, **NCAR/TN-398+STR**, 117pp.

Grell, G. A., Dudhia, J., and Stauffer, D. R., 1995: *A description of the Fifth-generation Penn State/NCAR Mesoscale Model (MM5)*, NCAR Technical Note, **NCAR/TN-398+STR**, 122pp.

Grell, G. A., Emeis, S., Stockwell, W. R., Schoenemeyer, T., Forkel, R., Michalakes, J., Knoche, R., and Seidl, W., 2000: *Application of a multiscale, coupled MM5/chemistry model to the complex terrain of the VOTALP valley campaign*, Atmospheric Environment, **34**, 1435–1453, doi:10.1016/S1352-2310(99)00402-1.

Gyakum, J. R., 1983a: *On the Evolution of the QE II Storm. I: Synoptic Aspects*, Mon. Weather Rev., **111**, 1137–1155.

Gyakum, J. R., 1983b: *On the Evolution of the QE II Storm. II: Dynamic and Thermodynamic Structure*, Mon. Weather Rev., **111**, 1156–1173.

Hakim, G. J., Keyser, D., and Bosart, L. F., 1996: *The Ohio valley wave-merger cyclogenesis event of 25-26 january 1978. Part II: Diagnosis using quasigeostrophic potential vorticity inversion*, Mon. Weather Rev., **124**, 2176–2205.

Holton, J., 1979: An introduction to dynamic meteorology, Academic Press Inc.

Homar, V., Ramis, C., Romero, R., Alonso, S., a Moya, J. G., and Alarcón, M., 1999: *A case of convection development over the western Mediterranean sea: A study through numerical simulations*, Meteorol. Atmos. Phys., **71**, 169–188.

Homar, V., Ramis, C., and Alonso, S., 2002a: *A deep cyclone of African origin over the Western Mediterranean: diagnosis and numerical simulation*, Ann. Geophys., **20**, 93–106.

Homar, V., Romero, R., Ramis, C., and Alonso, S., 2002b: *Numerical study of the October 2000 torrential precipitation event over eastern Spain: Analysis of the synoptic-scale stationarity*, Ann. Geophys., **20**, 2047–2066.

Homar, V., Gayà, M., Romero, R., Ramis, C., and Alonso, S., 2003a: *Tornadoes over complex terrain: An analysis of the 28th August 1999 tornadic event in eastern Spain*, Atmos. Res., **67-68**, 301–317, doi:10.1016/S0169-8095(03)00064-4.

Homar, V., Romero, R., Stensrud, D., Ramis, C., and Alonso, S., 2003b: *Numerical diagnosis of a small, quasi-tropical cyclone over the western Mediterranean: Dynamical vs. boundary factors*, Q. J. Roy. Meteor. Soc., **129**, 1469–1490.

Hong, S.-Y. and Pan, H.-L., 1996: *Nonlocal boundary layer vertical diffusion in a medium-range forecast model*, Mon. Weather Rev., **124**, 2322–2339.

Horvath, K., Fita, L., Romero, R., and Ivancan-Picek, B., 2006: *A numerical study on the first phase of a deep Mediterranean cyclone: Cyclogenesis in the lee of the Atlas Mountains*, Meteorologische Z. 1, **15**, 133–146, doi:10.1127/0941-2948/2006/0113.

Hoskins, B. J., McIntyre, M. E., and Robertson, A. W., 1985: *On the use and significance of isentropic potential vorticity maps*, Q. J. Roy. Meteor. Soc., **111**, 877–946.

Houssos, E. E., Lolis, C. J., and Bartzokas, A., 2007: *The atmospheric conditions over Europe and the Mediterranean, favoring snow events in Athens, Greece*, Adv. in Geoscie., **12**, 127–135.

Huo, Z., Zhang, D.-L., Gyakum, J. R., and Stainforth, A. N., 1995: *A diagnostic analysis of the superstorm of march 1993*, Mon. Weather Rev., **123**, 1740–1761.

Huo, Z., Zhang, D.-L., and Gyakum, J., 1998: *An Application of Potential Vorticity Inversion to Improving the Numerical Prediction of the March 1993 Superstorm*, Mon. Weather Rev., **126**, 424–436, doi:10.1175/1520-0493(1998)126⟨0424:AAOPVI⟩2.0.CO;2.

Huo, Z., Zhang, D.-L., Gyakum, J. R., and Stainforth, A. N., 1999: *Interaction of potential vorticity anomalies in extratropical cyclogenesis. Part II: Sensitivity to initial perturbations*, Mon. Weather Rev., **127**, 2563–2575.

Ikawa, M. and Saito, K., 1991: *Description of a nonhydrostatic model developed at the forecast research department of the MRI*, Technical Reports of the Meteorological Research Institute, **28**.

IPCC, 2007: Climate Change 2007: The Physical Science Basis. Contribution of Working Group I to the Fourth Assessment Report of the Intergovernmental Panel on Climate Change, [Solomon, S., D. Qin, M. Manning, Z. Chen, M. Marquis, K.B. Averyt,M. Tignor and H.L. Miller (eds.)] Cambridge University Press, Cambridge, United Kingdom and New York, NY, USA.

Janjić, Z. I., 1990: *The Step-Mountain Coordinate: Physical Package*, Mon. Weather Rev., **118**, 1429–1443.

Janjić, Z. I., 1994: *The Step-Mountain Eta Coordinate Model: Further Developments of the Convection*, Mon. Weather Rev., **122**, 927–945.

Jordan, C. L., 1958: *Mean Soundings for the West Indies Area*, J. Meteorol., **15**, 91–97.

Kain, J. S., 2004: *The Kain-Fritsch Convective Parameterization: An Update*, K. Appl. Meteorol., **43**, 170–181.

Kain, J. S. and Fritsch, J. M., 1990: *A one-dimensional entraining/detraining plume model and its application in convective parameterization*, J. Atmos. Sci., **47**, 2748–2802, doi:10.1175/1520-0469(1990)047⟨2784:AODEPM⟩2.0.CO;2.

Kain, J. S. and Fritsch, J. M., 1993: *Convective parameterization for mesoscale models: The Kain-Fritsch scheme*, The Representation of Cumulus Convection in Numerical Models, Meteor. Monogr., **No. 24**, 165–170.

Kidd, C., Kniveton, D. R., Todd, M. C., and Bellerby, T. J., 2003: *Satellite Rainfall Estimation Using Combined Passive Microwave and Infrared Algorithms*, J. Hydrometeorol., **4**, 1088–1104.

Krichak, S. O. and Alpert, P., 2002: *A fractional approach to the factor separation method*, J. Atmos. Sci., **59**, 2243–2252.

Krichak, S. O., Tsidulko, M., and Alpert, P., 2004: *Monthly Synoptic Patterns Associated with Wet/Dry Conditions in the Eastern Mediterranean*, Theo. Appl. Climatolo., **65**, 215–229.

Kuo, Y. A., Shapiro, M. A., and Donall, E. G., 1991a: *The interaction between baroclinic and diabatic processes in a numerical simulation of a rapidly intensifying extratropical marine cyclone*, Mon. Weather Rev., **119**, 368–384.

Kuo, Y.-H., Reed, R. J., and Low-Nam, S., 1991b: *Effects of surface energy fluxes during the early development and rapid intensification stages of seven explosive cyclones in the western Atlantic*, Mon. Weather Rev., **119**, 457–476.

Lagouvardos, K. and Kotroni, V., 2005: *Improvement of high-resolution weather forecasts through humidity adjustment based on satellite data*, Q. J. Roy. Meteorol. Soc., **131**, 2695–2712.

Lagouvardos, K., Kotroni, V., Nickovic, S., Jovic, D., and Kallos, G., 1999: *Observations and model simulations of a winter sub-synoptic vortex over the central Mediterranean*, Meteorol. Appl., **6**, 371–383.

Leslie, L. M., LeMarshall, J. F., Morison, R. P., Spinoso, C., Purser, R., Pescod, N., and Seecamp, R., 1998: *Improved Hurricane Track Forecasting from the Continuous Assimilation of High Quality Satellite Wind Data*, Mon. Weather Rev., **126**, 1248ŏ20131 258, doi:10.1175/1520-0493(1998)126⟨1248:IHTFFT⟩2.0.CO;2.

Lilly, D. K., 1962: *On the numerical simulation of bouyant convection*, Tellus, **14**, 148–172.

Liu, Y., Zhang, D., and Yau, M. K., 1997: *A Multiscale Numerical Study of Hurricane Andrew (1992). Part I: Explicit Simulation and Verification*, Mon. Weather Rev., **125**, 3073–3093.

Lorenc, A. C., Ballard, S. P., Bell, R. S., Ingleby, N. B., Andrews, P. L. F., Barker, D. M., Bray, J. R., Clayton, A. M., Dalby, T., Li, D., Payne, T. J., and Saunders, F. W., 2000: *The Met. Office global three-dimensional variational data assimilation scheme*, Q. J. Roy. Meteor. Soc., **126**, 2991–3012.

Lorenz, E. N., 1963: *Deterministic Nonperiodic Flow*, J. Atmos. Sci., **20**, 130–141.

Lorenz, E. N., 1991: *Dimension of weather and climate attractors*, Nature, **353**, 241–244.

Louis, J.-F., 1979: *A parametric model of vertical eddy fluxes in the atmosphere*, Bound.-Lay. Meteorol., **17**, 187–202, doi:10.1029/2004GL019821.

Luque, A., Fita, L., Romero, R., and Alonso, S., 2007: *Tropical-like Mediterranean Storms: An Analysis from satellite*, Proceedings. 2007 Joint EUMETSAT/AMS Conference – Amsterdam, pp. 1–7.

Maheras, P., Flocas, H. A., Patrikas, I., and Anagnostopoulou, C., 2001: *A 40 year Objective climatology of Surface Cyclones in the Mediterranean Region: Spatial and Temporal Distribution*, Int. J. Climatol., **21**, 109–130.

Mak, M., 1997: *Influence of Surface Sensible Heat Flux on Incipient Marine Cyclogenesis*, J. Atmos. Sci., **55**, 820–834.

Martín, A., Romero, R., Homar, V., de Luque, A., and Alonso, S., 2007: *Sensitivities of a Flash Flood Event over Catalonia: A Numerical Analysis*, Mon. Weather Rev., **135**, 651–669, doi:10.1175/MWR3316.1.

Mellor, G. L. and Yamada, T., 1982: *Development of a turbulence closure model for geophysical fluid problems*, Rev. Geophys., **20**, 851–875.

Molteni, F., Buizza, R., Palmer, T. N., and Petroliagis, T., 1996: *The ECMWF Ensemble Prediction System: Methodology and validation*, Q. J. Roy. Meteor. Soc., **122**, 73–119, doi:10.1002/qj.49712252905.

Monserrat, S., Vilibić, I., and Rabinovich, A. B., 2006: *Meteotsunamis: atmospherically induced destructive ocean waves in the tsunami frequency band*, Nat. Hazard. Earth Syst. Sci., **6**, 1035–1051.

Montgomery, M. T. and Farrell, B. F., 1992: *Polar Low Dynamics*, J. Atmos. Sci., **49**, 2484–2505.

Ooyama, K., 1964: *A dynamical model for the study of tropical cyclone development*, Geofis. Int, **4**, 187–198.

Orlandi, A., Ortolani, A., Meneguzzo, F., Levizzani, V., Torricella, F., and Turk, F. J., 2004: *Rainfall assimilation in RAMS by means of the Kuo parameterisation inversion: method and preliminary results*, J. Hydrol., **288**, 20–35.

Pettersen, S. and Smebye, S. J., 1971: *On the development of extratropical cyclones*, Q. J. Roy. Meteor. Soc., **97**, 457–482.

Phillips, N. A., 1954: *Energy transformations and meridional circulations associated with simple baroclinic waves in a two-level, quasi-geostrophic model*, Tellus, **6**, 273–286.

Picornell, M. A., Jansà, A., Genovés, A., and Campins, J., 2001: *Automated database of mesocyclones from the Hirlam(INM)-0.5° analyses in the Western Mediterranean*, Int. J. Climatol., **21**, 335–354.

Pytharoulis, I., Craig, G. C., and Ballard, S. P., 2000: *The hurricane-like Mediterranean cyclone of January 1995*, Meteorol. Appl., **7**, 261–279.

Rabier, F., Thépaut, J.-N., and Courtier, P., 1998: *Extended assimilation and forecast experiments with a four-dimensional variational assimilation system*, Q. J. Roy. Meteor. Soc., **124**, 1861–1887.

Rabier, F., Järvinen, H., Klinker, E., Mahfouf, J.-F., and Simmons, A., 2000: *The ECMWF operational implementation of four-dimensional variational assimilation. I: Experimental results with simplified physics*, Q. J. Roy. Meteor. Soc., **126**, 1143–1170.

Ramis, C. and Jansà, A., 1983: *Condiciones meteorológicas simultáneas a la aparicioón de oscilaciones del nivel del mar de amplitud extraordinaria en el Mediterráneo occidental*, Rev. Geofísica (in spanish), **39**, 3542.

Ramis, C., Romero, R., Homar, V., Alonso, S., and Alarcón, M., 1998: *Diagnosis and Numerical simulation of a Torrential Precipitation Event in Catalonia (Spain)*, Meterol. Atmos. Phys., **69**, 1–21.

Ramis, C., López, J., and Arús, J., 1999: *Two cases of severe weather in Catalonia (Spain): a diagnostic study*, Meteorol. Appl., **6**, 11–27.

Rasmussen, E. and Zick, C., 1987: *A subsynoptic vortex over the Mediterranean with some resemblance to polar lows*, Tellus A, **39**, 408–425.

Reed, R. J., Stoelinga, M. T., and Kuo, Y.-H., 1992: *A model-aided study of the origin and evolution of the anomalously high potential vorticity in the inner region of a rapidly deeping marine cyclone*, Mon. Weather Rev., **120**, 893–913.

Reed, R. J., Kuo, Y.-H., Albright, M. D., Gao, K., Gua, Y.-R., and Huang, W., 2001: *Analysis and modeling of a tropical-like cyclone in the Mediterranean Sea*, Meteorol. Atmos. Phys., **76**, 183–202.

Reiser, H. and Kutiel, H., 2007a: *The rainfall regime and its uncertainty in Valencia and Larnaca*, Adv. in Geosci., **12**, 101106, doi:10.1029/2004GL019821.

Reiser, H. and Kutiel, H., 2007b: *Rainfall uncertainty in the Mediterranean: definition of the rainy season a methodological approach*, Theor. Appl. Climatol., pp. 65–+, doi: 10.1007/s00704-007-0343-z.

Reisner, J., Rasmussen, R., and Bruintjes, R., 1998: *Explicit Forecasting of Supercooled Liquid Water in Winter Storms Using the MM5 Mesoscale Model*, Q. J. Roy. Meteor. Soc., **124**, 1071–1107, doi:10.1002/qj.49712454804.

Reiter, E. R., 1975: Handbook for Forecasters in the Mediterranean: Weather Phenomena of the Mediterranean Basin, Environmental Prediction Research Facility, Naval Postgraduate School, Monterey, CA.

Roberts, R. D. and Rutledge, S., 2003: *Nowcasting Storm Initiation and Growth Using GOES-8 and WSR-88D Data*, Weather Forecast., **18**, 562–584.

Robinson, W. A., 1989: *On the structure of potential vorticity in baroclinic instability*, Tellus, **41A**, 275–284.

Romero, R., 2001: *Sensitivity of a Heavy Rain producing Western Mediterranean cyclone to embedded Potential Vorticity anomalies*, Q. J. Roy. Meteor. Soc., **127**, 2559–2597.

Romero, R., 2008: *A method for quantifying the impacts and interactions of potential vorticity anomalies in extratropical cyclones*, Q. J. Roy. Meteor. Soc., **in press**.

Romero, R. and Emanuel, K., 2006: *Space-time probability density of Mediterranean hurricane genesis in the light of an empirical tropical index*, 5a Assamble Hispano-Portuguesa de Geodesia y Geofisica, **(Spanish)**, 4.

Romero, R., Ramis, C., and Alonso, S., 1997: *Numerical simulation of an extreme rainfall event in Catalonia: Role of orography and evaporation from the sea*, Q. J. Roy. Meteor. Soc., **123**, 537–559.

Romero, R., Guijarro, J. A., Ramis, C., and Alonso, S., 1998: *A 30-year (1964 1993) Daily Rainfall data base for the Spanish Mediterranean regions: first exploratory study*, Int. J. Climatol., **18**, 541560.

Romero, R., Sumner, G., Ramis, C., and Genovés, A., 1999: *A classification of the atmospheric circulation patterns producing significant daily rainfall in the Spanish Mediterranean area*, Int. J. Climatol., **19**, 765–785.

Romero, R., Doswell, C. A., and Ramis, C., 2000: *Mesoscale Numerical Study of Two Cases of Long-Lived Quasi-Stationary Convective Systems over Eastern Spain*, Mon. Weather Rev., **128**, 3731–3751.

Romero, R., Doswell, C., and Riosalido, R., 2001: *Observations and fine-grid simulations of a convective outbreak in northeastern Spain: importance of diurnal forcing and convective cold pools*, Mon. Weather Rev., **129**, 2157–2182.

Rotunno, R. and Emanuel, K., 1987: *An Air-Sea Interaction Theory for Tropical Cyclones. Part II: Evolutionary Study Using a Nonhydrostatic Axisymmetric Numerical Model*, J. Atmos. Sci., **44**, 542–561.

Sánchez, A. C. J. and Fraile, R., 1992: *Statistical comparison of the properties of thunderstorms in different areas around the Ebro Valley (Spain)*, Atmos. Res., **28**, 237–257.

Sánchez, J., García, E., Marcos, J., and Dessens, J., 1999: *Formation of big and giant drops inside Mediterranean convective cells*, Proceedings of the EGS Plinius Conf. Maratea, Italy., **1**, 57–65.

Sanders, F., 1986: *Explosive cyclogensis in the West-central North Atlantic ocean, 1981-84. Part I: Composite structure and mean behavior*, Mon. Weather Rev., **114**, 1781–1794.

Sanders, F. and Gyakum, J. R., 1980: *Synoptic-Dynamic climatology of the 'Bomb'*, Mon. Weather Rev., **108**, 1589–1606.

Schulz, J., Jeans, M., stefan, E., and Schlussel, P., 1996: *Evaluation of satellite derived latent heat flux*, J. Climate, **10**, 2782–2795.

Smagorinsky, J., 1963: *General circulation experiments with the primitive equations.I: The basic experiment*, Mon. Weather Rev., **91**, 99–164.

Stauffer, D. R. and Seaman, N. L., 1990: *Use of Four-Dimensional Data Assimilation in a Limited-Area Mesoscale Model. Part I: Experiments with Synoptic-Scale Data*, Mon. Weather Rev., **118**, 1250–1277, doi:10.1175/1520-0493(1990)118⟨1250:UOFDDA⟩2.0.CO;2.

Stein, U. and Albert, P., 1993: *Factor Separation in Numerical Simulations*, J. Atmos. Sci., **50**, 2107–2115.

Stull, R. B., 1988: An introduction to boundary layer meteorology, Kluwer Academic Publishers.

Tayanç, M., Karaca, M., and Dalfes, H., 1998: *March 1987 Cyclone (Blizzard) over the Eastern Mediterranean and Balkan Region Associated with Blocking*, Mon. Weather Rev., **126**, 3036–3047, doi:10.1175/1520-0493(1998)126⟨3036:MCBOTE⟩2.0.CO;2.

Taylor, K. E., 2001: *Summarizing multiple aspects of model performance in a single diagram*, J. Geophys. Res., **106**, 7183–7192.

Thorpe, A. J., 1986: *Synoptic scale disturbances with circular symmetry*, Mon. Weather Rev., **114**, 1384–1389.

Toth, Z. and Kalnay, E., 1993: *Ensemble Forecasting at NMC: The Generation of Perturbations*, B. Am. Meteorol. Soc., **74**, 2317–2330.

Toth, Z. and Kalnay, E., 1997: *Ensemble Forecasting at NCEP and the Breeding Method*, Mon. Weather Rev., **125**, 3297–3319, doi:10.1175/1520-0493(1997)125⟨3297:EFANAT⟩ 2.0.CO;2.

Tous, M. and Romero, R., 2006: *Towards a European climatology of meteorological parameters associated to the genesis of severe storms*, Tethys, **3**, 9–17, doi:10.3369/tethys. 2006.3.02.

Trigo, I. F., Davies, T. D., and Bigg, G. R., 1999: *Objective Climatology of Cyclones in the Mediterranean Region*, J. Climate, **12**, 1685–1696.

Trigo, I. F., Bigg, G. R., and Davies, T. D., 2002: *Climatology of Cyclogenesis Mechanisms in the Mediterranean*, Mon. Weather Rev., **130**, 549–569.

Tripoli, G. J., Medaglia, C. M., Dietrich, S., Mugnai, A., Panegrossi, G., Pinori, S., and E. A. Smith, E. A., 2005: *The 9-10 November 2001 Algerian Flood: A Numerical Study.*, B. Am. Meteorol. Soc., **86**, 1229–1235.

Troen, I. and Mahrt, L., 1986: *A Simple Model of the Atmospheric Boundary Layer: Sensitivity to Surface Evaporation*, Bound-Lay Meteorol., **37**, 129–148.

Tsidulko, M. and Alpert, P., 2001: *Synergism of upper-level potential vorticity and mountains in Genoa lee cyclogenesisA numerical study*, Meteorol. Atmos. Phys., **78**, 261285.

Tudurí E. and Ramis, C., 1997: *The Enviromments of Significant Convective Events in the Western Mediterranean*, Weather Forecast., **12**, 294–306.

Tudurí E., Romero, R., López, L., Garcia, E., Sánchez, J., and Ramis, C., 2003: *The 14 July 2001 hailstorm in northeastern Spain: diagnosis of the meteorological situation*, Atmos. Res., **67-68**, 541–558.

Turk, F. J., Rohaly, G., Hawkins, J. D., Smith, E. A., Grose, A., Marzano, F. S., Mugnai, A., and Levizzani, V., 2000: *Analysis and assimilation of rainfall from blended SSMI, TRMM and geostationary satellite data*, 10th AMS Conference on Satellite Meteorology and Oceanography, Long Beach CA, 15 Jan 2000, pp. 66–69.

Uccelini, L. W., Keyser, D., Brill, K. F., and Wash, C. H., 1985: *The Presidents' Day Cyclone of 18-19 February 1979: Influence of upstream trough amplification and associated Tropopause folding on rapid cyclogenesis*, Mon. Weather Rev., **113**, 962–987.

Uppala, S., Kallberg, P., Simmons, A., Andrae, U., da Costa Bechtold, V., Fiorino, M., Gibson, J., Haseler, J., Hernandez, A., Kelly, G., Li, X., Onogi, K., Saarinen, S., and (...), 2005: *The ERA-40 re-analysis*, Q. J. Roy. Meteor. Soc., **131**, 2961–3012.

Whitaker, J. S., Uccellini, L. W., and Brill, K. F., 1988: *A Model-Based diagnostic study of the rapid development phase of the Presidents' Day cyclone*, Mon. Weather Rev., **116**, 2337–2365.

Wisse, J. S. P. and de Arellano, J. V.-G., 2004: *Analysis of the role of the planetary boundary layer schemes during a severe convective storm*, Ann. Geophys., **22**, 1861–1874.

WMO, 2002: *54 Edition of the Executive Council*, WMO – Annex V, `http://www.wmo.int/pages/prog/arep/wwrp/documents/WWRPe.pdf`, **945**, 137pp (95–99).

WMO, 2006: *Guidelines on Using Information from EPS in Combination with Single Higher Resolution NWP Forecasts*, WMO - CBS Expert Team on EPS, `http://www.wmo.int/pages/prog/www/DPFS/Documentation/Guidelines_ET-EPS2%006.pdf`, p. 2.

WMO, 2007: *FM 94XIII Ext. BUFR Binary universal form for the representation of meteorological data*, `http://www.wmo.int/pages/prog/www/WMOCodes/Operational/BUFR/FM94REG-11-%2007.pdf`, pp. 1–12.

Xu, M., Bao, J.-W., Warner, T. T., and Stensrud, D. J., 2001: *Effect of Time Step Size in MM5 Simulations of a Mesoscale Convective System*, Mon. Weather Rev., **129**, 502–516, doi:10.1175/1520-0493(2001)129⟨0502:EOTSSI⟩2.0.CO;2.

Zängl, G., 2002: *An Improved Method for Computing Horizontal Diffusion in a Sigma-Coordinate Model and Its Application to Simulations over Mountainous Topography*, Mon. Weather Rev.–notes and correspondence, **130**, 1423–1432, doi:10.1175/1520-0493(2002)130⟨1423:AIMFCH⟩2.0.CO;2.

Zeng, X., Pielke, R. A., and Eykholt, R., 1992: *Estimating the Fractal Dimension and the Predictability of the Atmosphere*, J. Atmos. Sci., **49**, 649–659.

Zhang, D. and Anthes, R. A., 1982: *A High-Resolution Model of the Planetary Boundary Layer–Sensitivity Tests and Comparisons with SESAME-79 Data*, J. Appl. Meteorol., **21**, 1594–1609.

Zhang, D. and Fritsch, J. M., 1986: *Numerical simulation of the meso-β scale structure and evolution of the 1977 Johnstown flood. Part I: Model description and verification*, J. Atmos. Sci., **43**, 1913–1943.

Zou, X. and Xiao, Q., 1999: *Studies on the Initialization and Simulation of a Mature Hurricane Using a Variational Bogus Data Assimilation Scheme*, J. Atmos. Sci., **57**, 836–860.